Controlling Charge and Spin Delocalization in Porphyrin Nanomaterials
–
Synthesis and Magnetic Resonance Studies



Sebastian M. Kopp

St John's College

University of Oxford

A thesis submitted for the degree of

Doctor of Philosophy

Hilary 2024

ABSTRACT

Controlling Charge and Spin Delocalization in Porphyrin Nanomaterials – Synthesis and Magnetic Resonance Studies

A thesis submitted for the degree of Doctor of Philosophy at the University of Oxford by Sebastian M. Kopp

The research presented in this thesis describes the synthesis and spectroscopic investigation of porphyrin nanomaterials with tailored electronic and magnetic properties. A detailed understanding of the factors that govern the distribution of charge and spin carriers in π-conjugated molecules is important for the rational design of new materials with potential applications in molecular electronic, spintronic, and photonic devices. Electron paramagnetic resonance (EPR) spectroscopy, steady-state and transient optical absorption spectroscopy, nuclear magnetic resonance (NMR) spectroscopy, and quantum chemical calculations were employed throughout this thesis to study charge and spin delocalization.

The delocalization of radical cations in edge-fused porphyrin nanoribbons was investigated. Information about the extent of radical delocalization was obtained from the hyperfine couplings probed by continuous-wave (cw) and pulse EPR techniques. The trend in the wavelength of the lowest energy optical transitions provided additional information about the polaron delocalization. The results confirm coherent radical delocalization over more than ten porphyrin units, and a remarkably non-uniform distribution of the electron spin density. This is the most delocalized polaron, yet reported, in π-conjugated molecular materials.

The electron and spin transfer dynamics of the radical cation and photogenerated triplet states in a weakly coupled porphyrin dimer were studied. Variable-temperature cw-EPR spectroscopy demonstrated the presence of reversible, intramolecular electron transfers in the radical cations in fluid solution, and the localization of charge carriers in frozen solution. The hyperfine and zero–field splitting interactions of the photogenerated triplet state confirm the localization of the exciton on one porphyrin unit on the timescale of the EPR experiments. These findings are important for the design of new molecular spintronic materials.

The delocalization of photogenerated triplet excitons of anionic porphyrin wires was investigated. The triplet excited states exhibit substantially smaller zero–field splitting interactions and shorter lifetimes compared to the triplet states in the neutral porphyrin oligomers. These results demonstrate that photoexcitation of reduced porphyrin oligomers increases the spatial delocalization of triplet excitons, which leads to the formation of the most delocalized triplet excited states reported so far in one-dimensional π-conjugated molecular materials.

A new class of porphyrin nanoring complexes consisting of edge-fused and butadiyne-linked porphyrin units was prepared by template-directed synthesis. The partially fused nanoring complexes exhibit a significantly stronger effective π-conjugation in comparison to previously investigated nanorings. The global charge delocalization and aromaticity of partially fused 8- and 12-porphyrin nanoring complexes were analyzed by NMR spectroscopy. Amplified global ring currents in agreement with Hückel's rule were observed in the oxidized and reduced nanorings, which opens new avenues for the engineering of cyclic molecular wires.

Acknowledgements

First and foremost, I would like to thank my supervisors, Prof. Harry Anderson and Prof. Christiane Timmel, for giving me the great opportunity to work jointly between their research groups, and to combine the worlds of supramolecular synthesis and EPR spectroscopy in many exciting and interesting projects. I am very thankful for all their support and mentorship, and their constant encouragement throughout my DPhil.

I am especially thankful to Dr. Henrik Gotfredsen for being a great mentor, introducing me to porphyrin and supramolecular chemistry, and the collaborative work on porphyrin nanoring complexes. I would also like to thank Janko Hergehahn for working closely with me in the field of porphyrin EPR and for always being there to discuss ideas. I am also thankful to Dr. Jie-Ren Deng for preparing the porphyrin nanoribbons investigated in this thesis and many helpful discussions. Many thanks also to Ashley Redman and Dr. William Myers for introducing me to EPR spectroscopy.

I would like to thank all past and current members of the Anderson and Timmel groups for the enjoyable time in Oxford. In particular, I am thankful to (in no particular order) Dr. Jeff Van Raden, Joshua Field, Dr. Lewis Antill, Jake Holmes, Dr. Arnau Rubio, Dr. Igor Rončević, Prakhar Gupta, Dr. Yueze Gao, Dr. Keith Andrews, Dr. Gabriel Moise, Jamie Gravell, Jonathon Clark, Ana Štuhec, Edward Champness, Tommy Pitcher, Patrick Murton, Carl Olavesen, and Daniel Cubbin, variously for working closely with me on different projects, helpful discussions, and for creating a supportive and fun environment in and outside the lab. I would also like to express my gratitude to Janko Hergenhahn, Dr. Henrik Gotfredsen, Dr. Lewis Antill, Edward Champness, Tommy Pitcher, Patrick Murton, Joshua Field, and Dr. Arnau Rubio for proofreading parts of this thesis.

Thank you also to Prof. Michael Wasielewski and his group at Northwestern University for hosting me for three months during my DPhil, and for giving me the opportunity to work on the EPR implementation of quantum logic gates in photogenerated spin-correlated radical pairs.

Finally, I would like to thank my parents, Andreas and Romy, and brother, Michael, for their constant support and encouragement, and for always being there for me!

List of Publications

1. **Global Aromaticity in a Partially Fused 8-Porphyrin Nanoring**. **S. M. Kopp**, H. Gotfredsen, J.-R. Deng, T. D. W. Claridge, H. L. Anderson, *J. Am. Chem. Soc.*, **2020**, *142*, 19393–19401.

2. **Cationic Polaron Delocalization in Porphyrin Nanoribbons**. **S. M. Kopp**, J.-R. Deng, A. J. Redman, H. Gotfredsen, R. M. J. Jacobs, H. L. Anderson, C. R. Timmel, *Chem*, **2024**, DOI: 10.1016/j.chempr.2024.07.011.

3. **Charge Delocalization and Global Aromaticity in a Partially Fused 12-Porphyrin Nanoring**. **S. M. Kopp**, H. Gotfredsen, J. Hergenhahn, A. R. Rubio, J.-R. Deng, H. Zhu, W. Stawski, and H. L. Anderson, *Chem*, **2024**, DOI: 10.1016/j.chempr.2024.06.034.

4. **Charge and spin transfer dynamics in a weakly coupled porphyrin dimer**. **S. M. Kopp**, A. J. Redman, I. Rončević, L. Schröder, L. Bogani, H. L. Anderson, C. R. Timmel, *J. Am. Chem. Soc.*, **2024**, *146*, 21476–21489.

5. **Increased Triplet State Delocalization in Charged Molecular Wires**. **S. M. Kopp**, J. Hergenhahn, K. B. Henbest, H. Gotfredsen, H. L. Anderson, C. R. Timmel, *in preparation*.

Supplement to Statement of Authorship

In Chapter 2, all porphyrin oligomers were synthesized and characterized by Dr. Jie-Ren Deng in the research group of Prof. Harry L. Anderson. Optical spectroelectrochemistry measurements were performed by the author in collaboration with Dr. Jie-Ren Deng with assistance from Dr. Robert M. J. Jacobs (Department of Chemistry). Processing and analysis of the spectroelectrochemistry results were performed by the author. ^{14}N HYSCORE measurements were performed by Ashley J. Redman in the research group of Prof. Christiane R. Timmel and simulated by the author under consultation of Ashley J. Redman. TD-DFT calculations of the neutral and oxidized porphyrin oligomers were performed by Dr. Jie-Ren Deng. All additional results were obtained and analyzed by the author.

In Chapter 3, all transient EPR measurements were performed by Ashley J. Redman in the research group of Prof. Christiane R. Timmel due to restricted access to the EPR spectrometers during the Covid-19 pandemic. The transient EPR results were analyzed and simulated by the author. The electron transmission coefficient of the porphyrin dimer radical cation was calculated by Lisa Schröder under the supervision of Dr. Igor Rončević in the research group of Prof. Harry L. Anderson. All additional results were obtained and analyzed by the author.

In Chapter 4, transient absorption spectroscopy was performed by the author in collaboration with Dr. Kevin B. Henbest in the research group of Prof. Christiane R. Timmel. The absorption spectra of the reduced porphyrin oligomers were obtained by Janko Hergenhahn in the research groups of Prof. Christiane R. Timmel and Prof. Harry L. Anderson with assistance from Dr. Robert M. J. Jacobs (Department of Chemistry). All additional results were obtained and analyzed by the author.

In Chapter 5, the regioselectively fluorinated tetrapyrdiyl templates $\mathbf{T4}_{\mathbf{1,4F}}$ and $\mathbf{T4}_{\mathbf{2,3F}}$ were synthesized by Dr. Henrik Gotfredsen in the research group of Prof. Harry L. Anderson. DFT calculations (geometry optimization, NICS, ACID, and TD-DFT) of the porphyrin nanoring complexes were performed by Dr. Jie-Ren Deng in the research group of Prof. Harry L. Anderson. NMR oxidation titrations were performed by the author in collaboration with Dr. Henrik Gotfredsen and analyzed by the author. All additional results were obtained and analyzed by the author.

In Chapter 6, the synthesis of the two hexapyridyl templates **T6$_A$** and **T6$_B$** and nanoring ***c*-P12[b$_6$f$_6$]** was initially performed by the author and scaled-up in collaboration with Dr. Henrik Gotfredsen in the research group of Prof. Harry L. Anderson. NMR binding studies of the nanoring complexes were performed by Dr. Henrik Gotfredsen. Oxidant **ThnBArF$_{20}$** was synthesized by Dr. Arnau Rodríguez-Rubio in the research group of Prof. Harry L. Anderson. DFT strain calculations and molecular dynamics simulations were performed by Janko Hergenhahn in the research groups of Prof. Harry L. Anderson and Prof. Christiane R. Timmel. NMR oxidation and reduction titrations were performed by the author with assistance from Dr. Henrik Gotfredsen. All additional results were obtained and analyzed by the author.

Contents

1 Introduction **1**

1.1 Porphyrins 2

1.2 Electron Paramagnetic Resonance Spectroscopy 7

1.2.1 Electron Spin 7

1.2.2 Spin Hamiltonian 9

1.2.2.1 Electron Zeeman Interaction 10

1.2.2.2 Nuclear Zeeman Interaction 12

1.2.2.3 Nuclear Quadrupole Interaction 12

1.2.2.4 Hyperfine Interactions 13

1.2.2.5 Zero–Field Splitting Interactions 18

1.2.3 Continuous-Wave and Pulse EPR Spectroscopy 23

1.2.3.1 Continuous-Wave EPR Spectroscopy 24

1.2.3.2 Broadening of EPR Transitions 26

1.2.3.3 Transient EPR Spectroscopy 27

1.2.3.4 Pulse EPR Spectroscopy 29

1.2.3.5 Semiclassical Description of Pulse EPR Experiments . 30

1.2.3.6 Orientation Selection 33

1.2.3.7 Relaxation 34

1.2.3.8 Mims ENDOR Spectroscopy 36

1.3 Charge and Spin Delocalization 41

1.3.1 Organic Mixed Valence Systems 43

1.3.2 Aromaticity on the Nanoscale 46

1.4 Prospective 51

2 Cationic Polaron Delocalization in Porphyrin Nanoribbons **53**

2.1 Abstract 54

2.2 Introduction 55

2.3 Results and Discussion 56

2.3.1 Synthesis of Porphyrin Oligomers 56

2.3.2 Continuous-Wave EPR Spectroscopy 57

2.3.3 Investigation of the Spin-Density Non-Uniformity 64

2.3.4 W-band Pulse EPR Spectroscopy 67

2.3.5 Mims ENDOR Spectroscopy 70
2.3.6 ^{14}N HYSCORE Spectroscopy 77
2.3.7 Accidental Oxidation of Extended Nanoribbons 79
2.3.8 Optical vis-NIR-MIR Spectroelectrochemistry 81
2.4 Summary and Conclusion 87
2.5 Methods 89
2.5.1 General Methods 89
2.5.2 Distributed Point-Dipole Simulations 94
2.6 Supplemental Results and Analysis 102

3 Charge and Spin Transfer Dynamics in a Weakly Coupled Porphyrin Dimer 108
3.1 Abstract 109
3.2 Introduction 110
3.3 Results and Discussion 113
3.3.1 Synthesis and Molecular Design 113
3.3.2 Absorption Spectroscopy 114
3.3.3 Continuous-Wave EPR Spectroscopy 116
3.3.4 Investigation of the Monomer Dihedral Angle Distribution . . . 124
3.3.5 Mims ENDOR Spectroscopy 126
3.3.6 Introduction to Exchange Broadening 129
3.3.7 Simulation of the Electron Transfer Dynamics 132
3.3.8 Investigation of the Triplet State Delocalization 139
3.4 Summary and Conclusion 145
3.5 Methods 147
3.5.1 General Methods 147
3.5.2 Synthetic Procedures 152
3.5.3 Distributed Point-Dipole Simulations 155
3.6 Supplemental Results and Analysis 160

4 Triplet State Delocalization in Charged Molecular Wires 167
4.1 Abstract 168
4.2 Introduction 168
4.3 Results and Discussion 170
4.3.1 Steady State Absorption Spectroscopy 170
4.3.2 Photogenerated Triplet States of ***b*-P2** and ***b*-P2**$^{2-}$ 174
4.3.2.1 Optical Transient Absorption Spectroscopy 174
4.3.2.2 Transient EPR Spectroscopy 178
4.3.3 Photogenerated Triplet States of ***b*-P4**$^{4-}$ and ***b*-P6**$^{6-}$ 186
4.3.3.1 Optical Transient Absorption Spectroscopy 186
4.3.3.2 Transient EPR Spectroscopy 189

4.4 Summary and Conclusions . . . 195
4.5 Methods . . . 197
4.6 Supplemental Results and Analysis . . . 200

5 Global Aromaticity in a Partially Fused 8-Porphyrin Nanoring 207
5.1 Abstract . . . 208
5.2 Introduction . . . 208
5.3 Results and Discussion . . . 210
5.3.1 Molecular Design and Synthesis . . . 210
5.3.2 UV-vis-NIR Absorption Spectroscopy . . . 215
5.3.3 NMR Spectroscopy . . . 217
5.3.4 Theoretical Analysis of Ring Currents . . . 222
5.3.5 Experimental Relative Ring Current Strengths . . . 225
5.4 Summary and Conclusions . . . 227
5.5 Methods . . . 228
5.5.1 General Methods . . . 228
5.5.2 Synthetic Procedures . . . 231
5.6 Supplemental Results and Analysis . . . 249

6 Charge Delocalization and Global Aromaticity in a Partially Fused 12-Porphyrin Nanoring 259
6.1 Abstract . . . 260
6.2 Introduction . . . 261
6.3 Results and Discussion . . . 262
6.3.1 Molecular Modelling and Template Design . . . 262
6.3.2 Template-Directed Synthesis . . . 266
6.3.3 Stability of the Ternary Template Complexes . . . 269
6.3.4 UV-vis-NIR Absorption Spectra . . . 271
6.3.5 Global Charge Delocalization in Oxidized Porphyrin Nanorings 273
6.3.6 Global Charge Delocalization in Reduced Porphyrin Nanorings 281
6.4 Summary and Conclusions . . . 283
6.5 Methods . . . 285
6.5.1 General Methods . . . 285
6.5.2 Synthetic Procedures . . . 287
6.6 Supplemental Results and Analysis . . . 302

References 321

1 Introduction

Contents

1.1 Porphyrins 2
1.2 Electron Paramagnetic Resonance Spectroscopy 7
1.2.1 Electron Spin 7
1.2.2 Spin Hamiltonian 9
1.2.2.1 Electron Zeeman Interaction 10
1.2.2.2 Nuclear Zeeman Interaction 12
1.2.2.3 Nuclear Quadrupole Interaction 12
1.2.2.4 Hyperfine Interactions 13
1.2.2.5 Zero–Field Splitting Interactions 18
1.2.3 Continuous-Wave and Pulse EPR Spectroscopy 23
1.2.3.1 Continuous-Wave EPR Spectroscopy 24
1.2.3.2 Broadening of EPR Transitions 26
1.2.3.3 Transient EPR Spectroscopy 27
1.2.3.4 Pulse EPR Spectroscopy 29
1.2.3.5 Semiclassical Description of Pulse EPR Experiments 30
1.2.3.6 Orientation Selection 33
1.2.3.7 Relaxation 34
1.2.3.8 Mims ENDOR Spectroscopy 36
1.3 Charge and Spin Delocalization 41
1.3.1 Organic Mixed Valence Systems 43
1.3.2 Aromaticity on the Nanoscale 46
1.4 Prospective 51

1.1 Porphyrins

Porphyrins are vital for many biological processes such as photosynthesis[1–3], oxygen transport[4, 5], and biocatalysis[4, 6, 7]. They are also intriguing building blocks for artificial molecular materials because of their electronic and optical properties. Porphyrins are derivatives of porphine **I-1**, which consists of four pyrrole units connected by four methine bridges in a planar conformation (Figure 1.1).[8] The atomic positions of porphyrins can be identified by their IUPAC systematic numbering or the common nomenclature employed in this thesis (Figure 1.1A,B). In the common nomenclature, the methine bridges are called *meso* positions, the pyrrole C-H positions are referred to as β, and the quarternary pyrrole carbons constitute the α positions.

Porphyrins exhibit a delocalized 18 π-electron conjugation pathway and are therefore Hückel aromatic ($4n$+2 π-e$^-$; $n = 4$) (Figure 1.1C). The aromatic ring current in a free-base porphyrin becomes evident from its ^{1}H NMR spectrum, which exhibits shielding of the N-H resonances inside the macrocycle ($\delta_H = -2$ to -4 ppm) and deshielding of the C-H resonances outside the macrocycle ($\delta_H = 11$ to 8 ppm).[9]

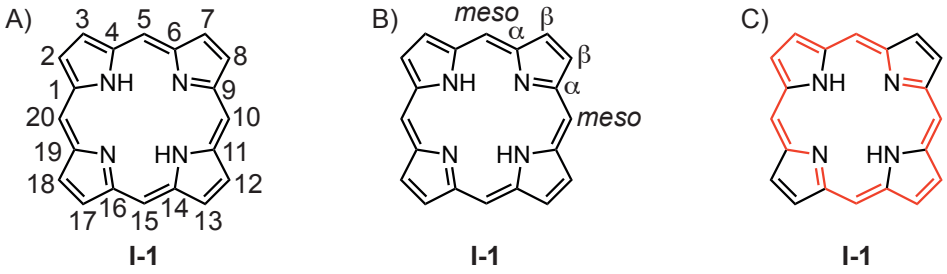


Figure 1.1: A) IUPAC and B) common nomenclature of porphine **I-1**. C) The 18 π-electron aromatic circuit of **I-1** is highlighted in red.

Porphyrins are typically synthesized by condensation of an aldehyde and pyrrole, or by condensation of the aldehyde with dipyrromethane to increase the efficiency of the porphyrin formation.[10, 11] Functionalization of the porphyrin core on its *meso* and β positions allows for the installation of a broad range of substituents to modify its electronic properties or to incorporate the porphyrin in complex molecular architectures.[12] Expansion or contraction of the porphyrin framework is another

active area of research that has allowed the synthesis of porphyrin-related compound families with unique properties.[13, 14]

Free-base porphyrins can act as square planar tetradentate ligands for various metal ions and form metalloporphyrin complexes with photophysical and electronic properties that are very different to the unbound free-base porphyrin.[15–17] Formation of the metalloporphyrin complexes is usually achieved by reacting the free-base porphyrin with an appropriate metal salt in a polar organic solvent. The following examples give an indication of the broad range of properties and applications of metalloporphyrins.

Terbium(III) and dysprosium(III) porphyrin complexes are single-molecule magnets at low temperatures and promising for high-density information storage.[18, 19] In addition, they can be used to generate spin polarized currents in single-molecule transistors.[20] Copper(II) porphyrins with d^9 electronic configuration are paramagnetic and are used as spin labels for EPR distance measurements in biological and supramolecular systems.[21–23] They have also been postulated as molecular qubits for quantum information processing.[24–26] Iron(II) and iron(III) porphyrins are essential for the function of heme proteins, which inspired their application as molecular catalysts for carbon dioxide and oxygen reductions.[27–29]

An important differentiation between metalloporphyrins is their ability to bind axial ligands such as pyridine to form square pyramidal or octahedral coordination complexes. Palladium(II) porphyrins with d^8 configuration do not bind additional ligands, whereas Mg(II) porphyrins can accommodate two axis ligands.[30, 31] Axial coordination of pyridine or imidazole to a nickel(II) porphyrin induces a spin crossover of the metal from a singlet state to a paramagnetic triplet state.[32] Zn(II) porphyrin complexes have a strong affinity towards one axial ligand. The strength of the ligand coordination can be quantified by the equilibrium binding constant K_F. In non-polar solvents, Zn-porphyrins have a high binding affinity towards an axial pyridine ligand ($K_\mathrm{F} \sim 10^4$ M^{-1}) to form a square pyramidal complex, whereas the affinity to a second pyridine ligand is negligible ($K_\mathrm{F} = 0.1$–1 M^{-1}) (Figure 1.2).[33–35]

This behaviour is very useful for the template-directed synthesis of supramolecular porphyrin assemblies.[36, 37]

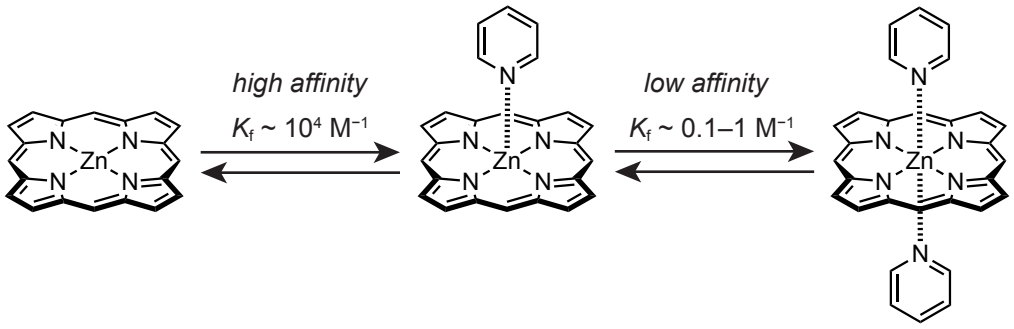
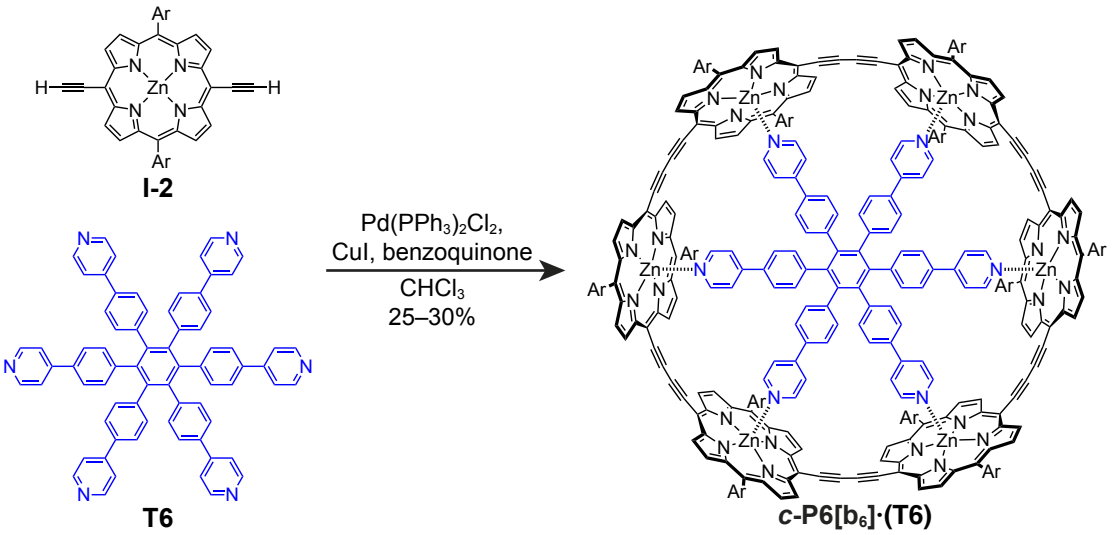


Figure 1.2: Schematic depiction of the axial coordination of pyridine to a Zn-porphyrin monomer in non-polar solvents. The porphyrin has a high affinity towards the first pyridine ligand and a negligible affinity towards the second pyridine.

Template-directed synthesis is a powerful tool for the synthesis of supramolecular structures such as catennanes, rotaxanes, knots, cages, capsules, macrocycles, and porphyrin nanomaterials.[36, 38–41] A formal definition of templates was provided by Busch[42] and refined by Sanders[43]: "*The template provides instructions for the formation of a single product from a substrate or substrates which otherwise have the potential to assemble and react in a variety of ways.*". In other words, the template directs the formation of the desired structure but is not part of the final molecule.

Zn-porphyrin nanorings such as ***c*-P6[$\mathbf{b_6}$]** are typically synthesized with oligopyridine templates. The pyridyl legs of the template coordinate to the central Zn(II) ions and arrange the porphyrin building blocks into a ring-shaped complex. The binding between the template and porphyrins is amplified by chelate cooperativity when several template legs coordinate to the same porphyrin structure.[44] The nanoring-template complex ***c*-P6[$\mathbf{b_6}$]·(T6)** is formed in a macrocyclization reaction (Scheme 1.1), after which the template can be removed by adding a large excess of a competing ligand such as 1,4-diazabicyclo[2.2.2]octane (DABCO). The first porphyrin nanoring was reported in 2008 by Anderson and co-workers with the synthesis of a butadiyne-linked cyclic porphyrin octamer ***c*-P8[$\mathbf{b_8}$]**.[45] Since then, the Anderson group has explored the template-directed synthesis of a range of

porphyrin nanomaterials including macrocycles, balls, and tubes.[36, 46–48] The study of these materials by optical, NMR, and EPR spectroscopy gives insight into fundamental processes such as photosynthetic light harvesting[49, 50], charge and spin delocalization[51, 52], aromaticity[53–56], and quantum interference[57].



Scheme 1.1: Template-directed synthesis of the butadiyne-linked porphyrin nanoring complex ***c*-P6[b$_6$]·(T6)**; Ar = solubilizing groups.

The UV-vis spectra of porphyrins exhibit two groups of absorption bands, the B or Soret band around 400 nm and the Q band at higher wavelengths (Figure 1.3C,F).[58] The origin of these electronic transitions can be rationalized using the Gouterman four orbital model (Figure 1.3).[59, 60] For a D_{4h} symmetric porphyrin such as zinc-tetraphenylporphyrin **I-3**, the Q and Soret absorption bands arise from transitions between the near-degenerate HOMO and HOMO−1 π orbitals a_{1u} and a_{2u} and the degenerate LUMO π^* orbitals e_{gx} and e_{gy} (Figure 1.3A,B). [58, 61–63] Due to the near-degeneracy of the π-π^* transitions $a_{1u} \rightarrow e_g$ and $a_{2u} \rightarrow e_g$, configuration interaction mixes the transitions. Constructive interactions give rise to the intense, high-energy Soret band ($S_0 \rightarrow S_2$) while destructive interactions result in the weak, quasi-forbidden Q band ($S_0 \rightarrow S_1$). In the D_{2h} symmetric monomer **I-4**, the degeneracy of the LUMOs is lifted, which results in splitting of the absorption bands for the x and y polarized states Q_x and Q_y (Q band), and B_x and B_y (Soret band) (Figure 1.3D,E). [61, 62]

Butadiyne-linked porphyrin oligomers show a progressive red-shift, broadening, and intensification of the Q band, and a broadening of the Soret band with increasing oligomer length.[64] The higher relative intensity of the Q band in porphyrin oligomers results from changes in the symmetry and energy of their frontier orbitals, which make the transition no longer quasi-forbidden.[65] The bathochromic shift of the Q band results from the increasing conjugation length, while the broadening of the transitions has been attributed to exciton coupling in different conformations following Kasha's model.[64, 66] In cyclic porphyrin oligomers such as nanoring ***c*-P6[$\mathbf{b_6}$]**, the lowest energy $S_0 \rightarrow S_1$ transition is dipole forbidden.[67–69] This can be qualitatively rationalized by a net cancellation of the head-to-tail aligned transition dipole moments of the individual porphyrin units and is corroborated by TD-DFT calculations.[67]

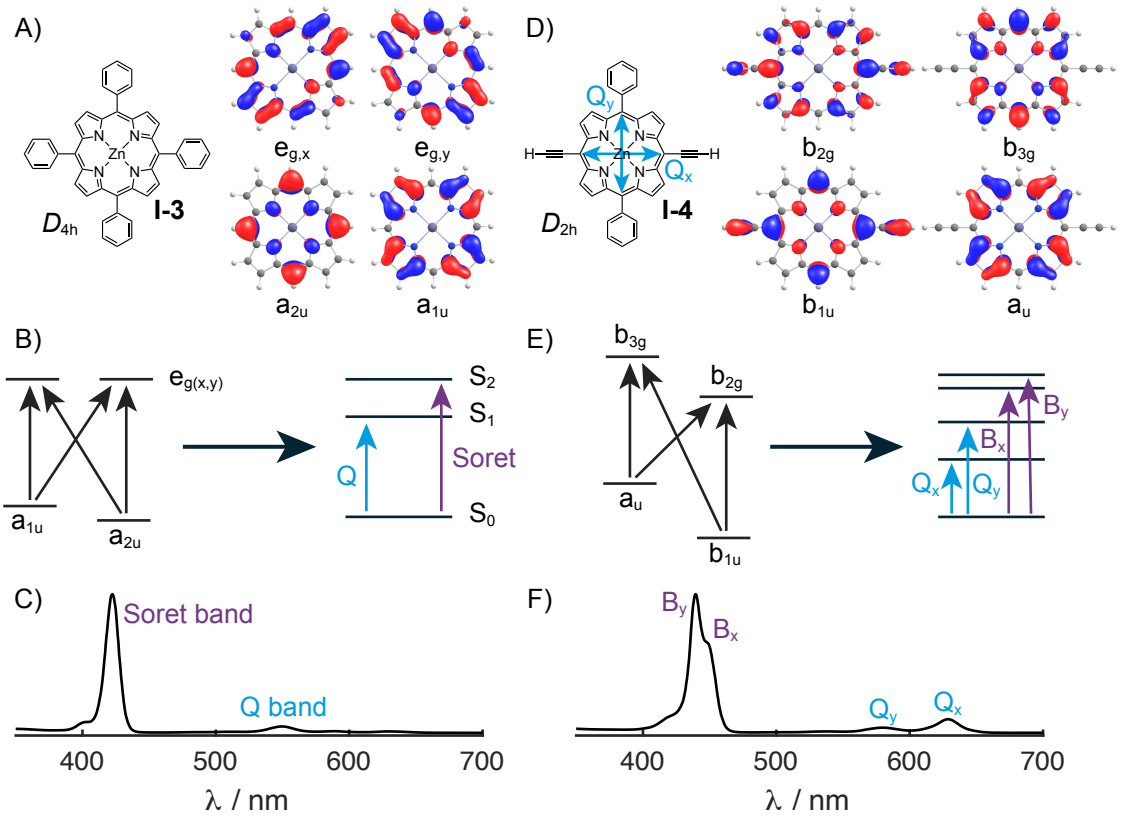


Figure 1.3: Chemical structure and DFT (B3LYP/def2-SVP; def2-TZVP(Zn)) calculated frontier orbitals of A) tetraphenylporphyrin **I-3** and D) monomer **I-4**. The phenyl substituents of the porphyrins were omitted in the DFT calculations to prevent deviations from an ideal D_{4h} or D_{2h} symmetry in the geometry optimizations. Gouterman four orbital transitions in B) **I-3** and E) **I-4**. UV-vis absorption spectra of C) **I-3** and F) **I-4** in toluene at 298 K.

1.2 Electron Paramagnetic Resonance Spectroscopy

Electron paramagnetic resonance (EPR) spectroscopy studies interactions of electron spins with an applied magnetic field, interactions of electron and nuclear spins, and interactions between different electron spins. This makes EPR spectroscopy a powerful tool for the investigation of paramagnetic species such as organic radicals, transition metals, photogenerated open-shell compounds, or defects in solids. Consequently, EPR techniques have found widespread application in chemistry, biology, materials science, and physics. For instance, EPR spectroscopy is used to obtain structural information about proteins or synthetic materials, to understand catalytic processes, to determine the spatial distribution of unpaired electrons, and to manipulate spins for quantum information processing. These applications are enabled by a wide range of continuous-wave and pulsed EPR techniques. In this section, the fundamental aspects of EPR relevant to the work in this thesis are discussed. The discussion is based on published introductions to EPR theory and techniques such as references [70–74].

1.2.1 Electron Spin

Spin is an intrinsic angular momentum of fundamental particles such as electrons.[75] The spin of an electron can be mathematically described as a vector $\boldsymbol{S}$ with associated eigenstates $|\, S, m_s\rangle$ and a magnitude of $\sqrt{S(S+1)}$. The spin quantum number S is equal to $\frac{1}{2}$ for all electrons, and the spin magnetic quantum number m_s describes the spin component along a defined axis. The spin angular momentum is quantized, and projection of $\boldsymbol{S}$ using the spin operators $\hat{\boldsymbol{S}}^2$ and $\hat{\boldsymbol{S}}_z$ gives the eigenvalues in equation 1.1.[1]

$$\begin{aligned} \hat{\boldsymbol{S}}^2 \,|\, S, m_s\rangle = \left(\hat{\boldsymbol{S}}_x^2 + \hat{\boldsymbol{S}}_y^2 + \hat{\boldsymbol{S}}_z^2\right) |\, S, m_s\rangle = \hbar^2 S(S+1) \,|\, S, m_s\rangle \\ \hat{\boldsymbol{S}}_z \,|\, S, m_s\rangle = \hbar m_s \,|\, S, m_s\rangle \end{aligned} \tag{1.1}$$

[1] The spin angular momentum operator $\hat{\boldsymbol{S}}$ is a vector with the general form $\left(\hat{S}_x\ \hat{S}_y\ \hat{S}_z\right)$. In this thesis, $\hat{\boldsymbol{S}}_x$, $\hat{\boldsymbol{S}}_y$, and $\hat{\boldsymbol{S}}_z$ are used in their matrix representation and written in bold font.

The spin operators $\hat{\boldsymbol{S}}_i$ $(i = x, y, z)$ correspond to the observable of the spin angular momentum projected onto the principal axis i and are given in equation 1.2 in units of $\hbar$ for an $S = \frac{1}{2}$ system.

$$\hat{\boldsymbol{S}}_x = \frac{1}{2}\begin{pmatrix} 0 & 1 \\ 1 & 0 \end{pmatrix} \quad \hat{\boldsymbol{S}}_y = \frac{1}{2i}\begin{pmatrix} 0 & 1 \\ -1 & 0 \end{pmatrix} \quad \hat{\boldsymbol{S}}_z = \frac{1}{2}\begin{pmatrix} 1 & 0 \\ 0 & -1 \end{pmatrix} \tag{1.2}$$

As seen in equation 1.1, projection of the spin angular momentum in the absence of a magnetic field along an arbitrarily defined axis (also referred to as space quantization axis) gives two discrete spin states: an $|\alpha\rangle$ or spin-up state with $m_s = +\frac{1}{2}$ and a $|\beta\rangle$ or spin-down state with $m_s = -\frac{1}{2}$. The spin state of an electron in the absence of external measurements exists as a superposition of $|\alpha\rangle$ and $|\beta\rangle$, and can be written as a linear combination of the two eigenstates following equation 1.3

$$\psi = c_1|\alpha\rangle + c_2|\beta\rangle \tag{1.3}$$

where normalization demands that $|c_1|^2 + |c_2|^2 = 1$. The wavefunction of the electron collapses when a measurement is carried out, and the probability P of observing the eigenstate $|\alpha\rangle$ in the measurement is given by equation 1.4.

$$P(|\alpha\rangle) = |\langle\alpha|\psi\rangle|^2 = |c_1|^2 \tag{1.4}$$

Experimental evidence of the quantized spin angular momentum was first provided by Stern and Gerlach in 1922.[76] A beam of silver atoms, which exhibit unquenched spin angular momentum and no orbital angular momentum, is deflected when passed through an inhomogeneous magnetic field, and two discrete spots are observed on a detection screen.

The spin angular momentum $\boldsymbol{S}$ of an electron gives rise to a magnetic moment $\boldsymbol{\mu}$, which is proportional to the electron's spin angular momentum following equation 1.5

$$\hat{\boldsymbol{\mu}} = -g\frac{e\hbar}{2m_e}\hat{\boldsymbol{S}} = -g\mu_B\hat{\boldsymbol{S}} \tag{1.5}$$

where μ_B is the Bohr magneton, $\hat{\boldsymbol{S}}$ is the spin angular momentum operator, m_e is the mass of the electron, and g accounts for the deviation of a quantum object from classical behaviour and can provide valuable information about the environment of the electron as discussed in Section 1.2.2.1. The g-value of a free electron is $g_e = 2.0023193043737$.[70] Nuclear spins also exhibit a magnetic moment that can be expressed analogous to equation 1.5. However, nuclear magnetic moments are considerably smaller than electron magnetic moments due to the larger mass of the nuclei.

1.2.2 Spin Hamiltonian

A systems with unpaired electrons and magnetic nuclei in an external magnetic field is characterized by the interactions of the electron and nuclear magnetic moments with the magnetic field, the interactions between electrons and nuclei, and electron-electron as well as nuclear-nuclear interactions. These interactions can be described using the electron and nuclear spin operators $\hat{\boldsymbol{S}}$ and $\hat{\boldsymbol{I}}$ and phenomenological constants, which form the spin Hamiltonian $\hat{\mathscr{H}}_{\mathbf{0}}$ in equation 1.6.

$$\begin{aligned}\hat{\mathscr{H}}_{\mathbf{0}} &= \hat{\mathscr{H}}_{\mathrm{EZ}} + \hat{\mathscr{H}}_{\mathrm{ZFS}} + \hat{\mathscr{H}}_{\mathrm{EE}} + \hat{\mathscr{H}}_{\mathrm{HF}} + \hat{\mathscr{H}}_{\mathrm{NZ}} + \hat{\mathscr{H}}_{\mathrm{NQ}} + \hat{\mathscr{H}}_{\mathrm{NN}} \\ &= \frac{\mu_B}{\hbar}\boldsymbol{B}_0\boldsymbol{g}\hat{\boldsymbol{S}} + \hat{\boldsymbol{S}}^T\boldsymbol{D}\hat{\boldsymbol{S}} + \sum_{i=1}^{n}\sum_{j\neq i}\hat{\boldsymbol{S}}_i^T\boldsymbol{J}\hat{\boldsymbol{S}}_j + \sum_{k=1}^{N}\hat{\boldsymbol{S}}^T\boldsymbol{A}_k\hat{\boldsymbol{I}}_k \\ &\quad -\mu_n\sum_{k=1}^{N}\frac{g_{n,k}}{\hbar}\boldsymbol{B}_0\hat{\boldsymbol{I}}_k + \sum_{I_k>\frac{1}{2}}\hat{\boldsymbol{I}}_k^T\boldsymbol{P}_k\hat{\boldsymbol{I}}_k + \sum_{i\neq k}\hat{\boldsymbol{I}}_i^T\boldsymbol{d}^{(i,k)}\hat{\boldsymbol{I}}_k\end{aligned} \tag{1.6}$$

The terms in equation 1.6 describe the following interactions: $\hat{\mathscr{H}}_{\mathrm{EZ}}$ is the electron Zeeman interaction, $\hat{\mathscr{H}}_{\mathrm{ZFS}}$ is the zero-field splitting, $\hat{\mathscr{H}}_{\mathrm{EE}}$ are the spin-spin interactions between electron pairs, $\hat{\mathscr{H}}_{\mathrm{HF}}$ are the hyperfine coupling interactions between the electron spins and the N nuclear spins, $\hat{\mathscr{H}}_{\mathrm{NZ}}$ are the nuclear Zeeman interactions, $\hat{\mathscr{H}}_{\mathrm{NQ}}$ are the nuclear quadrupole interactions for nuclei with spin quantum numbers $I > \frac{1}{2}$, and $\hat{\mathscr{H}}_{\mathrm{NN}}$ are the spin-spin interactions between pairs of nuclei. All of these interactions can influence the appearance of the EPR spectrum of a system. However, depending on the paramagnetic sample under investigation, some interactions are absent or too small to significantly influence the experimental results. Therefore, often only specific interactions need to be considered to describe the spin system.

The relevant interactions for the work in this thesis are electron Zeeman, nuclear Zeeman, nuclear quadrupole, hyperfine, and zero–field splitting interactions, which are discussed in turn in the following sections.

1.2.2.1 Electron Zeeman Interaction

The electron Zeeman term of the spin Hamiltonian (equation 1.7) describes the interaction between the magnetic moment arising from the electron spin angular momentum $\boldsymbol{S}$ and an applied magnetic field $\boldsymbol{B}_0$.

$$\hat{\mathscr{H}}_{\mathrm{EZ}} = \frac{\mu_B}{\hbar}\boldsymbol{B}_0\boldsymbol{g}\hat{\boldsymbol{S}} \tag{1.7}$$

All spatial information about an electron in its molecular environment is contained in the $\boldsymbol{g}$-tensor. The $\boldsymbol{g}$-tensor is a 3x3 matrix that is defined by three principal values g_x, g_y, and g_z and three Euler angles that determine the orientation of the principal tensor axes in the molecular frame. In an appropriate principal axis system, the electron Zeeman Hamiltonian $\hat{\mathscr{H}}_{\mathrm{EZ}}$ is described by equation 1.8

$$\begin{aligned}\hat{\mathscr{H}}_{\mathrm{EZ}} &= \frac{\mu_B}{\hbar}B_0\left(n_x, n_y, n_z\right)\begin{pmatrix} g_x & 0 & 0 \\ 0 & g_y & o \\ 0 & 0 & g_z \end{pmatrix}\begin{pmatrix} \hat{\boldsymbol{S}}_x \\ \hat{\boldsymbol{S}}_y \\ \hat{\boldsymbol{S}}_z \end{pmatrix} \\ &= \frac{\mu_B B_0}{\hbar}\sum_{i=x,y,z} n_i g_i \hat{\boldsymbol{S}}_i\end{aligned} \tag{1.8}$$

where n_x, n_y, and n_z are the components of the unit vector that defines the orientation of the magnetic field in the principal axis system of $\boldsymbol{g}$, and B_0 is the field strength.

The relationship between the principal values of $\boldsymbol{g}$ depends on the symmetry of the paramagnetic system. In the absence of symmetry, the $\boldsymbol{g}$-tensor is rhombic with $g_x \neq g_y \neq g_z$. Systems with axial symmetry display two equal principal g values $g_x = g_y = g_\perp$ while the third value is different $g_z = g_{||}$. The $\boldsymbol{g}$-tensor is only isotropic with $g_x = g_y = g_z$ for systems with cubic or higher symmetry. In fluid solutions with low viscosity and fast dynamic averaging of molecular orientations, the anisotropic $\boldsymbol{g}$-tensor is typically averaged to an isotropic scalar $g_{\mathrm{iso}} = \frac{1}{3}\left(g_x + g_y + g_z\right)$. Paramagnetic species in frozen solutions, powders, and single crystals have limited mobility, and

the anisotropy of the electron Zeeman interaction can be resolved at sufficiently high microwave frequencies (Figure 1.4).

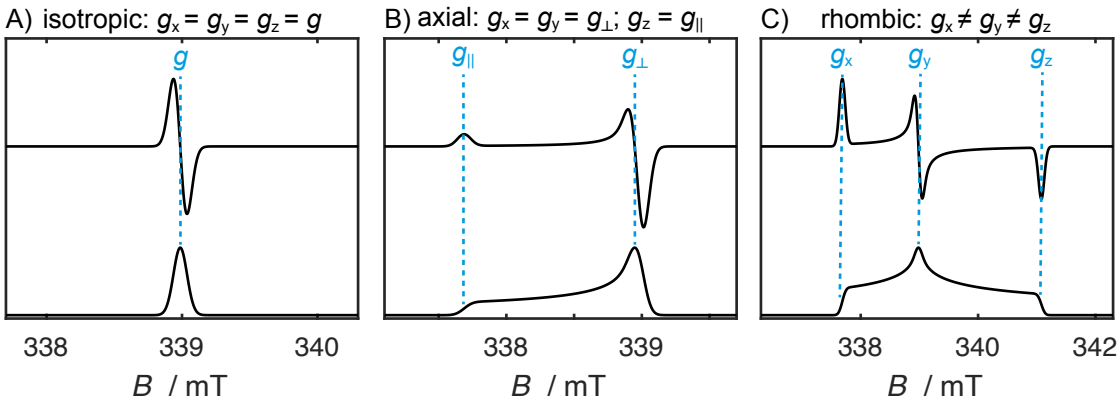


Figure 1.4: Simulated cw-EPR (top) and echo-detected field sweep (bottom) spectra of an $S = \frac{1}{2}$ species in a powder or frozen-solution with an isotropic, axial, and rhombic $\boldsymbol{g}$-tensor. Simulations were performed with a microwave frequency of 9.5 GHz and principal g-values A) $g_x = g_y = g_z = 2.0023$ (isotropic); B) $g_x = g_y = 2.0023$ and $g_z = 2.01$ (axial), C) and $g_x = 2.01$, $g_y = 2.0023$, and $g_z = 1.99$ (rhombic).

The deviation of the principal values of $\boldsymbol{g}$ from the free electron g_e value results from additional angular momentum contributions to the electron in a material. This is caused by the admixture of orbital angular momentum $\boldsymbol{L}$ from excited states into the ground state, which results in a second order pertubation of g_e expressed in equation 1.9

$$\boldsymbol{g} = g_e \mathbf{1} + 2\lambda\Lambda \tag{1.9}$$

where λ is the spin–orbit coupling constant and Λ describes the mixing between the ground and excited state (equation 1.10).

$$\Lambda_{ij} = \sum_{n\neq 0} \frac{\langle\psi_0|\hat{L}_i|\psi_n\rangle\langle\psi_n|\hat{L}_j|\psi_0\rangle}{E_0 - E_n} \quad (i,j = x,y,z) \tag{1.10}$$

The wavefunctions ψ_0 and ψ_n describe the ground state and n^{th} excited state of the unpaired electron, respectively, and $\hat{L}_x$, $\hat{L}_y$, and $\hat{L}_z$ are the components of the orbital angular momentum operator $\hat{\boldsymbol{L}}$. The energies of the ground and excited states are E_0 and E_n. Consequently, the $\boldsymbol{g}$-tensor deviates strongly from g_e in systems with

low-lying excited states and significant spin-orbit coupling. The principal g-values of organic radicals are typically close to g_e due to the high energy of their excited states. In contrast, metal ions exhibit strongly anisotropic $\boldsymbol{g}$-tensors that are often used to identify the paramagnetic metal and to obtain information about the symmetry of its coordination environment.

1.2.2.2 Nuclear Zeeman Interaction

The interaction of the magnetic moment arising from a nuclear spin angular momentum $\boldsymbol{I}$ with a magnetic field $\boldsymbol{B}_0$ is described by the nuclear Zeeman interaction in equation 1.11

$$\hat{\mathscr{H}}_{\mathrm{NZ}} = -\frac{g_n \mu_n}{\hbar} \boldsymbol{B}_0 \hat{\boldsymbol{I}} \tag{1.11}$$

where the spin quantum number I and g_n depend on the nucleus, and μ_n is the nuclear magneton. The spin active nuclei relevant for the work in this thesis are ^{1}H and ^{14}N with spin quantum numbers $I = \frac{1}{2}$ and 1, respectively.

Due to the higher mass of nuclei compared to electrons, the nuclear magneton is smaller than the Bohr magneton. Consequently, the nuclear Zeeman interaction is substantially smaller than the electron Zeeman interaction at the same magnetic field strength and has typically little influence on the EPR spectrum. Nuclear frequency spectra such as electron nuclear double resonance (ENDOR) spectra are however affected by the nuclear Zeeman interaction.

1.2.2.3 Nuclear Quadrupole Interaction

The charge distribution in nuclei with $I > \frac{1}{2}$ is non-spherical, and the deviation from a spherical distribution is quantified by the nuclear quadrupole moment Q. The nuclear quadrupole Hamiltonian in equation 1.12 describes the interaction of this non-spherical nuclear charge distribution with the electric field gradient eq around the nuclei

$$\hat{\mathscr{H}}_{\mathrm{NQ}} = \hat{\boldsymbol{I}}^T \boldsymbol{P} \hat{\boldsymbol{I}} \tag{1.12}$$

where $\boldsymbol{P}$ is the nuclear quadrupole tensor. In the appropriate coordinate system, $\boldsymbol{P}$ is diagonal and the Hamiltonian can be described following equation 1.13

$$\hat{\mathscr{H}}_{\mathrm{NQ}} = P_x \hat{I}_x^2 + P_y \hat{I}_y^2 + P_z \hat{I}_z^2 = \frac{e^2 qQ}{4I\hbar(2I-1)} \left[\left(3\hat{I}_z^2 - \hat{\boldsymbol{I}}^2 \right) + \eta \left(\hat{I}_x^2 - \hat{I}_y^2 \right) \right] \tag{1.13}$$

where $e^2 qQ\hbar$ is the nuclear quadrupole coupling constant and $\eta = \left(P_x - P_y \right) P_x^{-1}$ is the asymmetry parameter. The magnitude of the nuclear quadrupole interaction is determined by the charge of the nucleus, which is proportional to Q, and the distribution of electrons and additional nuclei around the nucleus, which determine the electric field gradient. The effects of nuclear quadrupole interactions on frozen solution EPR spectra are typically small and difficult to observe, but manifest as first-order splittings in the nuclear frequency spectra measured by ENDOR techniques.

1.2.2.4 Hyperfine Interactions

Hyperfine interactions between electron spins and nuclear spins in their proximity are one of the most important sources of structural information in EPR spectroscopy and are described by equation 1.14

$$\hat{\mathscr{H}}_{\mathrm{HF}} = \hat{\boldsymbol{S}}^T \boldsymbol{A} \hat{\boldsymbol{I}} = a_{\mathrm{iso}} \hat{\boldsymbol{S}}^T \hat{\boldsymbol{I}} + \hat{\boldsymbol{S}}^T \boldsymbol{T} \hat{\boldsymbol{I}} \tag{1.14}$$

The hyperfine tensor $\boldsymbol{A}$ consist of two contributions: the isotropic Fermi contact interaction that gives rise to the coupling a_{iso} and the anisotropic electron–nuclear dipole–dipole coupling expressed by the dipolar coupling tensor $\boldsymbol{T}$. The anisotropic hyperfine coupling contribution is averaged out in fluid solutions with low viscosity and fast dynamic averaging of molecular orientations, and only the isotropic hyperfine coupling a_{iso} is observed. Anisotropic hyperfine interactions are resolved in solid environments such as frozen solutions, powders, and single crystals. The isotropic hyperfine coupling is proportional to the electron spin density at a nucleus and described by equation 1.15

$$a_{\text{iso}} = \frac{2}{3}\frac{\mu_0}{\hbar} g_e \mu_B g_n \mu_n \left|\psi_0(0)\right|^2 \tag{1.15}$$

where μ_0 is the vacuum permeability and $\psi_0(0)$ is the electron wave function evaluated at the nucleus. Unpaired electrons in orbitals with *s*-character clearly contribute to the spin density on the nucleus and therefore a_{iso}. In addition, electrons in *p*-, *d*-, or *f*-, orbitals can also contribute to isotropic hyperfine interactions via spin polarization mechanisms. For instance, aromatic radicals with unpaired electrons in their π orbitals exhibit isotropic hyperfine couplings with protons attached to the π-system. The McConnell relationship[77, 78] relates the isotropic hyperfine interaction with these aromatic protons to the spin population in the $2p_z$ orbital of their α-carbon atoms following equation 1.16

$$^{1\text{H}}a_{\text{iso}} = c \cdot \rho_{p_z,C} \tag{1.16}$$

The semiempirical constant, c, expresses the proportionality between the spin population $\rho_{p_z,C}$ on the α-nucleus and a_{iso}. It is approximately -2.25 mT for all aromatic C-H bonds.[78] The hyperfine interaction arises from the perturbation of the C-H σ-bond density by the π-electron spin density, resulting in a net spin polarization on the ^{1}H nucleus.

The anisotropic hyperfine interaction can be described analogously to a classical dipole–dipole interaction between the electron and nuclear spins, and the elements of the traceless and symmetric dipolar tensor $\boldsymbol{T}$ are given by equation 1.17

$$T_{ij} = \frac{\mu_0}{4\pi\hbar} g_e \mu_B g_n \mu_n \left\langle \psi_0 \left| \frac{3r_i r_j - \delta_{ij} r^2}{r^5} \right| \psi_0 \right\rangle \tag{1.17}$$

where ψ_0 is the ground state electronic wave function, r_i and r_j are components of the vector connecting the electron and nuclear spin in the molecular coordinate system $(i, j = x, y, z)$, and δ_{ij} is the Kronecker symbol defined as $\delta_{ii} = 1$ and $\delta_{ij} = 0$ for $i \neq j$.

The anisotropic hyperfine interaction with a nucleus, i, can arise from interactions with an unpaired electron in a non-spherical orbital orbital of i (one-center interaction), and through-space interactions with spin centers not localized on i (two-center interaction). The latter interaction is dominant for ^{1}H nuclei and can be approximated with the distributed point-dipole formula in equation 1.18

$$\boldsymbol{T}_i = \frac{\mu_0}{4\pi\hbar} g_e \mu_B g_n \mu_n \sum_{k \neq i} \rho_k \frac{3\boldsymbol{n}_k \boldsymbol{n}_k^T - \mathbf{1}}{R_k^3} \tag{1.18}$$

where $\boldsymbol{T}_i$ is the anisotropic hyperfine tensor for the nucleus i, and the sum is over all spin centers k with a spin population, ρ_k, that are located at a distance, R_k, from i. The unit vector $\boldsymbol{n}_k$ defines the orientation of the vector connecting i and k in the molecular frame. Equation 1.18 is routinely used in the literature to obtain structural information from anisotropic hyperfine interactions.[79–81] In this thesis, the point-dipole approximation is used to calculate anisotropic hyperfine interactions from Mulliken spin populations.

In the high-field approximation, hyperfine interactions are much smaller than the electron Zeeman interaction and result in a splitting of the EPR transitions. In isotropic continuous-wave EPR spectra, the magnitude of a_{iso} can be determined from the distance between the peaks of the hyperfine structure, if they are sufficiently resolved. The hyperfine structure is determined by the number of nuclei, N, with a nuclear spin, I, that interact with the electron spin with the same hyperfine coupling, which results in $2NI+1$ hyperfine lines. The hyperfine lines are separated by the corresponding isotropic hyperfine coupling with relative intensities following Pascal's triangle. This is exemplified in Figure 1.5 in the simulated EPR spectra of a radical interacting with different numbers of equivalent ^{1}H $\left(I = \frac{1}{2}\right)$ and ^{14}N ($I = 1$) nuclei.

Hyperfine interactions are an important source of information to quantify the spin density distribution of delocalized radicals. As evident from equation 1.15 and the McConnell relationship[77, 78], the isotropic hyperfine interaction of an unpaired electron with a nucleus is proportional to the spin density interacting with

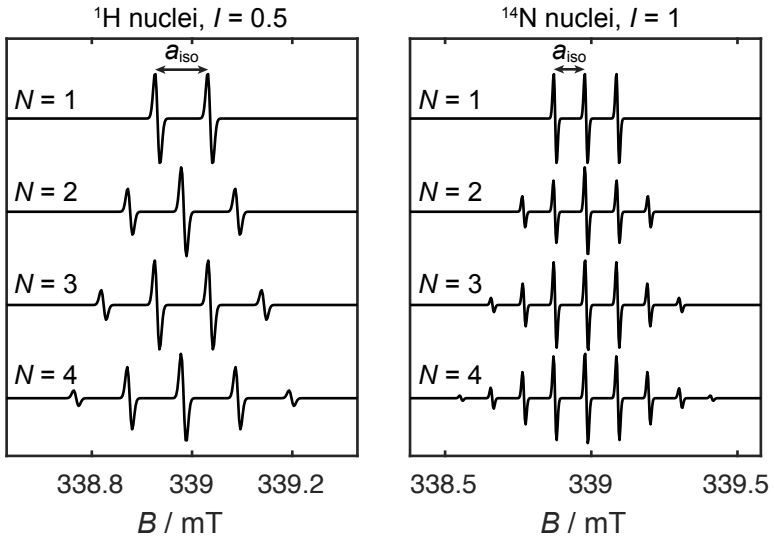


Figure 1.5: Isotropic X-band cw-EPR spectra of an electron spin coupled to N equivalent ^{1}H (left) or ^{14}N (right) nuclei. Simulations were performed at a microwave frequency of 9.5 GHz with $g = 2.0023$ and $a_{\mathrm{iso}} = 3$ MHz.

the nucleus. A delocalized radical that is distributed over many sites in a molecule has smaller spin populations on each given nucleus and consequently exhibits smaller isotropic hyperfine interactions compared to a more localized radical. This relationship was first quantified by James Norris to interpret the distribution of photogenerated radicals in the photosynthetic reaction center.[82] Since then, the Norris relationship in equation 1.19 was employed by many groups to obtain information about the distribution of organic π-radicals from continuous-wave EPR spectroscopy.[51, 83–86]

If hyperfine interactions are the main contribution to the spectral envelope width ΔB_N of a cw-EPR spectrum, and the radical spin density is completely and uniformly distributed over N repeat units of a one-dimensional molecular chain, the spectral envelope width of the oligomer is determined by the envelope width of the monomer repeat unit $\Delta B_{N=1}$ following equation 1.19.

$$\Delta B_N = \frac{\Delta B_{N=1}}{\sqrt{N}} \tag{1.19}$$

Here, complete and uniform spin distribution refers to an equal amount of spin density on each repeat unit of the chain with an identical distribution of spin density within the repeat units on the EPR time scale. The Norris trend in equation 1.19 is

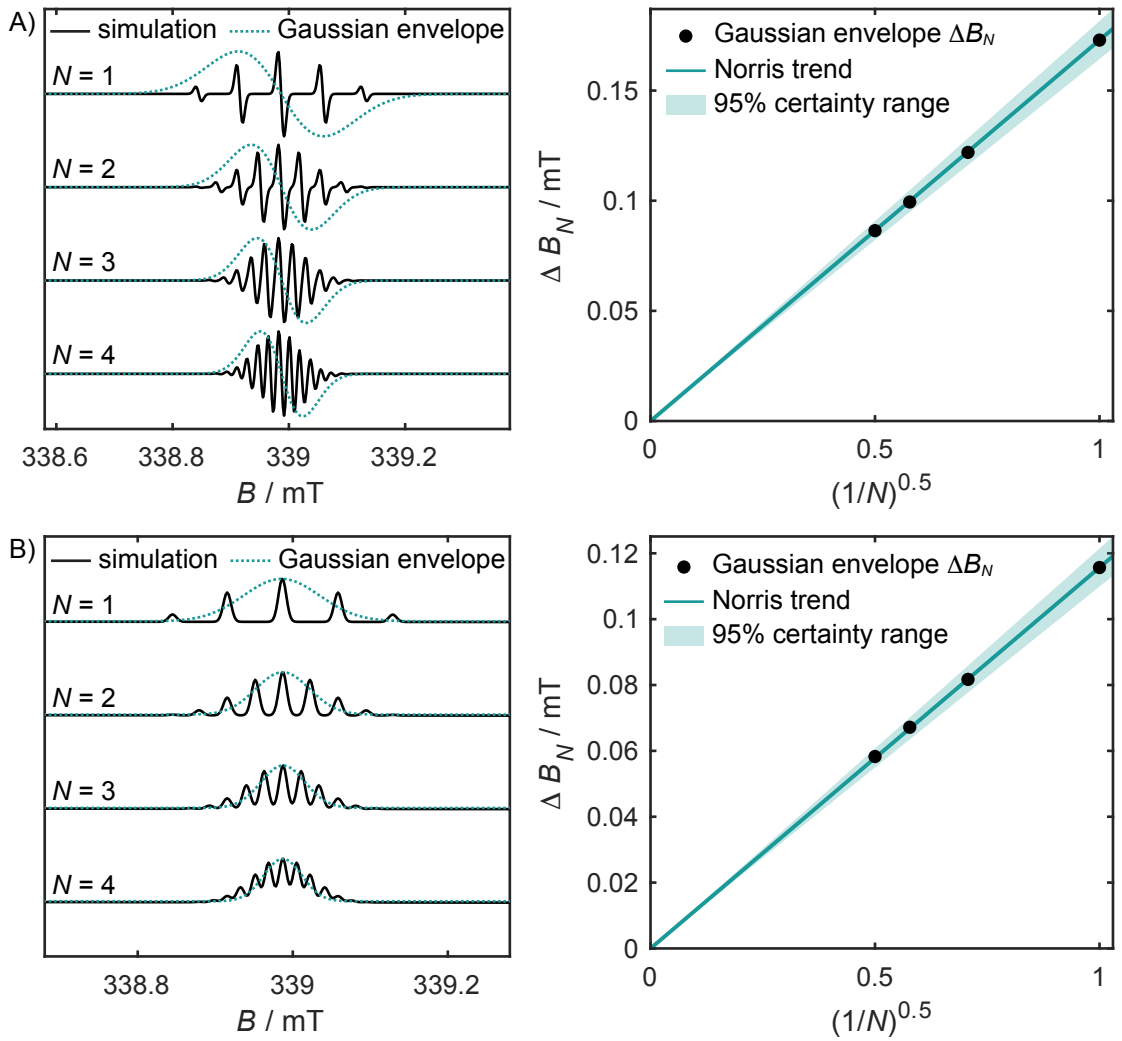


Figure 1.6: A) Derivative and B) absorptive simulations of the X-band EPR spectra of an $S = \frac{1}{2}$ radical distributed uniformly over $N = 1$–4 repeat units of a chain. In each repeat unit, the unpaired electron interacts with four equivalent ^{1}H nuclei with an isotropic hyperfine interaction $a_{\mathrm{iso}} = 2.0$ MHz/N. Simulations were performed with $g = 2.0023$ at a microwave frequency of 9.5 GHz. The spectral envelope widths ΔB_N were determined by fitting a Gaussian distribution to the experimental spectra. The agreement with the Norris trend is investigated by comparing ΔB_N vs $(1/N)^{0.5}$.

the result of an inversely proportional relationship between the isotropic hyperfine interactions in the oligomer repeat unit $a_{\mathrm{iso},N}$ and the hyperfine interactions in the monomer $a_{\mathrm{iso},N=1}$ (equation 1.20).

$$a_{\mathrm{iso},N} = \frac{a_{\mathrm{iso},N=1}}{N} \tag{1.20}$$

It should be noted that coherent spin delocalization and dynamic processes such as

fast radical hopping or dynamic migration of delocalized spins can all contribute to the apparent spin distribution in fluid solution at room temperature and are probed by the Norris relationship.[51, 83, 84] The ideal Norris behaviour is exemplified by simulations of a model system in Figure 1.6.

1.2.2.5 Zero–Field Splitting Interactions

The zero–field splitting Hamiltonian in equation 1.21 describes the interaction between electron spins in systems with $S > \frac{1}{2}$, which lifts the degeneracy of the $2S+1$ m_s sublevels in the absence of an external magnetic field

$$\hat{\mathscr{H}}_{\mathrm{ZFS}} = \hat{\boldsymbol{S}}^T \boldsymbol{D} \hat{\boldsymbol{S}} \tag{1.21}$$

where $\boldsymbol{D}$ is the symmetric, traceless zero–field splitting tensor. While zero–field splitting interactions play an important role in a variety of systems with multiple unpaired electrons, the following discussion will focus on theoretical aspects relevant to photogenerated, spin polarized triplet states ($S = 1$), which were extensively reviewed by Richert, Tait, and Timmel in reference [87].

In the principal coordinate system of the zero–field splitting interaction, $\hat{\mathscr{H}}_{\mathrm{ZFS}}$ can be written in terms of the two zero–field splitting parameters D and E following equation 1.22

$$\hat{\mathscr{H}}_{\mathrm{ZFS}} = D_x \hat{\boldsymbol{S}}_x^2 + D_y \hat{\boldsymbol{S}}_y^2 + D_z \hat{\boldsymbol{S}}_z^2 = D\left[\hat{\boldsymbol{S}}_z^2 - \frac{1}{3}S(S+1)\right] + E\left(\hat{\boldsymbol{S}}_x^2 - \hat{\boldsymbol{S}}_y^2\right) \tag{1.22}$$

where D and E are defined by the principal values of the traceless $\boldsymbol{D}$-tensor: $D = \frac{3}{2}D_z$ and $E = \frac{1}{2}\left(D_x - D_y\right)$. By convention, the coordinate system of the zero–field splitting $\boldsymbol{D}$-tensor is chosen so that $|D_z| \geq |D_x| \geq |D_y|$. Therefore, the axis of maximal dipolar coupling is along the zero–field splitting Z axis, and $|D| \geq 3|E|$. In the zero–field basis $|X\rangle$, $|Y\rangle$, and $|Z\rangle$, the energies of the triplet sublevels are determined by D and E following equation 1.23

$$\begin{aligned} \varepsilon_x &= -D_x = \frac{1}{3}D - E \\ \varepsilon_y &= -D_y = \frac{1}{3}D + E \\ \varepsilon_z &= -D_z = -\frac{2}{3}D \end{aligned} \tag{1.23}$$

The energetic ordering of the triplet sublevels depends on the sign and magnitude of D and E as shown in Figure 1.7A.

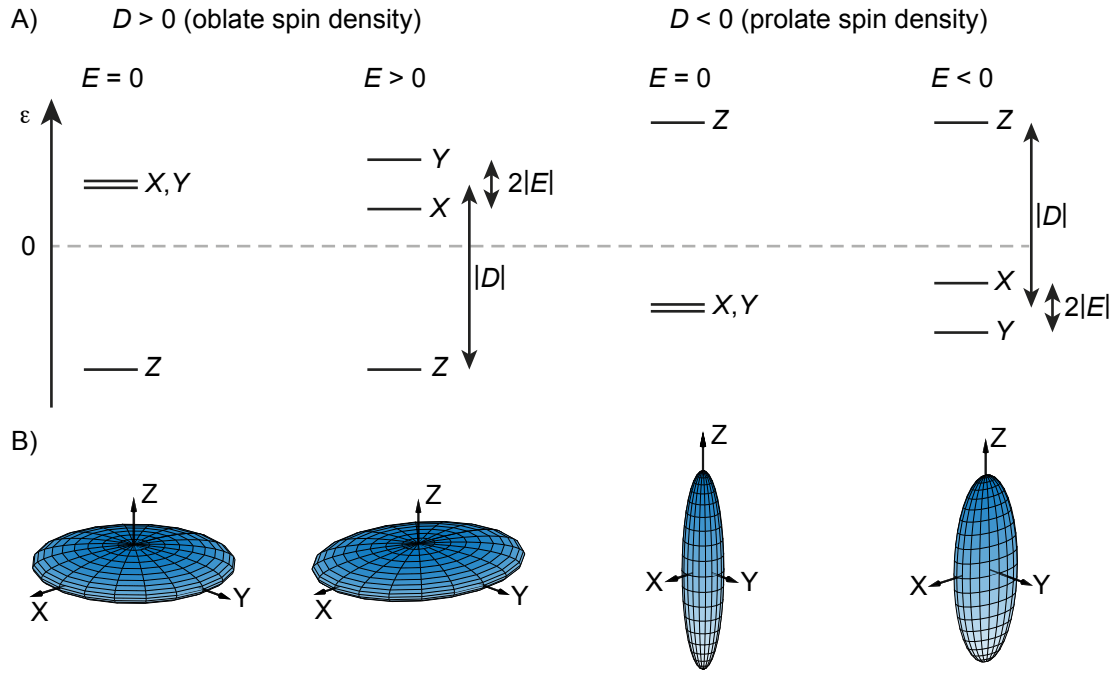


Figure 1.7: A) Energetic ordering of the zero–field triplet sublevels for an oblate ($D > 0$) and prolate ($D < 0$) spin density distribution without ($E \neq 0$) and with ($E = 0$) axial symmetry. B) Schematic visualization of the shape of the corresponding spin density distribution in the principal coordinate system of the zero–field interaction.

Two different interactions can give rise to zero–field splitting: spin–orbit coupling resulting in the coupling of the electron spin and orbital angular momenta, and spin–spin dipolar coupling between a pair of unpaired electrons. The spin-orbit contribution to the zero–field splitting is usually negligible for organic radicals, but becomes important for systems with large spin–orbit coupling constants such as transitions metals. Recent work by Moise, Redman *et al.*[88] has shown that spin–orbit contributions are also negligible in the photogenerated triplet states of Zn-porphyrins akin to the ones investigated in this thesis.

The spin–spin coupling contribution to the zero–field splitting Hamiltonian can be expressed analogously to classical magnetic dipole interactions following equation 1.24

$$\hat{\mathscr{H}}_{\mathrm{SSC}} = \frac{\mu_0}{4\pi\hbar} g_1 g_2 \mu_B^2 \left[\frac{\hat{\boldsymbol{S}}_1 \hat{\boldsymbol{S}}_2}{R^3} - \frac{3\left(\hat{\boldsymbol{S}}_1 \boldsymbol{r}\right)\left(\hat{\boldsymbol{S}}_2 \boldsymbol{r}\right)}{R^5} \right] \tag{1.24}$$

where $\boldsymbol{r}$ is the vector connecting the electron spins located at a distance R, and g_1 and g_2 are the g-values of the two electrons in their respective environments. In the context of this Hamiltonian, the zero–field splitting parameters D and E are given by equation 1.25

$$\begin{aligned} D &= \frac{3\mu_0}{16\pi h} \left(g_e \mu_B\right)^2 \left\langle \frac{1 - 3\cos^2\theta}{R^3} \right\rangle \\ E &= -\frac{3\mu_0}{16\pi h} \left(g_e \mu_B\right)^2 \left\langle \frac{\sin^2\theta \cos 2\phi}{R^3} \right\rangle \end{aligned} \tag{1.25}$$

where θ is the angle between the spin–spin vector and the dipolar Z axis, ϕ is the azimuthal angle of the spin–spin vector in the dipolar xy-plane, and the angular brackets indicate integration over the triplet wave function. The D parameter thus contains information about the mean interspin distance whereas E is a measure of the rhombicity of the $\boldsymbol{D}$-tensor. Systems with axial symmetry ($E = 0$) result in degenerate X and Y energy levels, while systems with lower symmetry are characterized by $E \neq 0$ (Figure 1.7A). The sign of D is determined by the $1 - 3\cos^2\theta$ term in equation 1.25 and is positive ($D > 0$) for an oblate spin density distribution and negative ($D < 0$) for a prolate shape of the spin density (Figure 1.7B). The sign of E depends on the assignment of the X and Y principal axes of the zero–field interaction and has no physical meaning.

The appropriate Hamiltonian to interpret the EPR spectrum of a triplet state consists of the Zeeman term $\hat{\mathscr{H}}_{\mathrm{EZ}}$ and the zero–field splitting term $\hat{\mathscr{H}}_{\mathrm{ZFS}}$ (equation 1.26).

$$\hat{\mathscr{H}} = \hat{\mathscr{H}}_{\mathrm{EZ}} + \hat{\mathscr{H}}_{\mathrm{ZFS}} = \frac{\mu_B}{\hbar} \boldsymbol{B}_0 \boldsymbol{g} \hat{\boldsymbol{S}} + \hat{\boldsymbol{S}}^T \boldsymbol{D} \hat{\boldsymbol{S}} \tag{1.26}$$

So far, the discussion in this section has exclusively focused on $\hat{\mathscr{H}}_{\mathrm{ZFS}}$ in the zero–field basis $|X\rangle$, $|Y\rangle$, and $|Z\rangle$, which can be expressed in terms of the three m_s sublevels of a triplet state following equation 1.27

$$
\begin{aligned}
|X\rangle &= \frac{1}{\sqrt{2}}\{|1,+1\rangle - |1,-1\rangle\} \\
|Y\rangle &= \frac{1}{\sqrt{2}}\{|1,+1\rangle + |1,-1\rangle\} \\
|Z\rangle &= |1,0\rangle
\end{aligned}
\tag{1.27}
$$

where $|1,-1\rangle$, $|1,0\rangle$, and $|1,+1\rangle$ are the wave functions for $m_s = -1$, 0, and 1, respectively. In the high-field approximation relevant for EPR spectroscopy at X-band frequencies, the electron Zeeman interaction is larger than the zero–field splitting interaction, and the Hamiltonian in equation 1.26 is typically expressed in the basis of $|T_+\rangle$, $|T_0\rangle$, and $|T_-\rangle$ labeled after their energetic ordering in the high–field limit. For an external magnetic field applied parallel to the Z-axis of the zero–field interaction tensor ($\boldsymbol{B}_0||\boldsymbol{Z}$), the relationship between the high–field and zero–field spin states is expressed by equation 1.28

$$
\begin{aligned}
|T_+\rangle &= c_1|X\rangle + c_2|Y\rangle \\
|T_0\rangle &= |Z\rangle \\
|T_-\rangle &= c_2|X\rangle - c_1|Y\rangle
\end{aligned}
\tag{1.28}
$$

where c_1 and c_2 are mixing coefficients that depend on the strength of the B_0 field.[89, 90] Analogous expressions can be obtained for ($\boldsymbol{B}_0||\boldsymbol{X}$) and ($\boldsymbol{B}_0||\boldsymbol{Y}$). If the B_0 field is aligned with a principal axis of the zero–field splitting tensor, the corresponding high–field state is independent of the magnetic field strength and equal to the energy at zero field, while the energy of the other two states increases or decreases as a function of B_0. This is exemplified by equation 1.29 for $\boldsymbol{B}_0||\boldsymbol{Z}$, and the expressions for $\boldsymbol{B}_0||\boldsymbol{X}$ and $\boldsymbol{B}_0||\boldsymbol{Y}$ can be derived analogously.

$$
\begin{aligned}
\varepsilon_{+,-} &= \frac{1}{3}D \pm \sqrt{E^2 + \left(\frac{g\mu_B}{h}B_0\right)^2} \\
\varepsilon_0 = \varepsilon_z &= -\frac{2}{3}D
\end{aligned}
\tag{1.29}
$$

Each orientation of the magnetic field with respect to the principal axes of the zero–field splitting tensor results in two allowed EPR transitions with $\Delta m_s = \pm 1$. This is schematically shown in Figure 1.8A for a triplet state with $D = +600$ MHz and

$E = -100$ MHz. In the absence of significant g-anisotropy, the powder EPR spectrum of a triplet state exhibits four turning points for a $\boldsymbol{D}$-tensor with axial symmetry and six turning points for a rhombic $\boldsymbol{D}$-tensor. The magnitude of the zero–field splitting parameters $|D|$ and $|E|$ can be determined from the position of the turning points, which are often referred to as canonical field positions (Figure 1.8B).

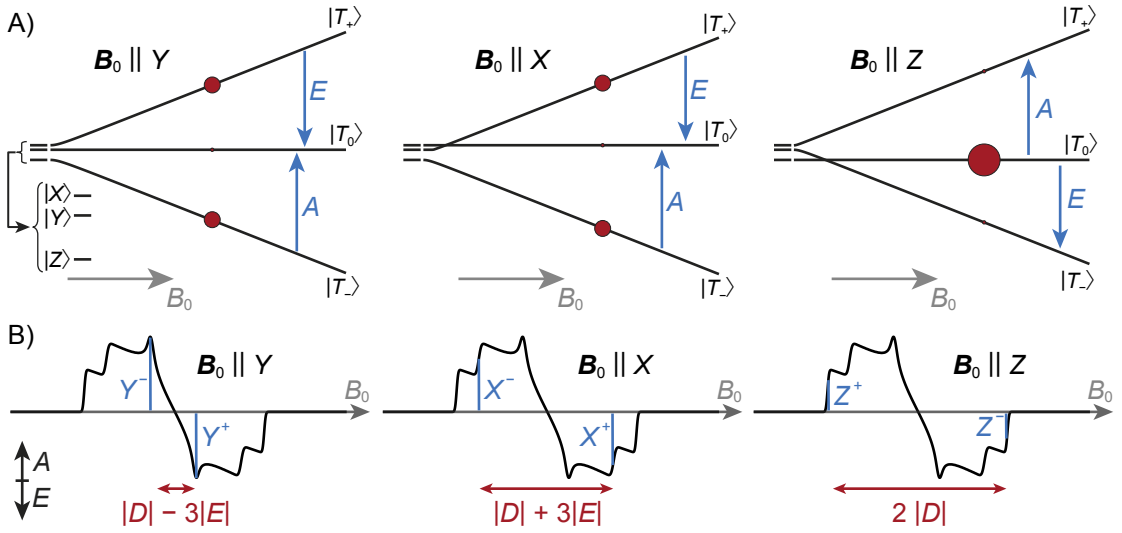


Figure 1.8: A) Energies of the triplet state sublevels for $D > 0$ and $E < 0$ as a function of the external magnetic field with strength B_0. The magnetic field vector $\boldsymbol{B}_0$ is aligned with the principal axes X, Y, and Z of the zero–field $\boldsymbol{D}$-tensor, respectively. The population of the high–field sublevels $|T_+\rangle$, $|T_0\rangle$, and $|T_-\rangle$ for a relative population of the zero–field sublevels $P_X : P_Y : P_Z = 0 : 0 : 1$ is indicated by the size of the red spheres. B) Simulated triplet state EPR spectrum for $D = +600$ MHz and $E = -100$ MHz at a microwave frequency of 9.5 GHz. The six canonical positions of the spectrum arise from the absorptive and emissive transitions in A), and are indicated by blue bars.

The photogenerated triplet states of the porphyrins investigated in this thesis are obtained by anisotropic intersystem crossing (ISC) from the photoexcited singlet state, and their polarization patterns arise from the selective population of the zero–field sublevels. For instance, preferential population of the $|Z\rangle$ zero–field sublevel gives rise to the *AAAEEE* (A = absorptive, E = emissive) polarization pattern shown in Figure 1.8. The population of the triplet sublevels in the high–field approximation is determined by the population of the zero–field sublevels, and the intensity of the EPR transitions is proportional to the population difference $P_0 - P_{\pm 1}$. For $\boldsymbol{B}_0 || \boldsymbol{Z}$, the population of the

high–field levels is given by equation 1.30, and analogous expressions are obtained for the other two canonical orientations $\boldsymbol{B}_0||\boldsymbol{X}$ and $\boldsymbol{B}_0||\boldsymbol{Y}$.

$$P_0 = P_z \qquad P_{\pm 1} = \frac{1}{2}\left(P_x + P_y\right) \tag{1.30}$$

1.2.3 Continuous-Wave and Pulse EPR Spectroscopy

Paramagnetic samples can be investigated by continuous-wave (cw) and pulse EPR techniques. Typically, the dominant interaction of the spin Hamiltonian discussed in Section 1.2.2 during an EPR experiment is the electron Zeeman interaction, which lifts the degeneracy of the $2S+1$ m_s sublevels of a spin system in the presence of an external magnetic field. Transitions between the different sublevels are then induced by microwave irradiation to obtain the EPR signal.

EPR experiments can be performed at different microwave frequencies and require stronger magnetic fields for higher frequencies. The work presented in this thesis was performed at X-band (∼9.5 GHz), Q-band (∼34 GHz), and W-band (∼95 GHz) frequencies. Higher microwave frequencies enhance the resolution of field-dependent interactions and can, for instance, help resolve the $\boldsymbol{g}$-anisotropy of organic radicals. Stronger magnetic fields furthermore improve the sensitivity of the measurements due to the larger energy difference between the spin sublevels that results in higher Boltzmann population differences. This is however accompanied by experimental challenges such as the need for superconducting magnets when working at W-band frequencies as well as reduced resonator dimensions and consequently smaller sample sizes.

Continuous-wave EPR spectra are acquired by continuously irradiating a sample with microwaves at a fixed frequency, while sweeping an external magnetic field. EPR transitions are detected at magnetic field strengths where the energetic splitting of the sublevels of the system matches the energy of the microwaves.

Pulse EPR is a useful technique to improve on the limited spectral and time resolution of cw-EPR, and to selectively investigate specific interactions of the spin Hamiltonian. Instead of continuous microwave irradiation, high intensity microwave pulses of varying lengths and shapes are used to perturb the spin system. Specific pulse sequences have been developed to investigate different properties of paramagnetic samples such as hyperfine interactions or relaxation times and are extensively reviewed in reference [70].

1.2.3.1 Continuous-Wave EPR Spectroscopy

The main components of a cw-EPR spectrometer are the microwave source, the electromagnet or superconducting magnet generating the external B_0 field, the resonator, and the detector. The magnetic field splits the m_s sublevels of the spin system so that transitions between the energy levels can be induced by microwave irradiation.

The microwaves emitted from the source are split into a signal and a reference arm in the microwave bridge to enable phase-sensitive signal detection. In the signal arm, the microwaves are passed to the resonator cavity *via* a circulator and an attenuator that adjusts the microwave power transmitted to the sample. The circulator directs the incident microwave irradiation to the resonator and the microwaves reflected by the sample to the detector.

Resonators are used in EPR spectroscopy to enhance the sensitivity of the measurements by focusing the microwave irradiation on the sample. They are specifically designed to generate standing waves in their cavities that maximize the magnetic field component $\boldsymbol{B}_1$ of the microwaves at the sample while the electric field component $\boldsymbol{E}_1$ is minimized. The minimization of the electric field is particularly important for samples in polar solvents with high dielectric constants, which absorb microwaves by interacting with with their $\boldsymbol{E}_1$ component. Typically, tuning of the microwaves emitted from the source is required to critically couple into the resonator. This is achieved by adjusting the frequency of the emitted microwaves to match the frequency of the resonator, and by controlling the amount of power entering the resonator using a

coupling element called an iris. Critical coupling is achieved when the microwave power reflected from the resonator is minimal. The sensitivity of the resonator is determined by its quality factor Q and the filling factor. A high quality factor means that the resonator efficiently stores microwave energy. The filling factor indicates the fraction of the magnetic energy stored in the resonator interacting with the sample.

A cw-EPR transition is observed when the microwave energy matches the energetic splitting of the spin levels ($\Delta E = h\nu_{\mathrm{mw}}$). Under these resonance conditions, microwave radiation is absorbed by the sample, which is detected indirectly by a change of the microwave reflection from the resonator. To increase the sensitivity of the EPR measurement, the magnetic field B_0 is modulated by an additional oscillating field with typical modulation frequencies of 100 kHz or less. If the microwave energy is on resonance, this results in a rapid oscillation of the EPR signal at the modulation frequency, which allows for its selective detection and a higher signal-to-noise ratio. The amplitude of the oscillating signal is proportional to the intensity change of the absorptive EPR line, which results in a derivative shape of the detected EPR transition. To avoid distortions of the spectral shape, the modulation amplitude B_m must be adjusted for each investigated system to maximize the signal intensity while ensuring that narrow features of the spectrum remain resolved ($B_m < \frac{1}{2}\Gamma$, where Γ is the narrowest peak-to-peak linewidth).

The intensity of the EPR transitions for stable radicals depends on the Boltzmann weighted population difference between the sublevels of the systems, the transition probability, and the relaxation times. The $\boldsymbol{B}_1$ induced transitions of the spin system equalize the population differences and perturb the system from its thermodynamic equilibrium. If the microwave power is too high, this population difference is saturated, ultimately reducing the signal intensity and distorting the observed EPR signal through power broadening. Therefore, the microwave power must be carefully adjusted to avoid saturation effects by remaining in the linear response regime in which a proportional relationship between microwave power and signal intensity is fulfilled.

1.2.3.2 Broadening of EPR Transitions

Experimentally observed EPR transitions are characterized by their linewidths and lineshapes, which can provide information about relaxation rates, dynamic processes, and the homogeneity of the sample. Homogeneously broadened EPR transitions are observed for ensembles of spins, also called spin packets, that are described by the same spin Hamiltonian and experience the same time-averaged magnetic field. The EPR lineshape of transitions arising from homogeneously broadened spin packets is Lorentzian with a peak-to-peak linewidth $\Gamma = \frac{2}{\sqrt{3}T_m}$, where T_m is the phase memory time introduced in Section 1.2.3.7 (Figure 1.9A).[70] Homogeneous broadening arises from fluctuating fields that can, for example, be caused by electron or nuclear spin flips.

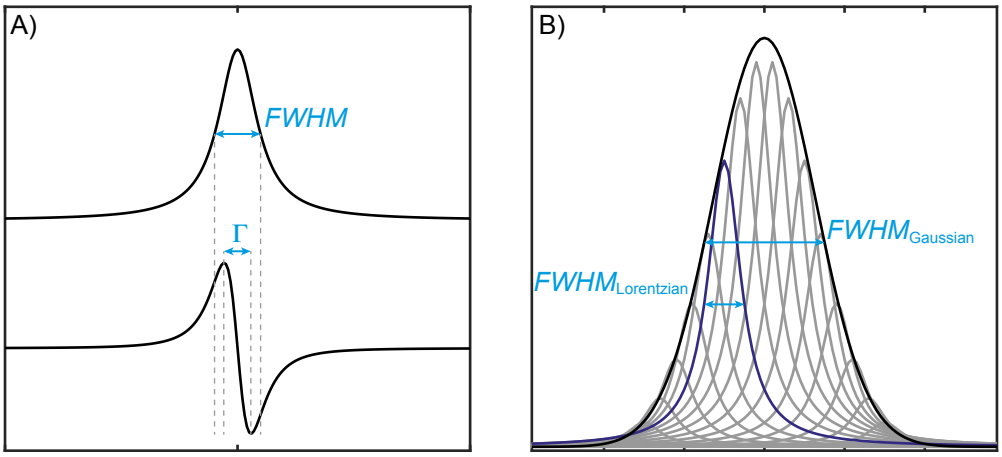


Figure 1.9: A) Absorptive and derivative Lorentzian lineshape of a homogeneously broadened EPR transition. The full width at half maximum (*FWHM*) and peak-to-peak linewidth Γ are indicated in the plot and are related by $\Gamma = \frac{FMWH}{\sqrt{3}}$. B) Inhomogeneously broadened line with a Gaussian shape arising from the superposition of multiple homogeneously broadened EPR transitions with different resonance frequencies. The intensity of the Gaussian line is normalized for better visualization.

Inhomogeneously broadened lines arise from the superposition of the homogeneously broadened EPR transitions of multiple spin packets with slightly different resonance positions, which gives rise to an unresolved Gaussian lineshape (Figure 1.9B). It can occur due to inhomogenous magnetic fields, unresolved hyperfine interactions, or a distribution of local magnetic fields resulting from anisotropic interactions in randomly oriented systems in the solid state (often referred to as strain effects).

Dynamic processes that modulate the environment of a paramagnetic center can also contribute to the apparent lineshape. Each paramagnetic molecule in fluid solution undergoes rotational diffusion with a tumbling rate that depends on the size and shape of the molecule, the solvent properties, and the available thermal energy. In first approximation, the rotational correlation time τ_c can be written based on the Stokes–Einstein relationship following equation 1.31

$$\tau_c = \frac{4\pi\eta R^3}{3k_B T} \tag{1.31}$$

where η is the viscosity of the solvent, R is the hydrodynamic radius, and $k_B T$ is the thermal energy at temperature T. More accurate descriptions of τ_c need to take the anisotropy of the molecular tumbling into account. The effects of tumbling on the width and shape of the EPR transitions depend on the magnitude of the anisotropic interactions, $\Delta\nu$, of the paramagnetic species and are typically dominated by g and hyperfine anisotropies for organic π-radicals. Here, $\Delta\nu$ is the spectral width to the anisotropic interactions in frequency units. Anisotropic broadening of the cw-EPR spectrum occurs when the tumbling rate of a molecule is insufficient for the complete dynamic averaging of the anisotropic interactions ($\tau_c > \frac{1}{\Delta\nu}$). In addition, dynamic chemical processes such as electron transfers or isomerizations can modulate the linewidth of the EPR transitions and provide information about the rate of the chemical process from the magnitude of exchange broadening. This effect is discussed in detail in Chapter 3.

1.2.3.3 Transient EPR Spectroscopy

Photogenerated, short-lived paramagnetic species such as spin-polarized triplet states can be investigated over a time range of a few nanoseconds to several hundred microseconds using time-resolved or transient continuous-wave EPR spectroscopy.[91–93] This technique is derived from traditional cw-EPR experiments introduced in Section 1.2.3.1 as continuous microwave irradiation is used in both cases to induce

EPR transitions. Unlike cw-EPR spectra of persistent radicals, transient continuous-wave EPR (tr-EPR) spectra are acquired with a transient recorder in absorption mode without field modulation.

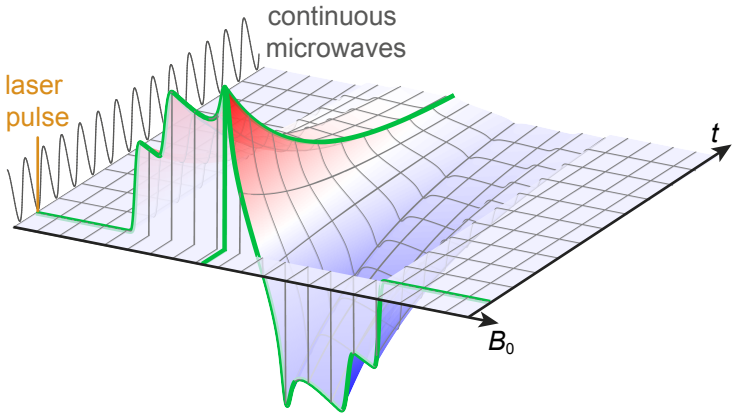


Figure 1.10: Schematic illustration of a transient continuous-wave EPR experiment. During the experiment transitions are induced by continuous microwave irradiation and the spectrum is recorded as a function of time, t, and magnetic field strength, B_0. The green lines highlight the EPR spectrum at a set time after photoexcitation, and the time evolution of the spectrum at a single field position.

The investigated paramagnetic species are generated with a short laser pulse that also acts as trigger for the data acquisition. The time evolution of the EPR signal is recorded at a fixed magnetic field strength B_0. Stepwise changes of B_0 followed by acquisition of the transient gives a two-dimensional spectrum as a function of time t and B_0 (Figure 1.10). The spectrum of the transient species at a set time after the laser pulse and the time evolution of the signal at a field position can be obtained from slices of the two-dimensional spectrum. The time-domain of tr-EPR spectra can be distorted by so-called Torrey oscillations that are caused by the precession of the magnetization vector $\boldsymbol{M}$ around the microwave magnetic field vector $\boldsymbol{B}_1$ in a rotating frame on resonance with the microwave frequency.[91] The frequency of the resulting transient nutations increases with increasing B_1 field strength. Therefore, low microwave powers are required to obtain reliable information about the evolution of transient species.

1.2.3.4 Pulse EPR Spectroscopy

The principal components of a pulse EPR spectrometer are analogous to a cw-EPR spectrometer and consist of the microwave source, the resonator, and the detector. During a pulse EPR experiment, short, high-power microwave pulses excite the paramagnetic sample, and the EPR signal is obtained by detecting emission from the excited sample. This fundamental difference between pulse and cw-EPR spectroscopy requires modifications of the experimental setup.

In a pulse EPR spectrometer, the continuous microwaves emitted from the source are passed through a pulse-forming unit with several channels that can create independent microwave pulses with varying lengths and phases. To obtain high-power pulses for exciting the investigated spin systems, the pulses generated by the pulse-forming unit are amplified in a TWT (traveling-wave tube) amplifier. These high-power pulses are directed to the resonator via a circulator and an attenuator.

Analogous to cw-EPR spectroscopy, resonators are used in pulse EPR experiments to concentrate the microwave energy at the sample. To efficiently excite spin packets over a wide range of resonance frequencies, wide resonator bandwidths are often desired for pulse EPR spectroscopy. The bandwidth of a resonator is characterized by its quality factor $Q = \nu_0/\Delta\nu$, where ν_0 is the center frequency and $\Delta\nu$ is the half-power bandwidth. Overcoupling of the resonator reduces its quality factor and increases the bandwidth, but also decreases the detection efficiency. After a pulse, the microwave power built up in the resonator is dissipated exponentially with a time constant $\tau_{\mathrm{rd}} = Q\pi^{-1}\nu_0^{-1}$. During this microwave ring-down, a protection switch isolates the detector from the resonator to shield it from the emitted high-power microwaves. Consequently, no signal can be detected during this period, typically referred to as deadtime, which is a fundamental limitation of pulse EPR spectroscopy. Overcoupling of the resonator reduces the deadtime. Quadrature detection is typically employed in pulse EPR spectroscopy to obtain an in-phase and an out-of-phase component of the signal.

For certain pulse EPR experiments, additional equipment is required. For instance, ENDOR experiments require a radiofrequency (rf) source and amplifier, as well as a resonator equipped with rf coils.

1.2.3.5 Semiclassical Description of Pulse EPR Experiments

As discussed in Section 1.2.1, the spin angular momentum $\boldsymbol{S}$ of an electron gives rise to the magnetic moment $\boldsymbol{\mu}$. Pulse EPR experiments are performed on macroscopic samples that consist of an ensemble of spins resulting in a macroscopic magnetization $\boldsymbol{M}$, which is defined as the vector sum of all individual magnetic moments $\boldsymbol{\mu}$ in the sample. This vector model can be used to intuitively describe simple pulse EPR experiments. For high-multiplicity systems or complicated pulse sequences, a more sophisticated density matrix treatment is required.

At thermal equilibrium, the magnetization vector $\boldsymbol{M}$ is aligned parallel to the external magnetic field, $\boldsymbol{B}_0$, which is conventionally defined along the Z-axis of the laboratory frame, and time independent. Application of a microwave pulse perpendicular to $\boldsymbol{M}$ perturbs the system from its thermal equilibrium and results in the tilting of $\boldsymbol{M}$ away from the Z-axis. The effects of microwave pulses on the spin dynamics of a system are conveniently described using a reference frame that rotates around the laboratory Z-axis with an angular frequency $\omega_{\text{rot}} = \omega_{\text{mw}}$, where ω_{mw} is the angular microwave frequency. In this rotating frame, the evolution of $\boldsymbol{M}$ is described by equation 1.32

$$\frac{d}{dt}\boldsymbol{M} = (\Delta\boldsymbol{\omega} + \boldsymbol{\omega}_1) \times \boldsymbol{M} \tag{1.32}$$

where $\boldsymbol{\omega}_1$ is the microwave amplitude vector and $\Delta\boldsymbol{\omega}$ is the offset between the resonance frequency of a spin packet and ω_{rot} as described by equation 1.33. A spin packet refers to an ensemble of spin systems with the same resonance frequency, where the electron and nuclear spins in each system experience the same time-averaged local fields.

$$\Delta\omega = \omega_0 - \omega_{\text{rot}} = 2\pi\left(\frac{g_e\mu_B B_0}{h} - \nu_{\text{mw}}\right) \tag{1.33}$$

As seen from equation 1.32, the precession of the magnetic moment $\boldsymbol{M}$ of a spin packet in the rotating frame is determined by its resonance frequency. Spin packets resonant with the microwave frequency ($\Delta\omega = 0$) are stationary in the rotating frame. Spin packets with resonance frequencies larger than ν_{mw} precess counterclockwise in the rotating frame ($\Delta\omega > 0$), while those with $\Delta\omega < 0$ precess clockwise.

The effect of a microwave pulse on a spin packet in the rotating frame is quantified by its flip angle θ, which defines the angle by which $\boldsymbol{M}$ is rotated, and is determined by the length t_p and amplitude of the pulse. The most common flip angles in pulse EPR experiments are $\frac{\pi}{2}$ ($\theta = 90°$) and π ($\theta = 180°$). The direction of the rotation is defined by the phase of the pulse.

Application of a $\frac{\pi}{2}$ pulse with $+y$ phase to a set of near resonant spin packets rotates the magnetization vector by 90° clockwise around the Y-axis of the rotating frame, which results in the alignment of the magnetization vector along the $+X$ axis in the XY plane. After the microwave pulse, the spin packets are precessing around the Z axis. The evolution of the magnetization of each spin packet is described by equation 1.34

$$\begin{pmatrix} 0 \\ 0 \\ M_0 \end{pmatrix} \xrightarrow{\left(\frac{\pi}{2}\right)_{+y}} \begin{pmatrix} M_0 \\ 0 \\ 0 \end{pmatrix} \xrightarrow{\tau} \begin{pmatrix} M_0\cos(\Delta\omega\tau) \\ M_0\sin(\Delta\omega\tau) \\ 0 \end{pmatrix} \tag{1.34}$$

where $(0, 0, M_0)$ describes the magnetization at thermal equilibrium along the Z axis, and τ is the time after the pulse. Precession of the magnetization vector in the XY plane induces a free induction decay (FID) signal that can be detected as a function of time. Dephasing of the individual spin packets results in the loss of the net transverse magnetization and the decay of the FID signal.

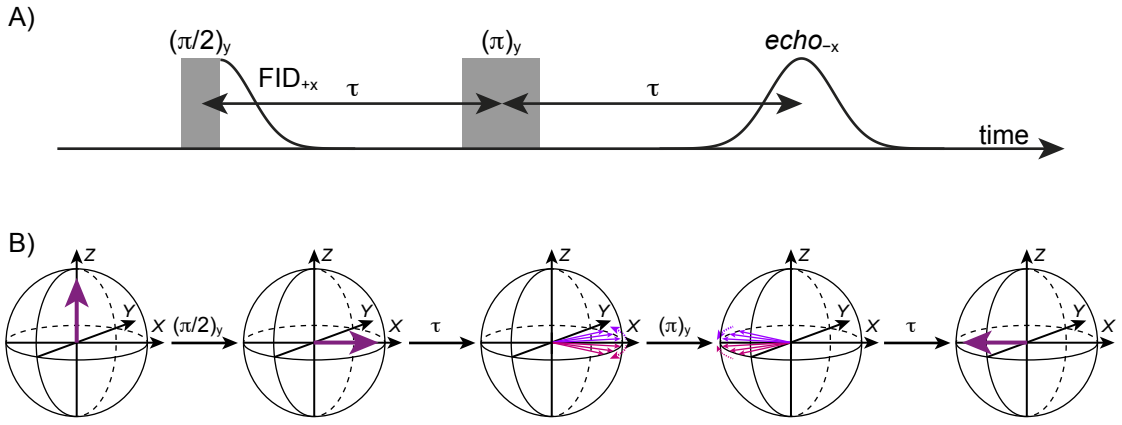


Figure 1.11: A) Schematic visualization of the two-pulse Hahn echo sequence. B) Vector representation of the evolution of magnetic moments during the Hahn echo pulse sequence in the rotating frame.

A primary echo is obtained with the two-pulse sequence $\left(\frac{\pi}{2}\right)_{+y} - \tau - (\pi)_{+y} - \tau - echo$ (Figure 1.11). As described above, the first pulse rotates the magnetization into the XY plane followed by dephasing of the individual spin packets during the free evolution time τ. The second microwave pulse rotates the magnetization vectors by 180° clockwise around the Y-axis. After the π-pulse, the spin packets continue to precess round Z with their characteristic frequencies and coherent spin packets refocus with $-x$ phase at time τ. This gives rise to the primary echo, or Hahn echo, which is formed by two back-to-back FIDs; a reverse FID during the rephasing of the spin packets followed by a second FID caused by the dephasing of the spin packets. The evolution of the magnetization of each spin packet during a Hahn echo experiment is described by equation 1.35.

$$\begin{pmatrix} 0 \\ 0 \\ M_0 \end{pmatrix} \xrightarrow{\left(\frac{\pi}{2}\right)_{+y}} \begin{pmatrix} M_0 \\ 0 \\ 0 \end{pmatrix} \xrightarrow{\tau} \begin{pmatrix} M_0 \cos(\Delta\omega\tau) \\ M_0 \sin(\Delta\omega\tau) \\ 0 \end{pmatrix} \xrightarrow{(\pi)_{+y}} \begin{pmatrix} M_0 \cos(\pi - \Delta\omega\tau) \\ M_0 \sin(\pi - \Delta\omega\tau) \\ 0 \end{pmatrix} \xrightarrow{\tau} \begin{pmatrix} -M_0 \\ 0 \\ 0 \end{pmatrix} \tag{1.35}$$

Pulse EPR spectra can be recorded by detecting the FID or the spin-echo and are obtained in absorption mode. In practice, FIDs often do not extend beyond the deadtime after the microwave $\frac{\pi}{2}$ pulse, and long microwave pulses with narrow excitation profiles are often required to observe the final part of the FID. Therefore, two-pulse spin-echo detection is used in many pulse EPR experiments as the final detection sequence.

1.2.3.6 Orientation Selection

The excitation bandwidth of a microwave pulse describes the range of resonance frequencies that are excited by the pulse. The excitation profile is approximately described by the Fourier transform of the pulse shape in the time domain.[70] For rectangular pulses, the excitation profile is inversely proportional to the pulse length t_p; in other words short microwave pulses excite spin packets over a broad frequency range. Since the introduction of arbitrary waveform generators (AWG) operating on the nanosecond timescale into many EPR laboratories, shaped pulses have become popular in pulse EPR spectroscopy to finely control the excitation profile.

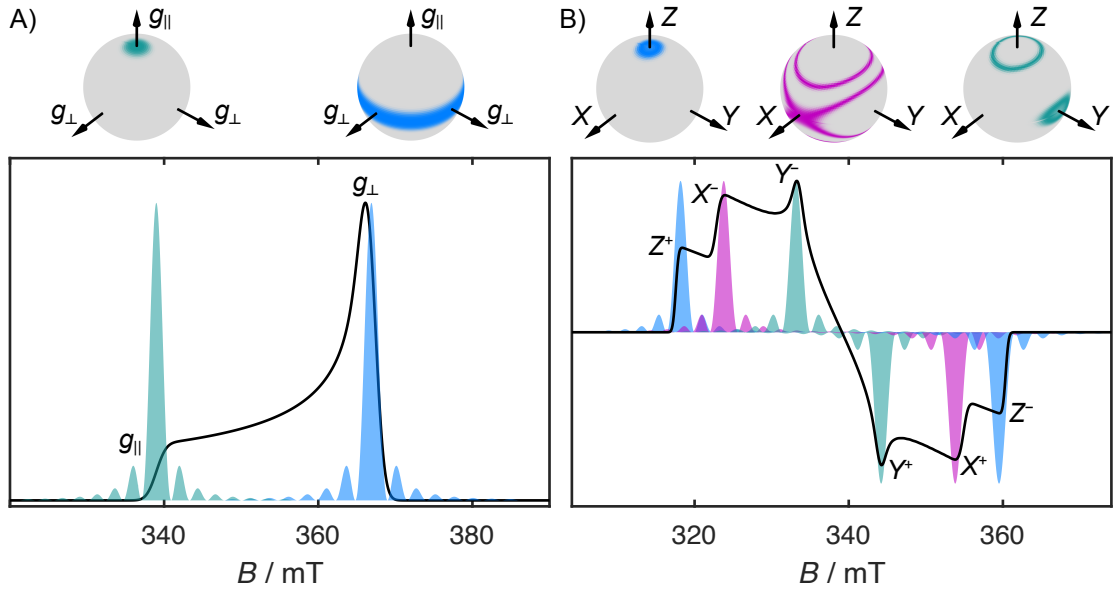


Figure 1.12: Calculated powder EPR spectra of A) an $S = \frac{1}{2}$ radical with an axial $\boldsymbol{g}$-tensor ($g_{||} = 2.0023$; $g_\perp = 1.85$), and B) a spin polarized triplet state with $D = 600$ MHz, $E = -100$ MHz, and $P_X : P_Y : P_Z = 0 : 0 : 1$ at a microwave frequency of 9.5 GHz. The fraction of the spectra excited with a 16 ns rectangular pulse at the canonical field positions is highlighted by the shaded areas. The excited orientations are plotted on the unit spheres above the simulated spectra with colours corresponding to the excitation profiles in the spectra. The grey areas of the unit spheres indicate orientations not excited by the pulses.

Still, the excitation bandwidth of typical microwave pulses is often insufficient to excite all spin packets in a sample with large anisotropic interactions such as $\boldsymbol{g}$-anisotropy or zero–field splitting interactions. Consequently, only a subset of molecular orientations relative to the external magnetic field are measured in the pulse EPR experiment. This phenomenon is called orientation selection and is illustrated for

an $S = \frac{1}{2}$ radical with an axial $\boldsymbol{g}$-tensor and a spin polarized triplet state with an orthorhombic $\boldsymbol{D}$-tensor in Figure 1.12.

Orientation selection can be exploited to obtain additional information about the interactions in a spin system. Excitation of a subset of orientations during a hyperfine experiment such as ENDOR provides information about the orientation of the hyperfine tensors and, if applicable, the nuclear quadrupole tensors in the principal coordinate system of the interaction that determines the orientation selection ($\boldsymbol{g}$-anisotropy or zero–field splitting).

1.2.3.7 Relaxation

During an EPR experiment, transitions between spin states are induced by continuous microwave irradiation or short, high-powered microwave pulses. The excited spin system returns to equilibrium through relaxation processes that arise from the interaction of the system with its environment. Longitudinal or spin-lattice relaxation processes change the relative population of the spin states to their equilibrium state with a relaxation time T_1, whereas transverse or spin-spin relaxation processes remove the phase coherence of the spin packets with a characteristic relaxation time T_2. Both relaxation processes are important in continuous-wave and pulse EPR experiments.

Spin-lattice relaxation recovers the thermal equilibrium of the spin system by dissipating energy of the excited system to its environment, *i.e.* the lattice. In liquids, Brownian motion and intramolecular structural dynamics modulate the anisotropic dipolar couplings that can arise from electron Zeeman, hyperfine, exchange, or electron dipole-dipole interactions.[70] This generates fluctuating local magnetic fields that can induce transitions between the electron spin states. In solids, longitudinal relaxation is caused by lattice vibrations that result in the absorption or stimulated emission of phonons by the paramagnetic system. Modulation of the spin–orbit coupling by lattice vibrations is often a major source of the fluctuating magnetic fields. Consequently, transition metal ions with large spin–orbit coupling constants exhibit faster spin-lattice relaxation than organic molecules.

Three major relaxation processes can contribute to the spin-lattice relaxation in solids, and their prevalence depends on the temperature, the magnetic field strength, and the nature of the spin system: in the direct process the lattice phonon energy matches the electron Zeeman energy and induces spin flips by phonon absorption or emission, the Raman process results from a two-phonon excitation-relaxation sequence involving a virtual state, and the Orbach process involves resonant two-phonon excitations-relaxations via a real high-energy state.[70, 71] The spin lattice relaxation time T_1 can be approximately measured with a pulse EPR inversion recovery experiment (contributions from spectral diffusion to the recovery constant can result in a deviation from T_1).

Spin-spin relaxation results in the loss of phase coherence in the XY plane of the rotating frame and is caused by dipole interactions with nearby spins without energy dissipation to the lattice. In pulse EPR spectroscopy, the phase memory time T_m is used as an empirical parameter to describe phase coherence and is determined from the decay of the primary echo with increasing interpulse delays τ. The phase memory time T_m encompasses any process that results in a loss of electron spin phase coherence and includes the intrinsic spin-spin relaxation time T_2. Spin transitions of a nuclear or electron spin B that is coupled to the electron spin A result in fluctuating local magnetic fields on A that in turn causes a spin transition of A. This energy conserving process is called a spin flip-flop. In dilute environments with isolated electron spins, nuclear spin flip-flops are the dominant source of decoherence, and the relaxation process is called nuclear spin diffusion. Larger coherence times can be achieved by replacing protons on the paramagnetic sample or in the solvent matrix with deuterons. The smaller magnetic moment and weaker dipole coupling between deuterons and electron spins reduces the prevalence of nuclear spin diffusion. Spin-lattice relaxation processes can also remove spin coherence and contribute to T_2. However, for spin systems at low temperature, T_1 is substantially longer than T_2 and the contributions of spin-lattice relaxation to the loss of phase coherence are negligible. Additional sources for the loss of electron spin phase coherence are spectral

diffusion for systems where only parts of the spectrum are excited, and instantaneous diffusion in systems with coupled electron spins.

To obtain an undistorted EPR signal, relaxation processes must dissipate the energy of the excited spin system fast enough to avoid saturation by repeated microwave excitation. This can be quantified with the saturation factor, s, in equation 1.36

$$s = \frac{1}{1 + \gamma^2 B_1^2 T_1 T_2} \tag{1.36}$$

where γ is the electron gyromagnetic ratio and B_1 is the strength of the microwave magnetic field. As discussed in Section 1.2.3.2, the spin-spin relaxation time T_2 also determines the peak-to-peak linewidth Γ of homogeneously broadened EPR transitions in a cw-EPR spectrum *via* lifetime broadening. Furthermore, during a pulse EPR experiment, spin-spin relaxation determines the maximum length of the pulse sequence, whilst spin-lattice relaxation dictates the minimum repetition time of the experiments.

1.2.3.8 Mims ENDOR Spectroscopy

Hyperfine couplings between electron and nuclear spins, introduced in Section 1.2.2.4, provide important information about the spatial distribution of the electron spin and its environment. These interactions are however often poorly resolved in cw-EPR and field sweep pulse EPR experiments and give rise to inhomogeneous broadening. To overcome this limitation, several pulse EPR experiments have been developed to measure the hyperfine interactions of a spin system directly. Two main classes of experiments can be differentiated based on the excited transitions: electron nuclear double resonance (ENDOR) experiments excite electron and nuclear transitions with a combination of microwave and radiofrequency pulses, while electron spin echo envelope modulation (ESEEM) experiments such as hyperfine sublevel correlation (HYSCORE) only excite electron transitions. Here, the Mims ENDOR pulse sequence used in this thesis to measure proton and nitrogen hyperfine interactions at different microwave frequencies is introduced.

Pulse ENDOR techniques are based on polarization transfer between electron and nuclear transitions and require spin-lattice relaxation times that are slower than the length of the pulse sequence. These experiments are therefore typically performed at low temperatures in a solid matrix. The Mims ENDOR pulse sequence consist of three non-selective microwave $\frac{\pi}{2}$ pulses that generate a stimulated echo, and a radiofrequency π pulse that is applied during the mixing time T (Figure 1.13A).[94]

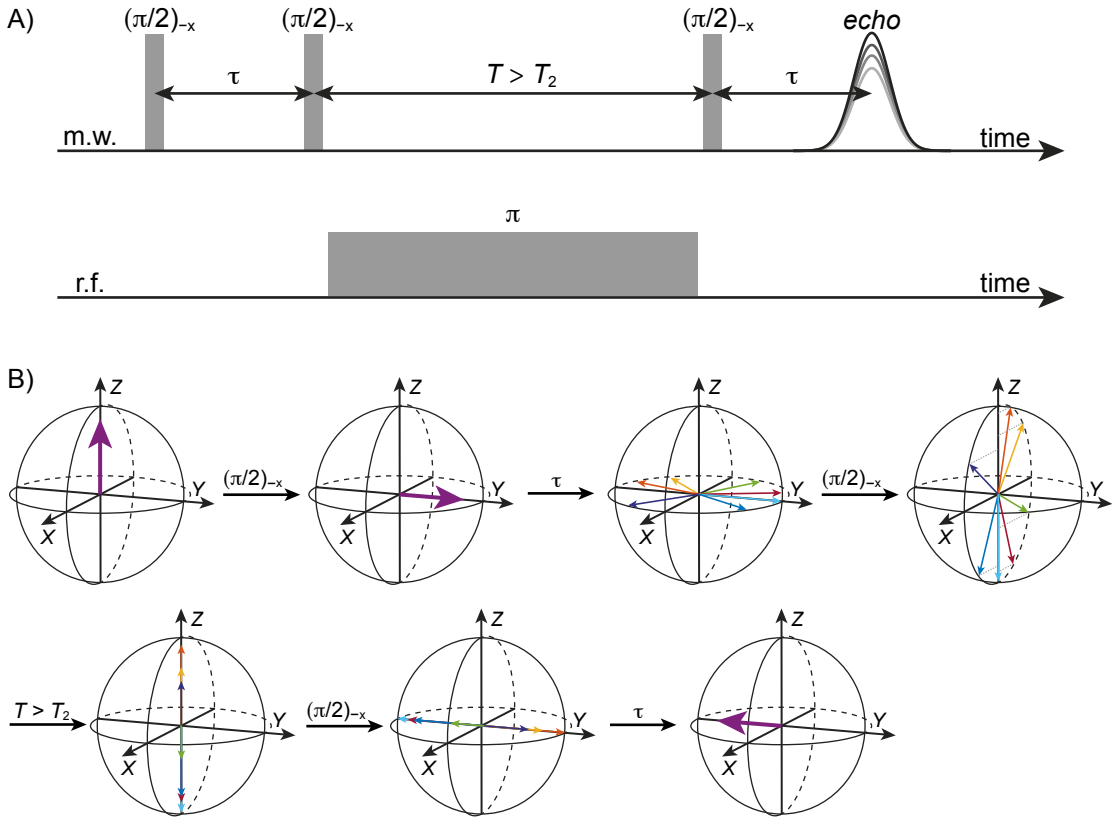


Figure 1.13: A) Schematic visualization of the Mims ENDOR pulse sequence. B) Vector model diagrams that show the evolution of the electron magnetization vectors in the rotating frame during the Mims ENDOR sequence. The large purple vectors indicate the net magnetization; smaller vectors correspond to individual spin packets.

In short, the first two $\frac{\pi}{2}$ pulses generate a grated polarization pattern over the EPR line which is stored during T as longitudinal magnetization along the Z axis of the rotating frame. In more detail, this can be visualized using the vector model introduced in Section 1.2.3.5: The first $\frac{\pi}{2}$ pulse results in a non-equilibrium magnetization in the XY plane (transverse magnetization), and the individual spin packets precess around the Z axis of the rotating frame during the interpulse delay τ. The precession frequency

and direction of the magnetization vectors depends on their resonance offset $\Delta\omega$, which depends amongst other factors on the magnitude of the hyperfine coupling. The second $\frac{\pi}{2}$ pulse transfers the coherences at time τ into polarizations along the Z axis. Due to the distribution of spin packets in the XY plane, the longitudinal magnetization varies sinusoidally over the EPR line with a periodicity of $\frac{2\pi}{\tau}$.[94] During the mixing time $T \gg T_2$, a selective radiofrequency π pulse is applied to the spin system followed by the third microwave $\frac{\pi}{2}$ pulse that transfer the electron populations to coherences for detection. If the radiofrequency pulse is off resonance with the nuclear spin transitions, the electron coherences refocus after the time τ and give rise to the stimulated echo. Radiofrequency pulses that induce a nuclear spin transition result in a frequency shift of the EPR polarization with a magnitude determined by the hyperfine interaction, which prevents the corresponding spin packets to refocus at time τ in the XY plane and reduces the echo intensity. The Mims ENDOR spectrum is obtained by stochastically varying the resonance frequency ν_{rf} of the rf π pulse over the desired frequency range while the stimulated echo intensity is recorded as a function of ν_{rf}.

The Mims ENDOR intensity I varies periodically as a function of the hyperfine interaction A and the interpulse delay τ following equation 1.37.

$$I = \frac{1}{4}\left(1 + \cos\left(A\tau\right)\right) \tag{1.37}$$

This results in maximum ENDOR efficiency for $\tau = \left(n + \frac{1}{2}\right)A^{-1}$ and a vanishing ENDOR effect for $\tau = nA^{-1}$ that gives rise to blindspots in the spectrum ($n = 0, 1, 2, ...$). To obtain an accurate description of the hyperfine interactions in a system, several Mims ENDOR spectra acquired with different τ values are typically combined to minimize distortions arising from the blindspots.

Mims ENDOR spectra have peaks at the radiofrequencies that induce nuclear spin transitions. In the weak coupling regime ($A < 2\nu_L$), the ENDOR transitions of an $S = \frac{1}{2}$ system are symmetrically split around the nuclear Larmor frequency ν_L, whereas hyperfine interactions in the strong coupling regime ($A > 2\nu_L$) result in transitions

centered at $\frac{A}{2}$ and split by $2\nu_L$. The nuclear Larmor frequency $\nu_L = g_n\mu_n B_0\hbar^{-1}$ is characteristic for each nucleus and increases linearly with the strength of the external magnetic field B_0.

As Mims ENDOR spectra are typically recorded in a solid matrix, the anisotropy of the hyperfine interactions can be resolved. Proton hyperfine interactions are typically much smaller than the corresponding Larmor frequency and appear in the weak coupling regime. Due to the smaller Larmor frequency of ^{14}N nuclei, hyperfine interactions can occur in the strong coupling regime at X-band frequencies, and higher B_0 field strengths at Q- or W-band frequencies are required to obtain ENDOR spectra in the weak coupling regime. The general structure of selected ^{1}H and ^{14}N Mims ENDOR spectra in the weak coupling regime is shown in Figure 1.14. Noticeably, the nuclear quadrupole interaction of the ^{14}N nuclei ($I = 1$) results in additional splitting of the ENDOR transitions and can cause complicated splitting patterns in the case of an orthorhombic nuclear quadrupole tensor and anisotropic hyperfine interactions.

Mims ENDOR spectroscopy of systems with multiple nuclei and similar hyperfine interactions often result in unresolved spectral shapes and prevents the direct identification of individual hyperfine interactions. In such cases, simulation of the ENDOR spectrum starting from calculated hyperfine tensors is required to determine the hyperfine interactions of the system. As discussed in Section 1.2.3.6, excitation of a subset of orientations in spectra with large g-anisotropy or zero–field splitting interactions can be used to obtain additional information about the relative orientation of the hyperfine tensors and the $\boldsymbol{g}$- or $\boldsymbol{D}$-tensor. Experimental ENDOR spectra typically exhibit a matrix peak at the Larmor frequency that arises from dipolar hyperfine interactions with distant nuclei of the molecule or the solvent. Using deuterated solvents for ^{1}H ENDOR experiments reduces the magnitude of the matrix peak.

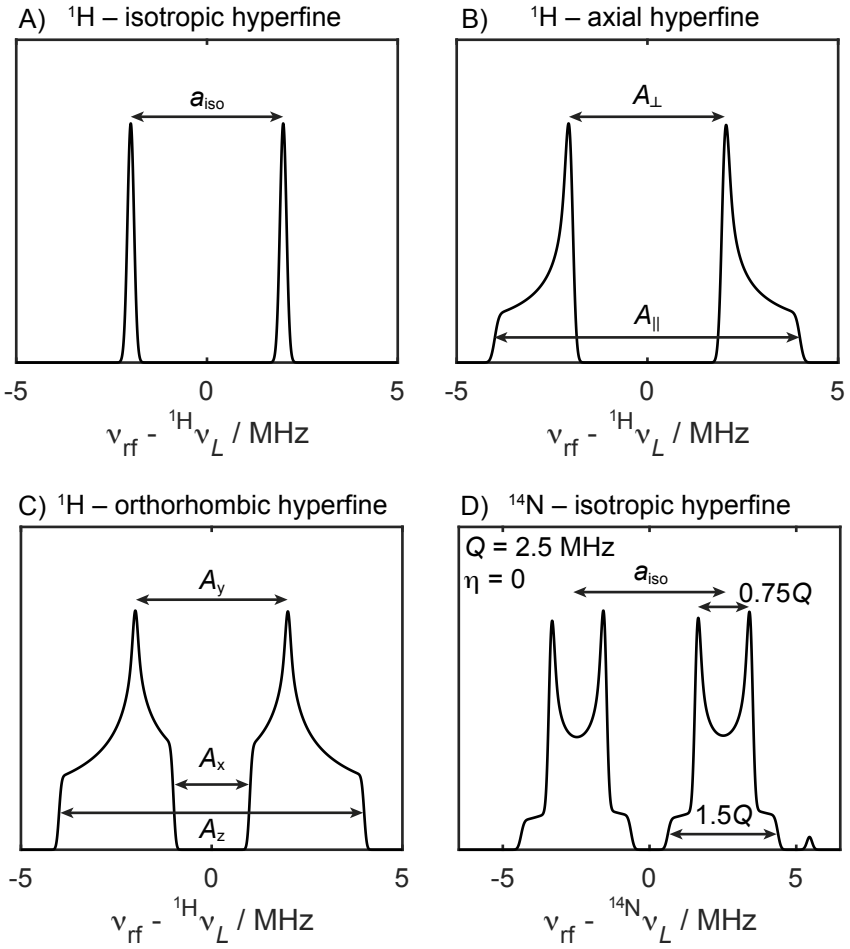


Figure 1.14: Simulated ^{1}H ENDOR spectra of a single nucleus with an A) isotropic, B) axial, and C) orthorhombic hyperfine tensor in the weak coupling regime. D) The simulated ENDOR spectrum for a single ^{14}N nucleus with an isotropic hyperfine interaction and an axial nuclear quadrupole tensor highlights the further splitting of the ENDOR transitions for nuclei with $I > \frac{1}{2}$.

Davies ENDOR with the microwave pulse sequence $\pi - T - \frac{\pi}{2} - \tau - \pi - \tau - echo$ and a radiofrequency π pulse applied during the mixing time T is an alternative way to measure hyperfine interactions.[95] Davies ENDOR spectra do not exhibit τ dependent blindspots and are generally used to measure hyperfine interactions larger than 6 MHz. A strong limitation of Davies ENDOR is its low sensitivity because the initial π pulse that generates polarization must be selective. In Mims ENDOR experiments, nonselective pulses with broad excitation bandwidths can be employed, which increases the number of spin packets contributing to the ENDOR signals and therefore the sensitivity.

1.3 Charge and Spin Delocalization

The origin of the field of molecular electronics dates back to the proposal by Aviram and Rattner in the early 1970s that a single molecule consisting of a donor and acceptor connected by a tunneling barrier can act as a molecular rectifier.[96] Since then, the idea of miniaturizing conventional electronic devices to the molecular scale has attracted substantial research that is motivated by the prospect of faster performances and higher packing densities of molecular semiconductors beyond the capabilities of silicon based electronic devices.[97–99] In addition, the quantum nature of charge transport in molecules can give rise to unique effects such as quantum interference[100, 101], the Coulomb blockade[102], and Kondo effects[102, 103] that are not accessible in the bulk materials.[99]

Porphyrins are versatile building blocks for single-molecule electronic devices due to their synthetic tractability, which allows for the rational design of their electronic properties, their distinctive redox chemistry that enables reversible oxidation and reduction of the porphyrin π-system, and their metal binding ability.[104–107] A variety of linkers have been explored in the literature to connect porphyrin monomers into molecular architectures.[108–111] Amongst them, π-conjugated butadiyne- and ethyne-linkers have gained particular interest as they convey moderate electronic coupling between neighbouring porphyrin units and direct a linear arrangement of monomers suitable for applications as molecular wires (Figure 1.15).[64, 108, 112]

Connecting neighbouring porphyrin units with three covalent bonds between their β and *meso* positions yields the edge-fused porphyrin tapes pioneered by Osuka in 2001 with strong π-conjugation along the molecular chain (Figure 1.15).[112, 113] The rational design and synthesis of porphyrin nanomaterials with tailored electronic properties opens up new applications in many areas of molecular electronics and requires a fundamental understanding of the relationship between the structure of a molecule and its ability to delocalize charge and spin density.

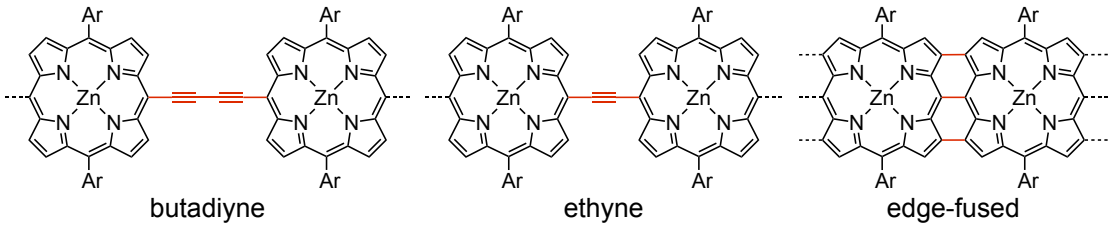


Figure 1.15: General chemical structure of butadiyne-, ethyne-, and β,*meso*,β-linked porphyrin oligomers; Ar = solubilizing group.

Porphyrin oligomers that efficiently delocalize charge carriers over long distances are promising candidates for applications as molecular wires.[51, 83, 114, 115] The effective delocalization length of a material can be studied by introducing charge carriers into the molecule *via* oxidation or reduction. The spatial delocalization of the radical is then determined using EPR or optical spectroscopy.[51, 83, 85, 116] EPR spectroscopy probes the interaction of the radical spin density with the molecular framework to determine the distribution of the spin carrier, whereas optical spectroscopy gives insight into the bathochromic shift of the lowest energy absorption band upon oxidation or reduction.

Additionally, the spin distribution of photogenerated triplet excitons in the photosynthetic reaction center and porphyrin based model systems has been extensively investigated by EPR spectroscopy and provided pivotal information for our understanding of photosynthetic light harvesting.[117–121] Porphyrin oligomers are also important model systems for investigating the spatial delocalization of triplet excitons in artificial molecular wires.[52, 87, 122–126] Achieving long range triplet delocalization in conjugated materials is important for the design of high-performance optoelectronic devices such as organic light-emitting diodes and organic photovoltaics.[127]

Cyclic molecular wires, with efficient electronic transmission around their circumference, can exhibit enhanced performance as organic semiconductors because their high symmetries lead to greater delocalization than in linear chains.[128–130] This is promising for applications in organic solar cells[130, 131], light-emitting diodes[132–135], photodetectors[136, 137], and sensors[138–140]. In addition,

global currents in molecular nanorings are directly related to the fundamental concept of aromaticity and are postulated as molecular analogues of persistent currents observed in mesoscopic metal rings.[54–56]

In the following sections, the concepts of organic mixed valency and aromaticity relevant to the work in this thesis will be introduced.

1.3.1 Organic Mixed Valence Systems

Organic mixed valence compounds consist of two or more redox centers with different formal oxidation states.[141, 142] Marcus theory[143, 144] provided the first theoretical framework to describe intramolecular electron transfer processes in mixed valence systems and was later extended to Marcus–Hush theory to allow for the analysis of mixed valence systems with large coupling between the individual redox sites.[145, 146] The two-state Marcus–Hush model for a general mixed valence system with two identical redox sites (a and b) of which one is oxidized is introduced below.[141, 145, 147]

The free energy of the two localized states Ψ_a and Ψ_b in the absence of coupling is described by their diabatic harmonic potentials in equation 1.38

$$\begin{aligned} \Psi_a &= \lambda x^2 \\ \Psi_b &= \lambda (x-1)^2 \end{aligned} \tag{1.38}$$

where x is the reaction coordinate of the intramolecular electron transfer and λ is the reorganization energy. The adiabatic ground and excited states Ψ_1 and Ψ_2 of the mixed valence system arise from the mixing of the diabatic states following equation 1.39

$$\begin{aligned} \Psi_1 &= c_{11}\Psi_a + c_{21}\Psi_b \\ \Psi_2 &= c_{12}\Psi_a + c_{22}\Psi_b \end{aligned} \tag{1.39}$$

where c_{ij} are the normalized mixing coefficients of the diabatic potentials. The squares of the mixing coefficients $|c_{ij}|^2$ determine the population of the charge carrier on each redox site in the ground or excited state. The free energy surfaces of the ground and

excited states, G_1 and G_2, are obtained following equation 1.40 by finding the solutions at each reaction coordinate x for which the secular determinant is equal to zero.

$$\begin{vmatrix} x^2 - G/\lambda & H_{ab}/\lambda \\ H_{ab}/\lambda & (x-1)^2 - G/\lambda \end{vmatrix} = 0 \tag{1.40}$$

Organic mixed valence systems can be classified based on the ratio of the electronic coupling between the individual redox sites, H_{ab}, and the reorganization energy as proposed by Robin and Day[148] (Figure 1.16): i) the electronic coupling between the individual sites is negligible ($H_{ab} \approx 0$) and the charge is predominantly localized on one site of the system (Robin–Day class I); ii) the electronic coupling is significant ($0 < 2H_{ab} < \lambda$) and the diabatic potentials of Ψ_a and Ψ_b mix to give rise to two adiabatic potentials with an energy gap of $2H_{ab}$ at the crossing point (Robin–Day class II); iii) the electronic coupling is so strong ($2H_{ab} > \lambda$) that the mixing results in adiabatic potentials with a single minimum and full charge delocalization over both sites (Robin–Day class III).

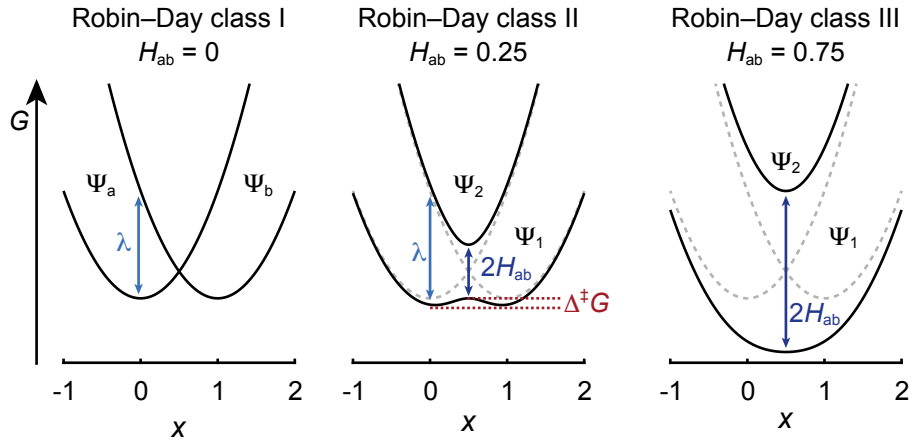


Figure 1.16: Potential energy surfaces for degenerate mixed valence compounds in the three Robin–Day coupling regimes of the two-state Marcus–Hush theory; x is the reaction coordinate for the electron transfer. The dashed lines indicate the potential surfaces of the diabatic potentials.

The vertical excitation energy of a mixed valence system with two minima in the ground state energy surface corresponds to the reorganization energy λ. Photoexcitation of a Robin–Day class I or II compound can result in a photoinduced

electron transfer and the observation of an intervalence charge-transfer (IV-CT) band that typically appears as the lowest energy transition in the optical absorption spectrum.[141] For a Robin–Day class III compound, the vertical excitation energy corresponds to twice the electronic coupling $2H_{ab}$.

The reorganization energy λ is the sum of two contributions: the outer reorganization energy λ_O, which describes the energy required by the solvent molecules to reorganize after an electron transfer, and the inner reorganization energy λ_I, which describes changes in the molecular geometry following the electron transfer. The inner reorganization energy is an intrinsic parameter of each mixed valence system, while the outer reorganization energy is determined by the dielectric properties of the solvent. In a simple approximation, λ_O is given by the dielectric continuum model in equation 1.41

$$\lambda_O = \frac{\Delta e^2}{4\pi\epsilon_0}\left[\frac{1}{2r_1}+\frac{1}{2r_2}-\frac{1}{r_{12}}\right]\left[\frac{1}{n^2}-\frac{1}{\epsilon}\right] \tag{1.41}$$

where Δe is the transferred charge, ϵ_0 is the vacuum permeability, r_1 and r_2 are the radii of the two spherical redox centers, r_{12} is the distance between the redox centers, n is the refractive index of the solvent, and ϵ is the solvent dielectric constant.[141, 143, 149] The rate of a thermally induced electron transfer k between the redox centers of a mixed valence system is given by the Arrhenius relationship in equation 1.42

$$k = A\exp\left(\frac{-\Delta^{\ddagger}G}{k_B T}\right) \tag{1.42}$$

where $\Delta^{\ddagger}G$ is the activation free energy and the pre-exponential factor A depends on the transmission probability through the transition state. In Marcus–Hush theory, the activation energy of a degenerate mixed valence compound is dominated by the reorganization energy and reduced by the magnitude of the electronic coupling H_{ab} following equation 1.43.

$$\Delta^{\ddagger}G = \frac{\lambda}{4} - H_{ab} \tag{1.43}$$

In the limit of a diabatic electron transfer with $H_{ab} \approx 0$, equation 1.43 is identical to the expression for the free energy of activation in Marcus theory.

Compared to their neutral analogues, radical cations of π-conjugated materials typically feature two characteristic low energy absorption bands P_1 and P_2 in their optical absorption spectra that approximately correspond to their HOMO → SOMO and SOMO → LUMO transitions, respectively (Figure 1.17).[150–152] The lowest energy absorption band of the radical cations is especially important for understanding their electronic structure and can be used to estimate the reorganization energy λ in Robin–Day class I/II systems and the electronic coupling energy H_{ab} in Robin–Day class III compounds. In addition, the trend in the lowest energy absorption band for a family of oligomers can be used to estimate the effective conjugation length.

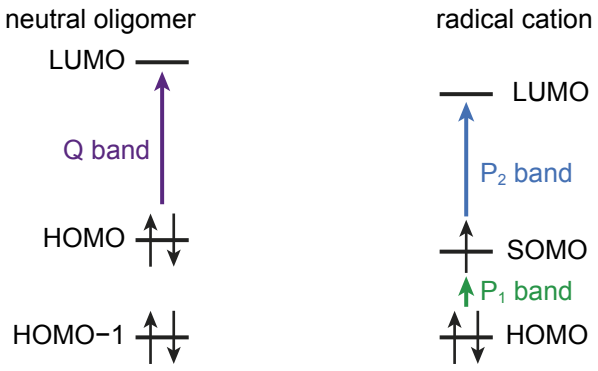


Figure 1.17: Schematic illustration of the optical signatures of a neutral and charged π-conjugated oligomer. HOMO, LUMO and SOMO denote the highest occupied molecular orbital, lowest unoccupied molecular orbital, and singly occupied molecular orbital, respectively.

1.3.2 Aromaticity on the Nanoscale

Aromaticity is one of the central concepts in chemistry and influences a wide range of molecular properties such as thermodynamic stability, chemical reactivity, molecular geometry, and magnetic susceptibility.[54, 153, 154] Hückel's rule is widely used to predict if a molecule is aromatic: conjugated macrocycles with $4n + 2$ π-electrons are aromatic whereas those with $4n$ π-electrons are antiaromatic.[155–157] This aromaticity rule was derived from Hückel molecular orbital theory, which is introduced

briefly below.[158, 159] The molecular orbitals of polyatomic molecules can be described by a linear combination of atomic orbitals (LCAO) following equation 1.44

$$\Psi = \sum_i c_i \phi_i \tag{1.44}$$

where Ψ is the wavefunction of the molecular orbital, ϕ_i is the wavefunction of an atomic orbital i, and c_i is the coefficient that determines the contribution of the atomic orbital to the molecular orbital.[160] In the Hückel approximation, the π orbital of a conjugated molecule is described as a linear combination of carbon $2p_z$ orbitals perpendicular to the molecular plane. The Hückel Hamiltonian can then be expressed as a function of the Coulomb integral α and the resonance integral β, which correspond to the energy of electrons in the carbon $2p_z$ orbital and the bonding energy between $2p_z$ orbitals, respectively. With the additional Hückel approximations that i) all carbon atoms are treated identically, ii) the resonance interactions between non-neighbouring atoms are 0, and iii) the resonance integrals between neighbouring atoms are equal, the general Hückel Hamiltonians for linear (equation 1.45) and cyclic (equation 1.46) π-systems are obtained.

$$\hat{\mathscr{H}}_{\text{chain}} = \begin{bmatrix} \alpha & \beta & 0 & \cdots & 0 \\ \beta & \alpha & \beta & \cdots & 0 \\ \vdots & \vdots & \vdots & \ddots & \beta \\ 0 & 0 & 0 & \beta & \alpha \end{bmatrix} \tag{1.45}$$

$$\hat{\mathscr{H}}_{\text{ring}} = \begin{bmatrix} \alpha & \beta & 0 & \cdots & \beta \\ \beta & \alpha & \beta & \cdots & 0 \\ \vdots & \vdots & \vdots & \ddots & \beta \\ \beta & 0 & 0 & \beta & \alpha \end{bmatrix} \tag{1.46}$$

Diagonalization of the Hamiltonians gives the molecular orbital energies in equations 1.47 and 1.48

$$E_{\text{chain}} = \alpha + 2\beta \cos\left(\frac{\pi(j+1)}{n+1}\right) \tag{1.47}$$

$$E_{\text{ring}} = \alpha + 2\beta \cos\left(\frac{2\pi j}{n}\right) \tag{1.48}$$

where n is the number of atomic orbitals contributing to the molecular orbital and j is a quantum number that can take values $j = 0, 1, \cdots, (n-1)$ for linear systems and $j = 0, \pm 1, \cdots, \pm\left(\frac{n}{2} - 1\right), \frac{n}{2}$ for cyclic systems.

The molecular orbital energies obtained from Hückel calculations are often presented using Frost–Musulin diagrams that give an intuitive picture of the molecular orbitals of cyclic systems. They are obtained by drawing a polygon with the same number of corners as carbon atoms in the conjugated molecule on a circle and placing a molecular orbital on each point where the polygon touches the circle.[161] The molecular orbital diagrams obtained from Hückel calculations of the $4n + 2$ π-systems 1,3,5-hexatriene and benzene and the $4n$ π-systems 1,3-butadiene and cyclobutadiene are shown in Figure 1.18. The total π-electron binding energies in

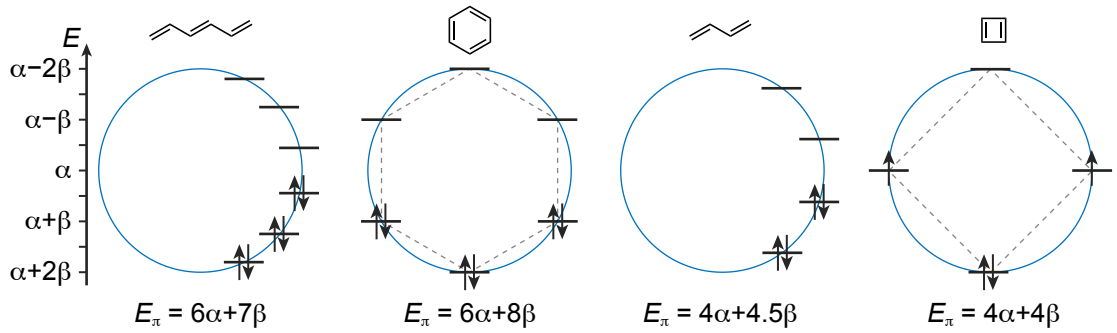


Figure 1.18: Hückel molecular orbital diagrams of the $4n + 2$ π-systems 1,3,5-hexatriene and benzene and the $4n$ π-systems 1,3-butadiene and cyclobutadiene. The total π-electron binding energies of the systems are given as E_π.

Figure 1.18 demonstrate that the aromatic $4n + 2$ π-electron macrocycle benzene is stabilized by 1β relative to its linear analogue while the antiaromatic $4n$ π-electron macrocycle cyclobutadiene is destabilized by 0.5β in comparison to 1,3-butadiene. In practice, the HOMO degeneracy of cyclobutadiene is typically lifted by a pseudo-Jahn-Teller distortion to give a closed-shell configuration with a small HOMO-LUMO energy gap.[162]

An exact quantum mechanical description of aromaticity has not yet been realized due to the lack of an appropriate operator that unambiguously defines the

concept.[154] Instead, a variety of experimental parameters such as bond-length alternation, energetic stabilization, or reactivity have been employed to provide indirect evidence for the aromaticity of a system.[163–167] In this thesis, the magnetic behaviour of a molecule is used to determine its aromaticity. Aromatic molecules sustain diatropic ring currents in an external magnetic field that create an induced magnetic field opposite to the external field inside the rings. Consequently, nuclei inside the aromatic macrocycle are shielded from the external field which results in an upfield shift (smaller chemical shift values δ) of their nuclear magnetic resonance (NMR) transitions. Nuclei outside the ring are deshielded and shifted to higher chemical shifts. Antiaromatic molecules sustain paratropic ring currents in the opposite direction which results in a deshielding of resonances in the ring and a shielding of resonances outside the ring.[54, 168]

Aromaticity was traditionally viewed as a property of small molecules, and it has been predicted by many theoretical studies that [N]annulenes would be non-aromatic for $N > 30$.[169–172] However, in recent years numerous larger conjugated macrocycles with global aromatic ring currents have been reported.[173–175] For instance, porphyrin nanoring complexes introduced in Section 1.1 exhibit global (anti)aromatic ring currents in their oxidized, reduced, and photoexcited states.[54–56, 176, 177] To date, the largest macrocycle exhibiting global charge delocalization and aromaticity is a butadiyne-linked 12 porphyrin nanoring ***c*-P12[$\mathbf{b_{12}}$]** in its 6+ oxidation state (162 π-electrons in the conjugation pathway, $n = 40$).[55] The presence and character of a global ring current around the circumference of a porphyrin nanoring complex is established based on the induced chemical shift differences of resonances inside and outside the ring. This is exemplified for the 6-porphyrin nanoring complex ***c*-P6[$\mathbf{b_6}$]·($\mathbf{T6_F}$)** first investigated by Peeks, Rickhaus, and Jirasek (Figure 1.19A).[55, 56]

The induced magnetic field lines are focused towards the internal edges of the ring and consequently, resonances located within the circumference of the ring will be affected to a larger extent by a global current than resonances located on the outside

(Figure 1.19B,C). The most characteristic resonances of the nanoring complex are the ^{1}H NMR signals of the trihexylsilyl (THS) solubilizing sidechains and the ^{19}F NMR signals of the CF_3 groups on the template. Interconversion of the THS environments pointing inside (THS_{in}) and outside (THS_{out}) the ring is slow on the NMR time scale.

In its neutral oxidation state, ***c*-P6[b_6]·($T6_F$)** does not exhibit global ring currents and each individual porphyrin unit is characterized by a localized aromatic ring current. The shielding of the THS_{in} and ^{19}F resonances inside the nanoring complex in its 2+ and 6+ oxidation states demonstrates the presence of a global diatropic ring current consistent with an aromatic character of the nanoring. In the 4+ oxidation state, the resonances inside the nanoring are deshielded by a global paratropic ring current around the circumference of the antiaromatic nanoring (Figure 1.19D). These observations are consistent with the Hückel $4n + 2$ rule for aromaticity (2+ state: 82 π-e^-, $4n + 2$, $n = 20$; 4+ state: 80 π-e^-, $4n$, $n = 20$; 6+ state: 78 π-e^-, $4n + 2$, $n = 19$).

The difference in chemical shift $\Delta\delta$ between resonances inside the nanoring complex in the presence of a global ring current and the corresponding resonances in the neutral nanoring complex is directly related to the strength of the induced ring current. This is evident from the Biot–Savart law that predicts a directly proportional relationship between the magnitude of the induced magnetic field and the strength of an induced ring current.[178] The aromaticity of a macrocycle can also be investigated by nucleus independent chemical shift (NICS) calculations: a grid of Banquo atoms is placed around the geometry optimized structure of the investigated molecule, and the NMR shielding of the atoms is calculated by density functional theory (DFT) (Figure 1.19B,C).[179] It should however be noted that the obtained shielding values are highly dependent on the DFT functional employed in the calculations and are best interpreted in combination with experimental NMR results.[180]

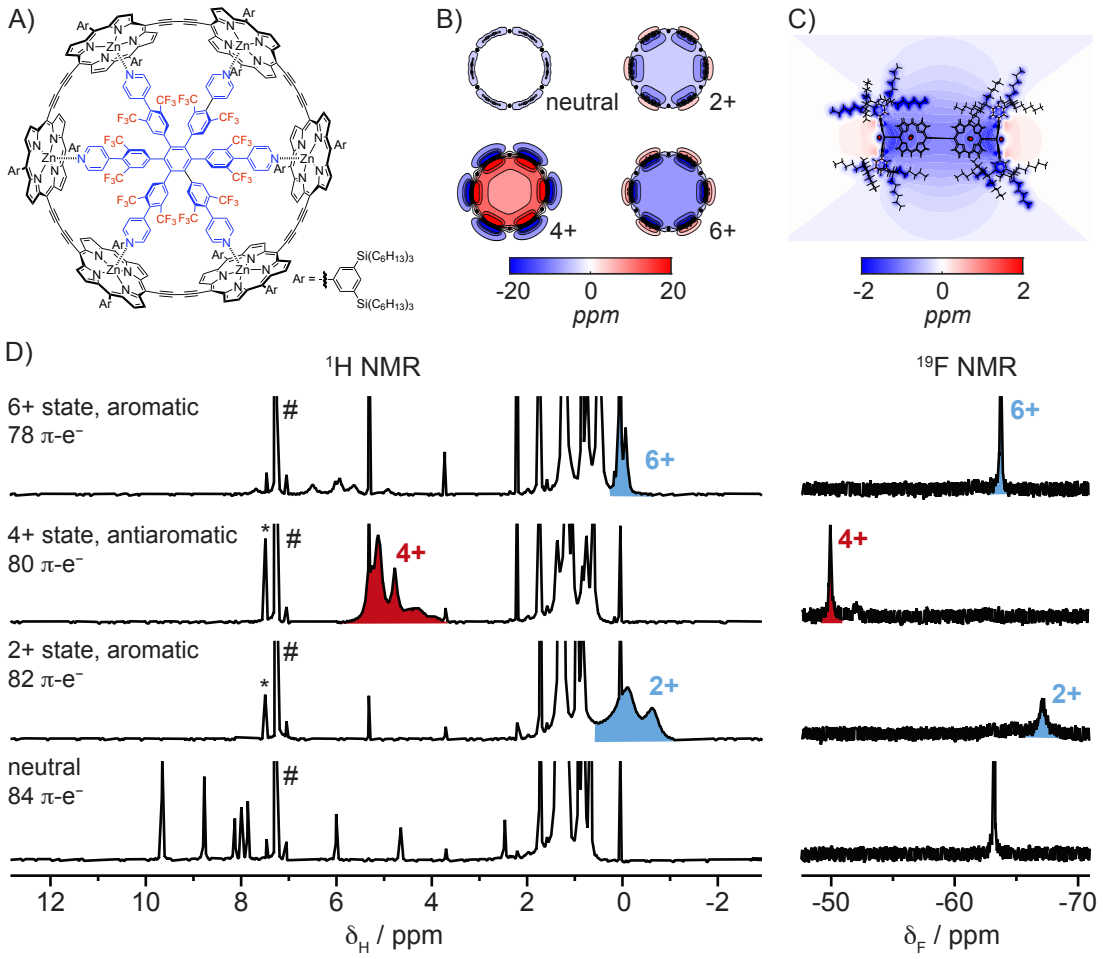


Figure 1.19: A) Chemical structure of the porphyrin nanoring complex ***c*-P6[b$_6$]·(T6$_F$)**. B) DFT (BLYP35/6-31G*) calculated NICS(0)$_{ZZ}$ grids in the plane of the 6-porphyrin nanoring in each investigated oxidation state. C) DFT (BLYP35/6-31G*) calculated NICS(0)$_{iso}$ values perpendicular to the molecular plane of ***c*-P6[b$_6$]** in its 2+ oxidation state. D) Experimental ^{1}H and ^{19}F NMR (500/471 MHz, 233 K, $CDCl_3$) spectra of ***c*-P6[b$_6$]·(T6$_F$)** in the predominat oxidation states 0, 2+, 4+, and 6+. THS$_{in}$ and CF_3 resonances indicating global antiaromaticity are highlighted in red; those indicating global aromaticity are highlighted in blue. Peaks assigned with # and * arise from $CHCl_3$ and neutral thianthrene, respectively.

1.4 Prospective

This thesis aims to demonstrate how changing the molecular or electronic structure of linear and cyclic porphyrin nanomaterials can be used to control charge and spin delocalization. To this end, synthesis, electron paramagnetic resonance and nuclear magnetic resonance spectroscopy, optical spectroscopy, quantum chemical calculations, and modeling are combined. In Chapter 2, the spatial delocalization of hole polarons in *β*,*meso*,*β*-triply linked porphyrin nanoribbons is investigated.

The strong electronic coupling conveyed by the three covalent bonds connecting neighbouring porphyrin units results in remarkably efficient polaron delocalization, which informs the potential application of porphyrin nanoribbons as molecular wires. In Chapter 3, the charge and spin transfer dynamics in a weakly coupled porphyrin dimer are studied. The intramolecular electron transfer dynamics in the radical cation of the porphyrin dimer inform the design of a proposed single-molecule spin valve. In addition, the electronic structure of the radical cation is compared with the spin distribution in the photogenerated triplet state of the dimer. Chapter 4 focuses on enhancing the delocalization of photogenerated triplet states in linear porphyrin wires. It is demonstrated that chemical reduction of the porphyrin wire followed by photoexcitation substantially increase the spatial distribution of the triplet state. The final two chapters focus on the synthesis of a new class of porphyrin nanoring complexes composed of both β,*meso*,β-edge-fused porphyrin tape dimers and butadiyne-linked porphyrins. It is shown that this molecular design can enhance the effective π-conjugation in the porphyrin nanoring complexes. The effects of this enhanced conjugation on the global charge delocalization and aromaticity in an oxidized partially fused 8-ring (Chapter 5) and an oxidized and reduced partially fused 12-ring (Chapter 6) are investigated.

2

Cationic Polaron Delocalization in Porphyrin Nanoribbons

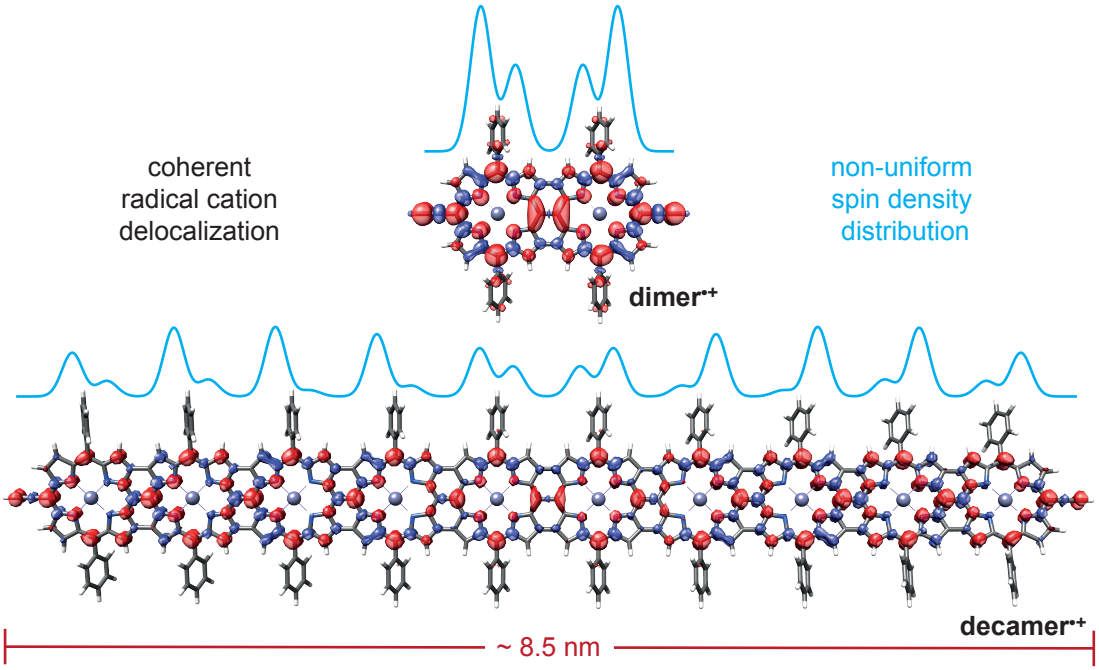
Contents

2.1 Abstract 54
2.2 Introduction 55
2.3 Results and Discussion 56
2.3.1 Synthesis of Porphyrin Oligomers 56
2.3.2 Continuous-Wave EPR Spectroscopy 57
2.3.3 Investigation of the Spin-Density Non-Uniformity 64
2.3.4 W-band Pulse EPR Spectroscopy 67
2.3.5 Mims ENDOR Spectroscopy 70
2.3.6 ^{14}N HYSCORE Spectroscopy 77
2.3.7 Accidental Oxidation of Extended Nanoribbons 79
2.3.8 Optical vis-NIR-MIR Spectroelectrochemistry 81
2.4 Summary and Conclusion 87
2.5 Methods 89
2.5.1 General Methods 89
2.5.2 Distributed Point-Dipole Simulations 94
2.6 Supplemental Results and Analysis 102

The work in this chapter was published in:

S. M. Kopp, J.-R. Deng, A. J. Redman, H. Gotfredsen, R. M. J. Jacobs, H. L. Anderson, C. R. Timmel, *Cationic Polaron Delocalization in Porphyrin Nanoribbons*, *Chem*, **2024**, DOI: 10.1016/j.chempr.2024.07.011.

2.1 Abstract



Long-range delocalization of unpaired electrons in organic π-conjugated oligomers is an important requirement to achieve high charge carrier mobilities in molecular transistors. In this chapter, the polaron delocalization in the radical cations of a series of β,*meso*,β-edge-fused porphyrin oligomers consisting of up to 18 porphyrin units is investigated by a combination of cw-EPR, ^{1}H and ^{14}N ENDOR, HYSCORE and vis-NIR-MIR absorption spectroscopy, supported by DFT calculations and simulations. The results demonstrate coherent delocalization of the radical cation over more than ten porphyrin units, which corresponds to an effective coherence length > 8.5 nm. This marks, to the best of my knowledge, the longest coherently delocalized polaron reported in π-conjugated materials to date. This study also shows a remarkably non-uniform distribution of the radical spin density and an increase in phase memory time with increasing delocalization length (up to $T_m \sim 4$ µs at 50 K). These findings open new avenues towards the design of molecular electronic and spintronic materials.

2.2 Introduction

The one-electron oxidation of a π-conjugated polymer to its radical cation results in a reorganization, or polarization, of the molecular framework and solvent environment.[141, 181, 182] This combination of the unpaired electron, positive charge, and associated structural changes comprise a hole polaron.[183] Maximizing the polaron spatial coherence lengths is essential for the design of organic semiconductors for efficient charge transport in organic solar cells and field-effect transistors.[184–191] In addition, organic polymers with long coherence times and extended polaron delocalization are promising building blocks to sustain spin-polarized currents in molecular spintronics,[192–195] and for fabricating single-molecule electronic devices. Charge transport through an electrode/molecule/electrode junction can either occur by direct tunneling or via multistep hopping.[196, 197] The former mechanism is favored by polaron states delocalized over the entire molecule and is desirable to achieve phase coherent charge transport over long distances.[114]

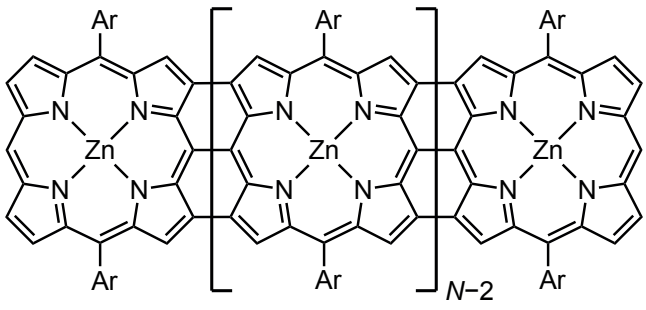


Figure 2.1: Structure of a β,*meso*,β-edge-fused porphyrin nanoribbon with N porphyrin repeat units. Ar is an aromatic solubilizing group.

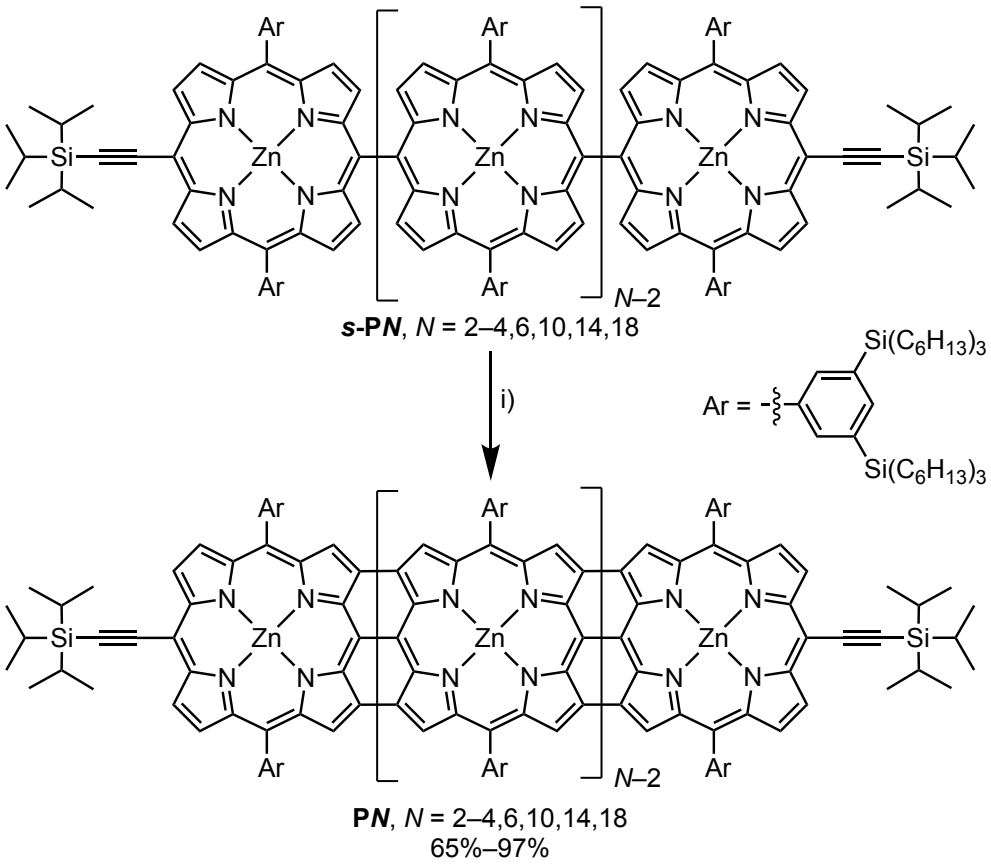
Porphyrin-based molecular wires with ethyne-links between their *meso* positions have been reported to exhibit long-range radical delocalization, with negative polarons spanning 7 porphyrin units (~7.5 nm) and positive polarons delocalized over 5 porphyrin units (~5.6 nm).[83, 85, 86, 116] This efficient polaron delocalization results in high single-molecule conductance.[195, 198, 199] The edge-fused porphyrin oligomers of the type shown in Figure 2.1 pioneered by Osuka are another promising class of molecular wires due to their steeply decreasing π-π^* energy gaps with

increasing oligomer length and the shallow length-dependence of their molecular conductance.[108, 113, 115, 200–203] Recent work has shown that these porphyrin nanoribbons exhibit phase-coherent charge-transport over eight porphyrin units in single-molecule transistors.[114] This has sparked interest in the extent of polaron delocalization in this family of molecular wires.

2.3 Results and Discussion

2.3.1 Synthesis of Porphyrin Oligomers

Meso-meso singly linked porphyrin oligomers with different lengths were synthesized by a combination of silver-mediated oxidative coupling and nickel-mediated Yamamoto coupling, and purified by recycling gel-permeation chromatography. The synthesis of all porphyrin oligomers investigated in this chapter was performed by Dr. Jie-Ren Deng in the research group of Prof. Harry L. Anderson and is reported in detail in his DPhil thesis. The *meso-meso*-singly-linked oligomers ***s*-P*N*** (N = 2–4, 6, 10, 14, 18) were obtained using a Yamamoto oligomerization, bromination of the terminal *meso* positions, and Sonogashira couplings to attach the terminal triisopropylsilyl (TIPS) acetylenes with isolated yields between 1% and 4% over five steps from unsubstituted porphyrin monomer. The role of the terminal TIPS-acetylene units is to protect the ends of the chain during oxidative fusion and to enhance solubility. Subjection of ***s*-P*N*** to oxidative fusion conditions with DDQ and $Sc(OTF)_3$ at 80 °C under argon for 2 hours afforded the β,*meso*,β-triply linked oligomers **P*N*** in good to excellent yields (Scheme 2.1). Monomer **P1** was synthesized as a reference compound following published procedures.[204] Bulky 3,5-bis(trihexylsily)phenyl substituents were attached to both peripheral *meso* positions of each porphyrin unit to improve the solubility of the fused porphyrin oligomers in common organic solvents such as toluene, and to inhibit aggregation. The oxidative fusion reactions of oligomers bearing TIPS-acetylene groups at the terminal *meso* positions were exceptionally efficient; no demetallation and partially fused products were identified from the UV-vis-NIR spectra of the products after the reaction. Partial oxidation of **P*N*** to



Scheme 2.1: Synthesis of β,*meso*,β-triply linked oligomers **P*N*** (N = 2–4, 6, 8, 10, 14, 18) from their singly linked precursors ***s*-P*N***; i) 2,3-dichloro-5,6-dicyano-*p*-benzoquinone (DDQ), $Sc(OTf)_3$, toluene, 80 °C, 2 h.

the radical monocations $\mathbf{PN}^{\bullet+}$ was achieved by addition of 0.5 equivalents tris(4-bromophenyl)-aminium hexachloroantimonate (**BAHA**) in a 1:1:1 solvent mixture of CD_2Cl_2:toluene-d_8:THF-d_8 which forms a glass at low temperatures.[51, 83]

2.3.2 Continuous-Wave EPR Spectroscopy

The room temperature cw-EPR spectra of the radical cations $\mathbf{P1}^{\bullet+}$ to $\mathbf{P4}^{\bullet+}$, $\mathbf{P6}^{\bullet+}$, and $\mathbf{P10}^{\bullet+}$ at X-band frequencies are shown in Figure 2.2A. The spectrum of $\mathbf{P1}^{\bullet+}$ is consistent with those previously reported for similar monomer cations.[51, 83] The nine prominent hyperfine lines in the spectrum arise from an isotropic coupling of $^{14}N a_{iso} = 4.07$ MHz to the four equivalent ^{14}N nuclei of the porphyrin and are further split by an isotropic hyperfine coupling of about $^{1}H a_{iso} = 1.0$ MHz to the four equivalent *ortho*-protons on the aryl rings. The spectrum of $\mathbf{P2}^{\bullet+}$ also shows a partially resolved

hyperfine pattern that arises from coupling to the eight ^{14}N nuclei, whereas the longer oligomers lack a resolved hyperfine structure due to substantial inhomogeneous broadening. If hyperfine interactions are the main contribution to the spectral envelope width ΔB_N and the radical spin-density is completely and uniformly delocalized, the Norris relationship in equation 1.19 can be applied to determine the delocalization length in the series of porphyrin nanoribbons $\mathbf{PN}^{\bullet+}$.[82] Here, complete and uniform delocalization refers to an equal amount of spin-density on each porphyrin unit in a chain with an identical distribution of this spin-density within the porphyrin units.

The spectral envelope widths of $\mathbf{PN}^{\bullet+}$ were determined by fitting the first derivative of a Gaussian or Lorentzian distribution to the cw-EPR spectra (Figure 2.29 and Figure 2.30). For $N \leq 10$, the lineshapes of all cw-EPR spectra are best described by a Gaussian envelope, which indicates that the main contribution to the spectral shape arises from unresolved hyperfine couplings. The Gaussian spectral envelop widths ΔB_N of $\mathbf{PN}^{\bullet+}$ (N = 1–4, 6, 10) are compared to the Norris trend in Figure 2.2C.

Although the width of the cw-EPR spectra for the series continuously decreases with increasing oligomer length, the experimental envelope widths deviate from the ideal values predicted by Norris by up to ~90%. Simulations of the cw-EPR spectra of $\mathbf{PN}^{\bullet+}$ with a constant Lorentzian line width $\Gamma_N = 0.07$ mT and the isotropic component $^{14}a_{\text{iso}}$ of the ^{14}N hyperfine interaction calculated with a distributed point-dipole model for completely delocalized spin density distributions (see Section 2.5.2 for details) provide an excellent agreement with the experimental spectra and replicate the trend in the experimental spectral widths (Figure 2.2B,C). Importantly, the isotropic hyperfine interactions used in these simulations are not equal for all ^{14}N nuclei. Instead, a non-uniform distribution of ^{14}N hyperfine interactions spanning all porphyrin units in each oligomer results in the excellent agreement with the experimental spectra (Figure 2.2D). The remarkable non-uniformity of the spin-density distribution in $\mathbf{PN}^{\bullet+}$ that results in the non-uniform hyperfine interaction pattern is discussed in detail in Section 2.3.3.

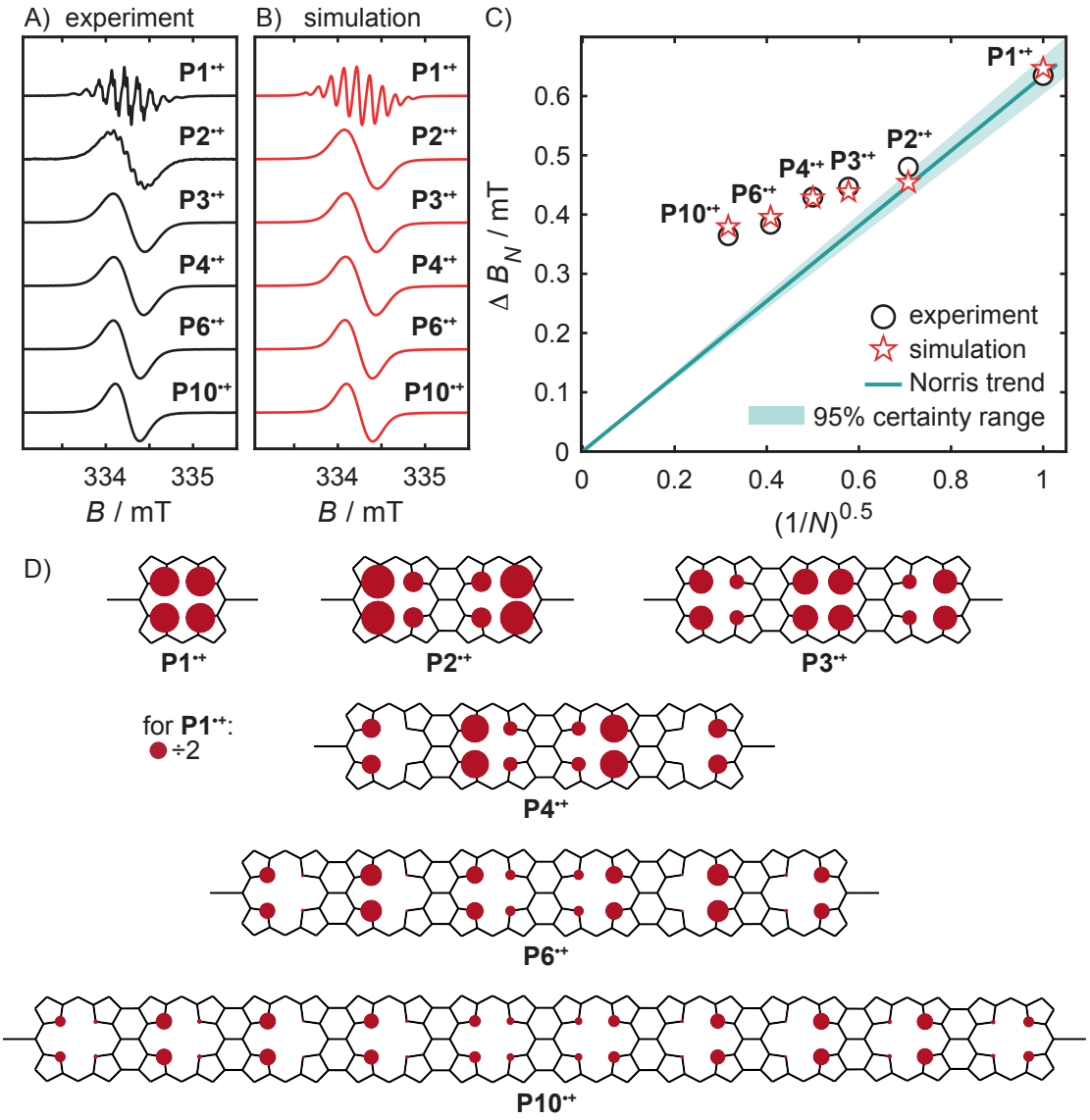


Figure 2.2: A) Experimental cw-EPR spectra of the radical cations $\mathbf{PN}^{\bullet+}$ (N = 1–4, 6, 10) acquired at 298 K in CD_2Cl_2:toluene-d_8:THF-d_8 1:1:1 at X-band frequencies. B) Simulated cw-EPR spectra of $\mathbf{PN}^{\bullet+}$ using the isotropic ^{14}N hyperfine couplings $^{14}N a_{iso}$ derived from a distributed point-dipole calculation. C) Comparison of the experimental and simulated Gaussian envelop widths ΔB_N vs $(1/N)^{0.5}$. The theoretical predicted ideal Norris trend is indicated by the green trend line. The light green shaded area represents the 95% confidence interval around the Norris trend based on a ±5% uncertainty in the experimental monomer spectrum width ΔB_1. D) Schematic representation of the isotropic ^{14}N hyperfine interactions in $\mathbf{PN}^{\bullet+}$ used to simulate the cw-EPR spectra. The radius of the red circle on each nucleus is proportional to the magnitude of $^{14}N a_{iso}$; for $\mathbf{P1}^{\bullet+}$ the shown radius is divided by two for a better visualization. Aryl and silyl solubilizing groups are omitted for clarity.

The spectral widths of $\mathbf{P14}^{\bullet+}$ and $\mathbf{P18}^{\bullet+}$ show an abrupt increase and deviate substantially from the trend observed for their shorter analogues (Figure 2.29 and

Figure 2.30). This is probably the result of significant anisotropic broadening, and prevents a more detailed analysis of their cw-EPR spectra in comparison to their shorter counterparts. The abrupt observation of anisotropic broadening in these oligomers is likely the result of the slow tumbling of the long, rigid, rod-shaped molecules in solution and the increasing anisotropy of specific ^{1}H hyperfine interactions with increasing oligomer length discussed in Section 2.3.5.

To determine if additional spin density distributions predicted by DFT can also describe the electronic structure of **PN**$^{\bullet+}$, their cw-EPR spectra were simulated based on an approach by Moise *et al.*[83] Following the McConnell relationship[77], the magnitude of the isotropic hyperfine coupling to each nitrogen atom $^{14\mathrm{N}}a_{\mathrm{iso}}$ is proportional to the spin population on the atom $^{14\mathrm{N}}\rho$:

$$^{14\mathrm{N}}a_{\mathrm{iso}} = c \cdot {}^{14\mathrm{N}}\rho \tag{2.1}$$

The proportionality constant c, also referred to as the McConnell constant, can reasonably be assumed to be identical for all ^{14}N nuclei in **PN**$^{\bullet+}$ due to their identical coordination environments in the porphyrin framework. The proportionality between the DFT predicted ^{14}N Mulliken spin populations and isotropic hyperfine interactions was determined for each DFT functional using the experimental hyperfine interactions $^{14\mathrm{N}}a_{\mathrm{iso}}$ in **P1**$^{\bullet+}$ and corresponding DFT calculated Mulliken populations $^{14\mathrm{N}}\rho$. These proportionality values and the DFT calculated ^{14}N spin populations of the longer oligomers were then used to simulate the DFT predicted cw-EPR spectra in Figure 2.3.

Calculations with B3LYP as functional and the 6-31G* basis set predict a non-uniform distribution of radical spin density over at least ten porphyrin units in **PN**$^{\bullet+}$ (Figure 2.3C). These spin densities give simulated cw-EPR spectra that are in excellent agreement with the experiment (Figure 2.3A,B) and were used to closely guide the spin density distributions behind the point-dipole calculations (see Section 2.5.2). The influence of the DFT functional on the calculated spin densities and subsequent cw-EPR simulations was investigated by screening additional functionals with different range-separation parameters ω and Hartree–Fock exchange, which strongly influence

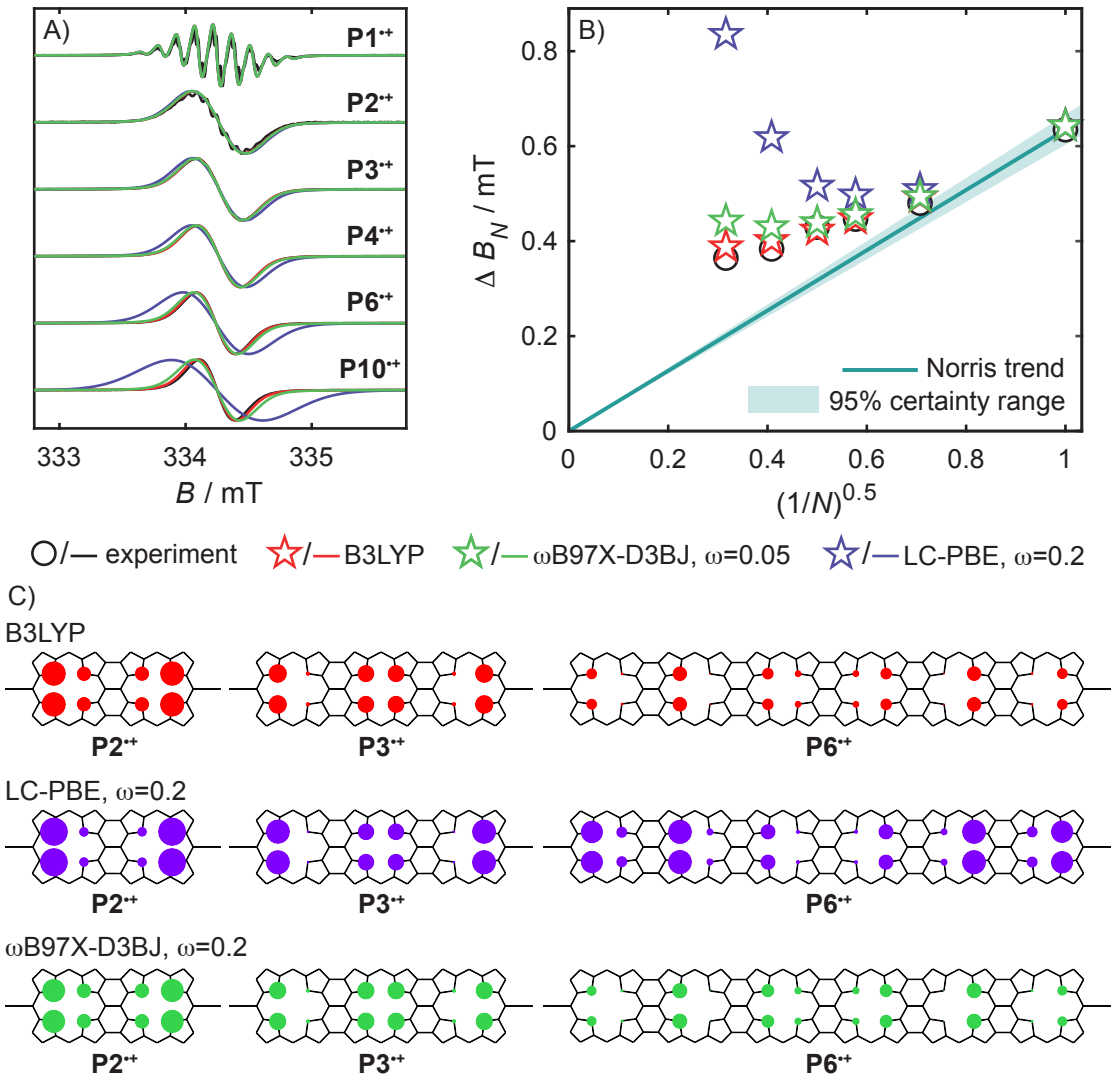


Figure 2.3: A) Comparison of the experimental and DFT (B3LYP, LC-PBE ω=0.2, ωB97X-D3BJ ω=0.05) predicted X-band cw-EPR spectra of $\mathbf{PN}^{\bullet+}$. B) Comparison of the trend in the spectral envelope widths ΔB_N of the experimental and DFT predicted cw-EPR spectra. C) Schematic visualization of the DFT calculated ^{14}N Mulliken spin densities $^{14}N\rho$ used for the simulation of the DFT predicted spectra. The spin density on each ^{14}N nucleus is represented by a circle centered on the nucleus with a radius proportional to its Mulliken spin population and a color consistent with A) and B). The basis set in all calculations was 6-31G*; phenyl solubilizing sidechains and silyl protecting groups are omitted for clarity.

the predicted electron delocalization.[205–207] Simulations based on calculations with the range separated functional ωB97X-D3BJ ($\omega = 0.05$) also reproduce the experimental data reasonably well but deviate more strongly from the experiment in longer oligomers than the B3LYP results. In contrast, DFT calculations with LC-PBE ($\omega = 0.2$) as functional result in an over-delocalization of spin density

onto the terminal porphyrin units, which results in a strong deviation from the experimental data. Importantly, all simulations that result in a close agreement with the experimental cw-EPR spectra are based on similar spin densities to the ones found with B3LYP, whereas different spin density distributions result in stark deviations from the experiment. This further strengthens the validity of the Mulliken populations calculated at the B3LYP level and suggests that the deviation from an ideal Norris trend results from the non-uniform spin distribution in the porphyrin nanoribbons with approximately equal amounts of spin density on each porphyrin unit and a remarkably different distribution of this spin density in the individual porphyrins.

As discussed in detail by Moise *et al.*,[83] it is necessary that the inherent line width Γ_N of the EPR transitions remains constant and small throughout an oligomer series for the Norris relationship to be applicable. Previous studies of the radical cations of butadiyne- and ethyne-linked porphyrin oligomers have shown that Γ_N remains approximately constant and similar to Γ_1.[51, 83] However, the increased rigidity and length of the porphyrin backbone in $\mathbf{PN}^{\bullet+}$ might lead to relevant changes in the rotational correlations times and consequently Γ_N as a function of oligomer size and warrants further investigation. First, the isotropic proton and nitrogen hyperfine interaction in $\mathbf{P1}^{\bullet+}$ were determined as ${}^{14}\mathrm{N}a_{\mathrm{iso}} = 4.07$ MHz and ${}^{1}\mathrm{H}a_{\mathrm{iso}} = 0.98$ MHz by least-squares fitting of the monomer cw-EPR spectrum. Subsequently, the cw-EPR spectra of the longer oligomers with $N = 2$–4, 6, 10 were simulated using fixed hyperfine couplings that impose complete and uniform spin delocalization ($a_N = a_{N=1}/N$) fundamental to the Norris relationship.[82, 83] The best fit to the experimental cw-EPR spectra was obtained by optimizing the inherent Lorentzian linewidth Γ_N. The results of these simulations are summarized in Table 2.1 and displayed in Figure 2.4.

If complete and uniform spin delocalization is imposed in the numerical simulation of the cw-EPR spectra of $\mathbf{PN}^{\bullet+}$, the inherent line width Γ_N required to fit the spectra increases non-linearly with increasing oligomer length (Figure 2.4, bottom right panel).

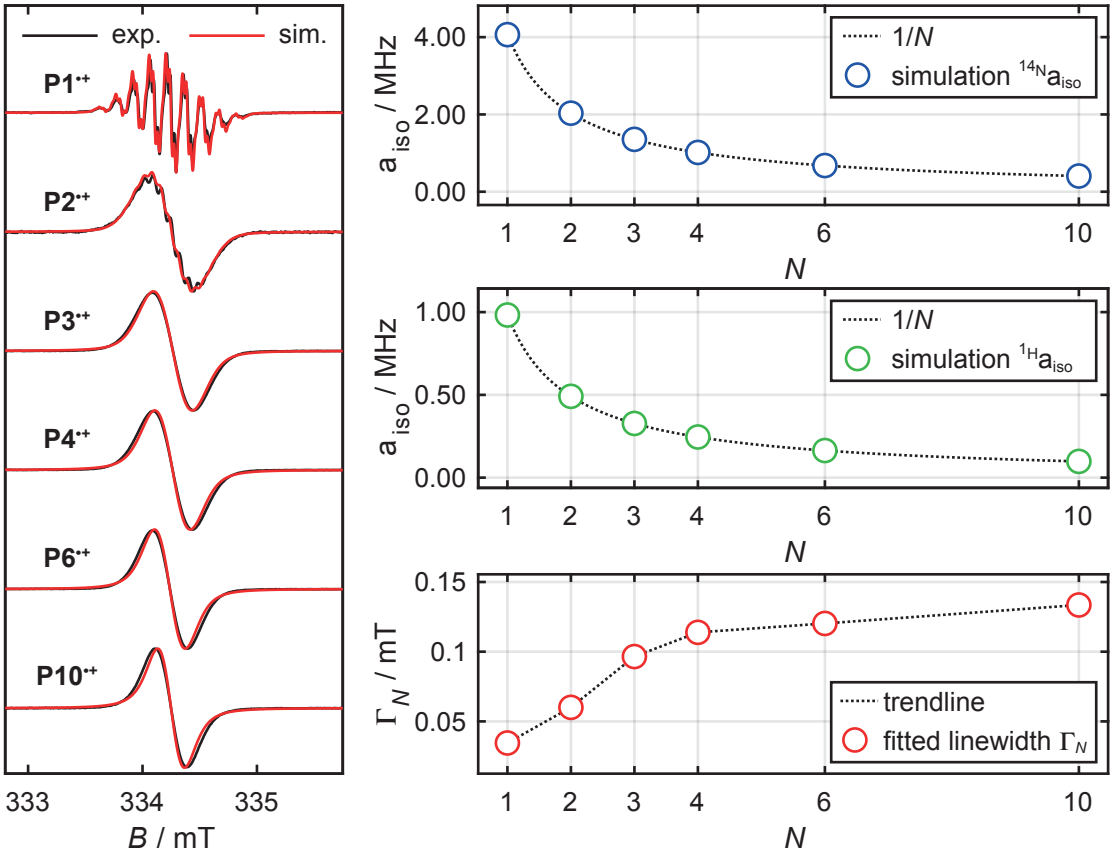


Figure 2.4: Numerical simulations of the X-band cw-EPR spectra of $\mathbf{PN}^{\bullet+}$ in CD_2Cl_2:toluene-d_8:THF-d_8 1:1:1 at 298 K. The field axis of all spectra was standardized for a microwave frequency of 9.37 GHz. The best fit to the monomer cw-EPR spectrum was found using a three-parameter least-squares fitting of the inherent Lorentzian linewidth Γ_N and the isotropic hyperfine couplings $^{14}N a_{iso}$ and $^{1}H a_{iso}$. The simulations of the longer oligomers were obtained by fitting Γ_N, while the hyperfine couplings were derived assuming complete and uniform spin density delocalization.

Table 2.1: Summary of the isotropic hyperfine couplings $^{14}N a_{iso}$ and $^{1}H a_{iso}$, and the best-fit Lorentzian linewidth Γ_N for the simulation of the cw-EPR spectra of $\mathbf{PN}^{\bullet+}$ (N = 1–4, 6, 10) with complete and uniform spin-density delocalization imposed in the hyperfine coupling trend.

	P1$^{\bullet+}$	**P2**$^{\bullet+}$	**P3**$^{\bullet+}$	**P4**$^{\bullet+}$	**P6**$^{\bullet+}$	**P10**$^{\bullet+}$
$^{14}N a_{iso}$ / mT	4.07	2.03	1.36	1.02	0.68	0.41
$^{1}H a_{iso}$ / mT	0.98	0.49	0.33	0.25	0.16	0.10
Γ_N / mT	0.03	0.06	0.10	0.11	0.12	0.13

The largest changes in Γ_N occur in the short oligomers with $\Gamma_4 \gg \Gamma_3 \gg \Gamma_2 \gg \Gamma_1$, while the longer oligomers display a more gradual increase in their linewidths ($\Gamma_{10} > \Gamma_6 > \Gamma_4$). This observation is not in agreement with a continuously increasing linewidth Γ_N

with increasing oligomer length expected if changes in the rotational correlation time cause the experimental trend in Figure 2.2C and rules out changes in Γ_N as a reason behind the deviation from an ideal Norris behaviour.

2.3.3 Investigation of the Spin-Density Non-Uniformity

DFT (B3LYP/6-31G*) calculated Mulliken spin populations were used to assess the non-uniformity of the spin-density distribution in $\mathbf{PN}^{\bullet+}$. The following analysis will focus exclusively on the Mulliken populations $^{14\mathrm{N}}\rho$ of the ^{14}N nuclei, which carry the largest amounts of spin-density in porphyrin radical cations and give rise to the ^{14}N hyperfine coupling interactions that dominate the shape of the cw-EPR spectra. The ^{14}N Mulliken spin populations $^{14\mathrm{N}}\rho$ visualized in Figure 2.5 show a non-uniform distribution of the spin populations in all studied systems apart from monomer $\mathbf{P1}^{\bullet+}$. Already in $\mathbf{P2}^{\bullet+}$ is the spin density non-uniformly distributed between the two sets of equivalent nitrogen atoms with the outer ^{14}N nuclei exhibiting higher spin population than the inner ones. An analogous pattern is found in the longer oligomers and results in alternating regions of high and low spin populations along the tape backbones. The non-uniformity of the spin distribution in $\mathbf{PN}^{\bullet+}$ was quantified using the non-uniformity parameter q.[83]

For each porphyrin unit, q was calculated following equation 2.2, where $^{14\mathrm{N}}\rho_+$ and $^{14\mathrm{N}}\rho_-$ are the Mulliken spin populations on the ^{14}N nuclei of a porphyrin unit with larger or smaller spin populations, respectively.

$$\begin{aligned} {}^{14\mathrm{N}}\rho_+ &= \frac{{}^{14\mathrm{N}}\rho_{\mathrm{sum}}}{2}(1+q) \\ {}^{14\mathrm{N}}\rho_- &= \frac{{}^{14\mathrm{N}}\rho_{\mathrm{sum}}}{2}(1-q) \end{aligned} \tag{2.2}$$

The sum of the ^{14}N Mulliken populations per porphyrin is $^{14\mathrm{N}}\rho_{\mathrm{sum}}$. The non-uniformity parameters q of $\mathbf{PN}^{\bullet+}$ and the mean non-uniformity parameters $q_{\varnothing}$ calculated as the average non-uniformity of all porphyrin units in an oligomer are summarized in Table 2.2.

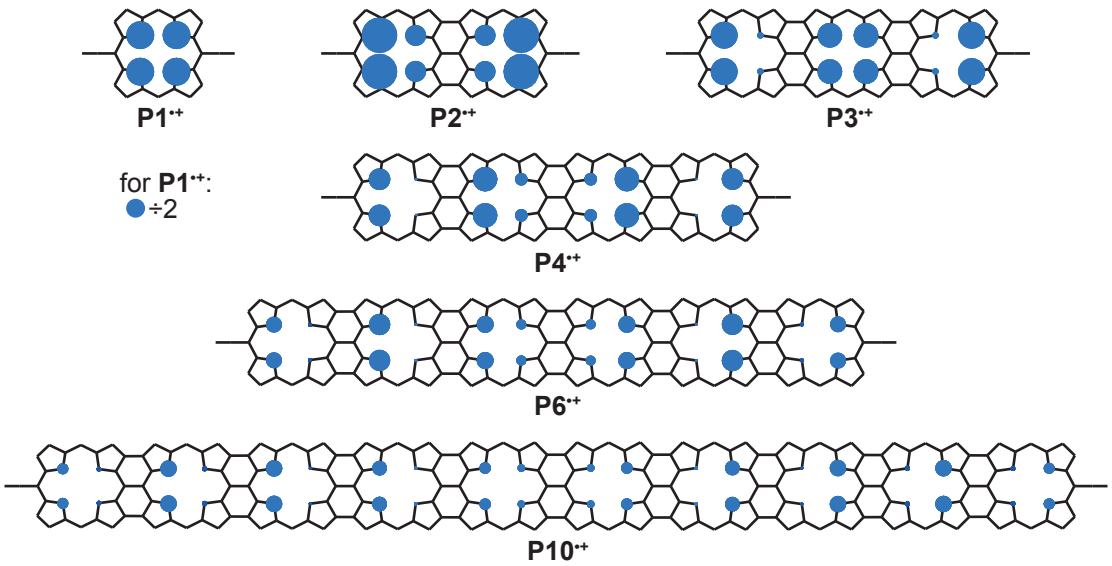


Figure 2.5: Schematic visualization of the DFT (B3LYP/6-31G*) calculated ^{14}N Mulliken spin populations $^{14}\rho$ of $\mathbf{PN}^{\bullet+}$ (N = 1–4, 6, 10). The spin population on each ^{14}N nucleus is represented by a blue circle centered on the nucleus with a radius proportional to $^{14}\rho$; for $\mathbf{P1}^{\bullet+}$ the shown radius is divided by two for a better visualization. Phenyl solubilizing sidechains and silyl protecting groups are omitted for clarity.

Table 2.2: Overview of the non-uniformity parameters of each porphyrin unit q_i and the mean non-uniformity $q_\varnothing$ in $\mathbf{PN}^{\bullet+}$ (N = 1–4, 6, 10) calculated with DFT (B3LYP/6-31G*) predicted ^{14}N Mulliken spin populations $^{14}\rho$.

	q_1	q_2	q_3	q_4	q_5	q_6	q_7	q_8	q_9	q_{10}	$q_\varnothing$
$\mathbf{P1}^{\bullet+}$	0.00										0.00
$\mathbf{P2}^{\bullet+}$	0.13	0.13									0.13
$\mathbf{P3}^{\bullet+}$	0.33	0.00	0.33								0.22
$\mathbf{P4}^{\bullet+}$	0.49	0.17	0.17	0.49							0.33
$\mathbf{P6}^{\bullet+}$	0.74	0.44	0.14	0.14	0.44	0.74					0.44
$\mathbf{P10}^{\bullet+}$	1.00	0.84	0.61	0.36	0.12	0.12	0.36	0.61	0.84	1.00	0.59

The analysis of the DFT calculated Mulliken spin populations highlights an increase in the mean non-uniformity of the spin distribution with increasing oligomer length. This trend is driven by a substantially increasing spin density non-uniformity towards the terminal porphyrin units in long oligomers. To compare the spin-density non-uniformity in $\mathbf{PN}^{\bullet+}$ with previous studies of ethyne- and butadiyne-linked porphyrin radical cations ***e*-PN**$^{\bullet+}$ and ***b*-PN**$^{\bullet+}$, their non-uniformity parameters q were determined from from literature reported Mulliken spin populations following the approach detailed above.[83] The non-uniformity parameters of ***e*-PN**$^{\bullet+}$ and ***b*-PN**$^{\bullet+}$

are summarized in Table 2.3, and the ^{14}N Mulliken spin population for the longest coherently delocalized polaron states of both oligomer classes are shown in Figure 2.6.

Table 2.3: Overview of the DFT (B3LYP/6-31G*) calculated non-uniformity parameters q_i of each porphyrin unit and the mean non-uniformity $q_\varnothing$ in ***b*-PN**$^{\bullet+}$ (N = 2,3) and ***e*-PN**$^{\bullet+}$ (N = 2–5).

	q_1	q_2	q_3	q_4	q_5	$q_\varnothing$
***b*-P2**$^{\bullet+}$	0.03	0.03				0.03
***b*-P3**$^{\bullet+}$	0.07	0.00	0.07			0.06
***e*-P2**$^{\bullet+}$	0.05	0.05				0.05
***e*-P3**$^{\bullet+}$	0.09	0.00	0.09			0.06
***e*-P4**$^{\bullet+}$	0.11	0.03	0.03	0.11		0.07
***e*-P5**$^{\bullet+}$	0.12	0.04	0.00	0.04	0.12	0.06

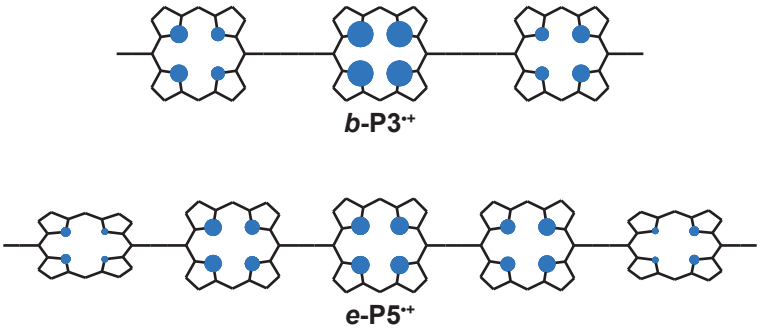


Figure 2.6: Schematic visualization of the DFT (B3LYP/6-31G*) calculated ^{14}N Mulliken spin populations $^{14}\rho$ of butadiyne- and ethyne-linked oligomers ***b*-P3**$^{\bullet+}$ and ***e*-P5**$^{\bullet+}$. The spin population on each ^{14}N nucleus is represented by a blue circle centered on the nucleus with a radius proportional to $^{14}\rho$. The ^{14}N Mulliken spin populations and geometry optimized structures were taken from reference [83]. Phenyl solubilizing sidechains and silyl protecting groups are omitted for clarity.

Analogous to the edge-fused porphyrin oligomers, ethyne- and butadiyne-linked porphyrin radical cations show increasingly non-uniform spin density distributions towards their terminal porphyrin units, albeit to a much smaller extent.[51, 83] The average of the mean spin-density non-uniformity of the different types of porphyrin oligomers increases in the order q(**PN**$^{\bullet+}$) = 0.34 $\gg$ q(***e*-PN**$^{\bullet+}$) = 0.06 $\gg$ q(***b*-PN**$^{\bullet+}$) = 0.04. This suggests that oligomers with stronger porphyrin-porphyrin electronic coupling exhibit more pronounced non-uniform spin distributions. The remarkably non-uniform spin distribution predicted by DFT for **PN**$^{\bullet+}$ is supported by the

interpretation of the EPR results in this chapter and demonstrates in unprecedented detail the coherent, wave-like delocalization of polaron states in porphyrin nanoribbons.

2.3.4 W-band Pulse EPR Spectroscopy

The $\boldsymbol{g}$-anisotropy of the porphyrin nanoribbon radical cations was investigated by W-band EPR spectroscopy. The echo-detected field sweep spectra of $\mathbf{PN}^{\bullet+}$ measured in a frozen solution of CD_2Cl_2:toluene-d_8:THF-d_8 1:1:1 at 50 K are consistent with a rhombic $\boldsymbol{g}$-tensor with small anisotropy as expected for organic π-radicals (Figure 2.7).[70, 208] Comparison of the principal values of the $\boldsymbol{g}$-tensors of $\mathbf{PN}^{\bullet+}$ in Figure 2.7B shows, that within the accuracy of the fitted values, the rhombicity of $\boldsymbol{g}$ does not increase with increasing oligomer length. The DFT predicted $\boldsymbol{g}$-tensors of $\mathbf{PN}^{\bullet+}$ with B3LYP as functional and the EPRII basis set are qualitatively consistent with the experimental data and correctly predict rhombic $\boldsymbol{g}$-tensors with small anisotropy, although the magnitudes of the principal components of $\boldsymbol{g}$ are predicted incorrectly (Table 2.4). Calculation of the $\boldsymbol{g}$-tensors for $\mathbf{P6}^{\bullet+}$ and $\mathbf{P10}^{\bullet+}$ was not feasible due to the large computational requirements.

The DFT calculated $\boldsymbol{g}$-tensors predict an alignment of the tensor principle axes with the out-of-plane axis (g_z), the axis along the aryl solubilizing sidechains (g_y), and the long axis of $\mathbf{PN}^{\bullet+}$ defined by the β,*meso*,β-triply fused motives (g_x). The predicted orientation of the principle axes of $\boldsymbol{g}$ is exemplified for $\mathbf{P2}^{\bullet+}$ in Figure 2.7C with the longer oligomers displaying analogous tensor orientations.

All investigated porphyrin nanoribbon radical cations show a field dependence of their phase memory times T_m at 50 K in CD_2Cl_2:toluene-d_8:THF-d_8 1:1:1 with longer coherence times observed at the field positions corresponding to g_x and g_y (Figure 2.8). The experimental two-pulse Hahn-echo decay spectra and stretched exponential fits used to determine T_m are shown in Figure 2.31. Anisotropic relaxation times have been reported in the literature for a variety of systems and were attributed to decoherence originating from changes in the effective g-values through molecular motion.[209–211]

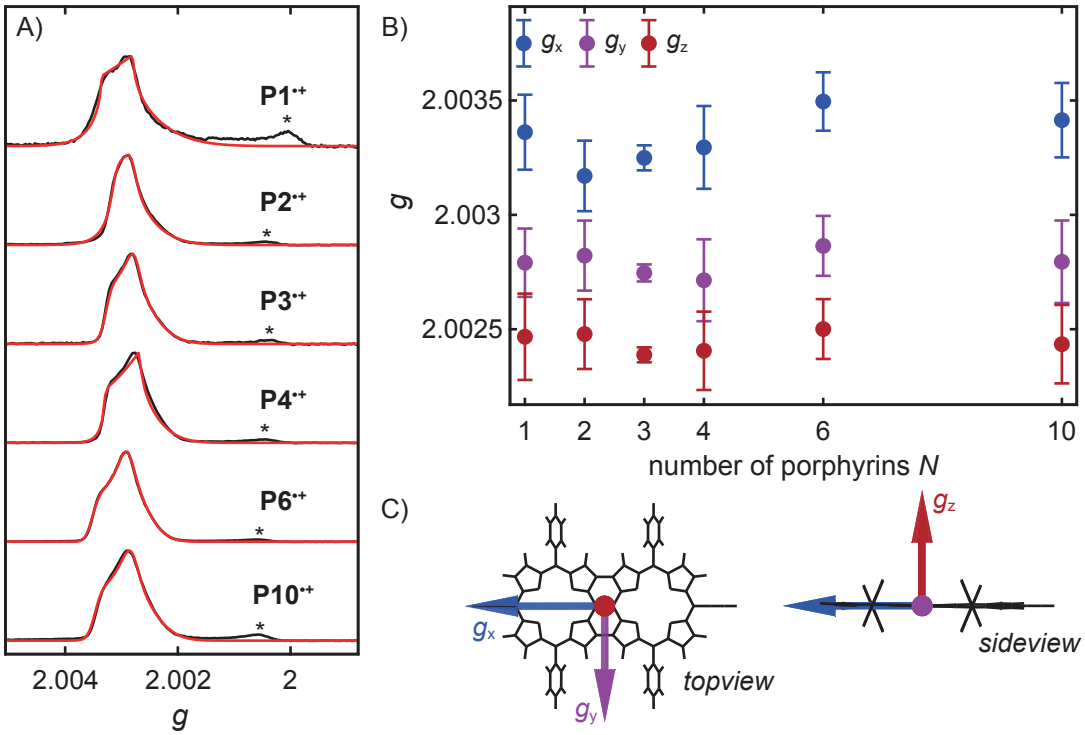


Figure 2.7: A) Experimental (black) and simulated (red) W-band echo-detected field sweep EPR spectra of $\mathbf{PN}^{\bullet+}$ (N = 1–4, 6, 10) recorded at 50 K in CD_2Cl_2:toluene-d_8:THF-d_8 1:1:1 and simulated with a rhombic $\boldsymbol{g}$-tensor; * denotes a background signal in the resonator. B) Representation of the anisotropic g-values of $\mathbf{PN}^{\bullet+}$ determined from the simulations shown in section A). The error margins show the 95% confidence intervals. C) Schematic visualization of the orientation of the principal axes of $\boldsymbol{g}$ in $\mathbf{P2}^{\bullet+}$ obtained from DFT calculations at the B3LYP/EPRII level of theory.

Table 2.4: Summary of the experimental g-values of $\mathbf{PN}^{\bullet+}$ (N = 1–4, 6, 10) determined from the simulation of the W-band echo-detected field sweep spectra and the DFT predicted g-values for N = 1–4 calculated with B3LYP as functional and the EPRII basis set.

		g_x	g_y	g_z
$\mathbf{P1}^{\bullet+}$	exp.	2.00336 ± 0.00017	2.00279 ± 0.00015	2.00247 ± 0.00019
	DFT	2.00307	2.00263	2.00238
$\mathbf{P2}^{\bullet+}$	exp.	2.00317 ± 0.00015	2.00282 ± 0.00015	2.00248 ± 0.00015
	DFT	2.00278	2.00265	2.00257
$\mathbf{P3}^{\bullet+}$	exp.	2.00325 ± 0.00005	2.00275 ± 0.00004	2.00239 ± 0.00003
	DFT	2.00302	2.00282	2.00237
$\mathbf{P4}^{\bullet+}$	exp.	2.00329 ± 0.00018	2.00271 ± 0.00018	2.00241 ± 0.00017
	DFT	2.00330	2.00307	2.00225
$\mathbf{P6}^{\bullet+}$	exp.	2.00350 ± 0.00013	2.00286 ± 0.00013	2.00250 ± 0.00013
$\mathbf{P10}^{\bullet+}$	exp.	2.00341 ± 0.00016	2.00280 ± 0.00018	2.00243 ± 0.00017

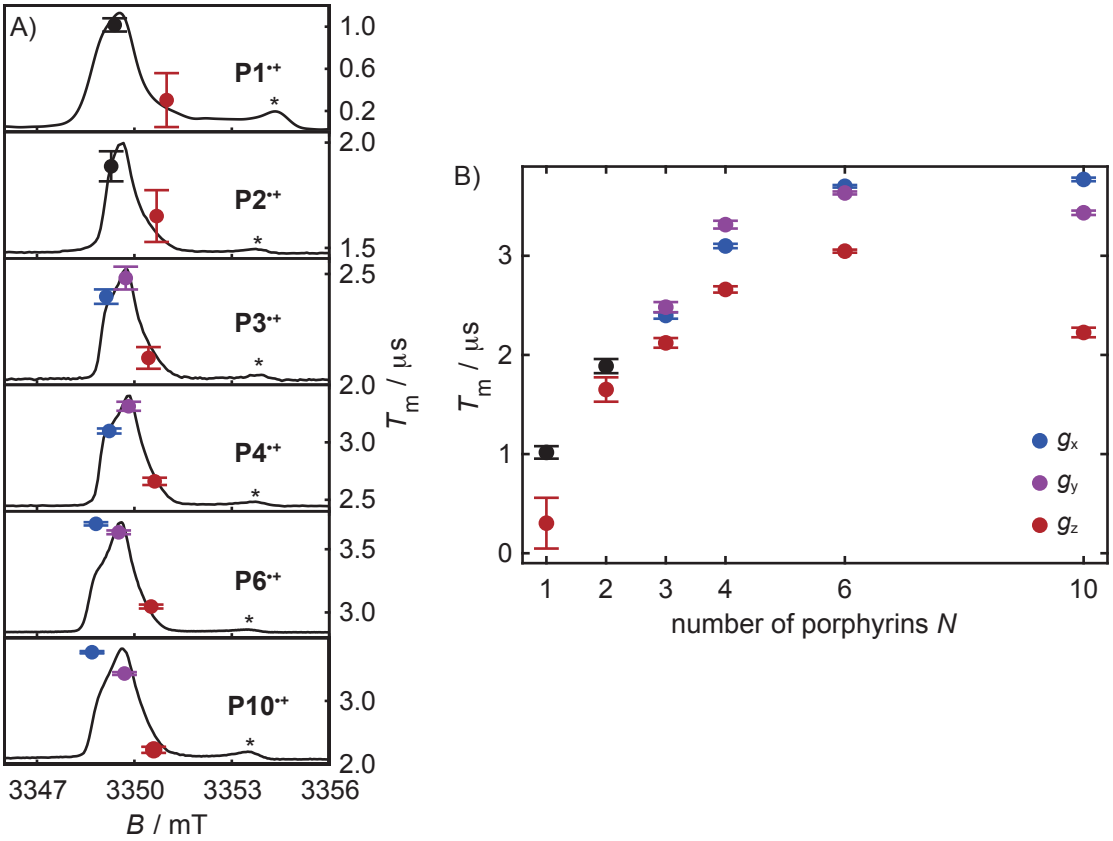


Figure 2.8: A) Echo-detected field sweep spectra of $\mathbf{PN}^{\bullet+}$ recorded at 50 K in CD_2Cl_2:toluene-d_8:THF-d_8 1:1:1 and corresponding field-dependent phase memory times T_m; * denotes a background signal in the resonator. B) Comparison of the coherence times T_m at field positions corresponding to the principal values of their anisotropic $\boldsymbol{g}$-tensors. The error margins show a 95% confidence interval of the fitted T_m values. For $\mathbf{P1}^{\bullet+}$ and $\mathbf{P2}^{\bullet+}$ the g_x and g_y field positions were not recorded separately and the reported coherence times correspond to $g_{x,y}$ (black).

Molecular oscillations along a particular axis result in small modulations of the effective g-value if the magnetic field is aligned with the oscillation axis and larger modulations of g for all other magnetic field orientations.[209] This suggests that libration movements in the porphyrin xy-plane dominate the relaxation processes in $\mathbf{PN}^{\bullet+}$ at 50 K. Noticeably, the phase memory times of $\mathbf{PN}^{\bullet+}$ (N = 1–4, 6, 10) continuously increase with increasing chain length under analogous acquisition conditions, as exemplified by the more than threefold increase in the phase memory time at the g_x field position from 1.0 µs for $\mathbf{P1}^{\bullet+}$ to 3.8 µs for $\mathbf{P10}^{\bullet+}$. This trend could be explained by smaller perturbations of the radical coherence *via* nuclear-spin diffusions due to smaller anisotropic hyperfine interactions in the longer oligomers.

2.3.5 Mims ENDOR Spectroscopy

The anisotropic ^{1}H and ^{14}N hyperfine interactions of $\mathbf{PN}^{\bullet+}$ were determined by pulse Mims ENDOR spectroscopy in frozen solutions at 50 K. Although decomposition of the Mims ENDOR spectra is not feasible due to the large number of nuclei with similar hyperfine couplings that contribute to the spectra, they still provide valuable insight into the electronic structure of the porphyrin radical cations: Dynamic polaron migration or electron hopping can occur rapidly on the EPR time-scale at room temperature and can therefore contribute to the apparent hyperfine interactions.[84] However, these processes are typically not observed by EPR spectroscopy at cryogenic temperatures in a frozen matrix, providing a better probe of the radical delocalization.[51, 83] In addition, due to the lack of dynamical averaging in a frozen solvent matrix, the anisotropic hyperfine interactions may be resolved, and ENDOR measurements provide additional information beyond what can be obtained from cw-EPR spectroscopy in the isotropic limit.

The W-band ^{1}H and ^{14}N Mims ENDOR spectra of $\mathbf{PN}^{\bullet+}$ (N = 1–4, 6, 10) are shown in Figure 2.9. The proton spectra were measured at field positions corresponding to $g_{x,y}$ and g_z while the nitrogen ENDOR spectra were acquired at the $g_{x,y}$ field position. All ^{1}H and ^{14}N ENDOR spectra are centered at the Larmor frequency of the relevant nucleus and split into symmetric peaks by the hyperfine interactions. This is characteristic for nuclei in the weak coupling limit with smaller hyperfine couplings than the Larmor frequency ($A < 2\nu_L$). Hyperfine spectroscopy is a powerful tool to probe the spin distribution of organic π-radicals. The magnitude of the individual hyperfine interactions, and consequently the width of the ENDOR signal, decreases for an increasingly delocalized radical (although the total number of hyperfine interactions increases) if the delocalization does not result in substantial changes to the hyperfine anisotropies.[82, 83] The width of the experimental ENDOR spectra of $\mathbf{PN}^{\bullet+}$ as a function of oligomer length is shown in Figure 2.10 with the full width at half maximum (*FWHM*) as measure of the spectral width.

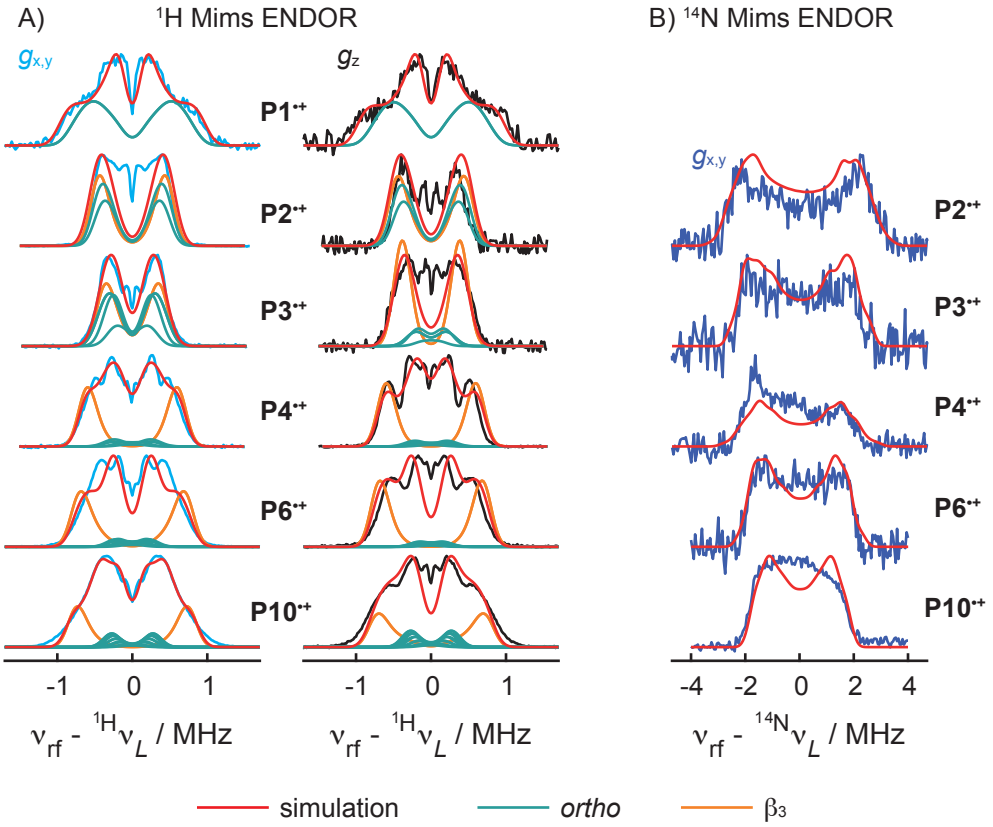


Figure 2.9: A) ^{1}H and B) ^{14}N Mims ENDOR spectra of $\mathbf{PN}^{\bullet+}$ acquired at 50 K in frozen CD_2Cl_2:toluene-d_8:THF-d_8 1:1:1 at W-band frequencies together with their simulations (red) using anisotropic hyperfine tensors derived from distributed point-dipole calculations. The ^{1}H Mims ENDOR spectra were recorded at field positions corresponding to $g_{x,y}$ (light blue) and g_z (black). The ^{14}N ENDOR spectra were recorded at the $g_{x,y}$ field position. The individual contributions to the ^{1}H Mims ENDOR spectra from the *ortho*- and β_3-hydrogens are highlighted in green and orange, respectively; see Figure 2.12 for an illustration of the ^{1}H hyperfine tensors.

The *FWHM* of the ^{14}N ENDOR spectra continuously decreases for $N = 2$–10 which indicates a sustained decrease of the largest ^{14}N hyperfine interaction (which determines the *FWHM*). This is consistent with coherent delocalization of the radical spin density over at least ten porphyrin units in $\mathbf{PN}^{\bullet+}$. The *FWHM* of the ^{1}H ENDOR spectra initially decreases as expected for an increasingly delocalized radical. Surprisingly, this trend is inverted for N>3 at the $g_{x,y}$ field position and N>2 at the g_z field position, with a continuously increasing *FWHM* accompanied by the emergence of a clearly resolved shoulder in the ^{1}H ENDOR spectra in Figure 2.9A. This behaviour is in stark contrast to the ^{14}N ENDOR results and previous reports on ethyne- and butadiyne-

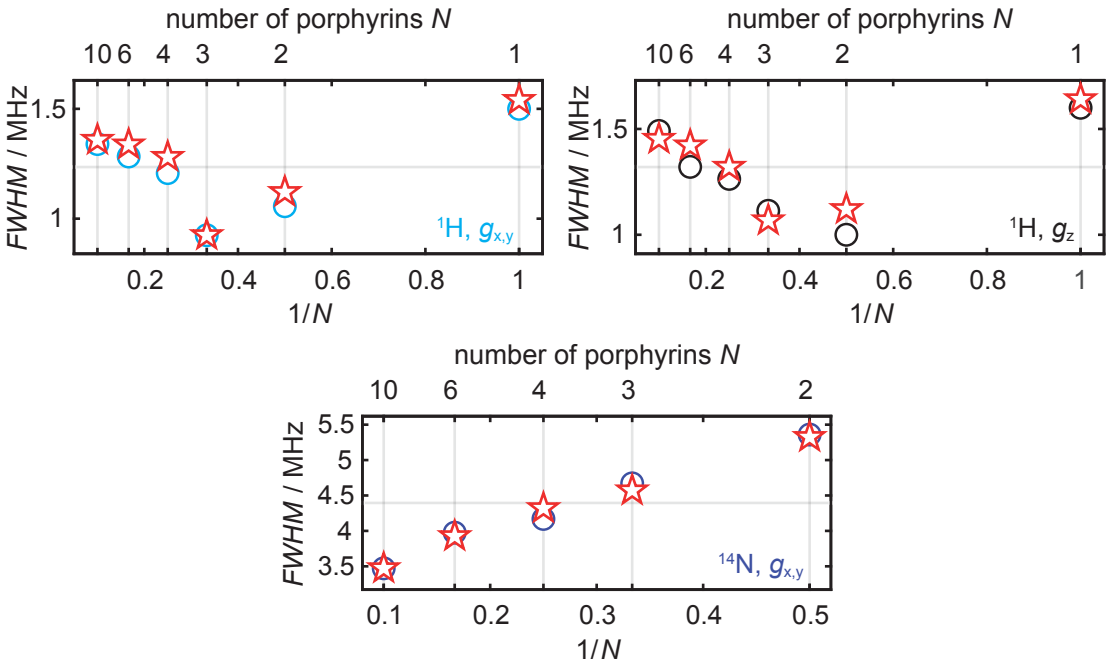


Figure 2.10: Trend of the full width at half maximum (*FWHM*) of the experimental and simulated ^{1}H and ^{14}N Mims ENDOR spectra of $\mathbf{PN}^{\bullet+}$ shown in Figure 2.9.

linked porphyrin radical cations, which exhibit continuously narrowing ^{1}H ENDOR widths until their effective polaron delocalization lengths are reached.[51, 83]

The surprising trend of the ^{1}H Mims ENDOR spectra of $\mathbf{PN}^{\bullet+}$ can be explained by computational simulation. It is not feasible to simulate the EPR spectra of $\mathbf{PN}^{\bullet+}$ using DFT-calculated hyperfine tensors, due to the high computational cost of accurately calculating hyperfine interactions in molecules with more than four porphyrin units. To overcome this limitation, the anisotropic hyperfine tensors were directly calculated from the spin density distributions in $\mathbf{PN}^{\bullet+}$ following the approach schematically summarized in Figure 2.11 and described in detail in Section 2.5.2. In brief, a spin distribution was assigned to each oligomer starting from DFT-calculated (B3LYP/6-31G*) Mulliken spin populations that were systematically modified to account for the effects of solubilizing sidechains and silyl protecting groups omitted in the calculations. The assigned spin populations show full delocalization of the radical cations over all porphyrin units in each oligomer (purple bars in Figure 2.11B). At the same time, the radical spin populations are non-uniformly distributed over the individual porphyrin

units for $N \geq 2$, as exemplified by the ^{14}N spin populations in Figure 2.11B (black circles). The isotropic component of the hyperfine tensors is proportional to the spin on each nucleus, while the anisotropic component was calculated via a distributed point-dipole approximation of the dipolar electron-nuclear interactions introduced in equation 1.18 of Chapter 1.[70, 79, 80] The full hyperfine tensors $^{1\mathrm{H}}\boldsymbol{A}$ and $^{14\mathrm{N}}\boldsymbol{A}$ obtained from this approach were employed in all relevant EPR simulations presented in this Chapter and are schematically visualized in Figure 2.27 and Figure 2.28.

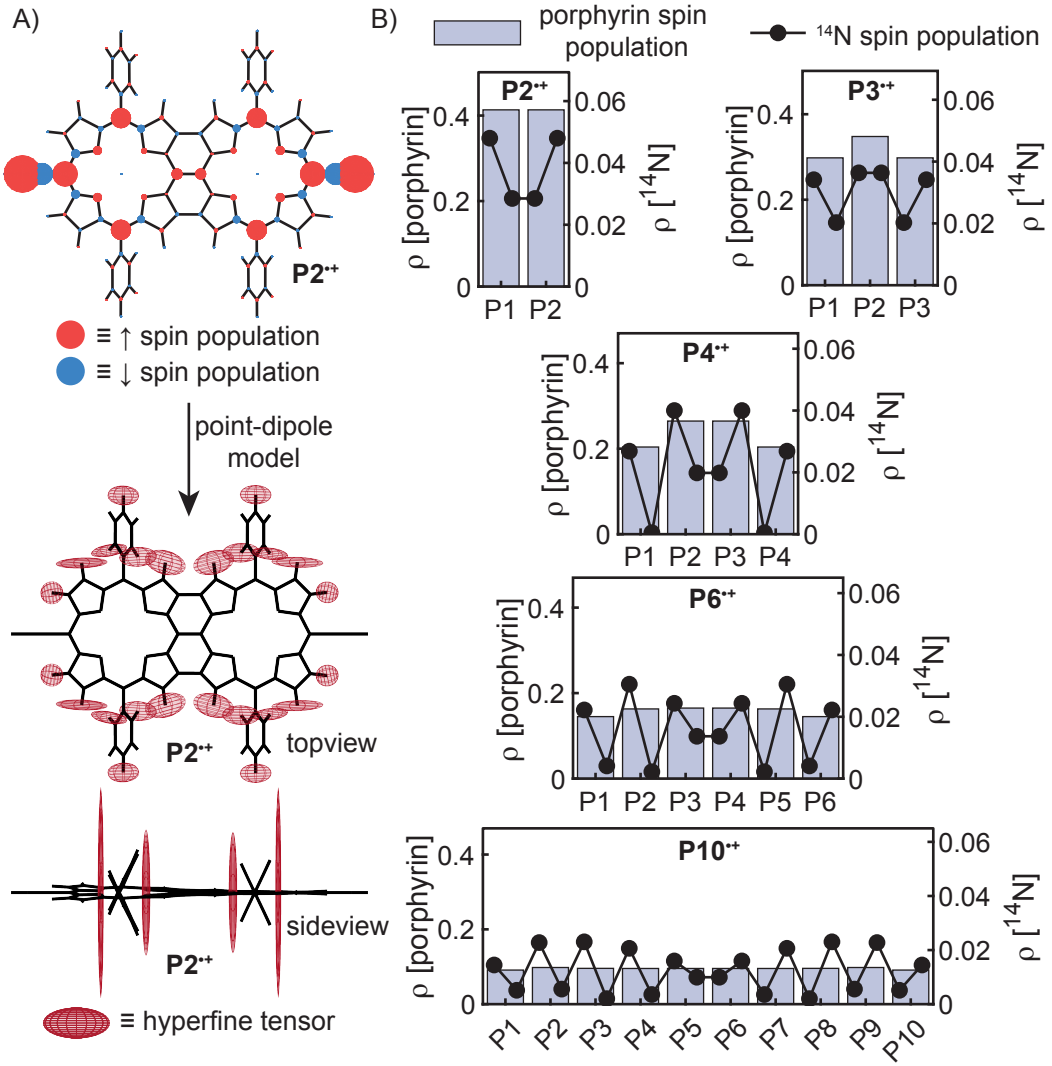


Figure 2.11: A) Representation of the approach to derive the ^{1}H and ^{14}N hyperfine interactions of $\mathbf{PN}^{\bullet+}$ from their Mulliken spin populations with a distributed point-dipole model (exemplarily shown for $\mathbf{P2}^{\bullet+}$). B) Visualization of the spin populations ρ of each porphyrin unit (purple bars) and set of ^{14}N nuclei (black circles) used to calculate the hyperfine interactions in $\mathbf{PN}^{\bullet+}$ (N = 2–4, 6, 10).

The simulated ^{1}H and ^{14}N Mims ENDOR spectra of $\mathbf{PN}^{\bullet+}$ (N = 1–4, 6, 10) shown in Figure 2.9 are in good agreement with the experimental spectra and qualitatively reproduce the trend in the experimental ENDOR *FWHM* as a function of oligomer length in Figure 2.10. This is strong evidence for a coherent radical delocalization over at least ten porphyrin units in $\mathbf{PN}^{\bullet+}$ on the EPR timescale in the frozen solution. The reason behind the discontinuous trend in the ^{1}H ENDOR *FWHM*, despite coherent delocalization over at least 10 porphyrin units in $\mathbf{PN}^{\bullet+}$, becomes evident from the simulations of the individual hyperfine contributions to the ENDOR spectra (Figure 2.9A). For $\mathbf{P1}^{\bullet+}$ and $\mathbf{P2}^{\bullet+}$, the width of the ^{1}H ENDOR spectra is determined by the anisotropic hyperfine couplings to the *ortho*-protons of the aryl side groups, which decrease, as expected, from the monomer to the dimer. However, from the trimer onwards, the largest anisotropic hyperfine interactions switch from the *ortho*-protons to the inner β-protons of the terminal porphyrin units (β_3-protons), as evident from the schematic visualization of the ^{1}H hyperfine tensors in Figure 2.12. This is accompanied by the emergence of a resolved shoulder in the experimental ^{1}H ENDOR spectra than can be directly attributed to the β_3 hyperfine interactions in $\mathbf{PN}^{\bullet+}$.

Changes in the protons with the largest anisotropic hyperfine interactions can occur with increasing oligomer length, as illustrated by the ethyne-linked porphyrin radical cation oligomers.[83] The sustained increase in the β_3 hyperfine interactions in the terminal porphyrin units is however so far a unique feature of $\mathbf{PN}^{\bullet+}$ and gives rise to the continuously increasing width of the ^{1}H ENDOR spectra. This increase is driven by a systematic redistribution of the spin density in the terminal porphyrin units with increasing oligomer length that locally overcompensates for the overall decrease of spin density per porphyrin with increasing radical delocalization (Figure 2.13). Ultimately, this change in the relative spin distribution, which is directly predicted by DFT calculations at the B3LYP/6-31G* level of theory, leads to larger anisotropic hyperfine contributions to $^{1\mathrm{H}}\boldsymbol{A}$ and consequently broader ^{1}H ENDOR spectra.

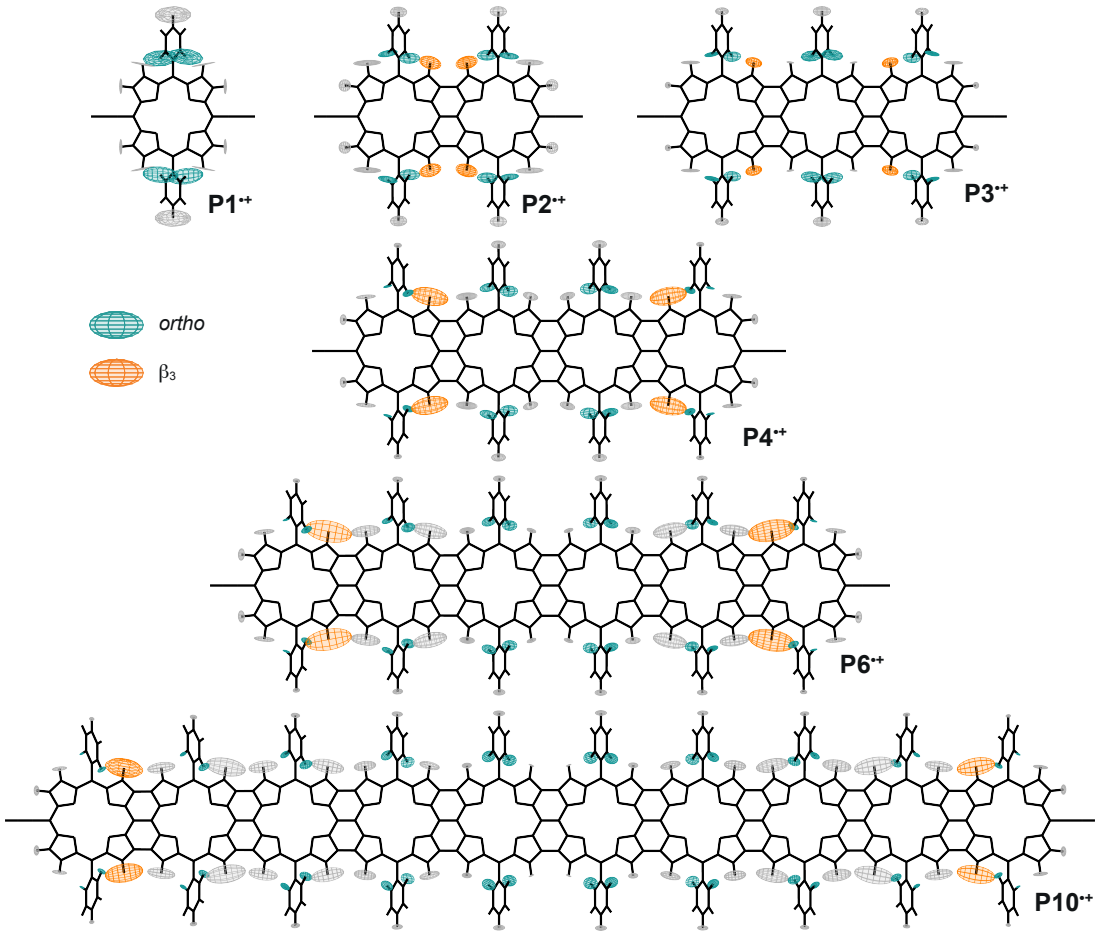


Figure 2.12: Visualization of the ^{1}H hyperfine coupling tensors $^{1\mathrm{H}}\boldsymbol{A}$ of $\mathbf{P}\boldsymbol{N}^{\bullet+}$ (N = 1–4, 6, 10). The tensors of the *ortho*- and β_3-protons that give rise to the individual contributions shown in Figure 2.9A are highlighted in green and orange, respectively; additional tensors are shown in grey as reference. The hyperfine tensors are represented as ellipsoids centred at the corresponding ^{1}H nuclei with dimensions proportional to the eigenvalues of $^{1\mathrm{H}}\boldsymbol{A}$ and are orientated in the molecular frame based on their Euler angles.

The hyperfine interactions in $\mathbf{P14}^{\bullet+}$ and $\mathbf{P18}^{\bullet+}$ were probed by W-band ^{1}H and ^{14}N Mims ENDOR spectroscopy in frozen solutions at 50 K and are compared to the ENDOR spectra of $\mathbf{P10}^{\bullet+}$ in Figure 2.14. The ^{1}H ENDOR spectra of $\mathbf{P14}^{\bullet+}$ measured at the $g_{x,y}$ and g_z field positions show a further increase in spectral width compared to $\mathbf{P10}^{\bullet+}$, whereas the spectral shape and width of $\mathbf{P14}^{\bullet+}$ and $\mathbf{P18}^{\bullet+}$ are virtually identical. No significant changes in the width and shape of the ^{14}N ENDOR spectra of $\mathbf{P}\boldsymbol{N}^{\bullet+}$ (N = 10, 14, 18) are evident within the signal to noise of the experimental data. This suggests a limit for coherent delocalization of the radical cation spin density between 10 and 14 porphyrin units in $\mathbf{P}\boldsymbol{N}^{\bullet+}$. Attempts to simulate the ENDOR

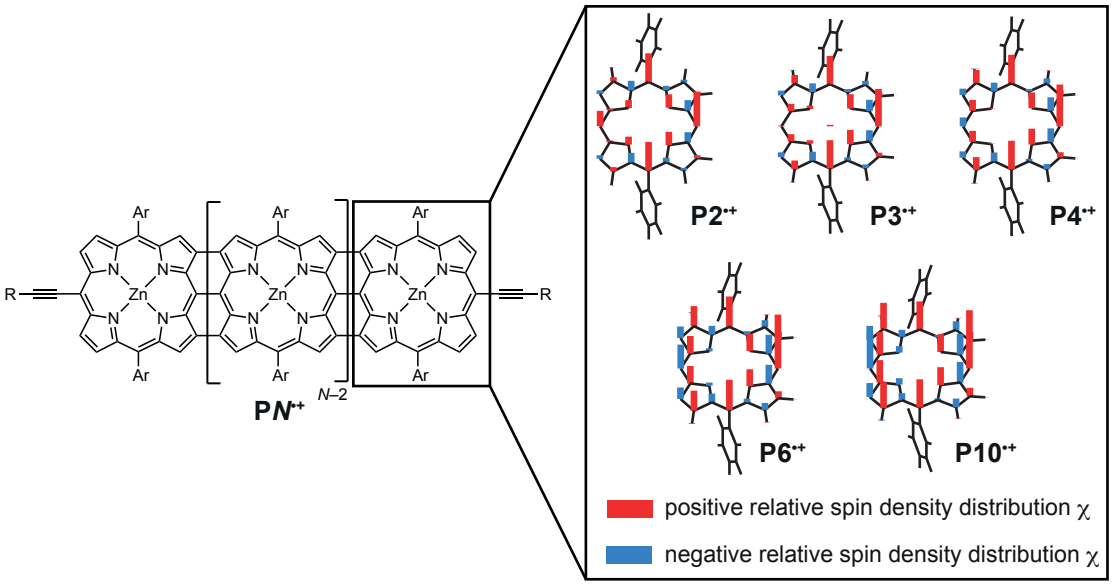


Figure 2.13: Schematic visualization of the trend in the relative spin density distributions χ in the outer porphyrin units of $\mathbf{PN}^{\bullet+}$ (N = 2–4, 6, 10). The relative spin density χ is defined as the fraction of spin density assigned to each individual atom in a subunit (see equation 2.5). The height of the coloured bars indicates the magnitude of the relative spin density χ for individual atoms. Positive relative spin density distributions are shown in red and negative ones in blue.

spectra of $\mathbf{P14}^{\bullet+}$ and $\mathbf{P18}^{\bullet+}$ to precisely determine the effective delocalization length were not successful. DFT calculations at the B3LYP/6-31G* level of theory predict a continuously increasing polaron delocalization which is not in agreement with the experimental observations, and the screening of different DFT functional to obtain a better agreement with the experimental trend was computationally too demanding for these large molecular structures.

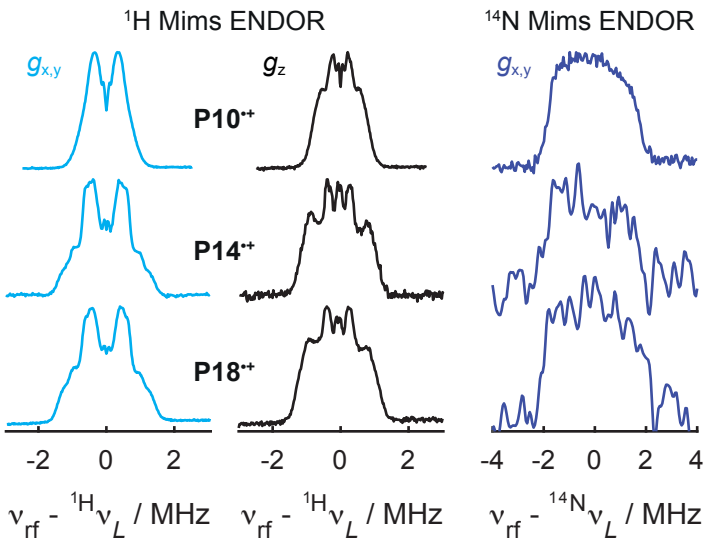


Figure 2.14: W-band ^{1}H and ^{14}N Mims ENDOR spectra of $\mathbf{PN}^{\bullet+}$ (N = 10, 14, 18) in frozen CD_2Cl_2:toluene-d_8:THF-d_8 1:1:1 at 50 K. The ^{1}H ENDOR spectra were recorded at field positions corresponding to $g_{x,y}$ and g_z while the ^{14}N ENDOR spectra were recorded at the $g_{x,y}$ field position.

2.3.6 ^{14}N HYSCORE Spectroscopy

The anisotropic ^{14}N hyperfine interactions of $\mathbf{PN}^{\bullet+}$ (N = 1–4) were measured by HYSCORE spectroscopy at X-band frequencies to complement the study of the hyperfine interactions by Mims ENDOR spectroscopy (Figure 2.15), and to provide additional evidence for the accuracy of the anisotropic hyperfine tensors obtained from the distributed point-dipole model. These measurements confirm the significant reduction in the nitrogen hyperfine couplings from $\mathbf{P1}^{\bullet+}$ to $\mathbf{P2}^{\bullet+}$, as indicated by the shift of the strongest signal contributions from the $(-,+)$ to the $(+,+)$ quadrant of the HYSCORE spectra. This trend continues for the HYSCORE spectrum of $\mathbf{P3}^{\bullet+}$ with a further reduced signal in the $(-,+)$ quadrant followed by a slightly higher spectral contribution in the $(-,+)$ quadrant for $\mathbf{P4}^{\bullet+}$. Simulations of the HYSCORE spectra using nitrogen hyperfine tensors obtained *via* the distributed point-dipole approximation are in good agreement with the experimental spectra. This provides additional evidence for the coherent delocalization of the radical spin density over at least four porphyrin units in $\mathbf{PN}^{\bullet+}$. In addition, the substantially better agreement of these simulations with the experimental spectra compared to simulations with DFT

calculated hyperfine interactions shown in Figure 2.32 further strengths the validity of the hyperfine tensors calculated *via* the distributed point-dipole approximation. The simulated spectra also reproduce the experimentally observed trend of a continuously reduced signal in the $(-,+)$ quadrant for $N = 1$–3 followed by a slight increase for $N = 4$ caused by an initial reduction of the largest out-of-plane nitrogen hyperfine coupling from 11.7 MHz in $\mathbf{P1}^{\bullet+}$ to 4.96 MHz in $\mathbf{P3}^{\bullet+}$ followed by an increase to 5.47 MHz in $\mathbf{P4}^{\bullet+}$ (Table 2.7). This is further experimental evidence for the non-uniform spin density distribution in $\mathbf{PN}^{\bullet+}$.

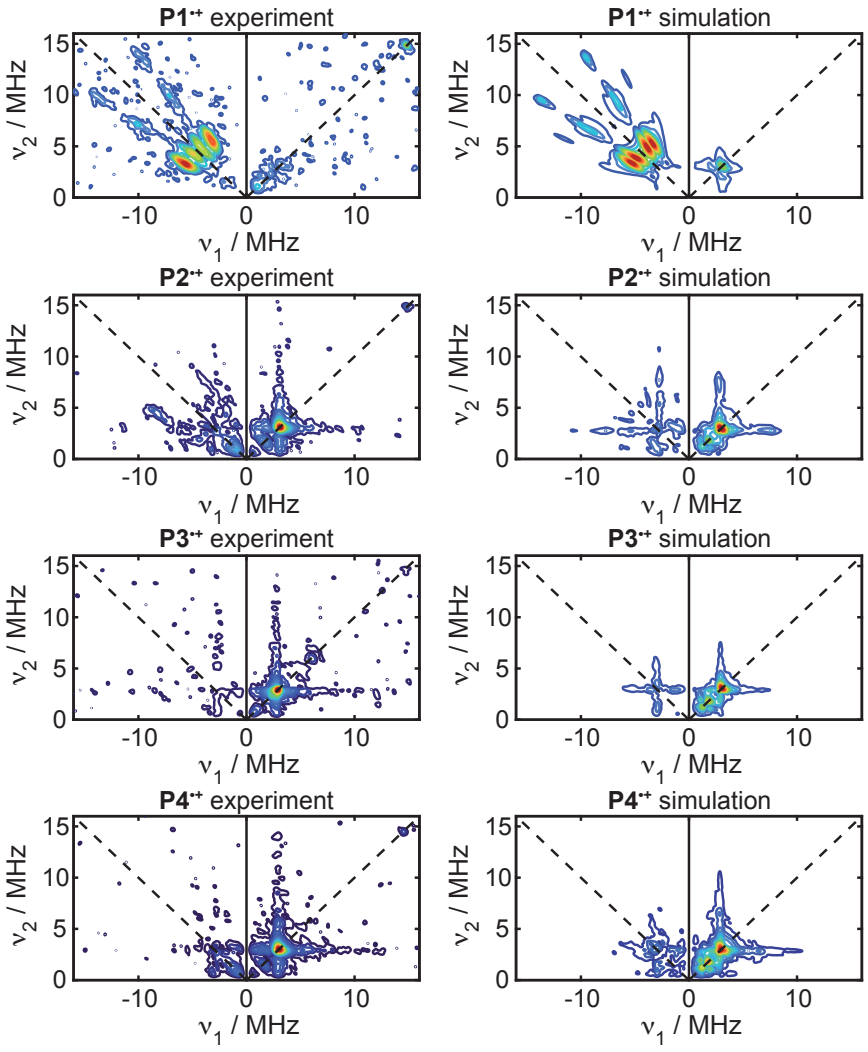


Figure 2.15: ^{14}N HYSCORE spectra of $\mathbf{P1}^{\bullet+}$ to $\mathbf{P4}^{\bullet+}$ measured at 80 K in frozen CD_2Cl_2:toluene-d_8:THF-d_8 1:1:1 at X-band frequencies at field positions corresponding to $g_{x,y}$. The simulated spectra were obtained using anisotropic ^{14}N hyperfine tensors $^{14}\boldsymbol{A}$ derived from distributed point-dipole calculations and ^{14}N quadrupole interactions calculated by DFT with B3LYP as functional and the EPRII basis set.

2.3.7 Accidental Oxidation of Extended Nanoribbons

The characterization of the edge-fused porphyrin nanoribbons ***PN*** by solution-phase ^{1}H NMR spectroscopy shows a substantial broadening of the proton resonances for $N > 4$ (Figure 2.16B), as previously reported by Osuka.[113, 212] This prompted the investigation of samples of ***PN*** prior to chemical oxidation by EPR spectroscopy. Cw-EPR spectra of **P2**, **P6**, and **P10** at 298 K and X-band frequencies without chemical oxidation confirm the closed-shell, diamagnetic character of **P2** and the emergence of increasing amounts of an EPR active, paramagnetic species in **P6** and **P10** (Figure 2.16A). Quantification of the radical content of the samples before and after chemical oxidation with **BAHA** by changes in the double-integrals of their cw-EPR spectra confirms that about 2% of **P6** and 12% of **P10** form radicals under ambient conditions.

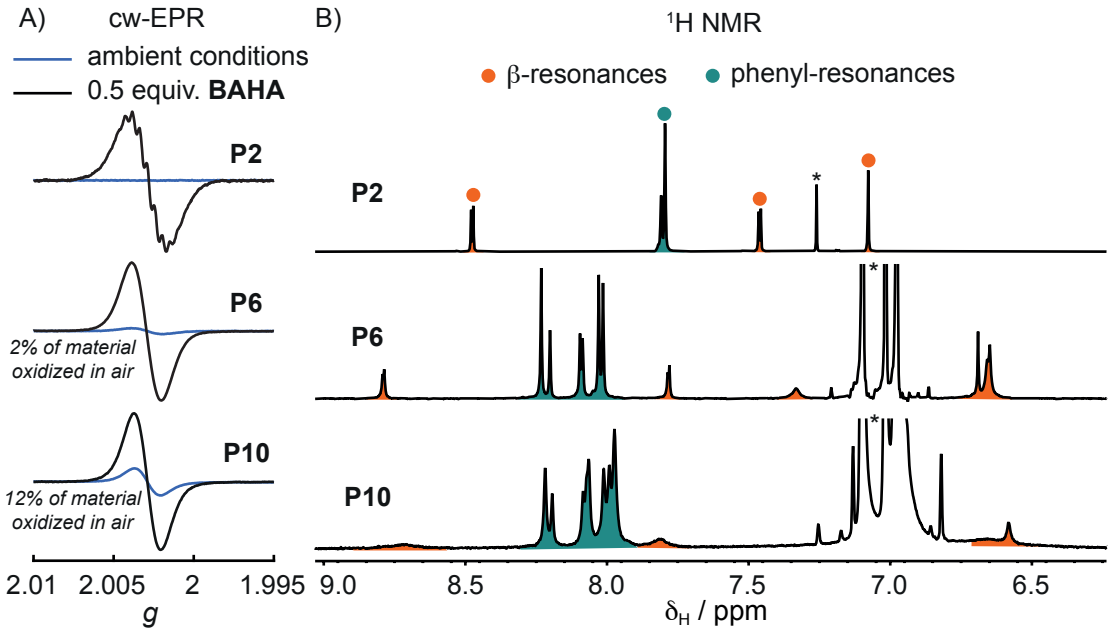


Figure 2.16: A) Comparison of the room temperature cw-EPR spectra of **P2**, **P6**, and **P10** in CD_2Cl_2:toluene-d_8:THF-d_8 1:1:1 at 298 K before (blue) and after (black) their chemical oxidation with 0.5 equivalents of **BAHA**. All measurements were performed with identical acquisition parameters to allow for the quantification of the open-shell character by double-integration. B) Aromatic region of the ^{1}H NMR spectra of **P2**, **P6**, and **P10** (298 K, toluene-d_8/$CDCl_3$); * = toluene-d_8/$CDCl_3$.

The nature of these radicals was investigated by a combination of room temperature X-band cw-EPR and W-band pulse EPR spectroscopy in frozen CD_2Cl_2:toluene-d_8:THF-d_8 1:1:1 at 50 K (Figure 2.17). The cw-EPR spectra and echo-detected field sweep spectra

of **P6** and **P10** both exhibit identical spectral shapes and $\boldsymbol{g}$-anisotropies with and without chemical oxidation. In addition, both species have identical anisotropic proton hyperfine interactions as confirmed by the identical width and shape of their ^{1}H Mims ENDOR spectra measured at field positions corresponding to $g_{x,y}$ and g_z. In combination, this spectroscopic evidence demonstrates that the partial open-shell character of **P6** and **P10** prior to chemical oxidation results from the spontaneous formation of their radical cations, presumably due to aerobic oxidation. No degradation of the partially oxidized samples was observed during purification by silica and size-exclusion chromatography or while they were stored as solid samples, which highlights the remarkable stability of the radical cations. Due to their even more extended π-systems, **P14** and **P18** exist predominantly as radical cations after exposure to air under ambient conditions. The formation of the radical cations shifts the optical absorption spectra to longer wavelengths, as discussed Section 2.3.8.

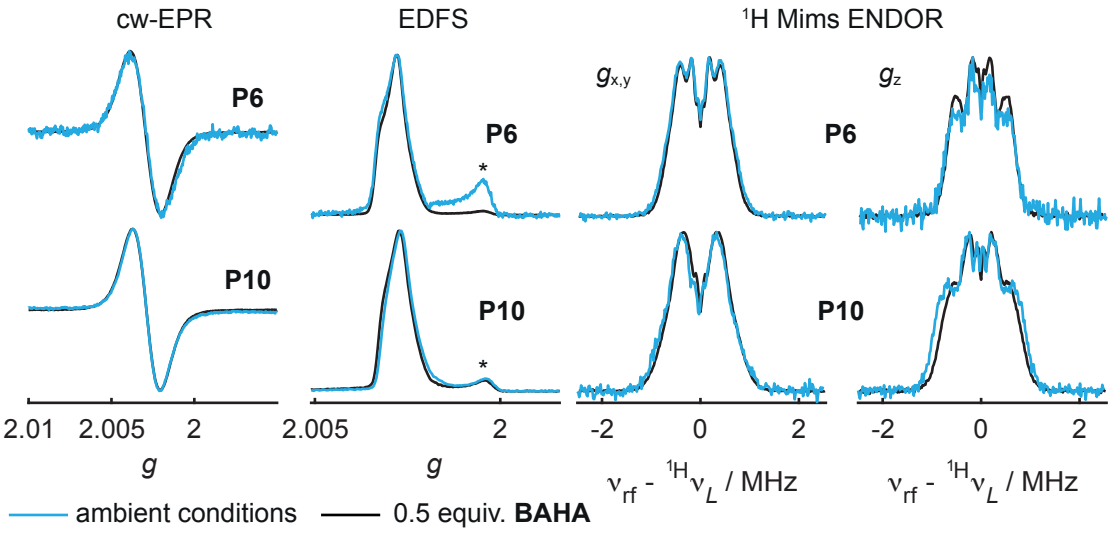


Figure 2.17: Comparison of the normalized room temperature X-band cw-EPR spectra, W-band echo-detected field sweep (EDFS) spectra, and W-band ^{1}H Mims ENDOR spectra of **P6**, and **P10** before (blue) and after (black) their chemical oxidation with 0.5 equivalents of **BAHA**. All W-band pulse EPR experiments were performed at 50 K in a frozen solution of CD_2Cl_2:toluene-d_8:THF-d_8 1:1:1 ; * = resonator background in the echo-detected field sweep spectra.

2.3.8 Optical vis-NIR-MIR Spectroelectrochemistry

Optical spectroscopy of organic mixed valence compounds such as **PN**$^{\bullet+}$ provides important information about their reorganization energy λ and electronic coupling energy H, and probes the polaron delocalization on a fs-time-scale in solution.[141, 213] A simple model to describe polaron delocalization is the Marcus–Hush theory which allows for the classification of mixed valence compounds based on the strength of the electronic coupling between the individual redox sites as proposed by Robin and Day (see Section 1.3.1 for details).[141, 145, 146, 148] Compared to their neutral analogues, radical cations of π-conjugated oligomers typically feature two characteristic low energy absorption bands P_1 and P_2 in their optical absorption spectra which approximately correspond to HOMO → SOMO and SOMO → LUMO transitions, respectively.[150–152]

The vis-NIR-MIR absorption spectra of **PN** were measured as a function of electrochemical oxidation in CH_2Cl_2 containing Bu_4NPF_6 (0.1 M) as electrolyte under an argon atmosphere. Deconvolution of the raw data gave the absorption spectra of several different oxidation states in each oligomer. The absorption spectra of **PN** in different oxidation states together with the 2D spectroelectrochemistry data that shows the evolution of the absorption profiles of **PN**$^{\bullet+}$ with increasing voltage are summarized in Figure 2.18. The absorption spectra of neutral and oxidized oligomers **P2** to **P4**, **P6**, **P10**, and **P18** obtained from spectroelectrochemistry are shown in Figure 2.19. The spectra of the neutral oligomers shown here are under slight electrochemical reduction to avoid the accidental oxidation observed under aerobic conditions.

The absorption spectra of neutral **PN** exhibit three characteristic peaks I, II, and III that originate from the B_y, B_x, and Q_x transitions of a porphyrin monomer, respectively.[200] TD-DFT calculations of **PN** with LC-ωHPBE ($\omega = 0.1$) as functional indicate that band III arises from the HOMO → LUMO transition in each neutral oligomer in agreement with previous reports.[113, 200, 212] The absorption spectra

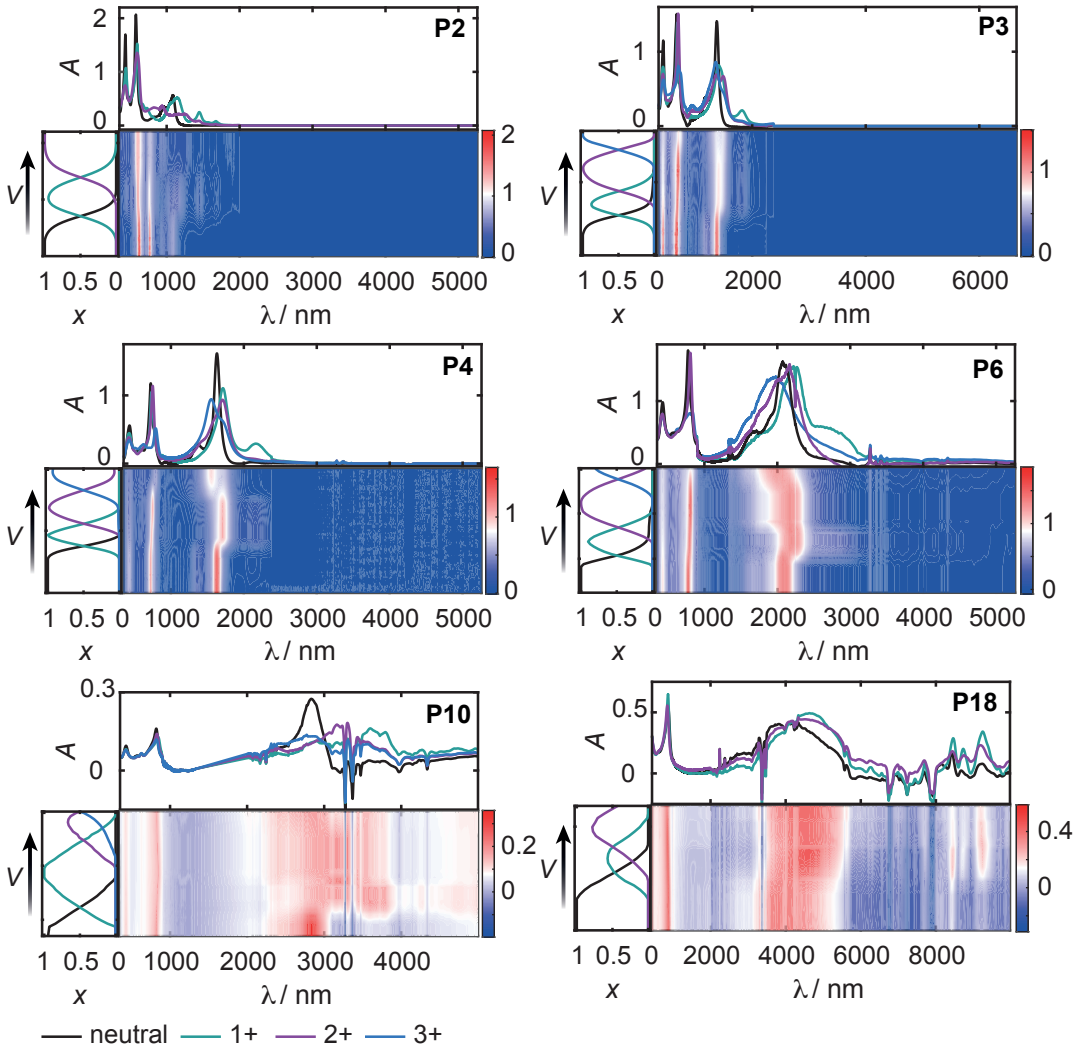


Figure 2.18: Deconvoluted spectroelectrochemistry data for the oxidation of **P*N*** (N = 2–4, 6, 10, 18) in CH_2Cl_2 (0.1 M Bu_4NPF_6). The resolved spectra for the individual oxidation states are shown above the contour plots. The speciation curves of the different oxidation states with increasing voltage are shown in the left subplots with x indicating the fraction of material in each oxidation state.

of the radical cations **P*N***$^{\bullet+}$ each exhibit an additional low energy absorption peak. This contrasts with the previously reported optical signatures of oxidized butadiyne-linked porphyrin oligomers which feature two distinct electronic transitions: P_1 at 2000–5000 nm and P_2 at around 1000 nm.[51] TD-DFT calculation of the excitation energies of **P*N*** and **P*N***$^{\bullet+}$ (N = 1–4, 6, 10) at the LC-ωHPBE/6-31G* ($\omega = 0.1$) level of theory are in good agreement with the experimental observations (Figure 2.19 and Figure 2.20). Attempts to perform TD-DFT calculations for **P18** and **P18**$^{\bullet+}$ were unsuccessful due to the extensive computational requirements.

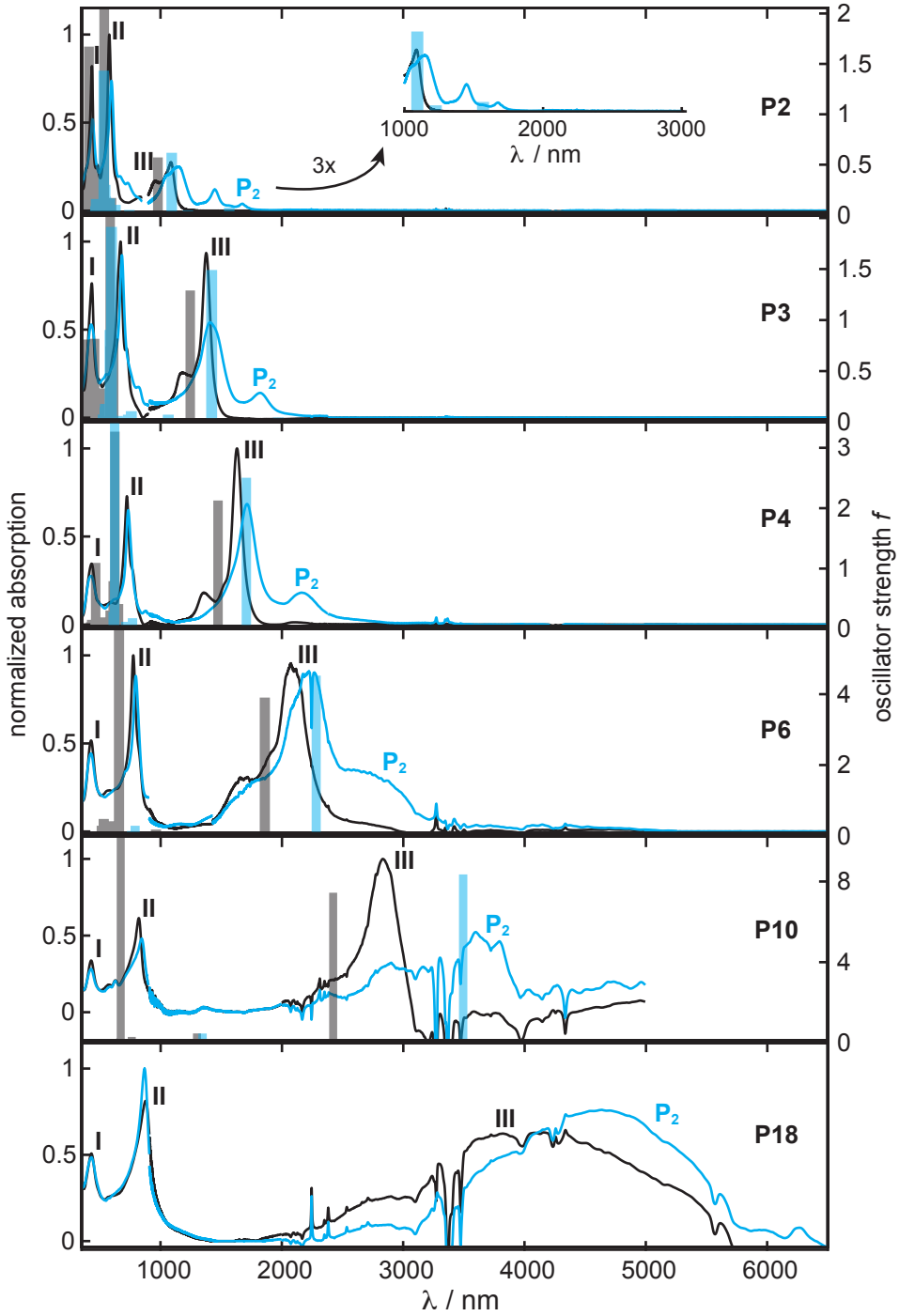


Figure 2.19: Vis-NIR-MIR normalized absorption spectra of ***PN*** (black) and ***PN***$^{\bullet+}$ (blue) from spectroelectrochemistry in CH_2Cl_2 (0.1 M Bu_4NPF_6, 298 K). The vertical bars indicate the TD-DFT (LC-ωHPBE/6-31G*; $\omega = 0.1$) calculated wavelengths and oscillator strengths f for the electronic transitions of the neutral and oxidized oligomers. Attempts to perform TD-DFT calculations for **P18** and **P18**$^{\bullet+}$ were unsuccessful due to the extensive computational requirements.

Comparison of the calculated electronic transitions to those observed in the deconvoluted experimental spectra suggest that the characteristic low energy absorption bands of $\mathbf{PN}^{\bullet+}$ mainly arise from SOMO → LUMO transitions and therefore correspond to the P_2 bands of the hole polarons. The P_1 bands of $\mathbf{PN}^{\bullet+}$ are dipole forbidden, merged with the SOMO → LUMO transition, or occur at relatively higher excitation energies depending on the length of the oligomer and functional employed in the TD-DFT calculations. Therefore, the following analysis focuses on the P_2 bands.

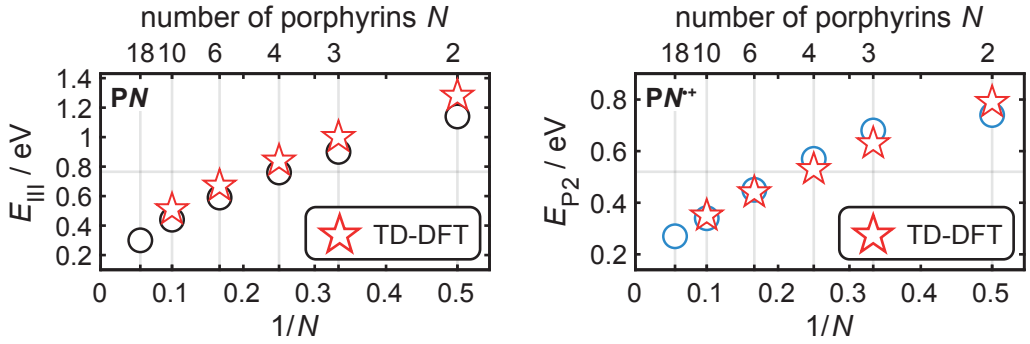


Figure 2.20: Trend in the experimental and TD-DFT (LC-ωHPBE/6-31G*; $\omega = 0.1$) calculated transition energies E for the lowest energy absorption bands of **PN** and the P_2 bands in $\mathbf{PN}^{\bullet+}$ in CH_2Cl_2.

Table 2.5: Summary of the experimental and TD-DFT calculated wavelengths λ and transition energies E for the long-wavelength absorption bands on **PN** and $\mathbf{PN}^{\bullet+}$ ($N = 2$–4, 6, 10, 18) in CH_2Cl_2. All TD-DFT calculations were performed with LC-ωHPBE ($\omega = 0.1$) as functional and the 6-31G* basis set with the PCM solvent model for CH_2Cl_2.

PN	$N = 2$	$N = 3$	$N = 4$	$N = 6$	$N = 10$	$N = 18$
$\lambda_{exp,III}$ / nm	1087	1378	1630	2088	2835	4080
$E_{exp,III}$ / eV	1.14	0.90	0.76	0.59	0.44	0.30
$\lambda_{LC\text{-}\omega HPBE,III}$ / nm	966	1245	1474	1860	2423	–
$E_{LC\text{-}\omega HPBE,III}$ / eV	1.28	1.00	0.84	0.67	0.51	–

$\mathbf{PN}^{\bullet+}$	$N = 2$	$N = 3$	$N = 4$	$N = 6$	$N = 10$	$N = 18$
λ_{exp,P_2} / nm	1674	1822	2161	2785	3600	4642
E_{exp,P_2} / eV	0.74	0.68	0.57	0.45	0.34	0.27
$\lambda_{LC\text{-}\omega HPBE,P_2}$ / nm	1567	1972	2322	2819	3495	–
$E_{LC\text{-}\omega HPBE,P_2}$ / eV	0.79	0.63	0.53	0.44	0.35	–

The lowest energy absorption bands (III) of **PN** and P_2 bands of $\mathbf{PN}^{\bullet+}$ exhibit a continuous bathochromic shift with increasing oligomer length which is replicated

by TD-DFT calculations and consistent with a continuous narrowing of their optical excitation gaps (Figure 2.20, Table 2.5). For the neutral oligomers **P*N***, the progressive bathochromic shift of band III does not saturate for $N \leq 18$ which suggests an effective conjugation length $N_{\text{eff}} \geq 18$ porphyrin units. In contrast, Osuka reported an effective conjugation length of 14–16 porphyrin units for **P*N***.[212] The radical cation P_2 bands show a similar trend to band III in the neutral oligomers, although with a clear shift to lower energies over the entire oligomer series. This points towards a limit of coherent radical delocalization beyond 18 porphyrin units in **P*N***$^{\bullet+}$.

To describe electron transfer processes in molecular chains comprised of N repeat units, Rathore and co-workers developed the multistate parabolic model (MPM) which extends the Marcus–Hush theory of mixed valence systems to an arbitrary number of electron transfer sites.[147] As for the Marcus–Hush model, the energies of the adiabatic states, G, are obtained following equation 2.3 by finding the solutions for which the secular determinant is equal to zero.

$$\begin{vmatrix} x^2-\epsilon/\lambda-G/\lambda & H/\lambda & 0 & \cdots & 0 \\ H/\lambda & (1-x)^2-G/\lambda & H/\lambda & \ddots & \vdots \\ 0 & H/\lambda & \ddots & H/\lambda & 0 \\ \vdots & \ddots & H/\lambda & (N-2-x)^2-G/\lambda & H/\lambda \\ 0 & \cdots & 0 & H/\lambda & (N-1-x)^2-\epsilon/\lambda-G/\lambda \end{vmatrix} = 0 \tag{2.3}$$

To account for the effect of the terminal electron withdrawing TIPS-acetylene groups on the hole stability on the adjacent porphyrin units, the energy of the terminal parabolas can be shifted by ϵ.[147] Division by λ gives a model that expresses the coupling between neighbouring porphyrin units with a single parameter (H/λ). The vertical excitation energy $\Delta G_{\text{abs},i}/\lambda$ from the ground state to the excited state i is described by equation 2.4.

$$\Delta G_{\text{abs},i}/\lambda = G_i/\lambda - G_0/\lambda \tag{2.4}$$

where G_i/λ and G_0/λ are the free energies of the excited state and ground state, respectively. To model the electron delocalization in **P*N***$^{\bullet+}$, equation 2.3 was solved for each

oligomer ($N = 3$, 4, 6, 10, and 18) and the obtained excitation energies $\Delta G_{abs}(N)/\lambda$ normalized to give $\Delta G_{abs}(3)/\lambda = 1$ and fitted to the trend in the experimental P_2 band excitation energies E_{P_2}. Here, $\Delta G_{abs}(N)/\lambda$ corresponds to the excitation energy from the ground state to the second excited state ($\Delta G_{abs}(N)/\lambda = G_2(N)/\lambda - G_0(N)/\lambda$) to describe the experimental P_2 band. The calculated parabolas for each oligomer are shown in Figure 2.21A with the red arrows corresponding to the modelled P_2 excitations. The simulated values of $\Delta G_{abs}(N)/\lambda$ using $H/\lambda = 8.3$ and $\epsilon/\lambda = -2.4$ broadly match the trend in the normalized experimental excitation energies of the P_2 band (Figure 2.21B). The negative sign of ϵ/λ is consistent with a destabilization of the hole polaron on the terminal porphyrin units due to the TIPS-acetylene end groups. The best-fit value of H/λ is significantly larger than 0.5 which suggest that the porphyrin nanoribbon radical cations $\mathbf{PN}^{\bullet+}$ are best described as Robin–Day class III mixed valence systems. Peeks, Tait *et.al.* found that the electronic coupling in butadiyne-linked porphyrin radical cations corresponds to $H/\lambda = 1.2$.[51] This is further evidence for the substantially stronger electronic coupling in edge-fused porphyrin nanoribbon radical cations.

Beyond the qualitative classification of $\mathbf{PN}^{\bullet+}$ as Robin–Day class III systems, the multistate parabolic model struggles to accurately describe the electronic structure of the extended porphyrin radical cations. While DFT calculations and the in-depth analysis of the EPR data suggest a complete delocalization of the radical over all porphyrin units for $N \leq 10$ the MPM simulations wrongly predict that the electron density is distributed around the center of the oligomers. In addition, the simulated trend for $\Delta G_{abs}(N)/\lambda$ starts to saturate for $N \geq 10$, which is not observed for the experimental excitation energies. This suggests a limited suitability of the MPM approximation for electron transfer processes in very strongly coupled oligomers. Attempts to overcome these limitations by introducing additional long range coupling elements in the MPM Hamiltonian or by resorting to the multistate model did not improve the description of the electronic structure of $\mathbf{PN}^{\bullet+}$.[214]

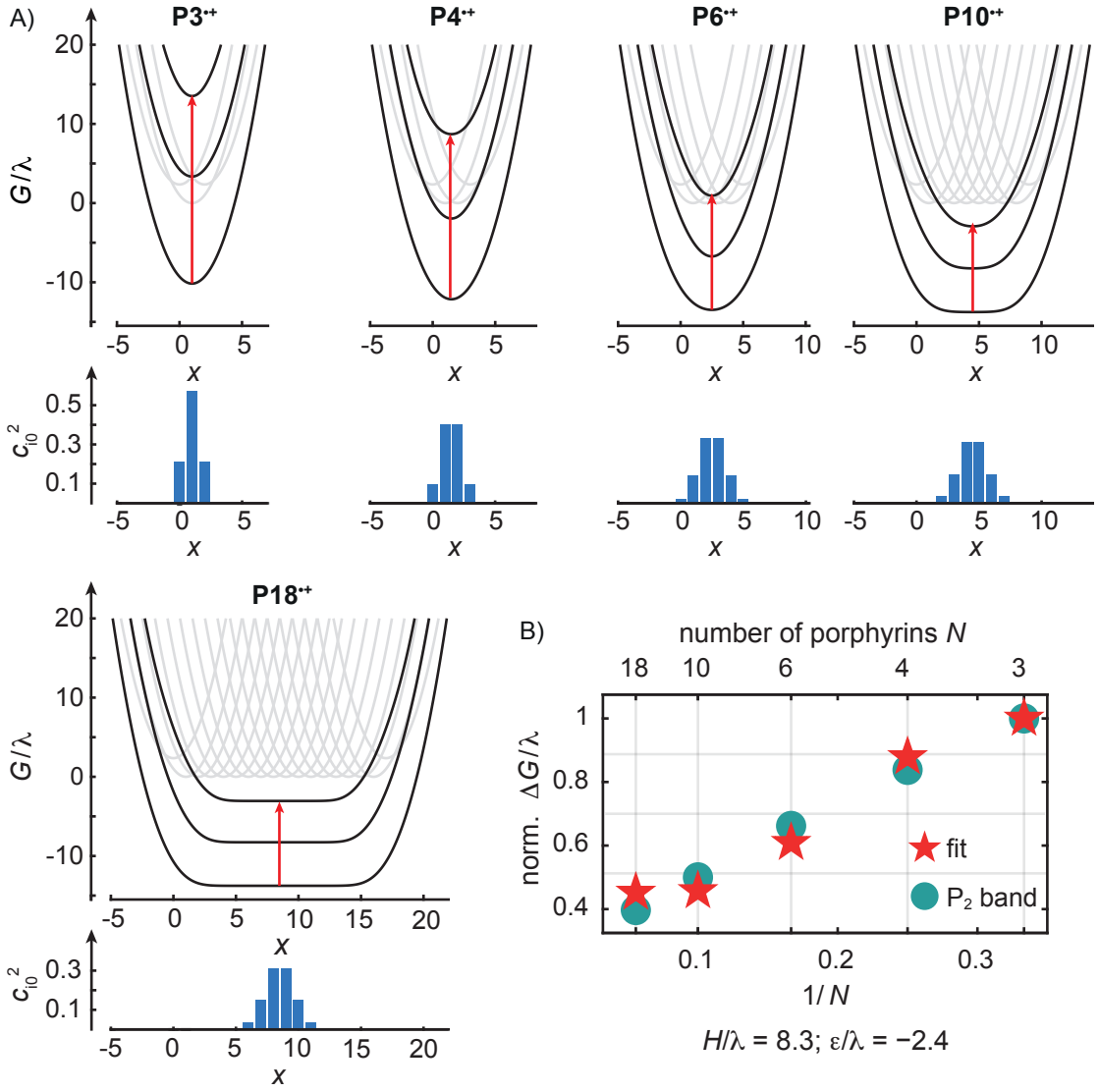


Figure 2.21: A) MPM simulations of $\mathbf{PN}^{\bullet+}$ (N = 3, 4, 6, 10, 18) using $H/\lambda = 8.3$ and $\epsilon/\lambda = -2.4$; x is the reaction coordinate of the electron transfer; ${c_{i0}}^2$ gives the density of the hole on each porphyrin unit. B) Normalized experimental excitation energies (green) and MPM simulated excitation energies $\Delta G_{abs}(N)/\lambda$ (red) for the P_2 absorption bands. The simulations were performed with $H/\lambda = 8.3$ and $\epsilon/\lambda = -2.4$ obtained by least-squares fitting of the simulated excitation energies to the experimental trend ($rmsd = 0.04$).

2.4 Summary and Conclusion

In this chapter, the extent of delocalization in the radical cations of a series of β,*meso*,β-triply linked porphyrin oligomers **PN** was investigated by a combination of EPR and optical spectroscopy and supporting DFT simulations. Cw-EPR spectroscopy at room temperature in solution, together with ^{1}H and ^{14}N Mims ENDOR spectroscopy in

frozen solutions at 50 K, demonstrate coherent polaron delocalization over 10 to 14 porphyrin units in $\mathbf{PN}^{\bullet+}$. These conclusions have been guided by simulations of the experimental spectra using ^{1}H and ^{14}N hyperfine interactions calculated from a fully delocalized spin density distribution in each oligomer via a distributed point-dipole approximation. The versatility and accuracy of this approach is highlighted by the fact that all cw-EPR spectra, ^{1}H and ^{14}N ENDOR spectra, and, where applicable, ^{14}N HYSCORE spectra, of an oligomer could be simulated with the same set of hyperfine interactions. The simulations also demonstrate that the deviation of the cw-EPR spectral width from an ideal Norris trend results from a non-uniform spin density distribution. The discontinuous trend in the ^{1}H ENDOR full width at half maximum is explained by a local redistributions of spin density and does not contradict a full delocalization of the radical spin density. This highlights the importance of theoretical modelling to guide the interpretation of experimental EPR results, and that discussions based merely on trends in the experimental spectra are insufficient to determine the delocalization of organic radicals. The continuous bathochromic shift of the P_2 lowest energy absorption band in the vis-NIR-MIR absorption spectra of $\mathbf{PN}^{\bullet+}$ in combination with TD-DFT calculations suggest an effective polaron delocalization length of more than 18 porphyrin units in $\mathbf{PN}^{\bullet+}$.

In conclusion, the combined spectroscopic analysis clearly shows radical cation delocalization over more than 10 porphyrins in $\mathbf{PN}^{\bullet+}$. This corresponds to an effective polaron delocalization length greater than 8.5 nm and marks, to the best of my knowledge, the longest coherent polaron delocalization reported in π-conjugated molecular materials to date.[83, 85, 116, 215] For comparison, the polaron coherence length in the widely studied organic semiconductor poly(3-hexylthiophene) (P3HT) is approximately 4–7 repeat units, which corresponds to 1.5-2.7 nm.[216, 217] These long delocalization lengths combined with the increasing coherence times in extended oligomers demonstrate that porphyrin nanoribbons are exceptionally effective molecular wires.

2.5 Methods

2.5.1 General Methods

EPR Sample Preparation

Samples of $\mathbf{PN}^{\bullet+}$ (N = 1–4, 6, 10, 14, 18) for EPR measurements were prepared in CD_2Cl_2:toluene-d_8:THF-d_8 1:1:1 and degassed using three freeze-pump-thaw cycles. For chemical oxidation, ~0.5 equivalents of tris(4-bromophenyl)-aminium hexachloroantimonate (**BAHA**) (1.0 mM in CD_2Cl_2) were added to a solution of the porphyrin oligomer (~200 μM in CD_2Cl_2:toluene-d_8:THF-d_8 1:1:1 for X-band cw-EPR measurements and typically ~400 μM in CD_2Cl_2:toluene-d_8:THF-d_8 1:1:1 for W-band pulse EPR measurements) under argon immediately before the EPR experiments. The 1:1:1 solvent mixture of CD_2Cl_2:toluene-d_8:THF-d_8 was chosen because it forms a glass at low temperatures and does not cause noticeable degradation of the porphyrin radical cations over several hours at 298 K. All radical cation samples were prepared in X-band EPR tubes (3.8 mm o.d.). For W-band measurements, an aliquot of sample was transferred from an X-band tube to the W-band tube (0.9 mm o.d.) using a thin glass capillary. For low-temperature measurements, the samples were flash-frozen in liquid nitrogen.

Continuous-Wave EPR Measurements

Continuous-wave X-band EPR spectra were acquired at 298 K on a Bruker EMX Micro spectrometer equipped with a high sensitivity Bruker probe head. EPR spectra were recorded at a microwave frequency of ~9.40 GHz with modulation amplitudes and frequencies of 0.1 G and 100 kHz, respectively. The microwave power was scanned to rule out spectral distortions due to saturation effects. The optimal microwave power used in all the cw-EPR spectra in this chapter was 2.0 mW or 1.26 mW corresponding to attenuations of 20 dB or 22 dB on our spectrometer, respectively. The reported spectra were obtained by combining several individually recorded scans to ensure that the signal intensity and shape remained constant over time.

Pulse EPR Measurements

Pulse EPR measurements were performed on a W-/X-band Bruker Elexsys 680 spectrometer equipped with helium gas flow cryostats from Oxford Instruments at 50 K. Echo-detected field sweep W-band EPR spectra were recorded by integrating the echo of the two-pulse Hahn echo sequence, $\frac{\pi}{2}-\tau-\frac{\pi}{2}-\tau-echo$, with pulse lengths $t_{\pi/2}=64$ ns and $t_{\pi}=128$ ns, an interpulse delay $\tau=300$ ns, and using a two-step phase cycle. Phase memory time measurements were performed using a two-pulse Hahn echo sequence with varying interpulse delay τ.

W-band ^{1}H and ^{14}N Mims ENDOR spectra were recorded with the pulse sequence $\frac{\pi}{2}-\tau-\frac{\pi}{2}-T-\frac{\pi}{2}-\tau-echo$ with a microwave pulse length $t_{\pi/2}=64$ ns. ^{1}H ENDOR measurements were performed with a radiofrequency pulse length $t_{\mathrm{rf}}=28$ µs with three different τ-values ($\tau=240$ ns, 300 ns, and 360 ns) to rule out distortions arising from the blind-spot characteristics of the Mims ENDOR sequence. ^{14}N ENDOR measurements were performed with a radiofrequency pulse length $t_{\mathrm{rf}}=70$ µs with two τ-values ($\tau=140$ ns and 160 ns). Before each ENDOR measurement, the power of the radiofrequency pulses was adjusted to obtain a π-pulse using a Rabi nutation experiment at the Larmor frequency ν_L of the investigated nuclei (about 140 MHz for ^{1}H and 10 MHz for ^{14}N).

X-band ^{14}N HYSCORE spectra were recorded with the pulse sequence $\frac{\pi}{2}-\tau-\frac{\pi}{2}-t_1-\pi-t_2-\frac{\pi}{2}-\tau-echo$ with microwave pulse lengths $t_{\pi/2}=16$ ns and $t_{\pi}=20$ ns and three different τ-values ($\tau=120$ ns, 170 ns, and 220 ns) to rule out distortions arising from blindspots. The delays t_1 and t_2 were incremented starting at 100 ns in 16 ns steps (256 x 256 data matrix). The experimental data were baseline corrected using a 3$^{\mathrm{rd}}$ order polynomal, apodised with a −80 dB side lobe suppression Dolph-Chebyshev window, and zero-filled to 4096 points in each dimension. The final spectrum was obtained as the absolute-value spectrum calculated after applying a 2D Fourier transform.

Spectroelectrochemistry

All optical spectroelectrochemistry (SEC) measurements were performed in an optically transparent thin layer electrochemistry (OTTLE) cell comprising a platinum gauze working electrode, a platinum wire counter electrode, and a Ag/AgCl reference electrode.[218] The measurements were performed in an electrolyte solution of 0.1 M tetra-n-butylammonium hexafluorophosphate (Bu_4NPF_6) in dry CH_2Cl_2. NIR and MIR measurements were performed using a Bruker Vertex 80 FT-IR spectrometer in rapid repeated measurement mode. The optical path was purged with dry N_2 for about 30 minutes after sample insertion. NIR spectra were collected with a CaF_2 beam splitter, tungsten source, and RT-InGaAS detector, and MIR spectra with a KBr beam splitter, Globar source and LN_2 cooled-MCT detector. Vis measurements were performed using a Cary 4000 UV-vis spectrophotometer in kinetics mode, and also purged with dry N_2. Measurements across the entire vis, NIR, and MIR range utilized background spectra acquired using the OTTLE cell containing the electrolyte solution of 0.1 M Bu_4NPF_6 in dry CH_2Cl_2. Spectra were collected every ~1.2 s in the NIR and MIR and ~30 s in the vis while a cyclic voltammetry experiment was performed in the OTTLE cell. The scan rate in the cyclic voltammogram was 0.01 mV/s for measurements in the NIR and MIR and 0.001 mV/s in the vis. The SEC data were symmetric around the upper inversion potential of the cyclic voltammogram consistent with the reversibility of the oxidations. The raw SEC data for each wavelength range (vis, NIR and MIR) were processed in python to remove noisy data on the edge of each wavelength region and to contain only the upward sweep of the cyclic voltammogram. The individual components contained in the spectral data and their speciation curves were extracted for each wavelength range using multivariate curve resolution with the MCR-ALS toolkit in MATLAB.[219–221] Subsequently, the deconvoluted spectra and 2D SEC data for each wavelength range were combined into the final data sets presented in this chapter.

Computational Methods

DFT geometry optimizations of the neutral and oxidized porphyrin oligomers were performed in Gaussian16 with the B3LYP functional and the 6-31G* basis set.[222–

226] The protecting groups on the terminal ethynes and the trihexylsilyl solubilizing sidechains were replaced with protons to increase the computational speed. The Mulliken spin populations of the radical cation geometries were obtained as part of the geometry optimizations. The stationary nature of the converged geometries was confirmed by the absence of imaginary vibrations in the frequency calculations for up to four porphyrin units in the oligomer. The dependence of the calculated Mulliken spin populations on the employed DFT functional was investigated by re-optimizing the geometries of the porphyrin radical cations with LC-PBE ($\omega = 0.2$)[227, 228], and ωB97X-D3BJ ($\omega = 0.05$)[229] as functionals using the ORCA package.[230, 231] Geometry optimizations with constrained geometries were also performed in ORCA. TD-DFT calculations[232] of of the neutral and oxidized porphyrin oligomers were performed for the first 64 excited states in Gaussian16 with B3LYP, LC-ωPBE ($\omega =$ 0.1 or 0.2)[233], or BLYP35[207] as functional and the 6-31G* basis set, using the PCM solvent model[234] (solvent = CH_2Cl_2). The hyperfine and nuclear quadrupole interaction parameters, and the principal values and orientation of the $\boldsymbol{g}$-tensors were calculated for the optimized structures of the radical cations with up to four porphyrin units with ORCA using B3LYP as defined in the Gaussian program system as functional and the EPRII base set, built specifically for the calculation of EPR hyperfine interaction values, for the C, N and H nuclei[235–237] and the 6-31G** basis set for Zn[225]. Calculations on the larger systems were not feasible due to the extensive computational requirements.

Simulation Methods

The cw-EPR spectra of the porphyrin radical cations were simulated with the EasySpin function *garlic*.[238] The anisotropic $\boldsymbol{g}$-tensors were obtained by least-squares fitting of the echo-detected field sweep EPR spectra using the EasySpin functions *esfit* and *pepper*. To reliably determine the magnitude of the principal values of $\boldsymbol{g}$, small offsets in the magnetic field axis of the W-band data were corrected by simultaneously fitting the W-band field sweep spectra and X-band cw-EPR spectra of the radical cations, using the cw-EPR spectra to determine the correct isotropic average of the fitted

$\boldsymbol{g}$-tensors. The phase memory times T_m were determined by fitting the echo decay time traces with a stretched exponential (stretching parameter d between 0.6 and 1.8) using the EasySpin function *esfit*.

The Mims ENDOR spectra were simulated using anisotropic hyperfine tensors calculated with the distributed point-dipole model described in Section 2.5.2. Simulations were performed separately for each ^{1}H or ^{14}N nucleus with the EasySpin function *saffron* using the relevant experimental τ-values, microwave pulse lengths $t_{\pi/2}$, and field positions, as well as an inherent linewidth of 0.25 MHz. The ^{14}N nuclear quadrupole interaction parameters Q and η did not vary considerably in the DFT calculations and therefore their average was used in the ^{14}N ENDOR simulations ($Q = 2.36$ MHz, $\eta = 0.68$). The final simulations were obtained as the sum of the individual spectra of all ^{1}H or ^{14}N nuclei. The ^{14}N HYSCORE spectra were simulated using anisotropic nitrogen hyperfine tensors obtained *via* the distributed point-dipole model or calculated by DFT at the B3LYP/EPRII level of theory. All simulations were performed with the EasySpin function *saffron* using the relevant experimental τ-values and microwave pulse lengths $t_{\pi/2}$. To increase the computational speed of the simulations, only one ^{14}N nucleus representative of each set of four equivalent ^{14}N nuclei was included in the simulations. The validity of this approximation was confirmed by comparing the HYSCORE simulation of $\mathbf{P1}^{\bullet+}$ with one representative nucleus with an analogous simulation including all four ^{14}N nuclei, which resulted in virtually identical spectra. The ^{14}N nuclear quadrupole interaction parameters Q and η did not vary considerably in the DFT calculations. Therefore, the average DFT predicted quadrupole parameters Q and η for each set of equivalent ^{14}N nuclei were used in the HYSCORE simulations.

Multiparabolic model simulations of the spectroelectrochemistry data were performed with home-written MATLAB routines as detailed in the relevant section of this chapter.

2.5.2 Distributed Point-Dipole Simulations

Step 1: assignment of the spin density distribution

The spin density distributions used in the point-dipole calculations were closely guided by DFT-calculated Mulliken spin populations computed at the B3LYP/EPRII level of theory for optimized geometries of $\mathbf{PN}^{\bullet+}$. To systematically adjust the DFT assigned spin density distributions, each molecule was formally divided into subunits defined as the two terminal acetylene groups, the individual porphyrin units, and the aryl groups attached to each porphyrin unit. This classification is exemplified for $\mathbf{P2}^{\bullet+}$ in Figure 2.22A. For each subunit, the relative spin density distributions χ_i were calculated using the DFT predicted Mulliken spin densities following equation 2.5:

$$\chi_i = \frac{\rho_i}{\rho_{\text{subunit}}} \tag{2.5}$$

where ρ_i is the amount of spin density assigned to an individual atom i and ρ_{subunit} is the total amount of spin density assigned collectively to all atoms in the subunit. This definition allows for a redistribution of spin density between the subunits of $\mathbf{PN}^{\bullet+}$ without modifying how the spin density is distributed to each individual atom. The magnitude of the relative spin density distributions is exemplified for the two porphyrin subunits in $\mathbf{P2}^{\bullet+}$ in Figure 2.22B.

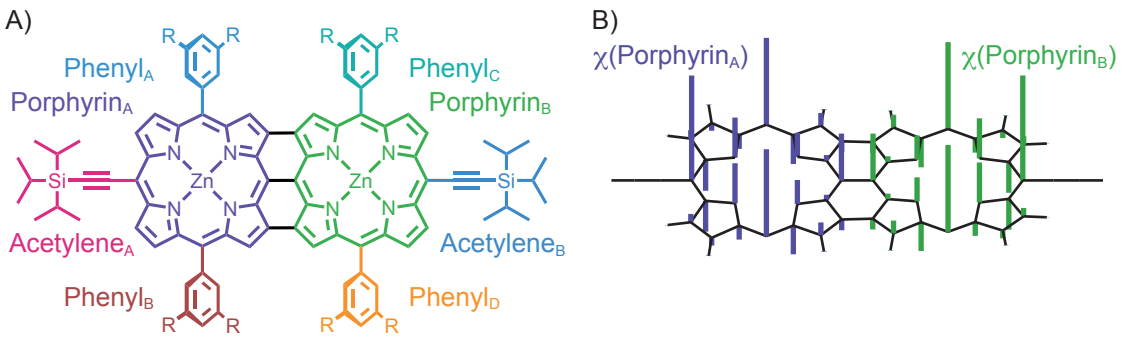


Figure 2.22: A) Visualization of the subunit assignment in $\mathbf{P2}^{\bullet+}$; R = Si(C_6H_{13})$_3$. B) Schematic representation of the relative spin density distributions χ_i for atoms assigned to the two porphyrin subunits in $\mathbf{P2}^{\bullet+}$. The height of the coloured bars indicates the magnitude of the relative spin density χ_i assigned to the individual atoms; positive/negative values are shown above/below the molecular plane. The phenyl substituents are omitted for clarity.

Using the DFT calculated spin densities as a starting point, the following systematic modifications could be implemented where necessary to refine the spin density

distribution to obtain a better agreement with the experimental data in subsequent EPR spectra simulations:

1. Variation of the spin density assigned to the terminal acetylene groups: The end groups of the porphyrin nanoribbons are triisopropylsilyl (TIPS) terminated acetylenes that are slightly electron-withdrawing, as evident from the optical spectroelectrochemistry measurements. The TIPS groups were omitted in all DFT calculations to increase the computational speed. To still account for their electron withdrawing effect, the spin density assigned to the terminal acetylene groups of $\mathbf{P1}^{\bullet+}$ and $\mathbf{P2}^{\bullet+}$ in the point-dipole simulations was increased by 75% compared to the DFT assigned spin densities. The excess spin density was removed uniformly from the other subunits of the molecules.

2. Variation of the spin density assigned to the phenyl solubilizing sidechains: The amount of spin density delocalized from each porphyrin onto its two phenyl substituents is determined by the dihedral angle between the porphyrin plane and the sidegroups which modulates their π-orbital overlap. In all DFT optimized geometries of $\mathbf{P}\boldsymbol{N}^{\bullet+}$, this dihedral angle is about 66°. These calculations neglect however the influence of the sterically demanding trihexylsilyl solubilizing sidechains attached to the *meta*-positions of each phenyl group. The steric interaction between the sidechains of neighboring porphyrin units is expected to favor larger dihedral angles and therefore a smaller orbital overlap for oligomers with more than three porphyrin units. To account for this effect, the amount of spin density delocalized from each porphyrin unit to its phenyl substituent was reduced stepwise from 3.8% in $\mathbf{P1}^{\bullet+}$ to 1.3% in $\mathbf{P10}^{\bullet+}$.

The distribution of spin density between the porphyrin subunits in $\mathbf{P}\boldsymbol{N}^{\bullet+}$ was directly taken from DFT calculations and only marginally adjusted where necessary to optimize the agreement with the experiment. In all oligomers, the spin density distribution employed for the point-dipole calculations shows a complete delocalization of the radical spin density, consistent with DFT calculations at the B3LYP/6-31G* level of theory (Figure 2.23).

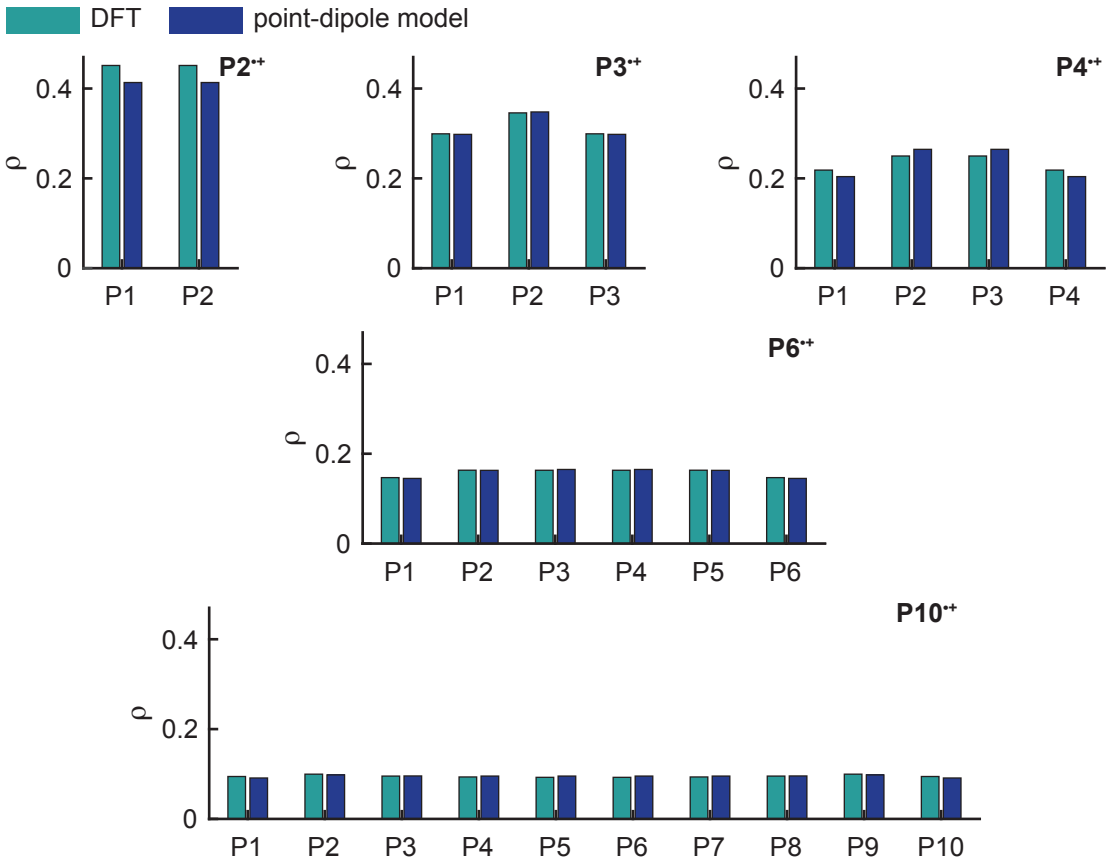


Figure 2.23: Schematic visualization of the distribution of the radical spin density ρ between the porphyrin subunits in $\mathbf{PN}^{\bullet+}$ (N = 2–4, 6, 10) predicted by DFT calculations with B3LYP as functional and the 6-31G* basis set (green) and implemented in the point-dipole simulations (blue).

To account for the π-radical character of $\mathbf{PN}^{\bullet+}$, spin densities assigned to sp^2-hybridized atoms were modelled to be localized in in *p*-type orbitals and split above and below the respective aromatic plane of the molecule. This is exemplified in Figure 2.24 for the spin distribution in $\mathbf{P2}^{\bullet+}$. The distance between the spin centers and the aromatic plane was optimized to give the best agreement between hyperfine tensors calculated by DFT and the point-dipole model for an identical spin density distribution and set to ±52 pm in all point-dipole calculations.

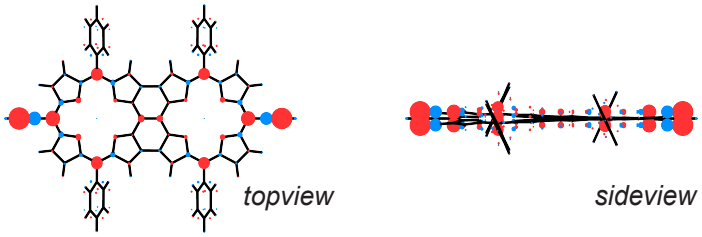


Figure 2.24: Visualization of the π-orbital type spin density centers in **P2**$^{\bullet+}$ used for the point-dipole calculations. The spin density at each point in space is represented by a sphere located at the position of the spin center with a radius proportional to the magnitude of its assigned spin density. Red spheres represent excess spin-up and light-blue spheres indicate excess spin-down densities.

Step 2: calculation of the dipolar hyperfine coupling contribution

The dipolar hyperfine tensor $\boldsymbol{T}_i$ of each ^{1}H and ^{14}N nucleus in **PN**$^{\bullet+}$ (N = 1–4, 6, 10) was calculated using the spin density distributions established in step 1. The through-space dipole-dipole interactions between nucleus i and and the discrete spin centers were approximated using the point-dipole model introduced in equation 1.18 in Chapter 1.

Step 3: calculation of the isotropic hyperfine coupling contribution

The isotropic contribution $a_{\mathrm{iso},i}$ to the hyperfine tensor of each ^{1}H and ^{14}N nucleus i was calculated based on the directly proportional relationship between $a_{\mathrm{iso},i}$ and the spin density assigned to the nucleus ρ_i.[77] The calculation of the McConnel proportionality constant for the nitrogen nuclei in **PN**$^{\bullet+}$ is discussed in Section 2.3.2. The proportionality factor used in this model was obtained based on DFT calculated Mulliken spin populations with B3LYP as functional and is $^{14\mathrm{N}}c$ = 48.9 MHz. McConnell's seminal work related the isotopic hyperfine interactions of aromatic protons to the amount of spin density on the carbon atom they are attached to.[77] This relationship was approximated for better implementation in the simulations by assuming a directly proportional relationship between $^{1\mathrm{H}}a_{\mathrm{iso},i}$ and $^{1\mathrm{H}}\rho_{\mathrm{i}}$. This approximation is valid as all relevant ^{1}H nuclei in **PN**$^{\bullet+}$ are directly attached to the porphyrin or phenyl π-framework and therefore assigned similar fractions of spin density relative to their α-carbons in the DFT calculations underpinning step 1.

The optimal ^{1}H McConnell constant for all protons in $\mathbf{PN}^{\bullet+}$ was determined by simulating the ^{1}H ENDOR spectrum of $\mathbf{P1}^{\bullet+}$ using ^{1}H hyperfine tensors $^{1\mathrm{H}}\boldsymbol{A}$ calculated with a range of proportionality constants $^{1\mathrm{H}}c$ (Figure 2.25). The best fit simulation was obtained with $^{1\mathrm{H}}c = 800$ MHz, which was subsequently used for all hyperfine calculations of $\mathbf{PN}^{\bullet+}$.

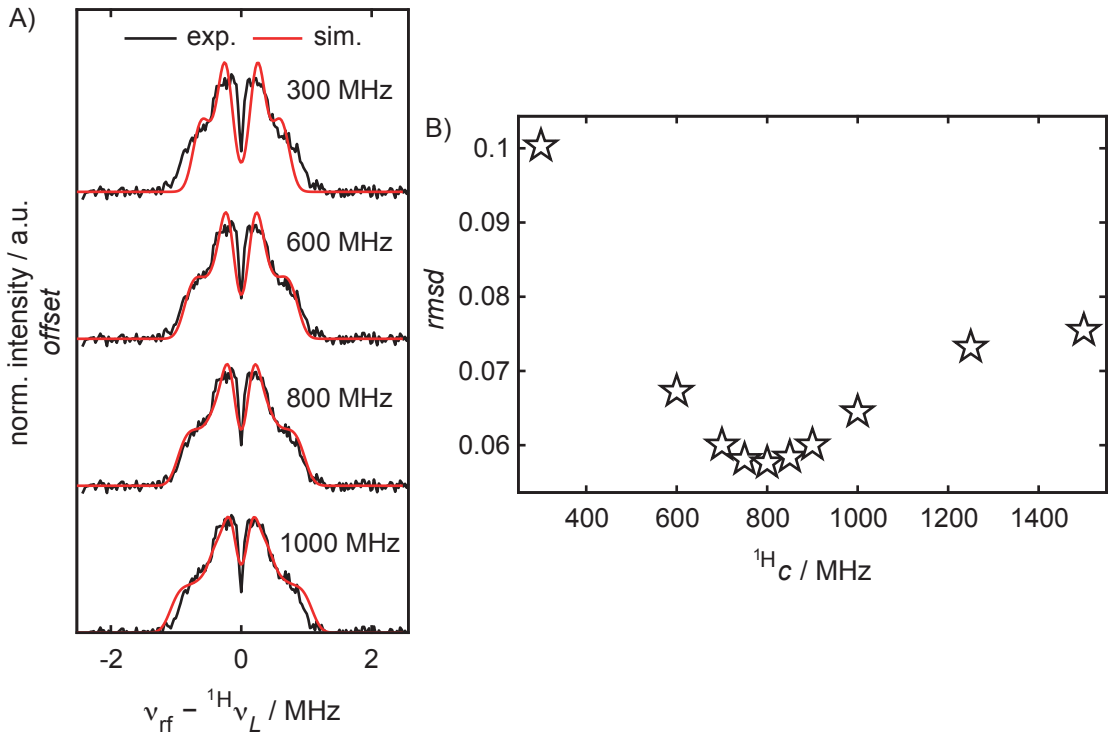


Figure 2.25: A) Overview of selected simulations of the W-band ^{1}H Mims ENDOR spectrum of $\mathbf{P1}^{\bullet+}$ with different ^{1}H McConnell constants $^{1\mathrm{H}}c$ employed in the calculation of the proton hyperfine tensors. B) Root-mean-square deviation (*rmsd*) of the experimental and simulated ENDOR spectra for different McConnell constants employed in the model. The experimental spectrum was recorded in CD_2Cl_2:toluene-d_8:THF-d_8 1:1:1 at 50 K at the field position corresponding to $g_{x,y}$.

Step 4: calculation of the final hyperfine tensor

The final hyperfine tensors $\boldsymbol{A}_i$ were calculated by combining the dipolar and isotropic hyperfine contributions $\boldsymbol{T}_i$ and $a_{\mathrm{iso},i}$ derived in steps 2 and 3, respectively. The spin distributions and ^{1}H and ^{14}N hyperfine coupling tensors calculated for $\mathbf{PN}^{\bullet+}$ ($N = 1$–4, 6, 10) with this model are shown in Figure 2.26, Figure 2.27, and Figure 2.28.

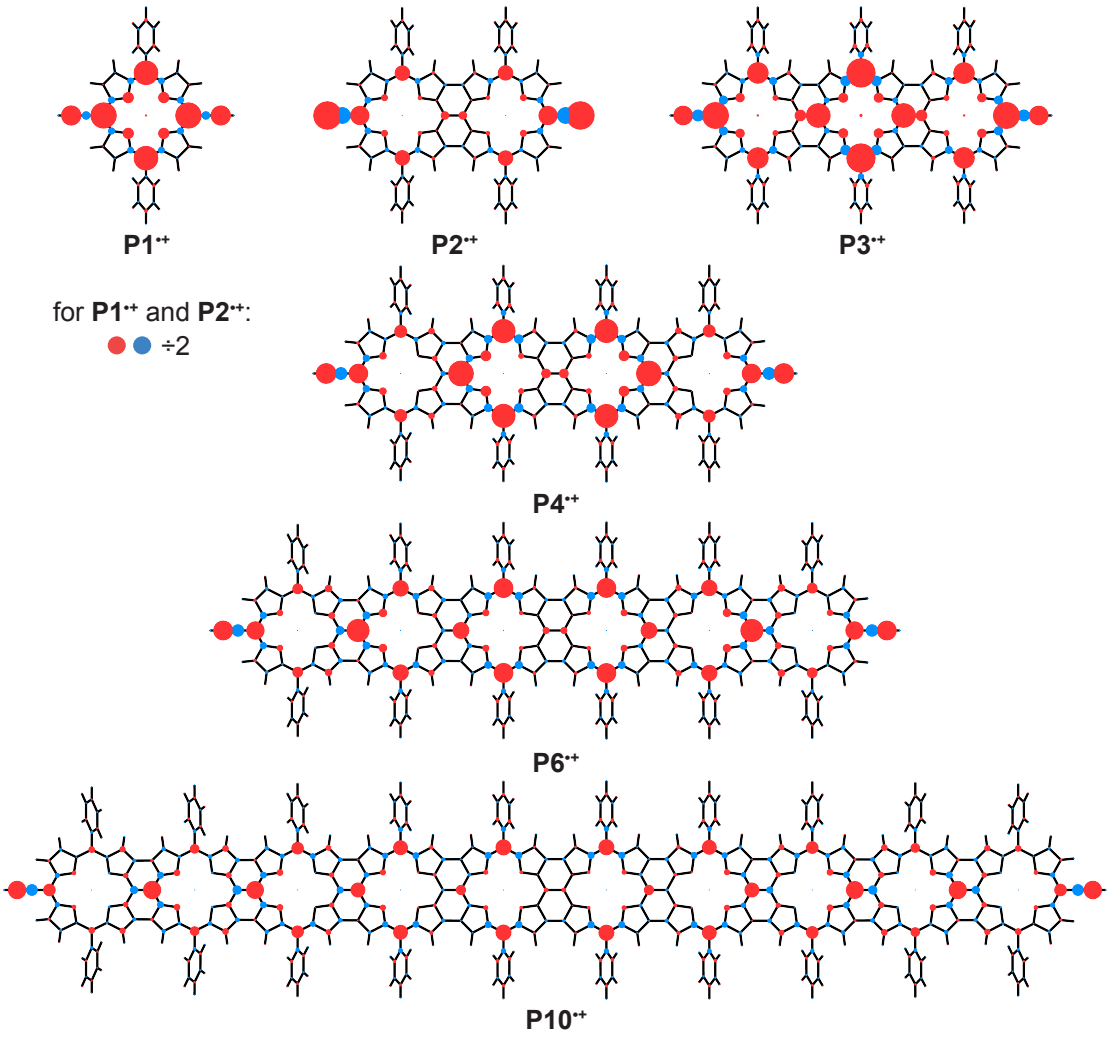


Figure 2.26: Visualization of the spin populations used to calculate the ^{1}H and ^{14}N hyperfine tensors of $\mathbf{PN}^{\bullet+}$ (N = 1–4, 6, 10) *via* the distributed point-dipole model. The spin density on each nucleus is represented by spheres centered on the nucleus with a radius proportional to its spin population. Red spheres represent excess spin-up and light-blue spheres indicate excess spin-down density.

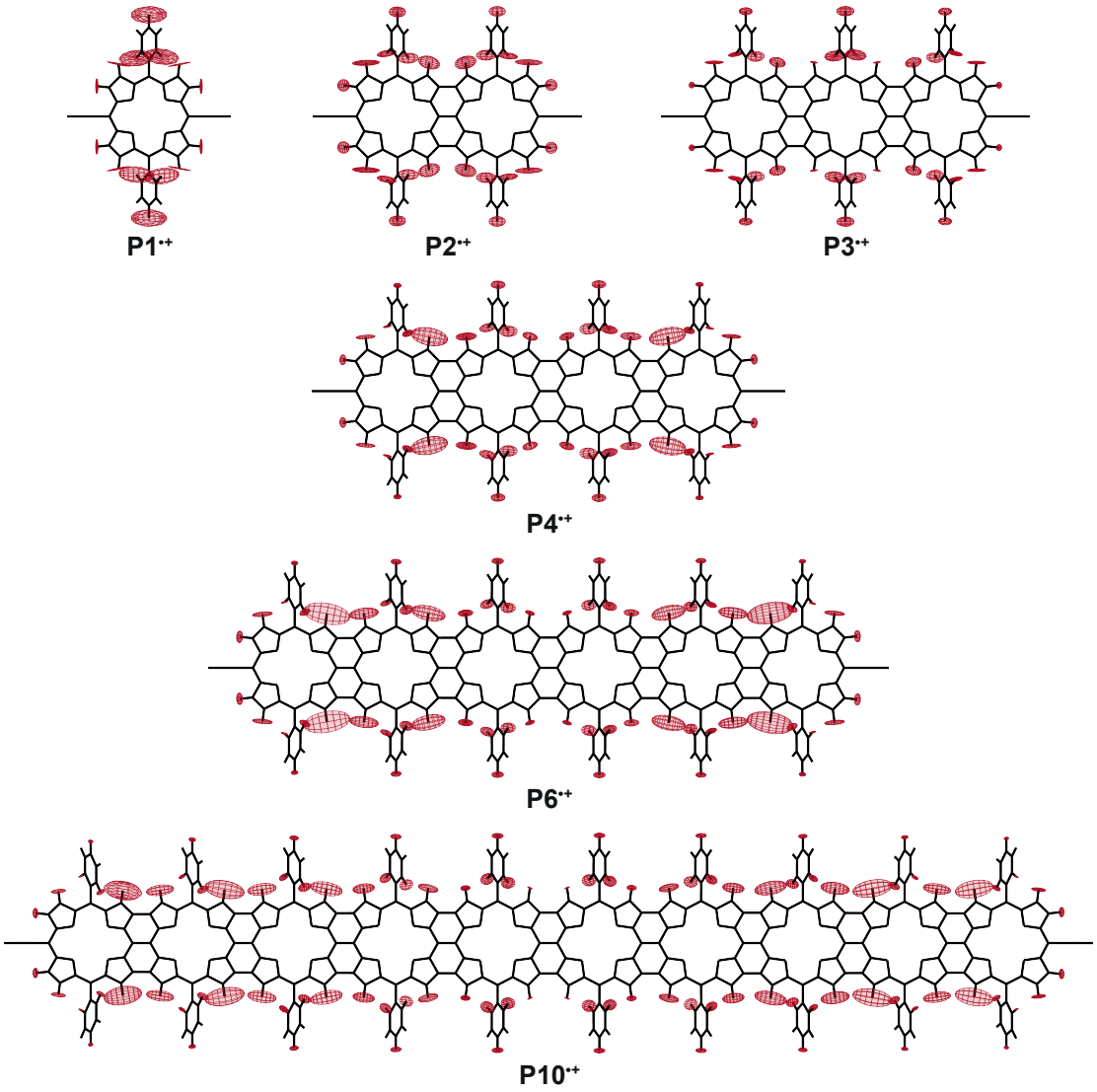


Figure 2.27: Visualization of the ^{1}H hyperfine coupling tensors $^{1\mathrm{H}}\boldsymbol{A}$ of $\mathbf{PN}^{\bullet+}$ (N = 1–4, 6, 10) calculated *via* the distributed point-dipole model. The tensors are represented as ellipsoids centred at the corresponding ^{1}H nuclei with dimensions proportional to the eigenvalues of $^{1\mathrm{H}}\boldsymbol{A}$ and are oriented in the molecular frame based on their Euler angles.

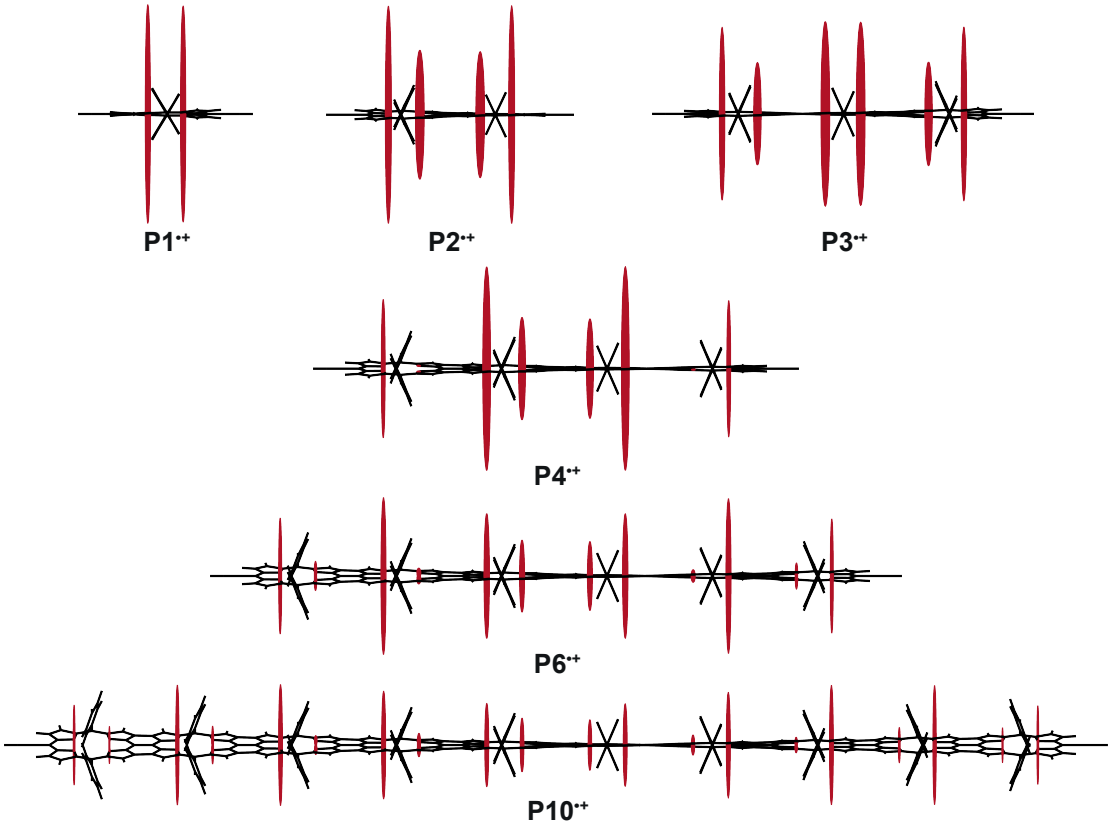


Figure 2.28: Visualization of the ^{14}N hyperfine coupling tensors $^{14}\boldsymbol{A}$ of $\mathbf{P}\boldsymbol{N}^{\bullet+}$ (N = 1–4, 6, 10) calculated *via* the distributed point-dipole model. The tensors are represented as ellipsoids centred at the corresponding ^{14}N nuclei with dimensions proportional to the eigenvalues of $^{14}\boldsymbol{A}$ and are oriented in the molecular frame based on their Euler angles.

2.6 Supplemental Results and Analysis

Continuous-Wave EPR Lineshape Analysis

The linewidth analysis of the room-temperature cw-EPR spectra was performed by fitting the first derivative of the following Gaussian normal distribution to the normalized data:

$$G(B) = \sqrt{\frac{2}{\pi}} \frac{1}{\Delta B_N} \exp\left[-2\left(\frac{B - B_0}{\Delta B_N}\right)\right] \tag{2.6}$$

where B, B_0, and ΔB_N are the magnetic field, the center field, and the width of the Gaussian spectral envelope, respectively. The fitting was performed using the built-in MATLAB function *lsqnonlin*. The resulting values of ΔB_N are summarized in Table 2.6 and plotted against $(1/N)^{0.5}$ in Figure 2.29.

The normalized data were also fitted to the first derivative of the following Lorentzian function:

$$L(B) = \frac{2}{\pi\sqrt{3}} \frac{1}{\Delta B'_N} \left[1 + \frac{4}{3}\left(\frac{B - B_0}{\Delta B'_N}\right)^2\right]^{-1} \tag{2.7}$$

where $\Delta B'_N$ is the width of the Lorentzian spectral envelope. The fitted values of $\Delta B'_N$ are summarized in Table 2.6 and plotted against $(1/N)^{0.5}$ in Figure 2.30.

Table 2.6: Summary of the Gaussian and Lorentzian spectral envelope widths ΔB_N and $\Delta B'_N$ of the cw-EPR spectra of $\mathbf{PN}^{\bullet+}$ (N = 1–4, 6, 10, 14, 18) at X-band frequencies in CD_2Cl_2:toluene-d_8:THF-d_8 1:1:1 at 298 K.

	$\mathbf{P1}^{\bullet+}$	$\mathbf{P2}^{\bullet+}$	$\mathbf{P3}^{\bullet+}$	$\mathbf{P4}^{\bullet+}$	$\mathbf{P6}^{\bullet+}$	$\mathbf{P10}^{\bullet+}$	$\mathbf{P14}^{\bullet+}$	$\mathbf{P18}^{\bullet+}$
ΔB_N / mT	0.6333	0.4662	0.4457	0.4295	0.3902	0.3552	0.7530	0.5735
$\Delta B'_N$ / mT	0.5330	0.3939	0.3757	0.3614	0.3279	0.2975	0.5898	0.4709

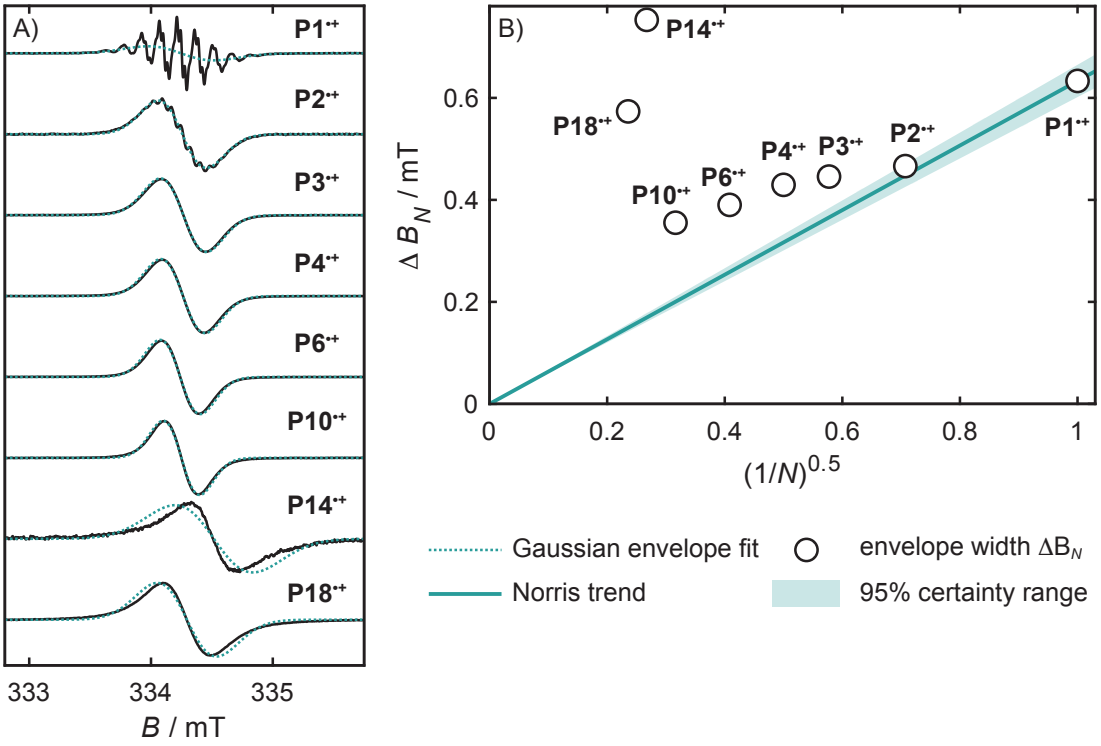


Figure 2.29: A) Linewidth analysis of the X-band cw-EPR spectra (black lines) of porphyrin oligomers $\mathbf{PN}^{\bullet+}$ (N = 1–4, 6, 10, 14, 18) in CD_2Cl_2:toluene-d_8:THF-d_8 1:1:1 at 298 K using a derivative Gaussian function to model the spectral envelope (dashed green lines). The field axis of all experimental cw-EPR spectra was standardized for a microwave frequency of 9.37 GHz. B) The agreement of the experimental spectral envelope trend with the Norris trend is investigated by plotting the best-fit Gaussian envelope width ΔB_N against $N^{-0.5}$. The theoretical predicted ideal Norris trend is indicated by the green trend line. The light green shaded area represents the 95% confidence interval around the Norris trend based on a ±5% uncertainty in the monomer spectrum width ΔB_1.

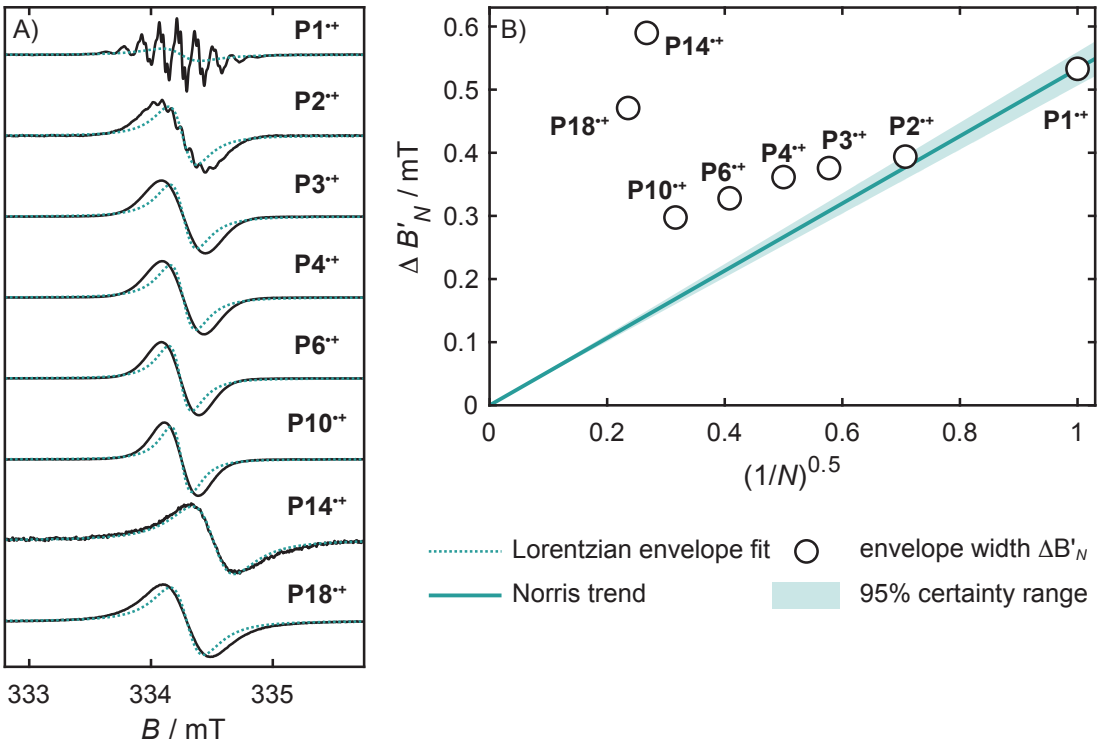


Figure 2.30: Linewidth analysis of the X-band cw-EPR spectra of porphyrin oligomers $\mathbf{P}N^{\bullet+}$ (N = 1–4, 6, 10, 14, 18) in CD_2Cl_2:toluene-d_8:THF-d_8 1:1:1 at 298 K using a derivative Lorentzian spectral envelope function. See the caption of Figure 2.29 for details.

Phase Memory Time Measurements

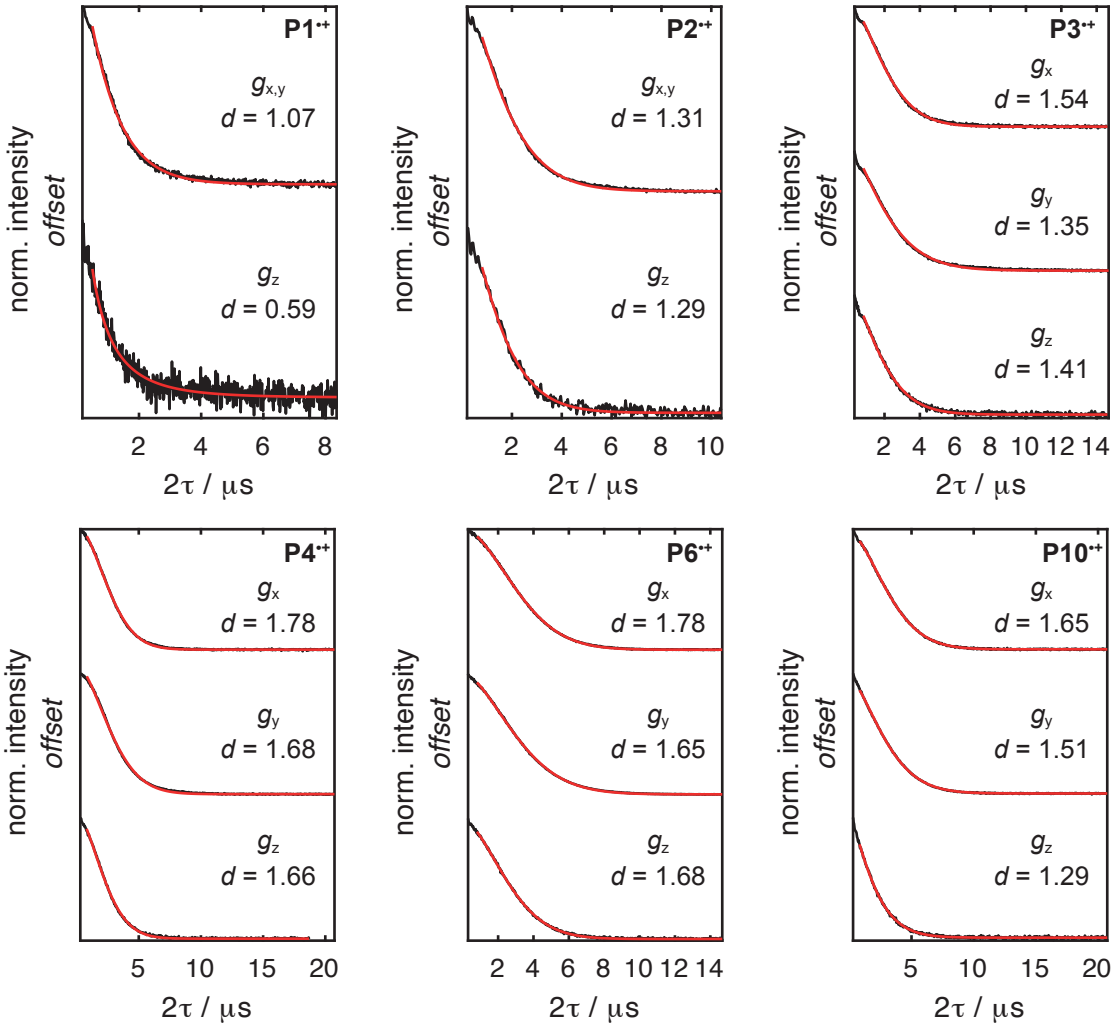


Figure 2.31: Experimental (black) and simulated (red) two-pulse Hahn echo decay spectra of $\mathbf{PN}^{\bullet+}$ at field positions corresponding to the principle values of the anisotropic $\boldsymbol{g}$-tensors in CD_2Cl_2:toluene-d_8:THF-d_8 1:1:1 at 50 K and W-band frequencies. The stretching parameters d of the exponential decays used in the simulations are given for each spectrum.

^{14}N HYSCORE Spectroscopy

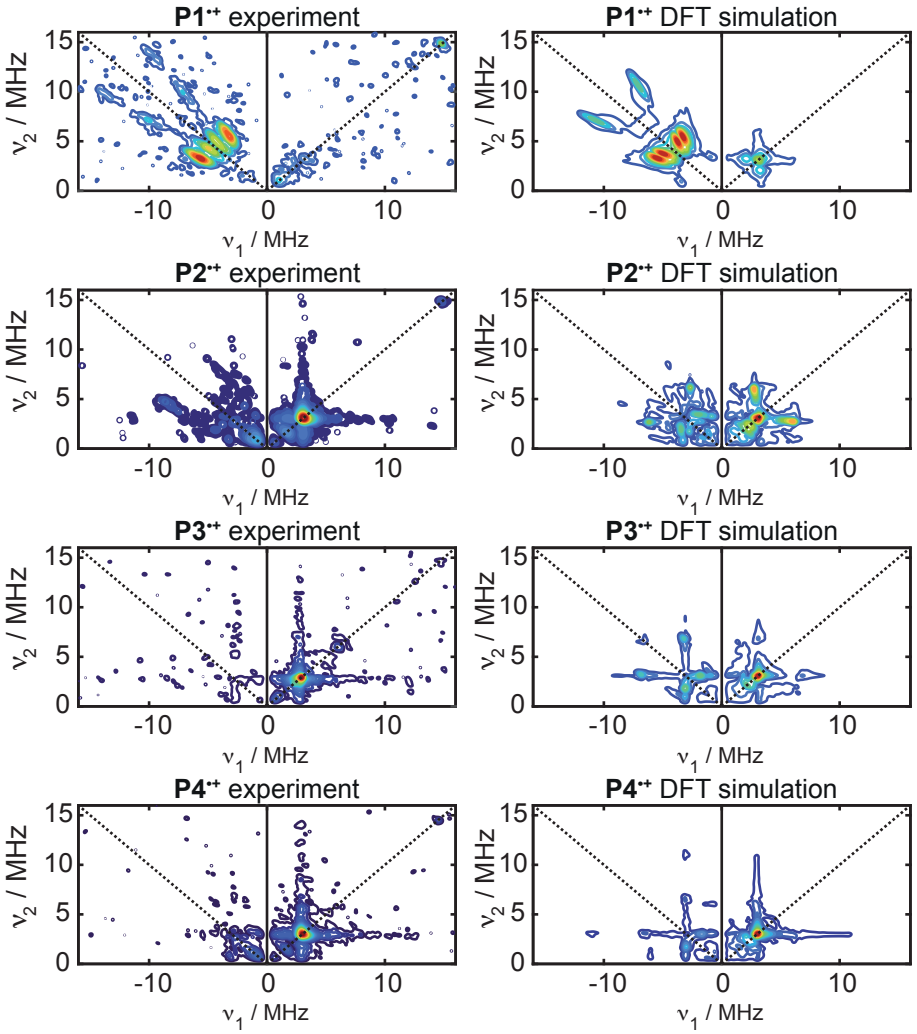


Figure 2.32: Experimental (80 K, CD_2Cl_2:toluene-d_8:THF-d_8 1:1:1) and simulated ^{14}N HYSCORE spectra of $\mathbf{PN}^{\bullet+}$ (N = 1–4) recorded at X-band frequencies at field positions corresponding to $g_{x,y}$. The simulated spectra were obtained using anisotropic ^{14}N hyperfine tensors $^{14\mathrm{N}}\boldsymbol{A}$ and ^{14}N quadrupole interactions calculated by DFT with B3LYP as functional and the EPRII basis set.

Table 2.7: Summary of the DFT (B3LYP/EPRII) and point-dipole predicted principal values of the ^{14}N hyperfine tensors $^{14}\boldsymbol{A}$ and the nuclear quadrupole parameters Q and η used to simulate the X-band ^{14}N HYSCORE spectra of $\mathbf{PN}^{\bullet+}$ ($N = 1$–4). The simulation parameters are given for each set of equivalent ^{14}N nuclei (N-I to N-IV). The numbering of the equivalent ^{14}N nuclei begins with the outermost set of nitrogen atoms in a given oligomer.

		$^{14}\boldsymbol{A}$ point-dipole / MHz	$^{14}\boldsymbol{A}$ DFT / MHz	Q / MHz	η
P1$^{\bullet+}$	N-I	[0.36 0.20 11.7]	[−0.12 −0.37 9.83]	2.27	0.82
P2$^{\bullet+}$	N-I	[0.16 0.28 6.61]	[−0.08 −0.25 6.28]	2.33	0.76
	N-II	[0.27 0.06 3.85]	[−0.17 −0.32 3.72]	2.36	0.70
P3$^{\bullet+}$	N-I	[0.13 0.21 4.67]	[−0.06 −0.20 4.43]	2.34	0.74
	N-II	[0.21 0.05 2.72]	[−0.16 −0.25 0.88]	2.41	0.62
	N-III	[0.25 0.13 4.96]	[−0.03 −0.15 4.77]	2.35	0.73
P4$^{\bullet+}$	N-I	[0.09 0.18 3.67]	[−0.01 −0.11 3.84]	2.37	0.71
	N-II	[0.09 0.02 0.05]	[−0.06 −0.16 −0.22]	2.43	0.60
	N-III	[0.24 0.16 5.47]	[0.00 −0.12 4.44]	2.34	0.75
	N-IV	[0.19 0.03 2.69]	[−0.07 −0.16 2.07]	2.38	0.68

3

Charge and Spin Transfer Dynamics in a Weakly Coupled Porphyrin Dimer

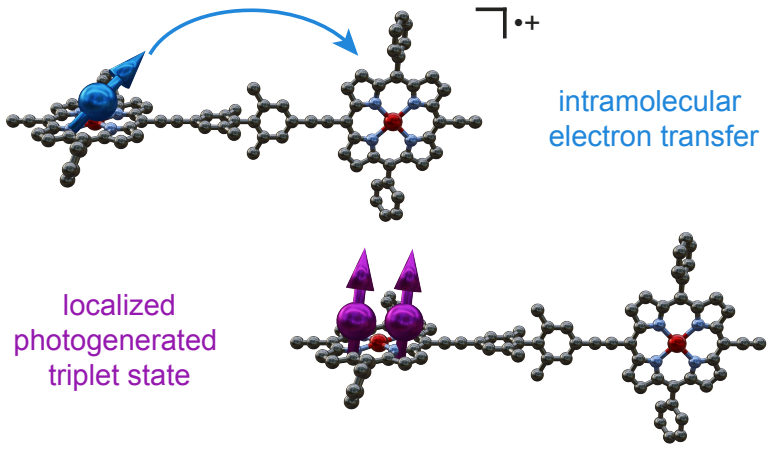
Contents

3.1 Abstract 109
3.2 Introduction 110
3.3 Results and Discussion 113
3.3.1 Synthesis and Molecular Design 113
3.3.2 Absorption Spectroscopy 114
3.3.3 Continuous-Wave EPR Spectroscopy 116
3.3.4 Investigation of the Monomer Dihedral Angle Distribution . 124
3.3.5 Mims ENDOR Spectroscopy 126
3.3.6 Introduction to Exchange Broadening 129
3.3.7 Simulation of the Electron Transfer Dynamics 132
3.3.8 Investigation of the Triplet State Delocalization 139
3.4 Summary and Conclusion 145
3.5 Methods 147
3.5.1 General Methods 147
3.5.2 Synthetic Procedures 152
3.5.3 Distributed Point-Dipole Simulations 155
3.6 Supplemental Results and Analysis 160

The work in this chapter was published in:

S. M. Kopp, A. J. Redman, I. Rončević, L. Schröder, L. Bogani, H. L. Anderson, C. R. Timmel, *Charge and spin transfer dynamics in a weakly coupled porphyrin dimer*, *J. Am. Chem. Soc.*, **2024**, *146*, 21476–21489.

3.1 Abstract



The dynamics of electron and spin transfer in the radical cation and photogenerated triplet states of a tetramethylbiphenyl-linked zinc-porphyrin dimer were investigated using a combination of multiple techniques, including variable-temperature cw-EPR, proton ENDOR, transient EPR, and optical spectroscopy. The conclusions are further supported by density functional theory calculations, and comparison to reference compounds. The results are discussed in the context of the relevant parameters for the design of a single-molecule spin valve, and the creation of a novel platform for the photogeneration of high-multiplicity spin states.

Frozen-solution cw-EPR and room-temperature near-IR spectra of the dimer monocation demonstrate that the radical cation is spatially localized on one side of the dimer at any point in time, while the cw-EPR spectra at 298 K reveal rapid hopping of the radical spin density between both sites of the dimer *via* reversible intramolecular electron transfers. The hyperfine interactions are modulated during the electron transfer and can be quantified using ENDOR spectroscopy. This allowed the simulation of the variable-temperature cw-EPR spectra with a two-site exchange model and provided information on the temperature-dependence of the electron transfer rate. The electron transfer rates range from about 54 MHz at 298 K to about 10 MHz at 200 K. The activation enthalpies $\Delta^{\ddagger}H$ of the electron transfer were determined as $\Delta^{\ddagger}H = 9.55$ kJ mol^{-1} and $\Delta^{\ddagger}H = 5.67$ kJ mol^{-1} in a 1:1:1 solvent mixture of

CD_2Cl_2:toluene-d_8:THF-d_8 and in 2-methyltetrahydrofuran, respectively, consistent with a Robin–Day class II mixed valence compound. Investigation of the spin density distribution of the photogenerated triplet state of the Zn-porphyrin dimer reveals localization of the triplet spin density on a nanosecond time scale on one half of the dimer at 20 K in 2-methyltetrahydrofuran and at 250 K in a polyvinylcarbazole film. These results impact the design of single-molecule spintronic devices by quantifying fundamental parameters for relevant building blocks, and offer the first step towards a novel platforms for photogenerated high-multiplicity spin states.

3.2 Introduction

Much of our recent understanding of the fundamental principles that govern electron transfer processes has come from the study of organic mixed valence compounds, which consist of two or more redox centers with different formal oxidation states.[141, 143, 213, 239–243] Moreover, because of their impressive chemical tunability, organic mixed valence compounds have found application in single-molecule electronic devices,[188, 244–246] organic light-emitting diodes, [247, 248] near-IR dyes,[249–251] organic superconductors[252, 253] and semiconductors,[182, 254, 255] and organic solar cells.[186, 187, 256]

These applications raise important, and still unanswered, questions about how the single elements that form functional mixed valence compounds can be rationally tuned to influence their performance. For example: spin valves typically require[257–262] a high energy barrier between the functional elements (Figure 3.1), while the Pauli spin blockade observed in two-quantum-dots nanoelectronic devices[263–265] needs low tunneling barriers. It is currently not well understood how efficient different linking groups are in producing electronic tunneling barriers, and this prevents the rational design of fully molecular electronic elements, such as molecular spin-valves or double-dots.[257–262] It is thus important to create a library of linkers with which electronic tunneling barriers can be carefully calibrated by chemical design.

Organic mixed valence systems can be classified based on the strength of the electronic coupling between the individual redox sites as proposed by Robin and Day[148] and introduced in Section 1.3.1. Due to their ability to coherently delocalize charge carriers over long distances, Robin–Day class III mixed valence compounds have been extensively investigated for applications as molecular wires in single-molecule conductance experiments.[51, 83, 86, 114, 266–268] On the other hand, many molecular electronics elements would require class II systems with reduced electronic coupling, and a single-molecule tunneling spin valve would need a particularly high tunneling barrier (Figure 3.1).[269–271]

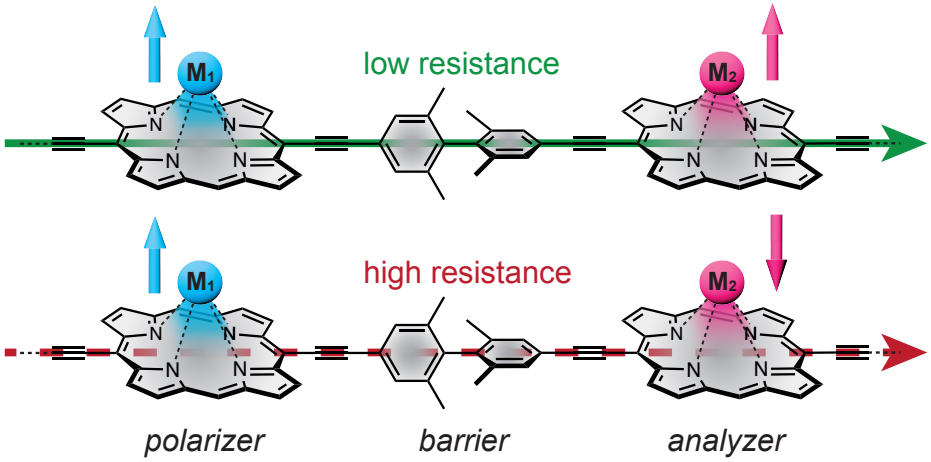


Figure 3.1: Schematic illustration of the general design of a single-molecule tunneling spin vale consisting of two different paramagnetic metalloporphyrin complexes (blue and pink) connected by a twisted biphenyl barrier. The current flowing through the device can be controlled by the mutual alignment of the metal magnetic moments (blue and pink arrows). For the same sign of the exchange coupling between the conductance electrons and both metalloporphyrin units, low resistance (top) and high resistance (bottom) states are obtained with parallel and antiparallel aligned magnetic moments, respectively.

The proposed prototype molecular spin valve consists of two different paramagnetic metalloporphyrin complexes that are independent single-molecule magnets at low temperature and act as spin polarizer and spin analyzer, creating and reading out a spin polarized current, respectively (Figure 3.1). The different magnetic anisotropy barriers of the paramagnetic metal porphyrin complexes allow for a selective inversion of their magnetic moments and the preferential spin polarization of the conductance electrons by an external magnetic field.[19, 20] This enables reversible switching

between low resistance and high resistance states. If the sign of the exchange coupling between the metal ions and the conductance electrons is the same for both metalloporphyrin units, low resistance and high resistance states are obtained with parallel and antiparallel aligned magnetic moments of the metals, respectively. For an efficient performance as a spin valve, the nature of the linker between the porphyrin complexes is crucial, as it must convey sufficient electronic coupling to sustain a current *via* single-electron transfer events, while preserving the independence of the two magnetic centers. The height of the tunnelling barrier between the two spin centers determines the magnitude of the magnetoresistance.[269] The resulting spin valve could be used as a magneto-responsive switch because its electrical resistance is expected to change in response to an external magnetic field, leading to applications as non-volatile memory devices, or for implementing logic operations in single-molecule conductance measurements.

In this chapter, a combination of variable-temperature cw-EPR spectroscopy, ^{1}H Mims ENDOR spectroscopy, optical spectroscopy, and supporting DFT calculations and simulations are used to investigate the electronic structure of a tetramethylbiphenyl-linked Zn-porphyrin dimer mixed valance compound that acts as a model system for the porphyrin backbone of the proposed spin valve. To simulate the electron transfer dynamics in this mixed valence system, a robust approach was developed to quantify hyperfine interactions, that cannot be resolved by cw-EPR spectroscopy, using Mims ENDOR spectroscopy. Previously, the inability to resolve these hyperfine couplings limited the quantitative investigation of electron transfer dynamics in Zn-porphyrin nanostructures.[84, 272–274]

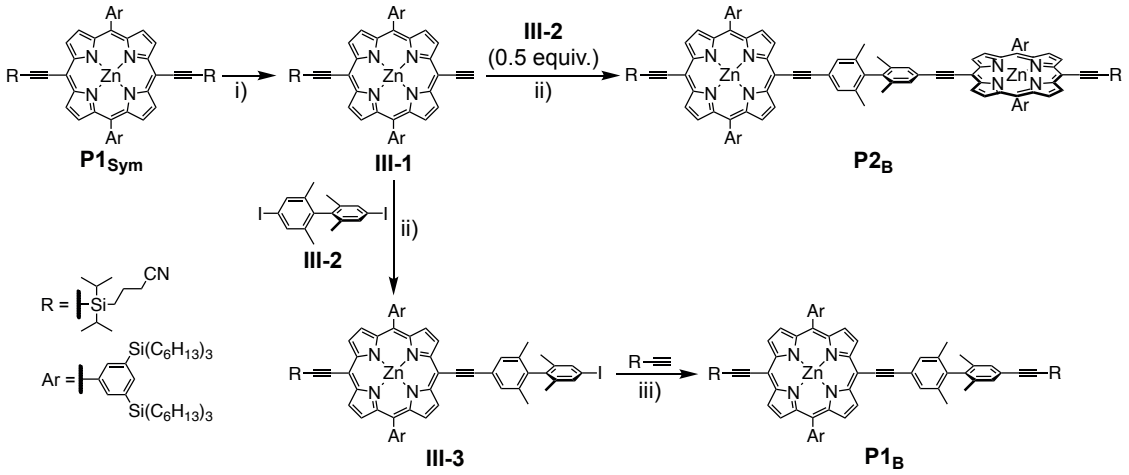
The spin transfer dynamics of the radical cation mixed valence compound are further compared to the dynamics of a photogenerated triplet state on the same porphyrin backbone. Molecular architectures with two decoupled porphyrin sites could also be used as platforms for generating high-multiplicity spin states for quantum information processing.[275] Recent work on photoexcited chromophore-radical or

chromophore-metal systems has shed light on a broad range of highly tunable trip-doublet and quartet states with potential applications in molecular spintronics and as multilevel qudit systems.[276–281] Therefore, a molecule that allows for the formation of a photogenerated triplet state adjacent to a redox active, tunable, ground-state porphyrin unit with a metal binding site would be a versatile platform for investigating high-multiplicity spin states. In this chapter, the delocalization of the photogenerated triplet state in a tetramethylbiphenyl-linked Zn-porphyrin dimer is investigated using transient cw-EPR and ^{1}H Mims ENDOR spectroscopy.

3.3 Results and Discussion

3.3.1 Synthesis and Molecular Design

Porphyrin dimer $\mathbf{P2_B}$ was designed to feature two redox-active zinc porphyrin units connected *via* a twisted tetramethyl biphenyl bridge (Scheme 3.1). Porphyrin monomer $\mathbf{P1_B}$ was chosen to model a single site of $\mathbf{P2_B}$. The steric demand of the methyl substituents on the 2,2',6,6' positions of the biphenyl groups of $\mathbf{P1_B}$ and $\mathbf{P2_B}$ results in a perpendicular orientation of the two phenyl units. This type of twisted bridge has previously been used to hold two chromophores in a linear arrangement while avoiding direct π-conjugation.[282–284] Two factors are expected to lead to a high barrier to charge hopping in $\mathbf{P2_B}^{\bullet+}$: a) the twist in the central biphenyl, and b) the fact that the planes of the two porphyrins tend to be orthogonal. Terminal alkyne units were included in $\mathbf{P2_B}$ so that the dimer could be incorporated into a molecular wire. Bulky 3,5-bis(trihexylsilyl)phenyl substituents were attached to both peripheral *meso* positions of each porphyrin unit to achieve high solubility and inhibit aggregation. Biphenyl-porphyrin monomer $\mathbf{P1_B}$ and biphenyl-linked porphyrin dimer $\mathbf{P2_B}$ were synthesized from the symmetric porphyrin monomer $\mathbf{P1_{Sym}}$ as summarized in Scheme 3.1. Monodeprotection of $\mathbf{P1_{Sym}}$ followed by a two-fold Sonogashira coupling of **III-1** with 4,4'-diiodo-2,2',6,6'-tetramethyl-1,1'-biphenyl **III-2**, and purification by recycling gel-permeation chromatography (GPC), afforded dimer $\mathbf{P2_B}$ in 45% yield. Sonogashira coupling of the deprotected monomer **III-1** with 0.9 equivalents of **III-2** followed



Scheme 3.1: Synthesis of biphenyl-porphyrin monomer $\mathbf{P1_B}$ and biphenyl-linked porphyrin dimer $\mathbf{P2_B}$ from the symmetric monomer $\mathbf{P1_{Sym}}$. Reaction conditions: i) TBAF, $CHCl_3$, 21 °C, 30 min, 50%; ii) XPhos Pd G4, CuI, toluene/*i*-Pr_2NH (2:1), 70 °C, 3 h, $\mathbf{P2_B}$: 45%; iii) $Pd(PPh_3)_2Cl_2$, CuI, toluene/*i*-Pr_2NH (5:1), 45 °C, 2 h, 15% over two steps.

by recycling GPC and a second Sonogashira coupling to attach the cyanopropyldiisopropylsilyl (CPDIPS) acetylene to the biphenyl group gave biphenyl-porphyrin monomer $\mathbf{P1_B}$ in 15% yield over two steps. Monomer $\mathbf{P1_{Sym}}$ and biphenyl derivative **III-2** were synthesized following published procedures.[285, 286] Partial oxidation of $\mathbf{P1_{Sym}}$ and $\mathbf{P1_B}$ to their radical cations $\mathbf{P1_{Sym}}^{\bullet+}$ and $\mathbf{P1_B}^{\bullet+}$ was achieved by addition of 0.5 equivalents tris(4-bromophenyl)-aminium hexachloroantimonate (**BAHA**) in a 1:1:1 solvent mixture of CD_2Cl_2:toluene-d_8:THF-d_8 or 2-methyltetrahydrofuran (MTHF), which both form a glass at low temperatures.[51, 83, 87] Radical cation $\mathbf{P2_B}^{\bullet+}$ was obtained by chemical oxidation with 0.25 equivalents **BAHA** to prevent oxidation of both porphyrin units in $\mathbf{P2_B}$.

3.3.2 Absorption Spectroscopy

Optical spectroscopy of organic mixed valence systems such as $\mathbf{P2_B}^{\bullet+}$ can provide important information about their reorganization energy λ and the electronic coupling H between different sites of the molecule, and probes the delocalization of the radicals on a fs-timescale in solution.[141, 213] Compared to their neutral analogues, radical cations of π-conjugated materials typically feature two characteristic low-energy absorption bands P_1 and P_2 that approximately correspond to HOMO → SOMO and

SOMO → LUMO transitions, respectively.[150–152] The absorption spectra of neutral and oxidized $\mathbf{P1}_{\mathbf{Sym}}$, $\mathbf{P1}_{\mathbf{B}}$, and $\mathbf{P2}_{\mathbf{B}}$ were measured during an oxidation titration with **BAHA** in $CHCl_3$ and are shown in Figure 3.2.

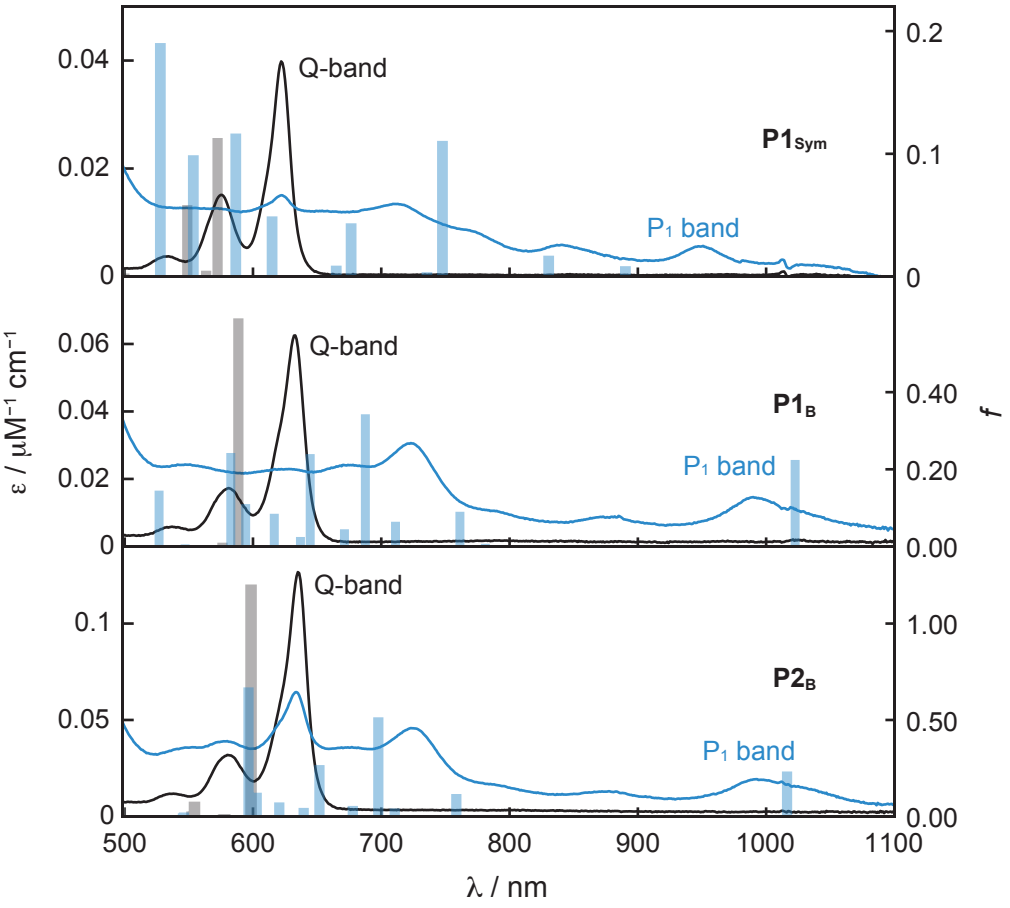


Figure 3.2: UV-vis-NIR absorption spectra of neutral (black) and oxidized (blue) $\mathbf{P1}_{\mathbf{Sym}}$, $\mathbf{P1}_{\mathbf{B}}$, and $\mathbf{P2}_{\mathbf{B}}$ in $CHCl_3$ (298 K). The absorption spectra of the radical cations $\mathbf{P1}_{\mathbf{Sym}}{}^{\bullet+}$, $\mathbf{P1}_{\mathbf{B}}{}^{\bullet+}$, and $\mathbf{P2}_{\mathbf{B}}{}^{\bullet+}$ were obtained by oxidation with 1 equivalent **BAHA** (see Figure 3.24 for the full oxidation titrations). The vertical bars indicate the TD-DFT (LC-ωPBE/6-31G*; $\omega = 0.1$) calculated wavelengths and oscillator strengths f for the electronic transitions of the neutral and oxidized compounds in the absence of vibronic coupling.

The spectra of neutral $\mathbf{P1}_{\mathbf{Sym}}$, $\mathbf{P1}_{\mathbf{B}}$, and $\mathbf{P2}_{\mathbf{B}}$ show a characteristic Q-band absorption with lowest energy absorption bands at 622 nm, 633 nm, and 635 nm, respectively. In the spectra of their respective radical cations, the lowest energy electronic transitions are shifted to 950 nm, 993 nm, and 993 nm.

TD-DFT calculations of the excitation energies of neutral and oxidized $\mathbf{P1}_{\mathbf{Sym}}$, $\mathbf{P1}_{\mathbf{B}}$, and $\mathbf{P2}_{\mathbf{B}}$ with LC-ωPBE, ω=0.1 as functional and the 6-31G* basis set are in

good agreement with the experimental observations (Figure 3.2, vertical bars). The calculated electronic transitions for the neutral compounds indicate that the Q-band absorptions arise from HOMO → LUMO transitions, as expected from the Gouterman four orbital model.[58–60] The lowest energy absorption bands of $\mathbf{P1_{Sym}}^{\bullet+}$, $\mathbf{P1_B}^{\bullet+}$, and $\mathbf{P2_B}^{\bullet+}$ arise mainly from HOMO → SOMO transitions and correspond to the P_1 bands of the hole polarons. The slight bathochromic shift of the Q-band absorption of $\mathbf{P1_B}$ compared to $\mathbf{P1_{Sym}}$ results from an extension of the conjugated π-system by one phenyl group in the biphenyl-porphyrin systems. The lack of a further red-shift of the lowest-energy absorption band of $\mathbf{P2_B}$ is evidence of the electronic decoupling of the two porphyrin sites by the twisted biphenyl linker. The P_1 bands of $\mathbf{P1_B}^{\bullet+}$ and $\mathbf{P2_B}^{\bullet+}$ are shifted toward longer absorption wavelengths by about 40 nm ($\Delta E_{\text{Abs}} = 0.06$ eV) relative to the P_1 band of $\mathbf{P1_{Sym}}^{\bullet+}$, which points towards a partial delocalization of the radical cation onto one half of the biphenyl-linker. The identical lowest-energy absorption bands of $\mathbf{P1_B}^{\bullet+}$ and $\mathbf{P2_B}^{\bullet+}$ stem from the same radical distribution in both systems and demonstrate the localization of the hole on one site of $\mathbf{P2_B}^{\bullet+}$. TD-DFT calculations on $\mathbf{P2_B}^{\bullet+}$ predict a very weak ($f = 0.0006$) intervalence charge-transfer (IV-CT) band at 2032 nm, and observation of this band would allow a more in-depth analysis of the electronic structure; however, this band appears to be too broad and weak to be observed experimentally.

3.3.3 Continuous-Wave EPR Spectroscopy

The cw-EPR spectra of the radical cations $\mathbf{P1_{Sym}}^{\bullet+}$, $\mathbf{P1_B}^{\bullet+}$, and $\mathbf{P2_B}^{\bullet+}$ at 298 K in CD_2Cl_2:toluene-d_8:THF-d_8 1:1:1 and MTHF at X-band frequencies are shown in Figure 3.3. The spectrum of $\mathbf{P1_{Sym}}^{\bullet+}$ is consistent with previous reports for this radical cation and the cw-EPR spectrum of a similar porphyrin monomer $\mathbf{P1}^{\bullet+}$ in Chapter 2, and consists of nine prominent hyperfine lines that arise from an isotropic coupling of $^{14}N a_{\text{iso}} = 3.99$ MHz to the four equivalent ^{14}N nuclei, which are further split by an isotropic coupling of $^{1}H a_{\text{iso}} = 0.94$ MHz to the four equivalent *ortho* protons of the *meso* aryl groups.[83] The cw-EPR spectra of $\mathbf{P1_B}^{\bullet+}$ exhibit partially resolved hyperfine structures that arise from an isotropic coupling of $^{14}N a_{\text{iso}} = 3.99$ MHz to

the four equivalent ^{14}N nuclei. The ^{1}H hyperfine couplings are not resolved in these spectra due to additional hyperfine interactions, which lead to the inhomogeneous broadening of the spectra. The room-temperature cw-EPR spectra of $\mathbf{P2_B}^{\bullet+}$ lack a resolved hyperfine structure and are narrower than the spectra of $\mathbf{P1_B}^{\bullet+}$. If hyperfine interactions are the main contribution to the spectral envelope and the radical spin density is distributed completely and uniformly over both sites of $\mathbf{P2_B}^{\bullet+}$ on the EPR timescale, the cw-EPR spectra can be described using the Norris relationship in equation 1.19 of Chapter 1.

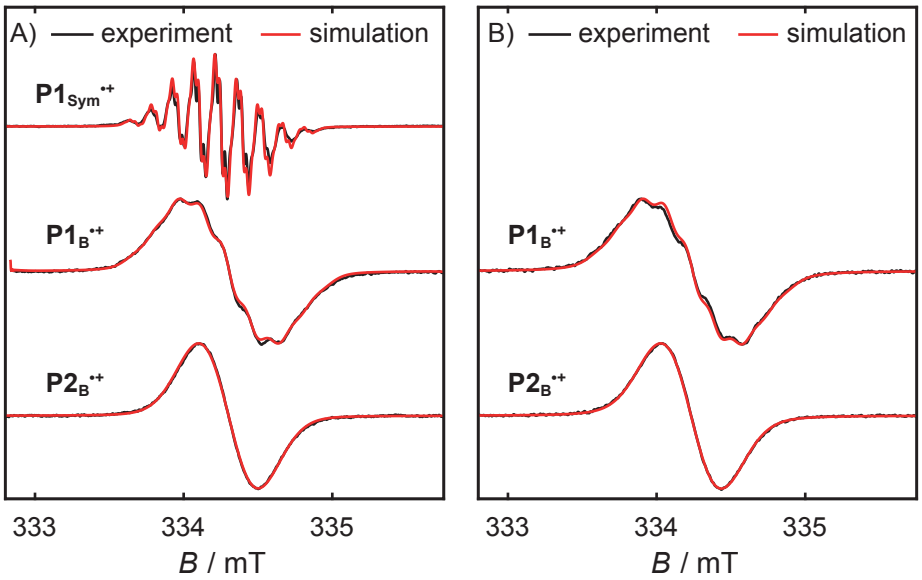


Figure 3.3: Experimental cw-EPR spectra of the radical cations $\mathbf{P1S_{Sym}}^{\bullet+}$, $\mathbf{P1_B}^{\bullet+}$, and $\mathbf{P2_B}^{\bullet+}$ (black) acquired at 298 K in A) CD_2Cl_2:toluene-d_8:THF-d_8 1:1:1 and B) 2-methyltetrahydrofuran at X-band frequencies. The simulated cw-EPR spectra (red) of $\mathbf{P1_{Sym}}^{\bullet+}$ and $\mathbf{P1_B}^{\bullet+}$ were obtained by least-squares fitting of the isotropic ^{14}N hyperfine interactions $^{14}a_{iso}$, and in the case of $\mathbf{P1_{Sym}}^{\bullet+}$ the isotropic hyperfine coupling $^{1}a_{iso}$ to four equivalent ^{1}H nuclei. Dimer $\mathbf{P2_B}^{\bullet+}$ was simulated by assuming a complete and uniform distribution of the radical spin density over both porphyrin units on the EPR timescale with $^{14}a_{iso}\left(\mathbf{P2_B}^{\bullet+}\right) = 0.5 \cdot {}^{14}a_{iso}\left(\mathbf{P1_B}^{\bullet+}\right)$. The hyperfine interactions and linewidth contributions used in the simulations are summarized in Table 3.1.

The numerical simulations of the cw-EPR spectra of $\mathbf{P2_B}^{\bullet+}$ under the assumption of complete and uniform spin distribution $\left({}^{14}a_{iso}\left(\mathbf{P2_B}^{\bullet+}\right) = 0.5 \cdot {}^{14}a_{iso}\left(\mathbf{P1_B}^{\bullet+}\right)\right)$ on the EPR timescale, which is fundamental to the Norris relationship, are in excellent agreement with the experimental spectra (Figure 3.3). Identical isotropic hyperfine interactions $^{14}a_{iso}$ were used to simulate the cw-EPR spectra in the two different

solvent environments, which suggests that the spin density distribution in the porphyrin systems is independent of the solvent environment at 298 K. Simulations of $\mathbf{P1_B}^{\bullet+}$ and $\mathbf{P2_B}^{\bullet+}$ were performed using a pseudo-Voigtian lineshape with Gaussian and Lorentzian peak-to-peak linewidth contributions summarized in Table 3.1. No Gaussian linewidth contributions were required to simulate the spectra of $\mathbf{P1_{Sym}}^{\bullet+}$ due to the absence of large, unresolved hyperfine interactions.

Table 3.1: Summary of the isotropic ^{14}N hyperfine interactions $^{14}a_{iso}$, number of equivalent nitrogen nuclei ^{14}n, and Gaussian and Lorentzian linewidth contributions Γ_G and Γ_L used for the simulation of the X-band cw-EPR spectra of $\mathbf{P1_{Sym}}^{\bullet+}$, $\mathbf{P1_B}^{\bullet+}$, and $\mathbf{P2_B}^{\bullet+}$ in CD_2Cl_2:toluene-d_8:THF-d_8 1:1:1 and 2-methyltetrahydrofuran.

CD_2Cl_2:toluene-d_8:THF-d_8 1:1:1	$^{14}a_{iso}$ / mT	^{14}n	Γ_G / mT	Γ_L / mT
$\mathbf{P1_{Sym}}^{\bullet+}$	3.99	4	0.00	0.03
$\mathbf{P1_B}^{\bullet+}$	3.99	4	0.14	0.05
$\mathbf{P2_B}^{\bullet+}$	2.00	8	0.14	0.05

2-methyltetrahydrofuran	$^{14}a_{iso}$ / mT	^{14}n	Γ_G / mT	Γ_L / mT
$\mathbf{P1_{Sym}}^{\bullet+}$	–	–	–	–
$\mathbf{P1_B}^{\bullet+}$	3.99	4	0.13	0.08
$\mathbf{P2_B}^{\bullet+}$	2.00	8	0.13	0.08

The agreement of the room-temperature cw-EPR spectra of $\mathbf{P1_B}^{\bullet+}$ and $\mathbf{P2_B}^{\bullet+}$ in CD_2Cl_2:toluene-d_8:THF-d_8 1:1:1 and MTHF with the Norris relationship was further investigated by analyzing the trend of their Gaussian spectral envelope widths ΔB_N *vs* $N^{-0.5}$ in Figure 3.4. The excellent description of the spectral envelopes of $\mathbf{P1_B}^{\bullet+}$ and $\mathbf{P2_B}^{\bullet+}$ by derivative Gaussian normal distributions indicates that the main contribution to their spectral shapes arises from hyperfine interactions. The spectral envelope widths ΔB_N of the monomer and dimer are slightly higher in MTHF compared to CD_2Cl_2:toluene-d_8:THF-d_8 1:1:1 which is probably the result of small changes in the relaxation behavior between the two solvent systems. The trend of the best-fit Gaussian spectral envelopes of $\mathbf{P1_B}^{\bullet+}$ and $\mathbf{P2_B}^{\bullet+}$ in both solvent systems closely follows the ideal Norris trend (Figure 3.4C), which is determined by the monomer spectral envelope width ΔB_1. This implies fast hopping of the radical spin density over both sites of $\mathbf{P2_B}^{\bullet+}$

on the EPR timescale at 298 K. The lack of a bathochromic shift in the NIR absorption spectrum of $\mathbf{P2_B}^{\bullet+}$ shows that the apparent spin density distribution is the result of fast reversible intramolecular electron transfers and not coherent delocalization.

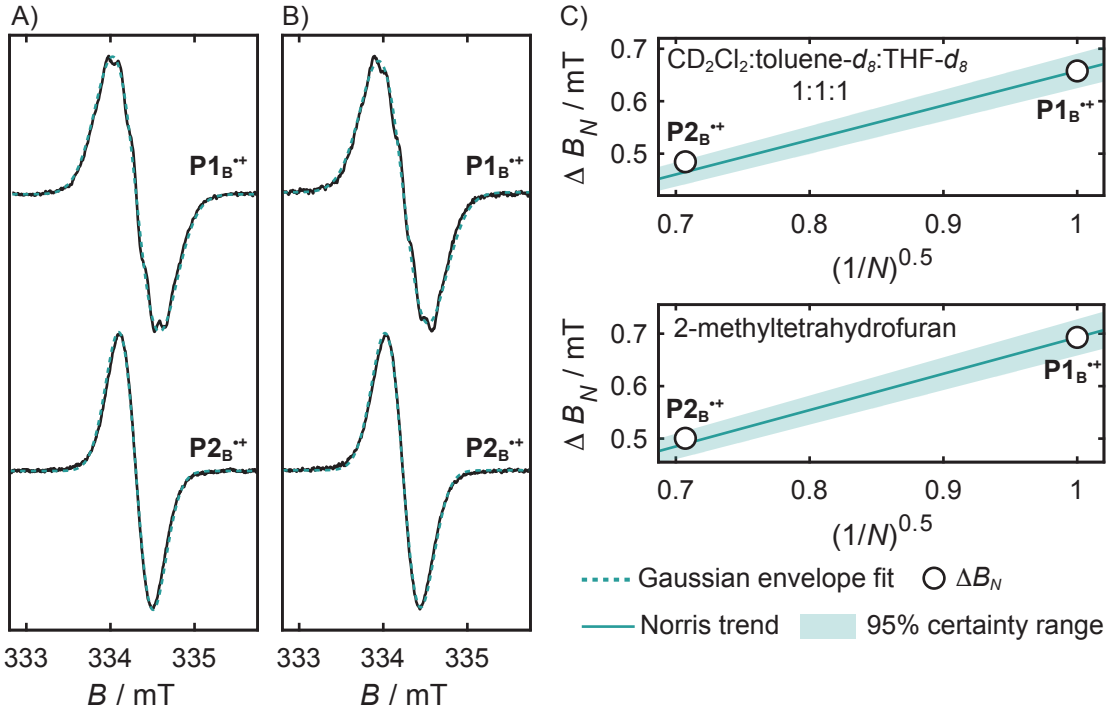


Figure 3.4: Linewidth analysis of the cw-EPR spectra (black) of $\mathbf{P1_B}^{\bullet+}$ and $\mathbf{P2_B}^{\bullet+}$ at 298 K and X-band frequencies in A) CD_2Cl_2:toluene-d_8:THF-d_8 1:1:1 and B) 2-methyltetrahydrofuran using derivative Gaussian normal distributions to model the spectral envelopes (dashed green lines). C) The agreement of the experimental spectral envelope trend with the Norris relationship is investigated by plotting the best-fit Gaussian envelope width ΔB_N in CD_2Cl_2:toluene-d_8:THF-d_8 1:1:1 and 2-methyltetrahydrofuran against $N^{-0.5}$. The theoretical predicted Norris trend is indicated by the green trend line and determined by the monomer envelope width ΔB_1. The light green shaded area represents the 95% confidence interval around the Norris trend based on a ±5% uncertainty in the monomer envelope width ΔB_1.

Dynamic chemical processes such as electron transfers result in linewidth changes of the cw-EPR transitions and provide information about the rate of the chemical process from the magnitude of exchange broadening (see Section 3.3.6 for a detailed discussion of exchange broadening).[287–290] To obtain insights into the kinetics of the reversible intramolecular electron transfer in $\mathbf{P2_B}^{\bullet+}$, the temperature-dependence of the cw-EPR spectra of $\mathbf{P1_B}^{\bullet+}$ and $\mathbf{P2_B}^{\bullet+}$ in CD_2Cl_2:toluene-d_8:THF-d_8 1:1:1 and MTHF was investigated by variable-temperature cw-EPR spectroscopy between 100 K and 298 K at X-band frequencies (Figure 3.5 and Figure 3.6). Variable-temperature

spectroscopy in MTHF enables the investigation of the intramolecular electron transfer over a larger temperature range in fluid solution due to its lower melting point, and provides insight into the solvent dependence of the transfer dynamics. The variable-temperature cw-EPR spectra of the butadiyne-linked porphyrin dimer cation ***b*-P2**$^{\bullet+}$ shown in Figure 3.7 were measured as a reference to differentiate between dynamic lineshape effects that result from the intramolecular electron transfer in **P2$_B$**$^{\bullet+}$ and anisotropic broadening due to slower tumbling at low temperatures. The size and shape of ***b*-P2** is comparable to **P2$_B$** and the rotational correlation times of both molecules are expected to be similar under identical conditions. The investigation of ***b*-P2**$^{\bullet+}$ by Peeks, Tait, *et al.*[51] demonstrated coherent delocalization of the radical spin density over both porphyrin units (Robin–Day class III). Therefore, temperature-dependent linewidth changes in the cw-EPR spectrum of ***b*-P2**$^{\bullet+}$ arise from anisotropic broadening and indicate insufficient rotational averaging of ***b*-P2**$^{\bullet+}$ and **P2$_B$**$^{\bullet+}$.

The fluid-phase variable-temperature cw-EPR spectra of **P1$_B$**$^{\bullet+}$ between 298 K and 175 K in CD_2Cl_2:toluene-d_8:THF-d_8 1:1:1 are virtually identical, indicating that the hyperfine interactions and the intrinsic Lorentzian linewidths Γ_L in **P1$_B$**$^{\bullet+}$ are essentially temperature-independent above 175 K (Figure 3.5A). In contrast, the fluid-phase cw-EPR spectra of **P2$_B$**$^{\bullet+}$ exhibit a continuous broadening of their spectral envelope with decreasing temperature (Figure 3.5B), which is highlighted by the superimposed variable temperature cw-EPR spectra of **P2$_B$**$^{\bullet+}$ in Figure 3.25. The cw-EPR spectra of ***b*-P2**$^{\bullet+}$ are virtually unchanged between 298 K and 225 K but show features consistent with anisotropic broadening at 200 K and 175 K (Figure 3.5D). Consequently, the broadening of the cw-EPR spectra of **P2$_B$**$^{\bullet+}$ between 298 K and 225 K can be attributed to a slower rate k_{ex} of the intramolecular electron transfer, whereas at 200 K and 175 K exchange broadening and anisotropic broadening both contribute to the lineshape. The spectral envelope of **P2$_B$**$^{\bullet+}$ remains narrower than that of **P1$_B$**$^{\bullet+}$ in all fluid-phase measurements in CD_2Cl_2:toluene-d_8:THF-d_8 1:1:1 which suggests that the intramolecular electron transfer in **P2$_B$**$^{\bullet+}$ remains fast on the EPR timescale (Figure 3.5C). The cw-EPR spectra of **P1$_B$**$^{\bullet+}$ and **P2$_B$**$^{\bullet+}$ in frozen

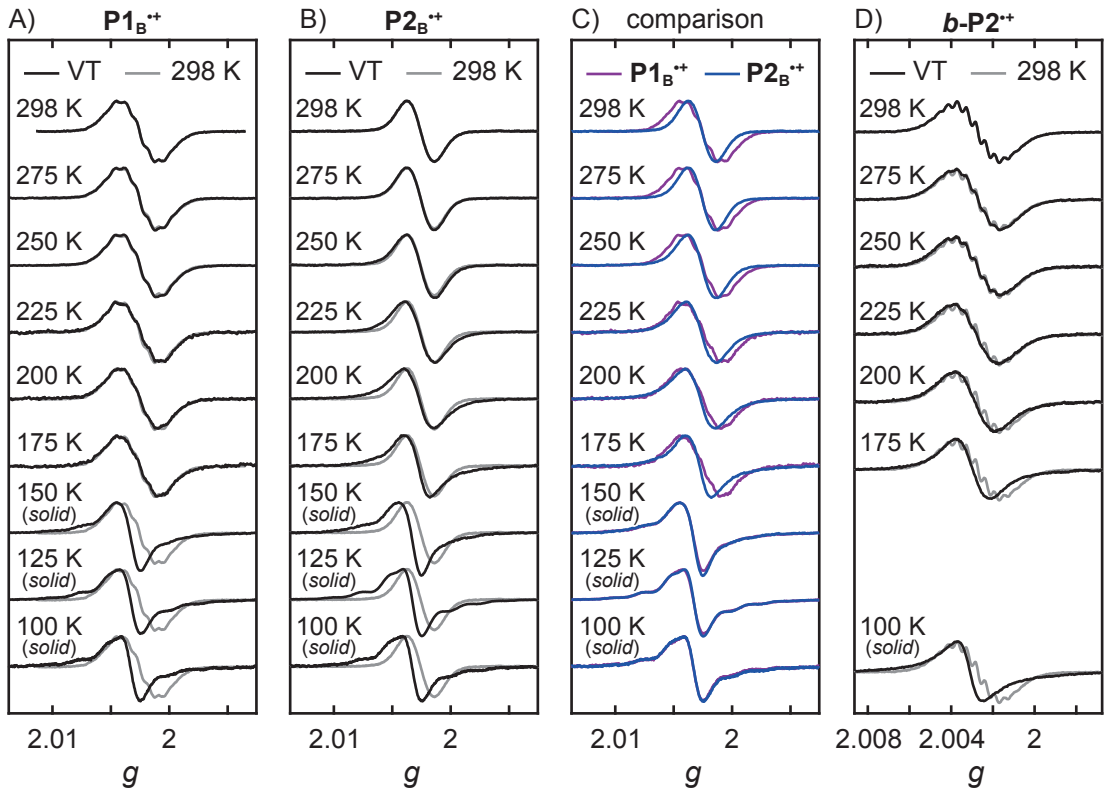


Figure 3.5: Variable-temperature (VT) cw-EPR spectra of A) $\mathbf{P1_B}^{\bullet+}$, B) $\mathbf{P2_B}^{\bullet+}$, and D) ***b*-P2**$^{\bullet+}$ in CD_2Cl_2:toluene-d_8:THF-d_8 1:1:1 between 298 K and 175 K in fluid solution and between 150 K and 100 K in a frozen glass at X-band frequencies. At each temperature, the variable-temperature spectrum (black) is compared to the corresponding spectrum at 298 K (gray). C) Comparison of the variable-temperature cw-EPR spectra of $\mathbf{P1_B}^{\bullet+}$ (purple) and $\mathbf{P2_B}^{\bullet+}$ (blue).

CD_2Cl_2:toluene-d_8:THF-d_8 1:1:1 show anisotropic broadening and are temperature-independent between 150 K and 100 K. The identical spectra of $\mathbf{P1_B}^{\bullet+}$ and $\mathbf{P2_B}^{\bullet+}$ at 100 K demonstrate the localization of the radical electron on one porphyrin unit in $\mathbf{P2_B}^{\bullet+}$ on the EPR timescale, which is supported by the simulation of these cw-EPR spectra (*vide infra*). This localization is probably caused by a combination of the reorganization energy associated with electron transfer, the lack of flexibility of the porphyrin backbone in the frozen solution, and possibly the localization of the $SbCl_6^-$ counter ion. In contrast, the frozen solution cw-EPR spectral envelope of ***b*-P2**$^{\bullet+}$ remains narrower than the spectral envelope of $\mathbf{P1_{Sym}}^{\bullet+}$ consistent with coherent delocalization of the radical spin density over both porphyrin units in the dimer.[51]

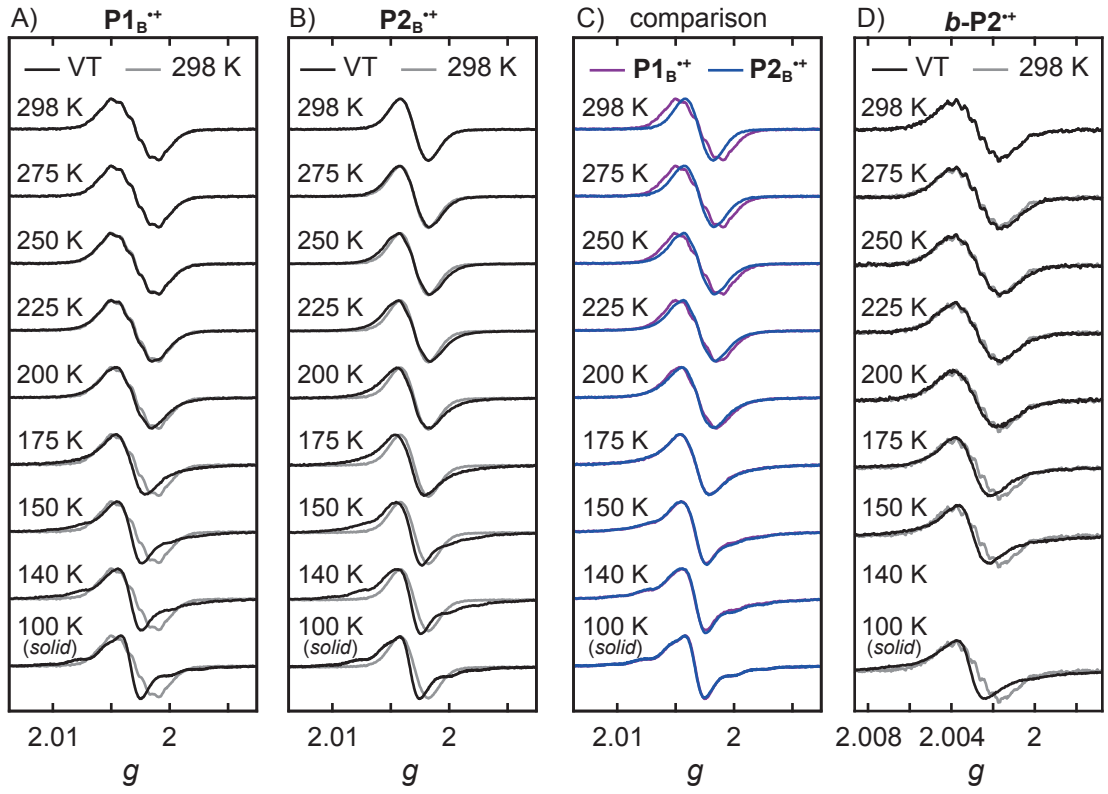


Figure 3.6: Variable-temperature (VT) cw-EPR spectra of A) $\mathbf{P1_B}^{\bullet+}$, B) $\mathbf{P2_B}^{\bullet+}$, and D) $\boldsymbol{b}$-$\mathbf{P2}^{\bullet+}$ in 2-methyltetrahydrofuran between 298 K and 140 K in fluid solution and at 100 K in a frozen glass at X-band frequencies. At each temperature, the variable-temperature spectrum (black) is compared to the corresponding spectrum at 298 K (gray). C) Comparison of the variable-temperature cw-EPR spectra of $\mathbf{P1_B}^{\bullet+}$ (purple) and $\mathbf{P2_B}^{\bullet+}$ (blue).

The variable temperature cw-EPR spectra of $\mathbf{P1_B}^{\bullet+}$, $\mathbf{P2_B}^{\bullet+}$, and $\boldsymbol{b}$-$\mathbf{P2}^{\bullet+}$ in MTHF exhibit a similar behaviour (Figure 3.6). The cw-EPR spectra of $\mathbf{P1_B}^{\bullet+}$ and $\boldsymbol{b}$-$\mathbf{P2}^{\bullet+}$ between 298 K and 225 K are virtually temperature-independent, while the cw-EPR spectra of $\mathbf{P2_B}^{\bullet+}$ exhibit increasing exchange broadening with decreasing temperature (Figure 3.6A,B,D). All fluid-phase cw-EPR spectra exhibit increasing anisotropic broadening between 200 K and 140 K and suggest localization of the radical spin density on one porphyrin unit of $\mathbf{P2_B}^{\bullet+}$ on the EPR timescale below 200 K (Figure 3.6C). The temperature at which hopping becomes slow in MTHF (200 K) is higher than in CD_2Cl_2:toluene-d_8:THF-d_8 1:1:1 (175 K) due to the higher viscosity of MTHF[291] and possibly its higher polarity, which increase the outer reorganization energy of the electron transfer. The virtually identical spectra of $\mathbf{P1_B}^{\bullet+}$ and $\mathbf{P2_B}^{\bullet+}$ in frozen MTHF at 100 K confirm that the radical in $\mathbf{P2_B}^{\bullet+}$ remains localized on the EPR time scale.

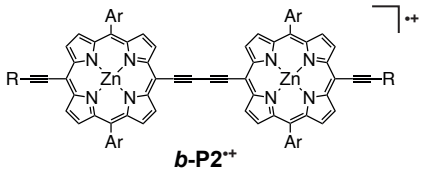


Figure 3.7: Chemical structure of the butadiyne-linked porphyrin dimer radical cation ***b*-P2**$^{\bullet+}$; Ar = 3,5- bis(trihexylsilyl)phenyl.

The frozen solution X-band cw-EPR spectra of $\mathbf{P1_B}^{\bullet+}$ and $\mathbf{P2_B}^{\bullet+}$ in CD_2Cl_2:toluene-d_8:THF-d_8 1:1:1 and 2-methyltetrahydrofuran at 100 K can be simulated with an anisotropic $\boldsymbol{g}$-tensor, anisotropic ^{14}N hyperfine interactions, ^{14}N quadrupole interactions, and an anisotropic linewidth (Figure 3.8).

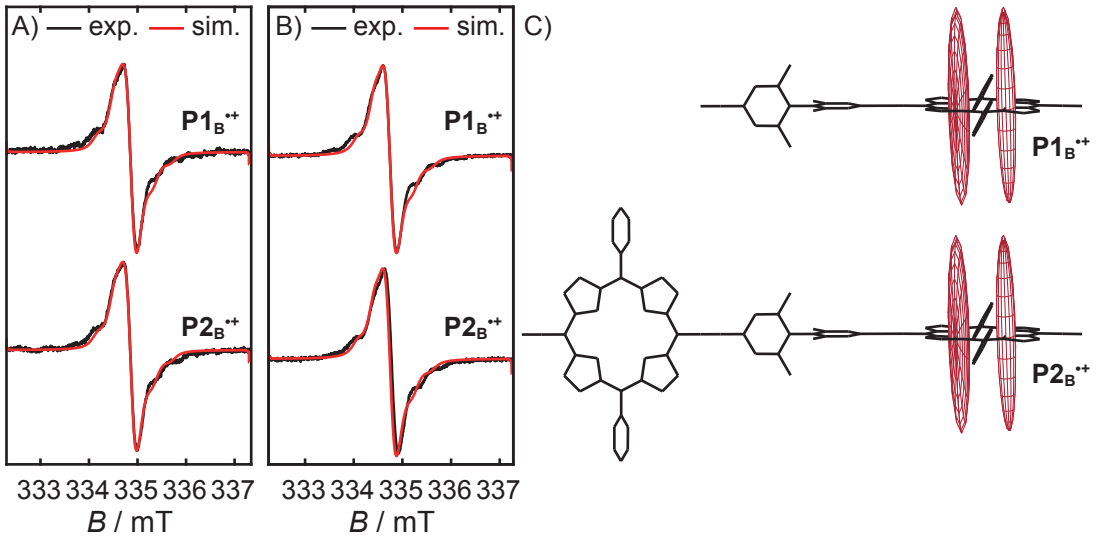


Figure 3.8: Experimental (black) and simulated (red) cw-EPR spectra of $\mathbf{P1_B}^{\bullet+}$ and $\mathbf{P2_B}^{\bullet+}$ at 100 K and X-band frequencies in frozen A) CD_2Cl_2:toluene-d_8:THF-d_8 1:1:1 and B) 2-methyltetrahydrofuran. C) Pictorial representation of the ^{14}N hyperfine coupling tensors $^{14}\boldsymbol{A}$ of $\mathbf{P1_B}^{\bullet+}$ and $\mathbf{P2_B}^{\bullet+}$ obtained from the distributed point-dipole model for $\Delta = 96.1\%$ and used to simulate the cw-EPR spectra. The hyperfine tensors are shown as ellipsoids centered at the corresponding ^{14}N nuclei with dimensions proportional to the eigenvalues of $^{14}\boldsymbol{A}$ and are oriented in the molecular frame based on their Euler angles.

The ^{14}N hyperfine tensors used in the simulations were calculated using the distributed point-dipole model for a spin density ratio $\Delta = 96.1\%$ (see Section 3.5.3 for details). The DFT (B3LYP/EPRII) calculated ^{14}N nuclear quadruple interaction parameters Q and η did not vary considerably between the different nitrogen nuclei, and their average was used in the simulations ($Q = 2.38$ MHz, $\eta = 0.58$). The good

agreement between the experimental and simulated cw-EPR spectra strengthens the validity of the hyperfine tensors obtained from the point-dipole calculations. The cw-EPR spectra of $\mathbf{P1_B}^{\bullet+}$ and $\mathbf{P2_B}^{\bullet+}$ in both solvent systems could be simulated with the same set of hyperfine interactions, which is evidence for the localization of the radical spin density on one porphyrin unit in $\mathbf{P2_B}^{\bullet+}$, and suggests that the hyperfine interactions are independent of the solvent system.

3.3.4 Investigation of the Monomer Dihedral Angle Distribution

The extent of radical delocalization between the porphyrin and biphenyl parts of $\mathbf{P1_B}^{\bullet+}$ depends on the π-conjugation between the two segments, which is modulated by their dihedral angle Φ (Figure 3.9A). To determine whether a distribution of dihedral angles must be taken into account for the analysis of $\mathbf{P1_B}^{\bullet+}$, the rotation barrier ΔE_{rot} between the biphenyl and porphyrin parts was calculated for different dihedral angles Φ using equation 3.1,

$$\Delta E_{\text{rot}} = E(\Phi) - E(0°) \tag{3.1}$$

where $E(\Phi)$ is the energy of the DFT optimized structure of $\mathbf{P1_B}^{\bullet+}$ with a constrained dihedral angle Φ and $E(0°)$ is the minimum energy corresponding to the optimized structure with $\Phi = 0°$. Geometry optimizations of $\mathbf{P1_B}^{\bullet+}$ were performed at the ωB97X-D3BJ/6-31G* level of theory for two range-separation parameters $\omega = 0.05$ and $\omega = 0.2$ to account for different extents of radical delocalization from the porphyrin to the biphenyl fragment. Higher rotation barriers ΔE_{rot} were obtained for $\omega = 0.05$ consistent with a larger delocalization of the radical spin density (Figure 3.9B). Using the Boltzmann relationship in equation 3.2, the population ratio of dihedral angles was calculated at 298 K and 175 K, just above the glass formation temperature of CD_2Cl_2:toluene-d_8:THF-d_8 1:1:1, using the DFT calculated rotation barriers.

$$\frac{P(\Phi)}{P(0°)} = \exp\left(\frac{-\Delta E_{\text{rot}}}{RT}\right) \tag{3.2}$$

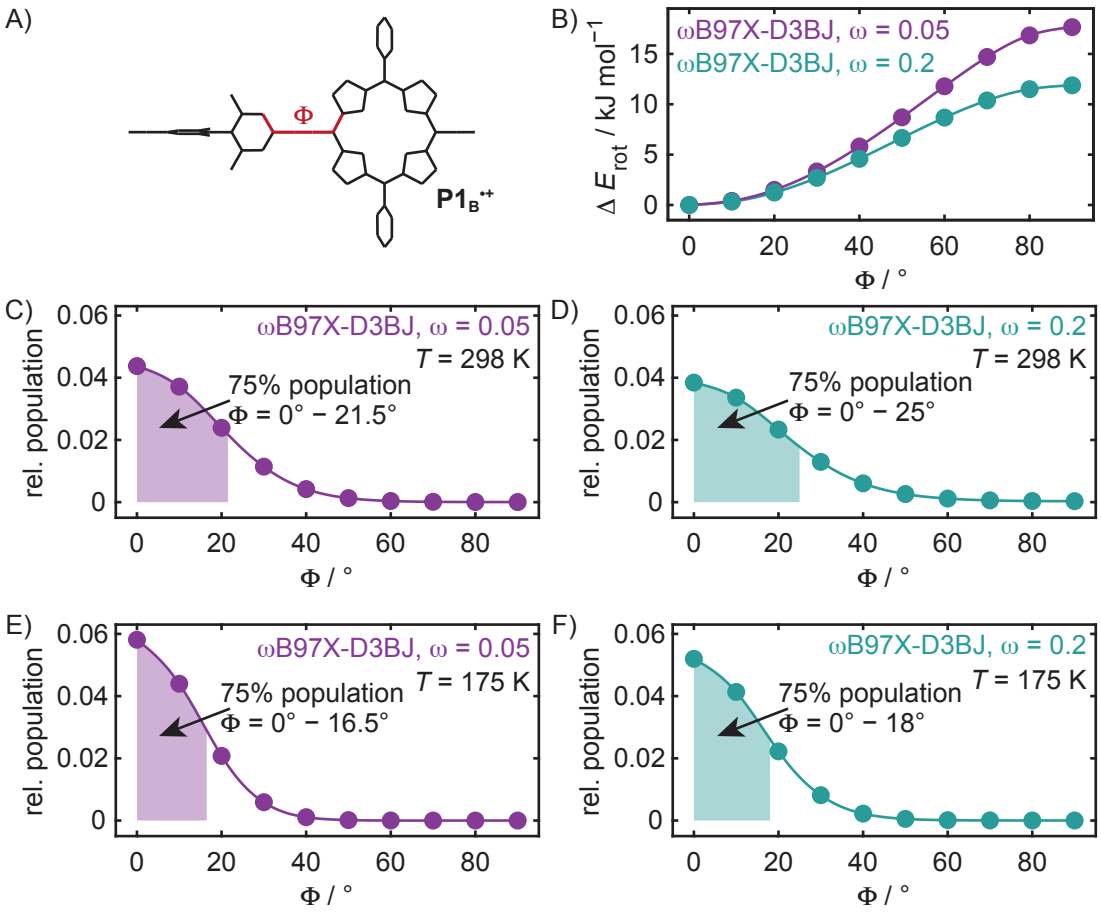


Figure 3.9: A) Schematic depiction of the dihedral angle Φ between the porphyrin and biphenyl parts of $\mathbf{P1_B}^{\bullet+}$. DFT calculated rotation barriers ΔE_{rot} for different dihedral angles Φ in $\mathbf{P1_B}^{\bullet+}$ calculated with ωB97X-D3BJ as functional with range-separation parameters $\omega = 0.05$ and $\omega = 0.2$ and the 6-31G* basis set. C)–F) Boltzmann weighted distributions of dihedral angles in $\mathbf{P1_B}^{\bullet+}$ at 298 K and 175 K obtained from the DFT calculated rotation barriers. The shaded areas indicate the dihedral angles that account for 75% of the populated geometries. DFT calculations for the different geometries of $\mathbf{P1_B}^{\bullet+}$ with constrained dihedral angles were performed in 10° steps (indicated by the solid dots) and interpolated to obtain the trends presented here.

The relative populations were subsequently normalized following equation 3.3 and are shown in Figure 3.9C–F. Integrations were performed using the trendlines obtained from interpolation of the DFT-calculated values.

$$\text{relative population}\,(\Phi) = \frac{P\,(\Phi)\,/P\,(0°)}{\int_{\Phi=0°}^{\Phi=90°} P\,(\Phi)\,/P\,(0°)\,\mathrm{d}\Phi} \tag{3.3}$$

The predicted thermal populations of Φ are similar for calculations with both range-separation parameters. At 298 K, geometries with dihedral angles between Φ = 0°–

21.5° for $\omega = 0.05$ and $\Phi = 0°$–25° for $\omega = 0.2$ account for 75% of populated structures (Figure 3.9C,D). This distribution is slightly narrowed to $\Phi = 0°$–16.5° for $\omega = 0.05$ and $\Phi = 0°$–18° for $\omega = 0.2$ at 175 K, which represents the geometric distribution in frozen CD_2Cl_2:toluene-d_8:THF-d_8 1:1:1 (Figure 3.9E,F). Increasing the dihedral angle Φ in $\mathbf{P1_B}^{\bullet+}$ from 0° to 20° only marginally affects the predicted spin density distributions. This confirms that simulations based on the lowest-energy geometry of $\mathbf{P1_B}^{\bullet+}$ with $\Phi = 0°$ are sufficient to model the experimental spectra.

3.3.5 Mims ENDOR Spectroscopy

The anisotropic ^{1}H hyperfine interactions of $\mathbf{P1_{Sym}}^{\bullet+}$, $\mathbf{P1_B}^{\bullet+}$, and $\mathbf{P2_B}^{\bullet+}$ were measured by pulse Mims ENDOR spectroscopy in frozen CD_2Cl_2:toluene-d_8:THF-d_8 1:1:1 at 80 K and Q-band frequencies (Figure 3.10). Although decomposition of the ENDOR spectra is not feasible due to the large number of nuclei with similar hyperfine interactions, these spectra provide valuable insight into the spin delocalization of the radical cations. Because of the lack of dynamic averaging in a frozen solvent matrix, the anisotropic hyperfine interactions are resolved in the ENDOR measurements. Simulation of the ENDOR spectra can therefore be used to obtain information about the ^{1}H hyperfine interactions that are not resolved due to the inhomogeneous broadening of the room-temperature cw-EPR spectra. In addition, dynamic processes such as polaron migration and electron hopping can occur rapidly on the EPR timescale at room temperature and therefore contribute to the apparent spin density distribution.[84] However, these processes are typically not observed by EPR spectroscopy at cryogenic temperatures in a frozen matrix, which provides a better probe for the instantaneous radical distribution and hyperfine interactions.[51, 83]

The Q-band ^{1}H Mims ENDOR spectra of $\mathbf{P1_{Sym}}^{\bullet+}$, $\mathbf{P1_B}^{\bullet+}$, and $\mathbf{P2_B}^{\bullet+}$ are centered at the proton Larmor frequency $^{1\mathrm{H}}\nu_L$ and split into symmetric peaks by the hyperfine interactions. This is characteristic of nuclei in the weak coupling limit with hyperfine interactions smaller than the Larmor frequency $\left(^{1\mathrm{H}}\boldsymbol{A} < 2\,^{1\mathrm{H}}\nu_L\right)$. The ENDOR spectra of $\mathbf{P1_B}^{\bullet+}$ and $\mathbf{P2_B}^{\bullet+}$ are virtually identical, suggesting that both radical cations have the

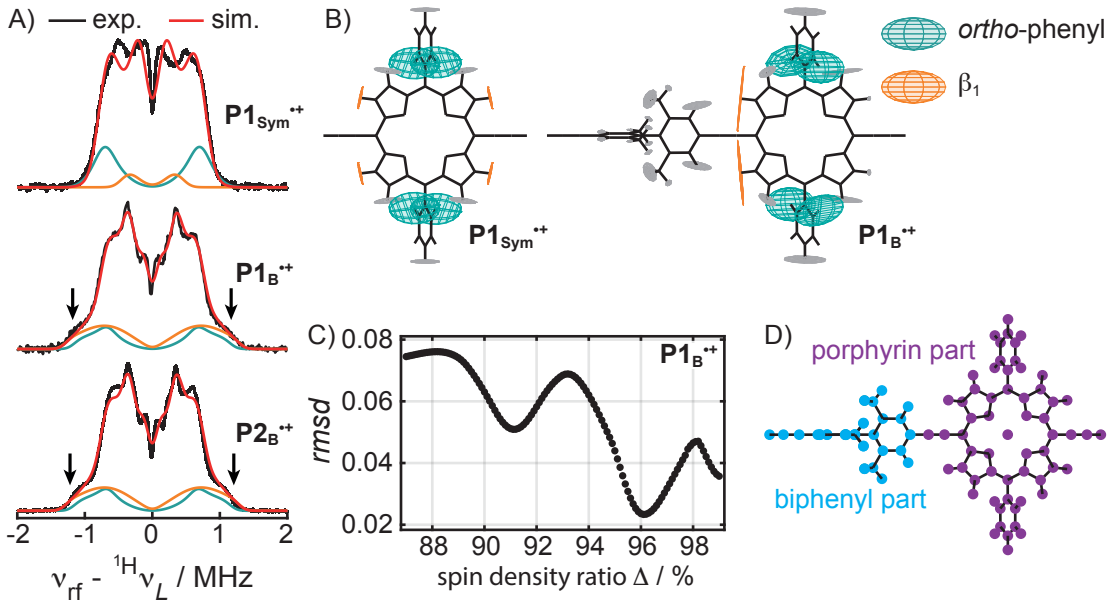


Figure 3.10: A) Experimental (black) and simulated (red) ^{1}H Mims ENDOR spectra of $\mathbf{P1_{Sym}}^{\bullet+}$, $\mathbf{P1_B}^{\bullet+}$, and $\mathbf{P2_B}^{\bullet+}$ recorded at Q-band frequencies in frozen CD_2Cl_2:toluene-d_8:THF-d_8 1:1:1 at 80 K. The spectrum of $\mathbf{P1_{Sym}}^{\bullet+}$ was simulated using anisotropic ^{1}H hyperfine tensors $^1\boldsymbol{A}$ obtained from DFT calculations at the B3LYP/EPRII level of theory. The spectra of $\mathbf{P1_B}^{\bullet+}$ and $\mathbf{P2_B}^{\bullet+}$ were simulated using hyperfine tensors calculated *via* the distributed point-dipole model for $\mathbf{P1_B}^{\bullet+}$ with a spin density ratio $\Delta = 96.1\%$. The individual contributions to the ^{1}H ENDOR spectra from the *ortho*- and β_1-hydrogens are highlighted in dark green and orange, respectively. B) Schematic representation of the anisotropic ^{1}H hyperfine tensors of $\mathbf{P1_{Sym}}^{\bullet+}$ and $\mathbf{P1_B}^{\bullet+}$. The tensors of the *ortho*- and β_1-protons that give rise to the highlighted transitions in A) are shown in dark green and orange, respectively; additional tensors are shown in grey as a reference. C) Root-mean-square deviation (*rmsd*) between the experimental and simulated ^{1}H Mims ENDOR spectra of $\mathbf{P1_B}^{\bullet+}$ as a function of Δ. D) Schematic visualization of the formal separation of $\mathbf{P1_B}^{\bullet+}$ in a porphyrin (purple) and biphenyl (blue) fragment.

same anisotropic proton hyperfine interactions. This is consistent with a localization of the radical spin density on one porphyrin unit in $\mathbf{P2_B}^{\bullet+}$ on the EPR timescale and provides additional evidence that the radical cation is not coherently delocalized over both porphyrin units.

Simulation of the ENDOR spectra of $\mathbf{P1_B}^{\bullet+}$ and $\mathbf{P2_B}^{\bullet+}$ using DFT-calculated hyperfine tensors is not feasible due to an over-delocalization of the radical spin density from the porphyrin to the biphenyl part for a wide range of DFT functionals with different range-separation parameters (Figure 3.20). To overcome this limitation, the distributed point-dipole model described in Section 3.5.3 was used to calculate the ^{1}H hyperfine

interactions in $\mathbf{P1_B}^{\bullet+}$ from a systematically assigned spin density distribution. In brief, $\mathbf{P1_B}^{\bullet+}$ was formally divided into a porphyrin and biphenyl subunit (Figure 3.10D). The extent of radical delocalization between the subunits is quantified by the spin density ratio Δ which is defined as the fraction of spin density on the porphyrin subunit. Variation of the spin density ratio Δ allows for the systematic screening of the radical delocalization with a single fitting parameter. The spin density assigned to each subunit is distributed to individual nuclei in agreement with DFT calculations. The optimal spin density ratio to describe $\mathbf{P1_B}^{\bullet+}$ was determined by comparing the experimental ^{1}H Mims ENDOR spectrum of $\mathbf{P1_B}^{\bullet+}$ in CD_2Cl_2:toluene-d_8:THF-d_8 1:1:1 with a range of simulated spectra using hyperfine tensors $^{1H}\boldsymbol{A}$ calculated with the distributed point-dipole model for a series of spin density ratios Δ (Figure 3.23). The best agreement between the experimental and simulated spectra was found for $\Delta = 96.1\%$ as judged by their root-mean-square deviation (*rmsd*, Figure 3.10C).

The ^{1}H Mims ENDOR spectra of $\mathbf{P1_B}^{\bullet+}$ and $\mathbf{P2_B}^{\bullet+}$ in Figure 3.10 were simulated with identical hyperfine tensors $^{1H}\boldsymbol{A}$ calculated for the optimal spin density ratio $\Delta = 96.1\%$. Noticeably, both ENDOR spectra exhibit a resolved shoulder corresponding to a hyperfine interaction of approximately 2.7 MHz that is absent in the spectrum of $\mathbf{P1_{Sym}}^{\bullet+}$ (Figure 3.10A; arrows). The origin of this feature becomes evident from the simulations of the individual hyperfine contributions to the ENDOR spectra (Figure 3.10A,B). For $\mathbf{P1_{Sym}}^{\bullet+}$, the width of the ENDOR spectrum is determined by the hyperfine interactions with the *ortho*-protons of the aryl side groups (dark green). The introduction of the biphenyl unit in $\mathbf{P1_B}^{\bullet+}$ desymmetrizes the porphyrin and changes the environment around the porphyrin β protons. This results in a substantial increase of the largest principal component of the anisotropic hyperfine interactions with the β_1-protons (orange) that determine the width of the ENDOR spectra of $\mathbf{P1_B}^{\bullet+}$ and $\mathbf{P2_B}^{\bullet+}$ and give rise to the pronounced shoulder.

Apart from subtle intensity changes, the ^{1}H Mims ENDOR spectra of $\mathbf{P1_B}^{\bullet+}$ and $\mathbf{P2_B}^{\bullet+}$ in frozen MTHF at 80 K and Q-band frequencies are virtually identical to the

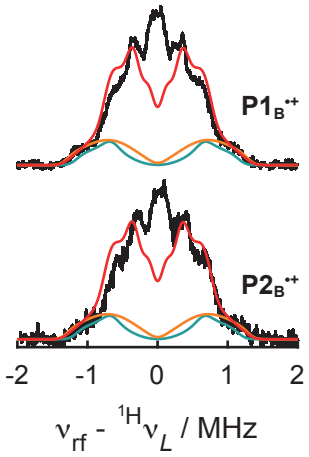


Figure 3.11: Experimental (black) and simulated (red) ^{1}H Mims ENDOR spectra of $\mathbf{P1_B}^{\bullet+}$ and $\mathbf{P2_B}^{\bullet+}$ recorded at Q-band frequencies in frozen 2-methyltetrahydrofuran at 80 K. The spectra were simulated using hyperfine tensors calculated with the distributed point-dipole model for a spin density ratio $\Delta = 96.1\%$. The individual contributions to the ^{1}H ENDOR spectra from the *ortho*- and β_1-hydrogens are highlighted in dark green and orange, respectively.

ENDOR spectra in CD_2Cl_2:toluene-d_8:THF-d_8 1:1:1 and can be simulated with the same anisotropic ^{1}H hyperfine tensors (Figure 3.11). The intense peak at the ^{1}H Larmor frequency of the Mims ENDOR spectra recorded in MTHF results from weak dipolar hyperfine interactions with the protonated solvent matrix. These ENDOR spectra are additional evidence for the localization of the radical on one porphyrin unit of $\mathbf{P2_B}^{\bullet+}$ in frozen MTHF on the EPR timescale and suggest that the proton hyperfine interactions in $\mathbf{P1_B}^{\bullet+}$ and $\mathbf{P2_B}^{\bullet+}$ are independent of the solvent systems in frozen solution.

3.3.6 Introduction to Exchange Broadening

The influence of the reversible intramolecular electron transfer between the two degenerate redox sites of $\mathbf{P2_B}^{\bullet+}$ on the cw-EPR spectra of the system can be modelled as a two-state chemical exchange process in which the radical spin density is either distributed over one half or the other half of $\mathbf{P2_B}^{\bullet+}$ (Figure 3.12). This electron transfer results in the modulation of hyperfine interactions, which means that hyperfine couplings to the nuclei on one half of $\mathbf{P2_B}^{\bullet+}$ result in in the absence of couplings to the corresponding nuclei on the other half, and *vice versa*. Consequently, the symmetry related nuclei on both sides of $\mathbf{P2_B}^{\bullet+}$ are dynamically equivalent with identical time-averaged hyperfine interactions but different instantaneous hyperfine couplings.

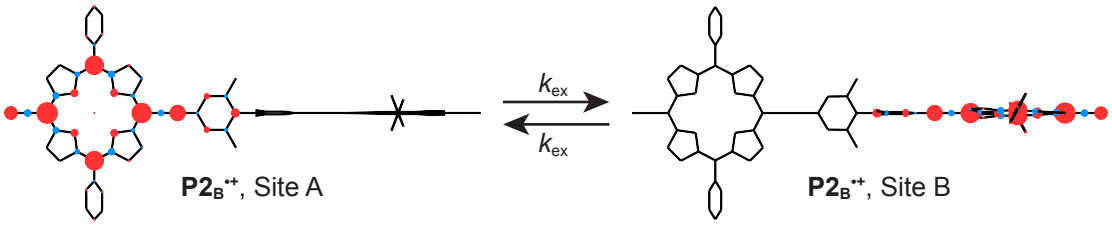


Figure 3.12: Schematic visualization of the redistribution of spin density during the reversible intramolecular electron transfer in $\mathbf{P2_B}^{\bullet+}$. The spin population on each nucleus is represented by a sphere centered on the atom with a radius proportional to the magnitude of its assigned spin population. Red spheres represent excess spin-up and light-blue spheres indicate excess spin-down populations.

The effects of a modulation of hyperfine interactions for dynamically equivalent nuclei on the cw-EPR spectrum of the system are exemplified for a simple model system using numerical linewidth equations reported in an account by Fraenkel[288] and derived from relaxation-matrix theory[292] and the generalized Bloch equations[293–295]. The model system consists of a free electron that alternatingly interacts with two ^{14}N nuclei with an isotropic hyperfine interaction of 30 MHz (Figure 3.13A). Simulations of the exchange broadened EPR spectra were performed with a magnetic field strength $B = 320$ mT and an intrinsic transverse relaxation time $T_{2,0} = 10^{-7}$ s. Exchange induced frequency shifts of the EPR transitions are negligible in this simple example and are therefore omitted in the discussions. It is also assumed that the nuclear-spin quantum number m of both nuclei is identical before and after the electron transfer.

The angular frequencies $\omega(M)$ of the one-electron-two-nuclei model system are given to first order by equation 3.4:

$$\omega(M) = \omega_0 + |\gamma_e| M \frac{a_\mathrm{I} + a_\mathrm{II}}{2} \tag{3.4}$$

where γ_e is the gyromagnetic ratio of the free electron, $\omega_0/2\pi$ is the electron-spin Larmor frequency, and a_I and a_II are the instantaneous hyperfine interactions on site A or B of the two-site exchange process. The quantum numbers M of the transitions are all possible combinations of the nuclear quantum numbers m of the two ^{14}N

nuclei: $M = m_{\mathrm{I}} + m_{\mathrm{II}}$. The Lorentzian lineshape $I_M(\omega)$ of the individual transitions M is given by equation 3.5.

$$I_M(\omega) = \frac{T_2(M)}{\pi}\left\{1 + T_2^2(M)\left[\omega - \omega(M)\right]^2\right\}^{-1} \tag{3.5}$$

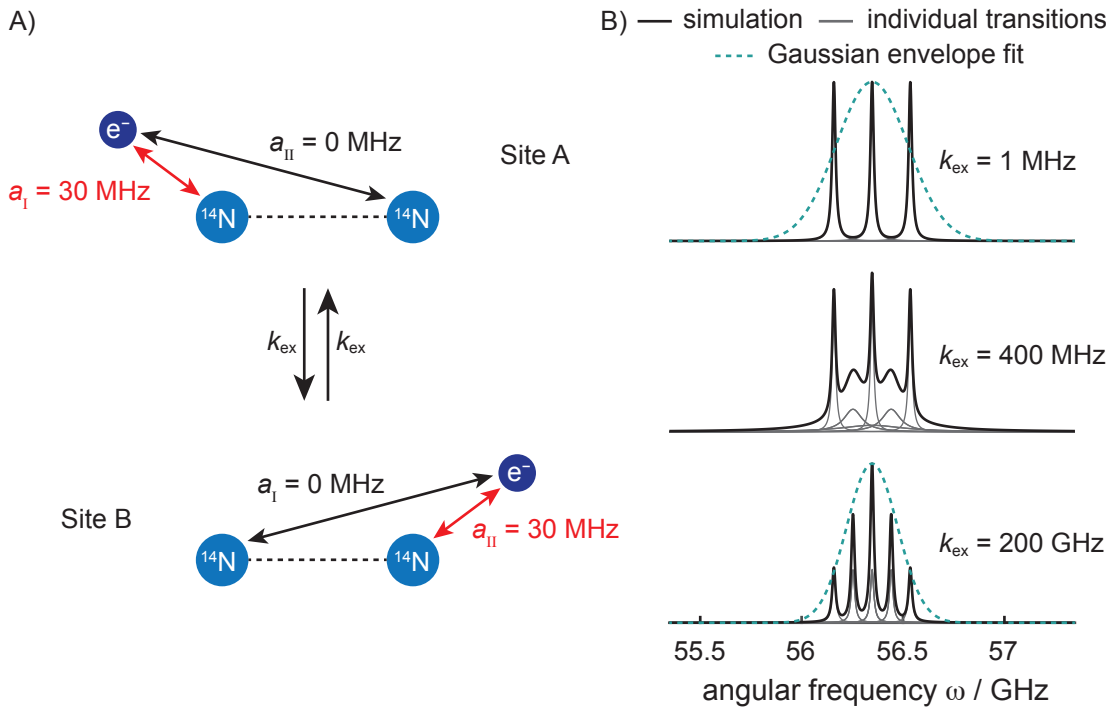


Figure 3.13: A) Pictorial representation of the reversible intramolecular electron transfer with a modulation of hyperfine interaction in a simple model system. The free electron e^- alternatingly interacts with two ^{14}N nuclei with an isotropic hyperfine interaction $a = 30$ MHz and a transfer rate k_{ex} between the nuclei. B) Numerical simulations of the absorptive EPR spectra of the model system in A) for transfer rates k_{ex} in the slow (top), intermediate (middle), and fast (bottom) exchange regime. The Gaussian spectral envelopes were obtained by least-squares fitting of a Gaussian normal distribution to the simulated spectra.

The transverse relaxation time $T_2(M)$ of each transition depends on the rate of the exchange process following equation 3.6.

$$T_2^{-1}(M) = T_2^{-1}(m_{\mathrm{I}}, m_{\mathrm{II}}) = \gamma_e^2 \tau \left\langle (\delta a)^2 \right\rangle (m_{\mathrm{I}} - m_{\mathrm{II}})^2 + T_{2,0}^{-1} \tag{3.6}$$

where $\left\langle (\delta a)^2 \right\rangle = 0.25\,(a_{\mathrm{I}} - a_{\mathrm{II}})^2$ is the mean square deviation of the hyperfine splitting and $T_{2,0}$ is the intrinsic transverse relaxation time of the system and independent from the nuclear transition. The lifetime τ depends on the exchange rate k_{ex} between sites A and B and is calculated following equation 3.7.

$$\tau = \frac{1}{2k_{ex}} \tag{3.7}$$

As shown in the numerical simulations in Figure 3.13B, the appearance of the EPR spectra of the simple model system is determined by the rate of the electron transfer k_{ex} between the two nuclei. In the slow exchange limit $\left(\tau > (|\gamma_e||\delta a|)^{-1}\right)$ the spectrum consists of a triplet with identical amplitudes for each transition as expected for the hyperfine coupling pattern of an $I = 1$ nucleus. For an intermediate electron transfer rate, the simulated spectrum is exchange broadened and exhibits an alternating line-width effect.[288] In the fast exchange limit $\left(\tau^2 < \left(\gamma_e^2 \left\langle (\delta a)^2 \right\rangle\right)^{-1}\right)$, a five line spectrum with relative amplitudes 1:2:3:2:1 is observed and the Gaussian envelope width of the spectrum is smaller by a factor of about $2^{-0.5}$ compared to the envelope width in the slow exchange limit. These simulations highlight the importance of accurate knowledge about the instantaneous hyperfine interactions of the radical cation on the individual redox sites of $\mathbf{P2_B}^{\bullet+}$. The trend in the model system simulations is consistent with the qualitative discussion of the variable-temperature cw-EPR spectra of $\mathbf{P2_B}^{\bullet+}$ in Section 3.3.3 and supports the conclusion of fast electron transfer at 298 K, intermediate electron transfer rates in the fluid phase below 298 K, and localization of the radical on the EPR timescale in frozen solution.

3.3.7 Simulation of the Electron Transfer Dynamics

The temperature-dependence of the rate constant k_{ex} for reversible intramolecular electron transfer in $\mathbf{P2_B}^{\bullet+}$ was determined by simulating the variable-temperature cw-EPR spectra of $\mathbf{P1_B}^{\bullet+}$ and $\mathbf{P2_B}^{\bullet+}$ between 298 K and 200 K at X-band frequencies. Simulations were performed for a range of electron transfer rates k_{ex}, and the best-fit simulations were identified from the smallest root-mean-square deviations (*rmsd*) between the experimental and simulated spectra. The error margins of k_{ex} were determined as the electron transfer rates with a 5% larger *rmsd* than the minimum *rmsd*. All simulations were performed with a two-site chemical exchange model implemented by Stoll[296] and Kozhanov[297] in MATLAB[221] based on the EasySpin[238] software package in which the radical spin density is distributed

over one half or the other half of $\mathbf{P2_B}^{\bullet+}$ (Figure 3.12). To increase the speed of the simulations, the chemical exchange model was called from a custom written MATLAB routine that enabled the parallel simulation of multiple spectra using a *parfor*-loop architecture included in the MATLAB parallel computing toolbox (see Section 3.6 for details about the MATLAB code).

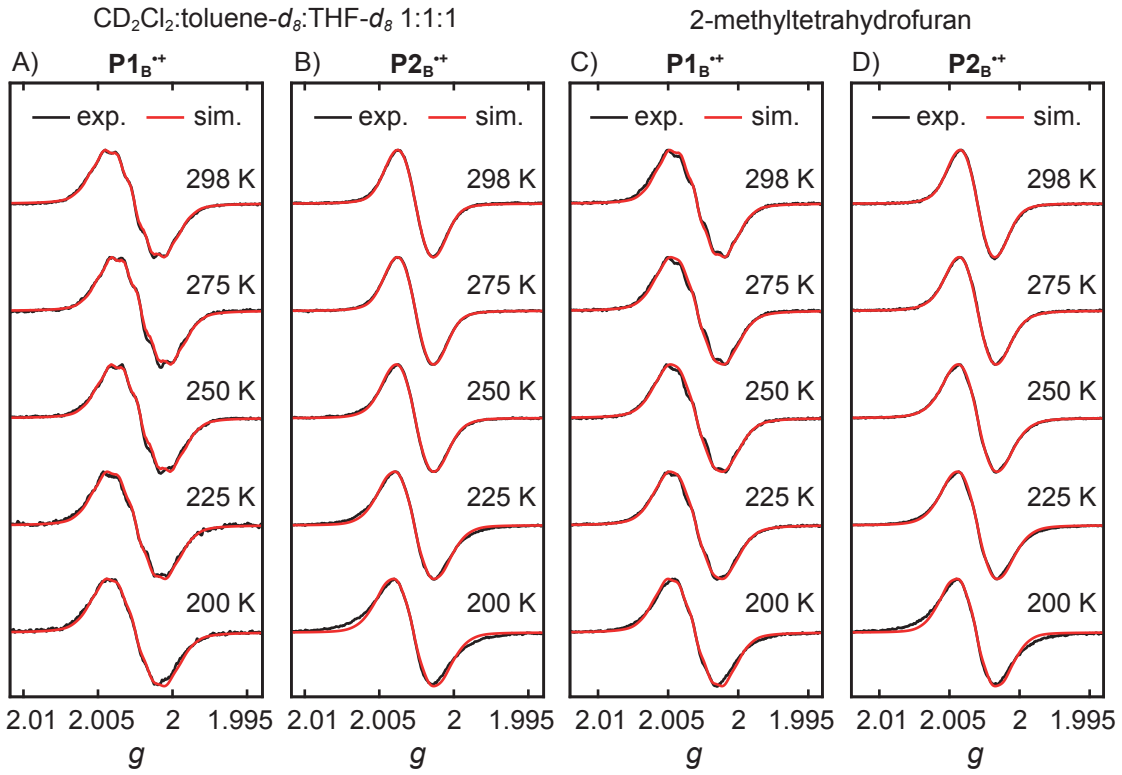


Figure 3.14: Comparison of the experimental (black) and simulated (red) variable temperature cw-EPR spectra of $\mathbf{P1_B}^{\bullet+}$ and $\mathbf{P2_B}^{\bullet+}$ at X-band frequencies in CD_2Cl_2:toluene-d_8:THF-d_8 1:1:1 (A+B) and 2-methyltetrahydrofuran (C+D) between 298 K and 200 K. Simulations were performed with a two-site chemical exchange model. The monomer spectra were simulated in the slow exchange limit with $k_{ex} = 10^{-10}$ MHz.

The best-fit simulations in CD_2Cl_2:toluene-d_8:THF-d_8 1:1:1 and MTHF are shown in Figure 3.14. Simulations of $\mathbf{P2_B}^{\bullet+}$ were obtained with the electron transfer rates k_{ex} summarized in Table 3.2. The trend in the root-mean-square deviation between the experimental and simulated variable-temperature cw-EPR spectra of $\mathbf{P2_B}^{\bullet+}$ as a function of k_{ex} is shown in Figure 3.26 and Figure 3.27.

The magnetic interactions of the unpaired electron with the two redox centers of $\mathbf{P2_B}^{\bullet+}$ involved in the intramolecular electron transfer are analogous to the magnetic

interactions in $\mathbf{P1_B}^{\bullet+}$ and need to be characterized in detail for an accurate simulation of the variable-temperature spectra. The inherent peak-to-peak linewidth Γ of the EPR transitions at each temperature was determined by simulating the cw-EPR spectra of $\mathbf{P1_B}^{\bullet+}$ with the chemical exchange model in the slow exchange limit ($k_{ex} = 10^{-10}$ MHz) and was subsequently used to describe the two redox sites in the simulation of the variable-temperature cw-EPR spectra of $\mathbf{P2_B}^{\bullet+}$ at the same temperature.

Table 3.2: Summary of the electron transfer rates k_{ex} with their lower and upper uncertainty boundaries resulting in the best-fit simulation of the variable temperature cw-EPR spectra of $\mathbf{P2_B}^{\bullet+}$ in CD_2Cl_2:toluene-d_8:THF-d_8 1:1:1 and 2-methyltetrahydrofuran. The uncertainty boundaries of k_{ex} were determined as the electron transfer rates resulting in root-mean-square deviations (*rmsd*) 5% larger than the minimum *rmsd*. The intensity of the experimental and simulated spectra was normalized to calculate the *rmsd*.

CD_2Cl_2:toluene-d_8:THF-d_8 1:1:1	298 K	275 K	250 K	225 K	200 K
k_{ex} / MHz	53.9	40.7	23.1	12.0	10.0
rmsd	0.0110	0.0105	0.0142	0.0240	0.0440
k_{ex} lower boundary / MHz	47.4	36.9	20.7	9.95	6.80
rmsd	0.0116	0.0110	0.0150	0.0252	0.0462
k_{ex} upper boundary / MHz	61.9	45.1	25.9	14.4	14.1
rmsd	0.0116	0.0110	0.0150	0.0252	0.0462

2-methyltetrahydrofuran	298 K	275 K	250 K	225 K	200 K
k_{ex} / MHz	27.9	22.0	14.8	10.2	7.16
rmsd	0.0113	0.0115	0.0112	0.0181	0.0422
k_{ex} lower boundary / MHz	25.6	20.0	13.5	8.64	4.66
rmsd	0.0118	0.0121	0.0117	0.0190	0.0443
k_{ex} upper boundary / MHz	30.5	24.2	16.1	11.9	10.3
rmsd	0.0118	0.0121	0.0117	0.0190	0.0443

As discussed in Section 3.3.6, exchange broadening of the cw-EPR spectra of $\mathbf{P2_B}^{\bullet+}$ for different electron transfer rates k_{ex} is caused by dynamic changes of hyperfine interactions. The magnitude of these interactions must be known to accurately simulate the exchange process. While the isotropic ^{14}N hyperfine interactions $^{14}N a_{iso}$ can be obtained from least-squares fitting of the cw-EPR spectrum of $\mathbf{P1_B}^{\bullet+}$ at 298 K, the proton hyperfine couplings are not resolved in the cw-EPR spectra (*vide supra*). Instead, the ^{1}H hyperfine interactions were probed by Mims ENDOR

spectroscopy and accurately simulated with ^{1}H hyperfine tensors $^{1H}\boldsymbol{A}$ calculated with the distributed point-dipole model for $\Delta = 96.1\%$. The five largest isotropic components of these hyperfine tensors summarized in Table 3.3 in combination with $^{14N}a_{iso}$ are sufficient to describe the hyperfine interactions modulated during the electron transfer process (Figure 3.15). It should be noted that the three individual ^{1}H nuclei in the biphenyl CH_3 group are not equivalent in the point-dipole simulations. To account for the fast dynamic averaging of the CH_3 protons through rapid rotation in solution, their $^{1H}a_{iso}$ hyperfine interactions were averaged to obtain the value used for the cw-EPR simulations. As discussed in Sections 3.3.3 and 3.3.5, the static hyperfine interactions in $\mathbf{P1_B}^{\bullet+}$ are identical in CD_2Cl_2:toluene-d_8:THF-d_8 1:1:1 and 2-methyltetrahydrofuran and temperature independent between 298 K and 200 K in both solvent systems. Therefore, the same magnetic interactions were used for all exchange broadening simulations.

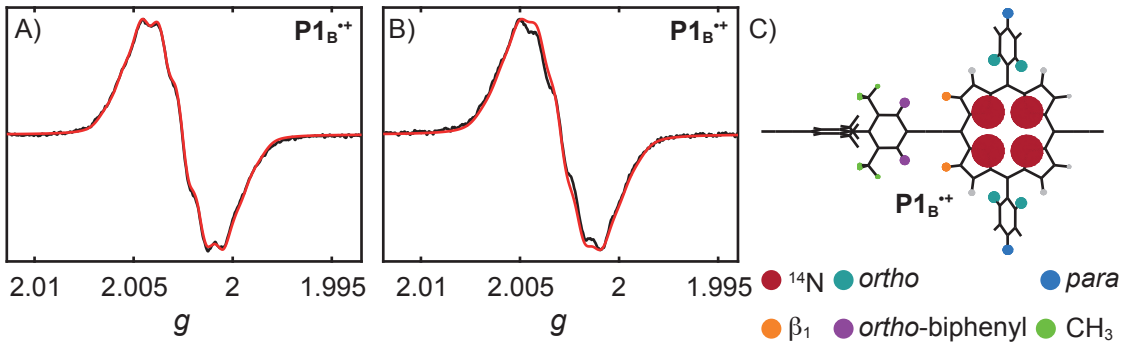


Figure 3.15: Experimental (black) and simulated (red) cw-EPR spectra of $\mathbf{P1_B}^{\bullet+}$ at 298 K and X-band frequencies in A) CD_2Cl_2:toluene-d_8:THF-d_8 1:1:1 and B) 2-methyltetrahydrofuran. Simulations were performed with the isotropic hyperfine interactions in Table 3.3 and Lorentzian peak-to-peak linewidths $\Gamma = 0.05$ mT in CD_2Cl_2:toluene-d_8:THF-d_8 1:1:1 and $\Gamma = 0.07$ mT in 2-methyltetrahydrofuran. C) Pictorial representation of the isotropic hyperfine interactions $^{1H}a_{iso}$ and $^{14N}a_{iso}$ used to simulate the cw-EPR spectra. The hyperfine interaction to each ^{1}H and ^{14}N nucleus is represented by a sphere centered on the atom with a radius proportional to the hyperfine coupling. Hyperfine interactions included in the simulations are color-coded (red: ^{14}N; teal: *ortho*-phenyl; blue: *para*-phenyl; orange: β_1; purple: *ortho*-biphenyl; green: CH_3) while interactions not included in the simulations are shown in grey as reference.

The simulations of the variable-temperature cw-EPR spectra of $\mathbf{P2_B}^{\bullet+}$ in CD_2Cl_2:toluene-d_8:THF-d_8 1:1:1 and MTHF quantify the decreasing rate of the electron transfer with decreasing temperature (Figure 3.14). The isotropic spectra of

Table 3.3: Summary of the isotropic ^{1}H and ^{14}N hyperfine interactions a_{iso} and the number of equivalent nuclei n for each interaction used to simulate the cw-EPR spectra of $\mathbf{P1_B}^{\bullet+}$ and the exchange broadened variable-temperature cw-EPR spectra of $\mathbf{P2_B}^{\bullet+}$.

	^{14}N	*ortho*-phenyl	*para*-phenyl	β_1	*ortho*-biphenyl	CH_3
a_{iso} / MHz	3.99	1.23	1.16	1.11	0.95	0.44
n	4	4	2	2	2	6

$\mathbf{P2_B}^{\bullet+}$ between 298 K and 225 K can be well simulated with the two-site exchange model, whereas the spectra at 200 K, with contributions of anisotropic broadening to the spectral shape, are no longer well described by the simulations, as evident from the larger root-mean-square deviations and uncertainty boundaries. Therefore, the following analysis will focus on the temperature range above 200 K. The temperature-dependence of the electron transfer rate k_{ex} between 298 K and 225 K in CD_2Cl_2:toluene-d_8:THF-d_8 1:1:1 and MTHF was investigated using the Eyring relationship in equation 3.8 to determine the activation enthalpy $\Delta^{\ddagger}H$ and activation entropy $\Delta^{\ddagger}S$ that govern the reversible intramolecular electron transfer in $\mathbf{P2_B}^{\bullet+}$

$$k_{ex} = \frac{\kappa k_B T}{h} \exp\left(-\frac{\Delta^{\ddagger}H}{RT}\right) \exp\left(\frac{\Delta^{\ddagger}S}{R}\right) \tag{3.8}$$

where k_B is the Boltzmann constant, R is the molar gas constant, h is Planck's constant, and κ is the electron transmission coefficient.[298, 299] Plots of $\ln\left(k_{ex}T^{-1}\right)$ versus T^{-1} for $\mathbf{P2_B}^{\bullet+}$ in CD_2Cl_2:toluene-d_8:THF-d_8 1:1:1 and MTHF are shown in Figure 3.16 and were used to determine $\Delta^{\ddagger}H$ and $\Delta^{\ddagger}S$ from the slope and intercept of the trendline between 298 K and 225 K, respectively. The error margins of $\Delta^{\ddagger}H$ and $\Delta^{\ddagger}S$ were determined from trendlines through the lower and upper uncertainty boundaries of the electron transfer rates. The kinetic parameters that govern the electron transfer in $\mathbf{P2_B}^{\bullet+}$ are given in Table 3.4.

Table 3.4: Summary of the activation enthalpies $\Delta^{\ddagger}H$ and entropies $\Delta^{\ddagger}S$ calculated with the Eyring equation with $\kappa = 0.035$ from the temperature dependence of the electron transfer rate k_{ex} in $\mathbf{P2_B}^{\bullet+}$ in CD_2Cl_2:toluene-d_8:THF-d_8 1:1:1 and 2-methyltetrahydrofuran.

	$\Delta^{\ddagger}H$ / kJ mol^{-1}	$\Delta^{\ddagger}S$ / kJ mol^{-1}
CD_2Cl_2:toluene-d_8:THF-d_8 1:1:1	9.55 ± 0.43	-36.5 ± 0.55
2-methyltetrahydrofuran	5.67 ± 0.55	-55.4 ± 1.3

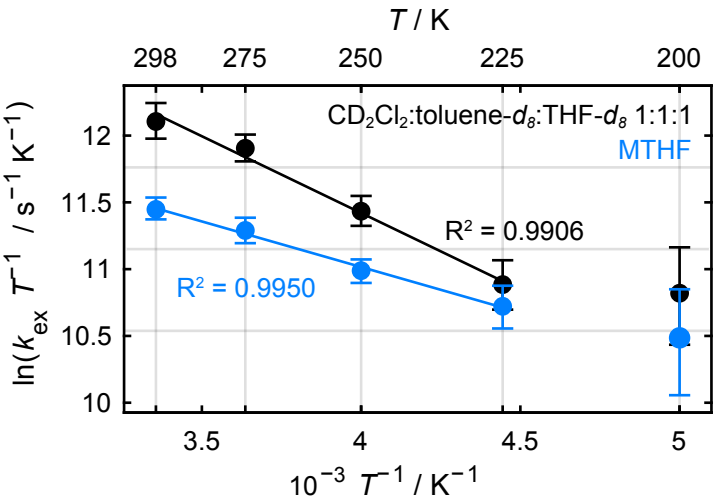


Figure 3.16: Eyring plots of $\ln(k_{ex}T^{-1})$ versus T^{-1} for $\mathbf{P2_B}^{\bullet+}$ in CD_2Cl_2:toluene-d_8:THF-d_8 1:1:1 (black) and 2-methyltetrahydrofuran (blue). The data points at 200 K were omitted from the linear regression analysis because the experimental cw-EPR spectra at this temperature exhibit anisotropic broadening.

The value of the electron transmission coefficient κ was estimated using theoretical modelling. The rate of the electron transfer in $\mathbf{P2_B}^{\bullet+}$ is determined by the overlap integral S_{AB} between Sites A and B of the two-state chemical exchange process (Figure 3.17A). The expectation value of the torsion angle Θ between the two phenyl groups of the 2,2',6,6'-tetramethylbiphenyl linker of $\mathbf{P2_B}^{\bullet+}$ and the resulting overlap integral S_{AB} were calculated by DFT between 298 K and 200 K to investigate the temperature dependence of the electronic coupling between Sites A and B. In the equilibrium geometry, the two phenyl groups are virtually orthogonal ($\Theta_{eq} = 90°$) resulting in a low overlap integral between the two symmetric charge-localized states (Figure 3.17A). The magnitude of S_{AB} is modulated by changes in the torsion angle Θ: as the temperature increases, a broader range of Θ becomes available which increases k_{ex} (Figure 3.17B). The extent of coupling between the electron transfer and nuclear vibrations ν_n was quantified by calculating the electron transmission coefficient following the Landau–Zener approach, which gave $\kappa = 0.035$.[300, 301] The small transmission coefficient ($\kappa \ll 1$) strongly indicates that the electron transfer in $\mathbf{P2_B}^{\bullet+}$ occurs in the non-adiabatic regime and proceeds slower than the nuclear motions ($k_{ex} < \nu_n$).

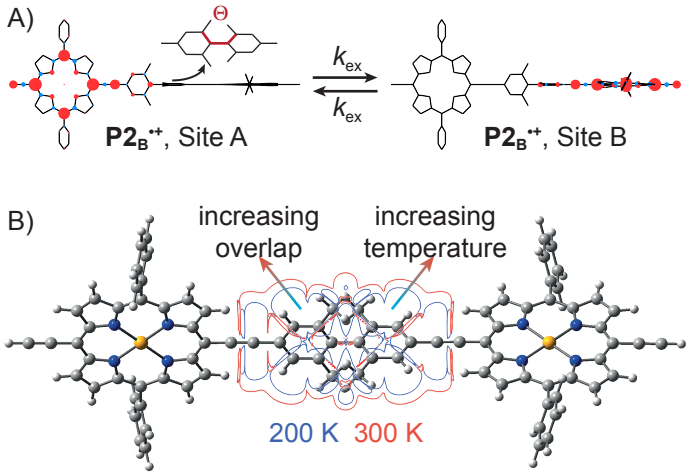


Figure 3.17: A) Schematic visualization of the redistribution of spin density during the reversible intramolecular electron transfer in $\mathbf{P2_B}^{\bullet+}$. The spin population on each nucleus is represented by a sphere centered on the atom with a radius proportional to the magnitude of its assigned spin population. The torsion angle Θ between the phenyl parts of the tetramethylbiphenyl linker is shown in the insert. B) Overlap between the localized charge states in $\mathbf{P2_B}^{\bullet+}$ at 200 K and 300 K calculated with LC-ωPBE as functional and the def2-SVP basis set visualized for the isofactor 10^{-11}.

As expected from Marcus–Hush theory, the electron transfer dynamics in $\mathbf{P2_B}^{\bullet+}$ are energetically and dynamically influenced by the polarity of the solvent, resulting in different activation enthalpies and entropies in CD_2Cl_2:toluene-d_8:THF-d_8 1:1:1 and MTHF.[143, 145, 146] Solvation effects contribute to the outer-sphere reorganization energy λ_o which is often calculated using a dielectric continuum model based on the static dielectric constant ϵ and the square of the refractive index n of the solvent.[143, 149] The implicit temperature dependence of λ_o and therefore $\Delta^{\ddagger}H$ due to the temperature dependence of ϵ and n is omitted in this analysis.[302] The activation enthalpies $\Delta^{\ddagger}H$ of the intramolecular electron transfer in $\mathbf{P2_B}^{\bullet+}$ in CD_2Cl_2:toluene-d_8:THF-d_8 1:1:1 and MTHF are of the same order of magnitude. The larger activation enthalpy in CD_2Cl_2:toluene-d_8:THF-d_8 1:1:1 compared to MTHF suggests a higher outer reorganization energy in the mixed solvent system. Further analysis of the solvent effects on the electron transfer dynamics in $\mathbf{P2_B}^{\bullet+}$ would require the in-depth characterization of the dielectric properties of the 1:1:1 solvent mixture of CD_2Cl_2:toluene-d_8:THF-d_8 and is beyond the scope of this work. The activation entropies $\Delta^{\ddagger}S$ were calculated for a transmission coefficient $\kappa = 0.035$

which approximates the dependence of the intramolecular electron transfer on nuclear vibrations by only considering the change in the biphenyl torsion angle. The negative sign of $\Delta^{\ddagger}S$ suggests that an ordered transition state of $\mathbf{P2_B}^{\bullet+}$ with sufficient electronic coupling between the porphyrin units is required for an efficient electron transfer.

3.3.8 Investigation of the Triplet State Delocalization

The transfer of triplet excitation is a closely related process to electron transfer, since they both involve electron exchange interaction.[121, 303–305] Therefore, the triplet excited state of the porphyrin dimer $\mathbf{P2_B}$ was investigated by transient EPR spectroscopy. The tr-EPR spectra of $^3\mathbf{P1_{Sym}}$, $^3\mathbf{P1_B}$, and $^3\mathbf{P2_B}$ in MTHF at 20 K and for $^3\mathbf{P1_B}$ and $^3\mathbf{P2_B}$ in a polyvinylcarbazole (PVK) film at 250 K were averaged between 300 ns and 400 ns after the laser pulse with depolarized light excitation at 532 nm and are shown in Figure 3.18. The spin polarization of all transient EPR spectra does not change significantly over time. The *AAAEEE* polarization patterns (A = absorptive, E = emissive) of the transient EPR spectra indicate a non-Boltzmann population of the triplet sublevels as expected for photogenerated porphyrin triplet states.[87, 306] This spin–polarization arises from different relative intersystem crossing rates to and relaxation rates from the individual triplet sublevels.

The line shapes and widths of the EPR spectra of photogenerated triplet states are dominated by their zero–field splitting (ZFS) interactions, that arises from the dipolar spin–spin interaction between the two triplet electrons and in some cases also from a spin–orbit interaction. Recent work by Moise, Redman *et al.* has shown that spin–orbit contributions to the zero–field splitting are negligible in Zn-porphyrins akin to the ones investigated here.[88] The following discussion will therefore focus exclusively on the spin–spin interaction, which can be defined by the two ZFS parameters D and E introduced in equation 1.25 in Chapter 1. The magnitudes of D and E are measures of the interspin distance and the orthorhombicity of the spin density distribution, respectively, and determine the distance between the turning points in the transient

EPR spectra. These turning points correspond to the canonical orientations of the zero-field splitting $\boldsymbol{D}$-tensor denoted as X, Y, and Z in Figure 3.18; the + and − superscripts refer to the $m_s = 0 \leftrightarrow m_s = +1$ and $m_s = -1 \leftrightarrow m_s = 0$ transitions, respectively. All other things being equal, an increasing delocalization of the triplet state should result in a reduction of $|D|$.[87] The sign of the D-parameter indicates the orientation of the ZFS tensor in the molecular frame: a positive D-value suggests an oblate spin density (Z axis of the $\boldsymbol{D}$-tensor is perpendicular to the porphyrin plane), whereas a negative D-value is consistent with a prolate spin density (Z axis of $\boldsymbol{D}$ is in the porphyrin plane).

The transient EPR spectrum of $^3\mathbf{P1}_{\mathbf{Sym}}$ in MTHF at 20 K is consistent with previous investigations of the photogenerated triplet state of this compound by Tait *et al.*[52, 307] The intersystem crossing in Zn-porphyrin monomers is driven by spin–orbit coupling due to mixing of the zinc d-orbitals with the π-system of the porphyrin and results in a preferential population of the out-of-plane sublevel of the triplet state.[308] For $^3\mathbf{P1}_{\mathbf{Sym}}$, this results in a preferential population of the Z sublevel (Table 3.5). Tait *et al.* assigned a positive sign to the D parameter of $^3\mathbf{P1}_{\mathbf{Sym}}$ using magnetophotoselection experiments, which is replicated by DFT calculations at the B3LYP/EPRII level of theory (Table 3.6).[307] The D-values of biphenyl porphyrins $^3\mathbf{P1}_{\mathbf{B}}$ and $^3\mathbf{P2}_{\mathbf{B}}$ are similar to $|D|$ for $^3\mathbf{P1}_{\mathbf{Sym}}$. This suggest a similar triplet state delocalization in all three systems consistent with a localization of the triplet state on one half of $^3\mathbf{P2}_{\mathbf{B}}$; in other words, there is no evidence for exciton mobility on the EPR timescale.

The 12% increase of $|E|$ for $^3\mathbf{P1}_{\mathbf{B}}$ and $^3\mathbf{P2}_{\mathbf{B}}$ compared to the value for $^3\mathbf{P1}_{\mathbf{Sym}}$ points towards a higher orthorhombicity of the spin density distribution. The preferential population of the Z sublevels in $^3\mathbf{P1}_{\mathbf{B}}$ and $^3\mathbf{P2}_{\mathbf{B}}$ and the position of the hyperfine transitions in the Mims ENDOR spectra (*vide infra*) suggest that the $\boldsymbol{D}$-tensors of $^3\mathbf{P1}_{\mathbf{B}}$ and $^3\mathbf{P2}_{\mathbf{B}}$ have approximately the same orientation as in $^3\mathbf{P1}_{\mathbf{Sym}}$, resulting in a positive D-parameter.

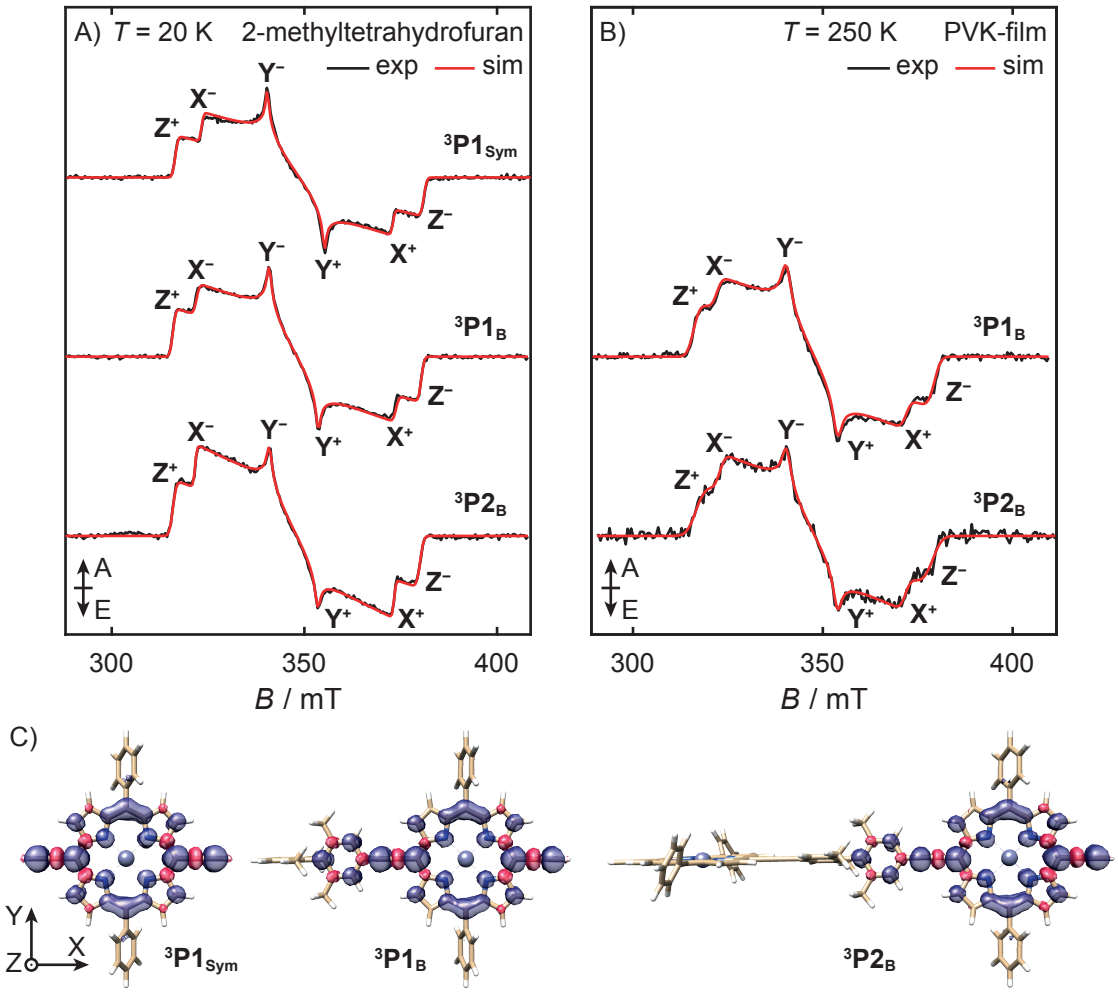


Figure 3.18: Comparison of the experimental (black) and simulated (red) transient EPR spectra of ^{3}**P1**$_{\mathbf{Sym}}$, ^{3}**P1**$_{\mathbf{B}}$, and ^{3}**P2**$_{\mathbf{B}}$ at X-band frequencies in A) 2-methyltetrahydrofuran at 20 K and B) a polyvinylcarbazole (PVK) film at 250 K. The experimental spectra are recorded as an average between 300 ns and 400 ns after the laser pulse with depolarized light at 532 nm. Simulations were performed with the parameters reported in Table 3.5. The ordering of the principal components of $\boldsymbol{D}$ was chosen as $|D_Z| > |D_X| > |D_Y|$ and the canonical field positions are indicated (A = absorption, E = emission). C) DFT calculated spin density distributions of ^{3}**P1**$_{\mathbf{Sym}}$, ^{3}**P1**$_{\mathbf{B}}$, and ^{3}**P2**$_{\mathbf{B}}$ using B3LYP as functional and the EPRII basis set.

The experimental D-values are qualitatively replicated by DFT calculations with B3LYP as functional and the EPRII basis set, which predict approximately identical magnitudes and a positive sign for the D-parameters of ^{3}**P1**$_{\mathbf{Sym}}$, ^{3}**P1**$_{\mathbf{B}}$, and ^{3}**P2**$_{\mathbf{B}}$ (Table 3.6). The discrepancy between the DFT calculated spin–spin contributions to the D-parameter and the experimental values is a know limitation for aromatic triplet states.[309, 310] The trend in the DFT calculated D-parameters for a series of compounds can however inform the interpretation of their experimental spectra.[87,

309, 310] The spin density distributions found in these calculations show a partial delocalization of the triplet spin density onto the biphenyl units of $^3\mathbf{P1_B}$ and $^3\mathbf{P2_B}$ but no triplet delocalization over both sites of $^3\mathbf{P2_B}$, as expected from the experimental data (Figure 3.18C). This localization is consistent with previous reports of localized triplet states in porphyrin nanostructures with a near-orthogonal arrangement of the neighboring porphyrin units at 20 K in 2-methyltetrahydrofuran.[126, 311]

Table 3.5: Zero-field splitting parameters D and E and relative sublevel populations of $^3\mathbf{P1_{Sym}}$, $^3\mathbf{P1_B}$,and $^3\mathbf{P2_B}$ determined through simulation of their transient EPR spectra presented in Figure 3.18.

	2-methyltetrahydrofuran		
	$\lvert D\rvert$ / MHz	$\lvert E\rvert$ / MHz	$p_X : p_Y : p_Z$
$^3\mathbf{P1_{Sym}}$	903 ± 2	163 ± 2	0.05 : 0.00 : 0.95
$^3\mathbf{P1_B}$	904 ± 2	182 ± 2	0.07 : 0.00 : 0.93
$^3\mathbf{P2_B}$	900 ± 2	183 ± 1	0.00 : 0.05 : 0.95

	PVK film		
	$\lvert D\rvert$ / MHz	$\lvert E\rvert$ / MHz	$p_X : p_Y : p_Z$
$^3\mathbf{P1_{Sym}}$	–	–	–
$^3\mathbf{P1_B}$	891 ± 4	170 ± 2	0.10 : 0.00 : 0.90
$^3\mathbf{P2_B}$	875 ± 6	166 ± 2	0.04 : 0.00 : 0.96

To investigate whether the triplet delocalization in $^3\mathbf{P2_B}$ can be extended at higher temperatures, the transient EPR spectra of $^3\mathbf{P1_B}$ and $^3\mathbf{P2_B}$ were measured in a PVK film at 250 K (Figure 3.18B). The approximately identical D-parameters and spectral widths of $^3\mathbf{P1_B}$ and $^3\mathbf{P2_B}$ suggest that the triplet state remains localized on one porphyrin unit in $^3\mathbf{P2_B}$. The smaller values of $|D|$ in the PVK film compared to 2-methyltetrahydrofuran could be the result of slightly different equilibrium geometries in the two environments. The absence of an increasing triplet state delocalization in $^3\mathbf{P2_B}$ probably results from a combination of the limited structural flexibility of the porphyrin dimer in the solid film environment and the intrinsically strong coupling between the two electrons comprising the exciton state.

Table 3.6: Experimental and DFT calculated zero–field splitting parameters for $^3\mathbf{P1}_{\mathbf{Sym}}$, $^3\mathbf{P1}_{\mathbf{B}}$, and $^3\mathbf{P2}_{\mathbf{B}}$.

	experiment		B3LYP/EPRII	
	D / MHz	$\lvert E\rvert$ / MHz	D / MHz	$\lvert E\rvert$ / MHz
$^3\mathbf{P1}_{\mathbf{Sym}}$	$+903 \pm 2$	163 ± 2	+501	122
$^3\mathbf{P1}_{\mathbf{B}}$	$+904 \pm 2$	182 ± 2	+492	135
$^3\mathbf{P2}_{\mathbf{B}}$	$+900 \pm 2$	183 ± 1	+481	133

The extent of triplet state delocalization in $^3\mathbf{P1}_{\mathbf{Sym}}$, $^3\mathbf{P1}_{\mathbf{B}}$, and $^3\mathbf{P2}_{\mathbf{B}}$ was further probed using proton hyperfine interactions measured by orientation-selective Mims ENDOR spectroscopy at the canonical field positions X^-, Y^-, and Z^- at 20 K in 2-methyltetrahydrofuran (Figure 3.19). Previous studies of $^3\mathbf{P1}_{\mathbf{Sym}}$ revealed that the largest hyperfine interactions are observed for the β_1 protons closest to alkyne bonds consistent with DFT calculations (Figure 3.19A).[52, 307] The transition selection ($m_s = 0 \leftrightarrow m_s = +1$ or $m_s = -1 \leftrightarrow m_s = 0$) during the ^{1}H ENDOR measurements provides information about the relative sign of the hyperfine interaction and the ZFS D-value. In the weak coupling regime, the triplet ENDOR spectrum is asymmetric around the Larmor frequency: in additon to a peak at the Larmor frequency from the T_0 state, for a positive D-value, a second peak is observed at $^{1\mathrm{H}}\nu_L + \boldsymbol{A}_i$ and $^{1\mathrm{H}}\nu_L - \boldsymbol{A}_i$ for the $T_0 \leftrightarrow T_-$ and $T_0 \leftrightarrow T_+$ transitions, respectively.[87]

The sign of the β_1 hyperfine interactions in $^3\mathbf{P1}_{\mathbf{Sym}}$ is negative following the assignment by Tait *et al.*.[307] This is in agreement with DFT calculated hyperfine tensors at the B3LYP/EPRII level of theory that also predict negative hyperfine interactions to the β_1 and *ortho*-biphenyl nuclei in $^3\mathbf{P1}_{\mathbf{B}}$ and $^3\mathbf{P2}_{\mathbf{B}}$. The observation of the prominent hyperfine interactions in $^3\mathbf{P1}_{\mathbf{Sym}}$,$^3\mathbf{P1}_{\mathbf{B}}$, and $^3\mathbf{P2}_{\mathbf{B}}$ at rf-frequencies smaller than $^{1\mathrm{H}}\nu_L$ at negative canonical positions is therefore consistent with a positive D-value in all investigated systems. Simulations of the ^{1}H ENDOR spectra of $^3\mathbf{P1}_{\mathbf{Sym}}$,$^3\mathbf{P1}_{\mathbf{B}}$, and $^3\mathbf{P2}_{\mathbf{B}}$ using the DFT calculated hyperfine tensors are broadly in agreement with the experimental spectra although the magnitude of the hyperfine interactions with nuclei on the biphenyl linker is strongly exaggerated (Figure 3.19B). This suggests an over delocalization of triplet spin density onto the biphenyl linker by DFT, analogous

to the over delocalization of the radical cation spin density (*vide supra*). The positions of the largest negative hyperfine transitions in the experimental ENDOR spectra were determined by fitting a Gaussian distribution to the principal hyperfine peaks and are summarized in Table 3.7 (see Figure 3.28 for the fitted spectra). The lack of a substantial reduction of the largest hyperfine tensors between $^{3}\mathbf{P1}_{\mathbf{B}}$ and $^{3}\mathbf{P2}_{\mathbf{B}}$ is additional evidence for the localization of the radical spin density on one half of $^{3}\mathbf{P2}_{\mathbf{B}}$.

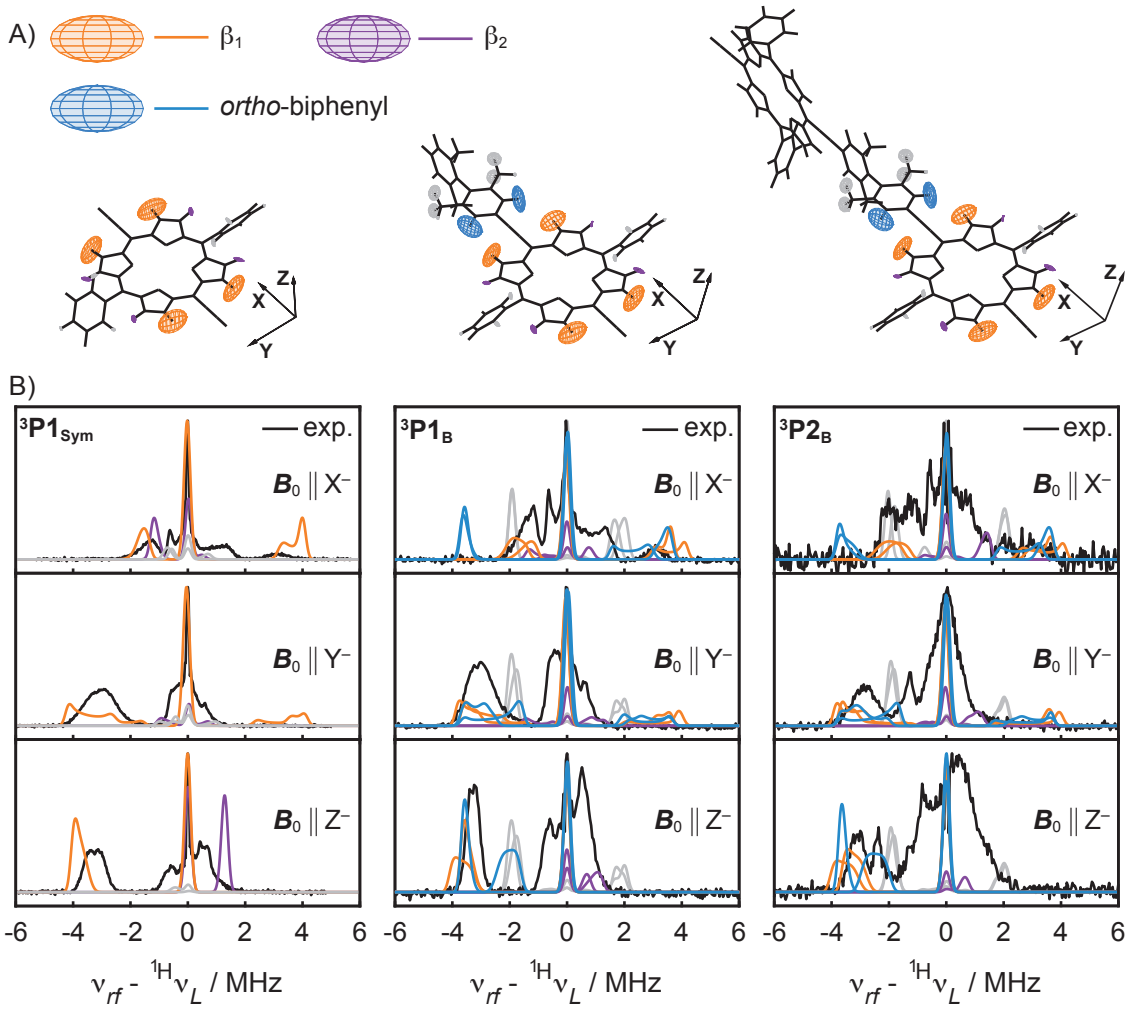


Figure 3.19: A) Schematic representation of the ^{1}H hyperfine tensors $^{1\mathrm{H}}\boldsymbol{A}$ in $^{3}\mathbf{P1}_{\mathbf{Sym}}$, $^{3}\mathbf{P1}_{\mathbf{B}}$, and $^{3}\mathbf{P2}_{\mathbf{B}}$ calculated at the B3LYP/EPRII level of theory. The tensors of the β_1, β_2, and *ortho*-biphenyl protons that give rise to the highlighted simulated transitions in B) are shown in orange, purple, and blue, respectively; additional tensors are shown in grey as a reference. The coordinate axes indicate the orientation of the $\boldsymbol{D}$-tensor in the molecular frame. B) Comparison of the experimental ^{1}H Mims ENDOR spectra of $^{3}\mathbf{P1}_{\mathbf{Sym}}$,$^{3}\mathbf{P1}_{\mathbf{B}}$, and $^{3}\mathbf{P2}_{\mathbf{B}}$ recorded at the X^{-}, Y^{-}, and Z^{-} field positions in 2-methyltetrahydrofuran at 20 K and X-band frequencies with the simulated ENDOR contributions of individual ^{1}H nuclei. Simulations were performed with anisotropic hyperfine tensors $^{1\mathrm{H}}\boldsymbol{A}$ shown in A).

Table 3.7: Summary of the largest negative ^{1}H hyperfine couplings along the *X*, *Y*, and *Z* directions of the zero-field splitting tensors in ^{3}**P1**$_{\mathbf{Sym}}$, ^{3}**P1**$_{\mathbf{B}}$, and ^{3}**P2**$_{\mathbf{B}}$ determined from fitting a Gaussian normal distribution to the principal hyperfine peaks. The distribution of the hyperfine interactions was determined from the full width at half maximum of the Gaussian.

	^{3}**P1**$_{\mathbf{Sym}}$	^{3}**P1**$_{\mathbf{B}}$	^{3}**P2**$_{\mathbf{B}}$
$^1H A_X$ / MHz	-1.35 ± 0.35	-1.35 ± 0.35	-1.55 ± 0.65
$^1H A_Y$ / MHz	-3.04 ± 0.64	-3.01 ± 0.56	-2.83 ± 0.55
$^1H A_Z$ / MHz	-3.25 ± 0.41	-3.27 ± 0.27	-3.07 ± 0.30

3.4 Summary and Conclusion

The electron and spin distribution of the radical cation and photogenerated triplet excited state of the biphenyl-linked porphyrin dimer **P2**$_{\mathbf{B}}$ were investigated by a combination of EPR and optical spectroscopy, DFT calculations, and theoretical modeling. Fluid-phase variable-temperature cw-EPR spectroscopy of **P2**$_{\mathbf{B}}^{\bullet+}$ in CD_2Cl_2:toluene-d_8:THF-d_8 1:1:1 and MTHF between 298 K and 225 K reveals thermally activated, intramolecular electron transfers between the two degenerate sites of **P2**$_{\mathbf{B}}^{\bullet+}$, consistent with a Robin–Day class II mixed valence compound in the nonadiabatic regime. A robust approach to quantify hyperfine interactions that cannot be resolved by cw-EPR spectroscopy, but are nevertheless crucial to simulate the electron transfer dynamics in **P2**$_{\mathbf{B}}^{\bullet+}$, has been demonstrated by investigating the ^{1}H hyperfine interactions of reference compound **P1**$_{\mathbf{B}}^{\bullet+}$ by ^{1}H Mims ENDOR spectroscopy and supporting simulations. This enables the quantification of the electron transfer dynamics in porphyrin nanostructures by fitting the variable-temperature cw-EPR spectra to a two-site exchange model, which was previously only possible by artificially introducing nuclei with large hyperfine interactions.[272, 273] The kinetic parameters that govern the intramolecular electron transfer in **P2**$_{\mathbf{B}}^{\bullet+}$ were quantified by investigating the temperature dependence of the electron transfer rate k_{ex}. The activation enthalpies $\Delta^{\ddagger}H$ that govern the electron transfer in **P2**$_{\mathbf{B}}^{\bullet+}$ highlight the presence of a large barrier between the porphyrin sites, which is promising for achieving high tunneling magnetoresistance ratios in a molecular spin valve.[269] At the same time, the observation of intramolecular electron transfer between the two sites of **P2**$_{\mathbf{B}}^{\bullet+}$ in CD_2Cl_2:toluene-d_8:THF-d_8 1:1:1 and MTHF suggests that the electronic coupling

remains sufficient to sustain a current. This makes $\mathbf{P2_B}$ an excellent candidate for the backbone for a proposed single-molecule spin valve.

Investigation of the spin density distribution of the photogenerated triplet state of $\mathbf{P2_B}$ using transient cw-EPR and ^{1}H Mims ENDOR spectroscopy at 20 K in MTHF confirms the localization of the triplet electrons on one half of the dimer. This localization is preserved at 250 K in a PVK film confirming that the orthogonal arrangement of the porphyrin units in $\mathbf{P2_B}$ prevents the delocalization of the triplet state over a wide range of temperatures and in different sample environments. These results demonstrate that chemical modifications of the electronic coupling in porphyrin nanostructures can be used to control the spin distribution of organic radicals and photogenerated triplet states in a solid matrix: butadiyne-linked porphyrins dimers with efficient interporphyrin electronic coupling exhibit coherent delocalization of their radical cations and triplet states in a frozen solution[51, 52, 307], whereas the weakly coupled biphenyl porphyrin dimer $\mathbf{P2_B}$ localizes doublet and triplet spin densities on one porphyrin unit under analogous conditions. These findings confirm that porphyrin nanostructures with weak electronic coupling between individual porphyrin units fulfill important design criteria for novel spintronic materials and are interesting for the design and synthesis of new molecular platforms for quantum information processing.

3.5 Methods

3.5.1 General Methods

EPR Sample Preparation

Samples of $\mathbf{P1_{Sym}}^{\bullet+}$, $\mathbf{P1_B}^{\bullet+}$, and $\mathbf{P2_B}^{\bullet+}$ for EPR measurements were prepared in CD_2Cl_2:toluene-d_8:THF-d_8 1:1:1 or 2-methyltetrahydrofuran and degassed with three freeze-pump-thaw cycles. For chemical oxidation, 0.5 equivalents of tris-(4-bromophenyl)ammoniumyl hexachloroantimonate (**BAHA**) (for $\mathbf{P1_{Sym}}$ and $\mathbf{P1_B}$) or 0.25 equivalents of **BAHA** (for $\mathbf{P2_B}$) (2.0 mM in CD_2Cl_2) were added to a solution of the porphyrin oligomer (~200 μM in CD_2Cl_2:toluene-d_8:THF-d_8 1:1:1 or 2-methyltetrahydrofuran) under argon just before the EPR experiments. All radical cation samples were prepared directly either in X-band EPR tubes (3.8 mm o.d.) or Q-band EPR tubes (2.0 mm o.d.). For low-temperature measurements, the samples were flash-frozen in liquid nitrogen.

Samples for transient EPR spectroscopy were prepared to a concentration of 150 μM in 2-methyltetrahydrofuran in X-band EPR tubes (3.8 mm o.d.). For the doped PVK-film preparation, stock solutions of PVK and porphyrin were prepared in toluene at 20 mg mL^{-1} and 1.5 mg mL^{-1}, respectively. The PVK stock solution was stirred at 40 °C until it was dissolved. The porphyrin and PVK stock solutions were combined in a ratio of 1:5 in an X-band EPR tube. The solvent was removed *in vacuo* to create a film on the inside of the tube.

Continuous-Wave EPR Measurements

Continuous-wave X-band EPR spectra were acquired on a Bruker EMX Micro spectrometer equipped with a high sensitivity Bruker probe head and an Oxford Instruments helium-flow cryostat. EPR spectra were recorded at a microwave frequency of ca. 9.40 GHz with modulation amplitudes and frequencies of 100 mT and 100 kHz, respectively. The microwave power was scanned to rule out spectral distortions due to saturation effects. The optimal microwave power used in the room temperature cw-EPR spectra in this chapter was 2.0 mW corresponding to an attenuation of 20 dB on

our spectrometer. The temperature during variable temperature cw-EPR experiments was controlled with an Oxford Instruments digital temperature controller using liquid nitrogen as cryogen. A waiting period of 1–1.5 hours between temperature changes or sample insertions and acquisition of the variable temperature cw-EPR spectra was used to ensure that thermal equilibrium was reached before the measurements. The reported spectra were obtained by combining several individually recorded scans to confirm that the signal shape remained constant over time.

^{1}H Mims ENDOR Spectroscopy

Pulse EPR measurements of the chemically generated radical cations were performed on a X-/Q-band Bruker Elexsys 580 spectrometer equipped with a helium gas flow cryostat from Oxford Instruments at 80 K. The ^{1}H Mims ENDOR spectra of $\mathbf{P1_{Sym}}^{\bullet+}$, $\mathbf{P1_B}^{\bullet+}$, and $\mathbf{P2_B}^{\bullet+}$ were recorded at Q-band frequencies in CD_2Cl_2:toluene-d_8:THF-d_8 1:1:1 or 2-methyltetrahydrofuran with the pulse sequence $\frac{\pi}{2}-\tau-\frac{\pi}{2}-T-\frac{\pi}{2}-\tau-echo$ with a microwave pulse length $t_{\pi/2}$ = 16 ns and a radiofrequency pulse length t_{rf} = 18 µs at the field position with the largest signal intensity (corresponding to $g_{x,y}$). All ^{1}H ENDOR spectra were acquired with three different τ-values (τ = 240 ns, 300 ns, and 360 ns) to rule out distortions arising from the blind-spot characteristics of the Mims ENDOR sequence. Before each ENDOR measurement, the power of the radiofrequency pulses was adjusted to obtain a π-pulse using a Rabi nutation experiment at the ^{1}H Larmor frequency $^{1\mathrm{H}}\nu_L$ (ca. 51.5 MHz).

Transient EPR Measurements

Photoexcitation of $\mathbf{P1_{Sym}}$, $\mathbf{P1_B}$, and $\mathbf{P1_B}$ was performed with depolarised light at 532 nm using either an Opotek Opolette He 355 LD optical parametric oscillator pumped by the third harmonic of a ND:YAG LASER or a Continuum Minilite Nd:YAG. The excitation energy was ~1–2 mJ/pulse at a repetition rate of 20 Hz or 15 Hz. The laser light was directed to the sample directly though the optical window of the cryostat. The X-band transient EPR spectra were recorded at 20 K and 250 K on a

X-/Q-band Bruker Elexsys 580 spectrometer equipped with a helium gas flow cryostat from Oxford Instruments with a microwave power of 0.2–1.5 mW.

The proton hyperfine interactions of the photogenerated triplet states were investigated at 20 K using transient Mims ENDOR spectroscopy with $t_{\pi/2} = 16$ ns and $t_{rf} = 15$ µs or 18 µs. All ^{1}H ENDOR spectra were acquired with three different τ-values ($\tau = 120$ ns, 180 ns, and 240 ns or 150 ns, 200 ns, and 250 ns) to rule out distortions arising from the blind-spot characteristics of the Mims ENDOR sequence. All ENDOR spectra were obtained by laser excitation at 532 nm.

Computational Methods

All DFT calculations for this work were performed using the Orca software package.[230, 231] Geometry optimization of $\mathbf{P1_{Sym}}$, $\mathbf{P1_B}$, $\mathbf{P2_B}$, $\mathbf{P1_{Sym}}^{\bullet+}$, $\mathbf{P1_B}^{\bullet+}$, $\mathbf{P2_B}^{\bullet+}$, $^3\mathbf{P1_{Sym}}$, $^3\mathbf{P1_B}$, and $^3\mathbf{P2_B}$ were performed with B3LYP as functional and the 6-31G* basis set.[223–226] The stationary nature of the converge geometries was confirmed by the absence of imaginary frequencies in the DFT calculated vibration spectra. The TD-DFT calculations of neutral and oxidized $\mathbf{P1_{Sym}}$, $\mathbf{P1_B}$, and $\mathbf{P2_B}$ were performed on their optimized geometries with LC-ωPBE ($\omega = 0.1$) as functional and the 6-31G* basis set with the conductor-like polarizable continuum model (CPCM) with chloroform as solvent.[227, 228, 312–315]

Simulation Methods

The cw-EPR spectra of the porphyrin radical cations at 298 K were simulated with the EasySpin function *garlic*.[238] The cw-EPR spectra in frozen CD_2Cl_2:toluene-d_8:THF-d_8 1:1:1 and 2-methyltetrahydrofuran were simulated with the EasySpin function *pepper*. The isotropic variable temperature cw-EPR spectra of $\mathbf{P1_B}^{\bullet+}$ and $\mathbf{P2_B}^{\bullet+}$ were simulated with a chemical exchange model implemented by Stoll and Kozhanov in MATLAB based on the EasySpin software package.[238, 296, 297] Simulations were performed using the Liouville simulation method for a general multisite exchange and identical inherent linewidths Γ for the exchanging sites. The magnetic interactions of the radical on the redox centers involved in the electron transfer in $\mathbf{P2_B}^{\bullet+}$ are analogous to the magnetic

interactions in $\mathbf{P1_B}^{\bullet+}$. All simulations were performed with an isotropic g-value and isotropic hyperfine interactions obtained either from least-squares fitting of the cw-EPR spectrum at 298 K or from the point-dipole simulations of the ^{1}H Mims ENDOR spectrum of $\mathbf{P1_B}^{\bullet+}$. The inherent linewidth Γ at each temperature was determined by simulating the cw-EPR spectra of $\mathbf{P1_B}^{\bullet+}$ using the chemical exchange model in the slow exchange limit ($k_{ex} = 10^{-10}$ MHz) and was subsequently used to describe the two redox sites in the simulation of the variable temperature cw-EPR spectra of $\mathbf{P2_B}^{\bullet+}$ at this temperature in the same solvent system. The cw-EPR spectra of $\mathbf{P2_B}^{\bullet+}$ were simulated for a range of electron transfer rates k_{ex} and the best-fit simulation was identified from the smallest root-mean-square deviation (*rmsd*) between the experimental and simulated spectra. The error margins of k_{ex} were determined as the electron transfer rates with a 5% deviation of their *rmsd* from the minimum *rmsd*. The simulations of all variable temperature cw-EPR spectra of $\mathbf{P1_B}^{\bullet+}$ and $\mathbf{P1_B}^{\bullet+}$ were performed by calling the chemical exchange model by Stoll and Kozhanov from a custom written MATLAB routine that allowed the simultaneous simulation of multiple spectra using a *parfor*-loop architecture included in the MATLAB parallel computing toolbox. All exchange simulations were performed on a high-performance computing cluster.

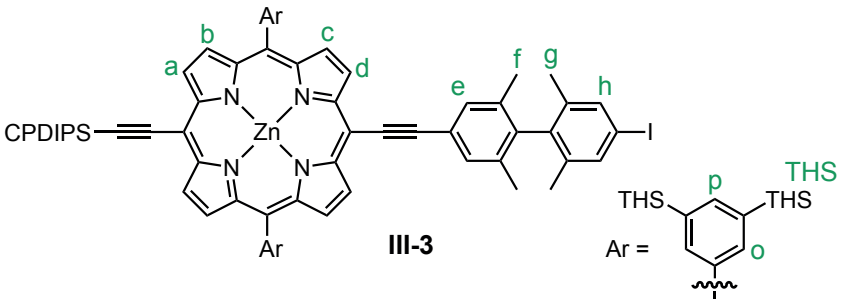
The ^{1}H Mims ENDOR spectra of the radical cations were simulated using anisotropic hyperfine tensors calculated with the distributed point-dipole model described in Section 3.5.3. The Mims ENDOR spectra of the photogenerated triplet states were simulated with ^{1}H hyperfine tensors calculated at the B3LYP/EPRII level of theory. The simulations were performed separately for each ^{1}H nucleus with the EasySpin function *saffron* using the relevant experimental τ-values, microwave pulse lengths $t_{\pi/2}$, and field positions, as well as an inherent linewidth of 0.25 MHz. The final simulations were obtained as the sum of the individual spectra of all ^{1}H nuclei.

The experimental continuous wave transient EPR spectra were baseline corrected in both dimensions using the pre-laser spectrum and the off-resonant transients. Simulations of the spin-polarised triplet state spectra were performed using the

EasySpin function *pepper*.[92] The zero-field splitting parameters D and E as well as the relative sublevel populations at zero-field were determined by least-squares fitting of the experimental time-resolved EPR data. The ordering of the principal components of $\boldsymbol{D}$ was chosen as $|D_Z| > |D_X| > |D_Y|$ for the analysis of the spectra.

3.5.2 Synthetic Procedures

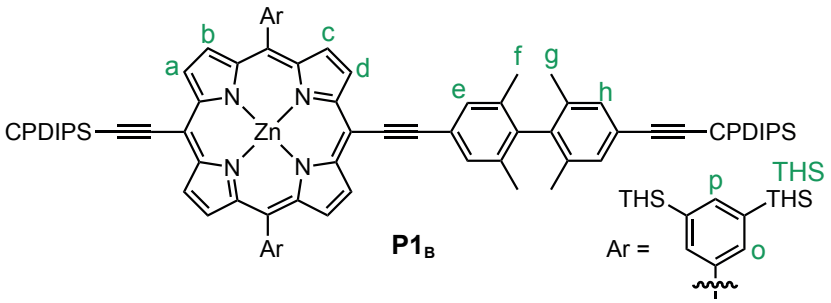
III-3:



III-3

In a Schlenk flask, porphyrin monomer **III-1** (100 mg, 1 equiv., 53 μmol) and 4,4'-diiodo-2,2',6,6'- tetramethyl-1,1'-biphenyl **III-2** (22.1 mg, 0.9 equiv., 47.7 μmol) were dissolved in dry toluene (10 mL) and *i*-Pr_2NH (3 mL) and subjected to two freeze-pump-thaw cycles. While frozen, CuI (0.2 mg, 1 μmol) and XPhos Pd G4 (2.74 mg, 3.2 μmol) were added from a stock solution in toluene followed by three additional freeze-pump-thaw cycles. After reacting for 3 hours at 45 °C, the reaction mixture was cooled to room temperature, passed through a short pad of silica ($CHCl_3$) and a size-exclusion column (toluene + 1% pyridine) and purified by recycling GPC (toluene + 1% pyridine) to afford the monocoupled product **III-3** (41.4 mg) in sufficient purity. ^{1}**H NMR** (500 MHz, $CDCl_3$, 298 K) $\delta_H = 9.82$ (d, $J = 4.6$ Hz, 2H, a), 9.69 (d, $J = 4.5$ Hz, 2H, d), 8.94 (d, $J = 4.5$ Hz, 2H, c), 8.93 (d, $J = 4.7$ Hz, 2H, b), 8.26 (s, 4H, o), 8.00 (s, 2H, p), 7.81 (s, 2H, e), 7.57 (s, 2H, h), 2.55 (t, $J = 6.8$ Hz, 2H, CPDIPS-CH_2), 2.22–2.17 (m, 2H, CPDIPS-CH_2), 2.05 (s, 6H, f), 1.97 (s, 6H, g), 1.57–0.79 (m, 170H, THS + CPDIPS-CH + CPDIPS-CH_3), 1.18–1.15 (m, 2H, CPDIPS-CH_2) ppm.

P1$_B$:

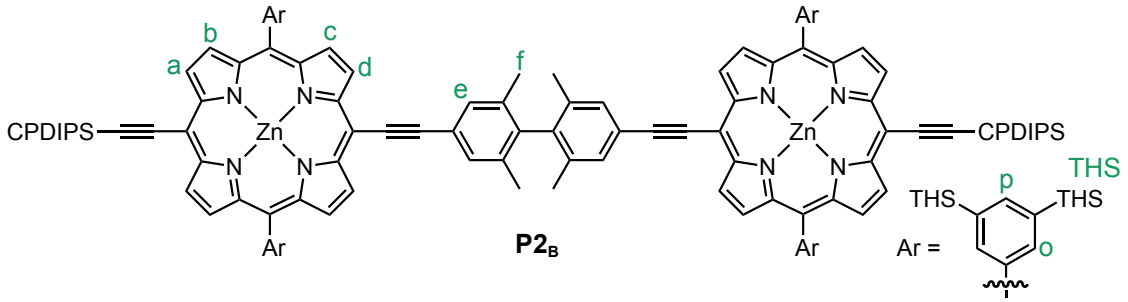


P1$_B$

Without further purification, **III-3** (35.8 mg, 1 equiv., 16.1 µmol), CuI (614 µg, 3.2 µmol), and $Pd(PPh_3)_2Cl_2$ (2.3 mg, 3.2 µmol) were dissolved in dry toluene (2 mL) and *i*-Pr_2NH (0.4 mL) and subjected to three freeze-pump-thaw cycles before cyanopropyldiisopropylsilylacetylene (13.4 mg, 0.01 mL, 4 equiv., 64.5 µmol) was added by syringe. The reaction mixture was stirred at 45 °C for 2 hours and passed through a silica pad ($CHCl_3$). The product was purified by flash column chromatography (20% CH_2Cl_2/$PE_{40\text{-}60}$ to 40% CH_2Cl_2/$PE_{40\text{-}60}$) to afford **P1$_B$** (23.4 mg, 10.2 µmol, 63%) as a green solid.

^{1}H NMR (500 MHz, $CDCl_3$, 298 K) δ_H = 9.83 (d, J = 4.6 Hz, 2H, a), 9.69 (d, J = 4.6 Hz, 2H, d), 8.94 (d, J = 4.6 Hz, 2H, c), 8.93 (d, J = 4.6 Hz, 2H, b), 8.26 (s, 4H, o), 8.00 (s, 2H, p), 7.81 (s, 2H, e), 7.34 (s, 2H, h), 2.55 (t, J = 6.8 Hz, 2H, CPDIPS-CH_2), 2.47 (t, J = 7.0 Hz, 2H, CPDIPS-CH_2), 2.23–2.17 (m, 2H, CPDIPS-CH_2), 2.05 (s, 6H, f), 2.00 (s, 6H, g), 1.96–1.89 (m, 2H, CPDIPS-CH_2), 1.50–0.88 (m, 188H, THS + CPDIPS-CH + CPDIPS-CH_3 + CPDIPS-CH_2) ppm. **MALDI-ToF** m/z 2298.840 (calculated for $[C_{146}H_{226}N_6Si_6Zn]^+ = [\mathbf{P1_B}]^+$: 2299.313). **UV-vis** ($CDCl_3$) λ / nm (ϵ / $\mu M^{-1}cm^{-1}$): 633 (0.063), 581 (0.017), 538 (0.005), 444 (0.458).

P2$_B$:



P2$_B$

In a Schlenk flask, porphyrin monomer **III-1** (76 mg, 2 equiv., 40.3 μmol) and 4,4'-diiodo-2,2',6,6'-tetramethyl-1,1'-biphenyl **III-2** (9.34 mg, 1 equiv., 20.2 μmol) were dissolved in dry toluene (8 mL) and *i*-Pr_2NH (3 mL) and subjected to two freeze-pump-thaw cycles. While frozen, CuI (0.12 mg, 0.6 μmol) and XPhos Pd G4 (2.00 mg, 2.3 μmol) were added from a stock solution in toluene followed by three additional freeze-pump-thaw cycles. After reacting for 4 hours at 45 °C, the reaction mixture was cooled to room temperature, passed through a short pad of silica ($CHCl_3$), and purified by flash column chromatography (20% CH_2Cl_2/$PE_{40\text{-}60}$ to 30% CH_2Cl_2/$PE_{40\text{-}60}$) to afford **P2$_B$** (36.0 mg, 9.1 μmol, 45%) as a green solid.

^{1}**H NMR** (500 MHz, $CDCl_3$, 298 K) δ_H = 9.87 (d, J = 4.6 Hz, 4H, a), 9.70 (d, J = 4.6 Hz, 4H, d), 8.95 (d, J = 4.6 Hz, 8H, b+c), 8.28 (d, J = 1.2 Hz, 8H, o), 8.01 (d, J = 1.2 Hz, 4H, p), 7.89 (s, 4H, e), 2.56 (t, J = 6.8 Hz, 4H, CPDIPS-CH_2), 2.24–2.17 (s+m, 16H, f + CPDIPS-CH_2), 1.20–1.16 (m, 4H, CPDIPS-CH_2) 1.55–0.81 (m, 340H, THS + CPDIPS-CH + CPDIPS-CH_3) ppm. **MALDI-ToF** m/z 3977.696 (calculated for $[C_{252}H_{396}N_{10}Si_{10}Zn_2]^+ = [\mathbf{P2_B}]^+$: 3977.569). **UV-vis** ($CDCl_3$) λ / nm (ϵ / $\mu M^{-1}cm^{-1}$): 635 (0.134), 581 (0.031), 537 (0.010), 447 (0.908).

3.5.3 Distributed Point-Dipole Simulations

The simulation of the Q-band ^{1}H Mims ENDOR spectra of $\mathbf{P1_B}^{\bullet+}$ and $\mathbf{P2_B}^{\bullet+}$ presented in Section 3.3.5 with DFT calculated hyperfine tensors is not feasible due to an over-delocalization of the radical spin density from the porphyrin part to the biphenyl part of $\mathbf{P1_B}^{\bullet+}$ for a wide range of DFT functionals with different range-separation parameters ω and amounts of exact Hartree–Fock exchange. All hyperfine tensor calculations were performed for the optimized geometry of $\mathbf{P1_B}^{\bullet+}$ with the EPRII basis set. The inaccurate prediction of the radical spin density distribution results in the calculation of inaccurate hyperfine tensors $^{1\mathrm{H}}\boldsymbol{A}$ as evident from the stark exaggeration of the largest anisotropic hyperfine contributions A_{max} in the simulated ^{1}H Mims ENDOR spectra of $\mathbf{P1_B}^{\bullet+}$ (Figure 3.20).

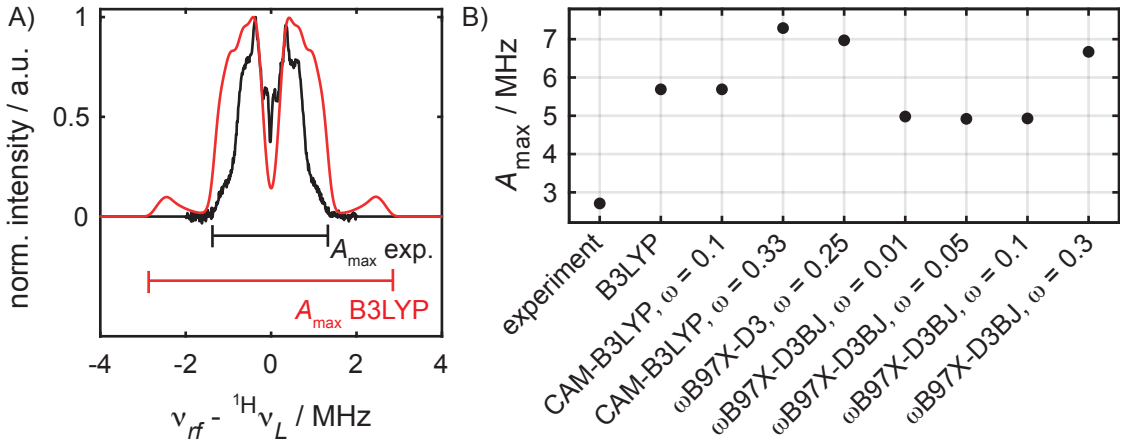


Figure 3.20: A) Experimental (black) and simulated (red) ^{1}H Mims ENDOR spectra of $\mathbf{P1_B}^{\bullet+}$ in CD_2Cl_2:toluene-d_8:THF-d_8 1:1:1 at 80 K and Q-band frequencies. The largest anisotropic hyperfine contributions A_{max} to the ENDOR spectra are determined from their width. B) Comparison of the experimental and simulated largest hyperfine contributions A_{max} to the ^{1}H Mims ENDOR spectra of $\mathbf{P1_B}^{\bullet+}$ using hyperfine tensors calculated with a range of DFT functionals and the 6-31G* basis set.

This limitation was overcome by using the distributed point-dipole model detailed below to calculate the ^{1}H and ^{14}N hyperfine interactions in $\mathbf{P1_B}^{\bullet+}$ for a range of spin density distributions between its porphyrin and biphenyl parts. The hyperfine interactions that resulted in the best simulation of the experimental ^{1}H ENDOR spectrum of $\mathbf{P1_B}^{\bullet+}$ were subsequently used to simulate the Mims ENDOR spectra of $\mathbf{P1_B}^{\bullet+}$ and $\mathbf{P2_B}^{\bullet+}$ in CD_2Cl_2:toluene-d_8:THF-d_8 1:1:1 and MTHF.

Step 1: assignment of the spin density distribution

To systematically adjust the spin density distribution in $\mathbf{P1_B}^{\bullet+}$, the monomer is formally divided into a porphyrin and biphenyl subunit (Figure 3.21A). For each subunit, the relative spin density distributions χ_i were calculated using DFT predicted Mulliken spin populations following equation 3.9:

$$\chi_i = \frac{\rho_i}{\rho_{\text{subunit}}} \tag{3.9}$$

The relative spin density distribution χ_i is defined as the amount of spin density assigned to an individual atom i relative to the total spin population assigned collectively to all atoms in the subunit ρ_{subunit}. This definition allows for a redistribution of spin density between the porphyrin and biphenyl parts of $\mathbf{P1_B}^{\bullet+}$ without modifying how the spin density is assigned to each individual atom. For a robust assignment of the relative spin density distributions, χ_i was separately calculated using Mulliken spin populations obtained from DFT calculations with B3LYP, CAM-B3LYP ($\omega = 0.1$), ωB97X-B3LYP ($\omega = 0.01$), ωB97X-B3LYP ($\omega = 0.05$), and ωB97X-B3LYP ($\omega = 0.1$) as functionals and the EPRII basis set. The functionals were chosen because the ^{1}H Mims ENDOR simulation of $\mathbf{P1_B}^{\bullet+}$ using their predicted hyperfine interactions deviated least from the experimental spectrum (Figure 3.20). The relative spin density distribution of each atom calculated with the five DFT functionals was averaged to give the final relative spin density distribution $\chi_{i,\text{av}}$ employed in the point-dipole model. Encouragingly, the relative spin densities of all atoms show only subtle deviations when calculated with Mulliken populations obtained with different DFT functionals (Figure 3.21B).

The spin density ratio Δ was defined as a quantitative measure of the radical delocalization in $\mathbf{P1_B}^{\bullet+}$ using equation 3.10:

$$\Delta = \frac{\rho\,(\text{porphyrin})}{\rho\,(\text{porphyrin}) + \rho\,(\text{biphenyl})} \tag{3.10}$$

where ρ (porphyrin) and ρ (biphenyl) are the total spin populations on the porphyrin and biphenyl subunits, respectively. Modification of the spin density ratio Δ followed by the distribution of the spin density assigned to the porphyrin and biphenyl subunits

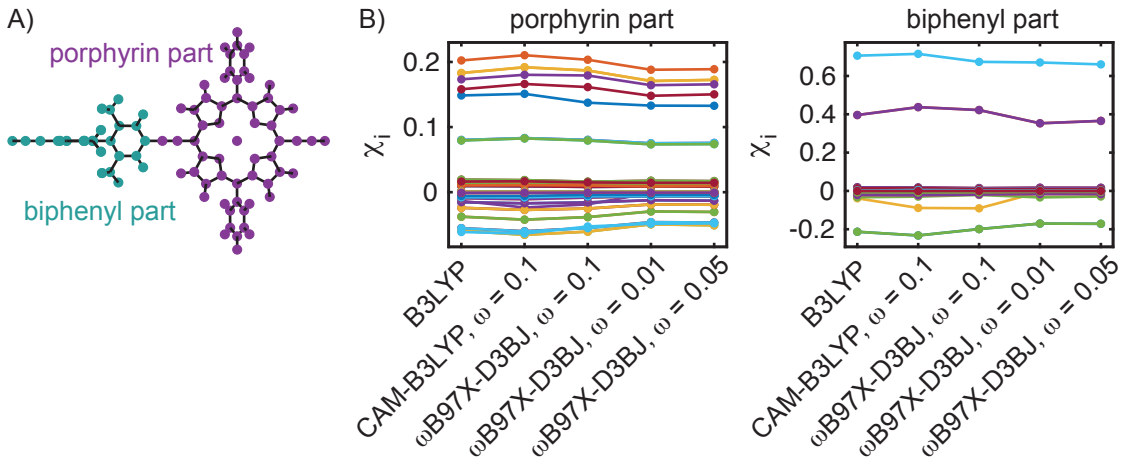


Figure 3.21: A) Schematic visualization of the separation of $\mathbf{P1_B}^{\bullet+}$ into a porphyrin (purple) and biphenyl (green) fragment. B) Trend in the relative spin density distribution χ_i for each atom in the porphyrin and biphenyl part of $\mathbf{P1_B}^{\bullet+}$ calculated using Mulliken spin populations obtained with different DFT functionals and the 6-31G* basis set. The connections between points of the same color are a guide to the eye for the functional dependence of χ_i for a given atom.

of $\mathbf{P1_B}^{\bullet+}$ to individual atoms using $\chi_{i,\mathrm{av}}$ allows for a systematic screening of radical delocalizations with a single fitting parameter.

To account for the π-radical character of $\mathbf{P1_B}^{\bullet+}$, spin densities assigned to sp^2-hybridized atoms were modelled to be localized in p-type orbitals and split above and below the respective aromatic plane of the molecule. This is exemplified for a spin density ratio $\Delta = 86.3\%$ predicted at the B3LYP/EPRII level of theory in Figure 3.22. The distance between the spin density and aromatic plane was set to ±52 pm in agreement with point-dipole simulations in Chapter 2.

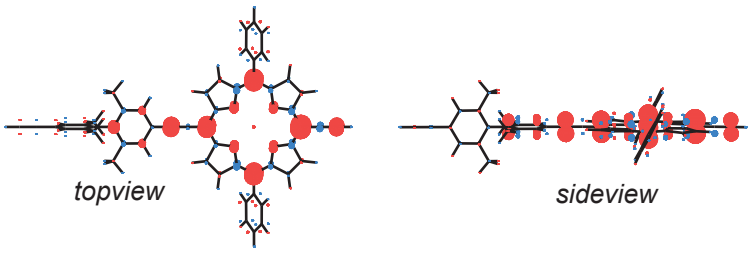


Figure 3.22: Visualization of the π-orbital type spin centers in $\mathbf{P1_B}^{\bullet+}$ for a spin density ratio $\Delta = 86.3\%$ predicted by DFT calculations at the B3LYP/EPRII level of theory. The spin populations at each point in space is represented by a sphere centered on the position of the spin center with a radius proportional to the magnitude of its assigned spin populations. Red spheres represent excess spin-up and light-blue spheres indicate excess spin-down populations.

Step 2: calculation of the dipolar hyperfine coupling contribution

The dipolar hyperfine tensor $\boldsymbol{T}_i$ of each ^{1}H and ^{14}N nucleus in $\mathbf{P1_B}^{\bullet+}$ was calculated using the spin density distributions established in step 1. The through space dipole-dipole interactions between nucleus i and the discrete spin centers were approximated using the point-dipole model introduced in equation 1.18 in Chapter 1.

Step 3: calculation of the isotropic hyperfine coupling contribution

The isotropic contribution $a_{\mathrm{iso},i}$ to the hyperfine tensor of each ^{1}H nucleus i was calculated based on the directly proportional relationship between $a_{\mathrm{iso},i}$ and the spin population assigned to the nucleus ρ_i.[77] McConnell's seminal work related the isotropic hyperfine interactions of aromatic protons to the amount of spin density on the carbon atom to which they are attached.[77] This relationship was approximated for a better implementation in the simulations by assuming a directly proportional relationship between ${}^{1H}a_{\mathrm{iso},i}$ and ${}^{1\mathrm{H}}\rho_i$. The proportionality constant c_i was calculated for each ^{1}H nucleus in $\mathbf{P1_B}^{\bullet+}$ using its DFT predicted Mulliken spin populations and isotropic hyperfine interactions with B3LYP, CAM-B3LYP ($\omega = 0.1$), ωB97X-B3LYP ($\omega = 0.01$), ωB97X-B3LYP ($\omega = 0.05$), and ωB97X-B3LYP ($\omega = 0.1$) as functionals and the EPRII basis set. The final proportionality constant $c_{i,\mathrm{av}}$ employed in the point-dipole model was obtained by averaging the McConnell constants for the different functionals. The isotropic hyperfine coupling to the ^{14}N nuclei ${}^{14\mathrm{N}}a_{\mathrm{iso}} = 3.99$ MHz was obtained from least-squares fitting of the room temperature cw-EPR spectra of $\mathbf{P1_B}^{\bullet+}$.

Step 4: calculation of the final hyperfine tensor

The final hyperfine tensors $\boldsymbol{A}_i$ were calculated by combining the dipolar and isotropic hyperfine contributions $\boldsymbol{T}_i$ and $a_{\mathrm{iso},i}\cdot\mathbf{1}$ derived in steps 2 and 3, respectively.

Step 5: fitting of the spin density ratio in $\mathbf{P1_B}^{\bullet+}$

The optimal spin density ratio to describe $\mathbf{P1_B}^{\bullet+}$ was determined by comparing the experimental Q-band ^{1}H Mims ENDOR spectrum of $\mathbf{P1_B}^{\bullet+}$ with a range of simulated spectra using anisotropic ^{1}H hyperfine tensors calculated *via* the distributed point-dipole model for a series of spin density ratios Δ (Figure 3.23). The best agreement between the experimental and simulated spectra was found for $\Delta = 96.1\%$ as judged by the root-mean-square deviation (*rmsd*) between the two spectra (Figure 3.23B).

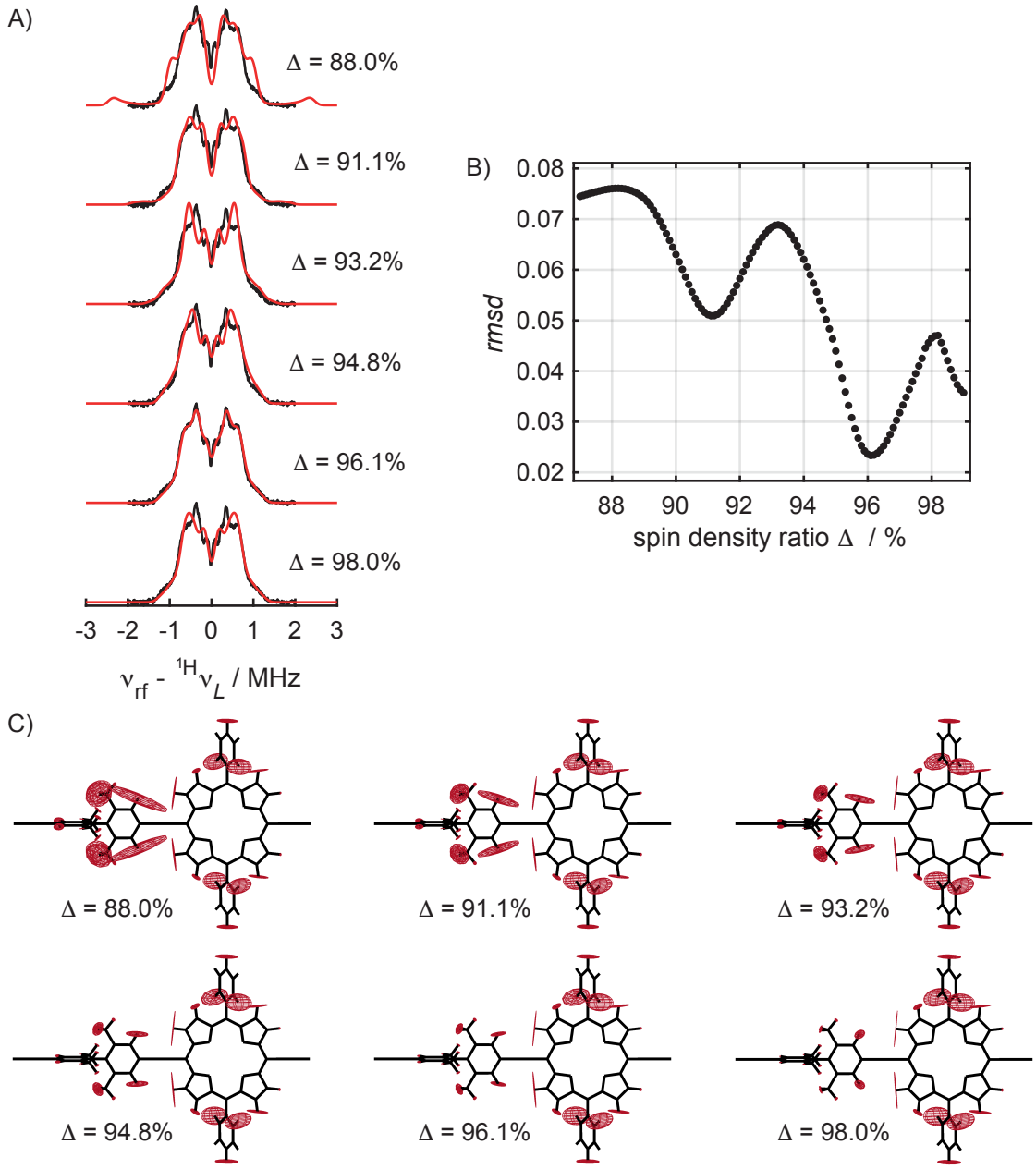


Figure 3.23: A) Experimental (black) and simulated (red) ^{1}H Mims ENDOR spectra of $\mathbf{P1_B}^{\bullet+}$ at Q-band frequencies in CD_2Cl_2:toluene-d_8:THF-d_8 1:1:1 at 80 K. The simulated spectra were obtained with anisotropic ^{1}H hyperfine tensors $^1\boldsymbol{A}$ calculated via the distributed point-dipole model for the respective spin density ratios Δ. B) Root-mean-square deviation (*rmsd*) between the experimental and simulated ^{1}H Mims ENDOR spectra of $\mathbf{P1_B}^{\bullet+}$ as a function of Δ. C) Pictorial representation of $^1\boldsymbol{A}$ for selected spin density ratios Δ. The tensors are shown as ellipsoids centered at the corresponding ^{1}H nuclei with dimensions proportional to the eigenvalues of $^1\boldsymbol{A}$ and are oriented in the molecular frame based on their Euler angles.

3.6 Supplemental Results and Analysis

UV-vis-NIR Oxidation Titrations

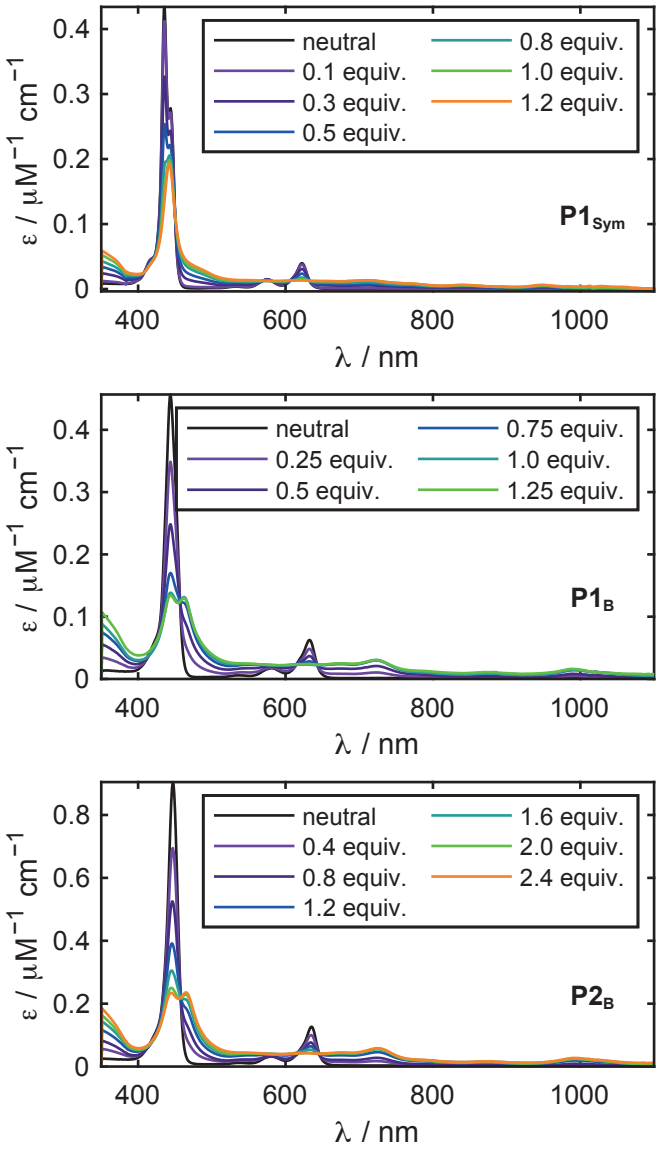


Figure 3.24: UV-vis-NIR absorption spectra of the oxidation titrations of $\mathbf{P1_{Sym}}$, $\mathbf{P1_B}$, and $\mathbf{P2_B}$ in $CHCl_3$ with **BAHA**. The oxidant was added to the porphyrin solutions from a stock solution in CH_2Cl_2 due to its limited solubility in $CHCl_3$.

Continuous Wave EPR Spectroscopy

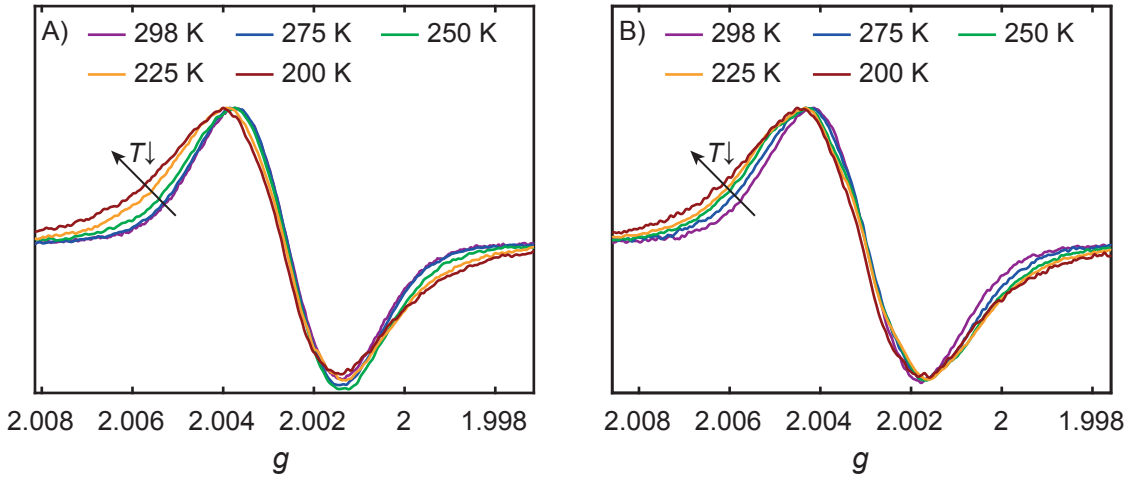


Figure 3.25: Superimposed variable temperature cw-EPR spectra of $\mathbf{P2_B}^{\bullet+}$ in A) CD_2Cl_2:toluene-d_8:THF-d_8 1:1:1 and B) 2-methyltetrahydrofuran to highlight the increasing exchange broadening.

Exchange Simulations

```
function [rate_vector,rmsd_vector,spec_sim_matrix] = HoppingRate_Fitting(start_rate,end_rate,rate_increment,g,lwpp,mwFreq,field_exp,spec_exp)

    % - Performs simulations of exchange broadened cw-EPR spectra
    % - Uses MATLAB parallel computing to increase simulation speed
    % - Calls function 'RMSD_calculation' to calculate root-mean-square deviation (rmsd) between experimental and simulated spectra

    %%% Input %%%
%     - start_rate: smallest exchange rate in MHz
%     - end_rate: largest exchange rate in MHz
%     - rate_increment: stepsize of exchange rate vector between start_rate and end_rate in MHz
%     - g: isotropic g-value
%     - lwpp: Lorentzian peak-to-peak linewidth of EPR transitions
%     - mwFreq: experimental microwave frequency in Hz
%     - field_exp: field-axis of experimental spectrum
%     - spec_exp: experimental spectrum

    %%% Output %%%
%     - rate_vector: array of all simulated exchange rates
%     - rmsd_vector: array of root-mean-square deviations between experimental and simulated spectra in the order of rate_vector
%     - spec_sim_matrix: collection of simulated spectra


    % normalization of experimental spectrum
    spec_exp = spec_exp./max(spec_exp);

    % generation of exchange rate vector
    rate_difference = end_rate - start_rate;
    n_points = round(rate_difference/rate_increment);
    rate_vector = linspace(start_rate,end_rate,n_points);

```

```
    rmsd_vector = zeros(size(rate_vector));
    spec_sim_matrix = zeros(numel(field_exp),n_points);

    % parameters to describe the spin system of the biphenyl-linked porphyrin dimer cation
    Nucs = '14N,1H,1H,1H,1H,1H,14N,1H,1H,1H,1H,1H';
    n = [4 4 2 2 2 6 4 4 2 2 2 6];
    A = [3.99 1.23 1.16 1.11 0.95 0.44 0 0 0 0 0 0]; % MHz
    xc = [7 8 9 10 11 12 1 2 3 4 5 6];

    % experimental parameters
    mwFreq = mwFreq./1e9;
    Range = [min(field_exp) max(field_exp)];
    nPoints = numel(field_exp);

    % simulation parameters specific to exchange function
    Method = 1
    reduce = 0;

    % simulations
    parfor ii = 1:n_points
        rate = rate_vector(ii);
        k = [0 rate;
             rate 0];
        Sys = struct('g',g,'Nucs',Nucs,'n',n,'A',A,'xc',xc,'lwpp',lwpp,'k',k);
        Exp = struct('mwFreq',mwFreq,'Range',Range,'nPoints',nPoints);
        Opt = struct('Method',Method,'reduce',reduce);

        [~,spec_sim] = exchange(Sys,Exp,Opt);
        spec_sim = spec_sim./max(spec_sim);
        spec_sim_matrix(:,ii) = spec_sim;

        [rmsd] = RMSD_calculation(spec_sim,spec_exp);
        rmsd_vector(ii) = rmsd;
    end
end
```

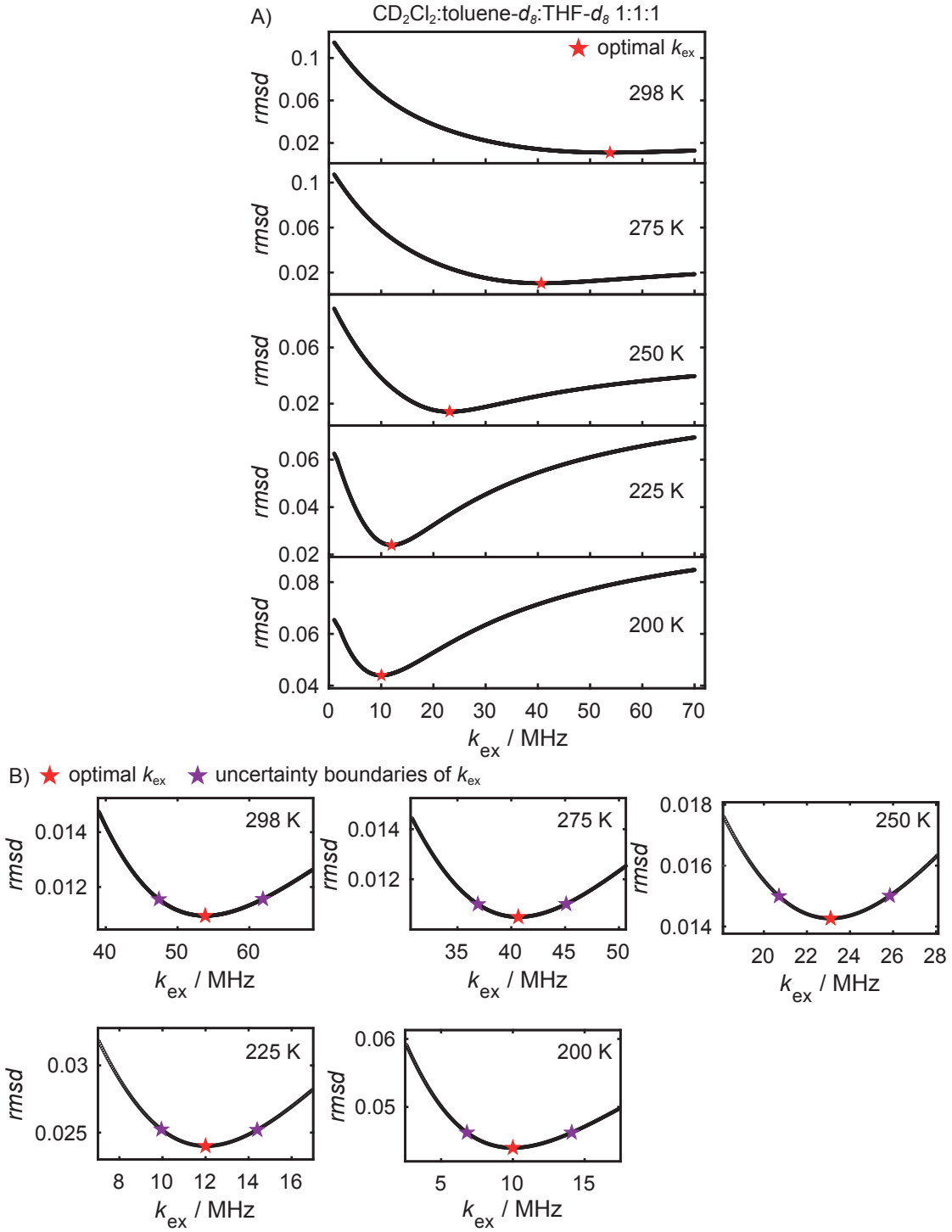


Figure 3.26: A) Root-mean-square deviation (*rmsd*) between the experimental and simulated cw-EPR spectra of $\mathbf{P2_B}^{\bullet+}$ at X-band frequencies in CD_2Cl_2:toluene-d_8:THF-d_8 1:1:1 between 298 K and 200 K as a function of the electron transfer rate k_{ex}. B) Enlarged regions of the *rmsd* curves in A) around their minima. The optimal electron transfer rates with the smallest root-mean-square deviations and their uncertainty boundaries with *rmsd* values 5% larger than the minimum are highlighted with red and purple stars, respectively.

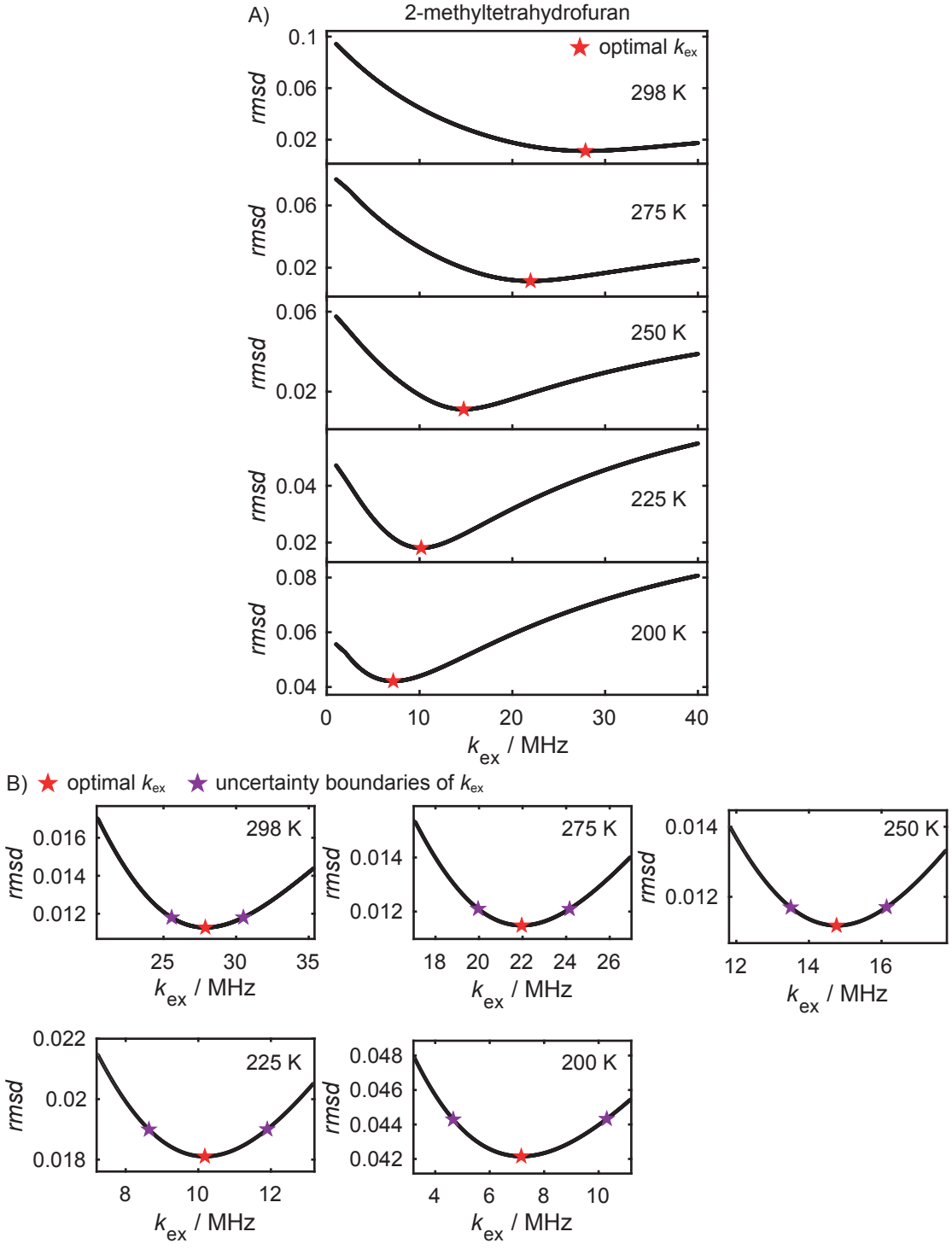


Figure 3.27: A) Root-mean-square deviation (*rmsd*) between the experimental and simulated cw-EPR spectra of $\mathbf{P2_B}^{\bullet+}$ at X-band frequencies in 2-methyltetrahydrofuran between 298 K and 200 K as a function of the electron transfer rate k_{ex}. B) Enlarged regions of the *rmsd* curves in A) around their minima. The optimal electron transfer rates with the smallest root-mean-square deviations and their uncertainty boundaries with *rmsd* values 5% larger than the minimum are highlighted with red and purple stars, respectively.

Transient EPR of Photogenerated Triplet States

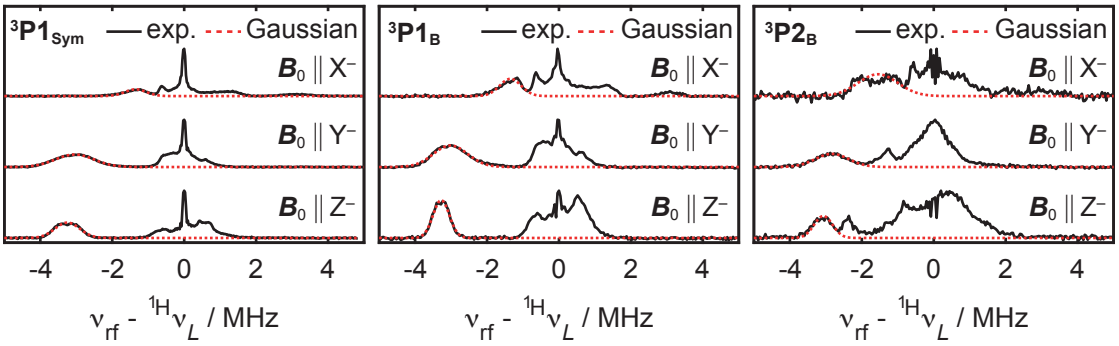


Figure 3.28: Experimental ^{1}H Mims ENDOR spectra of ^{3}**P1**$_{\mathbf{Sym}}$, ^{3}**P1**$_{\mathbf{B}}$, and ^{3}**P2**$_{\mathbf{B}}$ recorded at the X^-, Y^-, and Z^- field positions at 20 K in 2-methyltetrahydrofuran at X-band frequencies. The largest negative hyperfine couplings along the *X*, *Y*, and *Z* axes of the zero–field splitting tensor were determined by fitting a Gaussian to the principal hyperfine peak of the ENDOR spectra with the distribution of the hyperfine interactions determined from the full width at half maximum of the Gaussian.

4

Triplet State Delocalization in Charged Molecular Wires

Contents

4.1 Abstract 168
4.2 Introduction 168
4.3 Results and Discussion 170
4.3.1 Steady State Absorption Spectroscopy 170
4.3.2 Photogenerated Triplet States of ***b*-P2** and ***b*-P2**$^{2-}$ 174
4.3.2.1 Optical Transient Absorption Spectroscopy 174
4.3.2.2 Transient EPR Spectroscopy 178
4.3.3 Photogenerated Triplet States of ***b*-P4**$^{4-}$ and ***b*-P6**$^{6-}$ 186
4.3.3.1 Optical Transient Absorption Spectroscopy 186
4.3.3.2 Transient EPR Spectroscopy 189
4.4 Summary and Conclusions 195
4.5 Methods 197
4.6 Supplemental Results and Analysis 200

4.1 Abstract

The photoexcited triplet states of a series of negatively charged butadiyne-linked zinc porphyrin oligomers were investigated by optical transient absorption spectroscopy and transient continuous-wave EPR spectroscopy. Quantum chemical calculations and comparison to the triplet states of the neutral oligomers guided the interpretation of the spectroscopic data. The fully reduced oligomers consisting of an even-number of porphyrin units with one charge per porphyrin unit exhibit a closed-shell ground state and a substantial bathochromic shift of their lowest-energy absorption bands in comparison to the neutral oligomers. Photoexcitation of the charged oligomers results in the formation of the lowest-energy triplet excited state, which exhibits a shorter lifetime compared to previously investigated triplet states of neutral butadiyne-linked porphyrins. Transient EPR spectroscopy and supporting quantum chemical calculations highlight a substantially smaller electron–electron dipolar coupling in the photogenerated triplet states of the charged oligomers. This results in an about eight-fold reduction of $|D|$ in the fully reduced porphyrin hexamer triplet state compared to the neutral oligomer. This is attributed to a substantially increased delocalization of the triplet excited states in the reduced oligomers.

The results in this chapter highlight a new approach for the generation of highly delocalized triplet excited states by chemically reducing porphyrin oligomers prior to photoexcitation, which is expected to guide the design of novel molecular wires and platforms for quantum information processing.

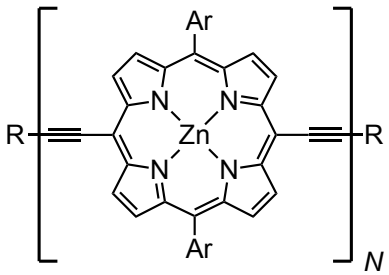
4.2 Introduction

Organic π-conjugated oligomers with tailored electronic and optical properties have attracted considerable interest as building blocks for molecular electronic and photonic devices.[110, 244, 316, 317] Consequently, understanding the factors that control exciton, charge, and spin delocalization in conjugated oligomers is paramount for the design of novel materials with properties tailored to specific applications.

Photogenerated triplet states are of particular interest due to their impact on the performance of optoelectronic devices such as organic light-emitting diodes and organic photovoltaics.[318–320] For instance, long-range delocalization of triplet excitons is important for increasing the power conversion efficiency in organic photovoltaics and enables efficient exciton harvesting following singlet fission.[319, 321, 322]

Molecular electron spins also fulfill the fundamental requirements to operate as quantum bits (qubits) for next generation quantum information processing.[323–325] Chemical synthesis can be used to obtain platforms for molecular qubits with atomic scale precision and enables the rational design of molecules with desired electronic properties. Photogenerated triplet states are promising for applications as three-level qutrits due to their initialization in a well-defined, spin-polarized quantum state following intersystem crossing.[325–327] Controlling the spatial delocalization of photoinitialized triplet states modulates the electron–electron dipolar coupling and electron–nuclear hyperfine interactions, and is therefore a versatile approach for modifying the properties of different qutrit candidates.

Triplet excitons are generally less delocalized than singlet excitons, which can be attributed to the better correlation of photogenerated triplet electrons *via* exchange interactions.[127, 328] Consequently, the design of materials with long range triplet state delocalization is a significant achievement. The delocalization of photogenerated triplet states of neutral porphyrin oligomers has been extensively investigated due to their promise for applications as molecular wires. Work in the Timmel and Anderson groups has highlighted the influence of different inter-porphyrin linkers, molecular geometries, and symmetry on the delocalization of triplet excited states in porphyrin nanomaterials.[52, 126, 307, 309, 329] Butadiyne-linked porphyrin oligomers of the type shown in Figure 4.1 are promising molecular wires and display coherent triplet state delocalization over two to three porphyrin units.[52, 307]



b*-P*N, N = 2, 4, 6

Figure 4.1: Chemical structure of butadiyne-linked porphyrin oligomers ***b*-P*N*** ($N = 2, 4, 6$); Ar = 3,5-bis(trihexylsilyl)phenyl, R = $Si(C_6H_{13})_3$.

In this chapter, the photogenerated triplet states in the negatively charged butadiyne-linked porphyrin oligomers ***b*-P2**$^{2-}$, ***b*-P4**$^{4-}$, and ***b*-P6**$^{6-}$ are investigated by transient optical absorption spectroscopy and transient continuous-wave EPR (tr-EPR) spectroscopy. Quantum chemical calculations and comparison to the triplet states in the neutral oligomers guide the interpretation of the tr-EPR spectra. The results demonstrate that chemical reduction of porphyrin wires prior to their photoexcitation substantially increases the triplet state delocalization.

4.3 Results and Discussion

4.3.1 Steady State Absorption Spectroscopy

The steady-state UV-vis-NIR absorption spectra of the neutral and reduced porphyrin oligomers ***b*-P*N*** and ***b*-P*N*$^{N-}$** provide important information about their electronic structure and the transitions that can be induced by photoexcitation. The UV-vis-NIR absorption spectra of ***b*-P*N*** ($N = 2, 4, 6$) were measured as a function of electrochemical reduction in THF containing Bu_4NPF_6 (0.1 M) as electrolyte under a nitrogen atmosphere. Deconvolution of the raw data gave the absorption spectra of the neutral and completely reduced porphyrin oligomers shown in Figure 4.2. In this chapter, complete reduction of an oligomer refers to the introduction of one charge per porphyrin unit.

The absorption spectra of neutral ***b*-P*N*** are consistent with previous reports of butadiyne-linked porphyrin oligomers and exhibit a high-energy Soret band and a low-energy Q-band that increases in relative intensity in the longer oligomers.[64, 65] The lowest energy absorption bands of ***b*-P2**, ***b*-P4**, and ***b*-P6** are observed at 727 nm ($E_{\mathrm{Abs}} = 1.71$ eV), 756 nm ($E_{\mathrm{Abs}} = 1.64$ eV), and 798 nm ($E_{\mathrm{Abs}} = 1.55$ eV), respectively. The continuous bathochromic shift of the Q-band transitions from ***b*-P2** to ***b*-P6** indicates an increased effective π-conjugation length. The lowest energy absorption bands in the spectra of the reduced porphyrin oligomers ***b*-P2**$^{2-}$, ***b*-P4**$^{4-}$, and ***b*-P6**$^{6-}$ are significantly red-shifted compared to their neutral analogues to 1128 nm ($E_{\mathrm{Abs}} = 1.10$ eV), 1446 nm ($E_{\mathrm{Abs}} = 0.86$ eV), and 1580 nm ($E_{\mathrm{Abs}} = 0.78$ eV), respectively.

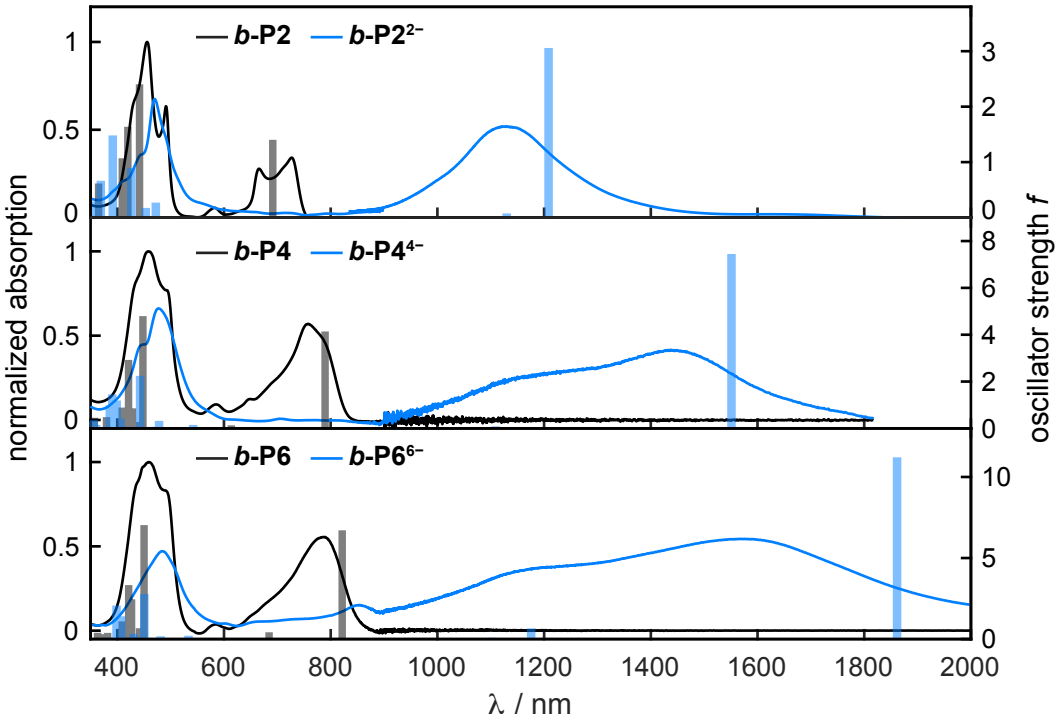


Figure 4.2: Steady-state UV-vis-NIR normalized absorption spectra of ***b*-P*N*** (black) and ***b*-P*N*$^{N-}$** (blue) ($N = 2, 4, 6$) from spectroelectrochemistry in THF (0.1 M Bu_4NPF_6, 298 K). The vertical bars indicate the TD-DFT (LC-ωHPBE/6-31G*; $\omega = 0.2$) calculated wavelengths and oscillator strengths f for the electronic transitions of the neutral and reduced oligomers in the absence of vibronic coupling.

TD-DFT calculations of the excitation energies of ***b*-P*N*** and ***b*-P*N*$^{N-}$** with LC-ωHPBE, $\omega = 0.2$ as functional and the 6-31G* basis set are in good agreement with the experimental observations, although the absorption energies of the long-

wavelength transitions of ***b*-P6** and the reduced oligomers are slightly underestimated in the calculations (Figure 4.2, vertical bars). The calculated electronic transitions of the neutral oligomers indicate that the Q-band absorptions arise from HOMO → LUMO transitions in agreement with previous reports.[330, 331] A singlet, closed-shell ground state was assumed in the TD-DFT calculations of the reduced oligomers due to the absence of a cw-EPR signal in frozen 2-methyltetrahydrofuran (MTHF) at 80 K (*vide infra*). In addition, Wilson and Arnold have reported a close agreement of their TD-DFT calculations of ***b*-P2**$^{2-}$ with the experimental spectrum using a closed-shell ground state.[330] The calculated lowest energy electronic transitions of ***b*-P*N***$^{N-}$ correspond to the $S_0 \rightarrow S_1$ excitation and indicate that the experimental absorption bands arise from HOMO → LUMO transitions (Figure 4.3A). TD-DFT calculations of ***b*-P*N*** and ***b*-P*N***$^{N-}$ were also performed with TPSSh and LC-ωHPBE ($\omega = 0.1$) as functionals (Figure 4.19 and Figure 4.20). While they support the assignment of the electronic transitions, the predicted excitation energies deviate more strongly from the experimental transitions.

The DFT (LC-ωHPBE/6-31G*; $\omega = 0.2$) calculated frontier orbital energies of ***b*-P*N*** show a reduction of the HOMO–LUMO gap from ***b*-P2** to ***b*-P6** (Figure 4.3A), consistent with the experimental and TD-DFT calculated Q-band transitions. Complete reduction of the porphyrin oligomers changes the HOMOs and LUMOs involved in the $S_0 \rightarrow S_1$ excitations causing a contraction of the orbitals accepting the additional electrons and an expansion of the remaining occupied and virtual orbitals (Figure 4.3A). This behaviour is qualitatively consistent with the interpretation of HOMO and LUMO energies as electron affinity and negative ionisation potential, respectively.[332] The HOMO–LUMO energy gap of ***b*-P*N***$^{N-}$ continuously narrows with increasing oligomer length as expected from the experimental absorption spectra.

The DFT calculated HOMOs and LUMOs of neutral and reduced ***b*-P2** and ***b*-P4** are visualized in Figure 4.3B–E. The HOMOs and LUMOs of ***b*-P2** and ***b*-P2**$^{2-}$ are delocalized over both porphyrin units, but exhibit different symmetries and coefficients

on individual atoms (Figure 4.3B,C) Twofold reduction of the porphyrin framework of ***b*-P2** results in the addition of two electrons into the LUMO. Consequently, the HOMO of ***b*-P2**$^{2-}$ and the LUMO of ***b*-P2** have the same spatial distribution and phase. Therefore, upon reduction of ***b*-P2**, the symmetric HOMO (g) and antisymmetric LUMO (u) become antisymmetric and symmetric, respectively, in ***b*-P2**$^{2-}$.

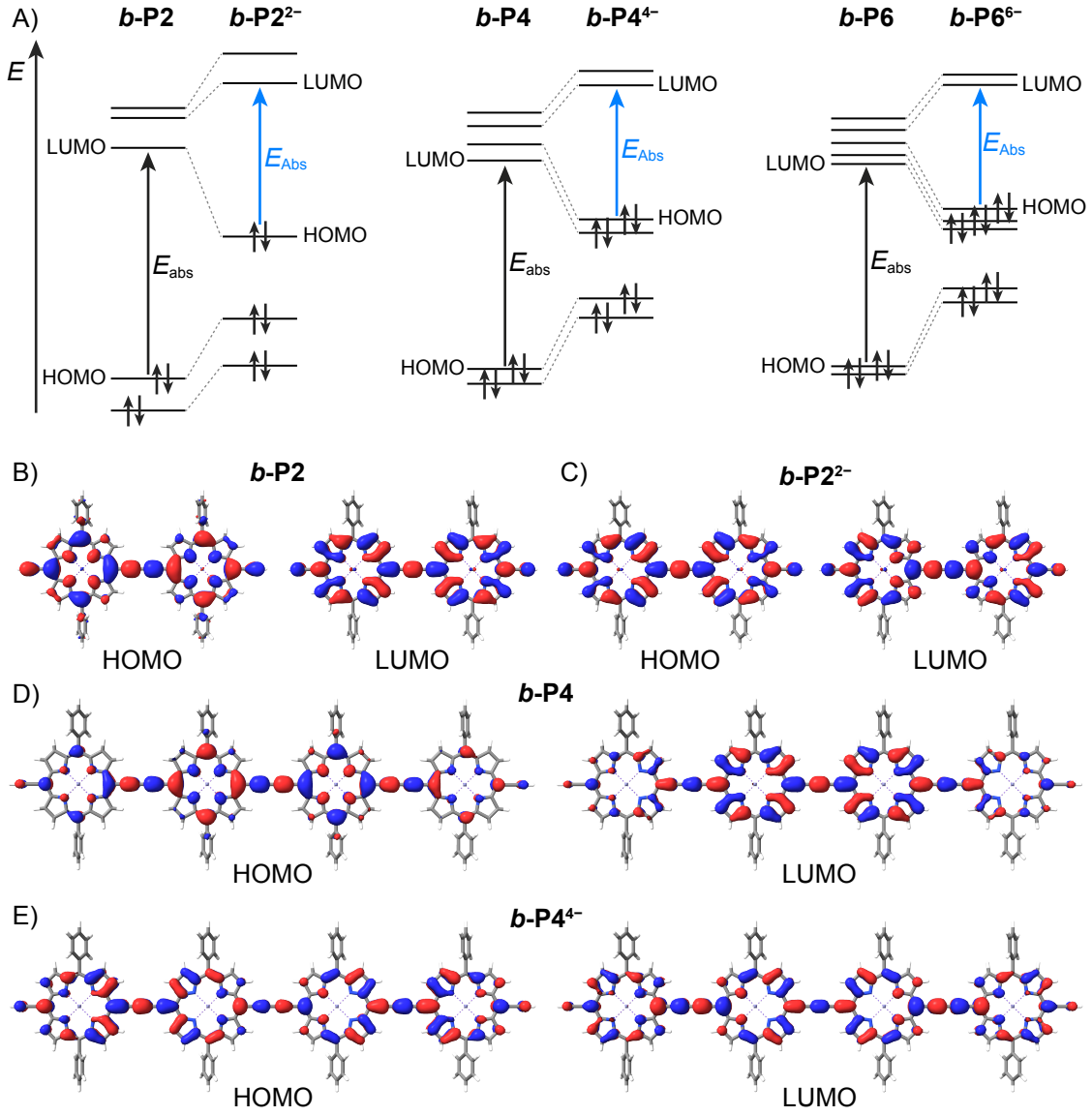


Figure 4.3: A) Representation of the DFT (LC-ωHPBE/6-31G*; $\omega = 0.2$) calculated relative energies of the frontier orbitals in ***b*-P*N*** and ***b*-P*N*$^{N-}$** ($N = 2, 4, 6$); the electronic transitions that predominantly contribute to the DFT calculated lowest energy absorption bands are highlighted by vertical arrows. Visual representation of the DFT (LC-ωHPBE/6-31G*; $\omega = 0.2$) calculated highest occupied molecular orbitals (HOMO) and lowest unoccupied molecular orbitals (LUMO) of B) ***b*-P2**, C) ***b*-P2**$^{2-}$, D) ***b*-P4**, and E) ***b*-P4**$^{4-}$ plotted for an isovalue of 0.015.

The HOMO and LUMO of ***b*-P4** are predominantly localized on the central two porphyrin units (Figure 4.3D). Fourfold reduction of ***b*-P4** changes the HOMO and LUMO delocalization substantially, and the frontier orbitals of ***b*-P4**$^{4-}$ extend over all porphyrin units of the oligomer. This is analogous to the behaviour of the porphyrin hexamer: the HOMO and LUMO are localized on the central porphyrin units in ***b*-P6** and are further extended towards the terminal porphyrin units in ***b*-P6**$^{6-}$ (Figure 4.21). The increasing delocalization of the HOMOs and LUMOs in ***b*-P4**$^{4-}$ and ***b*-P6**$^{6-}$ provides a promising avenue to modify the delocalization of photogenerated triplet states *via* their charge and is explored experimentally in the following sections.

4.3.2 Photogenerated Triplet States of *b*-P2 and *b*-P2^{2-}

4.3.2.1 Optical Transient Absorption Spectroscopy

The dynamical evolution of the excited states obtained after photoexcitation of ***b*-P2** and ***b*-P2**$^{2-}$ was investigated by transient absorption measurements at 80 K in frozen 2-methyltetrahydrofuran (MTHF). Pump excitation of ***b*-P2** at 450 nm yields the transient absorption spectra in Figure 4.4A. Negative features are observed between 465 and 500 nm, and between 643 and 750 nm, while broad positive features emerge between 500 and 640 nm and above 750 nm.

Transient kinetics monitored between 510 and 640 nm demonstrate the presence of two species with different decay profiles (Figure 4.4B). The short-lived species has completely decayed approximately 2 ns after photoexcitation, and was assigned to the S_1 excited state in previous investigations of butadiyne-linked porphyrin dimers.[333, 334] The broad positive features between 500 and 640 nm observed at early times result from excited state absorption of the S_1 state that gives rise to $S_1 \rightarrow S_n$ electronic transition.[334, 335] The time resolution of the transient kinetics is not sufficient to quantify the lifetime of S_1 more precisely.

Intersystem crossing (ISC) of the excited singlet state leads to the formation of the long-lived triplet excited state T_1, that decays monoexponentially with a lifetime $\tau = 3.02 \pm 0.02$ ms. The transient absorption spectrum of the T_1 state is characterized by excited state absorption arising from $T_1 \rightarrow T_n$ transitions between 470 and 640 nm and above 750 nm.[334–336] The negative features around 450 nm and between 640 and 720 nm closely resemble the shape of the steady state absorption of ***b*-P2** shown in Figure 4.2 and result from ground state bleaching.

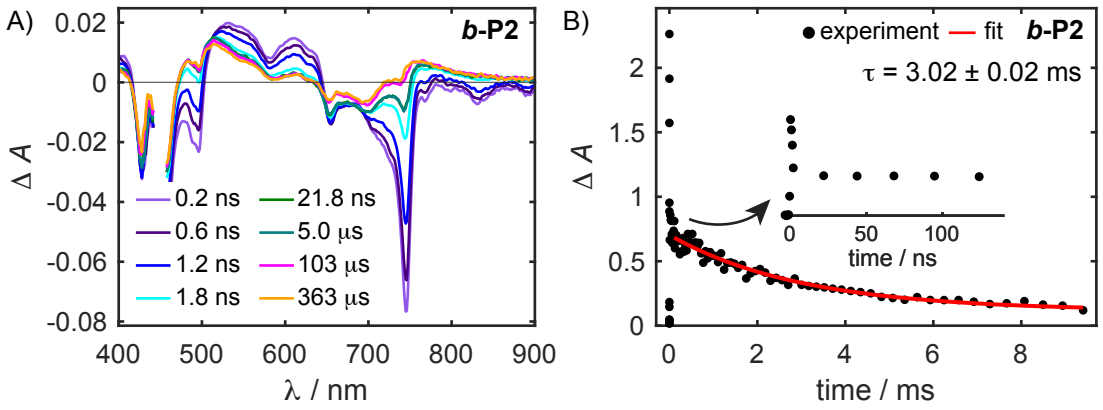


Figure 4.4: A) Time resolved transient absorption spectra of ***b*-P2** in frozen 2-methyltetrahydrofuran at 80 K following pump excitation at 450 nm. B) Transient kinetics of photoexcited ***b*-P2** monitored between 510 and 640 nm; the inset highlights the evolution of the transient species at early times. The triplet lifetime $\tau = 3.02 \pm 0.02$ ms was obtained by least-squares fitting of a monoexponential decay to the kinetic data after the decay of the S_1 state.

Pump excitation of ***b*-P2**$^{2-}$ at 450 nm followed by detection of the transient species in the UV-vis and NIR spectral regions yields the transient absorption spectra in Figure 4.5A and Figure 4.5B, respectively. The spectra exhibit positive features between 500 and 575 nm and 750 and 870 nm, and a negative feature between 1100 and 1300 nm. The negative feature appears at the same wavelengths as the HOMO → LUMO transition of ***b*-P2**$^{2-}$ and arises from ground state bleaching, whereas the positive features are assigned to excited state absorption of the photogenerated T_1 state. Transient kinetics monitored between 750 and 870 nm and 1100 and 1300 nm reveal a monoexponential decay of the positive and negative features with lifetimes $\tau = 51.9 \pm 3.6$ ns and $\tau = 53.3 \pm 4.8$ ns, respectively (Figure 4.5C,D). The lifetimes are the same within error and suggest that the decay of the spectral

features arises from relaxation of the photogenerated T_1 state to the S_0 ground state. Transient continuous-wave EPR (tr-EPR) spectroscopy and supporting calculations discussed in Section 4.3.2.2 confirm the formation of the lowest-energy triplet state T_1 following photoexcitation.

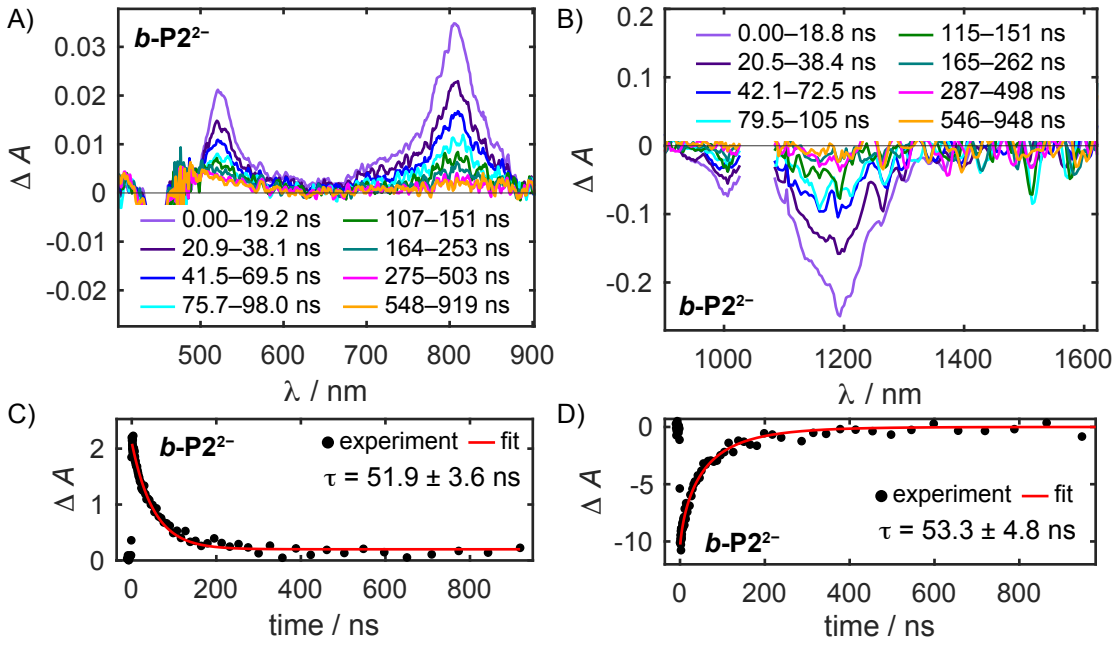


Figure 4.5: Time resolved transient absorption spectra of ***b*-P2** in frozen 2-methyltetrahydrofuran at 80 K following pump excitation at 450 nm detected in A) the UV-vis and B) the NIR spectral regions. The transient kinetics of photoexcited ***b*-P2**$^{2-}$ were monitored between C) 750 and 870 nm and D) 1100 and 1300 nm. The triplet lifetime τ was obtained by least-squares fitting of monoexponential functions to the kinetic data obtained for both wavelength ranges.

No singlet excited state is observed on the experimental timescale following photoexcitation of ***b*-P2**$^{2-}$, which indicates a shorter S_1 lifetime in ***b*-P2**$^{2-}$ compared to ***b*-P2**. Short singlet lifetimes are typically observed in π-conjugated polymers with small electronic bandgaps as expected from the energy gap law of nonradiative transitions.[337, 338] Internal conversion is often the dominant relaxation pathway in NIR chromophores such as ***b*-P2** and ***b*-P2**$^{2-}$, and the internal conversion rate k_{IC} is given by equation 4.1

$$k_{IC} \propto \exp(-\beta \Delta E) \tag{4.1}$$

where ΔE is the S_1–S_0 energy gap and β is a proportionality factor that depends on the geometric and vibrational characteristics of the transition.[338–340] The S_1–S_0 energy gaps of ***b*-P2** and ***b*-P2**$^{2-}$ obtained from TD-DFT (LC-ωHPBE/6-31G*; $\omega = 0.2$) calculations are 1.79 eV and 1.03 eV, respectively, consistent with faster $S_1 \rightarrow S_0$ internal conversion in ***b*-P2**$^{2-}$. Changes in the fluorescence and intersystem crossing rates can also contribute to the shorter S_1 lifetime in ***b*-P2**$^{2-}$.

A stark difference between the T_1 states of ***b*-P2** and ***b*-P2**$^{2-}$ is the substantially shorter triplet lifetime in ***b*-P2**$^{2-}$. Decay of the T_1 excited state can occur nonradiatively *via* direct $T_1 \rightarrow S_0$ transitions or reverse intersystem crossing to the S_1 state. In addition, phosphorescence from T_1 to S_0 can contribute to the T_1 decay. Phosphorescence rate constants are typically relatively small due to the spin forbidden nature of the process.[341] Therefore, triplet state lifetimes are particularly sensitive to nonradiative events governed by the energy gap law. This has been demonstrated for a series of butadiyne-linked porphyrin oligomers that exhibit decreasing triplet state lifetimes with increasing oligomer length, which was attributed to increased nonradiative deactivation processes due to the progressive decrease of the T_1 energy.[336]

It is therefore likely that the shorter T_1 lifetime of ***b*-P2**$^{2-}$ results from faster nonradiative decay rates. This could be caused by faster reverse intersystem crossing due to a smaller T_1–S_1 energy gap or faster $T_1 \rightarrow S_0$ decay due to a smaller T_1–S_0 energy gap, or a combination of both processes. In addition, a different spin–orbit coupling in the reduced dimer could also contribute to enhanced reverse intersystem crossing. A reduction of the T_1–S_0 energy gap from ***b*-P2** to ***b*-P2**$^{2-}$ is probable, due to the smaller S_0–S_1 energy gap and the requirement of sufficient overlap between the density of states of S_1 and T_1 at the T_1 energy for efficient ISC.[342] A more in-depth investigation of the reduced triplet lifetime in ***b*-P2**$^{2-}$ requires accurate knowledge about the relative energies of the S_0, S_1, and T_1 states from DFT calculations or experiments and is outside the scope of this investigation.

4.3.2.2 Transient EPR Spectroscopy

The triplet excited state of the doubly reduced porphyrin dimer ***b*-P2**$^{2-}$ was investigated by tr-EPR spectroscopy and compared to the photogenerated triplet state of ***b*-P2** previously characterized by Tait *et al.*[52, 307] Dimer ***b*-P2**$^{2-}$ was obtained by chemical reduction of ***b*-P2** with two equivalents of decamethylcobaltocene **CoCp*$_2$** and handled under strictly anaerobic conditions. A stepwise reduction titration of ***b*-P2** with **CoCp*$_2$** and investigation of each titration point by cw-EPR and tr-EPR spectroscopy confirmed the diamagnetic character of ***b*-P2**$^{2-}$, and that no transient species is observed following photoexcitation of ***b*-P2**$^{\bullet -}$ at 1000 nm (Figure 4.23). This supports the assignment of the observed transient species to the photoexcited dimer dianion ***b*-P2**$^{2-}$. The tr-EPR spectra of ^{3}***b*-P2** and ^{3}***b*-P2**$^{2-}$ in MTHF at 20 K were averaged over 400 ns after the laser pulse with depolarized light excitation at 532 nm and 1000 nm, respectively, and are shown in Figure 4.6A.

The *AAEAEE* (A = absorptive, E = emissive) polarization pattern of ^{3}***b*-P2**$^{2-}$ indicates a non-Boltzmann population of the triplet sublevels as expected for a photogenerated triplet state and is identical to the polarization pattern of ^{3}***b*-P2**. The spin polarization of ^{3}***b*-P2**$^{2-}$ does not change significantly over time as seen from the time domain of the tr-EPR spectrum in Figure 4.6B. The width of the tr-EPR spectrum of ^{3}***b*-P2**$^{2-}$ is substantially narrower than the spectral width of ^{3}***b*-P2**, which demonstrates that twofold reduction of the porphyrin backbone prior to photoexcitation successfully changes the nature of the spin polarized triplet state.

The tr-EPR spectra of the same sample of ***b*-P2**$^{2-}$ following laser excitation at 450 nm and 1000 nm in MTHF at 20 K are compared in Figure 4.7A and confirm that the polarization patterns and spectral shapes are independent of the excitation wavelength. Photoexcitation of ***b*-P2**$^{2-}$ at 450 nm and 1000 nm results in $S_0 \rightarrow S_n$ and $S_0 \rightarrow S_1$ electronic transitions, respectively, which is supported by TD-DFT calculations (LC-ωHPBE/6-31G*; $\omega = 0.2$) discussed in Section 4.3.1. As implied by Kasha's rule,[343] the upper singlet excited states of ***b*-P2**$^{2-}$ relax rapidly to the S_1 state *via* nonradiative

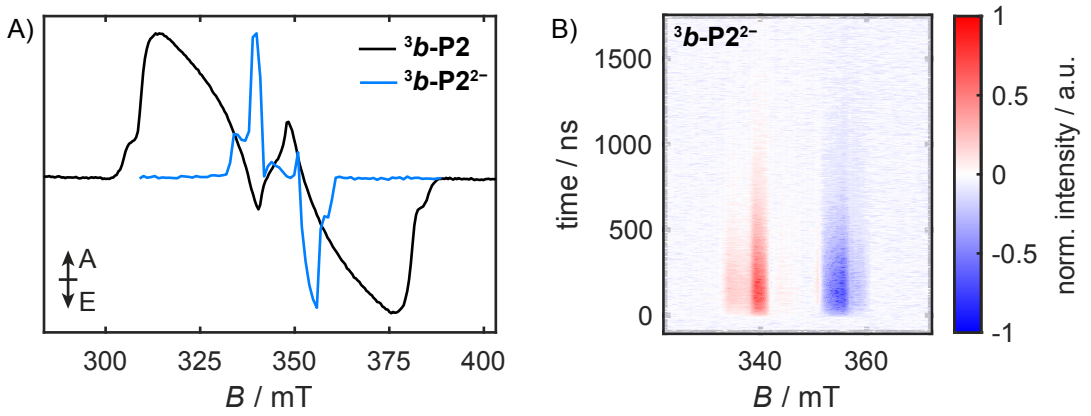


Figure 4.6: A) Comparison of the normalized experimental tr-EPR spectra of ^{3}***b*-P2** (black) and ^{3}***b*-P2**$^{2-}$ (blue) at X-band frequencies in 2-methyltetrahydrofuran at 20 K recorded as an average over 400 ns after the laser pulse with depolarized light at 532 nm and 1000 nm, respectively. The spectrum of ^{3}***b*-P2** was previously reported in reference [307]. B) Time domain of the tr-EPR spectrum of ^{3}***b*-P2**$^{2-}$.

processes. Consequently, ISC proceeds from S_1 to form the lowest-energy triplet excited state T_1 observed in both tr-EPR spectra.

The tr-EPR spectra of ^{3}***b*-P2**$^{2-}$ are temperature independent between 20 K and 80 K in frozen MTHF (Figure 4.7C). The transient kinetics of ^{3}***b*-P2**$^{2-}$ observed in the time domain of the tr-EPR spectra and monitored between 332 and 342 mT reveal a monoexponential decay of the triplet state with lifetimes $\tau = 348 \pm 2$ ns and $\tau = 193 \pm 5$ ns at 20 K and 80 K, respectively (Figure 4.7D). The increasing triplet lifetime with decreasing temperature is additional evidence for the predominant decay of T_1 via nonradiative processes. Molecular vibrations are typically smaller at lower temperature, which reduces the efficiency of nonradiative decay processes such as internal conversion or the Herzberg–Teller contributions to reverse ISC.[342, 344–346]

Comparison of the tr-EPR spectra of ^{3}***b*-P2** and ^{3}***b*-P2**$^{2-}$ demonstrates a substantially shorter triplet lifetime of ^{3}***b*-P2**$^{2-}$, which is in agreement with the transient absorption spectra discussed in Section 4.3.2.1. The differences in the triplet lifetimes of ^{3}***b*-P2**$^{2-}$ obtained by tr-EPR and transient absorption spectroscopy could result from different sample conditions such as concentration or glass morphologies caused by different freezing techniques. Attempts to perform transient absorption spectroscopy of ^{3}***b*-P2**$^{2-}$

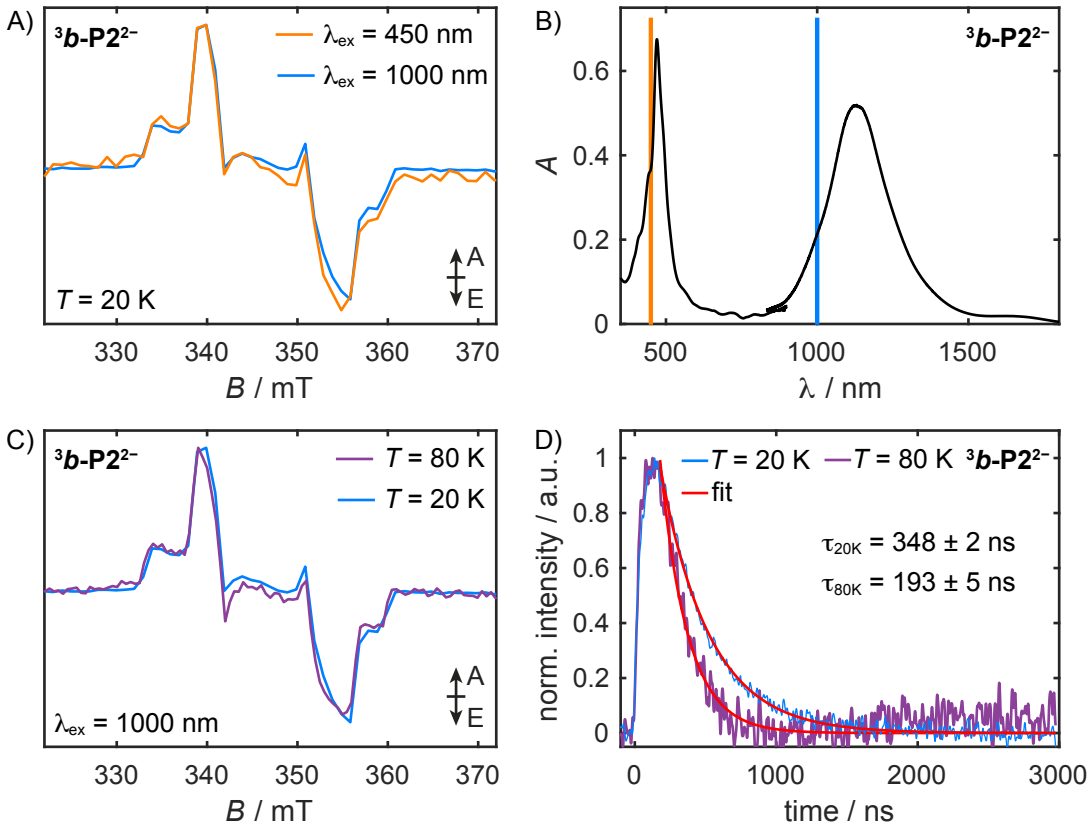


Figure 4.7: Comparison of the normalized tr-EPR spectra of the same sample of ***b*-P2**$^{2-}$ after photoexcitation at 450 nm (orange) and 1000 nm (blue) at X-band frequencies in 2-methyltetrahydrofuran at 20 K. B) Steady state UV-vis-NIR absorption spectrum of ***b*-P2**$^{2-}$ (THF, 298 K). The orange and blue bars indicate the excitation wavelengths, λ_{ex}, of the tr-EPR spectra in A). C) Comparison of the normalized tr-EPR spectra of the same sample of ***b*-P2**$^{2-}$ at 20 K (blue) and 80 K (purple) after photoexcitation at 1000 nm in 2-methyltetrahydrofuran. D) Transient kinetics of the tr-EPR spectra of ^{3}***b*-P2**$^{2-}$ shown in C) monitored between 332 and 342 mT. The triplet lifetimes τ were obtained by least-squares fitting of monoexponential decays to the kinetic data. The tr-EPR spectra were recorded as an average over 400 ns after the laser pulse.

at 20 K were unsuccessful due to the loss of optical transparency of frozen MTHF at about 50 K. The relatively short lifetime of ^{3}***b*-P2**$^{2-}$ even at 20 K prevented the investigation of the triplet state by pulse EPR spectroscopy.

ISC in Zn-porphyrin oligomers is driven by spin–orbit coupling due to mixing of zinc *d*-orbitals with the porphyrin π-system, and vibrations of the porphyrin framework.[52, 308, 347] The admixture of *d*-orbital character to the porphyrin π-system results in the preferential population of the out-of-plane triplet sublevel, whereas Herzberg–Teller vibronic coupling admixes $n\sigma^*$ states to the porphyrin π-system and results

in the preferential population of in-plane sublevels.[52, 308, 347, 348] The relative contributions of the spin–orbit and vibronic mechanism to the ISC are evident from the population of the zero–field triplet sublevels.[52] The lineshape and width of the EPR spectra of photogenerated triplet states are dominated by their zero–field splitting interactions, which arise due to dipolar spin–spin interactions between the triplet electrons in Zn-porphyrins.[52, 88, 308] The zero–field splitting parameters D and E introduced in equation 1.25 and relative sublevel populations of ^{3}***b*-P2** and ^{3}***b*-P2**$^{2-}$ were obtained by least-squares fitting of their tr-EPR spectra (Figure 4.8, Table 4.1).

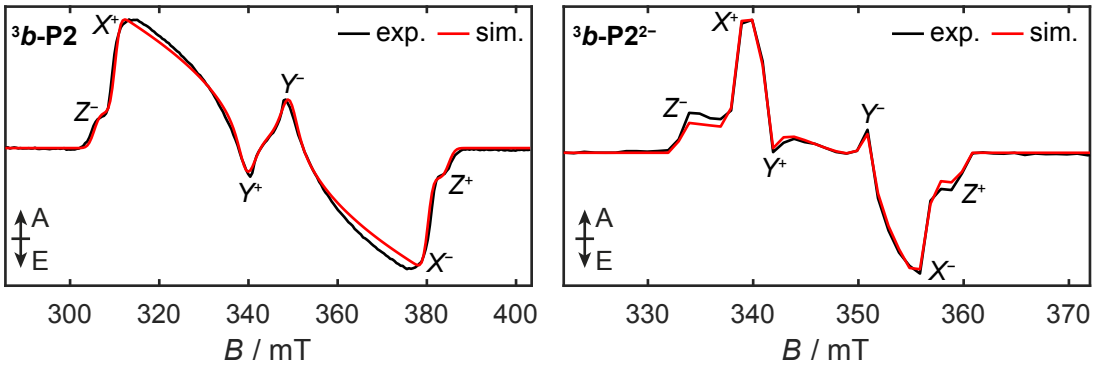


Figure 4.8: Experimental (black) and simulated (red) tr-EPR spectra of ^{3}***b*-P2** and ^{3}***b*-P2**$^{2-}$ at X-band frequencies in 2-methyltetrahydrofuran at 20 K. The experimental spectra were recorded as an average over 400 ns after the laser pulse with depolarized light at 532 nm (***b*-P2**) and 1000 nm (***b*-P2**$^{2-}$). The spectrum of ^{3}***b*-P2** was previously reported in reference [307]. Simulations were performed with the parameters reported in Table 4.1. The ordering of the principal components of $\boldsymbol{D}$ was chosen as $|D_Z| > |D_X| > |D_Y|$, and the canonical field positions are highlighted; A = absorption, E = emission, the + and − superscript refer to $m_s = 0 \leftrightarrow m_s = +1$ and $m_s = -1 \leftrightarrow m_s = 0$ transitions, respectively.

The orientation of the principal axes of the zero–field splitting $\boldsymbol{D}$-tensor in ^{3}***b*-P2** was assigned by Tait *et al.*, and showed that the axis of maximum dipolar coupling, Z, is aligned with the butadiyne axis of ***b*-P2**, whereas the X-axis is perpendicular to the molecular plane.[307] Magnetophotoselection experiments of ^{3}***b*-P2**$^{2-}$ discussed below demonstrate that the alignment of $\boldsymbol{D}$ is preserved in the doubly reduced dimer. Consequently, the preferential population of the X zero–field sublevels in ***b*-P2** and ***b*-P2**$^{2-}$ results from ISC driven by zinc spin–orbit coupling. Population of the Z sublevel results from Herzberg–Teller vibronic coupling and is slightly more prevalent in ^{3}***b*-P2**, which is probably the result of changes to the porphyrin vibrations in the

reduced dimer. The threefold reduction of the D-parameter in $^3\boldsymbol{b}$-**P2**$^{2-}$ compared to $^3\boldsymbol{b}$-**P2** together with the similar zero–field sublevel populations suggests a reduced dipolar coupling in the triplet state of $^3\boldsymbol{b}$-**P2**$^{2-}$.

Table 4.1: Zero-field splitting parameters D and E and relative sublevel populations of $^3\boldsymbol{b}$-**P2** and $^3\boldsymbol{b}$-**P2**$^{2-}$ determined through simulation of their tr-EPR spectra in Figure 4.8.

	$\lvert D\rvert$ / MHz	$\lvert E\rvert$ / MHz	$p_X : p_Y : p_Z$
$^3\boldsymbol{b}$-**P2**	1122 ± 4	285 ± 2	0.90 : 0.00 : 0.10
$^3\boldsymbol{b}$-**P2**$^{2-}$	375 ± 2	42 ± 1	0.96 : 0.00 : 0.04

Magnetophotoselection (MPS) experiments of $^3\boldsymbol{b}$-**P2**$^{2-}$ were used to determine the relative orientation of the principal axes of the zero–field splitting $\boldsymbol{D}$-tensor and the optical transition dipole moment $\boldsymbol{\mu}$ (Figure 4.9).[349–351] Linearly polarized light excites a subset of molecular orientations in a randomly oriented frozen solution with a probability of $\cos^2\theta$, where θ is the angle between the axis of the optical transition dipole moment and the polarization vector.[352] The orientation of the transition dipole moment of $^3\boldsymbol{b}$-**P2**$^{2-}$ for excitation at 1200 nm was determined by TD-DFT calculations (LC-ωPBE/6-31G*, $\omega = 0.2$), and is aligned with the long butadiyne axis of the dimer. Depending on the relative alignment to the light polarization axis and the static magnetic field $\boldsymbol{B}_0$, different orientations of the zero–field $\boldsymbol{D}$-tensor relative to $\boldsymbol{B}_0$ contribute more or less to the EPR spectrum (see Figure 1.8 for an introduction to orientation selection effects intrinsic to triplet EPR spectra). This results in changes of the relative intensities of the canonical transitions in the tr-EPR spectrum and provides information about the orientation of $\boldsymbol{D}$ and the sign of the zero–field splitting parameter, D. For instance, excitation of $^3\boldsymbol{b}$-**P2**$^{2-}$ with light polarized parallel to $\boldsymbol{B}_0$ excites orientations for which $\boldsymbol{D}_i \parallel \boldsymbol{\mu}$ is aligned with the magnetic field (Figure 4.9B). This enhances the intensity of the corresponding canonical transitions. Excitation with light polarized perpendicular to $\boldsymbol{B}_0$ selects molecules with other $\boldsymbol{D}$-axes aligned with the magnetic field and amplifies their respective canonical transitions (Figure 4.9A).

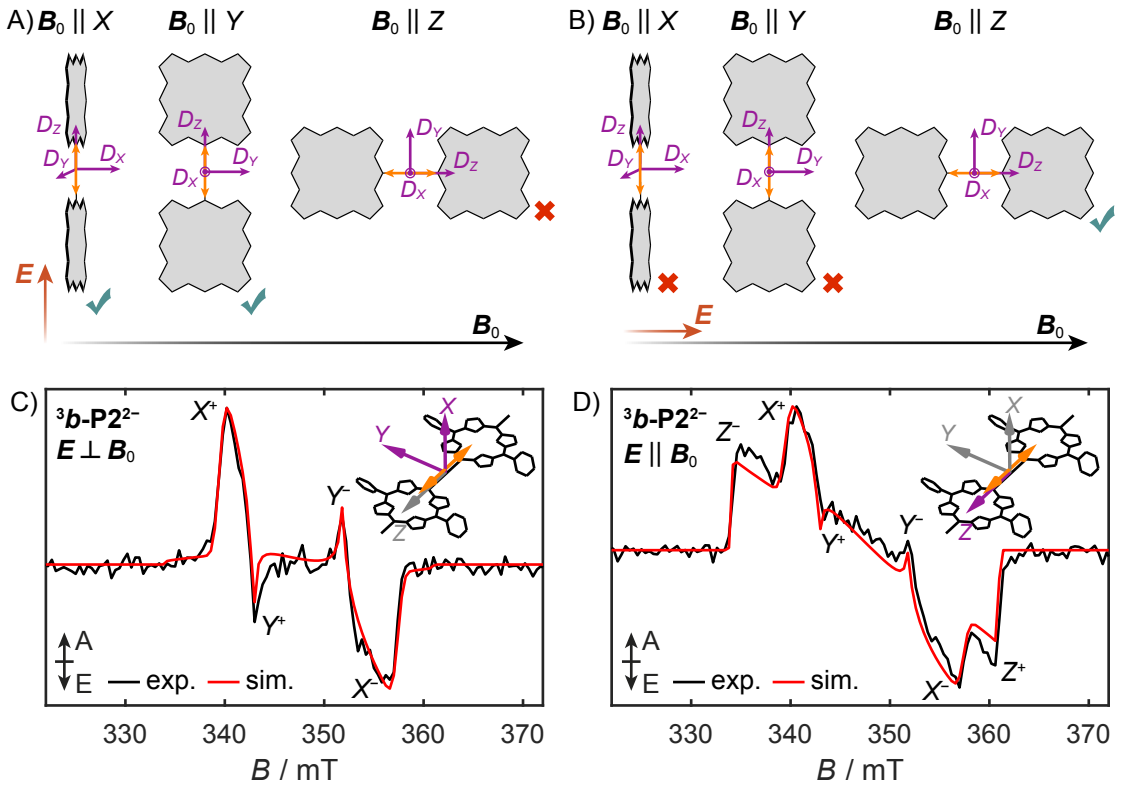


Figure 4.9: Schematic illustration of the selection effects during a magnetophotoselection (MPS) experiment for a porphyrin dimer with $D < 0$ and $E > 0$ with linearly polarized light excitation A) perpendicular ($\boldsymbol{E} \perp \boldsymbol{B}_0$) and B) parallel ($\boldsymbol{E} \parallel \boldsymbol{B}_0$) to the static magnetic field $\boldsymbol{B}_0$. Green ticks and red crosses indicate molecular orientations that contribute and do not contribute to the tr-EPR spectrum, respectively. The principal axes of the ZFS $\boldsymbol{D}$-tensor are shown in purple and the optical transition dipole moment in orange. Experimental (black) and simulated (red) MPS spectra of ^{3}***b***-**P2**$^{2-}$ at X-band frequencies in 2-methyltetrahydrofuran at 80 K with C) $\boldsymbol{E} \perp \boldsymbol{B}_0$ and D) $\boldsymbol{E} \parallel \boldsymbol{B}_0$. The experimental spectra were recorded as an average over 400 ns after the laser pulse with linearly polarized light at 1200 nm. Simulations were obtained from global least-squares fitting of the tr-EPR spectra for both laser orientations using the triplet parameters in Table 4.1. The insets show the orientation of the optical transition dipole moment (orange) obtained from TD-DFT calculations (LC-ωPBE/6-31G*, $\omega = 0.2$) and the principal axes of $\boldsymbol{D}$ obtained from the MPS simulations. The principal orientations of $\boldsymbol{D}$ that predominately contribute to the tr-EPR spectrum are shown in purple, while the others are shown in grey as a reference.

The MPS spectra of ^{3}***b***-**P2**$^{2-}$ were recorded at X-band frequencies in MTHF at 80 K and averaged over 400 ns after light excitation with linearly polarized light at 1200 nm (Figure 4.9C,D). Global simulation of both spectra with $\boldsymbol{E} \perp \boldsymbol{B}_0$ and $\boldsymbol{E} \parallel \boldsymbol{B}_0$ confirms that the zero–field Z axis is approximately colinear with the transition dipole moment and aligned with the long axis of the dimer. Consequently, the D-value of ^{3}***b***-**P2**$^{2-}$ is negative, which is consistent whith a prolate spin density distribution and analogous to

^{3}***b*-P2**.[307] No additional optical transition moment with a distinct orientation in the molecular frame of ***b*-P2**$^{2-}$ could be identified by TD-DFT calculations, which prevents the unambiguous assignment of the *X* and *Y* axes of ***D***. However, the preferential population of the zero–field *X* sublevel is evidence for the orientation of the *X* axis of ***D*** perpendicular to the molecular plane (*vide supra*).

To support the interpretation of the tr-EPR spectra, quantum chemical calculations were performed for ^{3}***b*-P2** and ^{3}***b*-P2**$^{2-}$ using DFT and complete active space self-consistent field (CASSCF) methods. Previous attempts to calculate the spin–spin contribution to the *D*-parameter of aromatic triplet states such as photogenerated porphyrin triplet states using DFT have shown that the magnitude of *D* is not correctly predicted in these calculations.[52, 88, 309, 310] This can be partially attributed to the incomplete description of the lowest-energy triplet state wavefunction in the DFT calculations.[309, 310] The trend in the DFT calculated *D*-parameters for a series of compounds can nevertheless provide important information about the nature of the triplet states.

The DFT predicted *D* values of ^{3}***b*-P2** and ^{3}***b*-P2**$^{2-}$ with B3LYP as functional and the EPRII basis set replicate the trend in the experimental *D* values with an about threefold smaller *D*-parameter for ^{3}***b*-P2**$^{2-}$ in comparison to ^{3}***b*-P2** (Table 4.2). The DFT calculated spin density distributions of ^{3}***b*-P2** and ^{3}***b*-P2**$^{2-}$ are visualized in Figure 4.10A and show a reduction of the spin density on the central butadiyne linker in ^{3}***b*-P2**$^{2-}$. The difference in the spin distribution in ^{3}***b*-P2** and ^{3}***b*-P2**$^{2-}$ was quantified by calculating the difference in their Mulliken spin populations $|\rho\left(^3\textbf{\textit{b}}\textbf{-P2}^{2-}\right)|-|\rho\left(^3\textbf{\textit{b}}\textbf{-P2}\right)|$, which confirms the redistribution of spin density from the central butadiyne linker to the porphyrin framework in the doubly reduced dimer (Figure 4.10B). This results in an about 10% increase in the distance between the average spin centers on both halves of the porphyrin dimer (Figure 4.10C, $d\left(^3\textbf{\textit{b}}\textbf{-P2}\right) = 12.78$ Å, $d\left(^3\textbf{\textit{b}}\textbf{-P2}^{2-}\right) = 14.12$ Å).

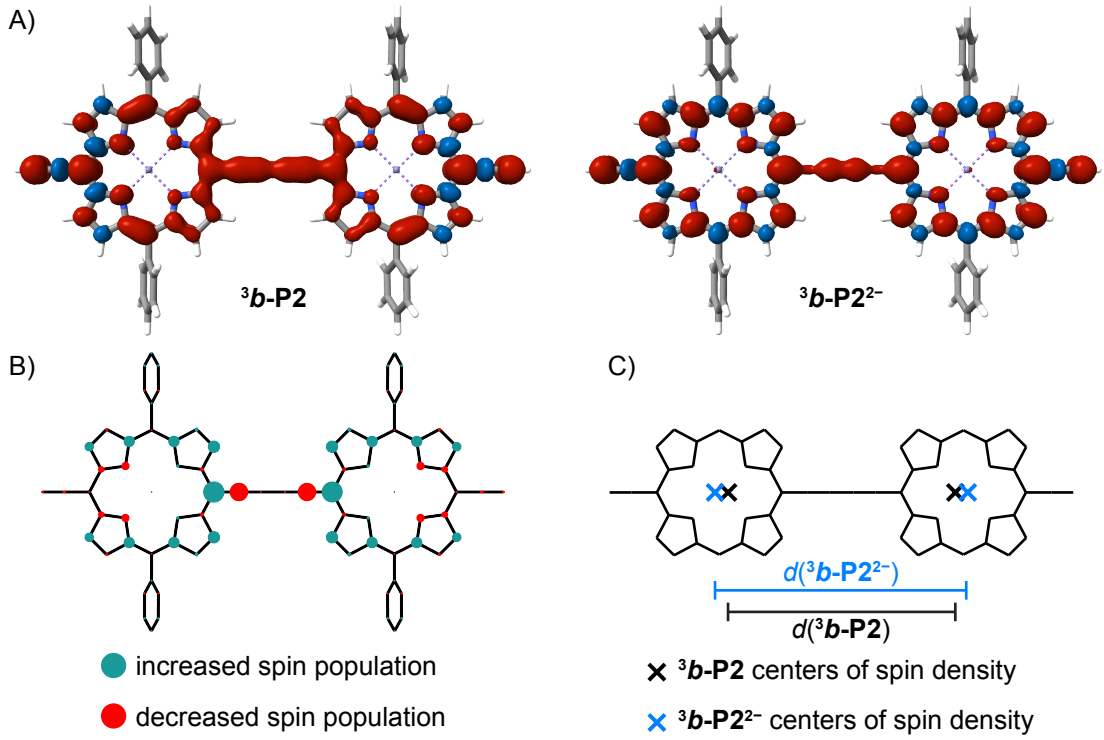


Figure 4.10: A) DFT (B3LYP/EPRII) calculated spin density distributions of the lowest-energy triplet excited states ^{3}***b***-**P2** and ^{3}***b***-**P2**$^{2-}$ plotted for an isovalue of 0.0012. B) Illustration of the difference in Mulliken spin populations between ^{3}***b***-**P2**$^{2-}$ and ^{3}***b***-**P2** calculated as $|\rho\left(^3\textbf{\textit{b}}\text{-}\textbf{P2}^{2-}\right)| - |\rho\left(^3\textbf{\textit{b}}\text{-}\textbf{P2}\right)|$. The radius of the circles is proportional to the spin population difference on each atom, and red and green circles indicate increased and decreased spin populations, respectively. C) Visualization of the centers of spin density in ^{3}***b***-**P2** (black) and ^{3}***b***-**P2**$^{2-}$ (blue) obtained as the weighted average of the position of the DFT calculated Mulliken spin populations in the left and right halves of the dimer. The distance between the spin centers is denoted as *d*.

The trend in the *D*-parameters obtained by CASSCF calculations is in even better agreement with the experimental results (Table 4.2), although the magnitude of the calculated values still deviates significantly from the experiment. The active space employed in the calculations presented here consists of four electrons and the four frontier molecular orbitals HOMO−1, HOMO, LUMO, and LUMO+1 (CAS(4,4)). The active molecular orbitals are analogous to the Gouterman four-orbital model[59, 60] and were obtained from single point calculations of ^{3}***b***-**P2** and ^{3}***b***-**P2**$^{2-}$ with TPSSh as functional and the def2-TZVP basis set for zinc and the def2-SVP basis set for the remaining nuclei. The quantitative agreement between the experimental and calculated *D* parameters might be improved with a larger active space, which is

however complicated by the extensive computational requirements.

Table 4.2: Comparison of the experimental zero–field splitting D parameters of ^{3}***b*-P2** and ^{3}***b*-P2**$^{2-}$ with results from quantum chemical calculations using DFT (B3LYP/EPRII) and CASSCF.

	$D\left(^3\textbf{\textit{b}}\text{-P2}\right)$ / MHz	$D\left(^3\textbf{\textit{b}}\text{-P2}^{2-}\right)$ / MHz	$D\left(^3\textbf{\textit{b}}\text{-P2}^{2-}\right) / D\left(^3\textbf{\textit{b}}\text{-P2}\right)$
experiment	−1122	−375	0.33
B3LYP/EPRII	−623	−230	0.37
CASSCF(4,4)	−733	−252	0.34

The spin densities of ^{3}***b*-P2** and ^{3}***b*-P2**$^{2-}$ obtained from the CASSCF calculations are shown in Figure 4.11 and are qualitatively consistent with the DFT predicted spin distributions. All quantum chemical calculations predict a negative sign of the D-parameters of ^{3}***b*-P2** and ^{3}***b*-P2**$^{2-}$, which is consistent with the experimental values and the prediction of prolate spin density distributions. In combination, DFT and CASSCF calculations provide clear evidence that the triplet states ^{3}***b*-P2** and ^{3}***b*-P2**$^{2-}$ are delocalized over both porphyrin units of the dimer. However, twofold reduction of the porphyrin backbone prior to photoexcitation results in a redistribution of the triplet spin density from the butadiyne linker to the porphyrin units, and a reduction of $|D|$.

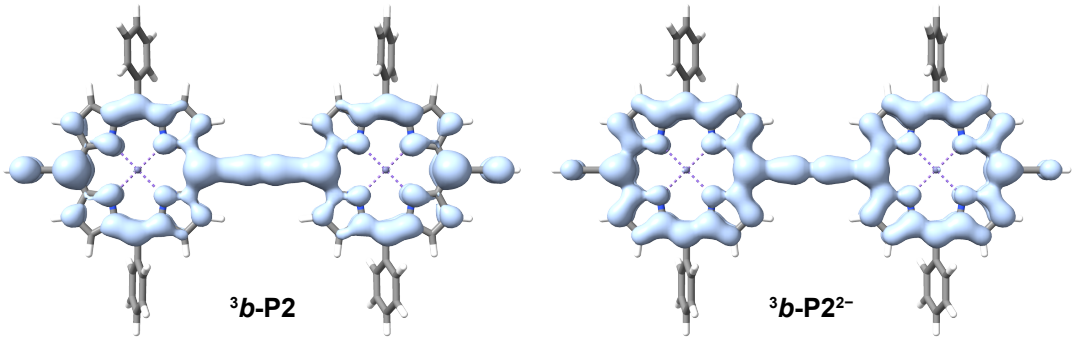


Figure 4.11: Spin densities of ^{3}***b*-P2** and ^{3}***b*-P2**$^{2-}$ obtained from CASSCF calculations with an active space of four orbitals and four electrons plotted for an isovalue of 0.00077.

4.3.3 Photogenerated Triplet States of *b*-P4^{4-} and *b*-P6^{6-}

4.3.3.1 Optical Transient Absorption Spectroscopy

To determine the effects of chemical reduction of the porphyrin backbone on the photogenerated triplet states of longer oligomers, tetramer ***b*-P4**$^{4-}$ and hexamer ***b*-**

P6^{6-} were investigated. Pump excitation of ***b*-P4**$^{4-}$ at 480 nm yields the transient absorption spectra in Figure 4.12A, which exhibit positive features between 500 and 650 nm, and 700 and 850 nm. The transient absorption spectra of ***b*-P6**$^{6-}$ following pump excitation at 480 nm are shown in Figure 4.12B and are similar to the spectra of ***b*-P4**$^{4-}$ with positive features between 500 and 630 nm, and 650 and 850 nm. However, the structure of the positive features at shorter wavelengths is more resolved in ***b*-P6**$^{6-}$.

No singlet excited state is evident in the transient absorption spectra following photoexcitation of ***b*-P4**$^{4-}$ or ***b*-P6**$^{6-}$. Instead, the observed transient species are assigned to the triplet excited states ^{3}***b*-P4**$^{4-}$ and ^{3}***b*-P6**$^{6-}$. The absence of optical features corresponding to the singlet excited states is consistent with the transient absorption measurements of ***b*-P2**$^{2-}$ discussed in Section 4.3.2.1. The transient kinetics of ***b*-P4**$^{4-}$ and ***b*-P6**$^{6-}$ were monitored between 700 and 850 nm and 650 and 850 nm, respectively, and are shown in Figure 4.12C and D. The photogenerated triplet state ^{3}***b*-P4**$^{4-}$ decays monoexponentially with a lifetime $\tau = 23.0 \pm 3.0$ ns in frozen MTHF at 80 K (Figure 4.12C), faster than ^{3}***b*-P2**$^{2-}$. This indicates a higher rate of the nonradiative decay processes as expected for a smaller T_1–S_0 energy gap in a larger π-conjugated system.

The transient kinetics of ^{3}***b*-P6**$^{6-}$ in Figure 4.12D could not be fitted to a monoexponential decay. Instead, a biexponential function with lifetimes $\tau_1 = 11.8 \pm 1.0$ ns and $\tau_2 = 156 \pm 13$ ns provides a good description of the experimental data, which indicates the presence of two distinct decay processes. The ratio of the pre-exponential factors obtained from least-squares fitting of the transient kinetics suggest an about 2.6 times higher prevalence of the faster decay process. The features in the transient absorption spectra of photoexcited ***b*-P6**$^{6-}$ do not change over time (Figure 4.12B), which confirms that both exponential decays are associated with ^{3}***b*-P6**$^{6-}$. Additional transient absorption measurements of ***b*-P6**$^{6-}$ under analogous conditions with pump excitation at 480 nm with half the laser power do not show substantial changes in the transient kinetics (Figure 4.22). This confirms that triplet-triplet annihilation does not noticeably contribute to the biexponential decay of ^{3}***b*-P6**$^{6-}$.

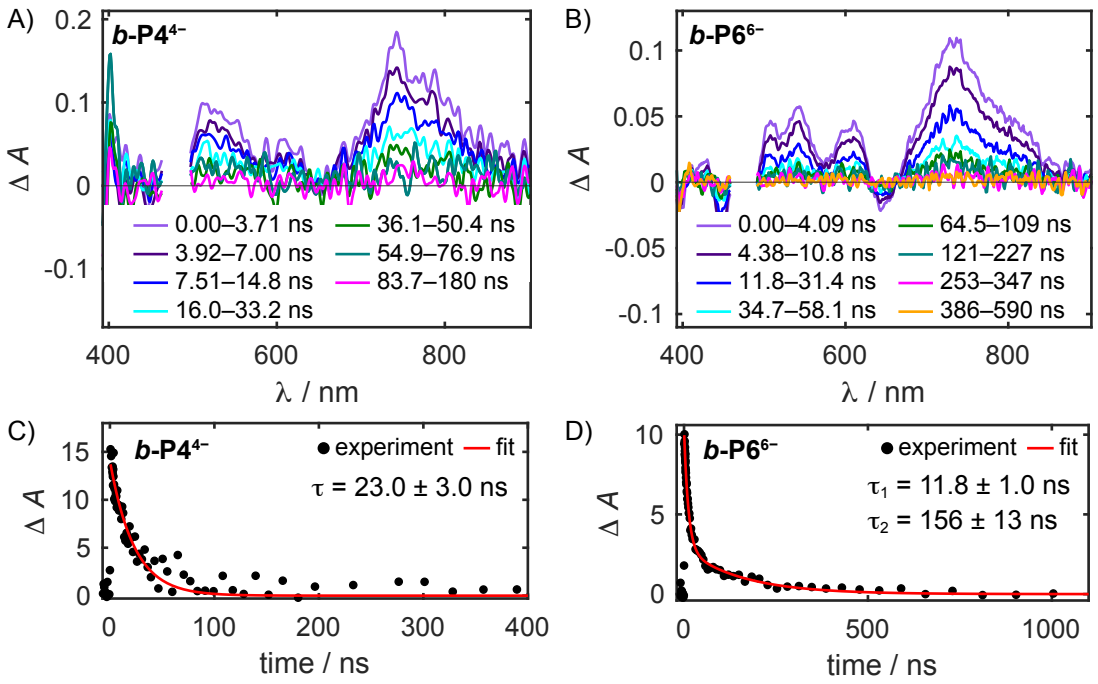


Figure 4.12: Time resolved transient absorption spectra of A) ***b*-P4**$^{4-}$ and B) ***b*-P6**$^{6-}$ in frozen 2-methyltetrahydrofuran at 80 K following pump excitation at 480 nm. C) Transient kinetics of photoexcited ***b*-P4**$^{4-}$ monitored between 700 and 850 nm and fitted to a monoexponential decay to determine the lifetime τ. D) Transient kinetics of photoexcited ***b*-P6**$^{6-}$ monitored between 650 and 850 nm. The data were fitted to a biexponential decay to obtain the lifetimes τ_1 and τ_2.

The decay of ^{3}***b*-P6**$^{6-}$ proceeding with a lifetime $\tau = 11.8$ ns is consistent with the reduction of the triplet lifetime with increasing oligomer length observed for ^{3}***b*-P2**$^{2-}$ and ^{3}***b*-P4**$^{4-}$. This suggests, that the fast contribution to the decay of ^{3}***b*-P6**$^{6-}$ can be tentatively assigned to nonradiative deactivation processes. Due to the increased structural flexibility of ***b*-P6**$^{6-}$ compared to the shorter oligomers, it is likely that a broader range of conformations is present in frozen MTHF. A plausible explanation for the slower contribution to the decay of ^{3}***b*-P6**$^{6-}$ could be the presence of molecular conformations for which nonradiative processes are reduced and the decay of ^{3}***b*-P6**$^{6-}$ is dominated by phosphorescence. However, further experimental and computational work is necessary to provide a clear explanation for the biexponential decay of ^{3}***b*-P6**$^{6-}$.

4.3.3.2 Transient EPR Spectroscopy

The triplet excited state of the fourfold reduced porphyrin tetramer ***b*-P4**$^{4-}$ was investigated by tr-EPR spectroscopy and compared to ^{3}***b*-P4** previously studied by Tait *et al.* (Figure 4.13).[52] Stepwise reduction of ***b*-P4** with **CoCp***$_2$ and investigation of the reduced samples by cw-EPR and tr-EPR spectroscopy confirms a diamagnetic ground state in ***b*-P4**$^{4-}$, and allowed for the unambiguous assignment of the observed transient species to ^{3}***b*-P4**$^{4-}$ (Figure 4.24). No transient species were observed following photoexcitation of ***b*-P4** in its 1−, 2− and 3− oxidation states at 1000 nm despite appreciable absorption coefficients of all species. This is probably the results of the substantially smaller HOMO–LUMO energy gaps of oligomers with fractional oxidation states of each porphyrin unit (e.g. ***b*-P4**$^{2-}$: $\lambda_{max} = 2904$ nm, $E_{Abs} = 0.43$ eV), which results in fast relaxation of the excited singlet state in agreement with the energy gap law. The tr-EPR spectra of ^{3}***b*-P4**$^{4-}$ following photoexcitation at 480 nm and 1000 nm are virtually identical, suggesting observation of the lowest energy triplet excited state T_1 (Figure 4.13B).

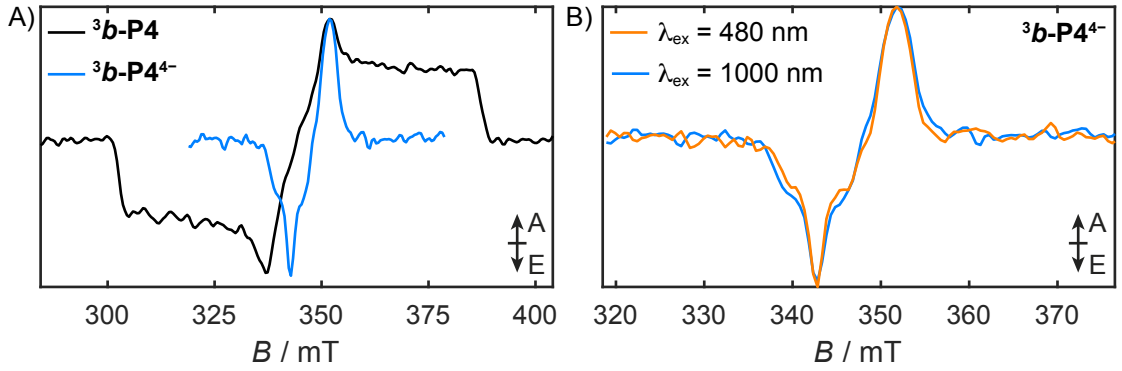


Figure 4.13: A) Comparison of the normalized experimental tr-EPR spectra of ^{3}***b*-P4** (black) and ^{3}***b*-P4**$^{4-}$ (blue) recorded as an average over 400 ns after the laser pulse with depolarized light at 830 nm and 1000 nm, respectively. The spectrum of ^{3}***b*-P4** was previously reported in reference [52]. B) Comparison of the normalized tr-EPR spectra for the same sample of ^{3}***b*-P4**$^{4-}$ after photoexcitation at 480 nm (orange) and 1000 nm (blue). All spectra were measured at X-band frequencies in 2-methyltetrahydrofuran at 20 K.

The tr-EPR spectra of ^{3}***b*-P4** and ^{3}***b*-P4**$^{4-}$ are compared in Figure 4.13A and exhibit both an *EEEAAA* polarization pattern consistent with a non-Boltzmann population of the triplet sublevels. The width of the tr-EPR spectrum of ^{3}***b*-P4**$^{4-}$ is substantially

narrower compared to the tr-EPR spectrum of ^{3}***b*-P4**. This is analogous to the behaviour of ^{3}***b*-P2** and ^{3}***b*-P2**$^{2-}$ discussed in Section 4.3.2.2 and provides further evidence that chemical reduction of a chromophore followed by photoexcitation is a powerful tool to modify the spin polarized triplet state. The zero–field splitting parameters D and E and relative sublevel populations of ^{3}***b*-P4** and ^{3}***b*-P4**$^{4-}$ were obtained by least-squares fitting of their tr-EPR spectra (Figure 4.14, Table 4.3) The $|D|$-parameter of ^{3}***b*-P4**$^{4-}$ is about five times smaller than in ^{3}***b*-P4** and about 1.6 times smaller than in ^{3}***b*-P2**$^{2-}$, which implies a further reduction of the dipolar coupling between the triplet electrons. Photoexcitation of ***b*-P4**$^{4-}$ also results in a smaller orthorhombicity of the triplet $\boldsymbol{D}$-tensor in comparison to ^{3}***b*-P4**, as seen from the smaller E-parameter. The overall reduction of D and E in ^{3}***b*-P4**$^{4-}$ limits the resolution of the individual canonical transitions and only results in a distinctive spectral feature for the low-field Z^- transition. The asymmetry of the tr-EPR spectrum of ^{3}***b*-P4**$^{4-}$ is attributed to increased $\boldsymbol{g}$-ansiotropy, which could be explained by a stronger spin–orbit contribution from excited states due to a closer energetic spacing of the electronic states in ***b*-P4**$^{4-}$.

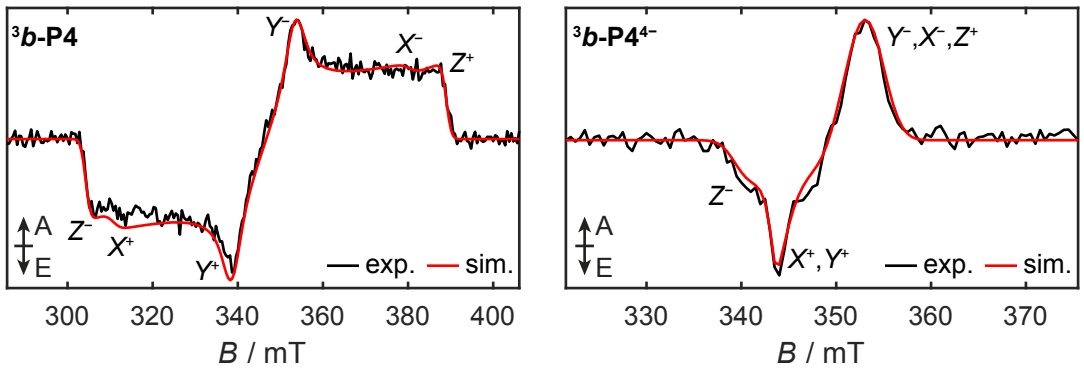


Figure 4.14: Experimental (black) and simulated (red) tr-EPR spectra of ^{3}***b*-P4** and ^{3}***b*-P4**$^{4-}$ at X-band frequencies in 2-methyltetrahydrofuran at 20 K. The experimental spectra were recorded as an average over 400 ns after the laser pulse with depolarized light at 830 nm (***b*-P4**) and 1000 nm (***b*-P4**$^{4-}$). Simulations were performed with the parameters reported in Table 4.3. The ordering of the principal components of $\boldsymbol{D}$ was chosen as $|D_Z| > |D_X| > |D_Y|$, and the canonical field positions are highlighted.

The orientation of the principal axes of $\boldsymbol{D}$ in ^{3}***b*-P4** was assigned by Tait *et al.* using magnetophotoselection experiments and showed the alignment of the Z and X axes with the butadiyne and out-of-plane axes of the molecule, respectively.[52]

Table 4.3: Zero-field splitting parameters D and E and relative sublevel populations of ^{3}***b*-P4** and ^{3}***b*-P4**$^{4-}$ determined through simulation of their tr-EPR spectra in Figure 4.14.

	$\lvert D\rvert$ / MHz	$\lvert E\rvert$ / MHz	$p_X : p_Y : p_Z$
^{3}***b*-P4**	1192 ± 4	259 ± 3	0.28 : 0.00 : 0.72
^{3}***b*-P4**$^{4-}$	235 ± 9	27 ± 4	0.00 : 0.48 : 0.52

This suggests a dominant contribution of Herzberg–Teller vibronic coupling to the ISC in photoexcited ***b*-P4**, resulting in the substantial population of the in-plane zero–field sublevel (Table 4.3). Magnetophotoselection experiments of ^{3}***b*-P4**$^{4-}$ after photoexcitation with linearly polarized light at 1450 nm demonstrate a colinear alignment of the zero–field Z axis with the TD-DFT calculated optical transition dipole moment along the butadiyne axis of ***b*-P4**$^{4-}$ (Figure 4.25). This confirms a negative sign of the D-value of ^{3}***b*-P4**$^{4-}$, and a prolate spin density distribution. The population of the zero–field Y sublevel in ^{3}***b*-P4**$^{4-}$ suggest a reorientation of the $\boldsymbol{D}$-tensor axes compared to ^{3}***b*-P4**, and an alignment of the Y axis of $\boldsymbol{D}$ perpendicular to the molecular plane. Consequently, the population of the Y and Z zero–field triplet sublevels of ^{3}***b*-P4**$^{4-}$ results from spin–orbit and vibronic contributions to the ISC, respectively. The smaller prevalence of vibronic effects in ^{3}***b*-P4**$^{4-}$ compared to ^{3}***b*-P4** is consistent with the trend observed for ^{3}***b*-P2** and ^{3}***b*-P2**$^{2-}$.

Quantum chemical calculations of ^{3}***b*-P4** and ^{3}***b*-P4**$^{4-}$ using DFT and CASSCF were performed to guide the interpretation of the tr-EPR spectra. The ratio of the DFT predicted D values matches the experimental observations with a fivefold reduction of $\lvert D\rvert$ in ^{3}***b*-P4**$^{4-}$ compared to ^{3}***b*-P4** (Table 4.4). The DFT predicted spin density distributions of ^{3}***b*-P4** and ^{3}***b*-P4**$^{4-}$ are shown in Figure 4.15A and display a substantially larger delocalization of the triplet state in the reduced porphyrin tetramer. In ^{3}***b*-P4**, the triplet spin density is predominantly localized on the central porphyrin units and butadiyne linker, in agreement with previous reports.[52] In contrast, the triplet spin density in ^{3}***b*-P4**$^{4-}$ is predominantly localized on the terminal porphyrin units, and the spin density on the central porphyrin units is substantially reduced (Figure 4.15A,B). The enhanced delocalization of the triplet state in ^{3}***b*-P4**$^{4-}$ results

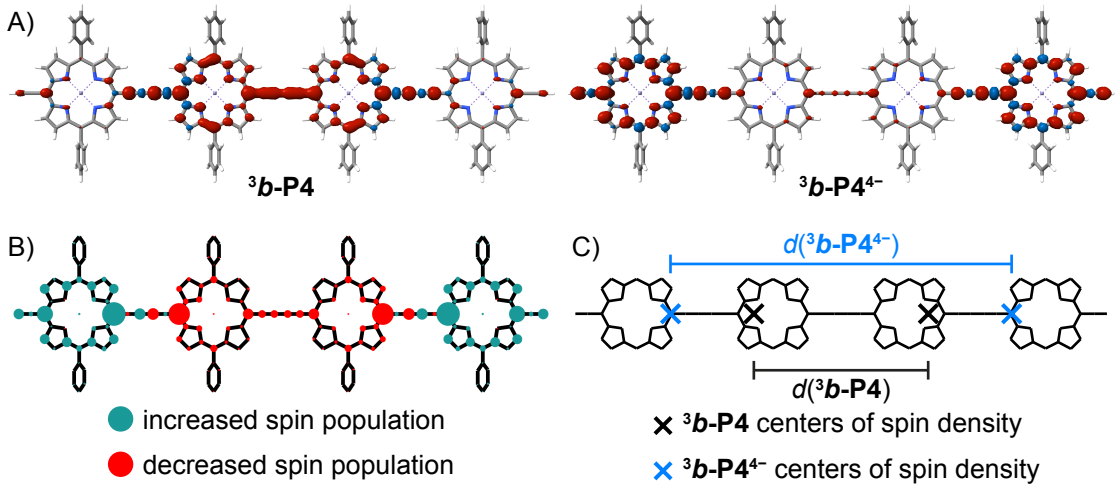


Figure 4.15: DFT (B3LYP/EPRII) calculated spin density distributions of the lowest-energy triplet state of ***b*-P4** and ***b*-P4**$^{4-}$ plotted for an isovalue of 0.0012. B) Illustration of the difference in Mulliken spin populations between ^{3}***b*-P4**$^{4-}$ and ^{3}***b*-P4** calculated as $|\,\rho\left(^3\textbf{\textit{b}}\text{-P4}^{4-}\right)\,| - |\,\rho\left(^3\textbf{\textit{b}}\text{-P4}\right)\,|$. The radius of the circles is proportional to the spin population difference on each atom, and red and green circles indicate increased and decreased spin populations, respectively. C) Visualization of the centers of spin density in ^{3}***b*-P4** (black) and ^{3}***b*-P4**$^{4-}$ (blue) obtained as the weighted average of the position of the DFT calculated Mulliken spin populations in the left and right halves of the tetramer. The distance between the spin centers is denoted as *d*, and was calculated as 17.4 Å and 34.1 Å in ^{3}***b*-P4** and ^{3}***b*-P4**$^{4-}$, respectively.

in an almost twofold increase in the distance between the average spin centers on both halves of the tetramer (Figure 4.15C, $d\left(^3\textbf{\textit{b}}\text{-P4}\right) = 17.4$ Å, $d\left(^3\textbf{\textit{b}}\text{-P4}^{4-}\right) = 34.1$ Å). The DFT predicted spin densities and the close agreement of the reduction in $|D|$ with the experimental observations provide strong evidence that reducing π-conjugated oligomers prior to photoexcitation is a powerful strategy for the generation of highly delocalized triplet states.

Table 4.4: Comparison of the experimental zero–field splitting D parameters of ^{3}***b*-P4** and ^{3}***b*-P4**$^{4-}$ with results from quantum chemical calculations using DFT (B3LYP/EPRII) and CASSCF.

	$D\left(^3\textbf{\textit{b}}\text{-P4}\right)$ / MHz	$D\left(^3\textbf{\textit{b}}\text{-P4}^{4-}\right)$ / MHz	$D\left(^3\textbf{\textit{b}}\text{-P4}^{4-}\right) / D\left(^3\textbf{\textit{b}}\text{-P2}\right)$
experiment	−1192	−235	0.20
B3LYP/EPRII	−507	−101	0.20
CASSCF(4,4)	−653	−485	0.74

CASSCF calculations of ^{3}***b***-**P4** and ^{3}***b***-**P4**$^{4-}$ with an active space of four electrons and four frontier orbitals qualitatively reproduce the observation of a smaller $|D|$-value in ^{3}***b***-**P4**$^{4-}$ and an increase of the triplet delocalization (Figure 4.16, Table 4.4). However, the ratio of the predicted D-parameters deviates substantially from the experimental values. This probably results from the exaggeration of the electron–electron dipolar coupling on ^{3}***b***-**P4**$^{4-}$ due to the allocation of more spin density to the central porphyrin units in comparison to DFT calculations. This suggest that better starting orbitals are required to describe ^{3}***b***-**P4**$^{4-}$ in CASSCF calculations.

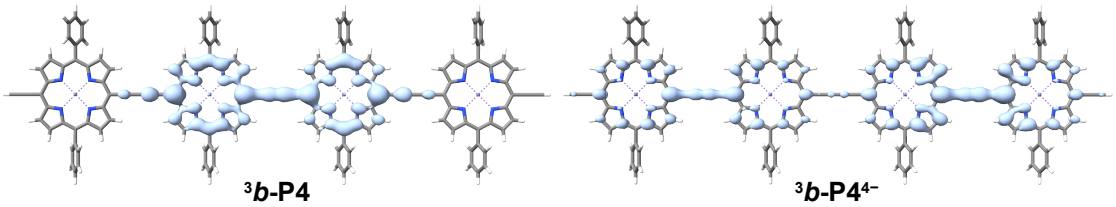


Figure 4.16: Spin densities of ^{3}***b***-**P4** and ^{3}***b***-**P4**$^{4-}$ obtained from CASSCF calculations with an active space of four orbitals and four electrons plotted for an isovalue of 0.0006.

The tr-EPR spectrum of ^{3}***b***-**P6**$^{6-}$ has a substantially smaller spectral width in comparison to the spectrum on ^{3}***b***-**P6**, as expected from the shorter oligomers discussed above (Figure 4.17A). Stepwise reduction of ^{3}***b***-**P6** with **CoCp***$_2$ and investigation of the titration points by cw-EPR and tr-EPR spectroscopy confirms the diamagnetic ground state of ^{3}***b***-**P6**$^{6-}$ and the assignment of the observed tr-EPR spectrum to ^{3}***b***-**P6**$^{6-}$ (Figure 4.26). The tr-EPR spectra of ^{3}***b***-**P6**$^{6-}$ following photoexcitation at 480 nm and 1000 nm are virtually identical, again suggesting observation of the lowest energy triplet excited state T_1 (Figure 4.17B).

The zero–field splitting parameters D and E and relative sublevel populations of ^{3}***b***-**P6** and ^{3}***b***-**P6**$^{6-}$ were obtained by least-squares fitting of their tr-EPR spectra (Figure 4.18, Table 4.5). The $|D|$-parameter of ^{3}***b***-**P6**$^{6-}$ is about 60% smaller than in ^{3}***b***-**P4**$^{4-}$, which indicates even further delocalization of the photogenerated triplet state. Preliminary DFT calculations of ^{3}***b***-**P6**$^{6-}$ also indicate substantial triplet state delocalization with large amounts of spin density assigned to the terminal porphyrin

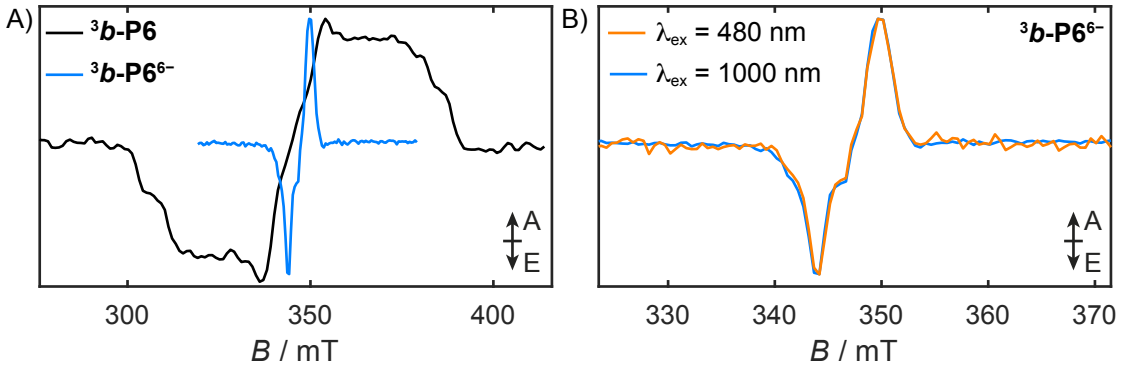


Figure 4.17: A) Comparison of the normalized experimental tr-EPR spectra of ^{3}***b*-P6** (black) and ^{3}***b*-P6**$^{6-}$ (blue) recorded as an average over 3 μs and 400 ns after the laser pulse with depolarized light at 830 nm and 1000 nm, respectively. B) Comparison of the normalized tr-EPR spectra for the same sample of ^{3}***b*-P6**$^{6-}$ after photoexcitation at 480 nm (orange) and 1000 nm (blue). All spectra were measured at X-band frequencies in 2-methyltetrahydrofuran at 20 K.

units. However, further computational work is required to confirm the validity of these calculations, as they exhibit noticeable spin contamination. Analogous to the discussion of ^{3}***b*-P4**$^{4-}$, population of the zero–field Y sublevel in ^{3}***b*-P6**$^{6-}$ suggest a reorientation of the $\boldsymbol{D}$-tensor axes compared to ^{3}***b*-P6**.

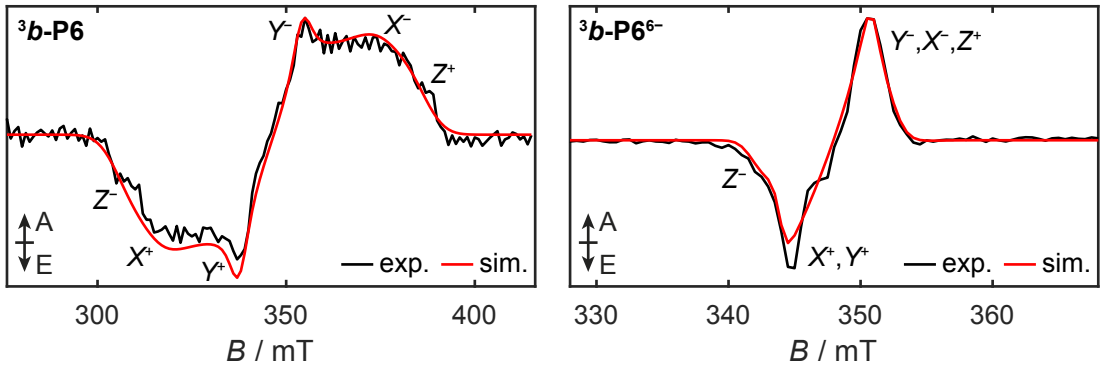


Figure 4.18: Experimental (black) and simulated (red) tr-EPR spectra of ^{3}***b*-P6** and ^{3}***b*-P6**$^{6-}$ at X-band frequencies in 2-methyltetrahydrofuran at 20 K. The experimental spectra were recorded as an average over 3 μs and 400 ns after the laser pulse with depolarized light at 830 nm (***b*-P4**) and 1000 nm (***b*-P4**$^{4-}$). Simulations were performed with the parameters reported in Table 4.5. The energetic ordering of the principal components of $\boldsymbol{D}$ was chosen as $|D_Z| > |D_X| > |D_Y|$, and the canonical field positions are highlighted.

Table 4.5: Zero-field splitting parameters D and E and relative sublevel populations of ^{3}***b*-P6** and ^{3}***b*-P6**$^{6-}$ determined through simulation of their tr-EPR spectra in Figure 4.18.

	$\lvert D\rvert$ / MHz	$\lvert E\rvert$ / MHz	$p_X : p_Y : p_Z$
^{3}***b*-P6**	1133 ± 19	222 ± 7	0.15 : 0.00 : 0.85
^{3}***b*-P6**$^{6-}$	143 ± 8	16 ± 4	0.00 : 0.41 : 0.59

4.4 Summary and Conclusions

The photogenerated, spin-polarized triplet states of a series of neutral and fully reduced butadiyne-linked porphyrin oligomers ***b*-P*N*** ($N = 2$, 4, 6) were investigated by optical transient absorption spectroscopy, tr-EPR spectroscopy, and supporting quantum chemical calculations. Steady-state UV-vis-NIR absorption spectroscopy and TD-DFT calculations of ***b*-P*N*$^{N-}$** show a continuously narrowing HOMO–LUMO gap with increasing oligomer length, and suggest that the $S_0 \rightarrow S_1$ electronic transitions proceed from closed-shell ground states. Transient absorption spectroscopy of ^{3}***b*-P2**$^{2-}$, ^{3}***b*-P4**$^{4-}$, and ^{3}***b*-P6**$^{6-}$ shows a substantially shorter triplet state lifetime in comparison with the photogenerated triplet states of the neutral oligomers. This phenomenon is attributed to faster nonradiative relaxation processes from the lowest-energy triplet exited states ^{3}***b*-P*N*$^{N-}$** due to smaller energy gaps in the charged oligomers.

Tr-EPR spectroscopy was used to characterize the triplet excited states ^{3}***b*-P*N*$^{N-}$** ($N = 2$, 4, 6). Comparison of the tr-EPR spectra of ^{3}***b*-P*N*$^{N-}$** with the spectra of the previously investigated triplet states ^{3}***b*-P*N*** demonstrated a substantially smaller dipolar coupling in the triplet states of the charged oligomers. Magnetophotoselection experiments on ^{3}***b*-P2**$^{2-}$ and ^{3}***b*-P4**$^{4-}$ show that the orientation of the axis of maximum dipolar coupling, Z, is identical in the neutral and reduced wires and approximately colinear with the butadiyne-axis of the oligomers. Consequently, ^{3}***b*-P2**$^{2-}$ and ^{3}***b*-P4**$^{4-}$ exhibit negative D-values and a prolate spin density distribution, which is correctly predicted by DFT and CASSCF(4,4) calculations. DFT calculations of ^{3}***b*-P*N*** and ^{3}***b*-P*N*$^{N-}$** ($N = 2$, 4) support the experimentally observed reduction of the zero–field $|D|$-values in the charged oligomers, and suggest that a larger delocalization of the triplet spin densities causes the reduction of $|D|$. In ^{3}***b*-P2**$^{2-}$, the increase

in triplet state delocalization is small and manifests as a reduction of spin density on the central butadiyne-linker. The spin density of ^{3}***b*-P4**$^{4-}$ is substantially more delocalized than in ^{3}***b*-P4** and predominantly distributed over the terminal porphyrin units. CASSCF(4,4) calculations are in excellent agreement with the experimental observations for ^{3}***b*-P2**$^{2-}$, but further computational work is required to obtain a better description of ^{3}***b*-P4**$^{4-}$. The sustained decrease of $|D|$ in ^{3}***b*-P6**$^{6-}$ compared to the shorter oligomers is preliminary evidence for an even further delocalization of the triplet state. However, further quantum chemical calculations are required to conclusively interpret the tr-EPR spectra of ^{3}***b*-P6**$^{6-}$.

The results in this chapter highlight a new approach for the generation of highly delocalized triplet excited states by chemically reducing porphyrin oligomers prior to photoexcitation. This exciting discovery provides insights into the design of materials for the rapid transport of triplet excitons and may enable the photogeneration of spin polarized triplet states with tailored electronic properties for quantum information processing. An important next challenge is the design of molecules with longer triplet state lifetime after chemical reduction to enable the manipulation of the triplet states by pulse EPR spectroscopy. Initial results from the photoexcitation of a doubly reduced butadiyne-linked Pd-porphyrin dimer show triplet state lifetimes in the order of several microseconds. Further work is currently ongoing to expand on this promising observation.

4.5 Methods

Sample Preparation

Samples of ^{3}***b*-PN**$^{N-}$ (N = 2, 4, 6) for EPR measurements were prepared in 2-methyltetrahydrofuran by addition of N equivalents of **CoCp*$_2$** to a solution of the porphyrin oligomer (~200 μM). All sample preparations and chemical reductions were performed under inert atmosphere by handling the EPR tubes in a MBraun LabStar Glovebox under N_2-atmosphere. A solution of decamethylcobaltocene **CoCp*$_2$** in THF was used as reducing agent. Prior to dissolving, **CoCp*$_2$** was sublimed under vacuum and the concentration of the stock solution was determined by quenching an aliquot of **CoCp*$_2$** solution with an excess of solid ferrocenium hexafluorophosphate under inert atmosphere. Evaporation of the solvent *in vacuo* and redissolving of the residuals in acetone-d_6 with *tert*-butyl benzene as an internal standard allowed for the quantification of **CoCp*$_2$** by ^{1}H NMR.[176] All samples were prepared directly in X-band EPR tubes (3.8 mm o.d.) and sealed with a silicone cap to preserve an anaerobic atmosphere during transport to the EPR spectrometer.

Samples of ^{3}***b*-PN**$^{N-}$ for transient absorption measurements were prepared directly in custom made borosilicate glass cuvettes with an optical path length of about 2–4 mm. The concentration of the porphyrin oligomers was adjusted to obtain an optical density of 0.8 at the wavelength with the largest extinction coefficient. The reduced porphyrin oligomers were prepared by addition of an excess of **CoCp*$_2$** to the porphyrin samples in 2-methyltetrahydrofuran in a MBraun LabStar Glovebox under N_2-atmosphere. The sample cuvettes were then removed from the Glovebox and connected to a Schlenk line, while preserving an anaerobic atmosphere, and flame sealed under reduced pressure.

Transient Absorption Spectroscopy

For transient absorption measurements, the third harmonic (355 nm) of an Nd:YAG Ekspla PL2210A laser is used to pump a tunable Ekspla PG400 optical parametric

generator (OPG). This produces the pump pulse with a repetition rate of 1 kHz. A series of three turning mirrors directs the pump pulse into an Ultrafast Systems EOS spectrometer. A 2 kHz probe pulse is generated by a Leukos STM-2-UV supercontinuum white light source and directed to the spectrometer through a fibre optic cable.

Samples for transient absorption measurements were inserted into the precooled cryostat at 80 K under a counter flow of helium. In each transient absorption scan, a magnetic field is applied in an ON/OFF/OFF/ ON pattern by a set of home-build Helmholtz field coils surrounding the sample. No magnetic field effects were observed for the investigated samples, and the optical spectra recorded with and without an applied magnetic field were combined to increase the signal-to-noise. A shutter, located along both the pump and probe beam paths, is opened and closed repeatedly to minimise sample irradiation. During each scan the sample undergoes six cycles of 15 s illumination and 3 min recovery. During the 15 s of illumination, the pump and probe beam run at an acquisition repetition rate of 1 kHz with a laser energy of 15 μJ for the pump excitation.

Transient Continuous-Wave EPR Spectroscopy

Photoexcitation of ^{3}***b*-PN** and ^{3}***b*-PN**$^{N-}$ was performed using an Ekspla laser with a repetition rate of 50 Hz and an excitation energy of $\sim$1 mJ/pulse. The laser light was directed to the sample though the optical window of the cryostat. The X-band transient EPR spectra were recorded at 20 K on a X-band Bruker Elexsys 680 spectrometer equipped with a helium gas flow cryostat from Oxford Instruments with a microwave power of 0.2–1.5 mW. Linearly polarized light with the desired excitation energy for magnetophotselelction experiments was obtained by combining a polarizer and $\lambda/2$ plate in the optical path. All other tr-EPR measurements were performed with depolarized light using a liquid crystal polymer depolarizer for the appropriate wavelength range. Protected silver mirrors were used as turning mirrors to ensure high reflectance of the laser light over a broad wavelength range.

Simulation Methods

The experimental transient EPR spectra were baseline corrected in both dimensions using the pre-laser spectrum and the off-resonant transients. Simulations of the spin-polarised triplet state spectra were performed using the EasySpin function *pepper*.[92] The zero–field splitting parameters D and E as well as the relative sublevel populations at zero-field were determined by least-squares fitting of the experimental time-resolved EPR data. The energetic ordering of the principal components of $\boldsymbol{D}$ was chosen as $|D_Z| > |D_X| > |D_Y|$ for the analysis of the spectra.

Computational Methods

The geometries of ***b*-PN** and ***b*-PN**$^{N-}$ (N = 2, 4, 6) were optimized in Turbomole using B3LYP as functional and the def2-SVP basis set.[353] The stationary nature of the converged geometries was confirmed by the absence of imaginary frequencies in the DFT calculated vibration spectra.

The geometries of the lowest-energy triplet excited states ^{3}***b*-PN** and ^{3}***b*-PN**$^{N-}$ were calculated in Orca with the B3LYP functional and the 6-31G* basis set without symmetry constraints.[226, 230, 231] The zero–field splitting parameters and spin densities of ^{3}***b*-PN** and ^{3}***b*-PN**$^{N-}$ were calculated in Orca using the triplet optimized geometries with B3LYP as functional and the EPRII basis set.[236, 237] Starting orbitals for CASSCF calculations of ^{3}***b*-P2**, ^{3}***b*-P2**$^{2-}$, ^{3}***b*-P4**, and ^{3}***b*-P4**$^{4-}$ were obtained from single point calculations with TPSSh as functional, and their order was adjusted, where necessary, through orbital rotations to obtain a symmetric pairing of spin orbitals.[354, 355] CASSCF calculations were performed with an active space of four electrons and four orbitals in Orca.

TD-DFT calculations[232] of neutral and fully reduced ***b*-PN** were performed using their optimized geometries in Gaussian 16 with the LC-ωHPBE (ω = 0.1 and 0.2) and TPSSh functionals, the 6-31G* basis set, and the PCM solvent model for THF.[222, 234]

4.6 Supplemental Results and Analysis

Steady State Absorption Spectroscopy

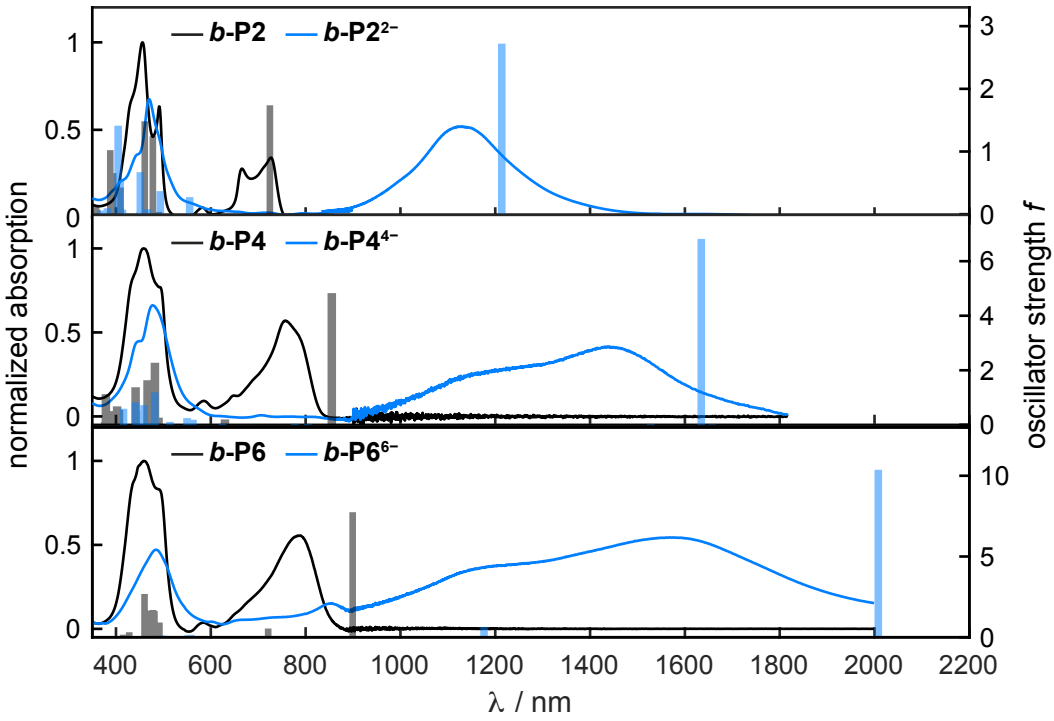


Figure 4.19: Steady-state UV-vis-NIR normalized absorption spectra of ***b*-P*N*** (black) and ***b*-P*N*$^{N-}$** (blue) ($N = 2$, 4, 6) from spectroelectrochemistry in THF (0.1 M Bu_4NPF_6, 298 K). The vertical bars indicate the TD-DFT (LC-ωHPBE/6-31G*; $\omega = 0.1$) calculated wavelengths and oscillator strengths f for the electronic transitions of the neutral and reduced oligomers in the absence of vibronic coupling.

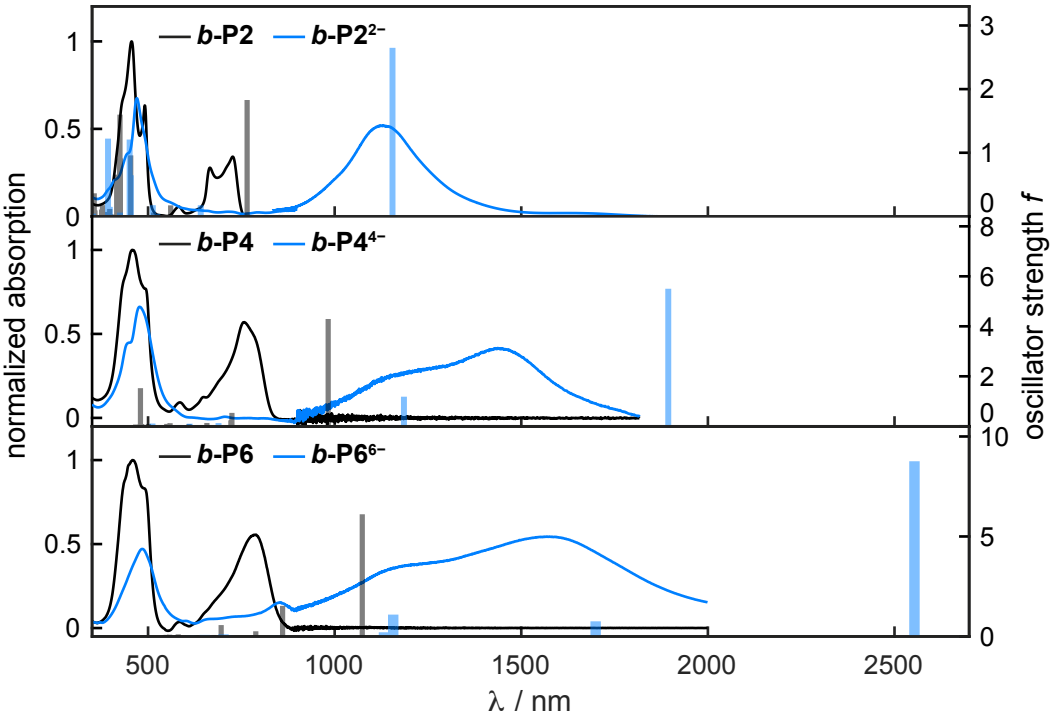


Figure 4.20: Steady-state UV-vis-NIR normalized absorption spectra of ***b*-P*N*** (black) and ***b*-P*N*$^{N-}$** (blue) ($N = 2$, 4, 6) from spectroelectrochemistry in THF (0.1 M Bu_4NPF_6, 298 K). The vertical bars indicate the TD-DFT (TPSSh/6-31G*) calculated wavelengths and oscillator strengths f for the electronic transitions of the neutral and reduced oligomers in the absence of vibronic coupling.

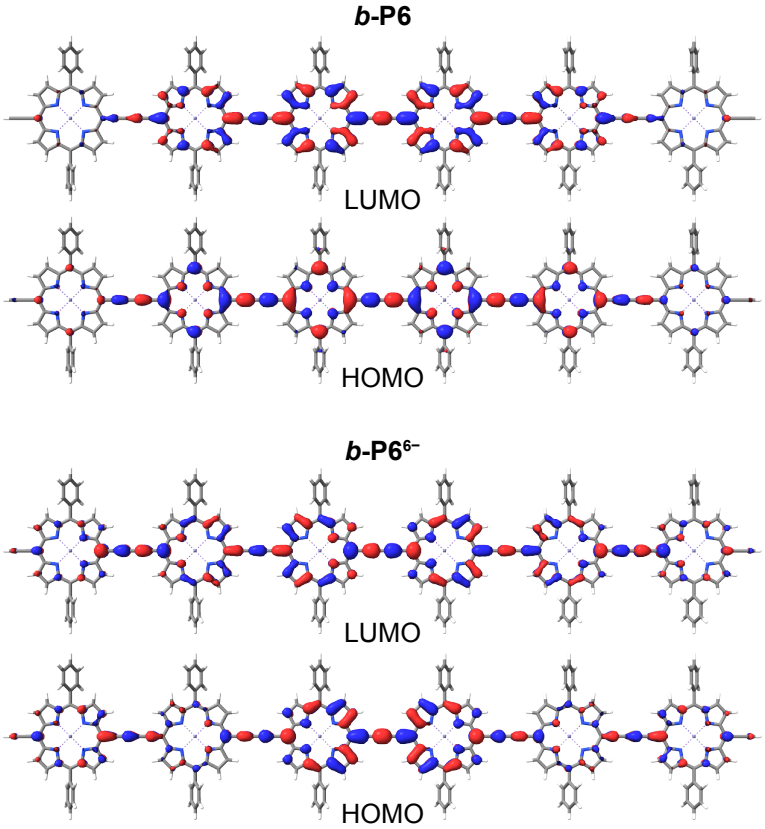


Figure 4.21: Visual representation of the DFT (LC-ωHPBE/6-31G*; $\omega = 0.2$) calculated highest occupied molecular orbitals (HOMO) and lowest unoccupied molecular orbitals (LUMO) of ***b*-P6** and ***b*-P6**$^{6-}$ plotted for an isovalue of 0.015

Transient Absorption Spectroscopy

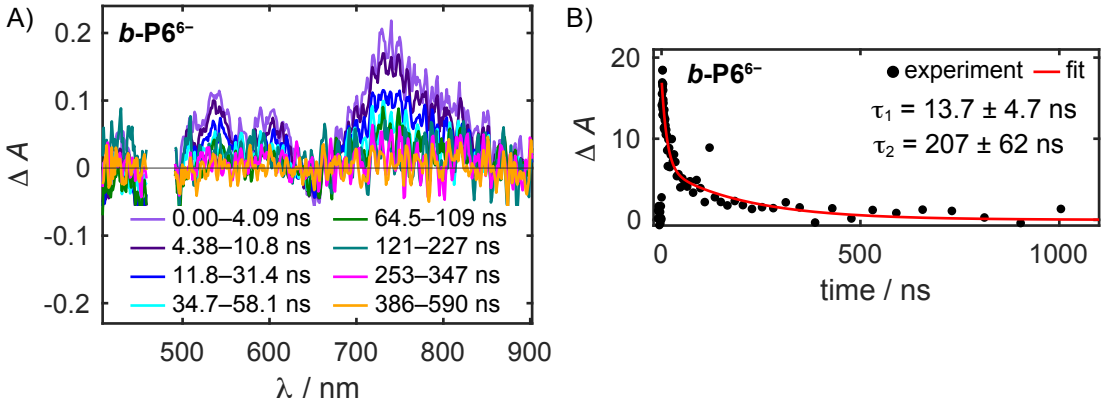


Figure 4.22: A) Time resolved transient absorption spectra of ***b*-P6**$^{6-}$ in frozen 2-methyltetrahydrofuran at 80 K following pump excitation at 480 nm with a laser pulse energy of about 7 μJ. B) Transient kinetics of photoexcited ***b*-P6**$^{6-}$ monitored between 650 and 850 nm and fitted to a biexponential decay to obtain the lifetimes τ_1 and τ_2.

Transient EPR Spectroscopy

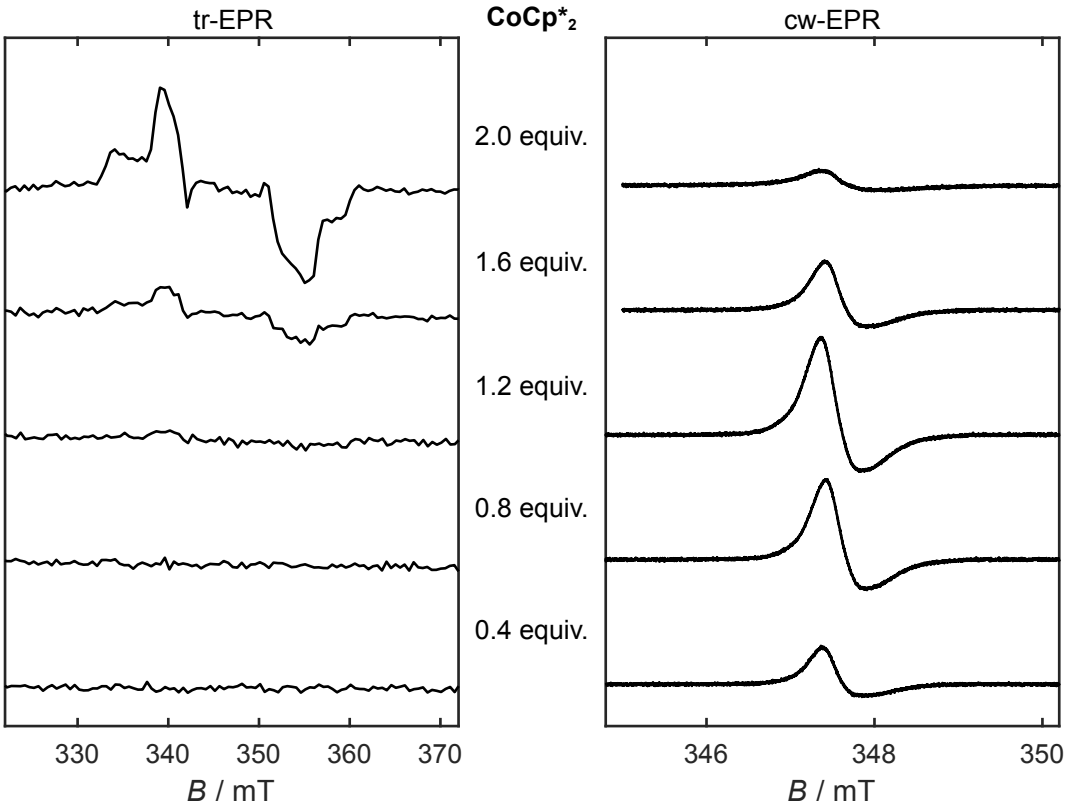


Figure 4.23: Reduction titration of ***b*-P2** with **CoCp*$_2$**. Each reduced sample was investigated by steady state cw-EPR spectroscopy and tr-EPR spectroscopy at X-band frequencies in frozen 2-methyltetrahydrofuran at 80 K. The tr-EPR spectra were recorded as an average over 400 ns after the laser pulse with depolarized light excitation at 1000 nm.

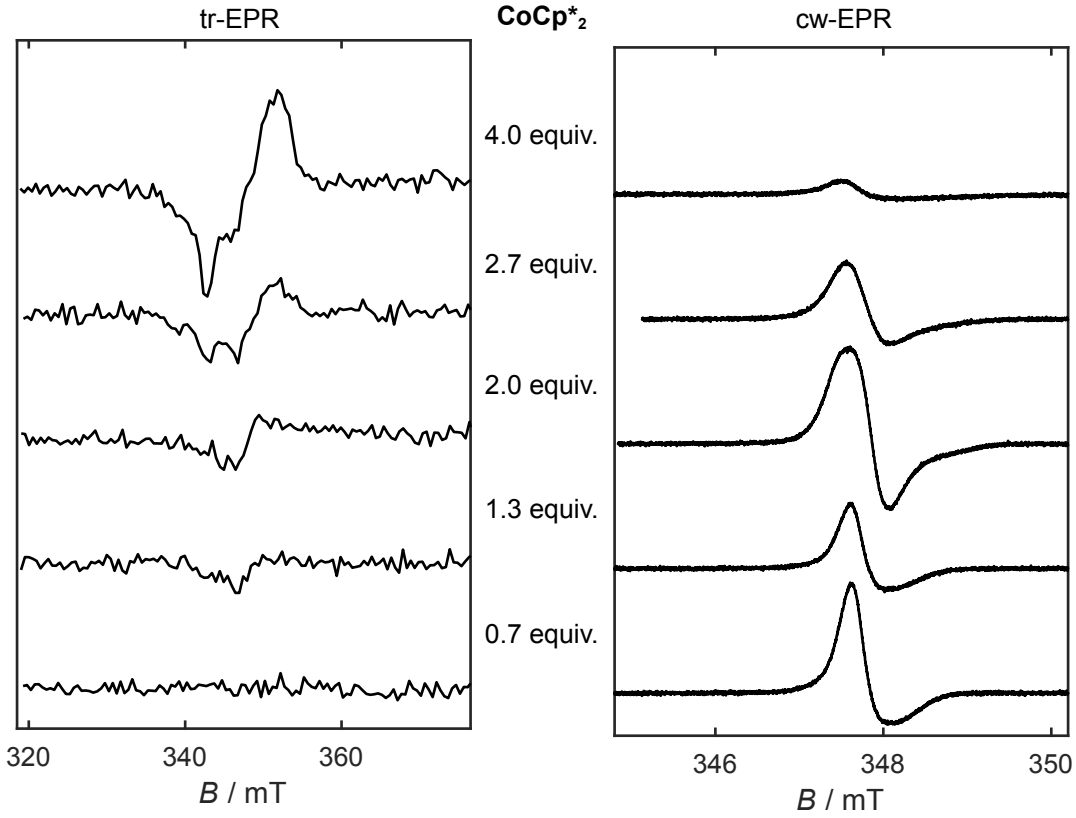


Figure 4.24: Reduction titration of ***b*-P4** with **CoCp*$_2$**. Each reduced sample was investigated by steady state cw-EPR spectroscopy and tr-EPR spectroscopy at X-band frequencies in frozen 2-methyltetrahydrofuran at 80 K. The tr-EPR spectra were recorded as an average over 400 ns after the laser pulse with depolarized light excitation at 1000 nm.

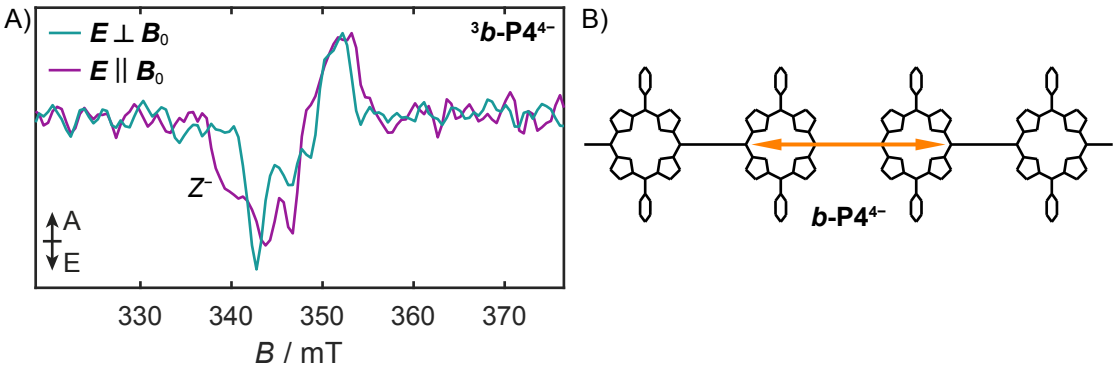


Figure 4.25: A) Magnetophotoselection spectra of ^{3}***b*-P4**$^{4-}$ with $\boldsymbol{E} \perp \boldsymbol{B}_0$ (dark green) and $\boldsymbol{E} \parallel \boldsymbol{B}_0$ (purple) at X-band frequencies in 2-methyltetrahydrofuran at 20 K. Both spectra were recorded as an average over 400 ns after the laser pulse with linearly polarized light at 1450 nm. B)Illustration of the orientation of the optical transition dipole moment (orange) in ***b*-P4**$^{4-}$ obtained from TD-DFT calculations (LC-ωPBE/6-31G*, $\omega = 0.2$).

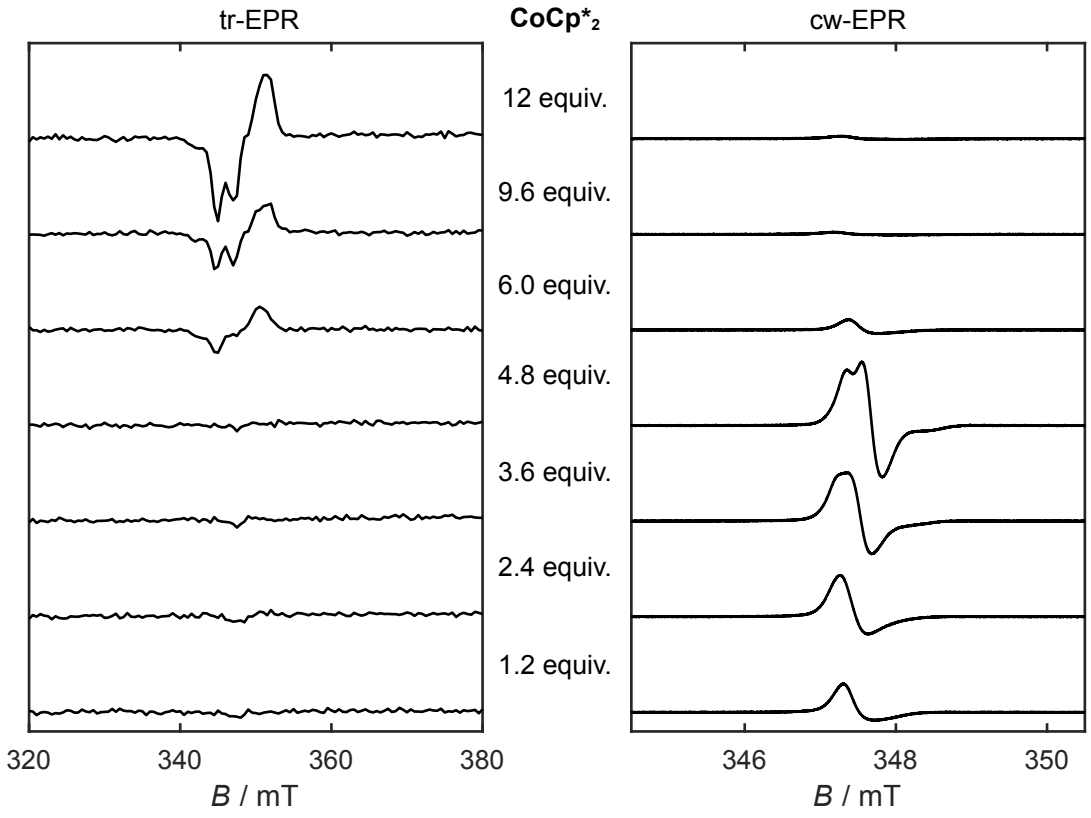


Figure 4.26: Reduction titration of ***b*-P6** with **CoCp*$_2$**. Each reduced sample was investigated by steady state cw-EPR spectroscopy and tr-EPR spectroscopy at X-band frequencies in frozen 2-methyltetrahydrofuran at 80 K. The tr-EPR spectra were recorded as an average over 400 ns after the laser pulse with depolarized light excitation at 1000 nm.

5

Global Aromaticity in a Partially Fused 8-Porphyrin Nanoring

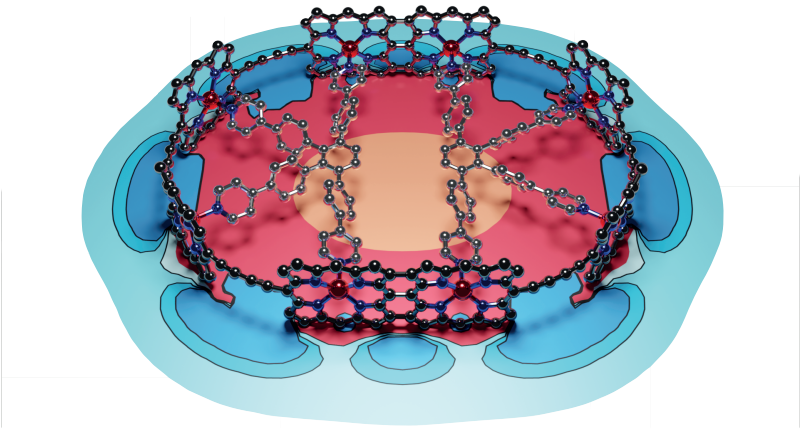
Contents

5.1 Abstract 208
5.2 Introduction 208
5.3 Results and Discussion 210
5.3.1 Molecular Design and Synthesis 210
5.3.2 UV-vis-NIR Absorption Spectroscopy 215
5.3.3 NMR Spectroscopy 217
5.3.4 Theoretical Analysis of Ring Currents 222
5.3.5 Experimental Relative Ring Current Strengths 225
5.4 Summary and Conclusions 227
5.5 Methods 228
5.5.1 General Methods 228
5.5.2 Synthetic Procedures 231
5.6 Supplemental Results and Analysis 249

The work in this chapter was published in:

S. M. Kopp, H. Gotfredsen, J.-R. Deng, T. D. W. Claridge, H. L. Anderson, *Global Aromaticity in a Partially Fused 8-Porphyrin Nanoring*, *J. Am. Chem. Soc.*, **2020**, *142*, 19393–19401.

5.1 Abstract



Template-directed synthesis has been used to prepare a fully π-conjugated cyclic porphyrin octamer, composed of both β,*meso*,β-edge-fused porphyrin tape units and butadiyne-linked porphyrins. The UV-vis-NIR spectra of this partially fused nanoring show that π-conjugation extends around the whole macrocycle, and that it has a smaller HOMO-LUMO gap than its all-butadiyne-linked analogue, as predicted by TD-DFT calculations. The ^{1}H NMR shifts of the bound templates confirm the disrupted aromaticity of the edge-fused porphyrins in the neutral nanoring. NMR oxidation titrations reveal the presence of a global paratropic ring current in its 4+ and 8+ oxidation states and of a global diatropic ring current in the 6+ state of the partially fused ring. The paratropic ring current in the 4+ oxidation state is about four times stronger than that in the all-butadiyne-linked cyclic octamer complex, whereas the diatropic current in the 6+ state is about 40% weaker. Two isomeric *K*-shaped tetrapyridyl templates with trifluoromethyl substituents at different positions were used to probe the distribution of the ring current in the 4+, 6+, and 8+ oxidation states by ^{19}F NMR, demonstrating that the ring currents are global and homogeneous.

5.2 Introduction

The edge-fused porphyrin nanoribbons pioneered by Osuka and studied in detail in Chapter 2 constitute the most "wire-like" family of soluble closed-shell oligomers, in the sense that their π-π*energy gaps fall steeply with increasing oligomer length, shifting

far into the IR,[108, 112, 113, 200, 212, 356–360] while their molecular conductances show only a shallow length-dependence.[201, 202, 267] Highly transmissive linear molecules with small bandgaps are in demand as components for single-molecule electronics[361] and as materials for thin-film devices.[362] Cyclic molecular wires, with efficient electronic transmission around the circumference of the ring, can exhibit enhanced performance as organic semiconductors because their high symmetries lead to greater delocalization than linear chains.[128] The presence of an aromatic (or antiaromatic) ring current is the most diagnostic signature of electronic delocalization in a molecular ring. Until recently, aromaticity was viewed as a property of small rings,[172] but in the past few years, global aromatic ring currents have been documented in large macrocycles with Hückel ($4n+2$) counts of 50-162 π-electrons and diameters of up to 5 nm.[55, 56, 173–177, 363] In this chapter, the first example of a fully π-conjugated macrocycle containing triply-linked porphyrin tape units together with an investigation of its global and local aromaticity is presented.

Previously, triply-linked porphyrin dimers have been incorporated into macrocycles by linking them with non-conjugated *meta*-phenylene bridges[364] or alkyl straps.[365] Osuka and co-workers also reported a remarkable triply linked square porphyrin tetramer with an antiaromatic cyclooctatetraene core.[366] The aromatic ring currents of the individual porphyrins are totally disrupted in this fused tetramer,[367] and the free-base N-H protons resonate at +13.3 and +12.2 ppm,[367] whereas a typical aromatic free-base porphyrin monomer gives an N-H ^{1}H NMR signal in the region between -2 to -4 ppm. A similar, but less dramatic, perturbation of the porphyrin ring currents is evident in porphyrin tapes. Free-base triply-linked porphyrin dimers give N-H signals at around +1.4 ppm,[357, 368–370] indicating that the aromatic (diatropic) ring current around the porphyrin is weaker than normal, while the naphthalene unit at the junction between the two porphyrins has a local antiaromatic (paratropic) ring current.[371–373]

Belt-shaped π-conjugated macrocycles have recently attracted great attention.[374–376] Nanobelts consisting of cyclic triply-linked porphyrin tapes[377] have not yet been synthesized, but a variety of arched porphyrin tapes have been reported,[378, 379] as well as porphyrin nanobelts lacking complete π-conjugation.[380, 381]

5.3 Results and Discussion

5.3.1 Molecular Design and Synthesis

The DFT (B3LYP/6-31G*) optimized geometry of the partially fused nanoring-template complex ***c*-P8[b_6f_2]·(T4)$_2$** (Figure 5.1) shows that two *K*-shaped **T4** templates fit well in the cavity of the ring. The complex is elliptical with approximate D_{2h} symmetry; its major and minor axis dimensions are 3.51 and 2.52 nm, respectively, measured between the centers of the butadiyne groups on the major axis (horizontal) and the centers of the β,*meso*,β-fused tape motifs (minor axis). The crystallographic Zn-Zn distances in β,*meso*,β-fused and butadiyne-linked porphyrin dimers are 0.85 and 1.35 nm, respectively.[64, 356, 357] This difference in Zn-Zn distance, together with the greater flexibility of butadiyne links, makes **T4** an extremely effective template for the synthesis of ***c*-P8[b_6f_2]**, because it prevents the formation of a stable 1:1 complex with linear porphyrin tetramer **H-*l*-P4[b_2f_1]-H**. The length of the four legs of **T4** is ideal for binding across butadiyne-linked porphyrin motifs, while the Zn-centers of the fused porphyrin dimer unit are too close together to chelate with a single **T4** molecule (Scheme 5.1).

The partially fused nanoring was synthesized by palladium-catalyzed oxidative coupling of the linear porphyrin tetramer **H-*l*-P4[b_2f_1]-H** in the presence of **T4** (Scheme 5.1A) to give ***c*-P8[b_6f_2]·(T4)$_2$** in 72% isolated yield (see Figure 5.2A for the analytical GPC trace of the crude reaction mixture). Please refer to Scheme 5.4 for the detailed synthetic pathway of ***c*-P8[b_6f_2]·(T4)$_2$** including the formation of the partially fused linear porphyrin tetramer. The all-butadiyne-linked analogue ***c*-P8[b_8]·(T4)$_2$** was synthesized from **H-*l*-P4[b_3]-H** and **T4** under identical reaction conditions in 37% yield (Scheme 5.1B).[382] This yield is comparable to those

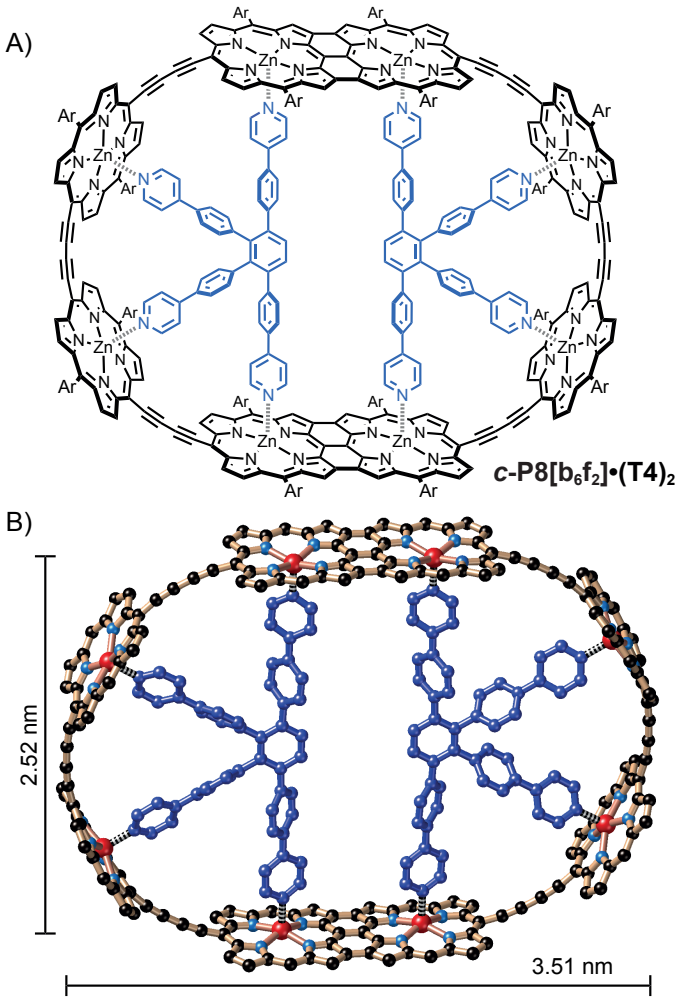
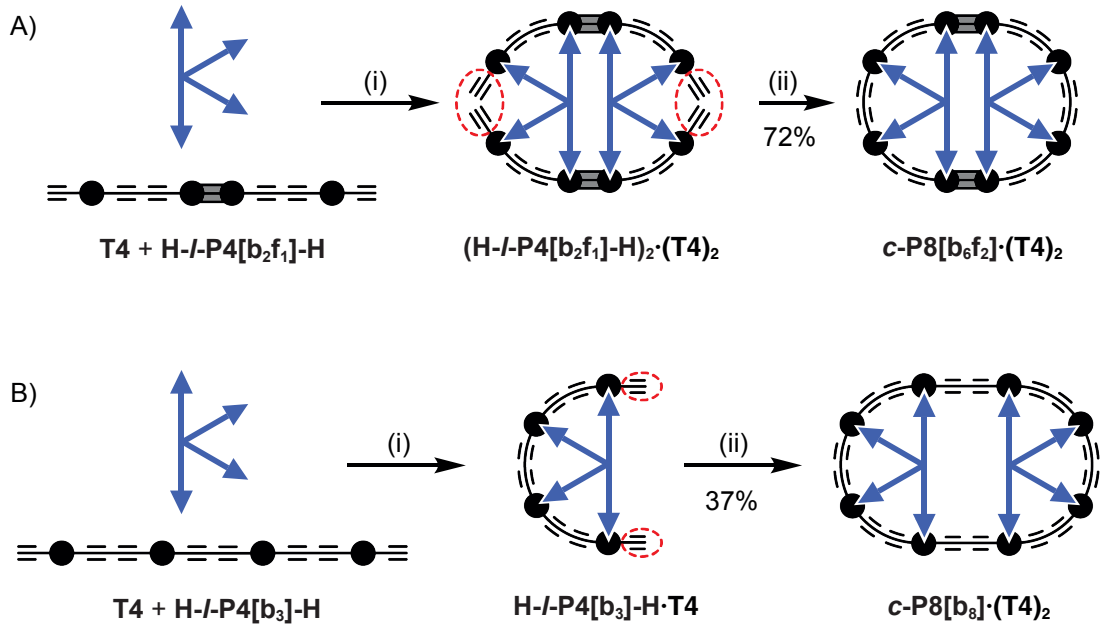


Figure 5.1: A) Chemical structure and B) calculated geometry of ***c*-P8[b_6f_2]·(T4)$_2$**. The geometry was optimized by DFT (LC-ωhPBE/6-31G*;$\omega = 0.1$); 3,5-bis(trihexylsilyl)-phenyl solubilizing groups were replaced by hydrogen to simplify the calculations. Hydrogen atoms are omitted for clarity. Ar = 3,5-bis(trihexylsilyl)phenyl.

previously reported for this and similar porphyrin nanorings (25–40%).[67, 382–384] The higher yield of ***c*-P8[b_6f_2]·(T4)$_2$** probably reflects the preorganization of the components in the 2:2 complex **(H-*l*-P4[b_2f_1]-H)$_2$·(T4)$_2$**. In contrast, **H-*l*-P4[b_3]-H** forms a 1:1 complex **H-*l*-P4[b_3]-H·T4**, which must couple intermolecularly, followed by an intramolecular coupling to form ***c*-P8[b_8]·(T4)$_2$**. This process is less efficient, as shown by the lower yield and complex analytical GPC trace of the crude reaction mixture (Figure 5.2B). Formation of a 2:2 complex by **H-*l*-P4[b_2f_1]-H** and **T4** was confirmed by ^{1}H diffusion NMR spectroscopy of the complex.[385] Relevant precursors and reference compounds for the synthesis and spectroscopic investigation of ***c***-

P8[b$_6$f$_2$]·(T4)$_2$ are summarized in Figure 5.3. Tetramer **Si-*l*-P4[b$_3$]-Si** was synthesized following a published procedure,[285] while octamer **H-*l*-P8[b$_5$f$_2$]-H** was isolated as a byproduct during the synthesis of ***c*-P8[b$_6$f$_2$]·(T4)$_2$** (Figure 5.2A).



Scheme 5.1: Representation of the template-directed synthesis of A) ***c*-P8[b$_6$f$_2$]·(T4)$_2$** and B) ***c*-P8[b$_8$]·(T4)$_2$**. Reaction conditions: (i) $CHCl_3$; (ii) $Pd(PPh_3)_2Cl_2$, CuI, 1,4-benzoquinone, *i*-Pr_2NH, $CHCl_3$, 20 °C.

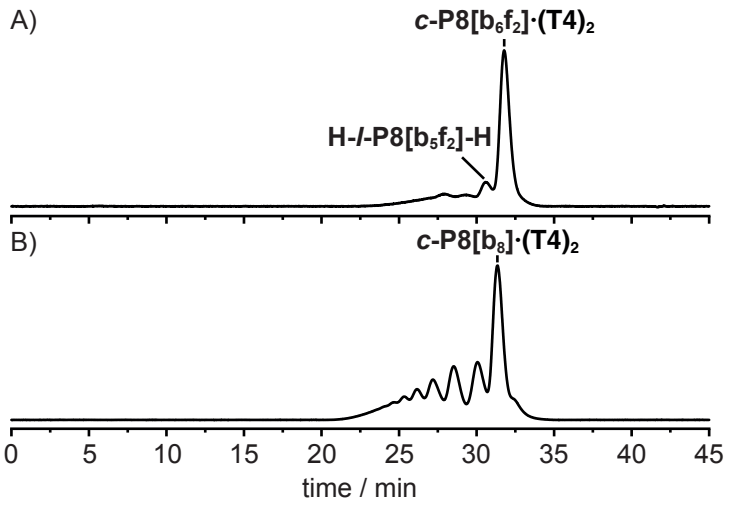
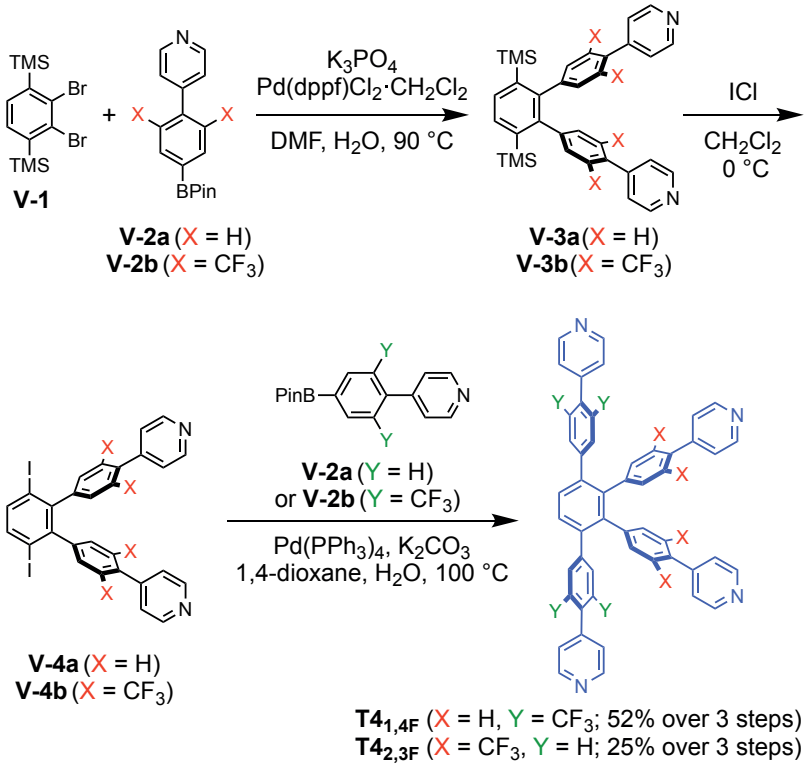


Figure 5.2: Comparison of the analytical GPC traces (THF + 1% pyridine, $\lambda_{ex} = 440$ nm) of the crude reaction mixtures for the synthesis of A) ***c*-P8[b$_6$f$_2$]·(T4)$_2$** and B) ***c*-P8[b$_8$]·(T4)$_2$** .

Two *K*-shaped **T4** templates with CF_3 groups positioned on the 1,4- or 2,3-legs, $\mathbf{T4_{1,4F}}$ and $\mathbf{T4_{2,3F}}$, respectively, were synthesized to probe the aromaticity in the edge-fused and butadiyne-linked regions of ***c*-P8[b$_6$f$_2$]** by ^{19}F NMR spectroscopy (Scheme 5.2).[55] Reaction of 2,3-dibromo-1,4-bis-(trimethylsilyl)benzene **V-1** with boronic ester **V-2** in a 2-fold Suzuki coupling introduced the pyridyl legs at the 2 and 3 positions of the template core. Unmasking of the 1 and 4 positions of **V-3** by substitution of the trimethylsilyl groups with iodine, followed by a further 2-fold Suzuki coupling, afforded templates $\mathbf{T4_{1,4F}}$ and $\mathbf{T4_{2,3F}}$. The regioselectively fluorinated complexes ***c*-P8[b$_6$f$_2$]·(T4$_{1,4F}$)$_2$** and ***c*-P8[b$_6$f$_2$]·(T4$_{2,3F}$)$_2$** and their all-butadiyne-linked counterparts ***c*-P8[b$_8$]·(T4$_{1,4F}$)$_2$** and ***c*-P8[b$_8$]·(T4$_{2,3F}$)$_2$** were formed by complexation of $\mathbf{T4_{1,4F}}$ and $\mathbf{T4_{2,3F}}$ with the respective free nanorings (Scheme 5.3, Scheme 5.4).



Scheme 5.2: Synthesis of regioselectively fluorinated templates $\mathbf{T4_{1,4F}}$ and $\mathbf{T4_{2,3F}}$.

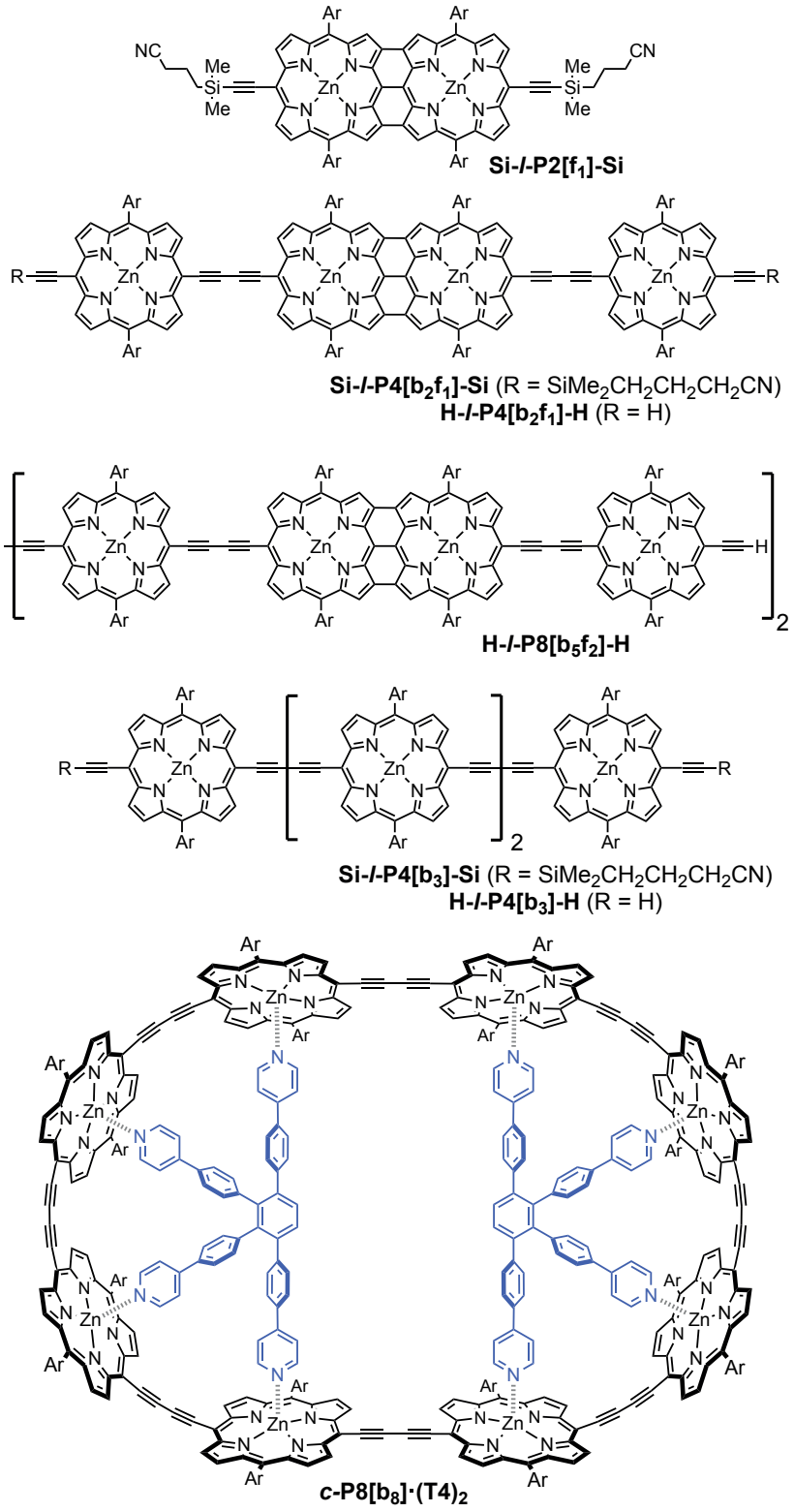


Figure 5.3: Chemical structures of synthetic precursors and reference compounds; Ar = 3,5-bis(trihexylsilyl)phenyl.

5.3.2 UV-vis-NIR Absorption Spectroscopy

As expected,[113, 200] the lowest energy absorption band of ***c*-P8[b$_6$f$_2$]·(T4)$_2$** (λ_{max} = 1304 nm) is substantially red-shifted compared with that of ***c*-P8[b$_8$]·(T4)$_2$** (λ_{max} = 860 nm; Figure 5.4A). Both template-free nanorings, ***c*-P8[b$_6$f$_2$]** (λ_{max} = 1158 nm) and ***c*-P8[b$_8$]** (λ_{max} = 759 nm), give spectra that are broader and more blue-shifted compared with the **T4** complexes, reflecting the more disordered, less π-conjugated, conformations of the template-free rings. The onset of the lowest energy absorption band of ***c*-P8[b$_6$f$_2$]** is approximately coincident with that of ***c*-P8[b$_6$f$_2$]·(T4)$_2$**. This indicates that ***c*-P8[b$_6$f$_2$]** is more rigid than ***c*-P8[b$_8$]**, as expected from the stiffness of the β,*meso*,β-fused tape unit.

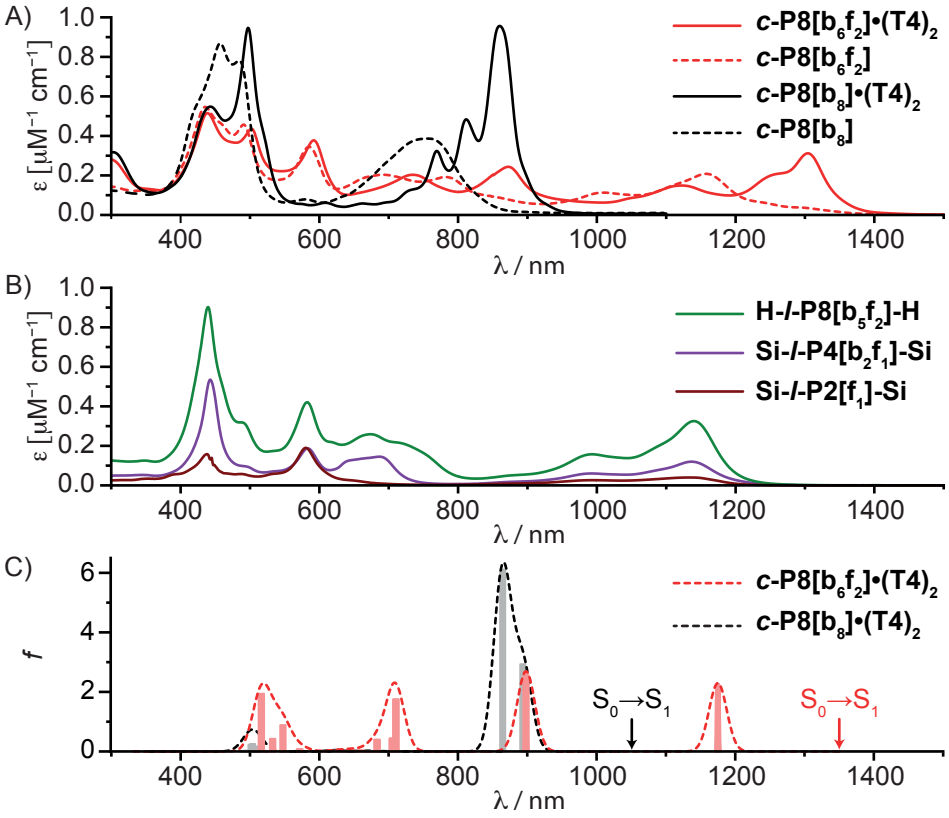


Figure 5.4: UV-vis-NIR absorption spectra of A) ***c*-P8[b$_6$f$_2$]**, ***c*-P8[b$_6$f$_2$]·(T4)$_2$**, ***c*-P8[b$_8$]**, and ***c*-P8[b$_8$]·(T4)$_2$**, and B) **H-*l*-P8[b$_5$f$_2$]-H**, **Si-*l*-P4[b$_2$f$_1$]-Si**, and **Si-*l*-P2[f$_1$]-Si** in $CHCl_3$ at 298 K.C) TD-DFT (LC-ωhPBE/6-31G* (ω = 0.1)) spectra of ***c*-P8[b$_6$f$_2$]·(T4)$_2$** and ***c*-P8[b$_8$]·(T4)$_2$** with envelopes plotted for a Gaussian line width of 50 nm. The arrows indicate the calculated position of the dipole forbidden $S_0 \rightarrow S_1$ transitions.

Comparison of the absorption spectra of the linear dimer **Si-*l*-P2[$\mathbf{f_1}$]-Si** (λ_{max} = 1133 nm), tetramer **Si-*l*-P4[$\mathbf{b_2f_1}$]-Si** (λ_{max} = 1137 nm), and octamer **H-*l*-P8[$\mathbf{b_5f_2}$]-H** (λ_{max} = 1140 nm, Figure 5.4B) shows that there is only weak communication between the edge-fused and butadiyne-linked porphyrin units. The absorption spectra of **H-*l*-P8[$\mathbf{b_5f_2}$]-H** and ***c*-P8[$\mathbf{b_6f_2}$]** are similar, although the peak for the cyclic compound is red-shifted by 18 nm and its absorption is more intense in the 1200–1400 nm region, reflecting an increase in π-conjugation in the closed ring. The calculated absorption spectra of ***c*-P8[$\mathbf{b_6f_2}$]·(T4)$_2$** and ***c*-P8[$\mathbf{b_8}$]·(T4)$_2$** from time-dependent DFT (TD-DFT) at the LC-ωhPBE/6-31G* ($\omega = 0.1$) level of theory (Figure 5.4C) reproduce the strong bathochromic shift of the lowest energy absorption band of ***c*-P8[$\mathbf{b_6f_2}$]·(T4)$_2$**. These calculations predict that $S_0 \rightarrow S_1$ transitions are dipole forbidden ($f = 0$) in both rings, and that the lowest energy absorption bands are dominated by $S_0 \rightarrow S_2$ transitions, as found in most π-conjugated macrocycles[386–388] such as porphyrin nanorings.[67–69] The natural transition orbitals for the $S_0 \rightarrow S_2$ transition of ***c*-P8[$\mathbf{b_6f_2}$]·(T4)$_2$** (Figure 5.5A) are concentrated around the two tape regions, but they also extend to the adjacent butadiyne and porphyrin units. In contrast, the natural transition orbitals for the $S_0 \rightarrow S_2$ transition in ***c*-P8[$\mathbf{b_8}$]·(T4)$_2$** (Figure 5.5B) are delocalized over the whole ring with the highest density on the most curved regions of the ellipse.

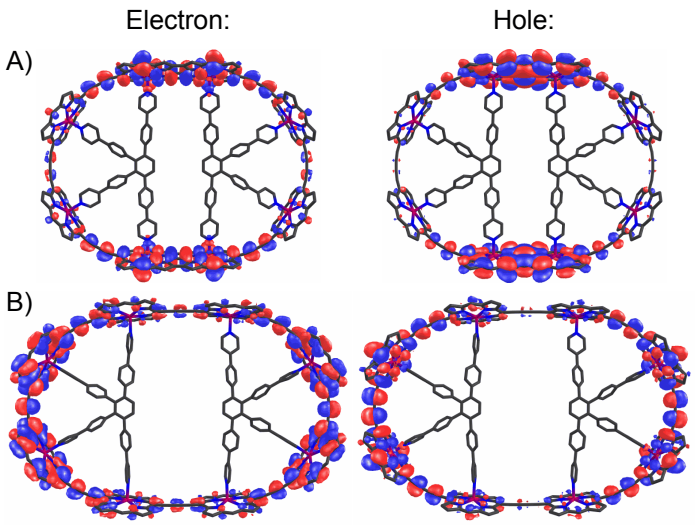


Figure 5.5: Initial (left) and final (right) state of representative natural transition orbital pairs for the $S_0 \rightarrow S_2$ transition of A) ***c*-P8[b$_6$f$_2$]·(T4)$_2$** and B) ***c*-P8[b$_8$]·(T4)$_2$** calculated at the LC-ωhPBE/6-31G* ($\omega = 0.1$) level of theory.

5.3.3 NMR Spectroscopy

^{1}H and ^{19}F NMR spectroscopy were used to confirm the structures of ***c*-P8[b$_6$f$_2$]·(T4)$_2$**, ***c*-P8[b$_6$f$_2$]·(T4$_{1,4F}$)$_2$**, and ***c*-P8[b$_6$f$_2$]·(T4$_{2,3F}$)$_2$** and to investigate the magnetic (de)shielding effects in the oxidized nanoring complexes. The labeled structures and ^{1}H NMR spectra of neutral ***c*-P8[b$_6$f$_2$]·(T4)$_2$** and ***c*-P8[b$_8$]·(T4)$_2$** are shown in Figure 5.6A,B. Two distinct environments are present in the partially fused nanoring complex which give rise to two α (α_1 and α_2) and β (β_1 and β_2) pyridyl template ^{1}H NMR resonances. In neutral ***c*-P8[b$_6$f$_2$]·(T4)$_2$**, the shielding of the α_1 and β_1-pyridyl protons ($\delta_H = 5.59$ and 6.34 ppm) by the local magnetic field of the fused porphyrin units is substantially weaker than the shielding of the α_2 and β_2 resonances ($\delta_H = 2.41$ and 5.23 ppm) close to the butadiyne-linked porphyrin region. This can be rationalized by the weaker aromatic character of the fused porphyrins, and by the paratropic ring current contribution from the central naphthalene unit (Figure 5.6C).[368–373]

^{1}H and ^{19}F NMR oxidation titrations were carried out by treating the porphyrin nanoring complexes with thianthrenium hexafluoroantimonate **ThnSbF$_6$** in CD_2Cl_2 at −50°C. The evolution of the NMR resonances during the oxidation titrations shows the

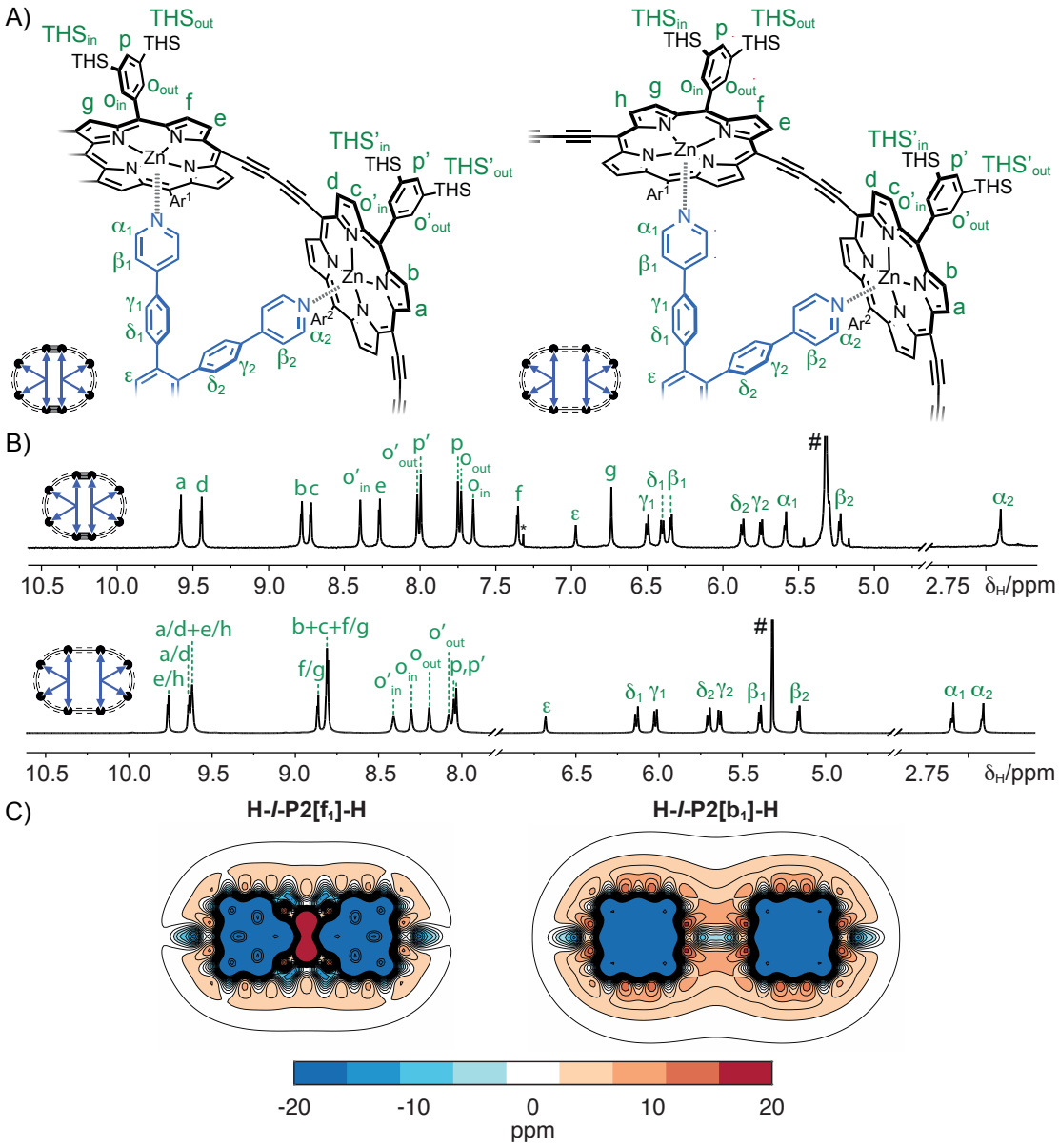


Figure 5.6: A) Symmetrical units of the molecular structures of the nanoring complexes ***c*-P8[b_6f_2]·(T4)$_2$** and ***c*-P8[b_8]·(T4)$_2$** with their respective labeling schemes. B) Assigned ^{1}H NMR (500 MHz, CD_2Cl_2, 298 K) spectra of ***c*-P8[b_6f_2]·(T4)$_2$** and ***c*-P8[b_8]·(T4)$_2$** . The THS signals at ca. δ_H = 1.7–0.5 ppm are omitted for clarity. Peaks assigned with # arise from CH_2Cl_2. C) NICS(0)$_{ZZ}$ plots of linear oligomers **H-*l*-P2[f_1]-H** and **H-*l*-P2[b_1]-H** calculated with LC-ωhPBE (ω = 0.1) as functional and the 6-31G* basis set.

emergence of characteristic ^{1}H and ^{19}F NMR signals from the 4+ to the 8+ oxidation state, that were assigned based on the equivalents of oxidant added to the complex. The endpoint of the NMR titrations was determined from the disappearance of the ^{1}H NMR resonances of thianthrene due to strong broadening caused by fast exchange between neutral thianthrene and excess **ThnSbF$_6$**. The complete progression of the ^{1}H and ^{19}F resonances during an NMR titration is exemplified for ***c*-P8[b$_6$f$_2$]·(T4$_{2,3F}$)$_2$** in Figure 5.7 (please refer to Figure 5.12, Figure 5.13, Figure 5.14, and Figure 5.15 for the complete oxidation titrations of ***c*-P8[b$_6$f$_2$]·(T4)$_2$**, ***c*-P8[b$_6$f$_2$]·(T4$_{1,4F}$)$_2$**, ***c*-P8[b$_8$]·(T4$_{1,4F}$)$_2$** and ***c*-P8[b$_8$]·(T4$_{2,3F}$)$_2$**, respectively). No NMR signals were observed for the 0, 1+, 2+, and 3+ oxidation states at −50 °C due to the poor solubility of the neutral and moderately charged nanoring complexes in cold CD_2Cl_2.[55, 56]

The labeled structures and ^{1}H NMR spectra of ***c*-P8[b$_6$f$_2$]·(T4)$_2$**, together with the ^{19}F NMR spectra of ***c*-P8[b$_6$f$_2$]·(T4$_{1,4F}$)$_2$**, and ***c*-P8[b$_6$f$_2$]·(T4$_{2,3F}$)$_2$**, in the neutral and oxidized states are shown in Figure 5.8. Figure 5.16, Figure 5.17, Figure 5.18, Figure 5.19, and Figure 5.20 show the NMR spectra of all investigated nanoring complexes in the prominent oxidation states. The ^{1}H NMR spectra of oxidized ***c*-P8[b$_6$f$_2$]·(T4)$_2$** reveal the presence of global antiaromatic and aromatic ring currents. Strong evidence for an antiaromatic ring current in the 4+ oxidation state is provided by deshielded α_1 and α_2 resonances ($\delta_H = 13.87$ and 16.39 ppm vs 8.62 and 8.56 ppm, respectively, in the free template). In the 6+ oxidation state, the template ^{1}H resonances are broad and poorly resolved, but the shielded **T4** envelope ($\delta_H = 3.8$–2.7 ppm) indicates that the 6+ state is globally aromatic. The ^{1}H NMR spectrum becomes sharp again in the 8+ state and the deshielded α_1 and α_2 resonances ($\delta_H = 8.97$ and 9.09 ppm, respectively) indicate the presence of a weak global antiaromatic ring current.

Additional evidence is provided by the ^{1}H NMR signals of the trihexylsilyl (THS) groups of the porphyrins. Interconversion of the THS environments pointing inside (THS_{in}) and outside (THS_{out}) the ring is slow on the NMR timescale, and the THS_{in}

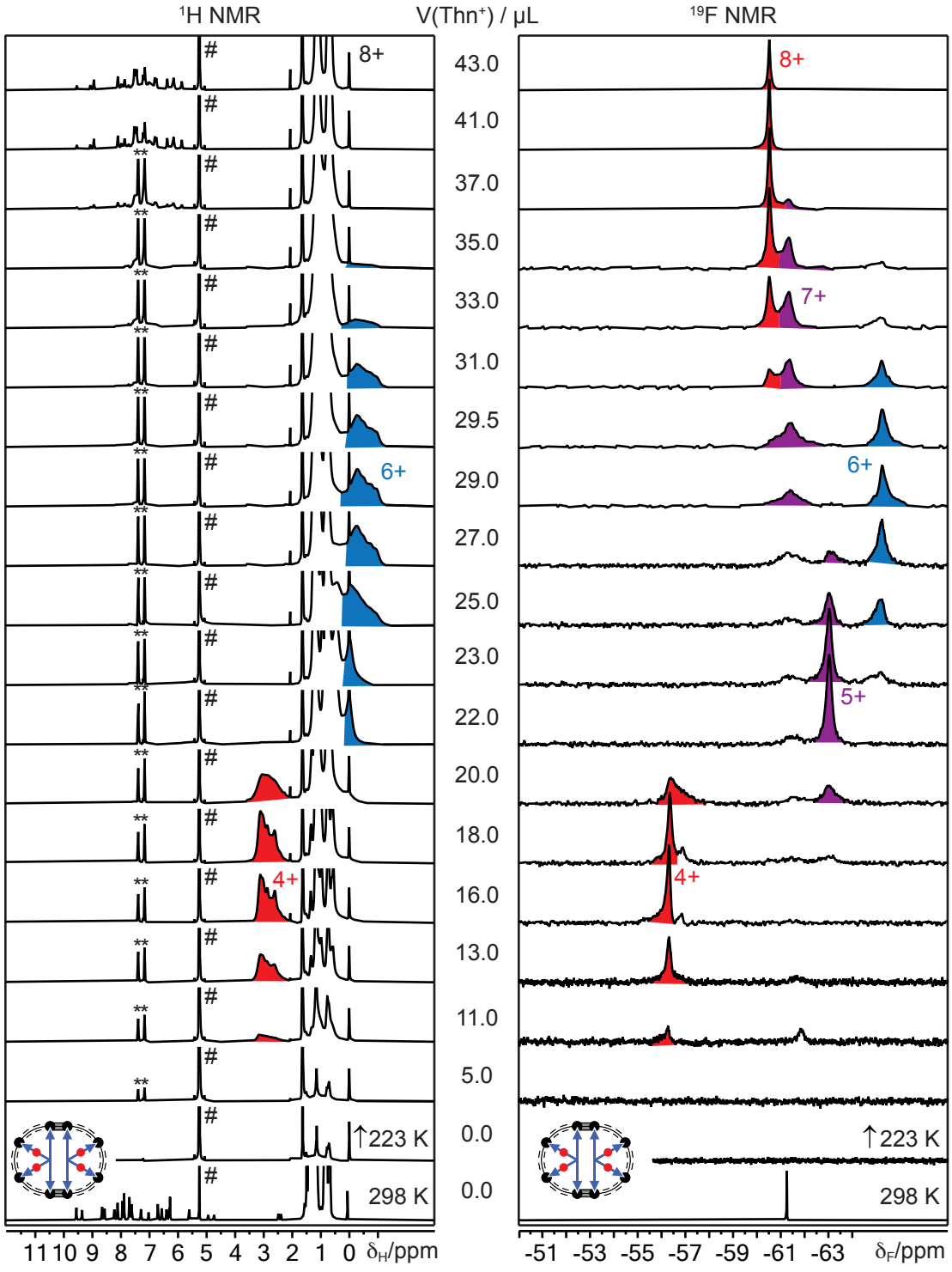


Figure 5.7: Summary of the ^{1}H and ^{19}F NMR titration of ***c*-P8[b$_6$f$_2$]·(T4$_{2,3F}$)$_2$** (500/471 MHz, 223 K) with **ThnSbF$_6$** in CD_2Cl_2; 4.5 µL Thn^+ solution contain about 1 equivalent of oxidant. Shifted $THS^{(\cdot)}_{in}$ and CF_3 resonances indicating global antiaromaticity are highlighted in red; those indicating global aromaticity are highlighted in blue. Odd-numbered oxidation states are highlighted in purple in the ^{19}F NMR spectra. Peaks assigned with # and * arise from CD_2Cl_2 and neutral thianthrene, respectively.

signals are readily assigned via their nuclear Overhauser correlations to template resonances. In each oxidation state, the THS_{out} signals appear essentially unshifted at 2.0–0.5 ppm, as they are located outside the induced magnetic cone of the global ring current. In contrast, the THS_{in} resonances (colored green in Figure 5.8B) are affected by the magnetic field induced by the global ring currents; they are deshielded in the antiaromatic 4+ and shielded in the aromatic 6+ oxidation state. In the fully oxidized 8+ state, the global antiaromatic character is too weak to cause a significant splitting of the THS resonances. The global ring currents deduced from the ^{1}H NMR spectra of ***c*-P8[$\mathbf{b_6f_2}$]·$\mathbf{(T4)_2}$** in the 4+, 6+, and 8+ oxidation states are seen more clearly from the ^{19}F NMR spectra of ***c*-P8[$\mathbf{b_6f_2}$]·$\mathbf{(T4_{1,4F})_2}$** and ***c*-P8[$\mathbf{b_6f_2}$]·$\mathbf{(T4_{2,3F})_2}$** in these same oxidation states (Figure 5.8B, right-hand panels). The ^{19}F resonance is deshielded by 5.95 and 5.15 ppm in the antiaromatic nanoring complexes ***c*-P8[$\mathbf{b_6f_2}$]·$\mathbf{(T4_{1,4F})_2}^{4+}$** and ***c*-P8[$\mathbf{b_6f_2}$]·$\mathbf{(T4_{2,3F})_2}^{4+}$**, respectively. Conversely, the ^{19}F resonance is shielded by 4.03 and 4.19 ppm in the aromatic 6+ states, respectively. In the marginally antiaromatic 8+ state, the ^{19}F resonance is deshielded by 0.41 and 0.76 ppm, respectively. The magnitudes of the shifts in the 4+, 6+, and 8+ oxidation states are consistent with the previous observation that global ring currents are strongest in mixed-valence systems, when the individual porphyrin units are in fractional oxidation states;[55] thus a strong ring current is observed in the 4+ state in which the average oxidation state of the porphyrin units is 0.5+.

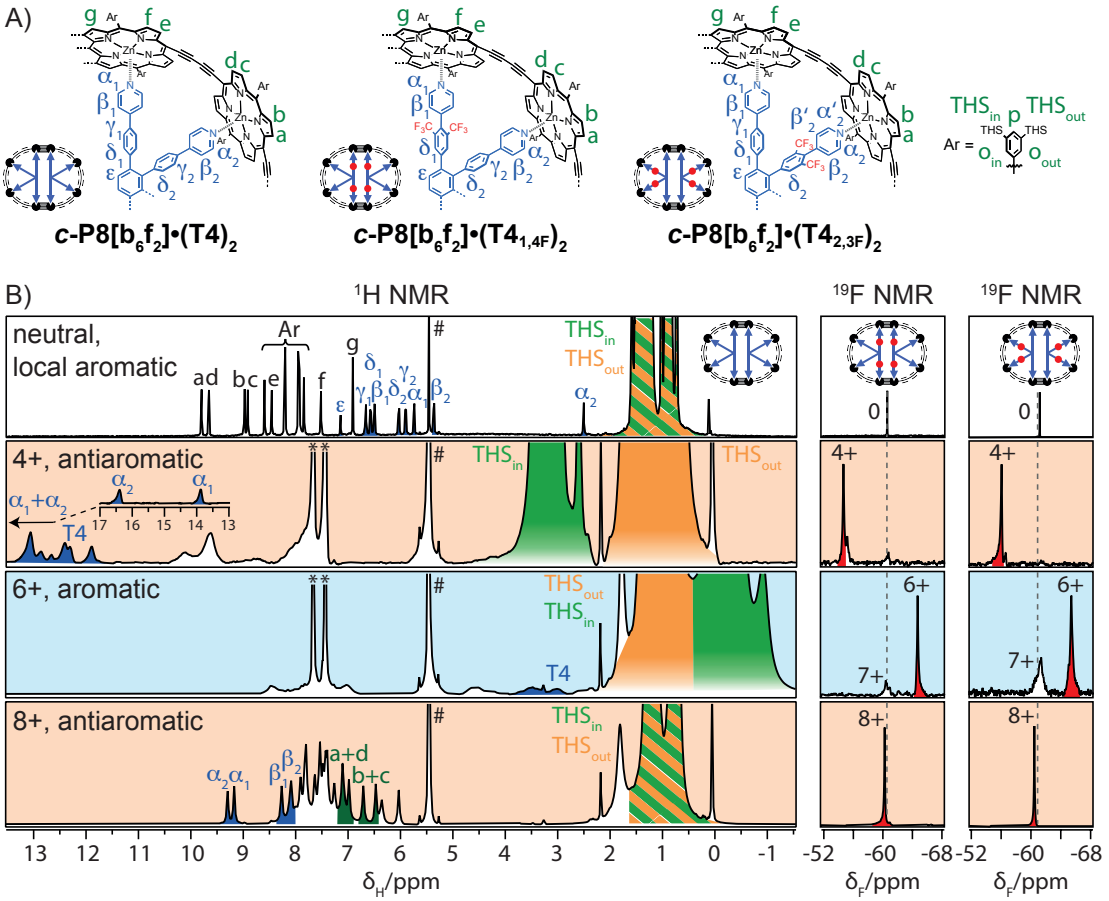


Figure 5.8: A) Symmetrical units of the molecular structures of the nanoring complexes ***c*-P8[b_6f_2]·(T4)$_2$** , ***c*-P8[b_6f_2]·(T4$_{1,4F}$)$_2$**, and ***c*-P8[b_6f_2]·(T4$_{2,3F}$)$_2$** with their respective labeling schemes and cartoon representations. B) ^{1}H NMR spectra of ***c*-P8[b_6f_2]·(T4)$_2$** and ^{19}F NMR spectra of ***c*-P8[b_6f_2]·(T4$_{1,4F}$)$_2$** and ***c*-P8[b_6f_2]·(T4$_{2,3F}$)$_2$** in the predominant oxidation states 0, 4+, 6+, and 8+; # and * denote CD_2Cl_2 and thianthrene signals, respectively. The dashed line in the ^{19}F NMR spectra indicates the chemical shift of the CF_3 resonance in the unbound template.

5.3.4 Theoretical Analysis of Ring Currents

The assignment of the (anti)aromatic character of the different oxidation states is supported by nucleus-independent chemical shift (NICS) and anisotropy of the induced current density (ACID) calculations shown in Figure 5.9. All calculations were performed at the LC-ωhPBE/6-31G* ($\omega = 0.1$) level of theory, which has previously been established to give reliable predictions for the global magnetic properties of oxidized porphyrin nanorings.[55] The calculations corroborate the existence of local aromaticity in the neutral state, global antiaromaticity in the 4+ state, and global

aromaticity in the 6+ state. The small positive NICS(0)$_{ZZ}$ values and the absence of a strong global ring current in the ACID calculations of the 8+ state suggest a mixture of global and local effects,leading only to weak deshielding of the template resonances.

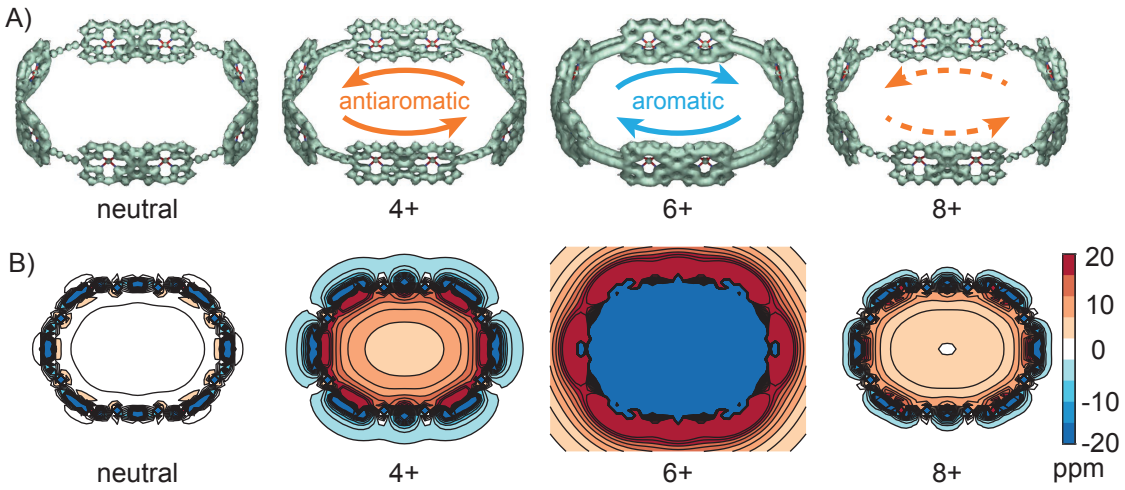


Figure 5.9: A) ACID isosurfaces (LC-ωhPBE/6-31G*, $\omega = 0.1$) of ***c*-P8[$\mathbf{b_6f_2}$]** in each oxidation state. Orange and blue arrows indicate the direction of global paratropic and diatropic ring currents, respectively. The magnetic field vector is pointing upward through the cavity of the nanorings. B) NICS(0)$_{ZZ}$ grids in the *xy* plane (LC-ωhPBE/6-31G*, ω=0.1) of ***c*-P8[$\mathbf{b_6f_2}$]** in each oxidation state.

The assignment of the global (anti)aromatic character of ***c*-P8[$\mathbf{b_6f_2}$]·(T4)$_2$$^{Q+}$** is also in agreement with Hückel's rule. The porphyrin tape units show two formal π-conjugation pathways (Figure 5.10). Depending on the pathway, each tape unit contributes either 16 or 20 electrons to the Hückel π-electron count. Together with the ten electrons per isolated porphyrin unit and the four electrons per butadiyne linker, this results in a total Hückel count of 104 or 96 π-electrons in the neutral nanoring ***c*-P8[$\mathbf{b_6f_2}$]**. Consequently, the delocalization pathways in the globally antiaromatic 4+ and 8+ oxidation states consist of $4n$ π-electrons (4+: 100/92 π-e$^-$; $n = 25/23$ and 8+: 96/88 π-e$^-$; $n = 24/22$), whereas the aromatic 6+ oxidation state exhibits a $4n$+2 π-electron (98/90 π-e$^-$; $n = 24/22$) pathway. The larger ACID isosurfaces at the *meso-meso* links of the porphyrin tape motifs of ***c*-P8[$\mathbf{b_6f_2}$]$^{4+}$** and ***c*-P8[$\mathbf{b_6f_2}$]$^{6+}$** suggests that the higher electron count pathways dominate the ring currents (Figure 5.9A).

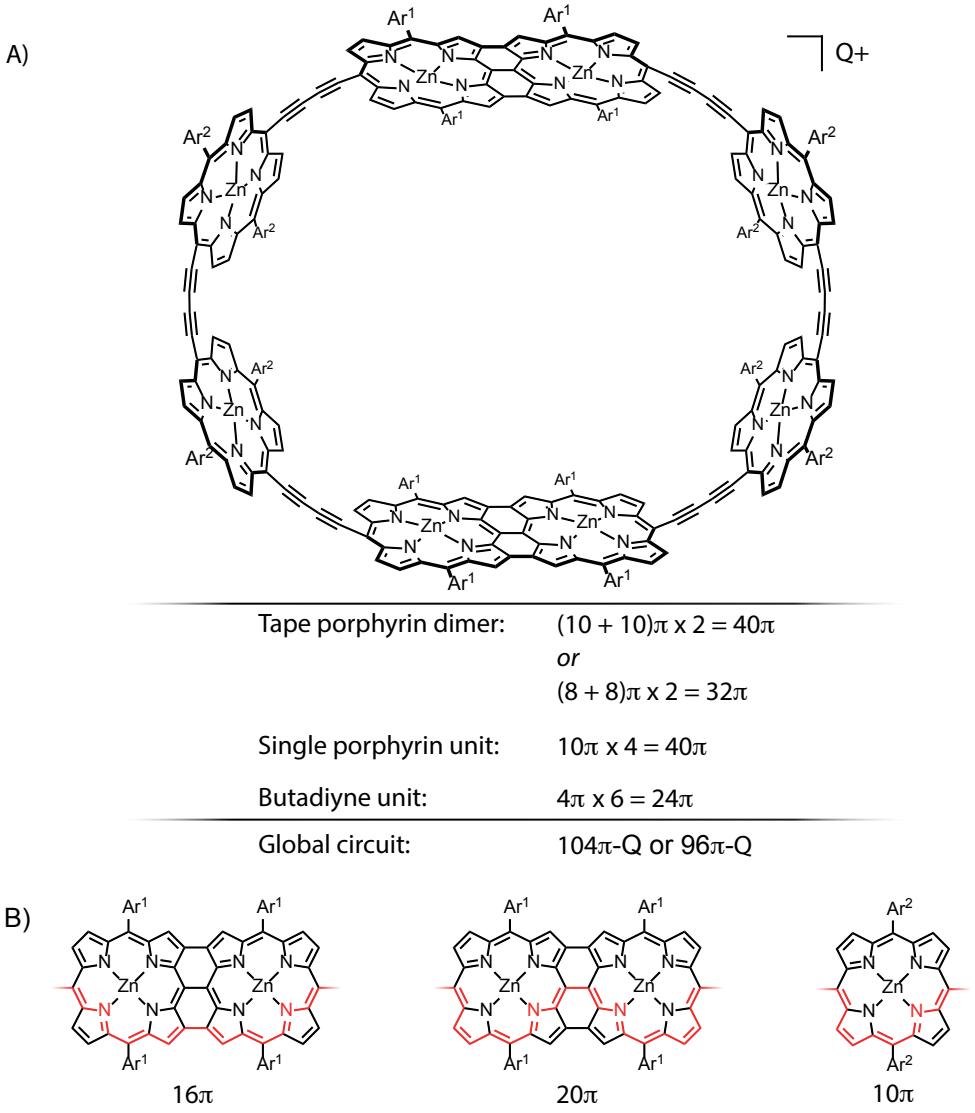


Figure 5.10: A) π-Electron count for the global ring circuit of ***c*-P8[$\mathbf{b_6f_2}$]** and B) possible delocalization pathways (in red) in the porphyrin tape dimer and single porphyrin units. The complete circuit consists of 2 tape dimers, 4 single porphyrin units, and 6 butadiyne links. A long and a short conjugation pathway exist for the tape dimer, contributing in total 20 π and 16 π-electrons, respectively, per unit. This leads to two possible π-electron counts for the global circuit: $104\pi - \mathrm{Q}$ or $96\pi - \mathrm{Q}$, where Q denotes the oxidation state of the system. $\mathrm{Ar}^1 = \mathrm{Ar}^2 =$ 3,5-bis(trihexylsilyl)phenyl.

5.3.5 Experimental Relative Ring Current Strengths

The fluorinated templates **T4$_{1,4F}$** and **T4$_{2,3F}$** were used to provide detailed information on the (de)shielding in the *β*,*meso*,*β*-fused and the butadiyne-linked regions of ***c*-P8[b$_6$f$_2$]**, and to compare the relative ring currents in ***c*-P8[b$_6$f$_2$]** and ***c*-P8[b$_8$]** (Table 5.1). The chemical shift difference of the CF_3 groups in the ^{19}F NMR spectra of a given oxidation state is defined in equation 5.1:

$$\Delta\delta_F = \delta_{F,\,\text{bound}} - \delta_{F,\,\text{unbound}} \tag{5.1}$$

where $\delta_{F,\,\text{bound}}$ is the chemical shift of the CF_3 resonances in the nanoring complex and $\delta_{F,\,\text{unbound}}$ is the chemical shift for the free template. This shift difference probes the induced magnetic field and scales with the strength of the ring current, as seen from the Biot–Savart law.[389]

Table 5.1: Summary of the observed ^{19}F chemical shift differences $\Delta\delta_F$ (in ppm) and chemical shift ratios φ_F for templates **T4$_{1,4F}$** and **T4$_{2,3F}$** when bound to nanorings ***c*-P8[b$_6$f$_2$]** and ***c*-P8[b$_8$]**, where Q is the oxidation state of the complex.

Q	$\Delta\delta_{1,4F}$(***c*-P8[b$_6$f$_2$]**·**(T4$_{1,4F}$)$_2$**)	$\Delta\delta_{1,4F}$(***c*-P8[b$_8$]**·**(T4$_{1,4F}$)$_2$**)	$\varphi_{1,4F}$
0	−0.12	−0.14	0.86
4+	5.83	1.48	3.94
5+	−1.55	–	–
6+	−4.15	−6.93	0.60
7+	−0.37	–	–
8+	0.29	0.73	0.40

Q	$\Delta\delta_{2,3F}$(***c*-P8[b$_6$f$_2$]**·**(T4$_{2,3F}$)$_2$**)	$\Delta\delta_{2,3F}$(***c*-P8[b$_8$]**·**(T4$_{2,3F}$)$_2$**)	$\varphi_{2,3F}$
0	−0.53	−0.62	0.85
4+	4.62	1.27	3.64
5+	−2.40	–	–
6+	−4.72	−7.16	0.66
7+	−0.61	–	–
8+	0.23	0.61	0.38

When compared with the *α*-pyridine protons, the CF_3 groups are further away from the porphyrin units, making the ^{19}F signals less sensitive than the *α*-pyridine

^{1}H resonances to the local disruption of aromaticity in the fused porphyrins. This is evident from the similar chemical shift differences of neutral ***c*-P8[$\mathbf{b_6f_2}$]·($\mathbf{T4_{1,4F}}$)$_2$** ($\Delta\delta_{1,4F} = -0.12$ ppm) and ***c*-P8[$\mathbf{b_8}$]·($\mathbf{T4_{1,4F}}$)$_2$** ($\Delta\delta_{1,4F} = -0.14$ ppm). Conversely, the ^{19}F signals provide a more sensitive probe of global ring currents because they are sharper and less influenced by local factors, such as the N–Zn interaction. The relative strengths of the global ring currents in the two nanorings ***c*-P8[$\mathbf{b_6f_2}$]** and ***c*-P8[$\mathbf{b_8}$]** were compared using the relative shift ratio φ_F, defined as the ratio of $\Delta\delta_F$ for the two systems in the same oxidation state following equation 5.2

$$\varphi_F = \frac{\Delta\delta_F\left(\textbf{\textit{c}-P8[b}_6\textbf{f}_2\textbf{]}\cdot\ (\textbf{T4}_{X,YF})_2{}^{Q+}\right)}{\Delta\delta_F\left(\textbf{\textit{c}-P8[b}_8\textbf{]}\cdot\ (\textbf{T4}_{X,YF})_2{}^{Q+}\right)} \tag{5.2}$$

where X,Y indicates the regiochemistry (1,4 or 2,3) and Q is the oxidation state. This analysis gives the values of φ_F listed in Table 5.1. In the 4+ state, $\varphi_F \approx 4$, implying that the paratropic ring current is about four times stronger in the partially fused ring, whereas in the 6+ state $\varphi_F \approx 0.6$, indicating that the global diatropic ring current is about 40% weaker than in the all-butadiyne-linked complexes. In the 8+ state, $\varphi_F \approx 0.4$, reflecting a weaker paratropic ring current in the partially fused ring. In all oxidation states, the difference between $\varphi_{1,4F}$ and $\varphi_{2,3F}$ is less than 10%, which supports the presence of homogeneous, global ring currents.

The stronger antiaromatic (paratropic) ring current in ***c*-P8[$\mathbf{b_6f_2}$]·(T4)$_2{}^{4+}$** and the weaker aromatic (diatropic) ring current in ***c*-P8[$\mathbf{b_6f_2}$]·(T4)$_2{}^{6+}$** compared with the all-butadiyne-linked system ***c*-P8[$\mathbf{b_8}$]·(T4)$_2{}^{4+}$** and ***c*-P8[$\mathbf{b_8}$]·(T4)$_2{}^{6+}$**, may be consequences of the smaller HOMO–LUMO gap of the partially fused nanoring. Systems with smaller excited state energy gaps for magnetically allowed transitions generally have larger paratropic contributions to the ring current.[390–392] The UV-vis-NIR absorption spectra and TD-DFT calculations in Section 5.3.2 establish a general trend toward smaller excitation gaps in the partially fused systems with a 0.26 eV smaller calculated excitation energy for the first magnetically allowed excitation ($S_0 \rightarrow S_1$) in ***c*-P8[$\mathbf{b_6f_2}$]·(T4)$_2$** ($\Delta E_{S0\rightarrow S1} = 0.92$ eV) compared to ***c*-P8[$\mathbf{b_8}$]·(T4)$_2$** ($\Delta E_{S0\rightarrow S1} = 1.18$ eV). This suggests that the magnetic excitation energies of the

oxidized, partially fused nanoring complexes are also likely smaller than those of the butadiyne-linked ring. The ^{19}F NMR titrations of ***c*-P8[$\mathbf{b_6f_2}$]·($\mathbf{T4_{1,4F}}$)$_2$** and ***c*-P8[$\mathbf{b_6f_2}$]·($\mathbf{T4_{2,3F}}$)$_2$** also exhibit well-defined signals for the 5+ and 7+ oxidation states (Figure 5.13, Figure 5.7). These odd-electron states were not observed in the titrations of ***c*-P8[$\mathbf{b_8}$]·($\mathbf{T4_{1,4F}}$)$_2$** and ***c*-P8[$\mathbf{b_8}$]·($\mathbf{T4_{2,3F}}$)$_2$** under identical conditions (Figure 5.14, Figure 5.15). The significant shift for the 5+ state ($\Delta\delta_F = -1.55$, -2.40; Table 5.1) might indicate an aromatic ring current, but there could also be contributions from the pseudocontact shift due to the unpaired electron.[393, 394] Further experimental and theoretical work is required to understand the ring currents of these odd-electron oxidation states.

5.4 Summary and Conclusions

The preparation of ***c*-P8[$\mathbf{b_6f_2}$]** illustrates a new strategy in template-directed synthesis: A geometrical mismatch between the template and porphyrin building block is used to disfavor formation of a 1:1 complex, thereby promoting formation of a 2:2 complex that is better preorganized to form the desired product. In the absence of the geometrical mismatch, the 1:1 complex between the template and the building block would predominate, because its entropy of formation is less unfavorable than that of the 2:2 complex. Destabilizing the 1:1 complex encourages two templates to bring two building blocks together, reducing the entropy of the coupling reaction by making it effectively intramolecular in the 2:2 complex. Comparison of the synthesis of ***c*-P8[$\mathbf{b_8}$]** from **H-*l*-P4[$\mathbf{b_3}$]-H** with the synthesis of ***c*-P8[$\mathbf{b_6f_2}$]** from **H-*l*-P4[$\mathbf{b_2f_1}$]-H** shows that this geometrical mismatch increases the yield of the 8-porphyrin nanoring by about a factor of two (from 37% to 72%). It seems likely that this principle could be applied to synthesize many other macrocycles. The most surprising conclusion from this study is that ***c*-P8[$\mathbf{b_6f_2}$]·($\mathbf{T4}$)$_2$** exhibits global antiaromatic and aromatic ring currents, in the 4+ and 6+ oxidation states, respectively. This is remarkable because β,*meso*,β-fused porphyrin dimers are much easier to oxidize than butadiyne-linked dimers.[357, 369, 395] Electronic delocalization over many sites generally requires a narrow distribution of site energies.[185] The difference in oxidation

potential between the different porphyrin units might have been expected to cause charge localization in these partially fused nanoring cations, but the ^{1}H and ^{19}F NMR shifts provide clear evidence for global ring currents, which implies coherent charge delocalization around the whole partially fused nanoring. The magnitude of the paratropic ring current in ***c*-P8[b_6f_2]·(T4)$_2^{4+}$** is about four times stronger than that in the all-butadiyne-linked analogue ***c*-P8[b_8]·(T4)$_2^{4+}$**, which may reflect the smaller HOMO–LUMO gap of the partially fused ring. The Hückel rule correctly predicts the direction of the ring current in these systems, even though the electron count is ambiguous: ***c*-P8[b_6f_2]·(T4)$_2^{4+}$** has a circuit of 100 or 92 electrons, depending on the chosen pathway, but either way it is $4n$ (antiaromatic), whereas ***c*-P8[b_6f_2]·(T4)$_2^{6+}$** has a circuit of 98 or 90 electrons, and either way it is $4n$+2 (aromatic). The ^{19}F NMR resonances of the fluorinated templates **T4$_{1,4F}$** and **T4$_{2,3F}$** provide a clear probe for the ring currents in these systems; the two isomers detect essentially the same effect, proving the ring current is homogeneous and global.

5.5 Methods

5.5.1 General Methods

NMR Oxidation Titrations

Oxidative NMR titrations of the porphyrin nanoring complexes were carried out similarly to previous descriptions.[55, 56] The nanoring complexes were transferred to J. Young NMR tubes, dissolved in CD_2Cl_2, and handled under argon using standard Schlenk techniques. A well-stirred suspension of the oxidant, thianthrenium hexafluoroantimonate (**ThnSbF$_6$**, E_{red} = 0.86 V versus Fc/Fc$^+$) in CD_2Cl_2 (ca. 20–30 mM), kept under argon was used for the titrations. The titrations were carried out using a Schlenk adaptor for the J. Young NMR tubes, enabling the addition of oxidant under a counterflow of argon. While having the NMR tube positioned in the Schlenk adaptor, the lower part of the tube was simultaneously immersed in a dry ice/acetone mixture (−78 °C) in a Dewar to preserve the integrity of the oxidized nanoring complexes. After the first addition of oxidant, the samples were kept at

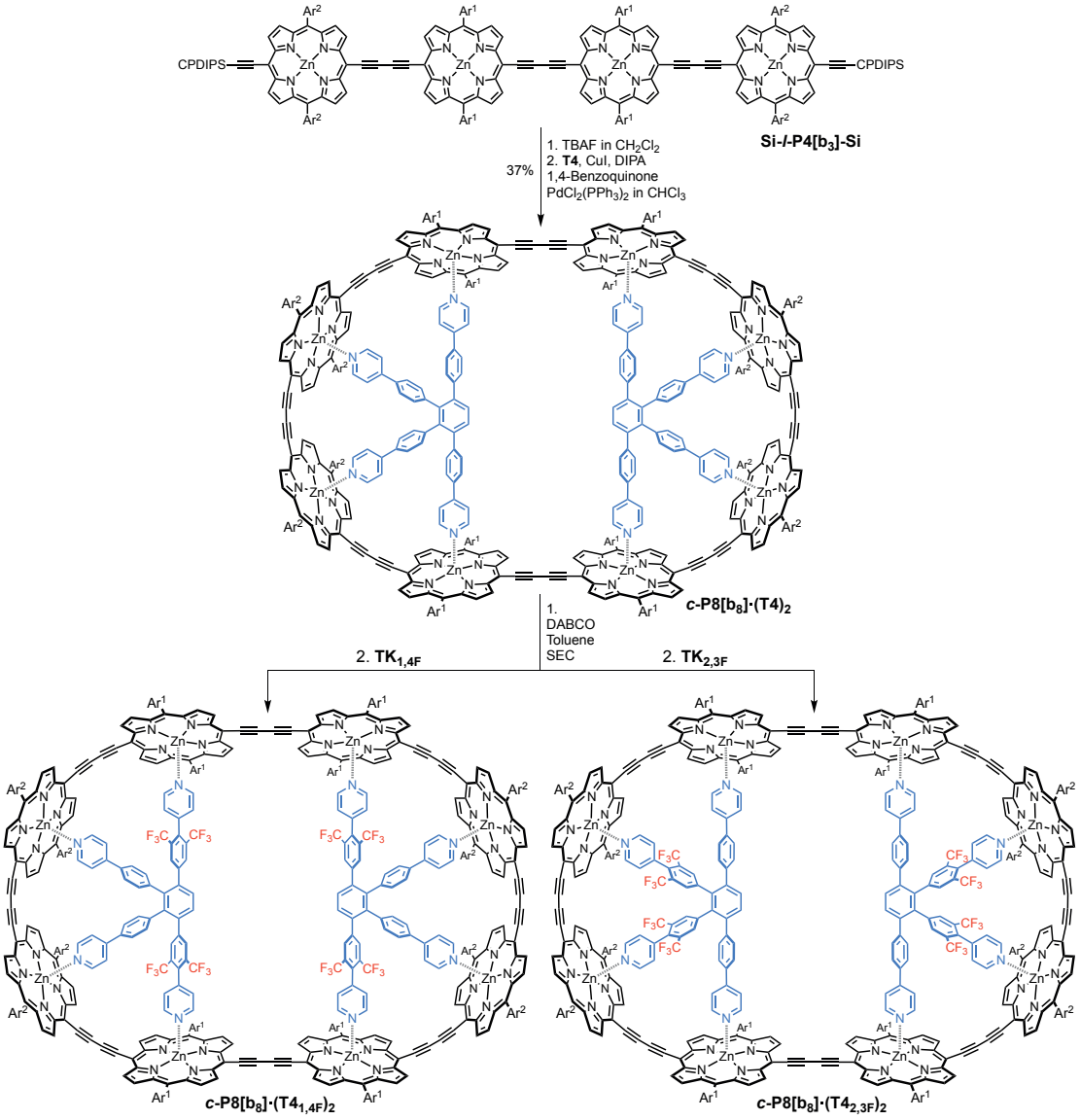
low-temperatures throughout the titration experiments using either a dry ice/acetone Dewar or the N_2 cooling (−50 °C) used for the NMR probe. Only during transfers (≤ 30 seconds) from the NMR instrument to the Dewar or from the NMR tube adaptor to the Dewar were the samples momentarily subjected to room temperature conditions. Prior to each titration, a ^{1}H spectrum was recorded at 298 K to confirm the integrity and purity of the porphyrin nanoring complex. At the end of a titration, the oxidized porphyrin nanoring complex was reduced using decamethylferrocene to recover the neutral state, as confirmed by ^{1}H NMR at 298 K. The titration endpoint (at which each porphyrin unit is oxidized to the 1+ state) is evident from the disappearance of the neutral oxidant (thianthrene) ^{1}H signals, resulting from signal broadening caused by exchange between neutral thianthrene and excess thianthrenium.

Computational Methods

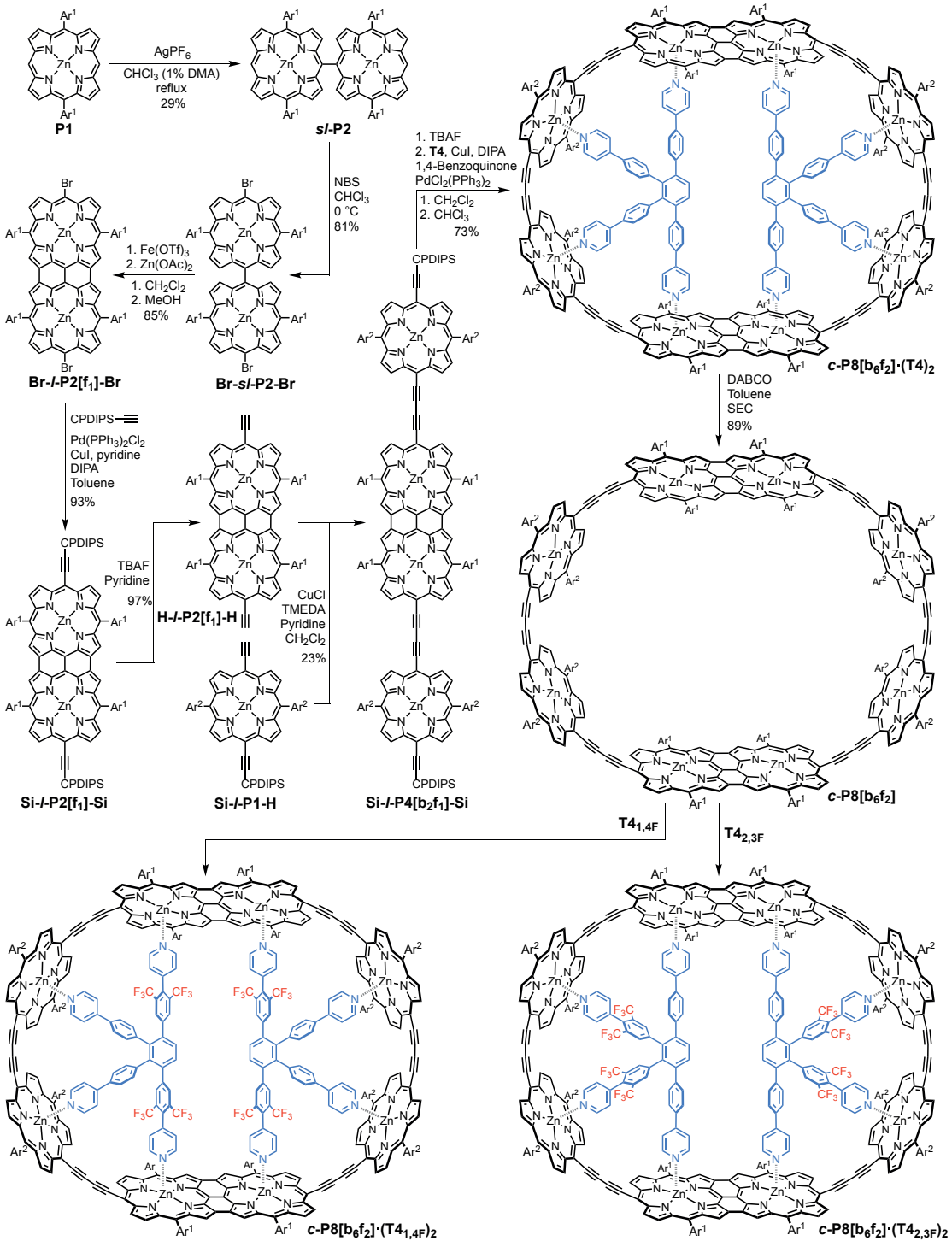
Molecular models were built in HyperChem™ 8.0 using the MM+ forcefield with parameters modified for the description of porphyrins.[396–399] The porphyrin *meso* aryl groups were replaced with H for all calculations. The resulting geometries were further optimized in MOPAC2016 using the PM7 level of theory and in the absence of symmetry.[400] The optimized structures were further refined by DFT calculations. DFT geometry optimizations of nanorings ***c*-P8[$\mathbf{b_6f_2}$]·$\mathbf{(T4)_2}$** and ***c*-P8[$\mathbf{b_8}$]·$\mathbf{(T4)_2}$**, and linear oligomers **H-*l*-P2[$\mathbf{f_1}$]-H**, **H-*l*-P2[$\mathbf{b_1}$]-H**, **H-*l*-P4[$\mathbf{b_2f_1}$]-H** and **H-*l*-P8[$\mathbf{b_5f_2}$]-H** were first performed using Gaussian 16/A.03 with B3LYP as functional and the 6-31G* basis set.[222–226] The stationary nature of the optimized geometries was confirmed by the absence of imaginary frequencies in the DFT frequency calculations. The geometries of the oxidized nanoring complexes were further optimized using the geometries of the neutral compounds as starting points with LC-ωhPBE (ω=0.1) as functional and the 6-31G* basis set,[233, 401–403] and the resulting structures were used for NICS, ACID and TD-DFT calculations. NICS/susceptibility calculations were performed using the gauge-independent atomic orbital (GIAO) method implemented in Gaussian16/A.03 at the LC-ωhPBE/6-31G* ($\omega = 0.1$) level of theory.[404] ACID calculations were performed with the continuous set of gauge transformations (CSGT)

method implemented in Gaussian09/D.01 at the LC-ωPBE/6-31G* ($\omega = 0.1$) level of theory.[405] Templates were removed prior to NICS and ACID calculations. TD-DFT calculations were performed in Gaussian16/A.03 for the first 64 excited states with LC-ωPBE ($\omega = 0.1$) as functional and the 6-31G* basis set.[232] Natural transition orbitals (NTOs) were calculated for the S_1 and S_2 excited states of ***c*-P8[$\mathbf{b_6f_2}$]·$\mathbf{(T4)_2}$** and ***c*-P8[$\mathbf{b_8}$]·$\mathbf{(T4)_2}$**.[406]

5.5.2 Synthetic Procedures

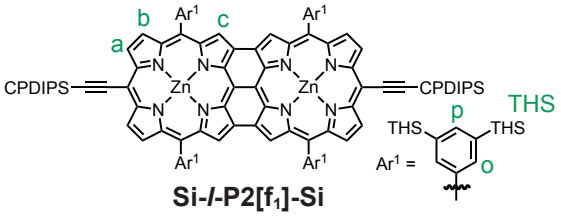


Scheme 5.3: Synthesis of ***c*-P8[b_8]·$(T4)_2$** and formation of fluorinated complexes ***c*-P8[b_8]·$(T4_{1,4F})_2$** and ***c*-P8[b_8]·$(T4_{2,3F})_2$**. $Ar^1 = Ar^2 = 3,5$-bis(trihexylsilyl)phenyl. CPDIPS = cyanopropyldiisopropylsilyl.



Scheme 5.4: Synthesis of ***c*-P8[b$_6$f$_2$]·(T4)$_2$** and free ***c*-P8[b$_6$f$_2$]**, and preparation of fluorinated complexes ***c*-P8[b$_6$f$_2$]·(T4$_{1,4F}$)$_2$** and ***c*-P8[b$_6$f$_2$]·(T4$_{2,3F}$)$_2$**. Ar^1 = Ar^2 = 3,5-bis(trihexylsilyl)phenyl. CPDIPS = cyanopropyldiisopropylsilyl.

Si-*l*-P2[f_1]-Si:

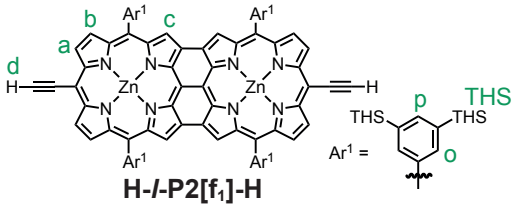


Si-*l*-P2[f_1]-Si

In a Schlenk flask, bromo-porphyrin dimer **Br-*l*-P2[f_1]-Br** (380 mg, 0.110 mmol, 1 equiv.), $Pd(PPh_3)_2Cl_2$ (16 mg, 0.023 mmol), and CuI (5 mg, 0.026 mmol) were dissolved in toluene (11 mL), *i*-Pr_2NH (2 mL), and pyridine (0.3 mL) and subjected to three freeze-pump-thaw cycles. Cyanopropyldiisopropylsilylacetylene (104 µL, 0.456 mmol, 4 equiv.) was added and the reaction mixture heated to 50 °C. After stirring for 2 hours, the mixture was cooled to room temperature, and the volatiles were removed *in vacuo*. The crude mixture was purified by flash column chromatography (SiO_2; eluent: 40% $CH_2Cl_2/PE_{40\text{-}60}$) to afford the desired product **Si-*l*-P2[f_1]-Si** (380 mg, 93%) as a dark green solid.

^{1}H NMR (500 MHz, $CDCl_3$, 298 K) $\delta_H = 8.41$ (d, $J = 4.6$ Hz, 4H, a), 7.81 (s, 4H, p), 7.78 (s, 8H, o), 7.47 (d, $J = 4.6$ Hz, 4H, b), 7.06 (s, 4H, c), 2.44 (t, $J = 6.8$ Hz, 4H, CPDIPS-CH_2), 2.04–1.95 (m, 4H, CPDIPS-CH_2), 1.01–0.97 (m, 4H, CPDIPS-CH_2), 1.45–0.75 (m, 340H, THS + CPDIPS-CH + CPDIPS-CH_3) ppm. **MALDI-ToF** *m/z* 3714.257 (calculated for $[C_{232}H_{376}N_{10}Si_{10}Zn_2]^+$: 3714.604). **UV-vis-NIR** ($CDCl_3$) λ_{max} / nm (log ϵ): 1133 (4.60), 994 (4.42), 580 (5.28), 487 (4.76), 438 (5.20).

H-*l*-P2[f_1]-H:



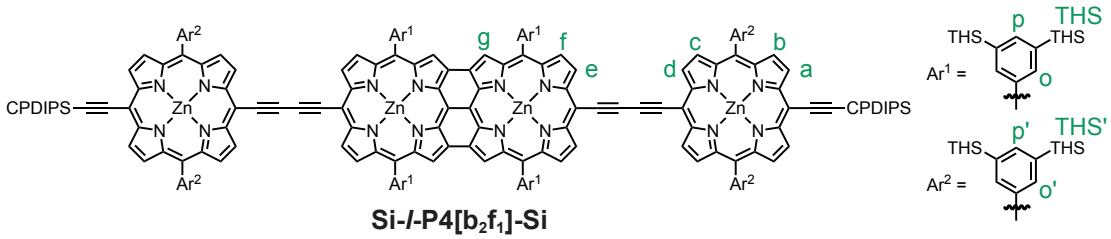
H-*l*-P2[f_1]-H

Si-*l*-P2[f_1]-Si (80 mg, 21.5 µmol) was dissolved in CH_2Cl_2 (10 mL) and pyridine (0.1 mL). TBAF (1.0 M in THF, 0.25 mL, 0.25 mmol) was added and the reaction

mixture was stirred for 25 minutes at room temperature before being passed through a pad of silica (eluent: 60% $CHCl_3$/$PE_{40\text{-}60}$ + 1% pyridine). The volatiles were removed *in vacuo* to afford **H-*l*-P2[f_1]-H** (70 mg, 97%) as a green solid.

^{1}H NMR (400 MHz, $CDCl_3$, 298 K) δ_H = 8.45 (d, J = 4.7 Hz, 4H, a), 7.81 (d, J = 1.2 Hz, 4H, p), 7.80 (d, J = 1.2 Hz, 8H, o), 7.48 (d, J = 4.7 Hz, 4H, b), 7.08 (s, 4H, c), 3.77 (s, 2H, d), 1.43–0.79 (m, 312H, THS) ppm.

Si-*l*-P4[b_2f_1]-Si:



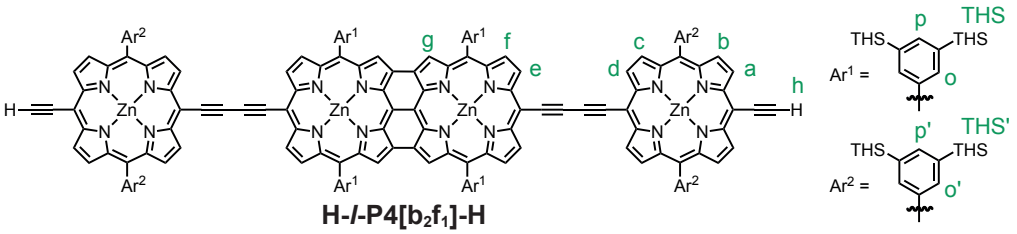
Si-*l*-P4[b_2f_1]-Si

In a 500 mL round bottom flask, **H-*l*-P2[f_1]-H** (70 mg, 20.9 μmol) and **Si-*l*-P1-H** (240 mg, 0.127 mmol) were dissolved in CH_2Cl_2 (10 mL) and pyridine (0.1 mL). CuCl (167 mg, 1.69 mmol) and TMEDA (0.25 mL) were added, and the mixture was stirred vigorously under an oxygen rich atmosphere. After 35 minutes, the reaction was filtered through a pad of silica (eluent: $CHCl_3$ + 1% pyridine) and concentrated *in vacuo*. The crude residue was purified by SEC (toluene + 1% pyridine) and further purified by recycling GPC (toluene + 1% pyridine) to afford **Si-*l*-P4[b_2f_1]-Si** (35 mg, 23%) as a green solid.

^{1}H NMR (500 MHz, $CDCl_3$, 298 K) δ_H = 9.73 (d, J = 4.6 Hz, 4H, d), 9.63 (d, J = 4.6 Hz, 4H, a), 8.88 (d, J = 4.6 Hz, 4H, c), 8.86 (d, J = 4.6 Hz, 4H, b), 8.59 (d, J = 4.5 Hz, 4H, e), 8.23 (s, o'), 7.99 (s, 4H, p'), 7.81 (s, 4H, p), 7.80 (s, 8H, o) 7.48 (d, J = 4.5 Hz, 4H, f), 6.96 (s, 4H, g), 2.54 (t, J = 6.8 Hz, 4H, CPDIPS-CH_2), 2.23–2.16 (m, 4H, CPDIPS-CH_2), 1.19–1.14 (m, 4H, CPDIPS-CH_2), 1.55–0.64 (m, 652H, THS + THS' + CPDIPS-CH + CPDIPS-CH_3) ppm. **^{13}C NMR** (126 MHz, $CDCl_3$, 298 K) δ_C = 155.9, 154.8, 154.2, 153.3, 153.1, 152.3, 150.8, 150.5, 144.9, 140.5, 139.3, 139.0, 138.8, 136.5, 135.3, 135.0, 133.3, 133.1, 132.3, 130.9, 129.4, 127.7, 124.6, 123.2, 119.9, 101.3, 33.7, 33.6, 31.8, 31.7, 31.1, 29.9, 24.2, 24.1, 22.82, 22.79,

21.8, 21.2, 18.8, 18.5, 14.3, 12.79, 12.77, 12.6, 12.5, 10.3, 1.2 ppm. **MALDI-ToF** *m/z* 7123.020 (calculated for $[C_{448}H_{716}N_{18}Si_{18}Zn_4]^+$: 7121.974). **UV-vis-NIR** ($CDCl_3$) λ_{max} / nm (log ϵ): 1137 (5.08), 992 (4.78), 687 (5.16), 583 (5.27), 443 (5.73).

H-*l*-P4[b_2f_1]-H:

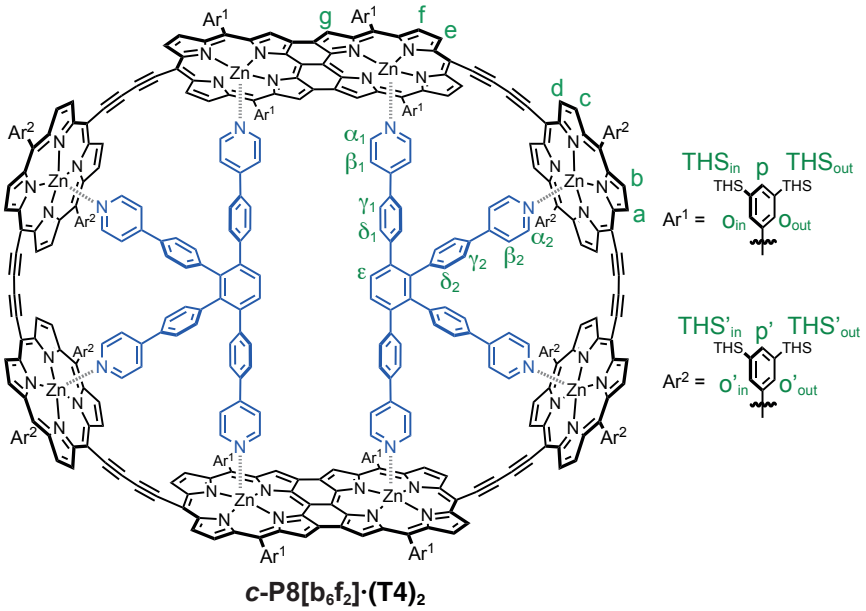


H-*l*-P4[b_2f_1]-H

Si-*l*-P4[b_2f_1]-Si (5.60 mg, 0.789 μmol) was dissolved in CH_2Cl_2 (2 mL) and pyridine (0.02 mL). TBAF (1.0 M in THF, 0.08 mL, 0.08 mmol) was added and the reaction mixture was stirred for 25 minutes at room temperature before being passed through a pad of silica (eluent: 20% CH_2Cl_2/$PE_{40\text{-}60}$ + 1% pyridine). The volatiles were removed *in vacuo* to afford **H-*l*-P4[b_2f_1]-H** (5.05 mg, 95%) as a green solid.

^{1}**H NMR** (400 MHz, $CDCl_3$) $\delta_H = 9.80$ (d, $J = 4.6$ Hz, 4H, d), 9.72 (d, $J = 4.6$ Hz, 4H, a), 8.96 (d, $J = 4.6$ Hz, 4H, c), 8.92 (d, $J = 4.6$ Hz, 4H, b), 8.67 (d, $J = 4.6$ Hz, 4H, e), 8.27 (d, $J = 1.1$ Hz, 8H, o'), 8.01 (t, $J = 1.1$ Hz, 4H, p'), 7.85 (d, $J = 1.2$ Hz, 8H, o), 7.84 (d, $J = 1.2$ Hz, 4H, p), 7.57 (d, $J = 4.6$ Hz, 4H, f), 7.08 (s, 4H, g), 4.19 (s, 2H, h), 1.49–0.80 (m, 624H, THS + THS') ppm.

***c*-P8[b_6f_2]·$(T4)_2$:**



***c*-P8[b_6f_2]·$(T4)_2$**

Procedure A: **H-*l*-P4[b_2f_1]-H** (5.05 mg, 0.747 μmol) and **T4** (0.52 mg, 0.753 μmol) were dissolved in $CHCl_3$ (2 mL) and sonicated for 2 hours to allow for the complex formation. A catalyst mixture of $PdCl_2(PPh_3)_2$ (0.33 mg, 0.470 μmol), CuI (0.47 mg, 2.47 μmol), 1,4-benzoquinone (1.08 mg, 10.0 μmol), and *i*-Pr_2NH (15 μL) in $CHCl_3$ (0.5 mL) was added, and the reaction progress was monitored by analytical GPC (THF + 1% pyridine). After 4 hours, the mixture was passed through a pad of silica (eluent: $CHCl_3$ + 1% pyridine) and concentrated *in vacuo*. The resulting residue was purified by SEC (toluene + 1% pyridine) before further purification by recycling GPC (toluene + 1% pyridine) to afford ***c*-P8[b_6f_2]·$(T4)_2$** (4.00 mg, 72%) as a brown solid and analytical amounts of **H-*l*-P8[b_5f_2]-H** as a green solid. Additional ***c*-P8[b_6f_2]·$(T4)_2$** was synthesized in two larger batches following procedure A: 1) **H-*l*-P4[b_2f_1]-H** (14.3 mg, 2.12 μmol), **T4** (1.47 mg, 2.13 μmol). Yield: 10.4 mg, 66%; 2) **H-*l*-P4[b_2f_1]-H** (17.4 mg, 2.57 μmol), **T4** (1.79 mg, 2.59 μmol). Yield: 12.1 mg, 63%.

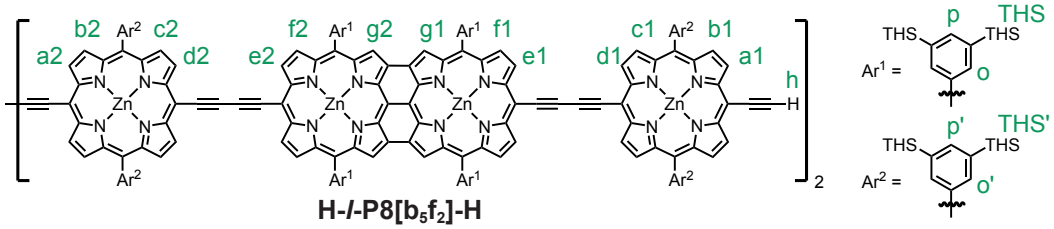
Procedure B (reduced equivalents of CuI): Following the general approach of procedure A, **H-*l*-P4[b_2f_1]-H** (16.3 mg, 2.41 μmol) and **T4** (2.34 mg, 3.39 μmol) were reacted using an adapted catalyst mixture of $PdCl_2(PPh_3)_2$ (1.06 mg, 1.51 μmol), CuI (0.54 mg, 2.84 μmol), 1,4-benzoquinone (3.49 mg, 32.3 μmol), and *i*-Pr_2NH

(48 µL). The reaction was monitored by analytical GPC (THF + 1% pyridine) and stopped after 14 hours when a 1:2 ratio of **H-*l*-P8[b$_5$f$_2$]-H** and ***c*-P8[b$_6$f$_2$]·(T4)$_2$** was reached. Workup and purification as described in procedure A gave **H-*l*-P8[b$_5$f$_2$]-H** (1.36 mg, 8%) for full characterization.

Characterization of ***c*-P8[b$_6$f$_2$]·(T4)$_2$**:

^{1}H NMR (600 MHz, CD_2Cl_2, 298 K) δ_H = 9.58 (d, J = 4.3 Hz, 8H, a), 9.45 (d, J = 4.3 Hz, 8H, d), 8.78 (d, J = 4.3 Hz, 8H, b), 8.72 (d, J = 4.3 Hz, 8H, c), 8.40 (s, 8H, o'$_{in}$), 8.27 (d, J = 4.3 Hz, 8H, e), 8.02 (s, 8H, o'$_{out}$), 7.99 (s, 8H, p'), 7.75 (s, 8H, p), 7.73 (s, 8H, o$_{out}$), 7.65 (s, 8H, o$_{in}$), 7.36 (d, J = 4.3 Hz, 8H, f), 6.97 (s, 4H, ϵ), 6.74 (s, 8H, g), 6.50 (d, J = 8.7 Hz, 8H, γ_1), 6.40 (d, J = 8.7 Hz, 8H, δ_1), 6.34 (d, J = 6.4 Hz, 8H, β_1), 5.87 (d, J = 8.8 Hz, 8H, δ_2), 5.75 (d, J = 8.8 Hz, 8H, γ_2), 5.59 (d, J = 6.4 Hz, 8H, α_1), 5.23 (d, J = 6.2 Hz, 8H, β_2), 2.41 (d, J = 6.2 Hz, 8H, α_2), 1.53–0.61 (m, 1248H, THS$_{in}$ + THS$_{out}$ + THS'$_{in}$ + THS'$_{out}$) ppm. **MALDI-ToF** *m/z* 13516 (calculated for $[C_{856}H_{1352}N_{32}Si_{32}Zn_8]^+$ = ***c*-P8[b$_6$f$_2$]$^+$**: 13513). **UV-vis-NIR** ($CDCl_3$) λ_{max} / nm (log ϵ): 1304 (5.49), 1254 (5.31), 1122 (5.17), 872 (5.39), 735 (5.31), 592 (5.58), 502 (5.64), 439 (5.71).

Characterization of **H-*l*-P8[b$_5$f$_2$]-H**:

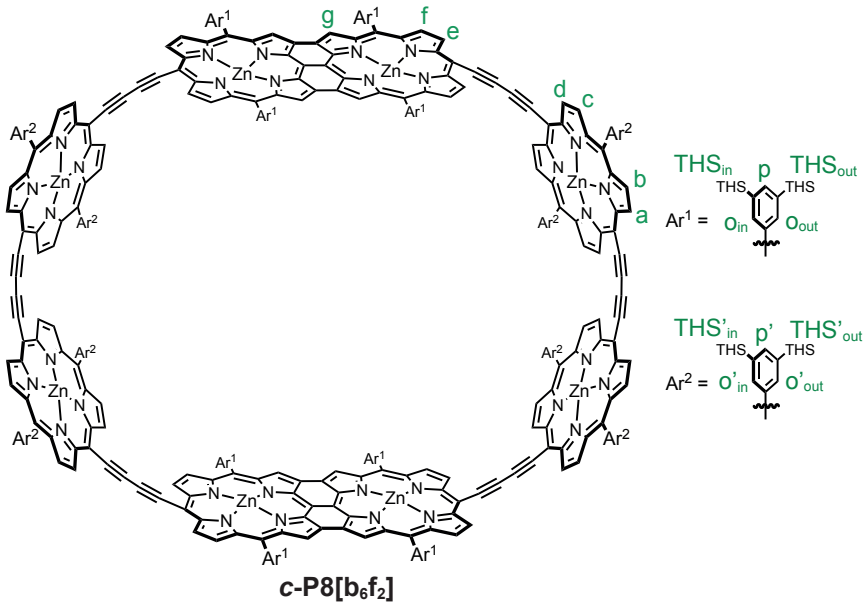


H-*l*-P8[b$_5$f$_2$]-H

^{1}H NMR (500 MHz, $CDCl_3$, 298 K) δ_H = 9.94 (d, J = 4.6 Hz, 4H, a1/a2), 9.85–9.82 (m, 4H, d1/d2), 9.81 (d, J = 4.5 Hz, 4H, d1/d2), 9.54 (d, J = 4.6 Hz, 4H, a1/a2), 9.01 (d, J = 4.6 Hz, 4H, b1/b2), 8.99 (d, J = 4.5 Hz, 4H, c1/c2), 8.97 (d, J = 4.5 Hz, 4H, c1/c2), 8.95 (d, J = 4.6 Hz, b1/b2), 8.70–8.66 (m, 8H, e1+e2), 8.32 (s, 8H, Ar^2 o'), 8.28 (s, 8H, Ar^2 o'), 8.04 (s, 4H, Ar^2 p'), 8.01 (s, 4H, Ar^2 p'), 7.88–7.83 (m, 24H, Ar^1), 7.60–7.56 (m, 8H, f1+f2), 7.09 (s, 8H, g1+g2), 3.73–3.63 (m, 2H, h), 1.56–0.69 (m, 1248H, THS + THS') ppm. **MALDI-ToF** *m/z* 13591

(calculated for $[C_{861}H_{1359}N_{33}Si_{32}Zn_8]^+ = [$**H-*l*-P8[b$_5f_2$]-H**+pyridine$]^+$: 13595). **UV-vis-NIR** ($CDCl_3$) λ_{max} / nm (log ϵ): 1140 (5.51), 993 (5.20), 719 (5.33), 673 (5.41), 582 (5.62), 440 (5.96).

***c*-P8[b$_6$f$_2$]**:

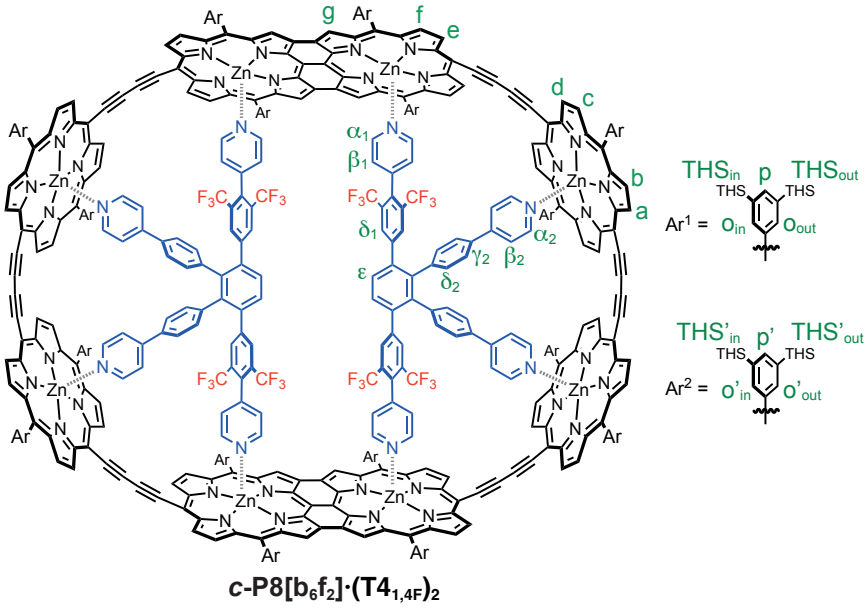


***c*-P8[b$_6$f$_2$]**

A 3.7 M (30%) solution of pyridine (15 mL) in toluene (35 mL) was eluted into a SEC column (toluene; diameter = 3.5 cm; height = 25 cm). A solution of the complex ***c*-P8[b$_6$f$_2$]·(T4)$_2$** (10.4 mg, 0.698 μmol) in toluene (5 mL) was loaded onto the SEC column and eluted through the pyridine solution with additional toluene. The collected fraction was washed with water (5 x 50 mL), dried over $MgSO_4$, and concentrated *in vacuo*. The crude residue was further purified by SEC ($CHCl_3$) to afford free nanoring ***c*-P8[b$_6$f$_2$]** (8.4 mg, 89%) as a brown solid.

^{1}H NMR (600 MHz, CD_2Cl_2, 298 K) δ_H = 9.72 (d, J = 4.5 Hz, 8H, a), 9.61 (d, J = 4.5 Hz, 8H, d), 8.85 (d, J = 4.5 Hz, 8H, b), 8.81 (d, J = 4.5 Hz, 8H, c), 8.51 (d, J = 4.5 Hz, 8H, e), 8.19 (s, 16H, o'), 7.97 (s, 8H, p'), 7.77 (s, 8H, p), 7.73 (s, 16H, o), 7.49 (d, J = 4.5 Hz, 8H, f), 6.92 (s, 8H, g), 1.48–0.72 (m, 1248H, THS + THS') ppm. **MALDI-ToF** m/z 13516 (calculated for $[C_{856}H_{1352}N_{32}Si_{32}Zn_8]^+$: 13513). **UV-vis-NIR** ($CDCl_3$) λ_{max} / nm (log ϵ): 1158 (5.32), 1009 (5.05), 782 (5.28), 691 (5.31), 585 (5.54), 491 (5.66), 435 (5.74).

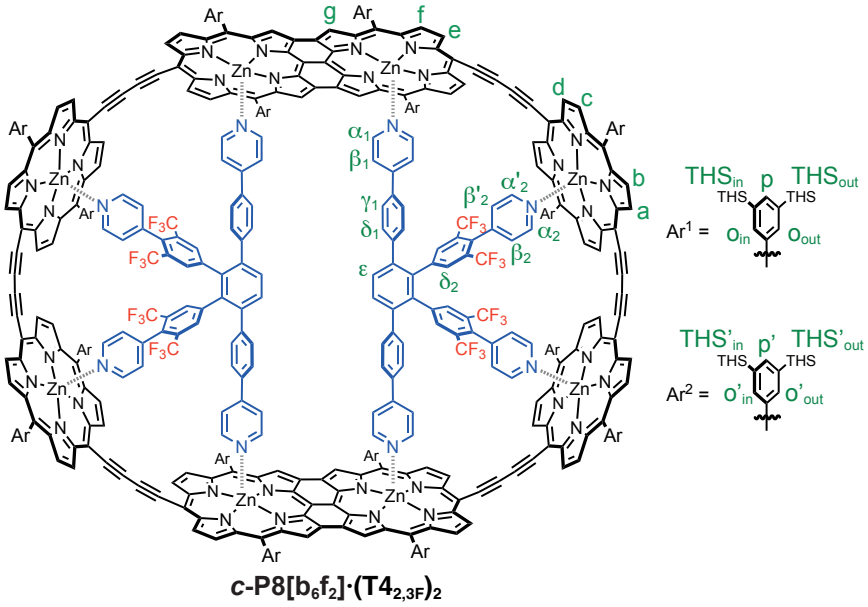
***c*-P8[b_6f_2]·($T4_{1,4F}$)$_2$:**



***c*-P8[b_6f_2]·($T4_{1,4F}$)$_2$**

^{1}H NMR (600 MHz, CD_2Cl_2, 298 K) δ_H = 9.57 (d, J = 4.3 Hz, 8H, a), 9.49 (d, J = 4.4 Hz, 8H, d),8.79 (d, J = 4.3 Hz, 8H, b), 8.75 (d, J = 4.4 Hz, 8H, c), 8.43 (s, 8H, o'_{in}), 8.26 (d, J = 4.4 Hz, 8H, e), 8.05 (s, 8H, o'_{out}), 8.03 (s, 8H, p'), 7.74 (s, 16H, p + o_{out}), 7.51 (s, 8H, o_{in}), 7.26 (d, J = 4.4 Hz, 8H, f), 7.20 (s, 4H, ϵ), 6.95 (s, 8H, δ_1), 6.72 (s, 8H, g), 6.07 (d, J = 6.2 Hz, 8H, β_1), 5.99 (d, J = 8.8 Hz, 8H, δ_2), 5.90 (d, J = 8.8 Hz, 8H, γ_2), 5.70 (d, J = 6.2 Hz, 8H, α_1), 5.25 (d, J = 6.9 Hz, 8H, β_2), 2.51–2.46 (m, 8H, α_2), 1.64–0.55 (m, 1248H, THS_{in} + THS_{out} + THS'_{in} + THS'_{out}) ppm. **^{19}F NMR** (470 MHz, CD_2Cl_2, 298 K) δ_F = −60.63 ppm. **MALDI-ToF** m/z 13515 (calculated for $[C_{856}H_{1352}N_{32}Si_{32}Zn_8]^+$ = ***c*-P8[b_6f_2]$^+$**: 13513).

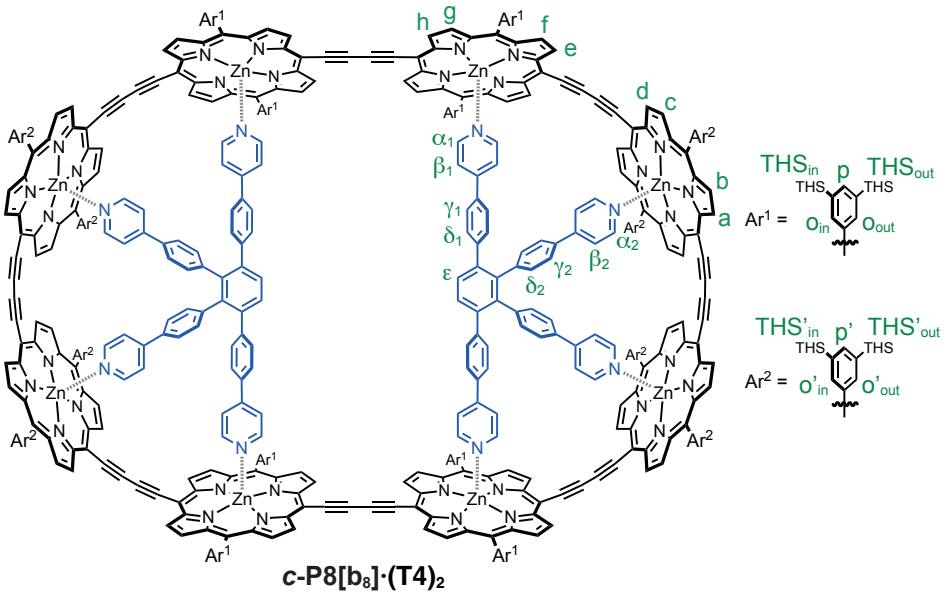
***c*-P8[b_6f_2]·($T4_{2,3F}$)$_2$:**



***c*-P8[b_6f_2]·($T4_{2,3F}$)$_2$**

^{1}H NMR (600 MHz, CD_2Cl_2, 298 K) δ_H = 9.67 (d, J = 4.4 Hz, 8H, a), 9.46 (d, J = 4.3 Hz, 8H, d), 8.76 (d, J = 4.4 Hz, 8H, b), 8.67 (d, J = 4.3 Hz, 8H, c), 8.33 (d, J = 4.4 Hz, 8H, e), 8.21 (s, 8H, o'$_{in}$), 8.03 (s, 8H, o'$_{out}$), 7.98 (s, 8H, p'), 7.79 (s, 8H, p), 7.77 (s, 8H, o$_{out}$), 7.71 (s, 8H, o$_{in}$), 7.38 (d, J = 4.4 Hz, f), 7.11 (s, 4H, ϵ), 6.78 (s, 8H, g), 6.65 (d, J = 8.4 Hz, 8H, γ_1), 6.47 (d, J = 8.4 Hz, 8H, δ_1), 6.39 (d, J = 6.7 Hz, 8H, β_1), 6.36 (s, 8H, δ_2), 5.70–5.66 (m, 8H, α_1), 5.00 (d, J = 6.6 Hz, 4H, β_2'), 4.81 (d, J = 6.5 Hz, 4H, β_2), 2.56–2.52 (m, 4H, α_2), 2.46–2.42 (m, 4H, α_2'), 1.50–0.67 (m, 1248H, THS$_{in}$ + THS$_{out}$ + THS'$_{in}$ + THS'$_{out}$) ppm. **^{19}F NMR** (470 MHz, CD_2Cl_2, 298 K) δ_F = −61.23 ppm. **MALDI-ToF** *m/z* 13515 (calculated for $[C_{856}H_{1352}N_{32}Si_{32}Zn_8]^+$ = ***c*-P8[b_6f_2]$^+$**: 13513).

***c*-P8[b$_8$]·(T4)$_2$:**



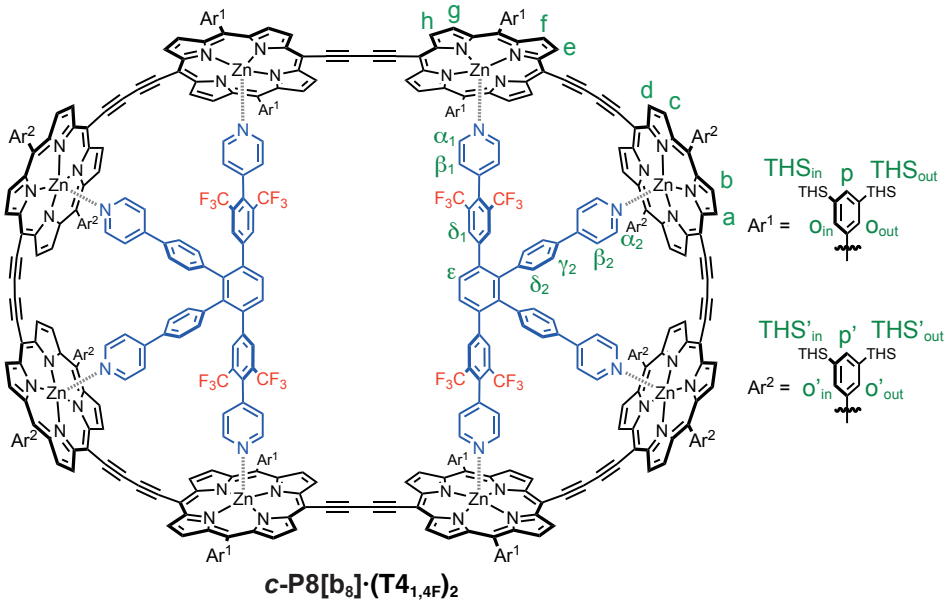
***c*-P8[b$_8$]·(T4)$_2$**

H-*l*-P4[b$_3$]-H (143 mg, 21.0 μmol) and **T4** (15.9 mg, 23.0 μmol) were dissolved in $CHCl_3$ (40 mL) and sonicated for 2 hours to allow for the complex formation. A catalyst mixture of $PdCl_2(PPh_3)_2$ (9.3 mg, 13.3 μmol), CuI (13.2 mg, 69.3 μmol), 1,4-benzoquinone (30.4 mg, 281 μmol), and *i*-Pr_2NH (0.42 mL) in $CHCl_3$ (10 mL) was added, and the reaction progress was monitored by analytical GPC (THF + 1% pyridine). After 4 hours, the mixture was passed through a pad of silica (eluent: $CHCl_3$ + 1% pyridine) and concentrated *in vacuo*. The crude residue was purified by SEC (toluene + 1% pyridine) before further purification by recycling GPC (toluene + 1% pyridine) to afford ***c*-P8[b$_8$]·(T4)$_2$** (53.2 mg, 37%) as a brown solid.

^{1}H NMR (600 MHz, CD_2Cl_2, 298 K) δ_H = 9.76 (d, J = 4.0 Hz, 8H, e/h), 9.64 (d, J = 4.1 Hz, 8H, a/d), 9.63–9.60 (m, 16H, a/d + e/h), 8.87 (d, J = 4.0 Hz, 8H, f/g), 8.84–8.77 (m, 24H, b + c + f/g), 8.41 (s, 8H, o'$_{in}$), 8.30 (s, 8H, o$_{in}$), 8.20 (s, 8H, o$_{out}$), 8.08 (s, 8H, o'$_{out}$), 8.05 (s, 8H, p), 8.03 (s, 8H, p'), 6.68 (s, 4H, ϵ), 6.14 (d, J = 9.5 Hz, 8H, δ_1), 6.02 (d, J = 9.5 Hz, 8H, γ_1), 5.70 (d, J = 8.7 Hz, 8H, δ_2), 5.64 (d, J = 8.7 Hz, 8H, γ_2), 5.39 (d, J = 7.3 Hz, 8H, β_1), 5.16 (d, J = 6.6 Hz, 8H, β_2), 2.64–2.55 (m, 8H, α_1), 2.46–2.36 (m, 8H, α_2), 1.59–0.71 (m, 1248H, THS$_{in}$ + THS$_{out}$ + THS'$_{in}$ + THS'$_{out}$) ppm. **UV-vis-NIR** ($CDCl_3$) λ_{max} / nm (log ϵ): 860 (5.98),

812 (5.68), 769 (5.51), 729 (5.09), 497 (5.98), 443 (5.74). **MALDI-ToF** *m/z* 13615 (calculated for $[C_{864}H_{1360}N_{32}Si_{32}Zn_8]^+$ = ***c*-P8[b$_8$]$^+$**: 13618).

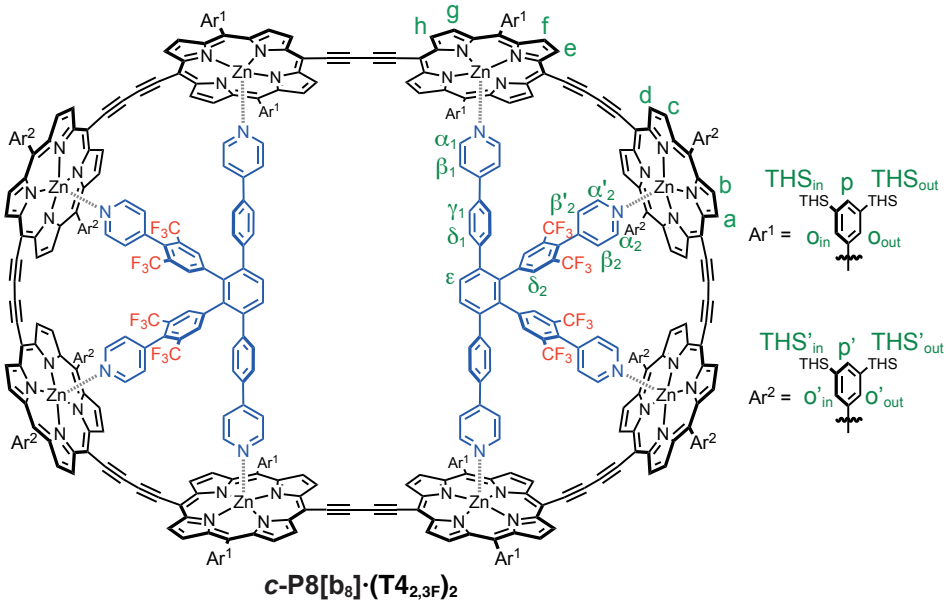
***c*-P8[b$_8$]·(T4$_{1,4F}$)$_2$**:



***c*-P8[b$_8$]·(T4$_{1,4F}$)$_2$**

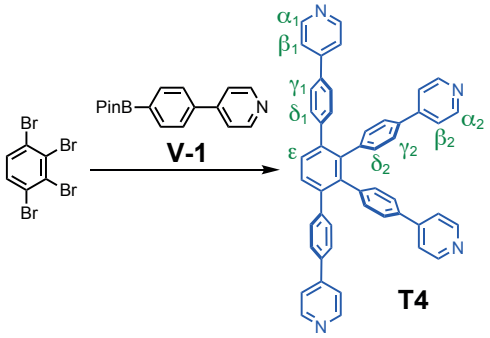
^{1}H NMR (600 MHz, CD_2Cl_2, 298 K) δ_H = 9.81 (d, J = 4.1 Hz, 8H, e/h), 9.68 (d, J = 4.2 Hz, 8H, a/d), 9.64–9.58 (m, 16H, a/d + e/h), 8.87–8.83 (m, 16H, b/c + f/g), 8.82 (d, J = 4.2 Hz, 8H, b/c), 8.75 (d, J = 4.1 Hz, 8H, f/g), 8.44 (s, 8H, o'$_{in}$), 8.22 (s, 8H, o$_{out}$), 8.13 (s, 8H, o$_{in}$), 8.11 (s, 8H, o'$_{out}$), 8.06 (s, 8H, p'), 8.00 (s, 8H, p), 6.83 (s, 4H, ϵ), 6.67 (s, 8H, δ_1), 5.82 (d, J = 8.7 Hz, 8H, δ_2), 5.77 (d, J = 8.7 Hz, γ_2), 5.19 (d, J = 6.6 Hz, 8H, β_2), 5.10 (d, J = 7.6 Hz, 8H, β_1), 2.57–2.52 (m, 8H, α_1), 2.50–2.44 (m, 8H, α_2), 1.66–0.57 (m, 1248H, THS$_{in}$ + THS$_{out}$ + THS'$_{in}$ + THS'$_{out}$) ppm. **^{19}F NMR** (470 MHz, CD_2Cl_2, 298 K) δ_F = −61.05 ppm. **MALDI-ToF** *m/z* 13615 (calculated for $[C_{864}H_{1360}N_{32}Si_{32}Zn_8]^+$ = ***c*-P8[b$_8$]$^+$**: 13618).

***c*-P8[b$_8$]·(T4$_{2,3F}$)$_2$:**



^{1}H NMR (600 MHz, CD_2Cl_2, 298 K) $\delta_H = 9.76$ (d, $J = 4.0$ Hz, 8H, e/h), 9.69 (d, $J = 4.4$ Hz, 8H, a), 9.68 (d, $J = 4.0$ Hz, 8H, e/h), 9.64 (d, $J = 4.3$ Hz, 8H, d), 8.89 (d, $J = 4.0$ Hz, 8H, f/g), 8.85 (d, $J = 4.0$ Hz, 8H, f/g), 8.78 (d, $J = 4.4$ Hz, 8H, b), 8.75 (d, $J = 4.3$ Hz, 8H, c), 8.37 (s, 8H, o_{in}), 8.21 (s, 16H, $o'_{in} + o_{out}$), 8.09 (s, 8H, o'_{out}), 8.05 (s, 8H, p), 8.01 (s, 8H, p'), 6.82 (s, 4H, ϵ), 6.18 (d, $J = 9.7$ Hz, 8H, δ_1), 6.17–6.13 (m, 16H, $\gamma_1 + \delta_2$), 5.44 (d, $J = 7.3$ Hz, 8H, β_1), 4.93 (d, $J = 6.3$ Hz, 4H, β'_2), 4.73 (d, $J = 6.0$ Hz, 4H, β_2), 2.74–2.66 (m, 8H, α_1), 2.52–2.46 (m, 4H, α_2), 2.45–2.41 (m, 4H, α'_2), 1.58–0.71 (m, 1248H, $THS_{in} + THS_{out} + THS'_{in} + THS'_{out}$) ppm. **^{19}F NMR** (470 MHz, CD_2Cl_2, 298 K) $\delta_F = -61.32$ ppm. **MALDI-ToF** *m/z* 13615 (calculated for $[C_{864}H_{1360}N_{32}Si_{32}Zn_8]^+$ = ***c*-P8[b$_8$]$^+$**: 13618).

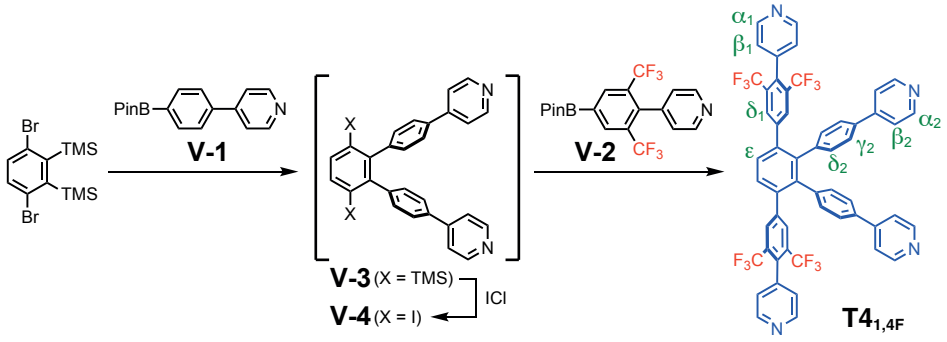
T4:



In a Schlenk flask, 1,2,3,4-tetrabromobenzene (356 mg, 0.904 mmol), boronic acid ester **V-1** (3.56 g, 12.7 mmol), and K_2CO_3 (3.90 g, 28.2 mmol) were dissolved in 1,4-dioxane (240 mL) and H_2O (50 mL) and subjected to two freeze-pump-thaw cycles. While the mixture was still frozen, $Pd(PPh_3)_4$ (406 mg, 351 µmol) was added followed by an additional freeze-pump-thaw cycle. The mixture was heated to 100 °C for 4 days, filtered through a short pad of silica (eluent: 20% MeOH/$CHCl_3$), and concentrated *in vacuo*. Purification by flash column chromatography (SiO_2, gradient elution: 0 to 10% MeOH/$CHCl_3$) followed by precipitation from $CHCl_3$/hexane afforded template **T4** (355 mg, 57%) as an off-white solid.

^{1}H NMR (500 MHz, $CDCl_3$, 298 K) δ_H = 8.64–8.60 (m, 4H, α_1), 8.58–8.54 (m, 4H, α_2), 7.62 (s, 2H, ϵ), 7.50 (d, J = 8.4 Hz, 4H, γ_1), 7.48–7.45 (m, 4H, β_1), 7.39–7.36 (m, 4H, β_2), 7.31 (d, J = 8.4 Hz, 4H, γ_2), 7.27 (d, J = 8.4 Hz, 4H, δ_1), 7.00 (d, J = 8.4 Hz, 4H, δ_2) ppm. **^{13}C NMR** (126 MHz, $CDCl_3$, 298 K) δ_C = 150.42, 150.35, 147.7, 147.6, 142.5, 140.8, 140.7, 139.8, 136.3, 135.5, 132.4, 130.7, 130.1, 126.5, 125.9, 121.5, 121.3 ppm. **HRMS** (ESI): *m/z* calcd for $C_{50}H_{35}N_4^+$ ($[M+H]^+$) 691.2856, found 691.2856.

$T4_{1,4F}$:

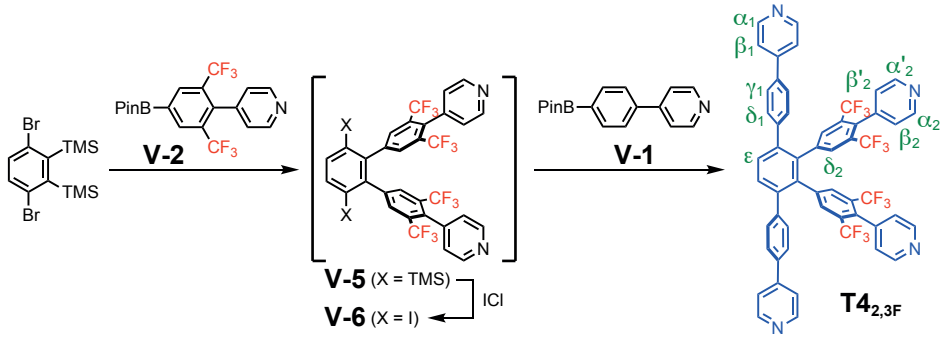


Step 1: A Schlenk flask charged with 1,4-bis(trimethylsilyl)-2,3-dibromobenzene (100 mg, 0.263 mmol), boronic acid ester **V-1** (185 mg, 0.657 mmol), K_3PO_4 (335 mg, 1.58 mmol), and $Pd(dppf)Cl_2 \cdot CH_2Cl_2$ (21.5 mg, 0.026 mmol) in DMF (2.5 mL) and H_2O (0.5 mL) was subjected to three freeze-pump-thaw cycles and heated to 90 °C. After stirring for 17 hours, the mixture was cooled to room temperature and filtered through a short pad of silica (eluent: 20% MeOH/$CHCl_3$). The crude mixture was purified by flash column chromatography (SiO_2, gradient elution: 1. 3/7 EtOAc/$CHCl_3$, 2. 3% MeOH/$CHCl_3$) to afford the bis-coupled product **V-3** (137 mg, 99%) as a pale, yellow solid containing minor impurities, presumably from desilylation. Step 2: The Suzuki-coupled product **V-3** (136 mg, 0.189 mmol) was dissolved in CH_2Cl_2 (3 mL) and cooled using an ice-water bath. A solution of iodine monochloride (1.13 mL, 1.13 mmol, 1.0 M in CH_2Cl_2) was added dropwise and the resulting mixture was stirred for one hour at which point complete conversion was confirmed by TLC. The orange suspension was transferred to a separatory funnel containing a sat. aq. solution of $Na_2S_2O_7$ (100 mL) and $CHCl_3$ (100 mL). The phases were thoroughly mixed and the organic phase separated. The aqueous phase was extracted once more with $CHCl_3$ (50 mL) and the combined organic extracts were washed with brine (100 mL) and H_2O (100 mL), dried over $MgSO_4$, filtered, and concentrated *in vacuo*. Purification by flash column chromatography (SiO_2, gradient elution: 0 to 5% MeOH/$CHCl_3$) gave the doubly iodinated product **V-4** (127 mg, 78%) as a purple-grey solid containing minor impurities. Step 3: A Schlenk flask charged with doubly iodinated product **V-4** (60 mg, 0.094 mmol), boronic acid ester **V-2** (98 mg,

0.236 mmol), and K_2CO_3 (78 mg, 0.566 mmol) in 1,4-dioxane (3 mL) and H_2O (0.5 mL) was subjected to two freeze-pump-thaw cycles and while the mixture was still frozen, $Pd(PPh_3)_4$ (27 mg, 0.024 mmol) was added, and three additional freeze-pump-thaw cycles were performed. The mixture was heated to 100 °C for 1.5 days, filtered through a short pad of silica (eluent: 15% MeOH/$CHCl_3$), and concentrated under reduced pressure. Purification by flash column chromatography (SiO_2, gradient elution: 0 to 7% MeOH/$CHCl_3$) gave the title compound **T4$_{1,4F}$** (62 mg, 68%) as a grey, off-white solid. Yield over 3 steps: 52%.

^{1}H NMR (500 MHz, $CDCl_3$) δ_H = 8.66–8.62 (m, 4H, α_1), 8.62–8.59 (m, 4H, α_2), 7.76 (s, 2H, ϵ), 7.74 (s, 4H, δ_1), 7.39 (d, J = 8.2 Hz, 4H, γ_2), 7.37–7.34 (m, 4H, β_2), 7.15 (br d, J = 5.4 Hz, 4H, β_1), 7.06 (d, J = 8.2 Hz, 4H, δ_2) ppm. **^{19}F NMR** (470 MHz, $CDCl_3$) δ_F = −60.49 ppm. **^{13}C NMR** (126 MHz, $CDCl_3$) δ_C = 150.5, 148.9, 147.5, 142.3, 141.9, 140.7, 139.2, 139.1, 137.3, 135.3, 132.1, 130.62 (q, $J_{C–F}$ = 5.6 Hz), 130.59 (q, $J_{C–F}$ = 30.3 Hz), 130.1, 126.6, 124.9 (br s), 122.9 (q, $J_{C–F}$ = 274.8 Hz), 121.5 ppm. **HRMS** (ESI): *m/z* calcd for $C_{54}H_{31}N_4F_{12}^+$ ([M+H]$^+$) 963.2352, found 963.2346.

$T4_{2,3F}$:



Step 1: A Schlenk flask charged with 1,4-bis(trimethylsilyl)-2,3-dibromobenzene (60 mg, 0.158 mmol), boronic acid ester **V-2** (165 mg, 0.394 mmol), K_3PO_4 (201 mg, 0.947 mmol), and Pd(dppf)Cl_2·CH_2Cl_2 (12.9 mg, 0.016 mmol) in DMF (3.0 mL) and H_2O (0.5 mL) was subjected to four freeze-pump-thaw cycles and heated to 90 °C. After stirring for 8.5 hours, the mixture was cooled to room temperature and filtered through a short pad of silica (eluent: 15% MeOH/$CHCl_3$). The crude mixture was purified by flash column chromatography (SiO_2, gradient elution: 10 to 20 to 30% EtOAc/toluene) to afford the bis-coupled product **V-5** (48 mg, 38%) as an off-white solid containing minor impurities, presumably from desilylation. Step 2: The Suzuki-coupled product **V-5** (48 mg, 0.060 mmol) was dissolved in CH_2Cl_2 (2 mL) and cooled using an ice-water bath. A solution of iodine monochloride (1.8 mL, 1.8 mmol, 1.0 M in CH_2Cl_2) was added dropwise and the resulting mixture was stirred for three hours at which point complete conversion was confirmed by TLC. The mixture was diluted with $CHCl_3$ (50 mL) and washed with a sat. aq. solution of $Na_2S_3O_7$ (2 x 50 mL), brine (100 mL), and H_2O (100 mL), dried over $MgSO_4$, filtered, and concentrated under reduced pressure. Purification by flash column chromatography (SiO_2, 3% MeOH/$CHCl_3$) gave the doubly iodinated product **V-6** (51 mg, 94%) as an off-white solid containing minor impurities. Step 3: A Schlenk flask charged with doubly iodinated product **V-6** (51 mg, 0.056 mmol), boronic acid ester **V-1** (63 mg, 0.225 mmol), and K_2CO_3 (93 mg, 0.674 mmol) in 1,4-dioxane (2 mL) and H_2O (0.5 mL) was subjected to two freeze-pump-thaw cycles, and while the mixture was

still frozen, $Pd(PPh_3)_4$ (19.5 mg, 0.017 mmol) was added, and three additional freeze-pump-thaw cycles were performed. The mixture was heated to 100 °C for 1.5 days, filtered through a short pad of silica (eluent: 15% MeOH/$CHCl_3$), and concentrated *in vacuo*. Purification by flash column chromatography (SiO_2, gradient elution: 0 to 7% MeOH/$CHCl_3$) followed by precipitation from $CHCl_3$/hexane 1:1 gave the title compound $\mathbf{T4_{2,3F}}$ (38 mg, 70%) as a white solid. Yield over 3 steps: 25%.
^{1}H NMR (500 MHz, $CDCl_3$) $\delta_H = 8.71$–8.65 (m, 4H, α_1), 8.62 (br d, $J = 3.8$ Hz, 4H, α_2 / α_2'), 7.77 (s, 2H, ϵ), 7.62 (d, $J = 8.3$ Hz, 4H, γ_1), 7.51–7.46 (m, 4H, β_1), 7.41 (s, 4H, δ_2), 7.31 (d, $J = 8.3$ Hz, 4H, δ_1), 7.10 (br d, $J = 3.8$ Hz, 2H, β_2 / β_2'), 6.96 (br d, $J = 3.8$ Hz, 2H, β_2 / β_2') ppm. **^{19}F NMR** (470 MHz, $CDCl_3$) $\delta_F = -60.70$ ppm. **^{13}C NMR** (126 MHz, $CDCl_3$) $\delta_F = 150.6$, 149.1, 148.8, 147.5, 141.9, 141.2, 140.7, 140.4, 137.7, 137.3, 135.4, 132.6 (q, $J_{C–F} = 5.0$ Hz), 131.4, 130.7, 130.4 (q, $J_{C–F} = 30.4$ Hz), 127.2, 124.8, 124.6, 122.6 (q, $J_{C–F} = 275.0$ Hz), 121.7 ppm. **HRMS** (ESI): *m/z* calcd for $C_{54}H_{31}N_4F_{12}^+$ ($[M+H]^+$) 963.2352, found 963.2344.

5.6 Supplemental Results and Analysis

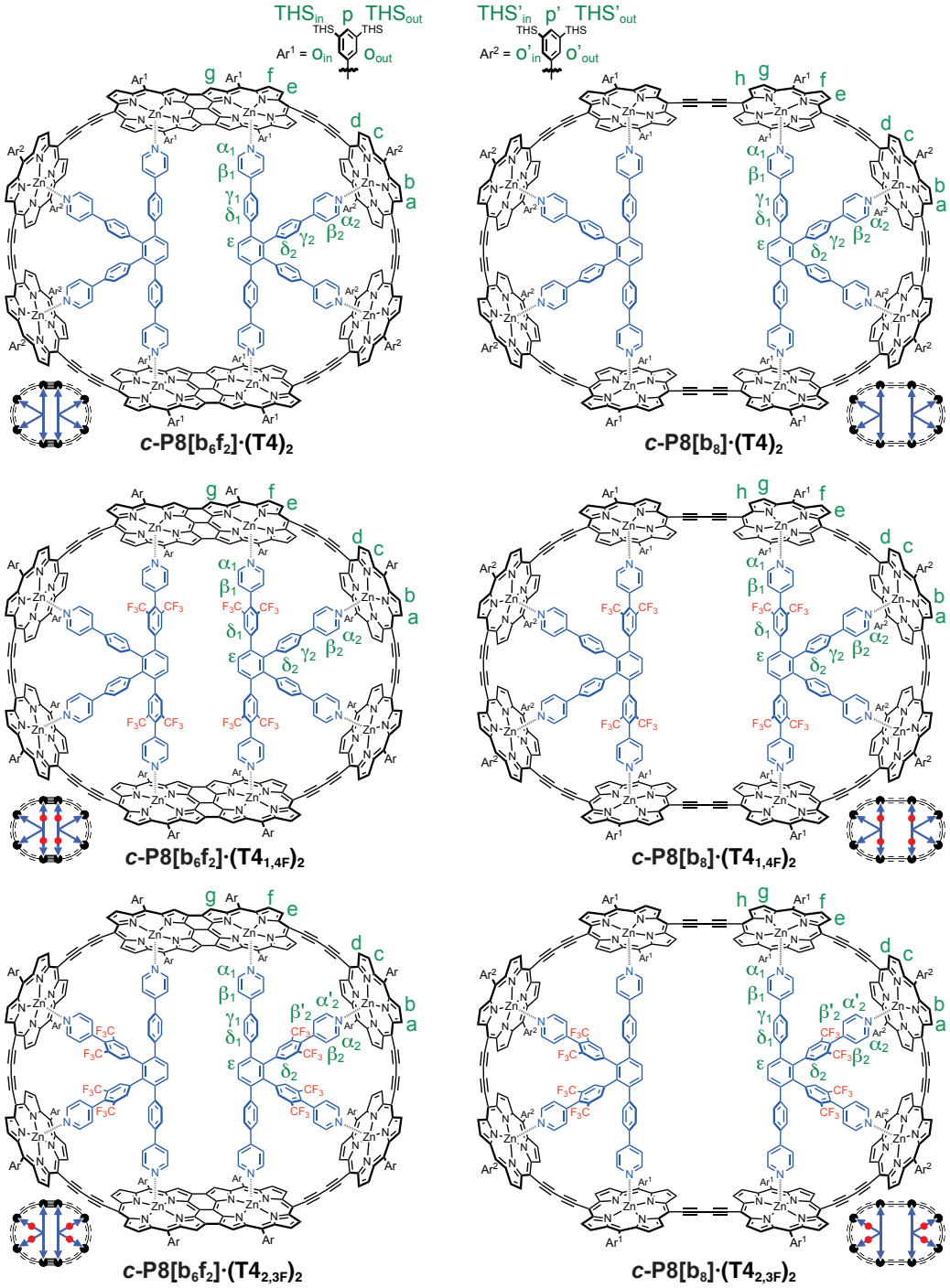


Figure 5.11: Overview of the chemical structures, cartoon representations, and NMR labeling schemes of the nanoring complexes investigated in this chapter. $Ar^1 = Ar^2 =$ 3,5-bis(trihexylsilyl)phenyl.

NMR of Oxidized Nanoring Complexes

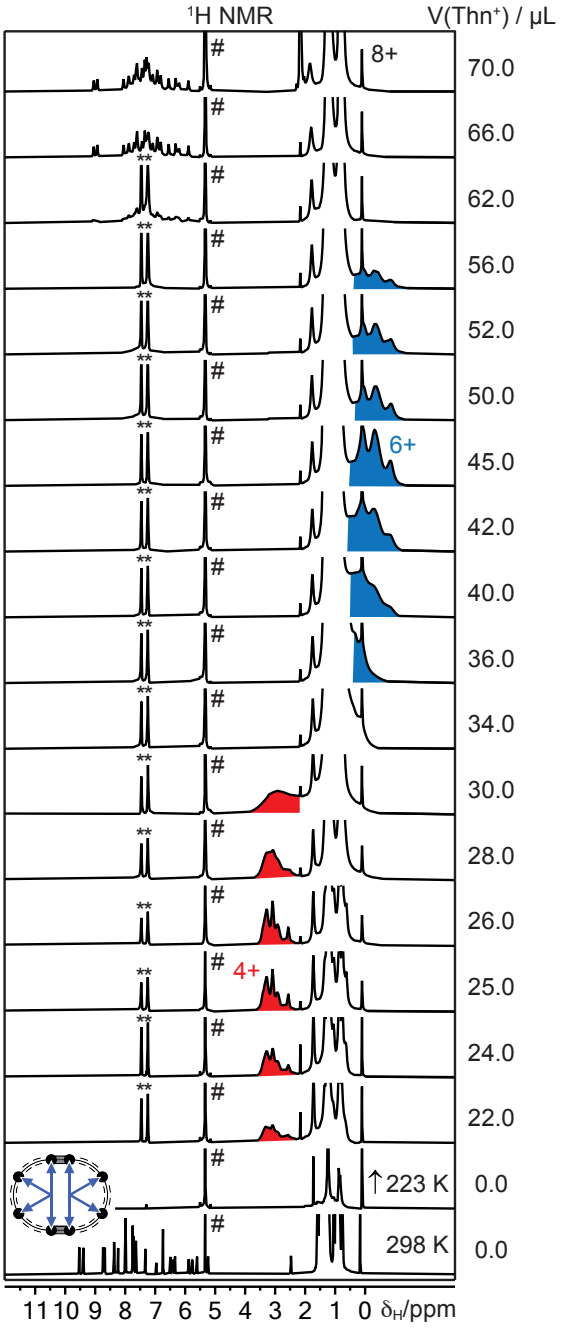


Figure 5.12: Summary of the ^{1}H NMR titration of ***c*-P8[b$_6$f$_2$]·(T4)$_2$** (500 MHz, 223 K) with **ThnSbF$_6$** in CD_2Cl_2; 6.5 µL Thn^+ solution contain about 1 equivalent of oxidant. Shifted $THS^{(\cdot)}_{in}$ resonances indicating global antiaromaticity are highlighted in red; those indicating global aromaticity are highlighted in blue. Peaks assigned with # and * arise from CD_2Cl_2 and neutral thianthrene, respectively.

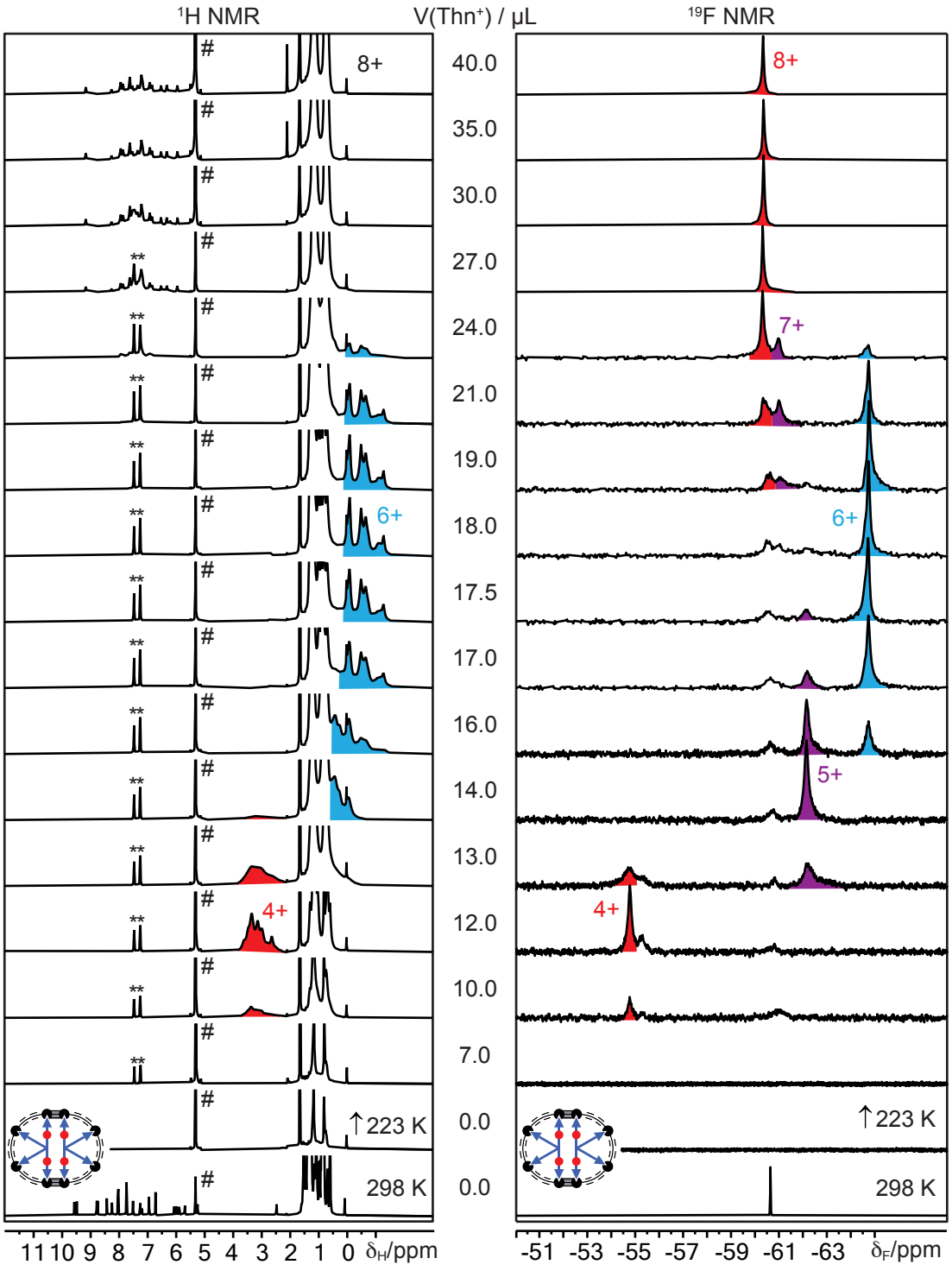


Figure 5.13: Summary of the ^{1}H and ^{19}F NMR titration of ***c*-P8[b$_6$f$_2$]·(T4$_{1,4F}$)$_2$** (500/471 MHz, 223 K) with **ThnSbF$_6$** in CD_2Cl_2; 3 µL Thn^+ solution contain about 1 equivalent of oxidant. Shifted $THS^{(\cdot)}{}_{in}$ and CF_3 resonances indicating global antiaromaticity are highlighted in red; those indicating global aromaticity are highlighted in blue. Odd-numbered oxidation states are highlighted in purple in the ^{19}F NMR spectra. Peaks assigned with # and * arise from CD_2Cl_2 and neutral thianthrene, respectively.

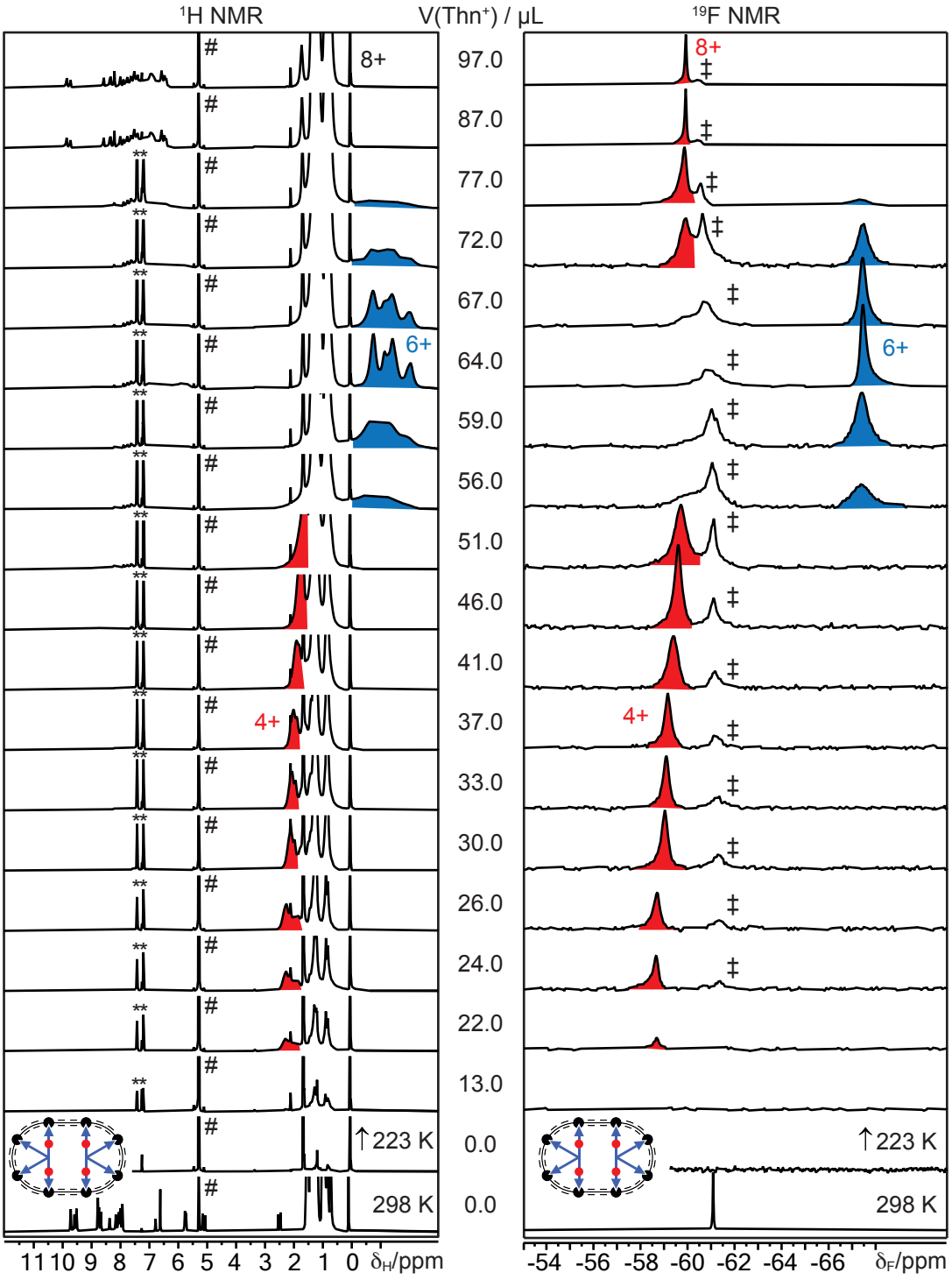


Figure 5.14: Summary of the ^{1}H and ^{19}F NMR titration of ***c*-P8[b$_8$]·(T4$_{1,4F}$)$_2$** (500/471 MHz, 223 K) with **ThnSbF$_6$** in CD_2Cl_2; 10 µL Thn^+ solution contain about 1 equivalent of oxidant. Shifted $THS^{(\cdot)}_{in}$ and CF_3 resonances indicating global antiaromaticity are highlighted in red; those indicating global aromaticity are highlighted in blue. Peaks assigned with # and * arise from CD_2Cl_2 and neutral thianthrene, respectively. Residual ^{19}F resonances assigned with ‡ indicate decomposed nanoring.

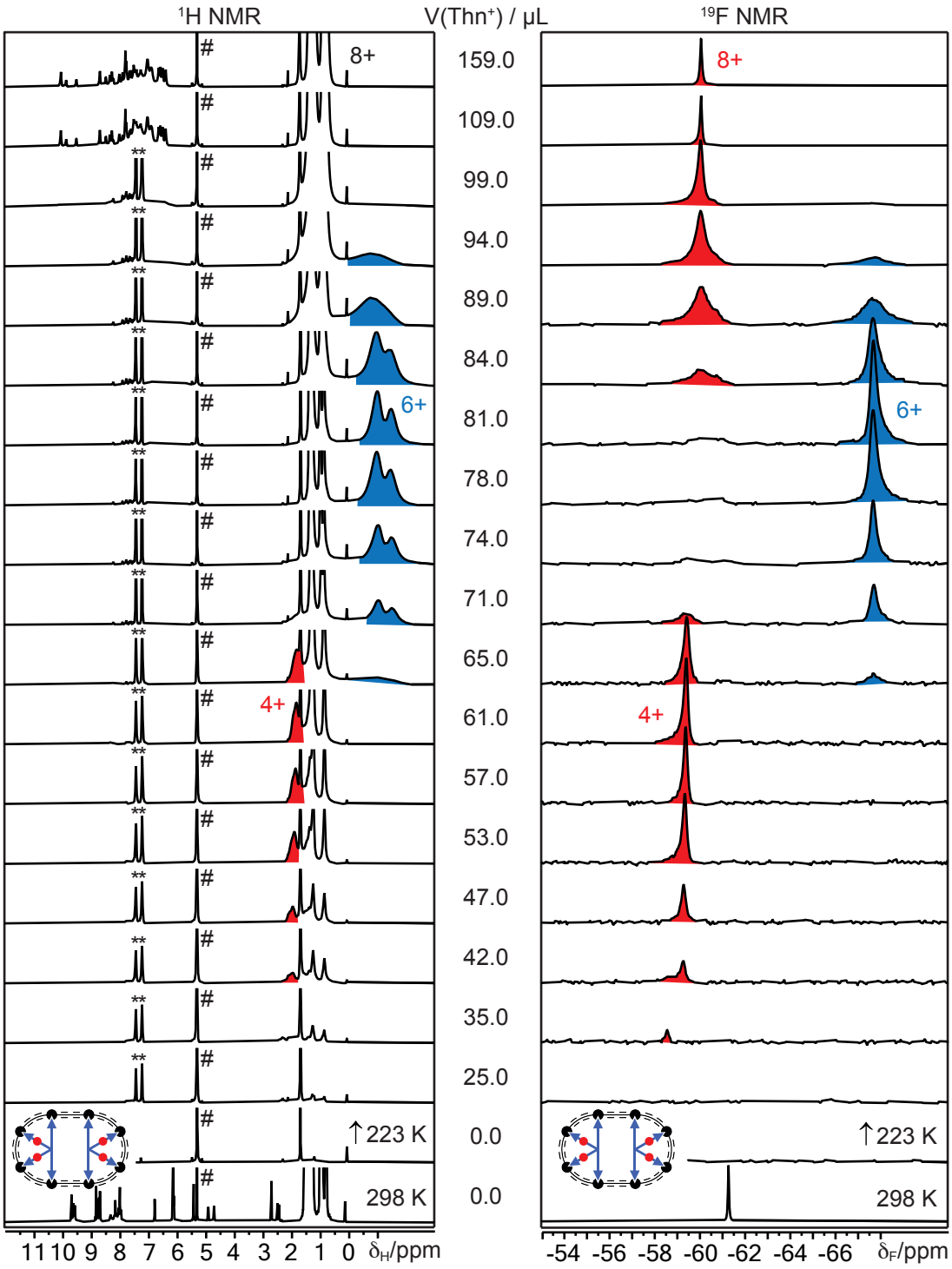


Figure 5.15: Summary of the ^{1}H and ^{19}F NMR titration of ***c*-P8[b$_8$]·(T4$_{2,3F}$)$_2$** (500/471 MHz, 223 K) with **ThnSbF$_6$** in CD_2Cl_2; 13.5 µL Thn^+ solution contain about 1 equivalent of oxidant. Shifted $THS^{(\cdot)}_{in}$ and CF_3 resonances indicating global antiaromaticity are highlighted in red; those indicating global aromaticity are highlighted in blue. Peaks assigned with # and * arise from CD_2Cl_2 and neutral thianthrene, respectively.

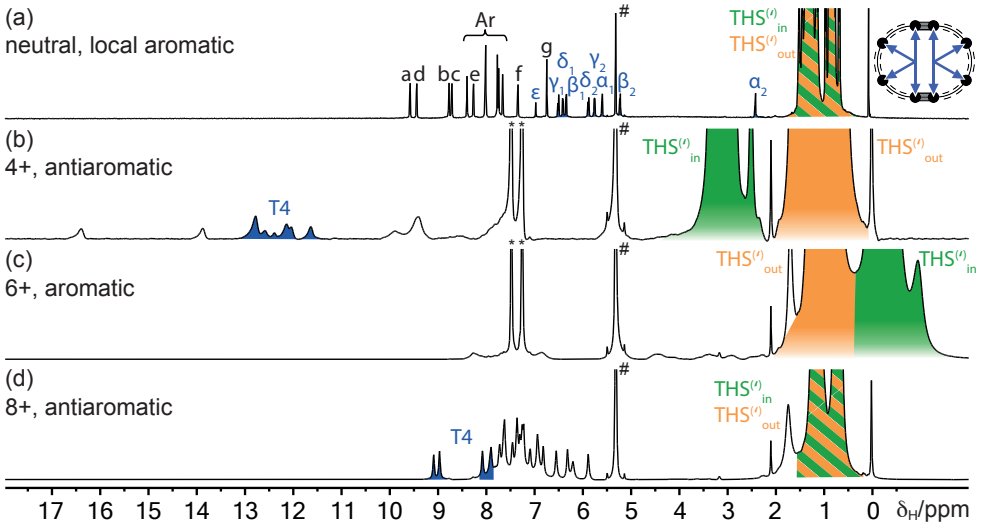


Figure 5.16: Summary of ^{1}H NMR (500 MHz, CD_2Cl_2) spectra of neutral (a, 298 K) and oxidized (b–d, 223 K) ***c*-P8[b$_6$f$_2$]·(T4)$_2$** obtained during an oxidation titration with **ThnSbF$_6$**. Refer to Figure 5.11 for labeling scheme. Peaks assigned with # and * arise from CD_2Cl_2 and neutral thianthrene, respectively. Unlabeled resonances were not unambiguously assigned.

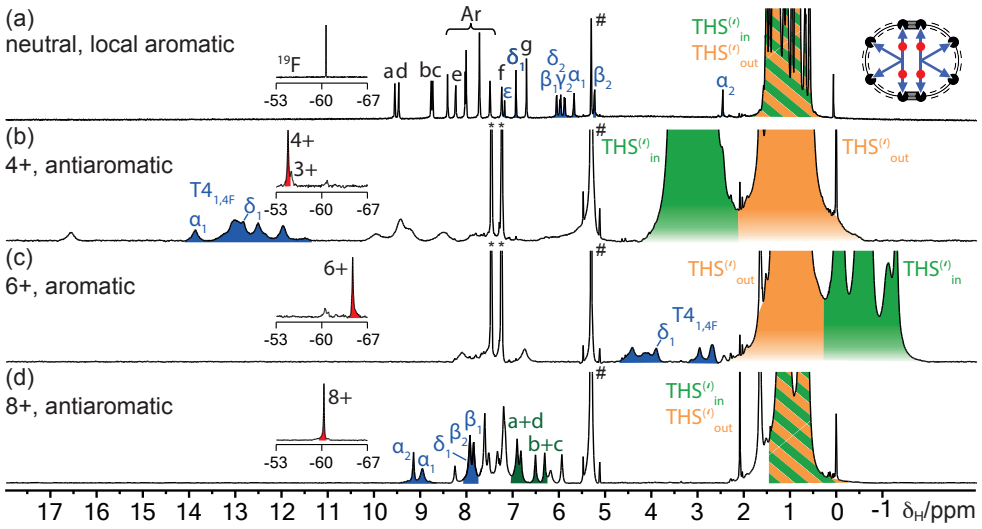


Figure 5.17: Summary of ^{1}H NMR (500 MHz, CD_2Cl_2) spectra of neutral (a, 298 K) and oxidized (b–d, 223 K) ***c*-P8[b$_6$f$_2$]·(T4$_{1,4F}$)$_2$** obtained during an oxidation titration with **ThnSbF$_6$**. The inserts show concomitantly recorded ^{19}F NMR (471 MHz, CD_2Cl_2) spectra of the CF_3 probes. Refer to Figure 5.11 for labeling scheme. Peaks assigned with # and * arise from CD_2Cl_2 and neutral thianthrene, respectively. Unlabeled resonances were not unambiguously assigned.

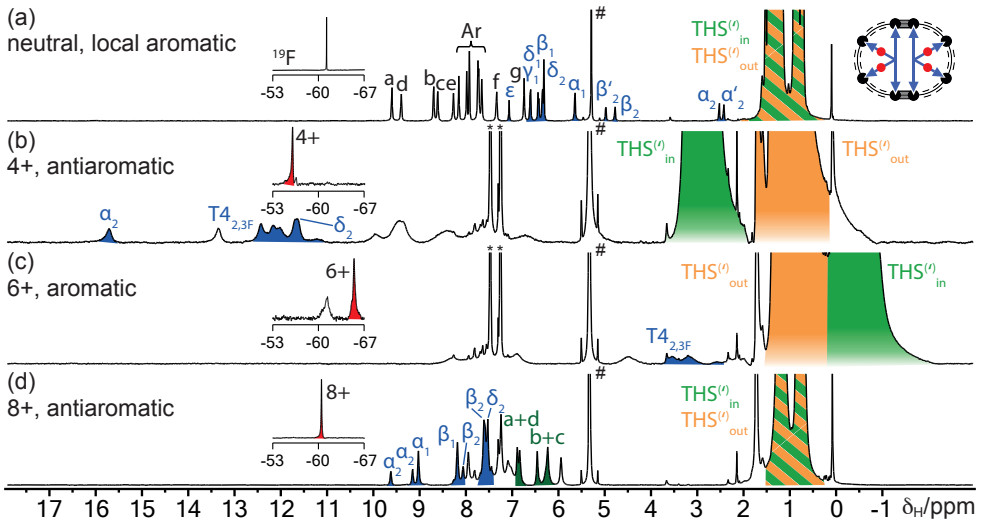


Figure 5.18: Summary of ^{1}H NMR (500 MHz, CD_2Cl_2) spectra of neutral (a, 298 K) and oxidized (b–d, 223 K) ***c*-P8[b_6f_2]·($T4_{2,3F}$)$_2$** obtained during an oxidation titration with **ThnSbF$_6$**. The inserts show concomitantly recorded ^{19}F NMR (471 MHz, CD_2Cl_2) spectra of the CF_3 probes. Refer to Figure 5.11 for labeling scheme. Peaks assigned with # and * arise from CD_2Cl_2 and neutral thianthrene, respectively. Unlabeled resonances were not unambiguously assigned.

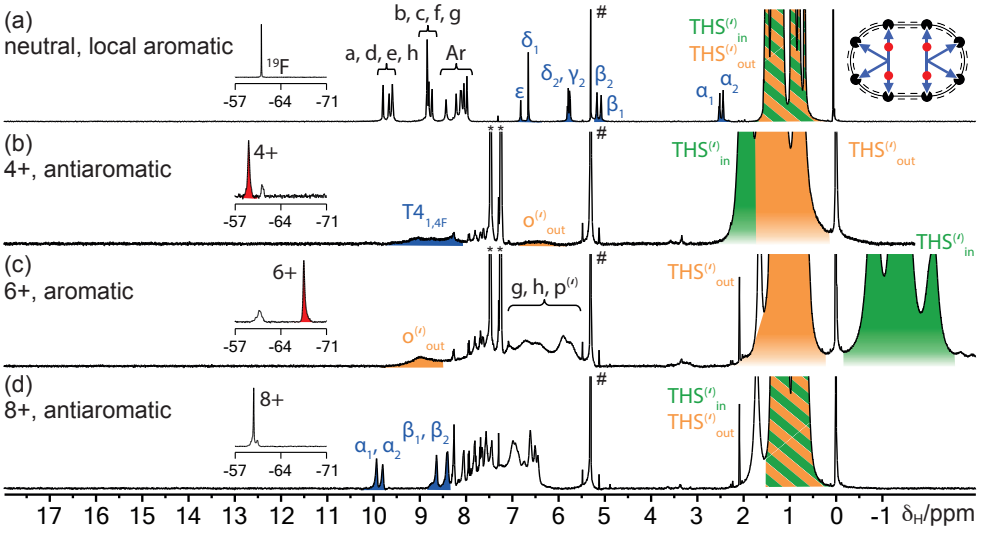


Figure 5.19: Summary of ^{1}H NMR (500 MHz, CD_2Cl_2) spectra of neutral (a, 298 K) and oxidized (b–d, 223 K) ***c*-P8[b_8]·($T4_{1,4F}$)$_2$** obtained during an oxidation titration with **ThnSbF$_6$**. The inserts show concomitantly recorded ^{19}F NMR (471 MHz, CD_2Cl_2) spectra of the CF_3 probes. Refer to Figure 5.11 for labeling scheme. Peaks assigned with # and * arise from CD_2Cl_2 and neutral thianthrene, respectively. Unlabeled resonances were not unambiguously assigned.

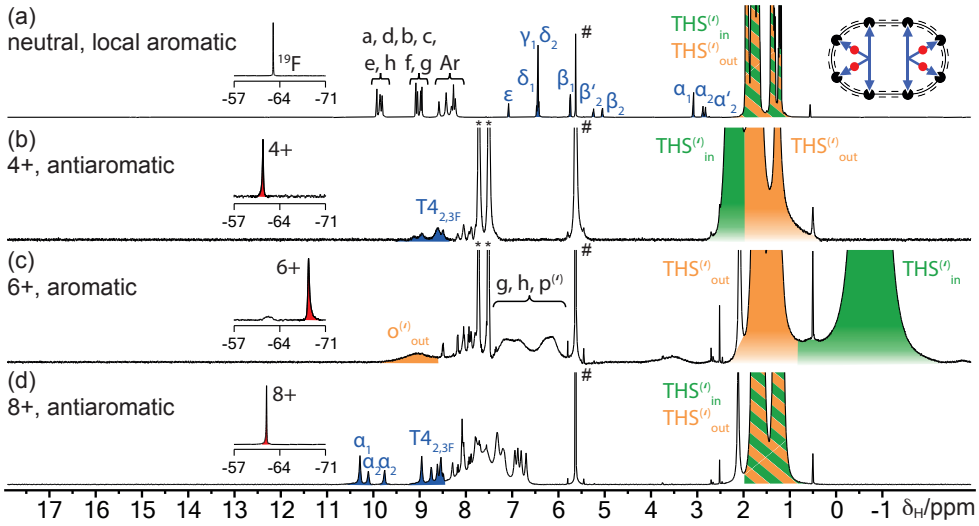


Figure 5.20: Summary of ^{1}H NMR (500 MHz, CD_2Cl_2) spectra of neutral (a, 298 K) and oxidized (b–d, 223 K) ***c*-P8[b$_8$]·(T4$_{2,3F}$)$_2$** obtained during an oxidation titration with **ThnSbF$_6$**. The inserts show concomitantly recorded ^{19}F NMR (471 MHz, CD_2Cl_2) spectra of the CF_3 probes. Refer to Figure 5.11 for labeling scheme. Peaks assigned with # and * arise from CD_2Cl_2 and neutral thianthrene, respectively. Unlabeled resonances were not unambiguously assigned.

Summary of Experimental Results and NICS Calculations

Negative NICS/$\Delta\delta$ values and $4n$+2 Hückel classification correspond to aromaticity; positive NICS/$\Delta\delta$ values and $4n$ Hückel classification to antiaromaticity. NICS(0) values were calculated in the center of the nanoring complexes using DFT (LC-ωhPBE/6-31G* (ω=0.1)) without template. The chemical shift differences $\Delta\delta_{\mathrm{THS}} = \delta_{\mathrm{THS}(^t)_{\mathrm{in}}} - \delta_{\mathrm{THS}(^t)_{\mathrm{out}}}$ were calculated using the average chemical shift of the respective multiplets. $\Delta\delta_{\mathrm{X}} = \delta_{\mathrm{X,bound}} - \delta_{\mathrm{X,unbound}}$ values describe the chemical shift differences of template resonances X = α_1, α_2, δ_1, and δ_2 in the nanoring complexes with respect to free template. $\Delta\delta_{\mathrm{F}} = \delta_{\mathrm{F,bound}} - \delta_{\mathrm{F,unbound}}$ values describe the ^{19}F chemical shift differences of the CF_3 groups with respect to free template. The chemical shift differences $\Delta\delta_{\mathrm{F}}$ for the oxidized nanoring complexes were calculated using the chemical shifts of unbound template in CD_2Cl_2 at 223 K: $\delta_{\mathrm{F}}(\mathbf{T4_{1,4F}}) = -60.59$ ppm; $\delta_{\mathrm{F}}(\mathbf{T4_{2,3F}}) = -60.69$ ppm.

Table 5.2: Summary of the calculated (NICS, ppm) and experimental ($\Delta\delta$, ppm) results for the study of global (anti)aromaticity in ***c*-P8[b_6f_2]·(T4)$_2$**; [a]local aromatic current observed.

***c*-P8[b_6f_2]·(T4)$_2$**	0	4+	6+	8+
n π-e$^-$	104/96	100/92	98/90	96/88
Hückel classification	$4n\pi$[a]	$4n\pi$	$4n$+2π	$4n\pi$
NICS(0)$_{ZZ}$	0.69	6.86	−37.5	3.97
NICS(0)$_{iso}$	−0.76	1.83	−12.7	1.37
$\Delta\delta_{THS}$	0	2.12	−1.53	−
$\Delta\delta_{\alpha_1}$	−3.03	5.25	−	0.35
$\Delta\delta_{\alpha_2}$	−6.15	7.83	−	0.53

Table 5.3: Summary of the calculated (NICS, ppm) and experimental ($\Delta\delta$, ppm) results for the study of global (anti)aromaticity in ***c*-P8[b_6f_2]·(T4$_{1,4F}$)$_2$**; [a]local aromatic current observed.

***c*-P8[b_6f_2]·(T4$_{1,4F}$)$_2$**	0	4+	6+	8+
n π-e$^-$	104/96	100/92	98/90	96/88
Hückel classification	$4n\pi$[a]	$4n\pi$	$4n$+2π	$4n\pi$
NICS(0)$_{ZZ}$	0.69	6.86	−37.5	3.97
NICS(0)$_{iso}$	−0.76	1.83	−12.7	1.37
$\Delta\delta_{THS}$	0	2.20	−1.61	−
$\Delta\delta_{\alpha_1}$	−2.94	5.25	−	0.34
$\Delta\delta_{\alpha_2}$	−6.12	7.97	−	0.56
$\Delta\delta_{\delta_1}$	−0.79	5.11	−3.83	0.20
$\Delta\delta_{1,4F}$	−0.12	5.83	−4.15	0.29

Table 5.4: Summary of the calculated (NICS, ppm) and experimental ($\Delta\delta$, ppm) results for the study of global (anti)aromaticity in ***c*-P8[b_6f_2]·(T4$_{2,3F}$)$_2$**; [a]local aromatic current observed.

***c*-P8[b_6f_2]·(T4$_{2,3F}$)$_2$**	0	4+	6+	8+
n π-e$^-$	104/96	100/92	98/90	96/88
Hückel classification	$4n\pi$[a]	$4n\pi$	$4n$+2π	$4n\pi$
NICS(0)$_{ZZ}$	0.69	6.86	−37.5	3.97
NICS(0)$_{iso}$	−0.76	1.83	−12.7	1.37
$\Delta\delta_{THS}$	0	1.76	−1.76	−
$\Delta\delta_{\alpha_1}$	−3.00	4.73	−	0.37
$\Delta\delta_{\delta_2}$	−1.05	4.30	−	0.12
$\Delta\delta_{2,3F}$	−0.53	4.62	−4.72	0.23

Table 5.5: Summary of the calculated (NICS, ppm) and experimental ($\Delta\delta$, ppm) results for the study of global (anti)aromaticity in ***c*-P8[$\mathbf{b_8}$]·($\mathbf{T4_{1,4F}}$)$_2$**; [a]local aromatic current observed.

***c*-P8[$\mathbf{b_8}$]·($\mathbf{T4_{1,4F}}$)$_2$**	0	4+	6+	8+
n π-e$^-$	112	108	106	104
Hückel classification	$4n\pi$[a]	$4n\pi$	$4n$+2π	$4n\pi$
NICS(0)$_{ZZ}$	0.53	8.64	−39.1	1.84
NICS(0)$_{iso}$	−0.68	2.12	−13.6	0.40
$\Delta\delta_{THS}$	0	1.17	−2.34	−
$\Delta\delta_{1,4F}$	−0.14	1.48	−6.93	0.73

Table 5.6: Summary of the calculated (NICS, ppm) and experimental ($\Delta\delta$, ppm) results for the study of global (anti)aromaticity in ***c*-P8[$\mathbf{b_8}$]·($\mathbf{T4_{2,3F}}$)$_2$**; [a]local aromatic current observed.

***c*-P8[$\mathbf{b_8}$]·($\mathbf{T4_{2,3F}}$)$_2$**	0	4+	6+	8+
n π-e$^-$	112	108	106	104
Hückel classification	$4n\pi$[a]	$4n\pi$	$4n$+2π	$4n\pi$
NICS(0)$_{ZZ}$	0.53	8.64	−39.1	1.84
NICS(0)$_{iso}$	−0.68	2.12	−13.6	0.40
$\Delta\delta_{THS}$	0	1.06	−2.34	−
$\Delta\delta_{\alpha_1}$	−5.98	−	−	1.45
$\Delta\delta_{2,3F}$	−0.62	1.27	−7.16	0.61

6

Charge Delocalization and Global Aromaticity in a Partially Fused 12-Porphyrin Nanoring

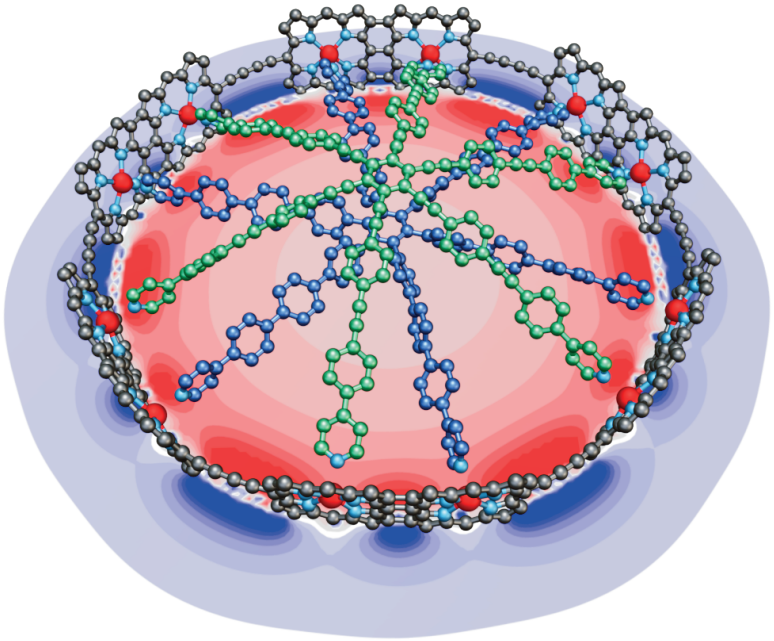
Contents

6.1 Abstract 260
6.2 Introduction 261
6.3 Results and Discussion 262
6.3.1 Molecular Modelling and Template Design 262
6.3.2 Template-Directed Synthesis 266
6.3.3 Stability of the Ternary Template Complexes 269
6.3.4 UV-vis-NIR Absorption Spectra 271
6.3.5 Global Charge Delocalization in Oxidized Porphyrin Nanorings 273
6.3.6 Global Charge Delocalization in Reduced Porphyrin Nanorings 281
6.4 Summary and Conclusions 283
6.5 Methods 285
6.5.1 General Methods 285
6.5.2 Synthetic Procedures 287
6.6 Supplemental Results and Analysis 302

The work in this chapter was published in:

S. M. Kopp, H. Gotfredsen, J. Hergenhahn, A. R. Rubio, J.-R. Deng, H. Zhu, W. Stawski, and H. L. Anderson, *Charge Delocalization and Global Aromaticity in a Partially Fused 12-Porphyrin Nanoring*, *Chem*, **2024**, DOI: 10.1016/j.chempr.2024.06.034.

6.1 Abstract



Aromatic and antiaromatic ring currents can reveal global electronic delocalization around the circumference of π-conjugated macrocycles. Here, the template-directed synthesis of a fully π-conjugated cyclic porphyrin 12-mer consisting of six β,*meso*,β-edge-fused porphyrin dimers connected by six butadiyne bridges is presented. The bathochromic shift of the lowest energy π-π* absorption band of this partially fused nanoring extends far into the NIR, confirming the strong conjugation around the circumference of the macrocycle. Investigation of the oxidized and reduced nanoring-template complex by ^{1}H and ^{19}F NMR spectroscopy demonstrates the presence of coherent global (anti)aromatic ring currents, consistent with DFT calculations. The stronger π-conjugation enables global charge delocalization even at low levels of oxidation or reduction. These findings open new avenues for the engineering of cyclic molecular wires.

6.2 Introduction

Molecular wire rings with efficient electronic transmission around their circumferences show promise for applications as materials in organic solar cells,[130, 131, 407, 408] light-emitting diodes,[132–135, 409] photodetectors,[136, 137] sensors,[138–140, 410] and as field effect transistors in molecular electronics.[128, 129, 411] Their high symmetries lead to greater electronic delocalization than linear wires for two reasons: the absence of ends allows every site in a ring to be equivalent, and the wavefunction of a cyclic wire approximates to that of a quantum particle on a ring, rather than a particle in a box. Global aromatic or antiaromatic ring currents can arise when a cyclic molecular wire is placed in a magnetic field and can be detected through the resulting pattern of local magnetic shielding and deshielding, providing evidence for electronic delocalization around the ring. In recent years, global (anti)aromatic ring currents have been observed in large π-conjugated macrocycles with Hückel circuits of up to 162 delocalized π-electrons and diameters of up to 5 nm. These molecular ring currents are analogues to the persistent currents in mesoscopic metal rings at low temperature.[54–56, 173, 175, 363, 385] Belt-shaped π-conjugated macrocycles have recently attracted interest due to their intriguing electronic properties and as hosts in supramolecular aggregates.[374, 412–415] Nanobelts exhibit enhanced π-conjugation in comparison to their nanoring counterparts, resulting in efficient global charge delocalization and highly tunable, size-dependent energy gaps.[412, 416, 417] Edge-fused porphyrin nanobelts such as ***c*-P12[$\mathbf{f}_{12}$]** in Figure 6.1, which have not yet been synthesized, are fascinating cyclic analogues of the β,*meso*,β-fused porphyrin nanoribbons pioneered by Osuka and investigated in Chapter 2 of this thesis.[113, 377, 418] Porphyrin nanoribbons display exceptional electronic delocalization resulting in π-π* absorption bands that extend far into the IR, and a shallow length-dependence of their molecular conductance.[108, 200, 201, 203, 267, 268]

The results in Chapter 5 show that incorporating two edge-fused porphyrin dimers in a butadiyne-linked cyclic porphyrin octamer (3:1 ratio of butadiyne and β,*meso*,β-fused porphyrin links) results in strong π-conjugation and amplifies the global ring

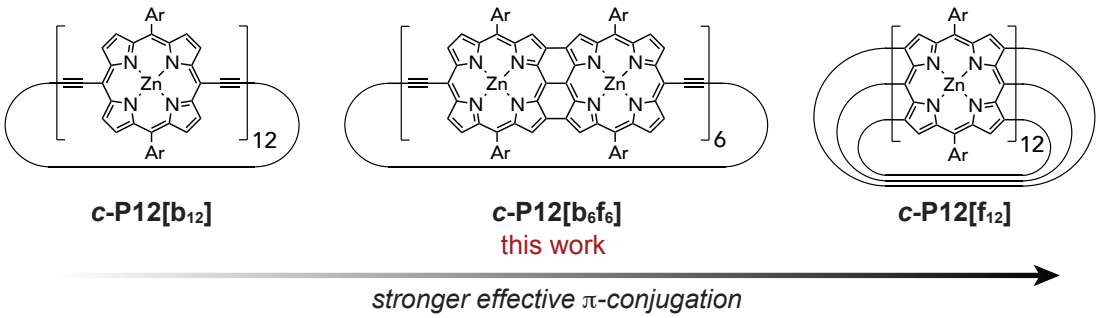


Figure 6.1: Chemical structures of butadiyne linked 12-porphyrin nanoring ***c*-P12[b$_{12}$]**, partially fused 12-ring ***c*-P12[b$_6$f$_6$]**, and porphyrin nanobelt ***c*-P12[f$_{12}$]** ordered with increasing strength of their effective π-conjugation; Ar = solubilizing sidechain.

currents in the oxidized nanoring.[385] The work in this chapter expands these promising results with the template-directed synthesis of a partially fused 12-porphyrin nanoring ***c*-P12[b$_6$f$_6$]**, consisting of six β,*meso*,β-fused porphyrin dimers connected by six butadiyne links (1:1 ratio of butadiyne and β,*meso*,β-fused linkers) and marks an important step towards investigating the electronic properties of fused porphyrin nanobelts (Figure 6.1).[377, 385]

6.3 Results and Discussion

6.3.1 Molecular Modelling and Template Design

The partially fused 12-porphyrin nanoring ***c*-P12[b$_6$f$_6$]** consists of six β,*meso*,β-fused porphyrin dimer units connected by six butadiyne links, resulting in an approximate D_{6h} symmetry. The calculated strain in this nanoring is 80.8 kJ mol^{-1}. This level of strain is intermediate between that of ***c*-P12[b$_{12}$]** (49.6 kJ mol^{-1}) and ***c*-P6[b$_6$]** (98.1 kJ mol^{-1}), indicating that ***c*-P12[b$_6$f$_6$]** is an attainable target for template-directed synthesis. Investigation of the strain distribution in ***c*-P12[b$_6$f$_6$]** using the StrainViz method introduced by Colwell *et al.*[419] indicates that 63% of the strain is localized in the butadiyne-linkers and adjacent meso-carbons, while only 37% of the strain is distributed over the edge-fused porphyrin dimers (Figure 6.2). Consequently, the fused porphyrin dimer units are only slightly curved and most of the deformation is accommodated by the butadiynes.

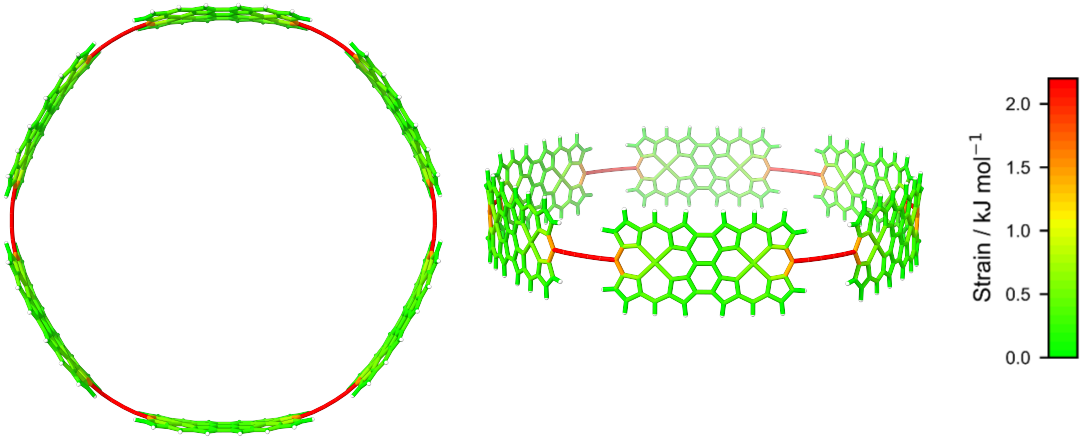


Figure 6.2: Topview (left) and sideview (right) of the StrainViz representation of the strain distribution in ***c*-P12[b_6f_6]**.

It would be difficult to design a single 12-legged template for directing the synthesis of ***c*-P12[b_6f_6]**. Instead, a 6-legged template was synthesized, such that two molecules of the template stack inside the cavity of ***c*-P12[b_6f_6]**. Previous work in the Anderson group has shown that the use of two stacked templates can be a very successful strategy for synthesizing large porphyrin nanorings such as ***c*-P12[b_{12}]**.[49, 420] Initially, the 6-legged template **T6$_A$** shown in Figure 6.3 was designed and synthesized based on preliminary molecular mechanics modelling using the MM+ force field (Figure 6.19) to direct the formation of ***c*-P12[b_6f_6]**.[421]

The Zn···Zn diameter of ***c*-P12[b_6f_6]** is 4.16 nm (for the DFT optimized structure with the Zn atoms 4-coordinate square planar). The average length of a N(pyridine)–Zn(porphyrin) coordinate bond is 2.16 Å and the zinc atom moves out of the plane of the porphyrin by 0.37 Å when it becomes 5-coordinate,[68] so the ideal N···N distance for a flat template to bind inside the cavity of ***c*-P12[b_6f_6]** is 3.65 nm. The calculated N···N diameter of **T6$_A$** is 3.90 nm, which means it is slightly too large for the cavity of the nanoring. It could however be anticipated that **T6$_A$** would be an effective template, since some doming is required for two templates to stack in the cavity of the nanoring. In addition, it has been shown that templates can be effective even when they are too large for the target nanoring, and that an exact geometric match between the template and the nanoring is not necessary because

large molecules tend to be flexible.[384, 420] However, in this case, the experimental results presented below show that $\mathbf{T6_A}$ failed to direct the synthesis of ***c*-P12[b$_6$f$_6$]**, and a second smaller template $\mathbf{T6_B}$ (Figure 6.3; calculated N···N diameter = 3.75 nm) needed to be synthesized to obtain the target nanoring.

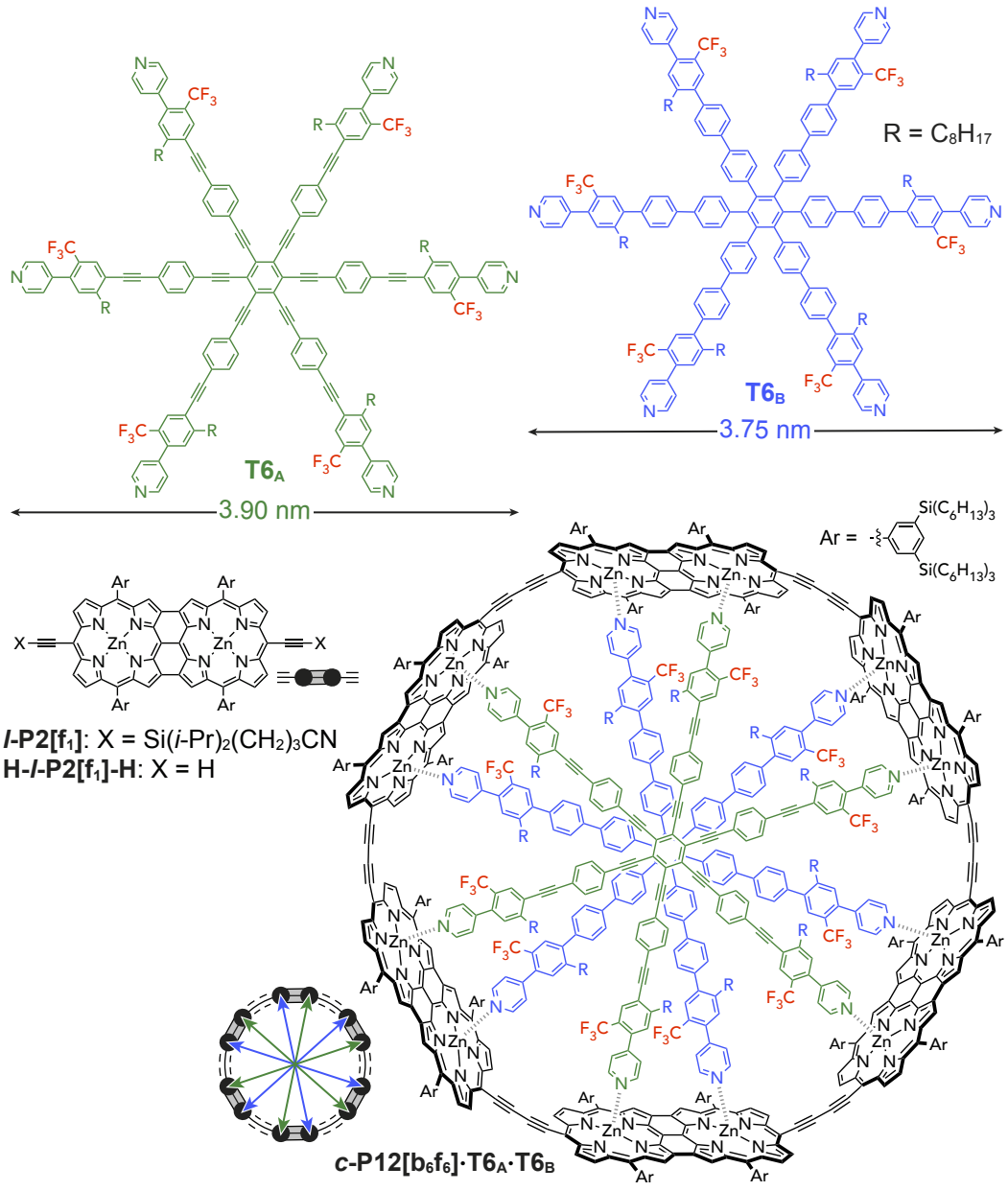


Figure 6.3: Chemical structures and selected cartoon representations of the two hexapyridyl templates, $\mathbf{T6_A}$ (green) and $\mathbf{T6_B}$ (blue), the fused porphyrin dimers ***l*-P2[f$_1$]** (X = Si(*i*-Pr)$_2$(CH$_2$)$_3$CN) and **H-*l*-P2[f$_1$]-H** (X = H), and the 1:1:1 template complex ***c*-P12[b$_6$f$_6$]·T6$_A$·T6$_B$**; R = *n*-octyl.

Both **T6$_A$** and **T6$_B$** feature six *n*-octyl chains to confer high solubility and six CF_3 groups to provide ^{19}F NMR probes for the magnetic (de)shielding arising from (anti)aromatic ring currents. **T6$_A$** has *para*-phenylene-ethynylene spokes, whereas **T6$_B$** is entirely linked by *para*-phenylene units, which makes **T6$_A$** flatter and more flexible. The DFT (B3LYP/6-31G*) calculated geometries of the molecular complexes ***c*-P12[b$_6$f$_6$]·(T6$_A$)$_2$**, ***c*-P12[b$_6$f$_6$]·(T6$_B$)$_2$** and ***c*-P12[b$_6$f$_6$]·T6$_A$·T6$_B$** are shown in Figure 6.4 and provide information about the fit of **T6$_A$** and **T6$_B$** in the cavity of ***c*-P12[b$_6$f$_6$]**. The doming of the stacked templates in the nanoring complexes can be quantified by the angle θ_{dome} between the 4-pyridyl carbon, the porphyrin Zn center, and the normal vector of the porphyrin plane (Figure 6.4C).

Binding of two templates **T6$_A$** to form ***c*-P12[b$_6$f$_6$]·(T6$_A$)$_2$** requires an average dome angle $\theta_{\text{dome}} = 16.2 \pm 3.2°$ to compensate for the poor fit between the template and nanoring dimensions, and results in a 12.1 Å spacing between the template cores. The average dome angle of **T6$_B$** in ***c*-P12[b$_6$f$_6$]·(T6$_B$)$_2$** is $9.1 \pm 2.4°$, which results in a 6.16 Å spacing between the central benzene units that is sufficient to accommodate the steric demand of the hexaphenylbenzene cores. Combining **T6$_A$** and **T6$_B$** to form the 1:1:1 complex ***c*-P12[b$_6$f$_6$]·T6$_A$·T6$_B$** results in the binding of **T6$_B$** close to the porphyrin plane with an average dome angle $\theta_{\text{dome}} = 4.6 \pm 0.9°$. The larger and more flexible template **T6$_A$** is domed above the porphyrin plane with $\theta_{\text{dome}} = 9.5 \pm 2.1°$ which results in a 5.20 Å spacing between the template cores. The smaller dome angles of **T6$_A$** and **T6$_B$** in ***c*-P12[b$_6$f$_6$]·T6$_A$·T6$_B$** compared to the 2:1 complexes ***c*-P12[b$_6$f$_6$]·(T6$_A$)$_2$** and ***c*-P12[b$_6$f$_6$]·(T6$_B$)$_2$** highlight the excellent accommodation of both templates in the nanoring cavity, which is supported by the reduction of steric clash between the stacked templates due to the flat hexaethynyl benzene core and the higher flexibility of **T6$_A$**. Noticeably, all template core distances exceed the typical limit for strong π-π-stacking interactions which suggest a limited stabilization of the nanoring complexes from interactions between the templates.[422, 423]

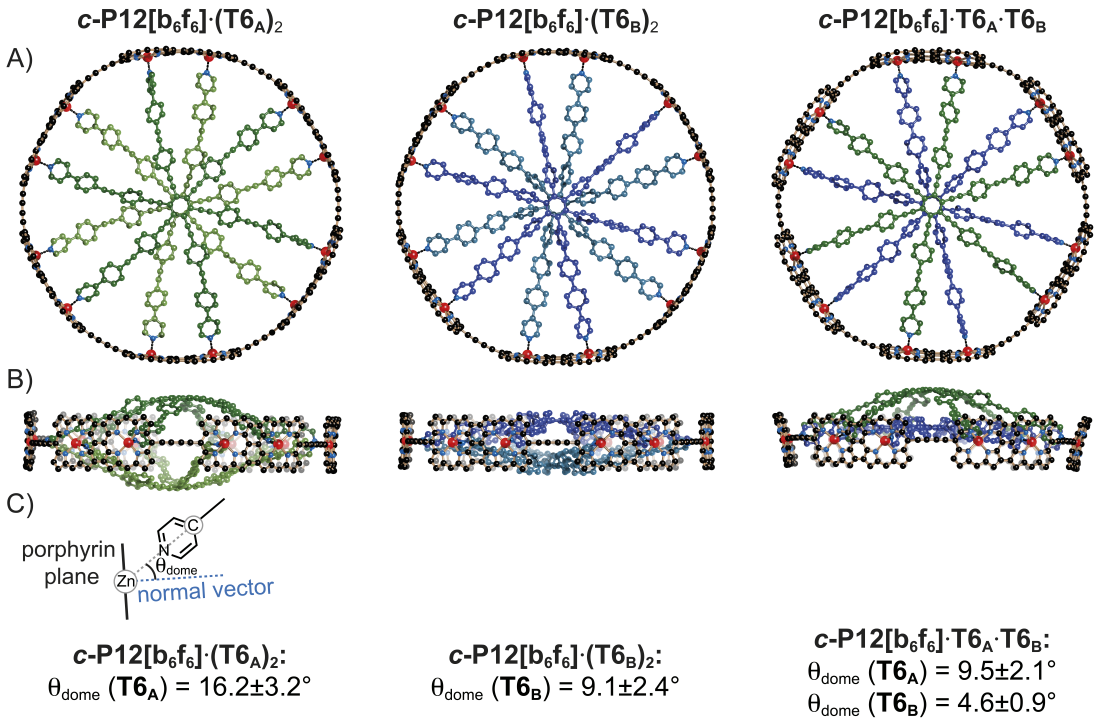


Figure 6.4: A) Topview and B) sideview of the geometry optimized structures of ***c*-P12[b_6f_6]·T6$_A$·T6$_B$**, ***c*-P12[b_6f_6]·(T6$_A$)$_2$**, and ***c*-P12[b_6f_6]·T6$_A$·T6$_B$** calculated with B3LYP as functional the 6-31G* basis set; aryl and octyl solubilizing groups and CF_3 units were replaced with hydrogen atoms to simplify the calculations; hydrogens are omitted for clarity. Templates **T6$_A$** and **T6$_B$** are shown in green and blue, respectively. Templates below the porphyrin plane in 2:1 complexes are shown in a lighter color. C) Definition of the template dome angle θ_{dome} in the nanoring complexes. The dome angles for each template leg of **T6$_A$** and **T6$_B$** in a complex were averaged to obtain the reported mean dome angles and standard deviations.

6.3.2 Template-Directed Synthesis

The synthesis of the partially fused 12-porpyrin nanoring ***c*-P12[b_6f_6]** was attempted by palladium-catalyzed oxidative coupling of the linear porphyrin dimer **H-*l*-P2[f_1]-H** under three different conditions: A) in the presence of two equivalents of **T6$_A$**, B) in the presence of two equivalents of **T6$_B$**, and C) in the presence of one equivalent of **T6$_A$** and one equivalent of **T6$_B$**. The analytical gel-permeation chromatography (GPC) traces of the crude reaction mixtures from these three reactions are compared with that of the product mixture from D) coupling **H-*l*-P2[f_1]-H** in the absence of any template in Figure 6.5. Surprisingly, coupling of **H-*l*-P2[f_1]-H** in the presence of **T6$_A$** does not yield any detectable amount of the target nanoring, but instead gives the linear dodecamer ***l*-P12[b_5f_6]** in about 70% analytical yield. In contrast, the reaction in the

presence of **T6$_B$** gives ***c*-P12[b$_6$f$_6$]** as the main product (~50% analytical yield) with ***l*-P12[b$_5$f$_6$]** as largest byproduct (~25% analytical yield). Coupling in the presence of a 1:1 mixture of **T6$_A$** and **T6$_B$** produces a 5:4 mixture of ***l*-P12[b$_5$f$_6$]** and ***c*-P12[b$_6$f$_6$]**. In the absence of a template, the reaction gave a mixture of high molecular weight polymers, which demonstrates that coupling proceeds efficiently.

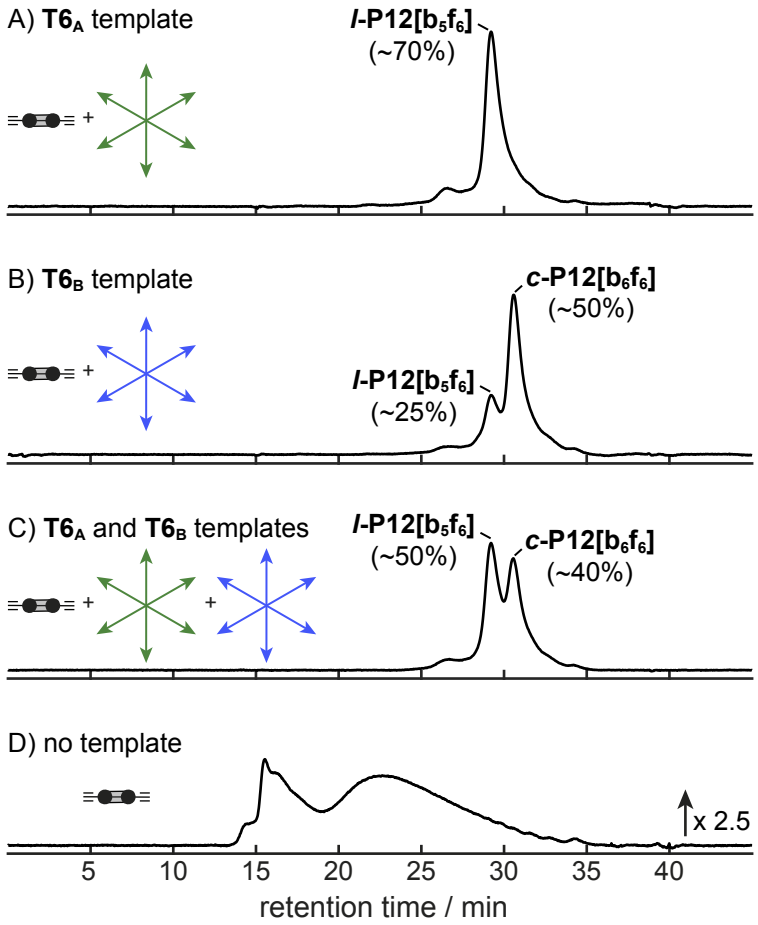


Figure 6.5: Area normalized gel permeation chromatography (GPC) traces of the crude reaction mixtures from the oxidative coupling of **H-*l*-P2[f$_1$]-H** under the control of different templates: A) in the presence of **T6$_A$**, B) in the presence of **T6$_B$**, C) in the presence of a 1:1 mixture of **T6$_A$** and **T6$_B$**, and D) in the absence of any template. The GPC traces were recorded with THF + 1% pyridine as eluent, detecting absorption at 500 nm. All reactions were performed under identical conditions in $CHCl_3$ with $Pd(PPh_3)_2Cl_2$, CuI, 1,4-benzoquinone, and *i*-Pr_2NH at 20 °C.

To understand the different performance of **T6$_A$** and **T6$_B$** in the synthesis of ***c*-P12[b$_6$f$_6$]**, the geometries of the open chain complexes ***l*-P12[b$_5$f$_6$]·(T6$_A$)$_2$** and ***l*-P12[b$_5$f$_6$]·(T6$_B$)$_2$** were optimized by DFT calculations at the B3LYP/6-31G* level

of theory (Figure 6.6A,B). Molecular dynamics simulations of ***l*-P12[b_5f_6]·($T6_A$)$_2$** and ***l*-P12[b_5f_6]·($T6_B$)$_2$** using modified AMBER force field parameters and the DFT optimized geometries as starting points were subsequently performed by Janko Hergenhahn to assess the feasibility of ring closure from the two reaction complexes (Figure 6.6C).[49, 424] The time averaged distance between the terminal acetylene carbon atoms of the ***l*-P12[b_5f_6]·($T6_B$)$_2$** complex is 0.99 ± 0.36 nm. While this is not close enough for successful ring closure, the terminal carbon atoms spent about 5% of the 100 ns molecular dynamics simulation at very short distances that are suitable for Glaser coupling (< 0.4 nm)[425], which suggests that ring closure is viable for the **$T6_B$** template. In comparison, the terminal acetylene carbon atoms of ***l*-P12[b_5f_6]·($T6_A$)$_2$** do not approach below 0.4 nm at any point during the simulations. This indicates that **$T6_A$** is too large to facilitate the ring closure reaction, which is consistent with experimental results.

The linear and cyclic dodecamers, ***l*-P12[b_5f_6]** and ***c*-P12[b_6f_6]**, were identified from their GPC retention times, mass spectra and NMR spectra. The MALDI-TOF mass spectra of both compounds are consistent with a porphyrin 12-mer, but the GPC retention time of ***l*-P12[b_5f_6]** (29.3 min) is shorter than that of ***c*-P12[b_6f_6]** (30.7 min). Together, these data indicate that ***l*-P12[b_5f_6]** is linear and that ***c*-P12[b_6f_6]** is cyclic, which is further confirmed by the fact that ***c*-P12[b_6f_6]** gives a sharp simple NMR spectrum (reflecting the high symmetry of the ring) whereas ***l*-P12[b_5f_6]** gives a more complex ^{1}H NMR spectrum.

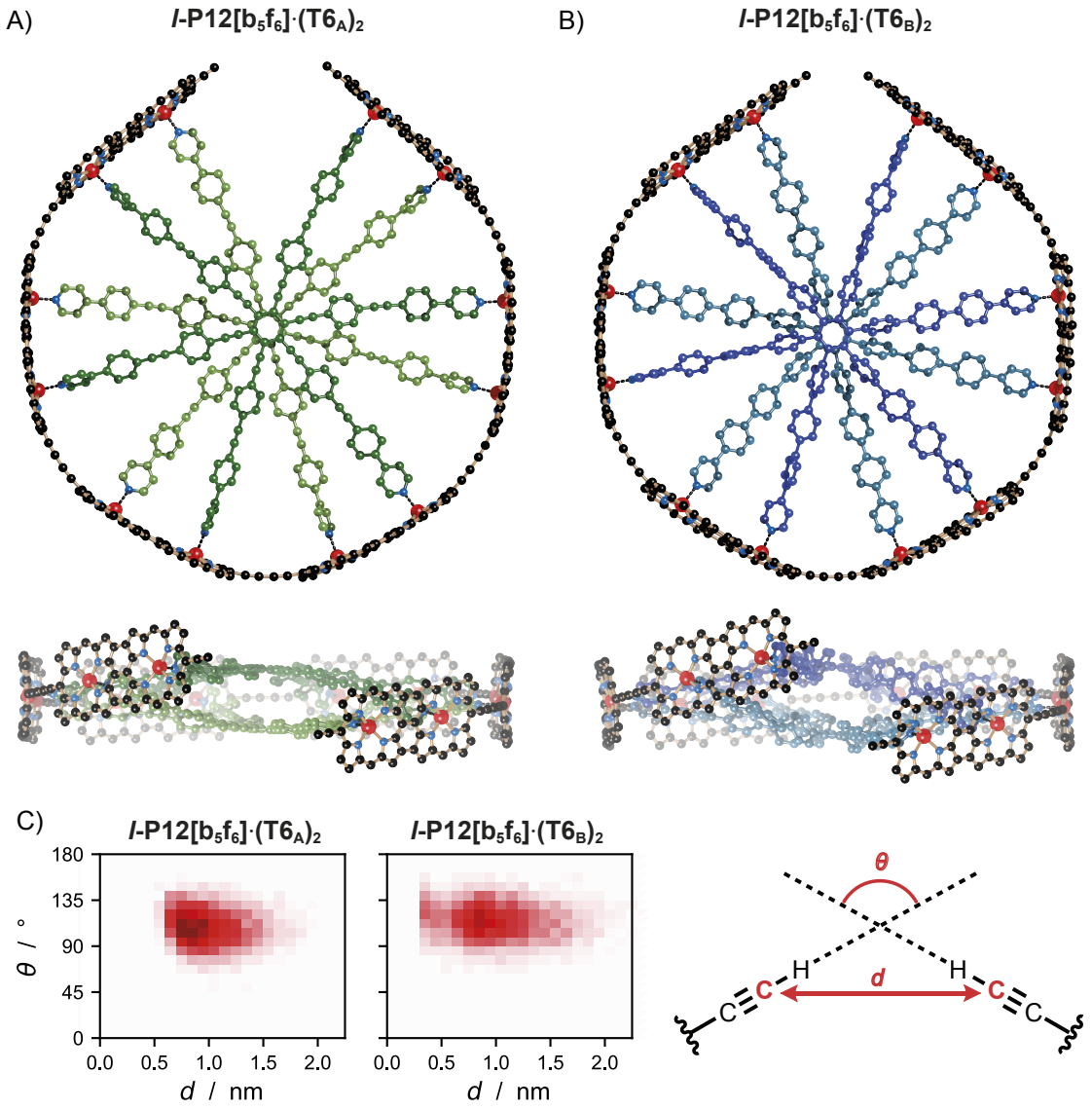


Figure 6.6: Top- and sideview of the DFT (B3LYP/6-31G*) optimized geometries of A) ***l*-P12[b$_5$f$_6$]·(T6$_A$)$_2$** and B) ***l*-P12[b$_5$f$_6$]·(T6$_B$)$_2$**. C) Distribution of end-to-end distances and angles of the terminal acetylene carbons in ***l*-P12[b$_5$f$_6$]·(T6$_A$)$_2$** and ***l*-P12[b$_5$f$_6$]·(T6$_B$)$_2$** obtained from molecular dynamics simulations.

6.3.3 Stability of the Ternary Template Complexes

^{19}F NMR spectroscopy was used to measure the relative stabilities of the three ternary complexes ***c*-P12[b$_6$f$_6$]·(T6$_A$)$_2$**, ***c*-P12[b$_6$f$_6$]·(T6$_B$)$_2$** and ***c*-P12[b$_6$f$_6$]·T6$_A$·T6$_B$**. Complexation of **T6$_A$** and **T6$_B$** with ***c*-P12[b$_6$f$_6$]** occurs rapidly in $CDCl_3$, and each template or template-complex gives a unique fluorine NMR signal. A competitive binding experiment was carried out by titrating a solution of ***c*-P12[b$_6$f$_6$]** into a 1:1 mixture of **T6$_A$** and **T6$_B$**. After equilibration, the concentrations of the three

ternary complexes were determined by integrating their ^{19}F NMR signals (Figure 6.7 and Figure 6.20).

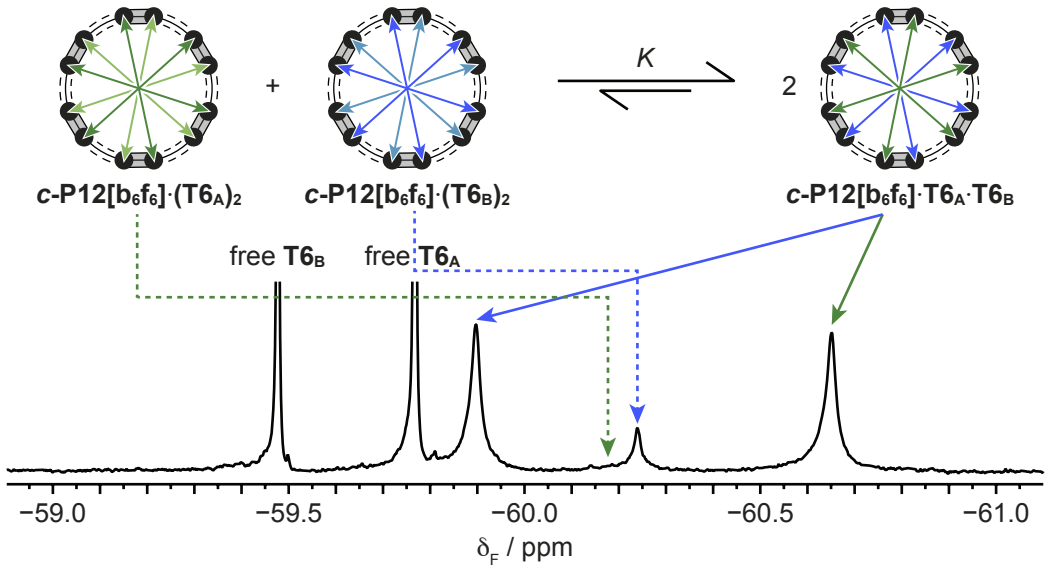


Figure 6.7: Cartoon representation of the competition experiment for the complexation of templates $\mathbf{T6_A}$ (green) and $\mathbf{T6_B}$ (blue) with porphyrin nanoring ***c*-P12[b$_6$f$_6$]**. The distribution of porphyrin nanoring complexes determined from ^{19}F NMR spectroscopy under thermodynamic equilibrium is ~88% ***c*-P12[b$_6$f$_6$]·T6$_A$·T6$_B$**, ~11% ***c*-P12[b$_6$f$_6$]·(T6$_B$)$_2$**, and <1% ***c*-P12[b$_6$f$_6$]·(T6$_A$)$_2$**. The ^{19}F NMR spectrum (471 MHz, 298 K, $CDCl_3$) shows the mixture of complexes at equilibrium.

The predominant species is the 1:1:1 complex ***c*-P12[b$_6$f$_6$]·T6$_A$·T6$_B$** (~88%), with a small amount of 2:1 complex ***c*-P12[b$_6$f$_6$]·(T6$_B$)$_2$** (~11%). No ^{19}F NMR signal was observed for ***c*-P12[b$_6$f$_6$]·(T6$_A$)$_2$** (<1%). Thus, the equilibrium constant *K* relating these three complexes must be greater than 700 (Figure 6.7). The 2:1 complex ***c*-P12[b$_6$f$_6$]·(T6$_B$)$_2$** is formed cleanly when two equivalents of $\mathbf{T6_B}$ are added to ***c*-P12[b$_6$f$_6$]** (Figure 6.21). In contrast, binding of a second molecule of $\mathbf{T6_A}$ to ***c*-P12[b$_6$f$_6$]·(T6$_A$)$_2$** is a weak process and a 6-fold excess of $\mathbf{T6_A}$ is required to form the 2:1 complex ***c*-P12[b$_6$f$_6$]·(T6$_A$)$_2$** (Figure 6.22). These experiments are consistent with the conclusion from the computational modelling in Section 6.3.1, that the cavity of ***c*-P12[b$_6$f$_6$]** is not large enough to easily accept two molecules of $\mathbf{T6_A}$.

6.3.4 UV-vis-NIR Absorption Spectra

The long-wavelength absorption band of ***c*-P12[b_6f_6]** peaks at λ_{max} = 1225 nm (E_{abs} = 1.01 eV). This band is strongly red-shifted when compared with the fused porphyrin dimer ***l*-P2[f_1]** (λ_{max} = 1133 nm; E_{abs} = 1.09 eV) confirming that there is efficient π-conjugation between the dimer units in the nanoring (Figure 6.8A).

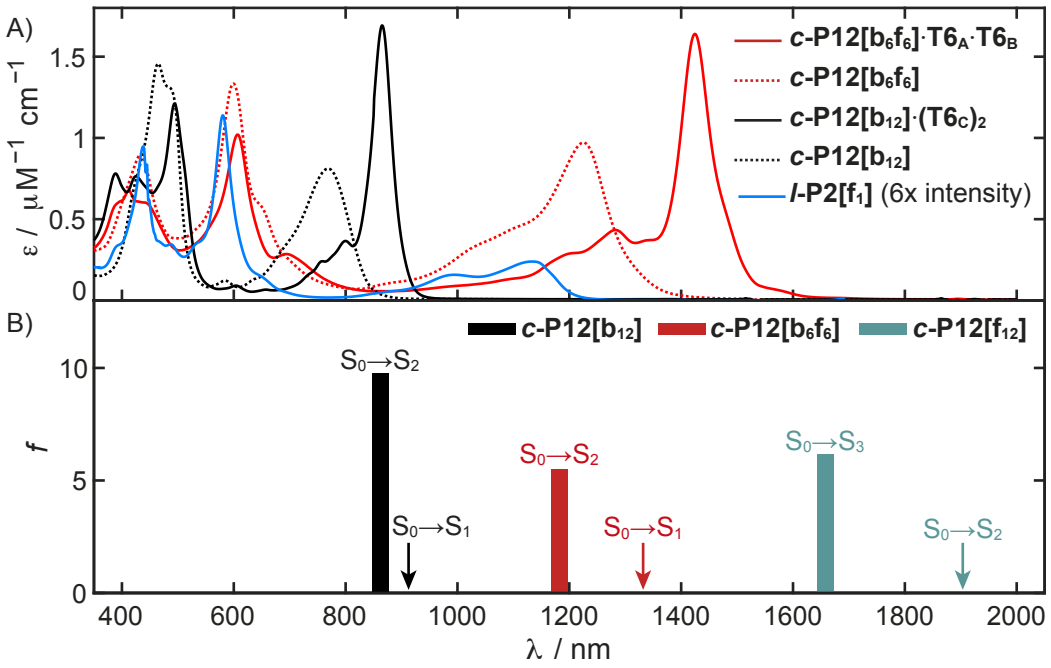


Figure 6.8: A) UV-vis-NIR absorption spectra of ***l*-P2[f_1]**, ***c*-P12[b_6f_6]**, ***c*-P12[b_6f_6]·$(T6_A)_2$**, ***c*-P12[b_{12}]**, and ***c*-P12[b_{12}]·$(T6_C)_2$** in $CHCl_3$ at 20 °C. B) TD-DFT (LC-ωHPBE/6-31G*; $\omega = 0.1$) predicted lowest energy electronic transitions of ***c*-P12[b_6f_6]**, ***c*-P12[b_{12}]**, and ***c*-P12[f_{12}]**. The positions of dipole forbidden electronic transitions are indicated by arrows.

The long-wavelength absorption band of the nanoring becomes even more red-shifted, and sharper, in the 1:1:1 complex ***c*-P12[b_6f_6]·$T6_A$·$T6_B$** (λ_{max} = 1425 nm; E_{abs} = 0.87 eV), showing that π-conjugation is amplified when the ring is locked into a circular conformation. The 1:2 complex ***c*-P12[b_6f_6]·$(T6_B)_2$** has a similar spectrum to the 1:1:1 complex, although it is slightly less redshifted (λ_{max} = 1420 nm) and broader, reflecting a less ordered geometry. The corresponding fully butadiyne-linked nanorings have much larger optical gaps; for example ***c*-P12[b_{12}]**, shown in Figure 6.1, exhibits a long wavelength absorption band at λ_{max} = 768 nm (E_{abs} = 1.61 eV), which shifts to 865 nm (E_{abs} = 1.43 eV) in the template complex ***c*-P12[b_{12}]·$(T6_C)_2$** (see

Figure 6.8A for a comparison of the absorption spectra of ***l*-P2[$\mathbf{f_1}$]**, ***c*-P12[$\mathbf{b_6f_6}$]**, ***c*-P12[$\mathbf{b_6f_6}$]·T6$_A$·T6$_B$**, ***c*-P12[$\mathbf{b_{12}}$]** and **c-P12[$\mathbf{b_{12}}$]·(T6$_C$)$_2$)**. Time-dependent DFT calculations of the lowest energy electronic transitions of ***c*-P12[$\mathbf{b_6f_6}$]** and ***c*-P12[$\mathbf{b_{12}}$]** (calculated with the LC-ωHPBE $\omega = 0.1$ functional and the 6-31G* basis set) reproduce the strong bathochromic shift of the lowest energy absorption band of the partially fused nanoring (Figure 6.8B). These calculations predict that the $S_0 \rightarrow S_1$ transitions are dipole forbidden ($f = 0$) in both nanorings, and that the lowest energy absorption bands predominantly arise from $S_0 \rightarrow S_2$ transitions, as found in most π-conjugated macrocycles[387, 388] such as porphyrin nanorings.[67–69]

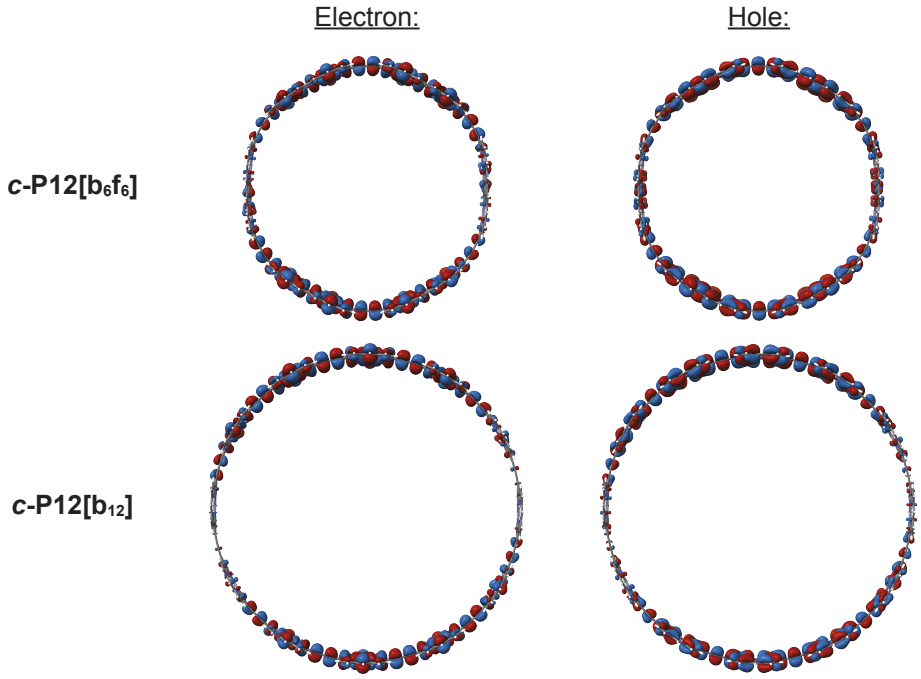


Figure 6.9: Initial (left) and final (right) states of the DFT (LC-ωHPBE/6-31G*; $\omega = 0.1$) calculated representative natural transition orbital pairs for the $S_0 \rightarrow S_2$ transitions of ***c*-P12[$\mathbf{b_6f_6}$]** and ***c*-P12[$\mathbf{b_{12}}$]** plotted for an isovalue of 0.0055.

The natural transition orbital pairs for the $S_0 \rightarrow S_2$ transitions in ***c*-P12[$\mathbf{b_6f_6}$]** and ***c*-P12[$\mathbf{b_{12}}$]** are predominantly centered on two opposite sides of the nanorings with a stronger involvement of the bridging porphyrin units in ***c*-P12[$\mathbf{b_6f_6}$]** consistent with a more extended π-conjugated system in the partially fused ring (Figure 6.9). TD-DFT calculations of a fully fused 12-porphyrin nanobelt predict a bathochromic shift of its lowest energy absorption band ($S_0 \rightarrow S_3$ transition) by 0.12 eV relative to

***c*-P12[b_6f_6]·$T6_A$·$T6_B$**, which confirms that the partially fused 12-ring complex is an important step in approaching the electronic structure of the nanobelt. Attempts to perform TD-DFT calculations for the porphyrin nanoring complexes were unsuccessful due to the extensive computational requirements.

6.3.5 Global Charge Delocalization in Oxidized Porphyrin Nanorings

^{1}H and ^{19}F NMR spectroscopy were used to investigate the magnetic (de)shielding effects in the oxidized nanoring complex ***c*-P12[b_6f_6]·$T6_A$·$T6_B$**, and to compare the behavior of the previously studied 12-porphyrin nanoring complex ***c*-P12[b_{12}]·$(T6_C)_2$** under identical conditions (Figure 6.10).[55]

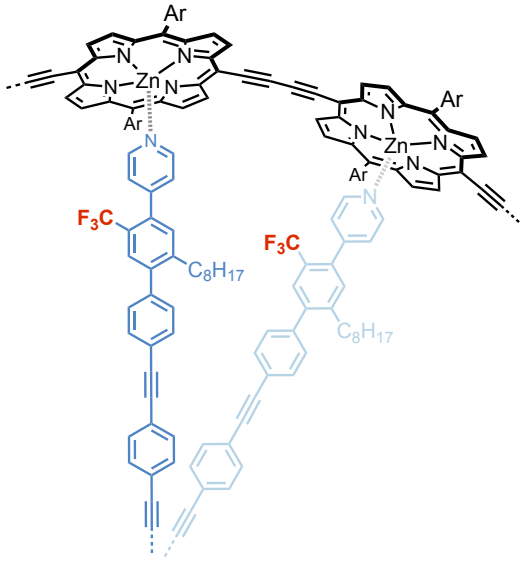


Figure 6.10: Chemical structure of the symmetric unit of ***c*-P12[b_{12}]·$(T6_C)_2$**.

The ^{19}F NMR oxidation titrations of both nanoring complexes are shown in Figure 6.11 (see Figure 6.23 and Figure 6.26 for the corresponding ^{1}H NMR spectra). Two distinct ^{19}F NMR resonances at −60.65 ppm and −59.89 ppm were observed for ***c*-P12[b_6f_6]·$T6_A$·$T6_B$** and assigned based on their chemical shift upon complexation and their ^{1}H -^{19}F heteronuclear Overhauser effect spectroscopy (HOESY) correlations to the CF_3 groups of **$T6_A$** and **$T6_B$**, respectively. ^{1}H and ^{19}F NMR oxidation titrations were performed by treating ***c*-P12[b_6f_6]·$T6_A$·$T6_B$** and ***c*-P12[b_{12}]·$(T6_C)_2$** with thianthrenium

tetrakis(pentafluorophenyl)borate **ThnBArF$_{20}$** in $CDCl_3$ at 298 K. These oxidation conditions were chosen because they enable the monitoring of early oxidation states by NMR spectroscopy (whereas in previous work, using thianthrenium hexafluoroantimonate **ThnSbF$_6$** in CD_2Cl_2 at 233 K, this was prevented by the low solubility of uncharged, or slightly charged, nanoring complexes).[55, 385] **ThnBArF$_{20}$** was synthesized from **ThnSbF$_6$** by exchanging the counterion of the oxidant using **KBArF$_{20}$** in acetonitrile followed by precipitation of the target compound from CH_2Cl_2 with pentane. The exchange of the counterion resulted in a good solubility of the thianthrenium salt in $CHCl_3$. UV-vis-NIR spectroscopy and square wave voltammetry of **ThnBArF$_{20}$** and **ThnSbF$_6$** confirm that exchanging the counterion does not affect the electronic structure and oxidation potential of **Thn$^+$** in solution (Figure 6.17 and Figure 6.18).

The different species observed in the NMR oxidation titrations of ***c*-P12[b$_6$f$_6$]·T6$_A$·T6$_B$** and ***c*-P12[b$_{12}$]·(T6$_C$)$_2$** were assigned to individual oxidation states using ^{19}F NMR speciation curves based on the equivalents of oxidant added (Figure 6.12). The relative abundance of each state was obtained from the intensity of the ^{19}F NMR signal at the chemical shift δ_F corresponding to the state, normalized by the maximum ^{19}F signal intensity at that δ_F. Virtually identical independent speciation curves were obtained using the ^{19}F NMR resonances of **T6$_A$** and **T6$_B$** in ***c*-P12[b$_6$f$_6$]·T6$_A$·T6$_B$** (Figure 6.28). The endpoint of the NMR titrations ($Q = 12+$) was determined from the disappearance of the ^{1}H NMR resonances of thianthrene and the ^{19}F NMR signals of $BArF_{20}^-$ due to strong exchange broadening caused by fast exchange with excess **ThnBArF$_{20}$** (Figure 6.23 and Figure 6.26).

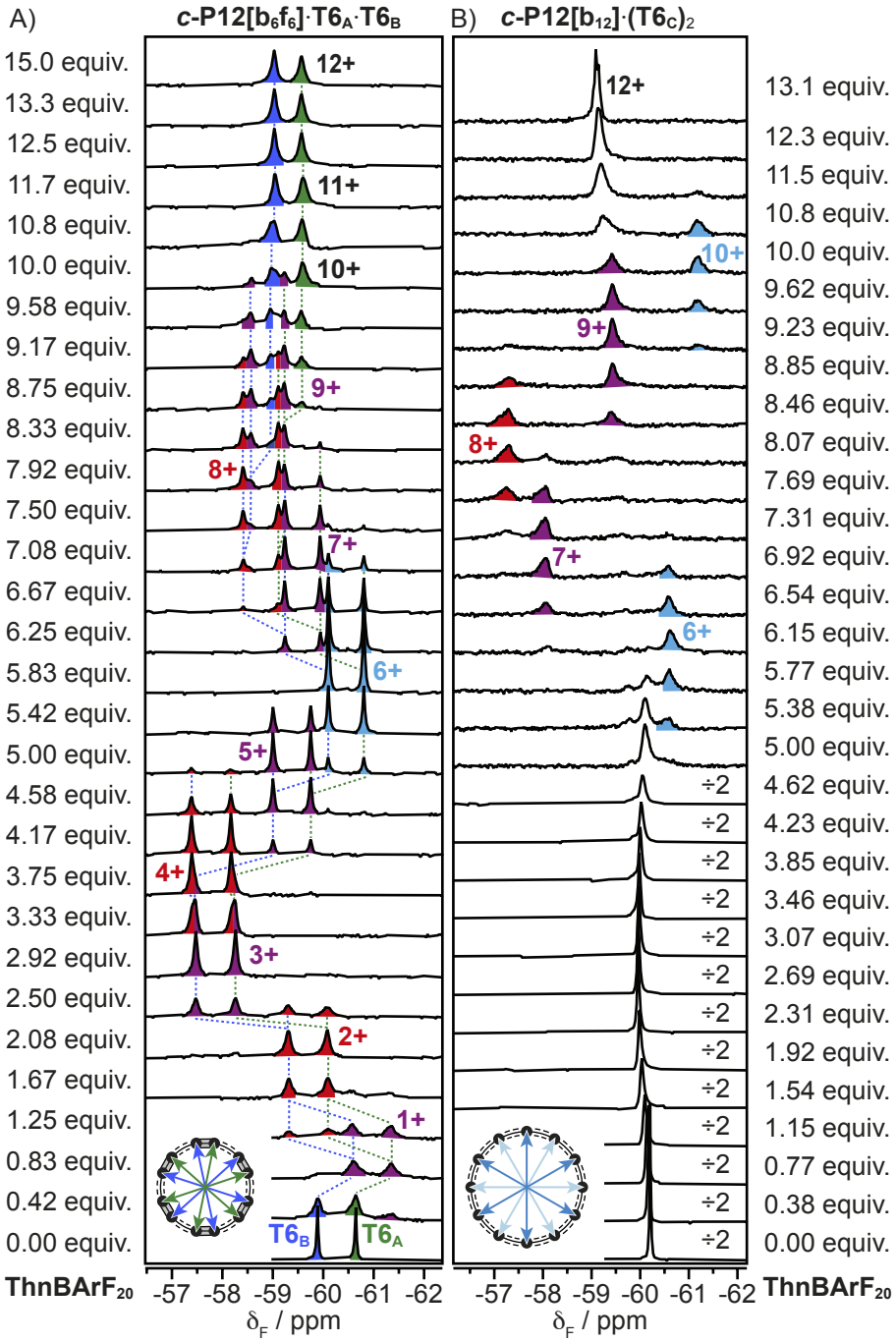


Figure 6.11: Experimental ^{19}F NMR (471 MHz, $CDCl_3$, 298 K) oxidation titrations of A) ***c*-P12[b_6f_6]·T6$_A$·T6$_B$** and B) ***c*-P12[b_{12}]·(T6$_C$)$_2$**. ^{19}F NMR signals indicating global aromaticity and antiaromaticity are colored in light blue and red, respectively; ^{19}F NMR resonances corresponding to odd-numbered oxidation states are shown in purple. ^{19}F resonances in the color of their respective templates (**T6$_A$**: green, **T6$_B$**: blue) indicate the absence of global (anti)aromaticity.

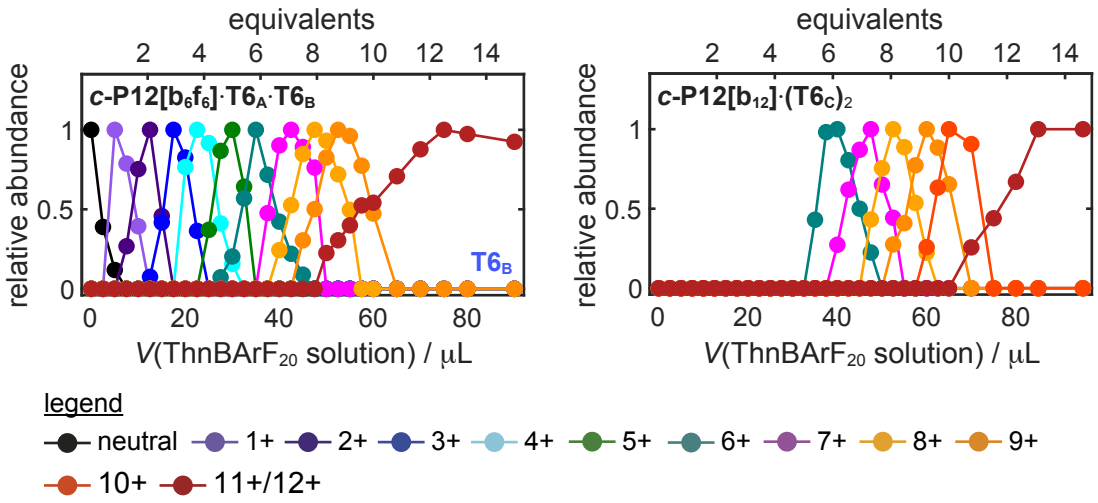


Figure 6.12: Speciation curves for the different oxidation states observed in the NMR oxidation titrations of ***c*-P12[b_6f_6]·$T6_A$·$T6_B$** and ***c*-P12[b_{12}]·$(T6_C)_2$**. The speciation curve of ***c*-P12[b_6f_6]·$T6_A$·$T6_B$** was calculated based on the ^{19}F NMR signals of **$T6_B$**. The relative abundance of each oxidation state was obtained as the intensity of the ^{19}F NMR signal of the state at the chemical shifts reported in Table 6.4 and Table 6.8 divided by its maximum signal intensity.

To quantify the extent of (de)shielding in the ^{19}F NMR spectra, the chemical shift difference $\Delta\delta_F$ was defined following equation 6.1:

$$\Delta\delta_F = \delta_Q - \delta_0 \tag{6.1}$$

where δ_Q is the chemical shift of the CF_3 resonances in the oxidation state Q and δ_0 is the chemical shift in the neutral nanoring complex. The shift differences summarized in Table 6.1 probe the induced magnetic field in the charged nanoring complexes and scale with the strength of the ring current according to the Biot–Savart law.[426] Quantification of the chemical shift difference relative to the ^{19}F resonances of the unbound templates broadly supports the assignment of global (anti)aromaticity in different oxidation states but does not account for the different environments of the CF_3 probes of **$T6_A$** and **$T6_B$** in ***c*-P12[b_6f_6]·$T6_A$·$T6_B$** (Table 6.4).

The ^{19}F NMR spectra of oxidized ***c*-P12[b_6f_6]·$T6_A$·$T6_B$** reveal the presence of global antiaromatic and aromatic ring currents from the deshielding ($\Delta\delta_F > 0$) and shielding ($\Delta\delta_F < 0$) of the CF_3 resonances, respectively (Figure 6.11A). In the 2+ oxidation

state, the ^{19}F resonances of $\mathbf{T6_A}$ and $\mathbf{T6_B}$ are deshielded with $\Delta\delta_F = 0.57$ ppm and 0.59 ppm, respectively, consistent with a weak global antiaromatic ring current. The chemical shift differences in the 4+ oxidation state are $\Delta\delta_F(\mathbf{T6_A}) = 2.47$ ppm and $\Delta\delta_F(\mathbf{T6_B}) = 2.50$ ppm and indicate the presence of a strong antiaromatic ring current. In the 6+ oxidation state, the ^{19}F resonances are shielded ($\Delta\delta_F(\mathbf{T6_A}) = -0.15$ ppm; $\Delta\delta_F(\mathbf{T6_B}) = -0.21$ ppm) which suggests a globally aromatic state. The subsequent deshielding of the ^{19}F resonances of $\mathbf{T6_A}$ ($\Delta\delta_F = 1.54$ ppm) and $\mathbf{T6_B}$ ($\Delta\delta_F = 1.48$ ppm) in the 8+ oxidation state suggests the emergence of a global antiaromatic ring current. Importantly, $\mathbf{T6_A}$ and $\mathbf{T6_B}$ exhibit similar chemical shift differences in each oxidations state (Table 6.1), which supports the presence of homogenous, global ring currents.

Table 6.1: Summary of the observed ^{19}F chemical shift differences $\Delta\delta_F$ for templates $\mathbf{T6_A}$ and $\mathbf{T6_B}$ in ***c*-P12[b$_6$f$_6$]** and $\mathbf{T6_C}$ in ***c*-P12[b$_{12}$]** in the oxidized nanoring complexes.

Q	***c*-P12[b$_6$f$_6$]·T6$_A$·T6$_B$**		**c-P12[b$_{12}$]·(T6$_C$)$_2$**
	$\Delta\delta_F(\mathbf{T6_A})$ / ppm	$\Delta\delta_F(\mathbf{T6_B})$ / ppm	$\Delta\delta_F(\mathbf{T6_C})$ / ppm
	oxidation		
0	0.00	0.00	0.00
2+	0.57	0.59	0.21
4+	2.47	2.50	0.20
6+	−0.15	−0.21	−0.43
8+	1.54	1.48	2.93
10+	1.05	0.89	−0.99
12+	1.08	0.86	1.05

Additional evidence for the magnetic (de)shielding in the 4+, 6+ and 8+ oxidation states is provided by the ^{1}H NMR signals of the trihexylsilyl (THS) groups of the porphyrins (Figure 6.23). Interconversion of the THS environments pointing inside (THS_{in}) and outside (THS_{out}) the nanoring is slow on the NMR timescale. Only the THS_{in} resonances are affected by the magnetic field induced by global ring currents[54–56, 385] and are deshielded in the 4+ and 8+ oxidation states and shielded in the 6+ oxidation state consistent with the $\Delta\delta_F$ values. The shift of the THS_{in} resonances in the 2+ oxidation state is too small to be clearly identified. The chemical shifts of the $\mathbf{T6_A}$ and $\mathbf{T6_B}$ ^{19}F resonances in the 10+, 11+, and 12+ oxidation states remain

virtually unchanged with increasing oxidation state, and no magnetic (de)shielding is observed for the THS_{in} resonances. This suggest that no global ring currents are present in ***c*-P12[$\mathbf{b_6f_6}$]·$\mathbf{T6_A}$·$\mathbf{T6_B}$** beyond the 8+ oxidation state.

Well-defined signals for the odd-electron 1+, 3+, 5+, 7+, and 9+ oxidation states can also be observed in the ^{19}F NMR titrations of ***c*-P12[$\mathbf{b_6f_6}$]·$\mathbf{T6_A}$·$\mathbf{T6_B}$**. The significant chemical shift differences observed in some of these states (e.g. 1+: $\Delta\delta_F(\mathbf{T6_A}) = -0.70$ ppm; 3+: $\Delta\delta_F(\mathbf{T6_A}) = 2.39$ ppm; 5+: $\Delta\delta_F(\mathbf{T6_A}) = 0.90$ ppm) might indicate the presence of (anti)aromatic ring currents in odd-electron oxidations states, but there could also be contributions from the pseudocontact shift due to the presence of unpaired electrons (Table 6.4).[393, 394] Further experimental and theoretical work is necessary to understand the magnetic (de)shielding in these states.

The assignment of the global (anti)aromatic character in the 4+, 6+ and 8+ oxidation states of ***c*-P12[$\mathbf{b_6f_6}$]·$\mathbf{T6_A}$·$\mathbf{T6_B}$** is in agreement with Hückel's rule.[155, 157] The edge-fused porphyrin dimer units have two formal π-conjugation pathways and contribute either 20 or 16 electrons to the π-electron count (Figure 6.13). Together with the four electrons per butadiyne linker, this results in a total count of 144 or 120 π-electrons in the neutral nanoring ***c*-P12[$\mathbf{b_6f_6}$]**. Consequently, the delocalization pathways in the globally antiaromatic 4+ and 8+ oxidation states consist of $4n$ π-electrons (4+: 140/116 πe^-; $n = 35/29$ and 8+: 136/112 πe^-; $n = 34/28$), whereas the globally aromatic 6+ state exhibits a $4n + 2$ π-electron pathway (138/114 πe^-; $n = 34/28$).

Nucleus independent chemical shift calculations ($NICS(0)_{ZZ}$, BLYP35/6-31G*) of ***c*-P12[$\mathbf{b_6f_6}$]** in the 0, 4+, 6+, and 8+ oxidation states are qualitatively in agreement with the experimental results and corroborate the presence of local aromaticity in the neutral nanoring, global antiaromaticity in the 4+ and 8+ states, and global aromaticity in the 6+ state (Figure 6.14).

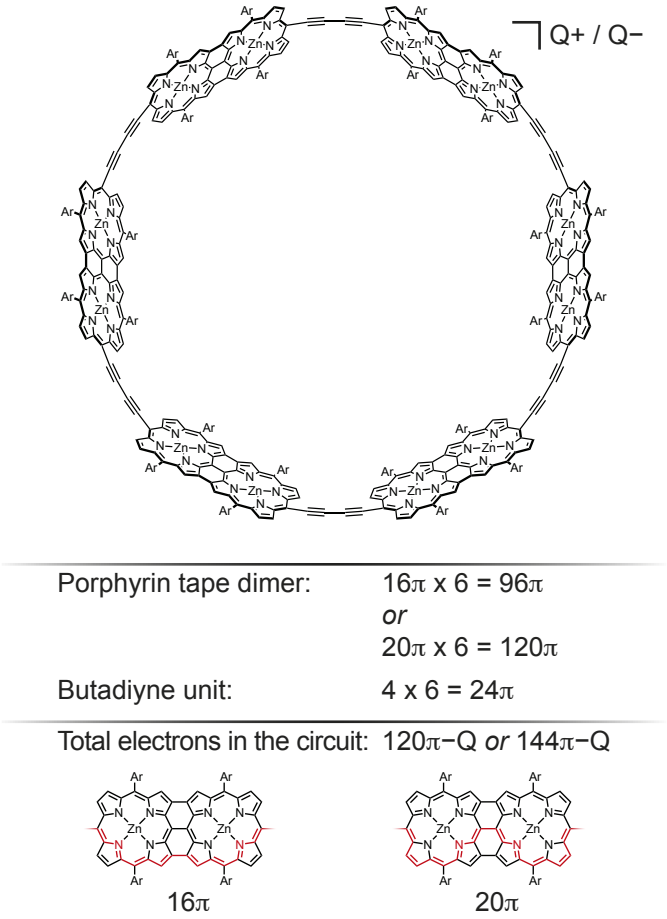


Figure 6.13: π-Electron count for the global ring circuit of ***c*-P12[$\mathbf{b_6f_6}$]** and possible delocalization pathways (red) in the porphyrin tape dimer units. The complete circuit consists of 6 tape dimers and 6 butadiyne links. A long and a short conjugation pathway exist for the porphyrin dimers that contribute a total of 20 or 16 π-electrons to the conjugation pathway, respectively. This leads to two possible π-electron counts of 144 $\pi e^- - Q$ or 120 $\pi e^- - Q$ for the global circuit where Q denotes the oxidation state. Ar = 3,5-bis(trihexylsilyl)phenyl.

Anomalous behavior arises in the 2+ oxidation state. The observed deshielding of the CF_3 resonance in [***c*-P12[$\mathbf{b_6f_6}$]·T6$_\mathbf{A}$·T6$_\mathbf{B}$**]$^{2+}$ indicates global antiaromatic character, which is not consistent with Hückel's rule; this species has a $4n+2$ π-conjugation pathway (142/118 πe^-; $n = 35/29$) and would be expected to be aromatic. Similar deshielding of the CF_3 resonances is also observed in the 2+ oxidation state of ***c*-P12[$\mathbf{b_6f_6}$]·(T6$_\mathbf{B}$)$_\mathbf{2}$** under the same conditions (Figure 6.24). This anomaly could be attributed to the formation of a triplet ground state; Baird's rule would then predict global antiaromaticity.[427] This interpretation is consistent with calculated NICS(0)$_{ZZ}$ maps, which predict shielding of resonances in the nanoring cavity for a singlet ground

state and a weak deshielding for a triplet ground state of ***c*-P12[b_6f_6]**$^{2+}$ (Figure 6.15).

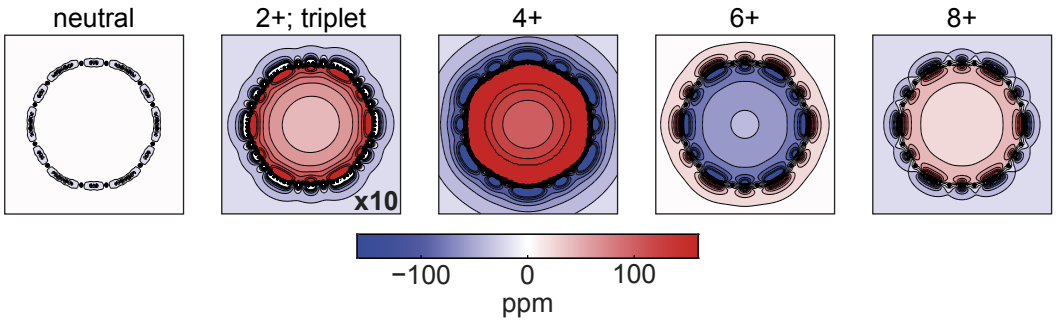


Figure 6.14: Nucleus independent chemical shift (NICS) calculations of ***c*-P12[b_6f_6]** in the predominant oxidation states 0, 2+, 4+, 6+, and 8+. The NICS(0)$_{ZZ}$ grids in the *xy*-plane of the nanoring were calculated with BLYP35 as functional and the 6-31G* basis set using optimized geometries of ***c*-P12[b_6f_6]** in each oxidation state. The NICS(0)$_{ZZ}$ values for the 2+ state were calculated for a triplet ground state and increased by a factor of 10 for better visualization.

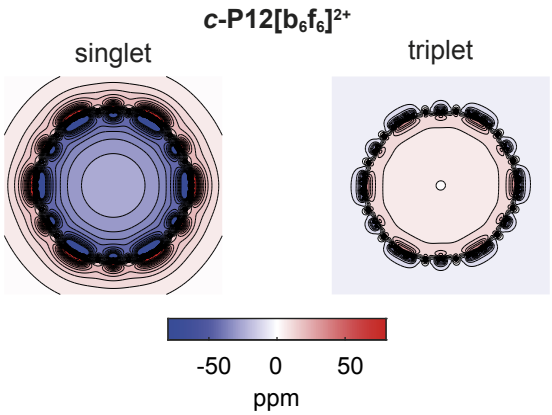


Figure 6.15: Comparison of the NICS(0)$_{ZZ}$ calculations (BLYP35/6-31G*) of ***c*-P12[b_6f_6]** in the 2+ oxidation state with a singlet and triplet ground state. The geometries of the nanoring in in the 2+ oxidation state were optimized with B3LYP as functional and the 6-31G* basis set for a singlet and triplet electronic configurations.

The ^{19}F NMR spectra of ***c*-P12[b_{12}]·($T6_C$)$_2$** are in agreement with the previously reported NMR investigation of the oxidized nanoring complex in CD_2Cl_2 at 223 K[55] and indicate the presence of global aromatic ring currents in the 6+ ($\Delta\delta_F = -0.43$) and 10+ ($\Delta\delta_F = -0.99$) oxidation states and a global antiaromatic ring current in the 8+ state ($\Delta\delta_F = 2.93$) (Figure 6.11B, Figure 6.26, and Figure 6.27). Rickhaus, Jirasek *et al.* concluded that no global ring current is observed in the 12+ oxidation state of ***c*-P12[b_{12}]·($T6_C$)$_2$**.[55] This is supported by the lack of magnetic (de)shielding of the

THS_{in} resonances in ***c*-P12[b_{12}]·($T6_C$)$_2^{12+}$**, although the deshielding of the ^{19}F NMR resonances by 1.05 ppm relative to the neutral nanoring complex and by 0.28 ppm relative to the CF_3 resonance of unbound $\mathbf{T6_C}$ might indicate a weak antiaromatic ring current in agreement with Hückel's rule (Table 6.8). There are no indications of global ring currents in the 2+ and 4+ oxidation states of ***c*-P12[b_{12}]·($T6_C$)$_2$** in stark contrast to the partially fused porphyrin nanoring complex. The comparison of the ^1H and ^{19}F NMR oxidation titrations of ***c*-P12[b_6f_6]·($T6_B$)$_2$** and ***c*-P12[b_{12}]·($T6_C$)$_2$** in $CDCl_3$ at 298 K and 233 K supports the conclusions on the global (anti)aromatic ring currents independent of temperature (Figure 6.24, Figure 6.25, Figure 6.26, Figure 6.27). However, the magnitude of the observed chemical shift differences $\Delta\delta_F$ at 233 K is typically larger than the corresponding $\Delta\delta_F$ at 298 K by a factor of two or more (Table 6.5, Table 6.6, Table 6.8, Table 6.9), which probably reflects the reduced conformational flexibility of the nanoring complexes at low temperature.

6.3.6 Global Charge Delocalization in Reduced Porphyrin Nanorings

The global charge delocalization and (anti)aromaticity in the reduced porphyrin nanoring complexes ***c*-P12[b_6f_6]·$T6_A$·$T6_B$** and ***c*-P12[b_{12}]·($T6_C$)$_2$** was investigated by ^1H and ^{19}F NMR spectroscopy. The ^{19}F NMR spectra of the 0, 2−, 4− and 6− oxidation states of ***c*-P12[b_6f_6]·$T6_A$·$T6_B$** are shown in Figure 6.16B. The complete NMR titration curve and the corresponding ^1H NMR spectra are shown in Figure 6.33. NMR reduction titrations were performed by treating ***c*-P12[b_6f_6]·$T6_A$·$T6_B$** and ***c*-P12[b_{12}]·($T6_C$)$_2$** with decamethylcobaltocene **CoCp*$_2$** in THF-d_8 at 298 K under strictly anaerobic conditions. The $\Delta\delta_F$ values in the different oxidation states are summarized in Table 6.2 and suggest the presence of homogeneous global aromatic ring currents in the 2− ($\Delta\delta_F(\mathbf{T6_A}) = -0.23$ ppm; $\Delta\delta_F(\mathbf{T6_B}) = -0.21$ ppm) and 6− ($\Delta\delta_F(\mathbf{T6_A}) = -0.79$ ppm; $\Delta\delta_F(\mathbf{T6_B}) = -0.82$ ppm) oxidation states and an antiaromatic ring current in the 4− state ($\Delta\delta_F(\mathbf{T6_A}) = 0.71$ ppm; $\Delta\delta_F(\mathbf{T6_B}) = 0.70$ ppm) of ***c*-P12[b_6f_6]·$T6_A$·$T6_B$**.

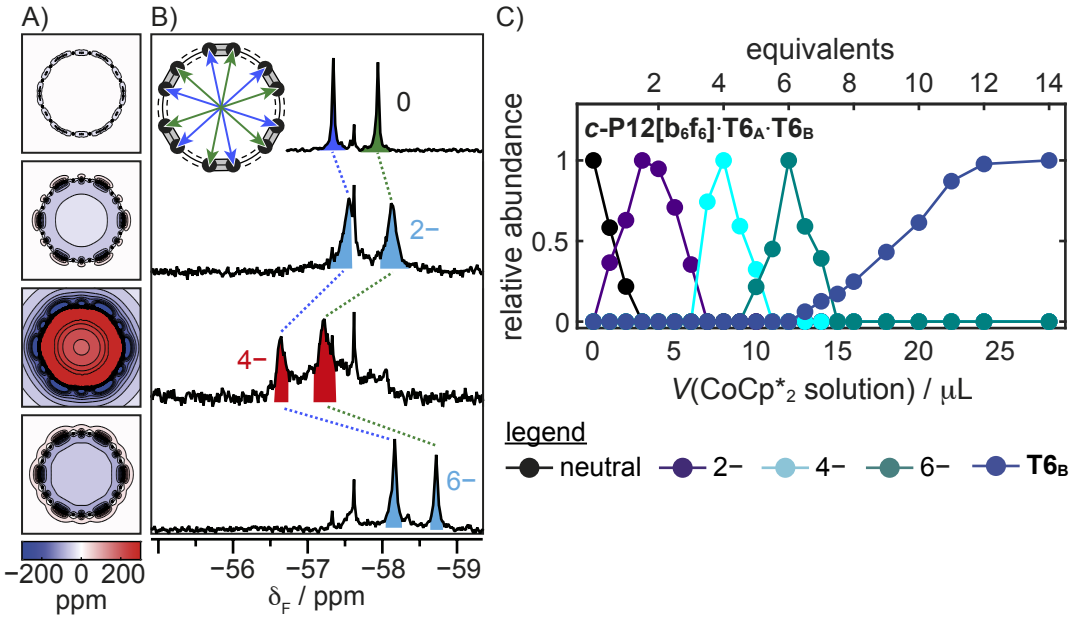


Figure 6.16: A) NICS(0)$_{ZZ}$ plots and B) experimental ^{19}F NMR spectra (471 MHz, THF-d_8, 298 K) of ***c*-P12[b$_6$f$_6$]·T6$_A$·T6$_B$** in the predominant oxidation states 0, 2−, 4−, and 6−. ^{19}F NMR signals indicating global aromaticity and antiaromaticity are colored in light blue and red, respectively. ^{19}F resonances in the color of their respective templates (**T6$_A$**: green, **T6$_B$**: blue) indicate the absence of global (anti)aromaticity. The NICS(0)$_{ZZ}$ grids in the *xy*-planes of ***c*-P12[b$_6$f$_6$]** were calculated with BLYP35 as functional and the 6-31G* basis set using the optimized geometry of the nanoring for each oxidation state. C) Speciation curve for the different species observed in the NMR reduction titration of ***c*-P12[b$_6$f$_6$]·T6$_A$·T6$_B$** based on the ^{19}F NMR signals of the **T6$_B$** template. The relative abundance of each species was obtained as the intensity of the ^{19}F NMR signal of the state divided by its maximum signal intensity. The intensities of the ^{19}F NMR signal in different oxidation states were obtained at the chemical shifts reported in Table 6.11.

Table 6.2: Summary of the observed ^{19}F chemical shift differences $\Delta\delta_F$ for templates **T6$_A$** and **T6$_B$** in ***c*-P12[b$_6$f$_6$]** and **T6$_C$** in ***c*-P12[b$_{12}$]** in the reduced nanoring complexes.

Q	***c*-P12[b$_6$f$_6$]·T6$_A$·T6$_B$**		**c-P12[b$_{12}$]·(T6$_C$)$_2$**
	$\Delta\delta_F$(**T6$_A$**) / ppm	$\Delta\delta_F$(**T6$_B$**) / ppm	$\Delta\delta_F$(**T6$_C$**) / ppm
	reduction		
2−	−0.23	−0.21	0.25
4−	0.71	0.70	0.28
6−	−0.79	−0.82	–

Further evidence for the global (anti)aromatic ring currents is provided by the magnetic (de)shielding of the THS$_{in}$ resonances, which are consistent with the $\Delta\delta_F$ values (Figure 6.33). Attempts to reduce ***c*-P12[b$_6$f$_6$]·T6$_A$·T6$_B$** beyond the 6− state were unsuccessful, and it appears that the two hexadentate templates dissociate from

the nanoring when ***c*-P12[b_6f_6]·$T6_A$·$T6_B$** is treated with more than six equivalents of **$CoCp^*_2$** (Figure 6.16C and Figure 6.33).

The assignment of the global (anti)aromatic character in the 2−, 4−, and 6− oxidation states of ***c*-P12[b_6f_6]·$T6_A$·$T6_B$** is in agreement with Hückel's rule: the delocalization pathways in the globally aromatic 2− and 6− states consist of $4n+2$ π-electrons (2−: 146/122 πe^-; $n = 36/30$ and 6−: 150/126 πe^-; $n = 37/31$), whereas the globally antiaromatic 4− state exhibits a $4n$ π-electron pathway (148/124 πe^-; $n = 37/31$). $NICS(0)_{ZZ}$ calculations of ***c*-P12[b_6f_6]** in the 0, 2−, 4−, and 6− oxidation states (BLYP35, 6-31G*) qualitatively agree with the experimental results and corroborate the presence of global aromaticity in the 2− and 6− states, and global antiaromaticity in the 4− state (Figure 6.16A).

The CF_3 ^{19}F NMR resonance of **$T6_C$** in reduced **c-P12[b_{12}]·($T6_C$)$_2$** as well as the THS_{in} porphyrin signals do not exhibit noticeable magnetic (de)shielding that would indicate the presence of global ring currents (Figure 6.34). In addition, the ^{19}F resonance of the template complex is increasingly broadened upon higher reduction and essentially disappears in the 6− state. This could be caused by rapid exchange of the weakly bound templates in the nanoring complex or the decomposition of the highly reduced complex and prevented the further investigation of **c-P12[b_{12}]·($T6_C$)$_2$** in the 8−, 10−, and 12− states.

6.4 Summary and Conclusions

The work in this chapter shows the preparation of a new porphyrin nanoring ***c*-P12[b_6f_6]** consisting of six β,*meso*,β-fused porphyrin dimers connected by six butadiyne links using template-directed synthesis. Complexation of two different hexapyridyl templates, **$T6_A$** and **$T6_B$**, with the porphyrin nanoring allowed for the formation of the stable 1:1:1 porphyrin nanoring complex ***c*-P12[b_6f_6]·$T6_A$·$T6_B$**, which is more strongly π-conjugated than the free nanoring and exhibits a π-π^* absorption band in the infrared ($\lambda_{max} = 1425$ nm, $E_{abs} = 0.87$ eV). This marks, to the best of my

knowledge, the smallest HOMO-LUMO gap for a neutral, π-conjugated molecular macrocycle.[385, 428]

Oxidized ***c*-P12[$\mathbf{b_6f_6}$]·$\mathbf{T6_A}$·$\mathbf{T6_B}$** exhibits global antiaromatic ring currents in its 4+ and 8+ oxidation states and a global aromatic ring current in its 6+ state. The ^{19}F NMR signals of the CF_3 probes of $\mathbf{T6_A}$ and $\mathbf{T6_B}$ in the nanoring complex appear at different chemical shifts but are (de)shielded to the same extent upon oxidation of ***c*-P12[$\mathbf{b_6f_6}$]·$\mathbf{T6_A}$·$\mathbf{T6_B}$**. This provides clear evidence for global ring currents and coherent charge delocalization around the entire nanoring. The Hückel rule correctly predicts the direction of the ring currents in the 4+, 6+, and 8+ oxidation sates of ***c*-P12[$\mathbf{b_6f_6}$]·$\mathbf{T6_A}$·$\mathbf{T6_B}$** despite the ambiguous π-electron count of 144 or 120 π-electrons in the neutral nanoring. Surprisingly, the ^{19}F resonances in the 2+ oxidation state of ***c*-P12[$\mathbf{b_6f_6}$]·$\mathbf{T6_A}$·$\mathbf{T6_B}$** are deshielded, despite its $4n + 2$ electron count. Independent observation of an analogous deshielding of the ^{19}F resonances in ***c*-P12[$\mathbf{b_6f_6}$]·$\mathbf{(T6_B)_2}^{2+}$** and supporting nucleus independent chemical shift calculations suggest the presence of a Baird antiaromatic triplet state in ***c*-P12[$\mathbf{b_6f_6}$]$^{2+}$**. Reduction of ***c*-P12[$\mathbf{b_6f_6}$]·$\mathbf{T6_A}$·$\mathbf{T6_B}$** results in a global aromatic ring currents in the 2− and 6− states and a global antiaromatic ring current in the 4− state, in agreement with Hückel's rule.

Comparison of the global ring currents in ***c*-P12[$\mathbf{b_6f_6}$]·$\mathbf{T6_A}$·$\mathbf{T6_B}$** and the all-butadiyne linked 12-porphyrin nanoring complex **c-P12[$\mathbf{b_{12}}$]·$\mathbf{(T6_C)_2}$** under identical experimental conditions demonstrates that a smaller formal oxidation state per porphyrin units is required to establish global charge delocalization in the partially fused nanoring: ***c*-P12[$\mathbf{b_6f_6}$]·$\mathbf{T6_A}$·$\mathbf{T6_B}$** starts exhibiting global ring currents in its 2+ oxidation state (charge per porphyrin unit $\approx$ +0.17) whereas the 6+ oxidation state is required to observe ring currents in **c-P12[$\mathbf{b_{12}}$]·$\mathbf{(T6_C)_2}$** (charge per porphyrin = +0.5). Analogous behavior is observed for the reduced porphyrin nanoring complexes, reflecting the stronger π-conjugation in ***c*-P12[$\mathbf{b_6f_6}$]·$\mathbf{T6_A}$·$\mathbf{T6_B}$**. These findings suggest that π-conjugated macrocycles with further enhanced electronic communication are promising candidates to achieve global charge delocalization in neutral nanorings and are expected to inform the design of novel cyclic molecular wires.

6.5 Methods

6.5.1 General Methods

NMR Titrations

Oxidative NMR titrations on porphyrin nanoring complexes were carried out in J. Young NMR tubes, dissolved in $CDCl_3$, and handled under argon using standard Schlenk techniques. A solution of the oxidant, thianthrenium tetrakis(pentafluorophenyl)borate (Thn^+, $E_{red} = 0.84$ V versus Fc/Fc^+) in $CDCl_3$ kept under argon was used for the titrations. The titrations were carried out using a Schlenk adaptor for the J. Young NMR tubes, enabling the addition of oxidant under a counterflow of argon. Samples were kept at 298 K for room temperature experiments or cooled in a dry ice/acetone bath (223 K) for titrations at low temperature. Prior to each titration, a ^1H NMR spectrum was recorded at 25 °C to confirm integrity and purity of the porphyrin nanoring complex. The titration endpoint (at which each porphyrin unit is oxidized to the 1+ state) is evident from the disappearance of the neutral oxidant (thianthrene) ^1H NMR signals and the ^{19}F NMR signals of the $BArF_{20}^-$ counterion, resulting from signal broadening caused by exchange between neutral thianthrene and excess oxidant.

Reductive NMR titrations were performed in J. Young NMR tubes by dissolving the nanoring complex in THF-d_8. All sample preparations and reductions were performed under inert atmosphere by handling the J. Young tubes in a MBraun LabStar Glovebox under N_2-atmosphere. A solution of decamethylcobaltocene **CoCp*$_2$** in THF-d_8 was used as reducing agent. Prior to dissolving, **CoCp*$_2$** was sublimed under vacuum and the concentration of the stock solution was determined by quenching an aliquot of **CoCp*$_2$** solution with an excess of solid ferrocenium hexafluorophosphate under inert atmosphere. Evaporation of THF-d_8 *in vacuo* and redissolving of the residuals in acetone-d_6 with *tert*-butyl benzene as an internal standard allowed for the quantification of **CoCp*$_2$** by ^1H NMR.[176]

Computational methods

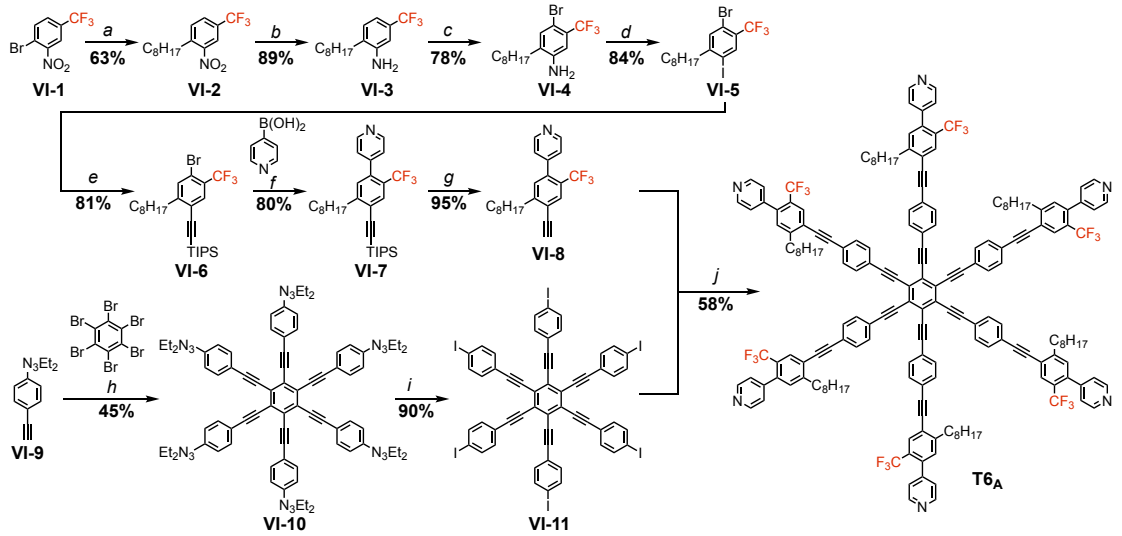
Initial molecular models were built in HyperChem™ 8.0 using the MM+ forcefield with parameters modified for the description of porphyrins and subsequently further refined by DFT.[396–399, 421] Aryl and octyl solubilizing groups and CF_3 units were replaced with H for all calculations to increase the computational speed.

DFT geometry optimizations of **T6$_A$**, **T6$_B$**, ***c*-P12[b$_6$f$_6$]**, ***c*-P12[b$_{12}$]**, ***c*-P12[f$_{12}$]**, ***c*-P12[b$_6$f$_6$]·T6$_A$·T6$_B$**, ***c*-P12[b$_6$f$_6$]·(T6$_A$)$_2$**, ***c*-P12[b$_6$f$_6$]·(T6$_B$)$_2$**, and ***c*-P12[b$_{12}$]·(T6$_C$)$_2$** were performed in Gaussian 16 with the B3LYP functional and the 6-31G* basis set.[222–226]

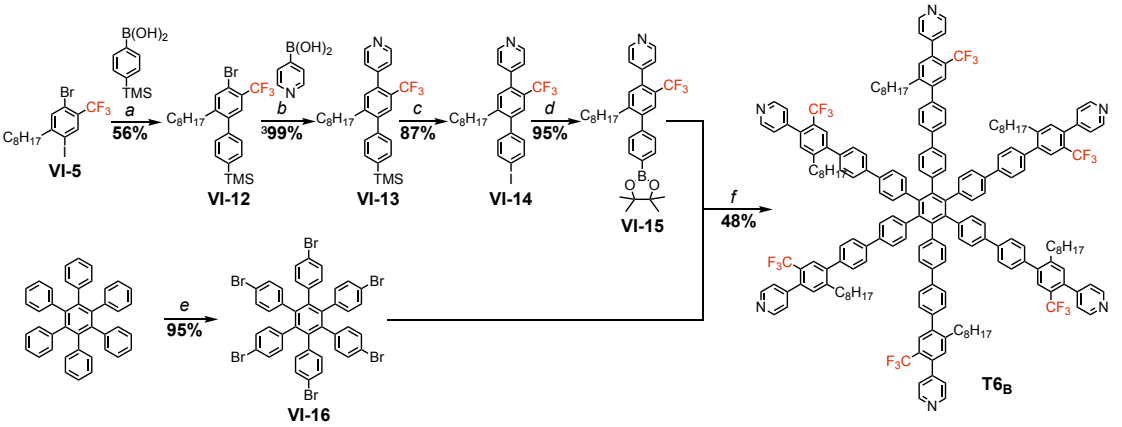
Nucleus independent chemical shift (NICS) calculations of ***c*-P12[b$_6$f$_6$]** and ***c*-P12[b$_{12}$]** in different oxidation states were performed using geometries of the free nanorings optimized by DFT (B3LYP/6-31G*) for each investigated oxidation state. NICS calculations were performed using the GIAO method, as implemented in Gaussian 16, with BLYP35 as functional and the 6-31G* basis set.[207, 404]

TD-DFT calculations of ***c*-P12[b$_6$f$_6$]**, ***c*-P12[b$_{12}$]**, and ***c*-P12[f$_{12}$]** were performed in Gaussian 16 with LC-ωHPBE ($\omega = 0.1$) as functional and the 6-31G* basis set, and the PCM solvent model (solvent = $CHCl_3$).[232, 401–403] Natural transition orbitals (NTOs) were calculated for the S_1 and S_2 excited states of ***c*-P12[b$_6$f$_6$]**, ***c*-P12[b$_{12}$]**, and ***c*-P12[f$_{12}$]**.[406]

6.5.2 Synthetic Procedures

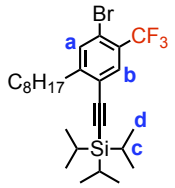


Scheme 6.1: Synthesis of template $\mathbf{T6_A}$. Reaction conditions a) *n*-$C_8H_{17}B(OH)_2$, $Pd(PPh_3)_4$, K_2CO_3, toluene/H_2O, reflux, 5 d, 63%; b) $SnCl_2{\cdot}2H_2O$, EtOH, 37% HCl, 60 °C, 16 h, 89%; c) NBS, MeCN, 0 °C, 1 h, 78%; d) $NaNO_2$, KI, *p*-TsOH·H_2O, MeCN/H_2O, 0 °C → r.t., 1 h, 84%; e) TIPS-acetylene, $Pd_2(dba)_3$, CuI, PPh_3, toluene, *i*-Pr_2NH_2, r.t., 2 h, 81%; f) $Pd(PPh_3)_2Cl_2$, K_2CO_3, dioxane/H_2O, 90 °C, 19 h, 80%; g) TBAF (1.0 M in THF), CH_2Cl_2, r.t., 30 min, 95%; h) $Pd(PPh_3)_4$, CuI, *i*-Pr_2NH, THF, 95 °C, 1 d, 45%; i) MeI neat, sealed tube, 135 °C, 14 h, 90%; j) $Pd(PPh_3)_4$, CuI, *i*-Pr_2NH, THF, 50 °C, 2.5 d, 58%.



Scheme 6.2: Synthesis of template $\mathbf{T6_B}$. Reaction conditions: a) $Pd(PPh_3)_2Cl_2$, K_2CO_3 in 1,4-dioxane/H_2O, 70 °C, 1.5 d, 56%; b) $Pd(PPh_3)_2Cl_2$, K_2CO_3, 1,4-dioxane/H_2O, 90 °C, 16 h, ≥99%; c) ICl in $CHCl_3$, r.t., 1.5 h, 94%; d) B_2pin_2, $Pd(dppf)Cl_2{\cdot}CH_2Cl_2$, KOAc, 1,4-dioxane, 90 °C, 16 h, 95%; e) Br_2 neat, 1 h, 95%; f) Xphos Pd G2, K_3PO_4 in 1,4-dioxane/H_2O, 90 °C, 3 d, 48%.

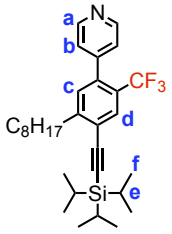
Compound VI-6:



In a Schlenk flask, 1-bromo-4-iodo-5-octyl-2-(trifluoromethyl)benzene **VI-5** (3.14 g, 6.77 mmol), $Pd_2(dba)_3$ (619 mg, 677 μmol), and CuI (270 mg, 1.35 mmol) were dissolved in *i*-Pr_2NH (25 mL) and toluene (50 mL) and subjected to three freeze-pump-thaw cycles. (Triisopropylsilyl)acetylene (1.51 mL, 6.77 mmol, 1 equiv.) was added and the reaction mixture was stirred at room temperature for 2.5 hours. The mixture was filtered through a short pad of SiO_2 (petroleum ether) and concentrated *in vacuo*. Purification by flash column chromatography (SiO_2, petroleum ether) afforded **VI-6** (2.82 g, 81%) as a yellow oil.

^{1}**H NMR** (500 MHz, $CDCl_3$, 298 K) δ_H = 7.70 (s, 1H, b), 7.53 (s, 1H, a), 2.81–2.77 (m, 2H, H_{Alkyl}), 1.66–1.60 (m, 2H, H_{Alkyl}), 1.35–1.24 (m, 10H, H_{Alkyl}), 1.13 (m, 21H, c+d), 0.88 (t, J = 6.9 Hz, 3H, $Alkyl_{CH3}$) ppm. ^{13}**C NMR** (126 MHz, $CDCl_3$, 298 K) δ_C = 150.66, 135.19, 131.90 (q, $J_{C–F}$ = 5.5 Hz), 127.80 (q, $J_{C–F}$ = 31.6 Hz), 122.85 (q, $J_{C–F}$ = 273.1 Hz), 122.57, 119.53, 103.29, 97.41, 34.81, 32.00, 30.56, 29.74, 29.61, 29.40, 22.80, 18.81, 14.24, 11.42 ppm.

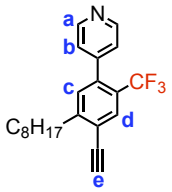
Compound VI-7:



To a deoxygenated mixture of 1-bromo-4-(triisopropylsilyl)acetylene-5-octyl-2-(trifluoromethyl)benzene **VI-6** (2.80 g, 5.42 mmol), pyridine-4-boronic acid (1.54 g, 10.8 mmol, 2 equiv.), and K_2CO_3 (6.10 g, 44.1 mmol) in dioxane (75 mL) and water (20 mL) was added $Pd(PPh_3)_2Cl_2$ (189 mg, 269 μmol, 0.05 equiv.) and the mixture was further degassed with a stream of argon. The reaction mixture was heated at 90 °C for 19 h, cooled to room temperature, washed with H_2O, dried over $MgSO_4$, filtered, and concentrated *in vacuo*. Flash column chromatography (SiO_2, 30% ethyl acetate/petroleum ether) afforded **VI-7** (2.23 g, 80%) as a yellow oil.

^{1}**H NMR** (500 MHz, $CDCl_3$, 298 K) δ_H = 8.67–8.63 (m, 2H, a), 7.81 (s, 1H, d), 7.26–7.23 (m, 2H, b), 7.11 (s, 1H, c), 2.88–2.83 (m, 2H, H_{Alkyl}), 1.69–1.63 (m, 2H, H_{Alkyl}), 1.39–1.23 (m, 10H, H_{Alkyl}), 1.16 (m, 18H, e+f), 0.87 (t, J = 6.9 Hz, 3H, $Alkyl_{CH3}$) ppm. ^{13}**C NMR** (126 MHz, $CDCl_3$, 298 K) δ_C = 149.55, 149.26, 147.59, 137.96, 131.83, 130.79 (q, $J_{C–F}$ = 5.3 Hz), 125.94 (q, $J_{C–F}$ = 31.0 Hz), 123.95, 123.73 (q, $J_{C–F}$ = 273.8 Hz), 123.54, 103.67, 97.19, 35.03, 31.99, 30.74, 29.83, 29.62, 29.40, 22.79, 18.83, 14.23, 11.45 ppm.

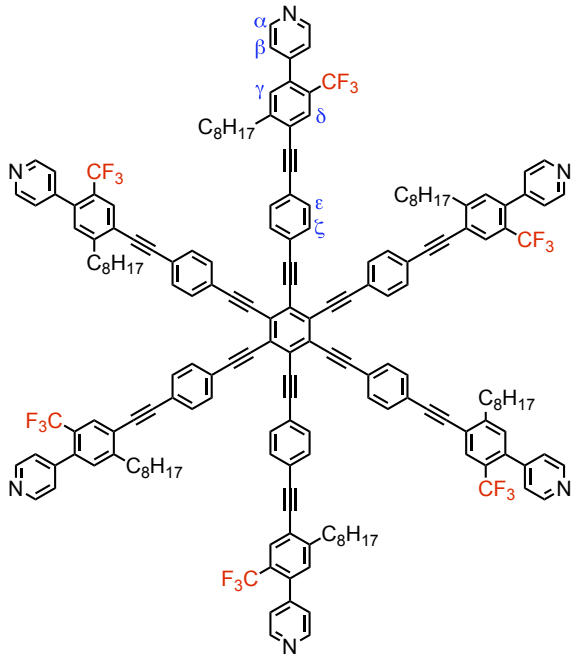
Compound VI-8:



To a solution of **VI-7** (307 mg, 0.595 mmol) in CH_2Cl_2 (20 mL) was added tetrabutylammonium fluoride (1.0 M in THF, 4.40 mL, 4.40 mmol, 7.5 equiv.) and the reaction mixture was stirred for 30 min at room temperature, poured into water (50 mL), and extracted with CH_2Cl_2 (3 x 30 mL). The combined organic extracts were dried over $MgSO_4$, filtered, and concentrated *in vacuo*. Purification of the crude material by flash column chromatography (SiO_2, gradient elution CH_2Cl_2 to EtOAc/CH_2Cl_2 3:7) afforded **VI-8** (203 mg, 95%) as a red oil.

^{1}**H NMR** (400 MHz, $CDCl_3$, 298 K) δ_H = 8.69–8.62 (m, 2H, a), 7.85 (s, 1H, d), 7.26–7.22 (m, 2H, b), 7.13 (s, 1H, c), 3.37 (s, 1H, e), 2.88–2.81 (m, 2H, H_{Alkyl}), 1.71–1.60 (m, 2H, H_{Alkyl}), 1.36–1.24 (m, 10H, H_{Alkyl}), 0.90–0.84 (m, 3H, $Alkyl_{CH3}$) ppm.

Template $T6_A$:

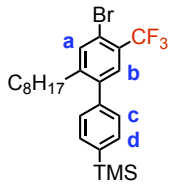


In a Schlenk flask, alkyne **VI-8** (240 mg, 669 μmol, 15 equiv.) and **VI-11** (64 mg, 44.7 μmol, 1 equiv.) were dissolved in THF (65 mL) and diisopropylamine (9 mL) and subjected to two freeze-pump-thaw cycles. While the mixture was still frozen, $Pd(PPh_3)_4$ (22 mg, 19.2 μmol) and CuI (4.6 mg, 24.9 μmol) were added followed by three additional freeze-pump thaw cycles. The mixture was heated to 50 °C for 2.5 days, cooled to room temperature, filtered through a short pad of silica (eluent: 20% MeOH/$CHCl_3$), and concentrated *in vacuo*. Purification by flash column chromatography (SiO_2, gradient elution 2% MeOH/$CHCl_3$ to 5% MeOH/$CHCl_3$) followed by precipitation from $CHCl_3$/MeOH afforded template $\mathbf{T6_A}$ (98 mg, 78%) as a yellow solid.

^{1}H NMR (600 MHz, $CDCl_3$, 298 K) $\delta_H = 8.67$ (d, $J = 6.0$ Hz, 12H, α), 7.91 (s, 6H, δ), 7.68 (d, $J = 8.3$ Hz, 12H, ζ), 7.61 (d, $J = 8.3$ Hz, 12H, ε), 7.28 (d, $J = 6.0$ Hz, 12H, β), 7.18 (s, 6H, γ), 2.98–2.90 (m, 12H, Ar-CH_2-), 1.78–1.71 (m, 12H, -CH_2-), 1.47–1.40 (m, 12H, -CH_2-), 1.39–1.33 (m, 12H, -CH_2-), 1.33–1.21 (m, 36H, -CH_3) ppm. **^{13}C NMR** (126 MHz, $CDCl_3$, 298 K) δ_C = 149.49, 148.91, 147.53, 138.30, 132.02, 131.97, 130.40 (q, J_{C-F} = 5.2 Hz), 127.74, 126.24 (q, J_{C-F} = 31.0 Hz), 123.97, 123.76, 123.69 (q, J_{C-F} = 273.7 Hz), 123.31, 122.97, 99.61, 94.40, 89.22, 89.13, 34.71,

31.97, 30.52, 29.65, 29.52, 29.35, 22.76, 14.22 ppm. **^{19}F NMR** (565 MHz, $CDCl_3$, 298 K) $\delta_F = -59.76$ ppm. **HRMS** (APCI) *m/z*: $[M+H]^+$ calcd. for $C_{186}H_{163}F_{18}N_6^+$ 2822.2646; found 2822.2599.

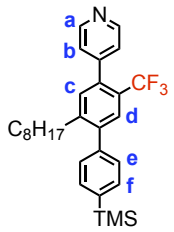
Compound VI-12:



To a deoxygenated mixture of 1-bromo-4-iodo-5-octyl-2-(trifluoromethyl)benzene **VI-5** (4.93 g, 10.65 mmol), (4-(trimethylsilyl)phenyl)boronic acid (2.07 g, 10.65 mmol), K_2CO_3 (8.83 g, 63.87 mmol) in 1,4-dioxane (100 mL) and water (30 mL) was added $Pd(PPh_3)_2Cl_2$ (374 mg, 0.532 mmol). The reaction mixture was heated to 50 °C for 1.5 d, cooled to room temperature, filtered through a short pad of SiO_2 (CH_2Cl_2 / petroleum ether 1:1), and concentrated under reduced pressure. Purification by flash column chromatography (SiO_2, petroleum ether) afforded the title compound as a pale-yellow oil (2.88 g, 56%).

^{1}H NMR (600 MHz, $CDCl_3$, 298 K) $\delta_H = 7.63$ (s, 1H, a), 7.59 (d, $J = 8.1$ Hz, 2H, c/d), 7.51 (s, 1H, b), 7.25 (d, $J = 8.1$ Hz, 2H, c/d), 2.62–2.55 (m, 2H, Ar-CH_2-), 1.53–1.45 (m, 2H, -octyl-), 1.29-1.24 (m, 2H, -octyl-), 1.23–1.15 (m, 8H, -octyl-), 0.87 (t, $J = 7.2$ Hz, 3H, -CH_3), 0.32 (s, 9H, TMS) ppm. **^{13}C NMR** (151 MHz, $CDCl_3$, 298 K) $\delta_C = 146.38, 141.20, 140.08, 139.98, 135.57, 133.49, 129.47$ (q, $J_{C-F} = 5.3$ Hz), 128.38, 127.42 (q, $J_{C-F} = 31.2$ Hz), 123.21 (q, $J_{C-F} = 273.0$ Hz), 118.52 (q, $J_{C-F} = 1.7$ Hz), 32.73, 31.94, 31.01, 29.35, 29.26, 29.20, 22.76, 14.23, −0.97 ppm. **^{19}F NMR** (377 MHz, $CDCl_3$, 298 K) $\delta_F = -65.23$ ppm.

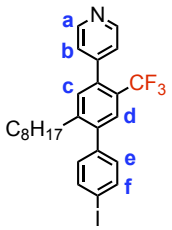
Compound VI-13:



To a deoxygenated mixture of aryl bromide **VI-12** (4.01 g, 8.26 mmol), pyridine-4-boronic acid hydrate (1.75 g, 12.4 mmol), K_2CO_3 (6.85 g, 49.6 mmol) in 1,4-dioxane (80 mL) and water (20 mL) was added $Pd(PPh_3)_2Cl_2$ (290 mg, 0.413 mmol). The reaction mixture was heated to 90 °C for 16 h, cooled to room temperature, filtered through a short pad of SiO_2 (EtOAc / petroleum ether 1:1), and concentrated under reduced pressure. Purification by flash column chromatography (SiO_2, gradient elution: EtOAc / petroleum ether 1:9 to 2:8) afforded the title compound as a pale-yellow oil (4.08 g, 99%).

^{1}H NMR (600 MHz, $CDCl_3$, 298 K) $\delta_H = 8.67$ (d, $J = 6.0$ Hz, 2H, a), 7.63–7.58 (m, 3H, d + e/f), 7.34–7.30 (m, 4H, b + e/f), 7.21 (s, 1H, c), 2.67–2.61 (m, 2H, Ar-CH_2-), 1.54–1.46 (m, 2H, octyl), 1.28–1.13 (m, 10H, octyl), 0.85 (t, $J = 7.2$ Hz, 3H, -CH_3), 0.33 (s, 9H, TMS) ppm. **^{13}C NMR** (151 MHz, $CDCl_3$, 298 K) $\delta_C = 149.43$, 148.12, 144.72, 142.15, 140.41, 140.00, 137.15 (q, $J_{C–F} = 1.7$ Hz), 133.49, 132.33, 128.50, 128.20 (q, $J_{C–F} = 5.2$ Hz), 125.58 (q, $J_{C–F} = 30.5$ Hz), 124.23, 124.12 (q, $J_{C–F} = 273.6$ Hz), 32.90, 31.94, 31.21, 29.45, 29.27, 29.21, 22.75, 14.22, −0.95 ppm. **^{19}F NMR** (377 MHz, $CDCl_3$, 298 K) $\delta_F = -59.38$ ppm.

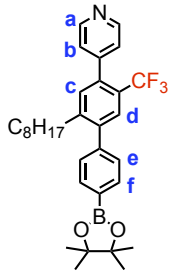
Compound VI-14:



A solution of ICl (2.67 g, 16.4 mmol) in $CHCl_3$ (15 mL) was added dropwise to a solution of aryl trimethylsilane **VI-13** (3.18 g, 6.57 mmol) in $CHCl_3$ (60 mL). The reaction mixture was stirred for 1.5 h, diluted with $CHCl_3$ (60 mL), and washed with sat. aqueous $Na_2S_2O_3$ (1 x 150 mL), H_2O (1 x 150 mL), and sat. aqueous Na_2CO_3 (1 x 150 mL), dried over Na_2SO_4, filtered, and concentrated under reduced pressure. Purification by flash column chromatography (SiO_2, EtOAc / petroleum ether 2:8) yielded the title compound as a colorless oil (3.32 g, 94%).

^{1}H NMR (600 MHz, $CDCl_3$, 298 K) δ_H = 8.67 (d, J = 5.6 Hz, 2H, a), 7.80 (d, J = 8.3 Hz, 2H, e/f), 7.55 (s, 1H, d), 7.31 (d, J = 5.6 Hz, 2H, b), 7.20 (s, 1H, c), 7.08 (d, J = 8.3 Hz, 2H, e/f), 2.65–2.58 (m, 2H, Ar-CH_2-), 1.50–1.43 (m, 2H, octyl), 1.28–1.14 (m, 10H, octyl), 0.86 (t, J = 7.2 Hz, 3H, -CH_3) ppm. **^{13}C NMR** (151 MHz, $CDCl_3$, 298 K) δ_C = 149.53, 147.81, 144.62, 140.94, 139.57, 137.72, 137.63 (q, $J_{C–F}$ = 2.0 Hz), 132.49, 131.08, 127.92 (q, $J_{C–F}$ = 4.9 Hz), 125.79 (q, $J_{C–F}$ = 30.8 Hz), 124.13, 123.99 (q, $J_{C–F}$ = 273.8 Hz), 93.66, 32.94, 31.94, 31.16, 29.46, 29.28, 29.21, 22.78, 14.25 ppm. **^{19}F NMR** (377 MHz, $CDCl_3$, 298 K) δ_F = −59.46 ppm.

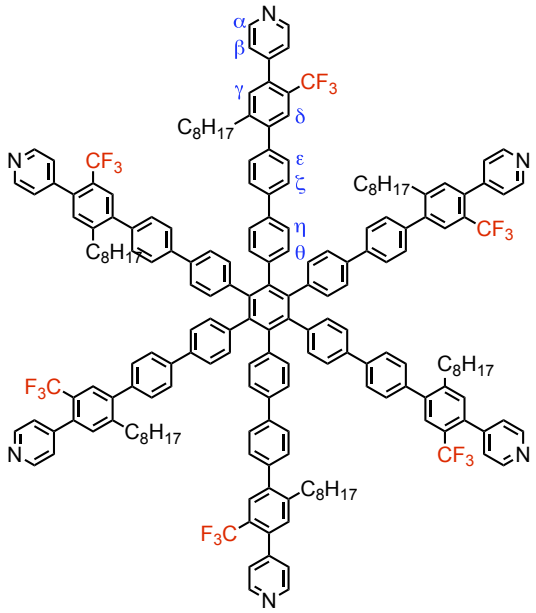
Compound VI-15:



To a deoxygenated mixture of aryl iodide **VI-14** (4.02 g, 7.48 mmol), B_2Pin_2 (2.09 g, 8.23 mmol), and KOAc (2.20 g, 22.4 mmol) in 1,4-dioxane (45 mL) was added $Pd(dppf)Cl_2{\cdot}CH_2Cl_2$ (305 mg, 0.374 mmol). The reaction mixture was heated to 90 °C for 16 h, cooled to room temperature, filtered through a short pad of SiO_2 (EtOAc / petroleum ether 1:1), and concentrated under reduced pressure. Purification by flash column chromatography (SiO_2, gradient elution: EtOAc / $CHCl_3$ 0:1 to 0.5:9.5) afforded the title compound as a yellow-brown oil (3.82 g, 95%).

^{1}H NMR (600 MHz, $CDCl_3$, 298 K) δ_H = 8.69–8.65 (m, 2H, a), 7.90 (d, J = 8.0 Hz, 2H, e/f), 7.58 (s, 1H, d), 7.35 (d, J = 8.0 Hz, 2H, e/f), 7.32 (d, J = 5.8 Hz, 2H, b), 7.20 (s, 1H, c), 2.65–2.59 (m, 2H, Ar-CH_2-), 1.50–1.43 (m, 2H, octyl), 1.38 (s, 12H, Bpin-CH_3), 1.26–1.22 (m, 2H, octyl), 1.21–1.11 (m, 8H, octyl), 0.85 (t, J = 7.2 Hz, 3H, -CH_3) ppm. **^{13}C NMR** (151 MHz, $CDCl_3$, 298 K) δ_C = 149.43, 148.06, 144.69, 142.92, 142.06, 137.30 (q, $J_{C–F}$ = 1.8 Hz), 134.95, 132.36, 128.57, 128.00 (q, $J_{C–F}$ = 5.0 Hz), 125.60 (q, $J_{C–F}$ = 30.8 Hz), 124.21, 124.09 (q, $J_{C–F}$ = 273.6 Hz), 84.13, 32.99, 31.91, 31.18, 29.48, 29.28, 29.19, 25.05, 22.74, 14.22 ppm. **^{19}F NMR** (377 MHz, $CDCl_3$, 298 K) δ_F = −59.40 ppm.

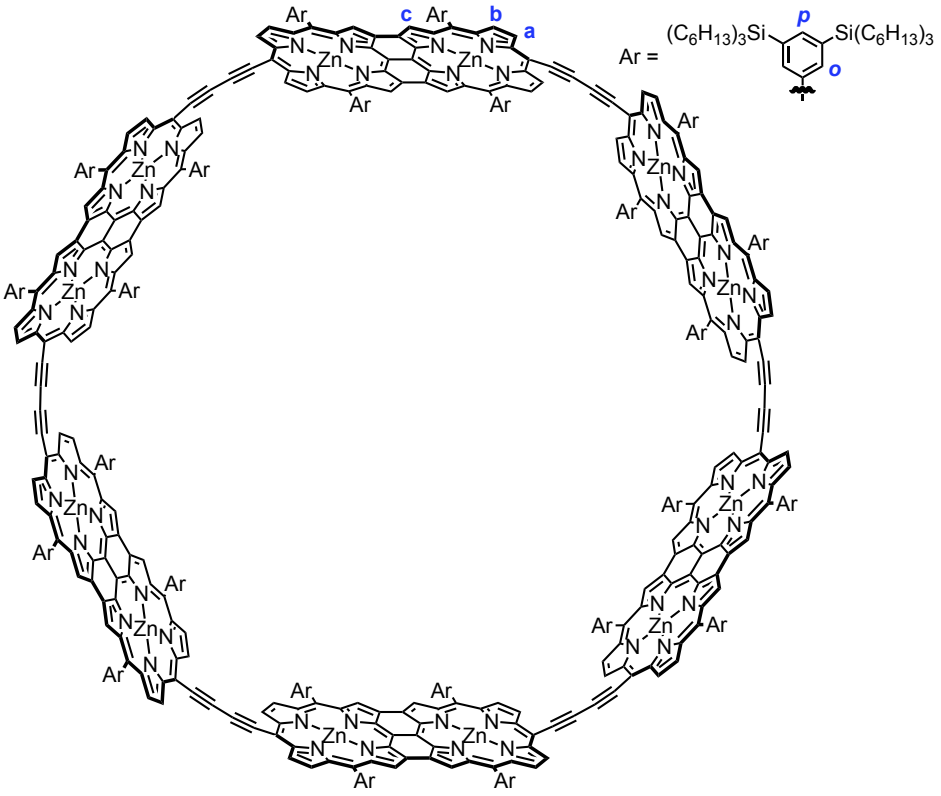
Template $T6_B$:



A mixture of hexa(*p*-bromophenyl)benzene (50.0 mg, 0.050 mmol), aryl-Bpin **VI-15** (533 mg, 0.992 mmol), and XPhos Pd G2 (23.4 mg, 0.030 mmol) in 1,4-dioxane (7.0 mL) was subjected to freeze-pump-thaw cycles (3 times). A deoxygenated aqueous solution of K_3PO_4 (1.0 M, 1.65 mmol, 1.65 mL) was added to the reaction flask and the mixture was heated to 50 °C for 3 h, followed by 90 °C for 3 days. The reaction mixture was cooled to room temperature, filtered through a short pad of SiO_2 (MeOH / $CHCl_3$ 15:85 + 1% Et_3N), and concentrated under reduced pressure. Purification by flash column chromatography (SiO_2, MeOH/$CHCl_3$ 4:96) followed by precipitation from $CHCl_3$ / petrol ether yielded the title compound (71 mg, 48%) as a white solid. **^{1}H NMR** (600 MHz, $CDCl_3$, 298 K) δ_H = 8.66 (d, J = 6.0 Hz, 12H, α), 7.59 (d, J = 8.1 Hz, 12H, ϵ), 7.56 (s, 6H, δ), 7.32 (d, J = 8.1 Hz, 12H, ζ), 7.31 (d, J = 8.2 Hz, 12H, η/θ), 7.29 (d, J = 6.0 Hz, 12H, β), 7.19 (s, 6H, γ), 7.10 (d, J = 8.2 Hz, 12H, η/θ), 2.67–2.60 (m, 12H, Ar-CH_2-), 1.51–1.45 (m, 12H, -CH_2-), 1.22–1.10 (m, 60H, -CH_2-), 0.79 (t, J = 7.1 Hz, 18H, -CH_3) ppm. **^{13}C NMR** (151 MHz, $CDCl_3$, 298 K) δ_C = 149.53, 147.90, 144.64, 141.65, 140.53, 140.17, 140.06, 138.91, 137.29, 137.20, 132.38, 132.24, 129.52, 128.14 (q, $J_{C–F}$ = 5.1 Hz), 126.84, 125.64 (q, $J_{C–F}$ = 30.5 Hz), 125.54, 124.14, 124.06 (q, $J_{C–F}$ = 273.6 Hz), 32.93, 31.88, 31.15, 29.44, 29.28, 29.14, 22.69, 14.18 ppm. **^{19}F NMR** (377 MHz, $CDCl_3$,

298 K) $\delta_F = -59.48$ ppm. **HRMS** (ESI$^+$) *m/z*: $[M+3H]^{3+}$ calcd. for $C_{198}H_{189}F_{18}N_6{}^{3+}$ 997.4890; found 997.4869.

***c*-P12[b_6f_6] and *l*-P12[b_5f_6]:**



A solution of **T6$_B$** (11.5 mg, 3.83 μmol) in $CDCl_3$ (10.9 mL) was added to a solution of **H-*l*-P2[f_1]-H** (37.8 mg, 11.3 μmol) in $CDCl_3$ (28.8 mL). The resulting mixture was sonicated for 15 minutes and then stirred at room temperature. A catalyst solution of $Pd(PPh_3)_2Cl_2$ (7.9 mg, 11.3 μmol), CuI (21.5 mg, 113 μmol), and 1,4-benzoquinone (24.4 mg, 225 μmol) in diisopropylamine (0.4 mL) and $CDCl_3$ (6.6 mL) was added to the reaction flask and it was stirred vigorously under oxygen. Progress of the reaction was monitored by analytical gel-permeation chromatography. After 2 days, the reaction mixture was filtered through a short pad of SiO_2 ($CHCl_3$ + 5% pyridine) and the solvent was removed by evaporation under reduced pressure. The crude mixture was passed through a size-exclusion column (toluene + 1% pyridine) to remove small molecular weight impurities and subsequently purified by preparative recycling gel-permeation chromatography (toluene + 1% pyridine), yielding partially

templated ***c*-P12[b_6f_6]**. The **$T6_B$** template was fully removed from the ring by size-exclusion chromatography (THF + 1% pyridine) by loading a solution of THF + 20% pyridine (200 mL) onto the column before eluting the templated ***c*-P12[b_6f_6]** sample through it. BHT stabilizer from the THF was removed from the free ***c*-P12[b_6f_6]** ring by size-exclusion chromatography ($CHCl_3$) and precipitation from CH_2Cl_2 / MeOH yielded ***c*-P12[b_6f_6]** (12.7 mg, 35%) as a dark blue solid and ***l*-P12[b_5f_6]** (5.3 mg, 15%), as the major byproduct, also as a dark blue solid.

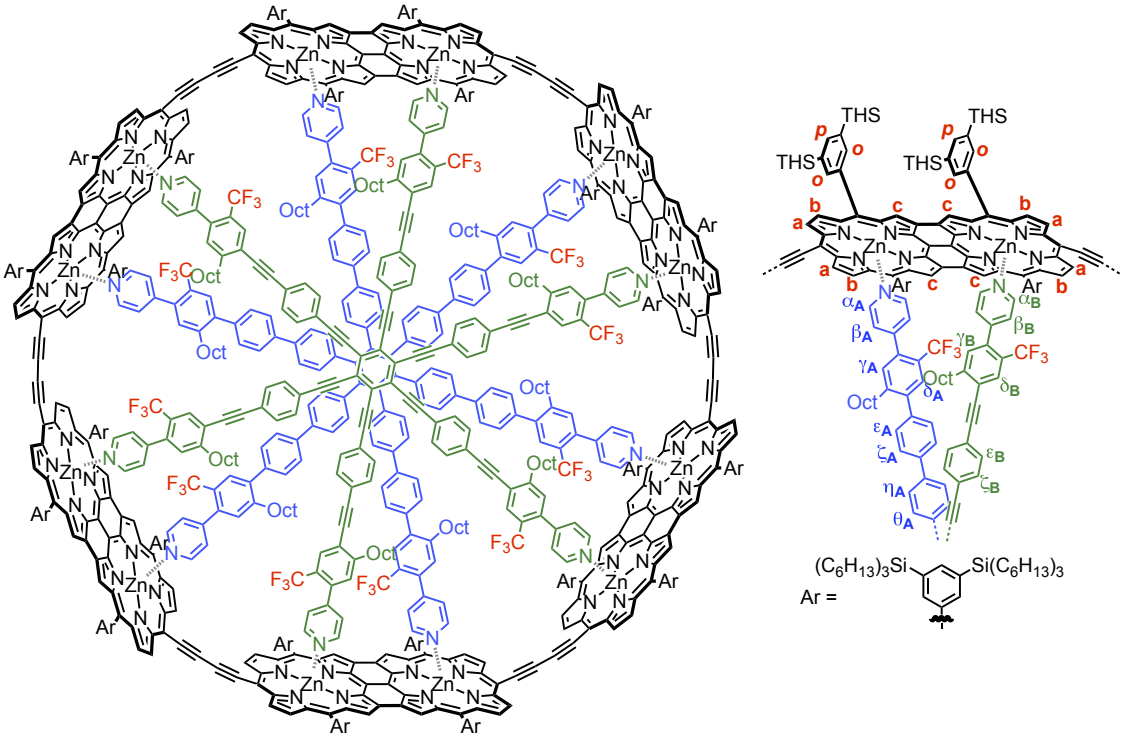
Characterisation of ***c*-P12[b_6f_6]**:

^{1}H NMR (600 MHz, CD_2Cl_2, 298 K) $\delta_H = 8.44$ (d, $J = 3.7$ Hz, 24H, a), 7.82 (s, 24H, p), 7.78 (s, 48H, o), 7.52 (d, $J = 3.7$ Hz, 24H, b), 6.97 (s, 24H, c), 1.45–1.36 (m, 288H, -CH_2-), 1.35–1.20 (m, 864H, -CH_2-), 0.89–0.83 (m, 288H, -CH_2-), 0.83–0.76 (m, 432H, -CH_3) ppm. **HRMS** (MALDI) *m/z*: $[M^\bullet]^+$ calcd. for $C1_{272}H_{2016}N_{48}Si_{48}Zn_{12}{}^{\bullet+}$ 20114; found 20112. **UV-vis-NIR** ($CDCl_3$) λ_{max} (log ϵ): 434 (0.90), 599 (1.33), 1225 (0.97) nm.

Characterisation of ***l*-P12[b_5f_6]**:

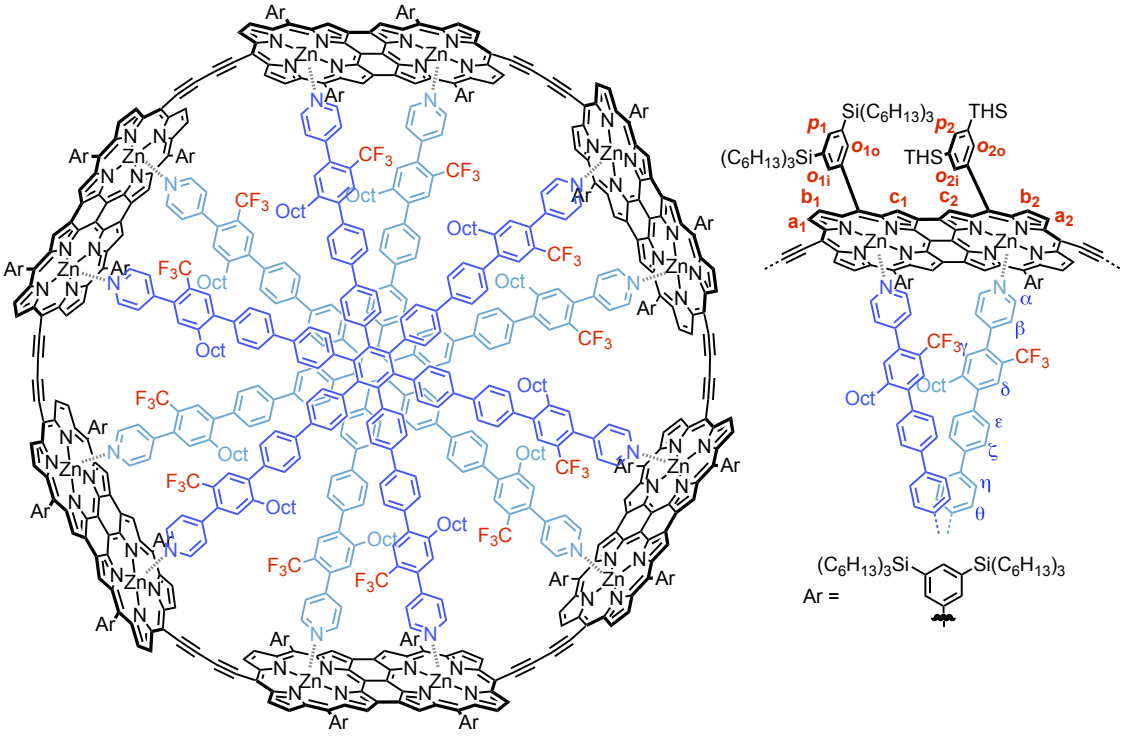
^{1}H NMR (700 MHz, CD_2Cl_2, 298 K) $\delta_H = 8.71$–8.30 (m, 24H, a), 8.00–7.66 (m, 72H, o + p), 7.66–7.44 (m, 24H, b), 7.31–6.86 (m, 24H, c), 3.22 (s, 2H, d), 1.47–1.23 (m, 1152H, THS), 0.91–0.79 (m, 720H, THS) ppm. **HRMS** (MALDI) *m/z*: $[M^\bullet]^+$ calcd. for $C_{1272}H_{2018}N_{48}Si_{48}Zn_{12}{}^{\bullet+}$ 20116; found 20139. **UV-vis-NIR** ($CDCl_3$) λ_{max} (log ϵ): 433 (0.78), 607 (1.10), 1240 (0.92) nm.

Characterization of *c*-P12[b_6f_6]·T6$_A$·T6$_B$:



^{1}**H NMR** (600 MHz, $CDCl_3$, 298 K) $\delta_H = 8.27$ (d, $J = 3.7$ Hz, 6H, a), 8.25–8.18 (m, 12H, a), 8.15 (d, $J = 3.7$ Hz, 6H, a), 7.80 (s, 6H, o), 7.78–7.71 (m, 36H, o + p), 7.66 (s, 12H, o), 7.63 (s, 6H, o), 7.60 (s, 12H, o), 7.41–7.33 (m, 18H, $\epsilon_A/\zeta_A + \delta_B$), 7.30–7.20 (m, 24H, b, overlapping with $CHCl_3$), 7.14–7.06 (m, 24H, $\zeta_B + \epsilon_B$), 7.07–7.00 (m, 18H, $\delta_A + \epsilon_A/\delta_A$), 6.98–6.90 (m, 12H, η_A), 6.76 (s, 12H, c), 6.71 (s, 6H, c), 6.69 (s, 6H, c), 6.61 (s, 6H, γ_B), 6.56 (d, $J = 7.8$ Hz, 6H, θ_A), 6.52 (s, 6H, γ_A), 6.39 (s, 24H, $\beta_A + \beta_B$), 6.00–5.85 (m, 18H, $\theta_A + \alpha_B$), 5.85–5.74 (m, 12H, α_A), 2.55–1.91 (m, 24H, Ar-CH_2-), 1.78–0.41 (m, 2052H, octyl + THS) ppm. ^{19}**F NMR** (565 MHz, $CDCl_3$, 298 K) $\delta_F = -59.87$ (**T6$_B$**), -60.63 (**T6$_A$**) ppm. **HRMS** (MALDI) *m/z*: $[M^\bullet]^+$ calcd. for $C_{1656}H_{2364}F_{36}N_{60}Si_{48}Zn_{12}{}^{\bullet+}$ 25930; found 25932. **UV-vis-NIR** ($CDCl_3$) λ_{max} (log ϵ): 412 (0.68), 607 (1.02), 695 (0.29), 1283 (0.43), 1425 (1.64) nm.

Characterization of *c*-P12[b_6f_6]·($T6_B$)$_2$:



^{1}H NMR (600 MHz, $CDCl_3$, 298 K) $\delta_H = 8.22$ (d, $J = 4.1$ Hz, 24H, a_1+a_2), 7.79 (s, 12H, o_{1i}/o_{2i}), 7.73 (s, 24H, p_1+p_2), 7.66 (s, 12H, o_{1i}/o_{2i}), 7.64 (s, 12H, o_{1o}/o_{2o}), 7.56 (s, 12H, o_{1o}/o_{2o}), 7.27–7.25 (m, 12H, b_1/b_2, overlapping with $CHCl_3$), 7.24 (d, $J = 4.1$ Hz, 12H, b_1/b_2), 7.20 (d, $J = 8.4$ Hz, 12H, η/θ), 7.14 (d, $J = 8.2$ Hz, 24H, ζ), 7.11 (d, $J = 8.7$ Hz, 12H, η/θ), 6.85–6.79 (m, 24H, $\delta + \eta/\theta$), 6.76 (d, $J = 8.2$ Hz, 24H, ϵ), 6.73 (s, 12H, c_1/c_2), 6.71 (s, 12H, c_1/c_2), 6.70–6.66 (m, 12H, η/θ), 6.52 (s, 12H, γ), 6.36–6.28 (m, 24H, β), 5.90–5.80 (m, 24H, α), 2.10–1.93 (m, 24H, Ar-CH_2-), 1.44–0.66 (m, 2016H, Oct + THS), 0.55 (t, $J = 7.2$ Hz, 36H, -CH_3) ppm. **^{19}F NMR** (471 MHz, $CDCl_3$, 298 K) $\delta_F = -60.26$ ppm. **HRMS** (MALDI) m/z: $[M^\bullet]^+$ calcd. for $C_{1668}H_{2388}F_{36}N_{60}Si_{48}Zn_{12}{}^{\bullet+}$ 26098; found 26103. **UV-vis-NIR** ($CDCl_3$) λ_{max} (log ϵ): 441 (0.75), 607 (1.23), 687 (0.34), 1282 (0.49), 1419 (1.30) nm.

$ThnBArF_{20}$:

Thianthrenium hexafluoroantimonate **$ThnSbF_6$** (100 mg, 0.22 mmol, 1.0 equiv.) was dissolved in dry CH_2Cl_2 (2.5 mL) under an argon atmosphere. Potassium tetrakis(pentafluorophenyl)borate **$KBArF_{20}$** (159 mg, 0.22 mmol, 1.0 equiv.) was dissolved in dry CH_3CN (2.5 mL) under an argon atmosphere and added to the **$ThnSbF_6$** solution. The dark purple mixture was stirred at room temperature for 15 minutes before filtration *via* a cannula into a dry Schlenk flask. The solvent was removed under vacuum to obtain a blue oil. The crude material was redissolved in dry CH_2Cl_2 (2.5 mL) and precipitated over 12 hours by layering with dry pentane (1.5 mL). Removal of the excess solution *via* cannula filtration afforded dark-purple crystals of thianthrenium tetrakis(pentafluorophenyl)borate **$ThnBArF_{20}$** (153 mg, 77%) that were dried *in vacuo* and stored under inert atmosphere.

UV-vis-NIR (CH_2Cl_2) λ_{max} (log ϵ): 551 (3.86) nm.

The exchange of the counterion from SbF_6^- to $BArF_{20}^-$ does not affect the electronic structure of the thianthrenium radical cation Thn^+ as confirmed by UV-vis-NIR absorption spectroscopy and square-wave voltammetry (Figure 6.17 and Figure 6.18).

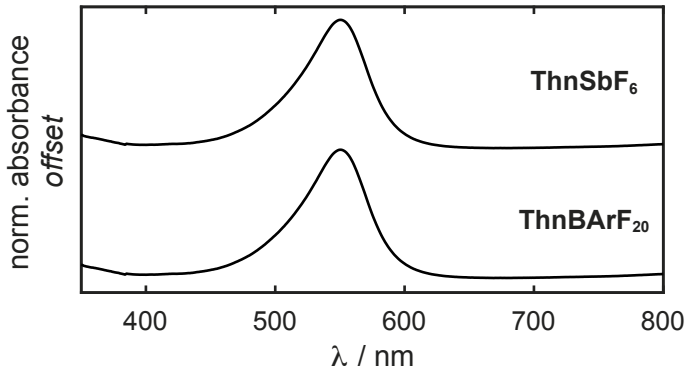


Figure 6.17: Normalized UV-vis-NIR absorption spectra of **$ThnSbF_6$** and **$ThnBArF_{20}$** in CH_2Cl_2 at 298 K.

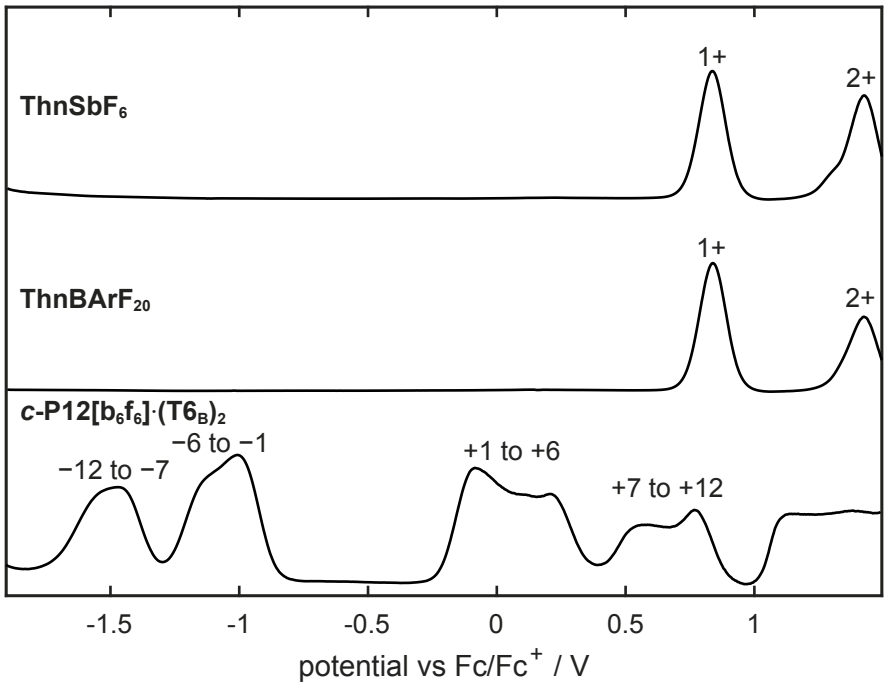


Figure 6.18: Square-wave voltammetry of **ThnSbF$_6$**, **ThnBArF$_{20}$**, and ***c*-P12[b$_6$f$_6$]·(T6$_B$)$_2$** in CH_2Cl_2 (0.1 M Bu_4NPF_6) versus the ferrocene/ferrocenium redox couple (Fc/Fc^+). The potential was swept from negative to positive values with a step size of 0.005 V, amplitude of 0.05 V, and a frequency of 2.0 Hz.

6.6 Supplemental Results and Analysis

Molecular Modelling

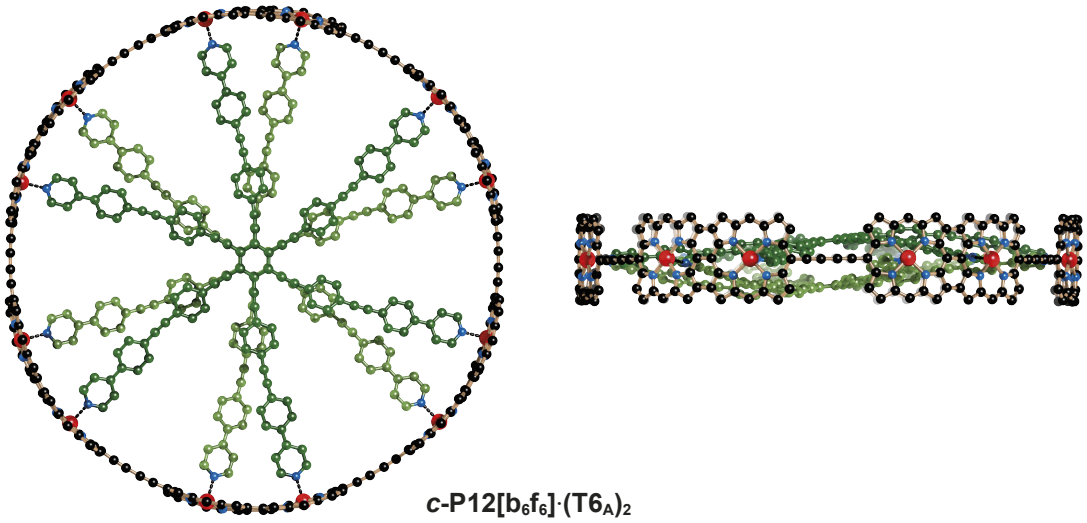


Figure 6.19: Topview (left) and sideview (right) of the HyperChem optimized geometry of ***c*-P12[b$_6$f$_6$]·(T6$_A$)$_2$** using the MM+ force field.

NMR Complexation Experiments

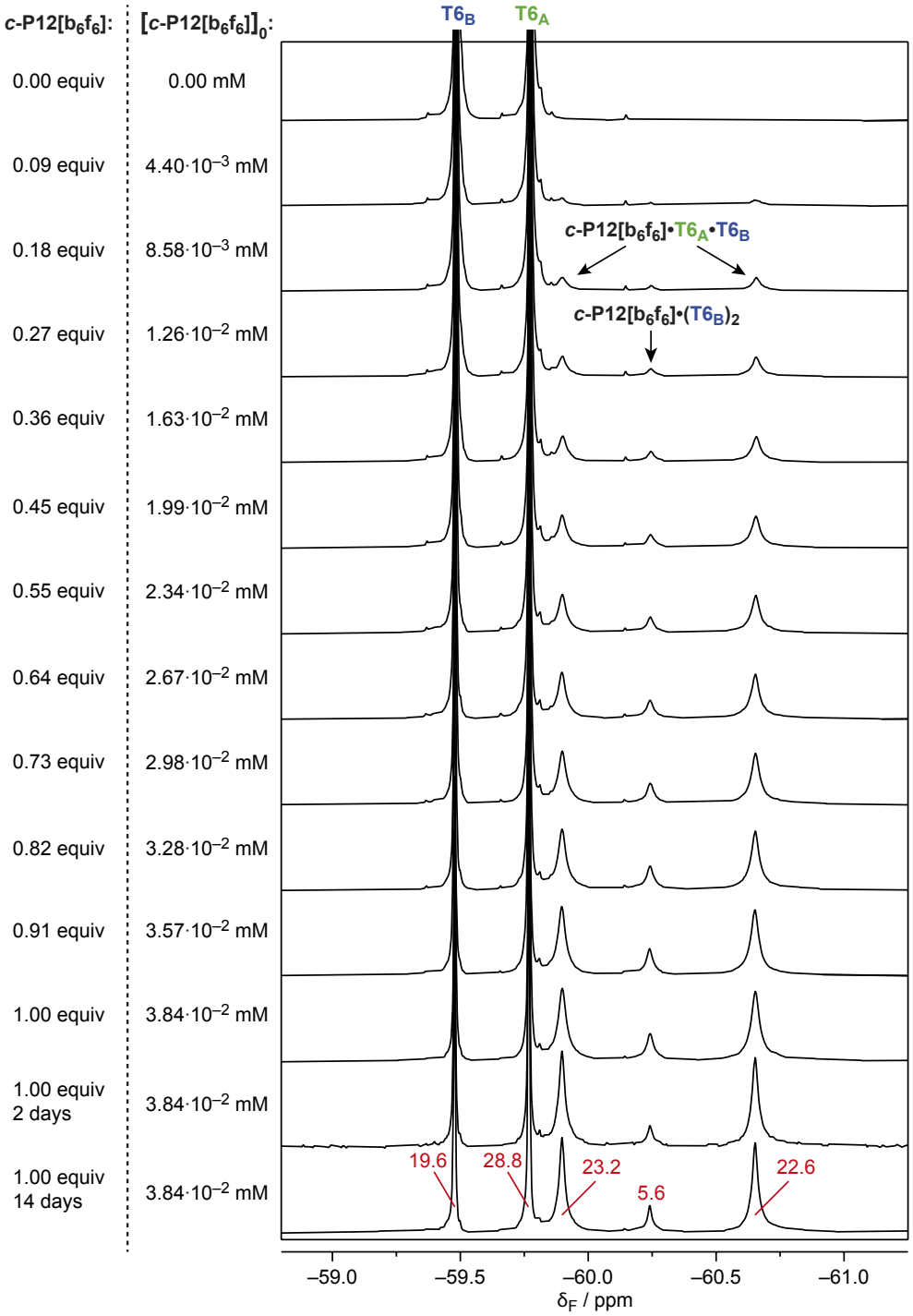


Figure 6.20: ^{19}F NMR titration (565 MHz, $CDCl_3$, 298 K) of ***c*-P12[b_6f_6]** (1.0 equiv) into a 1:1 mixture of **T6$_B$** (2.2 equiv.) and **T6$_A$** (2.2 equiv.); the total concentration of ***c*-P12[b_6f_6]** added is provided at each spectral point as $[$***c*-P12[b_6f_6]**$]_0$. At the end of the titration, the distribution between free templates and nanoring complexes did not change significantly over 14 days indicating that equilibrium was reached after 2 hours.

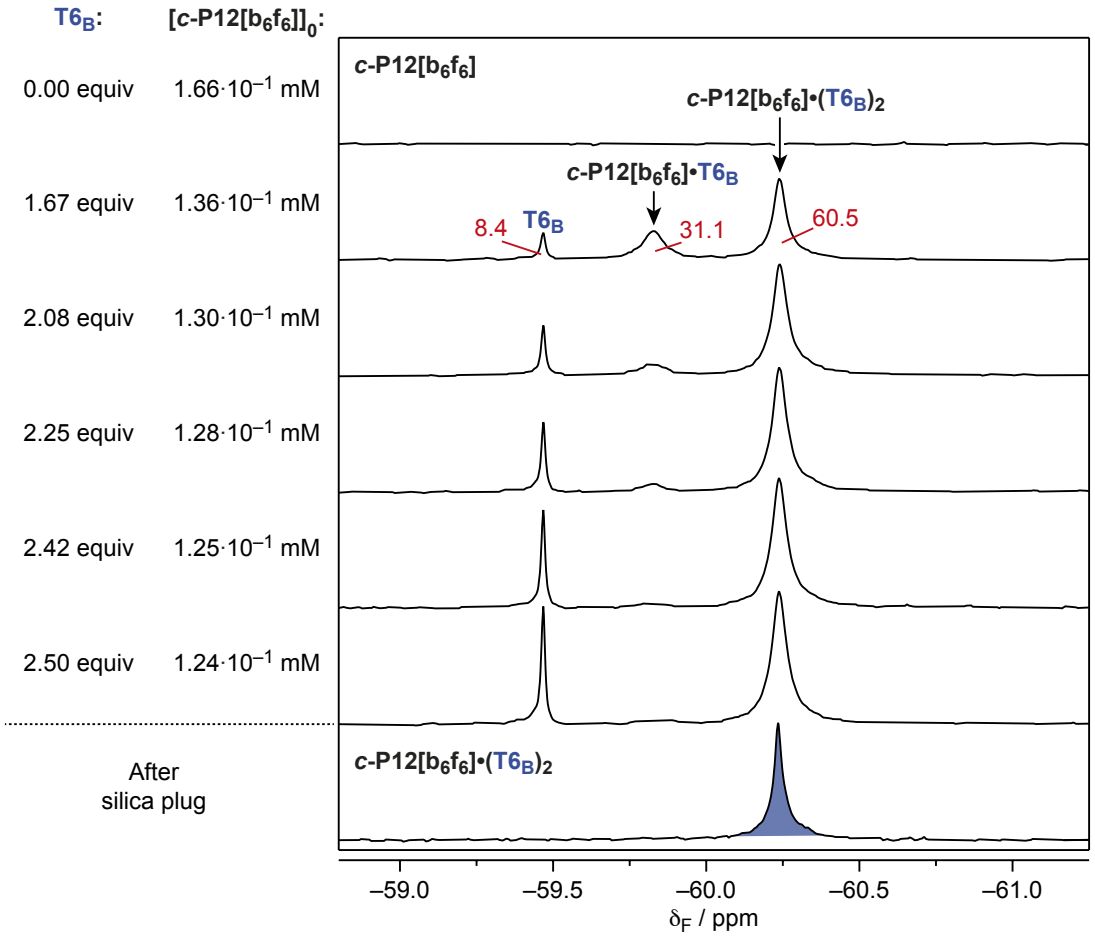


Figure 6.21: ^{19}F NMR formation titration (470 MHz, $CDCl_3$, 298 K) of ***c*-P12[b_6f_6]·($T6_B$)$_2$** starting from ***c*-P12[b_6f_6]** (top spectrum); the total concentration of ***c*-P12[b_6f_6]** added is provided at each spectral point as [***c*-P12[b_6f_6]**]$_0$. Excess unbound **$T6_B$** template was removed by passing the mixture through a short plug of silica ($CHCl_3$ / pentane = 1:1), yielding pure ***c*-P12[b_6f_6]·($T6_B$)$_2$**.

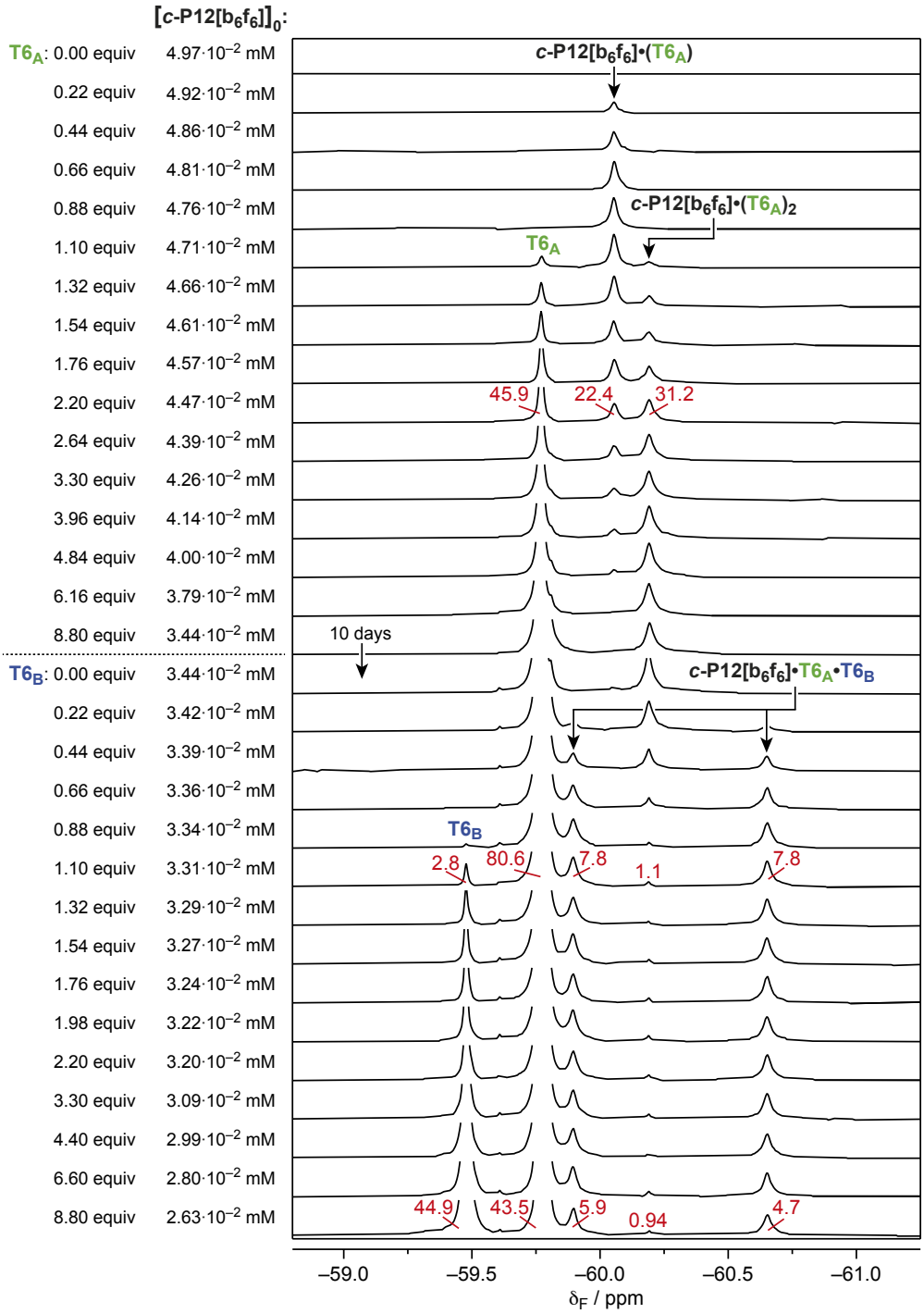


Figure 6.22: ^{19}F NMR titration (470 MHz, $CDCl_3$, 298 K) with stepwise addition of first **T6$_A$** (8.80 equiv.) into a solution of ***c*-P12[b$_6$f$_6$]**, followed by the addition of **T6$_B$** (8.80 equiv.); total concentration of ***c*-P12[b$_6$f$_6$]**added is provided at each spectral point as $[$***c*-P12[b$_6$f$_6$]**$]_0$. An excess of **T6$_A$** was needed to convert ***c*-P12[b$_6$f$_6$]·(T6$_A$)** into ***c*-P12[b$_6$f$_6$]·(T6$_A$)$_2$** during the time-course of the titration. Once **T6$_B$** was added to the ***c*-P12[b$_6$f$_6$]·(T6$_A$)$_2$**, replacement of one **T6$_A$** occurred immediately, giving the mixed complex ***c*-P12[b$_6$f$_6$]·T6$_A$·T6$_B$**.

NMR Oxidation Titrations and Speciation Curves

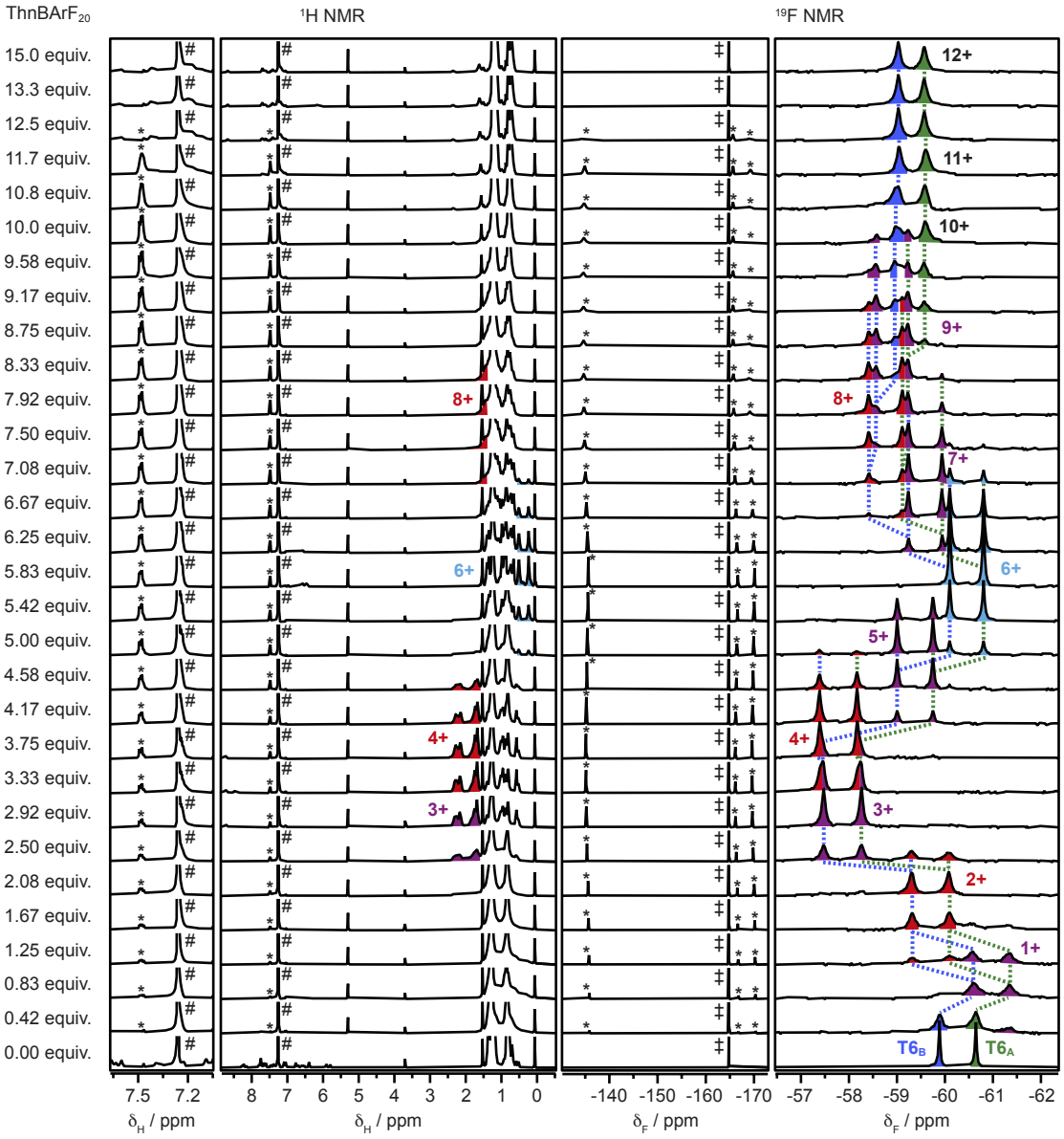


Figure 6.23: Summary of the ^{1}H and ^{19}F NMR titration of ***c*-P12[b_6f_6]·T6$_A$·T6$_B$** (500/471 MHz, 298 K) with **ThnBArF$_{20}$** in $CDCl_3$; 6 μL Thn^+ solution contain about 1 equivalent of oxidant. Shifted THS and CF_3 resonances indicating global antiaromaticity are highlighted in red; those indicating global aromaticity are highlighted in blue. Odd-numbered oxidation states are shown in purple. Peaks assigned with # and ‡ arise from $CHCl_3$ and C_6F_6, respectively. Resonances assigned with * in the ^{1}H and ^{19}F spectra arise from neutral thianthrene and the $BArF_{20}^-$ counterion, respectively.

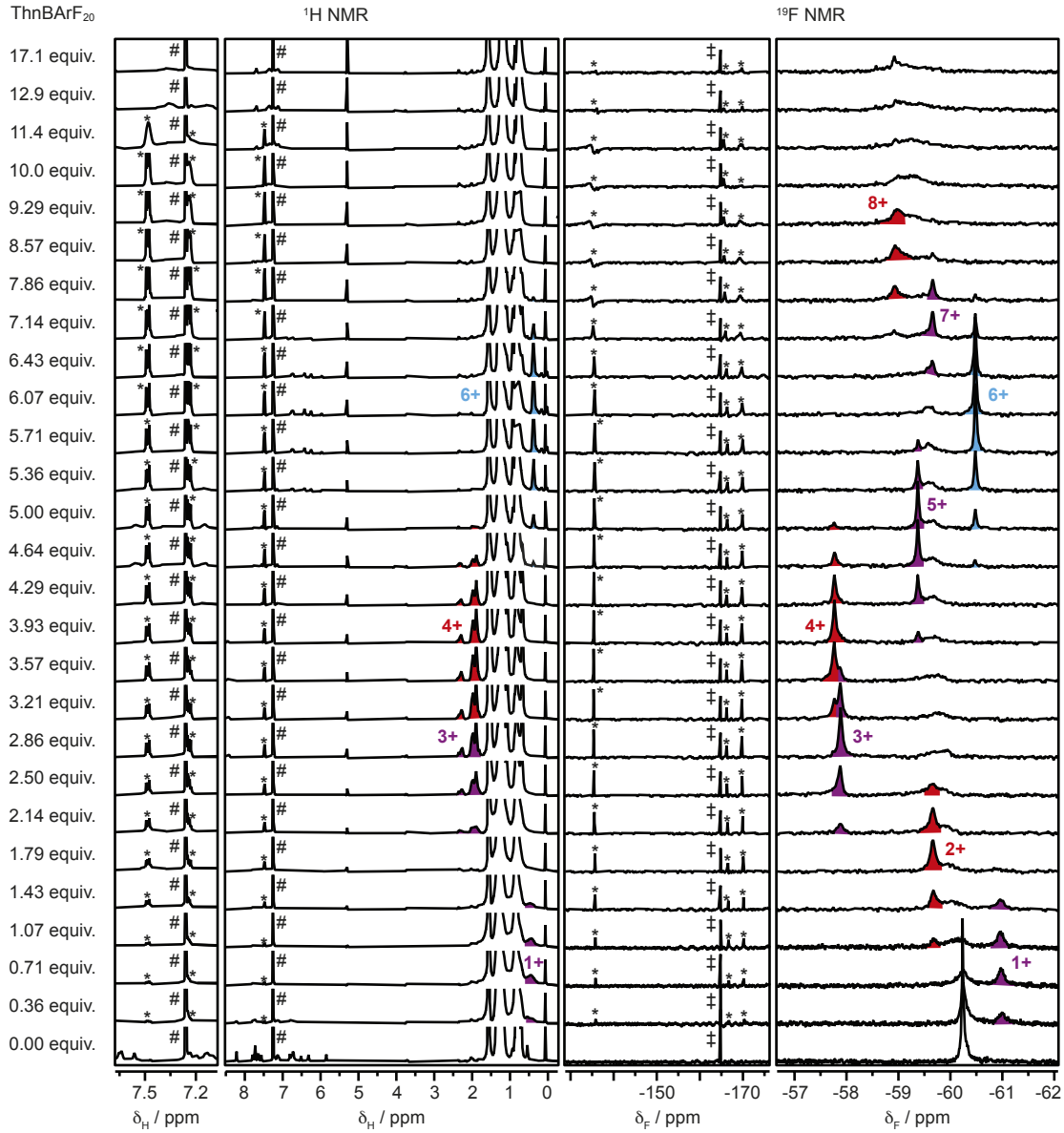


Figure 6.24: Summary of the ^{1}H and ^{19}F NMR titration of ***c*-P12[b$_6$f$_6$]·(T6$_B$)$_2$** (500/471 MHz, 298 K) with **ThnBArF$_{20}$** in $CDCl_3$; 7 μL Thn$^+$ solution contain about 1 equivalent of oxidant. Shifted THS and CF_3 resonances indicating global antiaromaticity are highlighted in red; those indicating global aromaticity are highlighted in blue. Odd-numbered oxidation states are shown in purple. Peaks assigned with # and ‡ arise from $CHCl_3$ and C_6F_6, respectively. Resonances assigned with * in the ^{1}H and ^{19}F spectra arise from neutral thianthrene and the $BArF_{20}^-$ counterion, respectively.

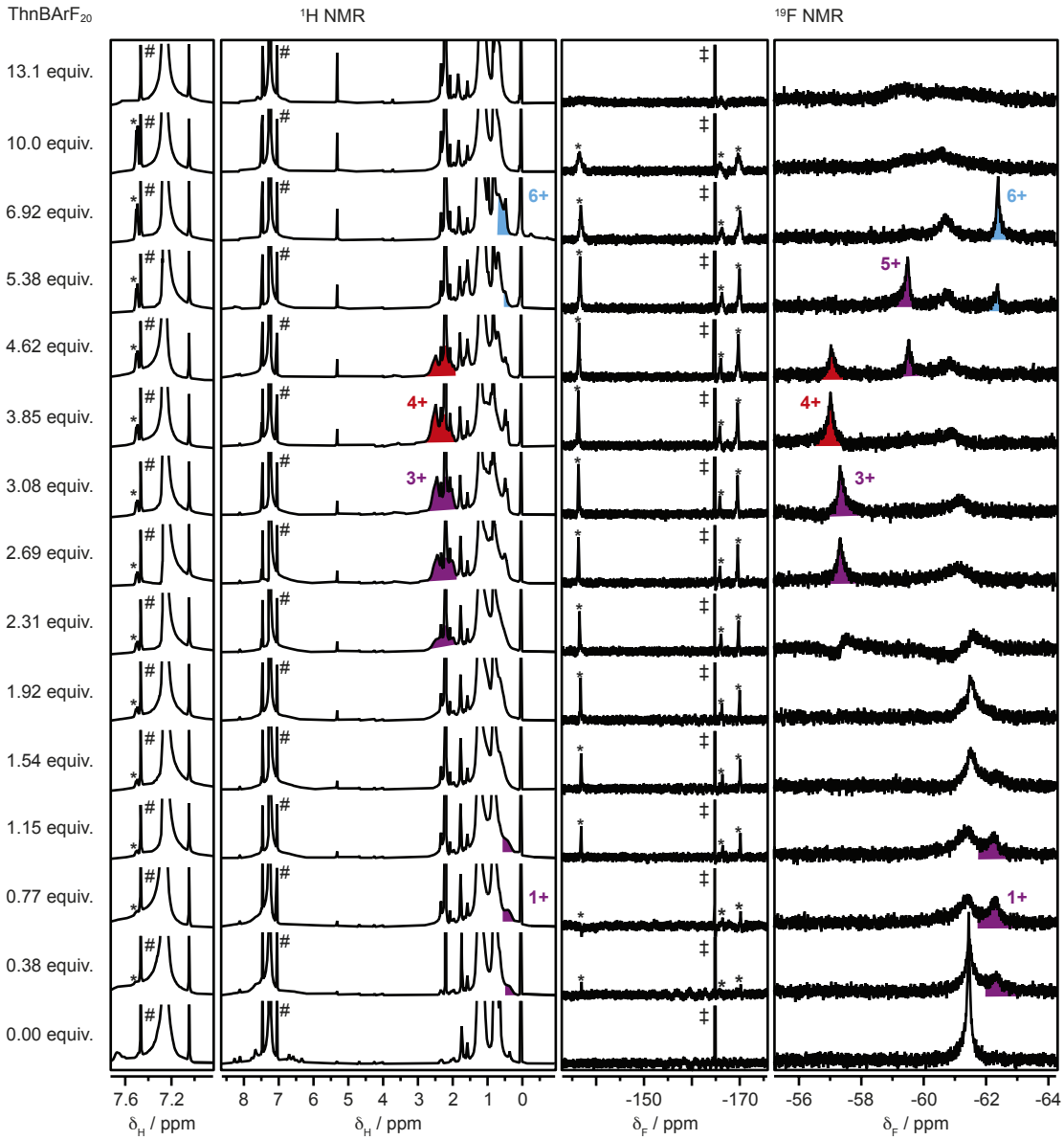


Figure 6.25: Summary of the ^{1}H and ^{19}F NMR titration of ***c*-P12[b$_6$f$_6$]·(T6$_B$)$_2$** (500/471 MHz, 233 K) with **ThnBArF$_{20}$** in $CDCl_3$; 6.5 μL Thn^+ solution contain about 1 equivalent of oxidant. Shifted THS and CF_3 resonances indicating global antiaromaticity are highlighted in red; those indicating global aromaticity are highlighted in blue. Odd-numbered oxidation states are shown in purple. Peaks assigned with # and ‡ arise from $CHCl_3$ and C_6F_6, respectively. Resonances assigned with * in the ^{1}H and ^{19}F spectra arise from neutral thianthrene and the $BArF_{20}^-$ counterion, respectively.

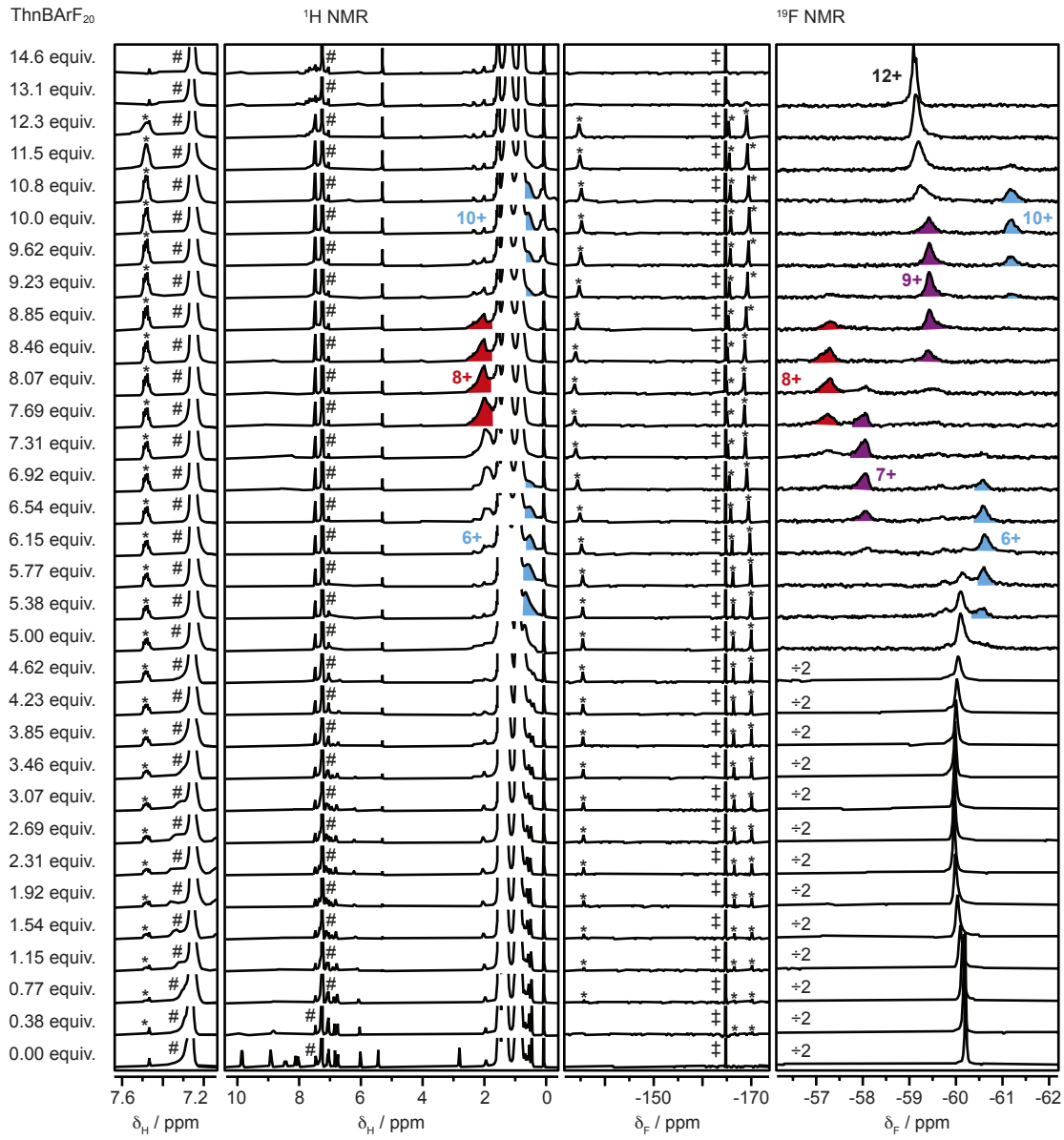


Figure 6.26: Summary of the ^{1}H and ^{19}F NMR titration of ***c*-P12[b$_{12}$]·(T6$_{C}$)$_{2}$** (500/471 MHz, 298 K) with **ThnBArF$_{20}$** in $CDCl_3$; 6.5 μL Thn^+ solution contain about 1 equivalent of oxidant. Shifted THS and CF_3 resonances indicating global antiaromaticity are highlighted in red; those indicating global aromaticity are highlighted in blue. Odd-numbered oxidation states are shown in purple. Peaks assigned with # and ‡ arise from $CHCl_3$ and C_6F_6, respectively. Resonances assigned with * in the ^{1}H and ^{19}F spectra arise from neutral thianthrene and the $BArF_{20}^-$ counterion, respectively.

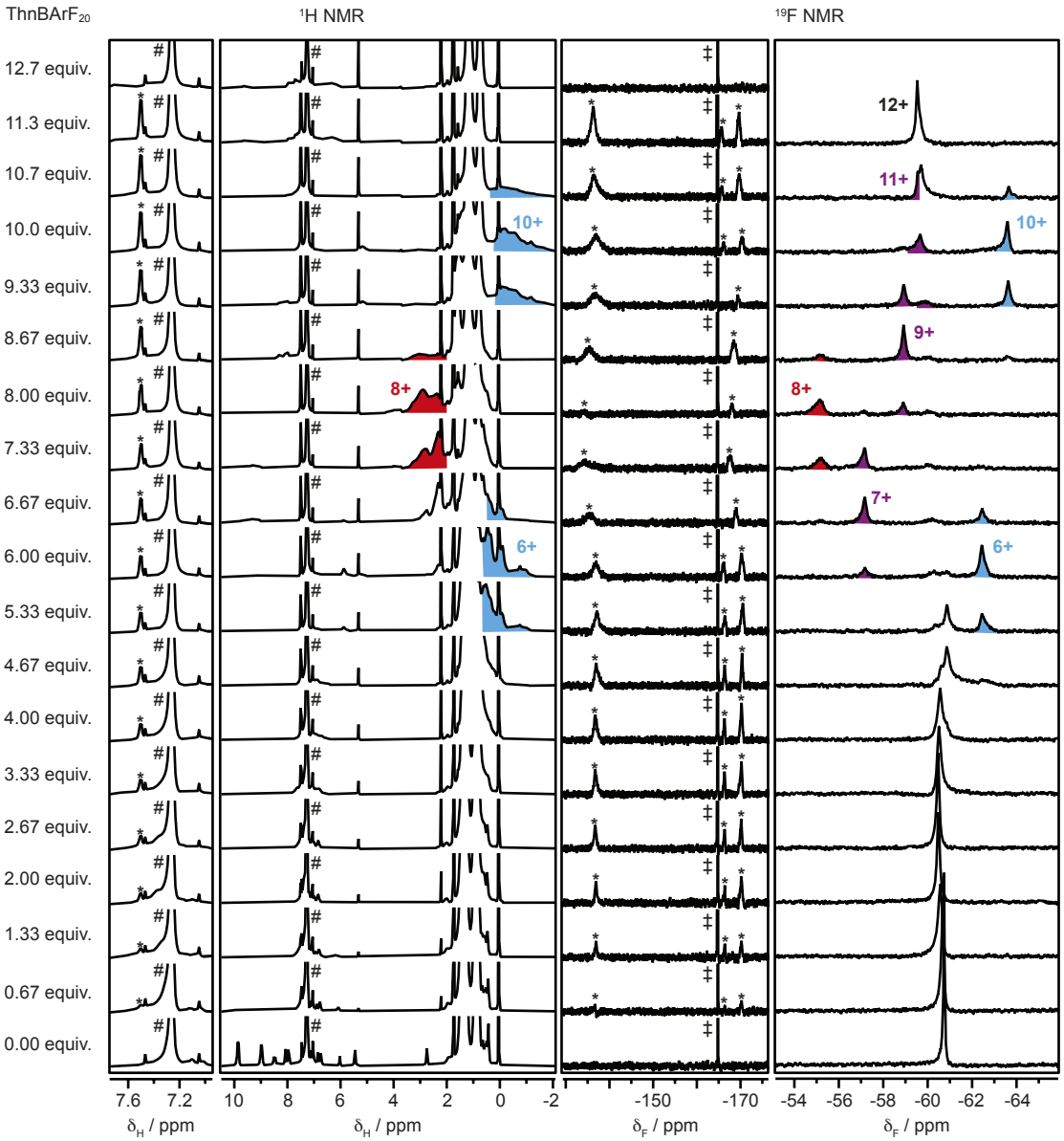


Figure 6.27: Summary of the ^{1}H and ^{19}F NMR titration of ***c*-P12[b$_{12}$]·(T6$_{C}$)$_2$** (500/471 MHz, 233 K) with **ThnBArF$_{20}$** in $CDCl_3$; 7.5 μL Thn^+ solution contain about 1 equivalent of oxidant. Shifted THS and CF_3 resonances indicating global antiaromaticity are highlighted in red; those indicating global aromaticity are highlighted in blue. Odd-numbered oxidation states are shown in purple. Peaks assigned with # and ‡ arise from $CHCl_3$ and C_6F_6, respectively. Resonances assigned with * in the ^{1}H and ^{19}F spectra arise from neutral thianthrene and the $BArF_{20}^-$ counterion, respectively.

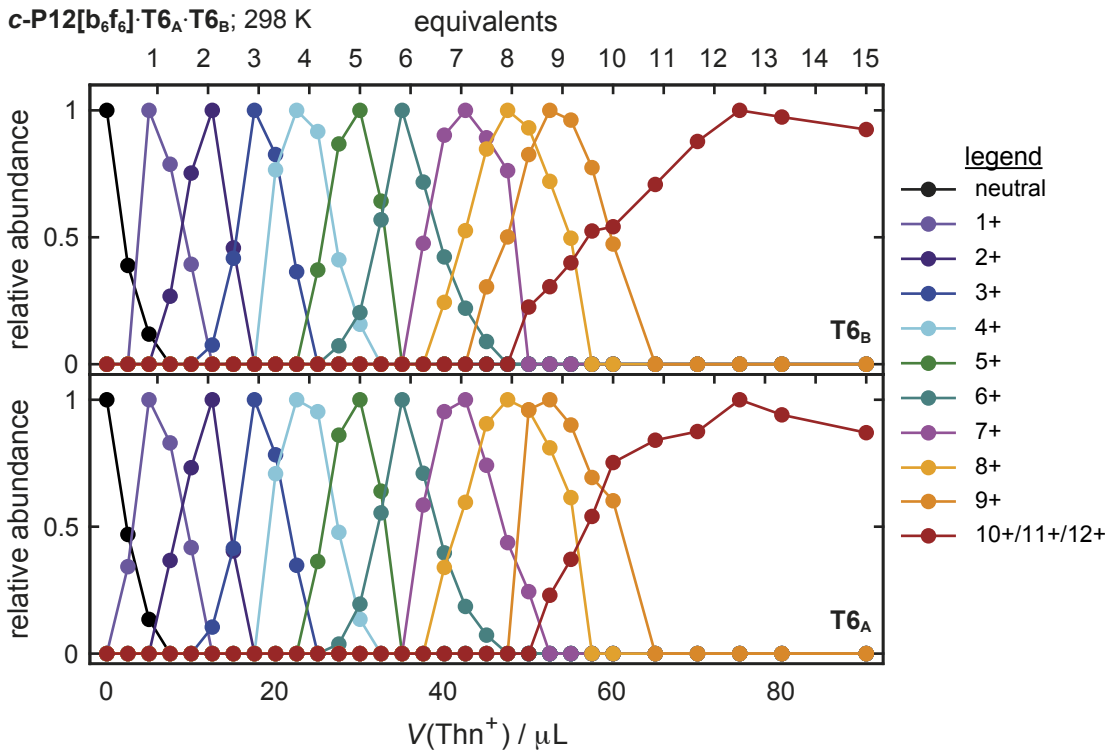


Figure 6.28: Speciation curve for the different oxidation states observed in the ^{19}F NMR titration of ***c*-P12[b_6f_6]·T6$_A$·T6$_B$** with **ThnBArF$_{20}$** in $CDCl_3$ at 298 K; 6 μL Thn$^+$ solution contain about 1 equivalent of oxidant. Two independent speciation curves were calculated using the ^{19}F NMR resonances of the two templates **T6$_B$** and **T6$_A$** and are shown in the top and bottom panels, respectively. The relative abundance of each oxidation state was obtained as the intensity of the ^{19}F NMR signals assigned to the oxidation state divided by the maximum ^{19}F signal intensity for the oxidation state. The intensities of the ^{19}F NMR signals of the CF_3 groups of **T6$_A$** and **T6$_B$** in the different oxidation states were obtained at the chemical shifts reported in Table 6.4.

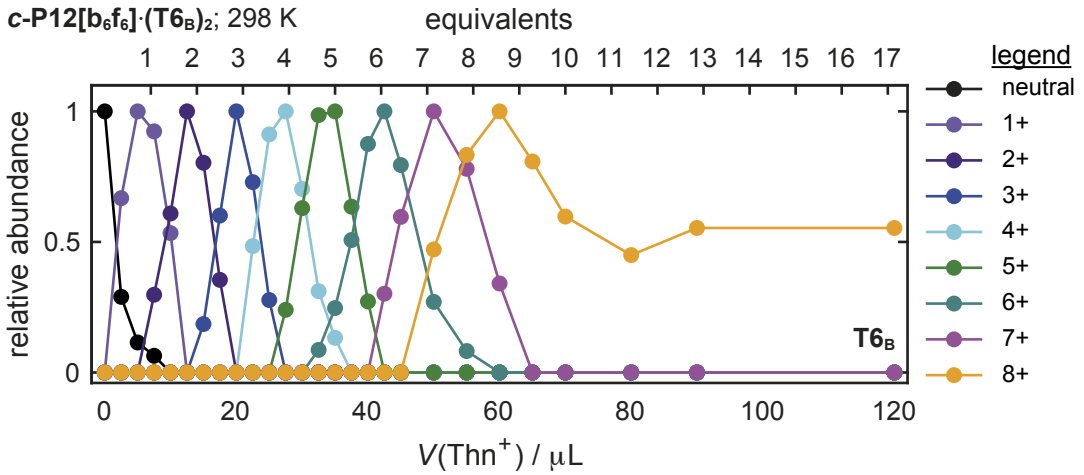


Figure 6.29: Speciation curve for the different oxidation states observed in the ^{19}F NMR titration of ***c*-P12[b_6f_6]·($T6_B$)$_2$** with **ThnBArF$_{20}$** in $CDCl_3$ at 298 K; 7 μL Thn^+ solution contain about 1 equivalent of oxidant. The relative abundance of each oxidation state was obtained as the intensity of the ^{19}F NMR signals assigned to the oxidation state divided by the maximum ^{19}F signal intensity for the oxidation state. The intensities of the ^{19}F NMR signals of the CF_3 groups of **$T6_B$** in the different oxidation states were obtained at the chemical shifts reported in Table 6.5.

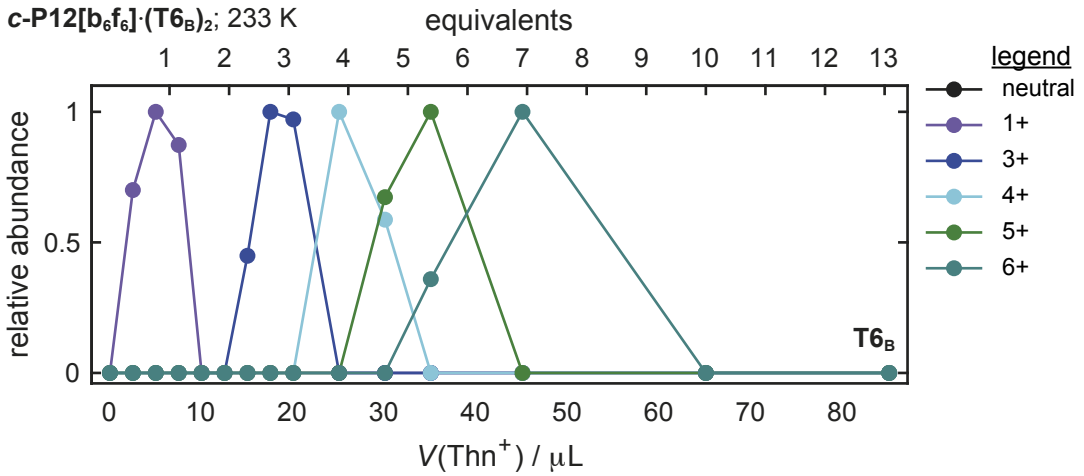


Figure 6.30: Speciation curve for the different oxidation states observed in the ^{19}F NMR titration of ***c*-P12[b_6f_6]·($T6_B$)$_2$** with **ThnBArF$_{20}$** in $CDCl_3$ at 233 K; 6.5 μL Thn^+ solution contain about 1 equivalent of oxidant. The relative abundance of each oxidation state was obtained as the intensity of the ^{19}F NMR signals assigned to the oxidation state divided by the maximum ^{19}F signal intensity for the oxidation state. The intensities of the ^{19}F NMR signals of the CF_3 groups of **$T6_B$** in the different oxidation states were obtained at the chemical shifts reported in Table 6.6.

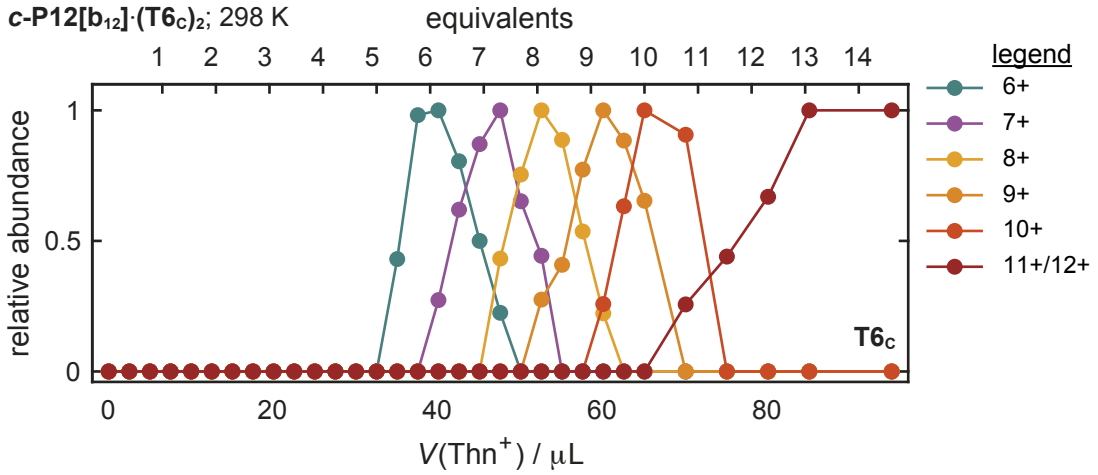


Figure 6.31: Speciation curve for the different oxidation states observed in the ^{19}F NMR titration of ***c*-P12[$\mathbf{b_{12}}$]·($\mathbf{T6_C}$)$_2$** with **ThnBArF$_{20}$** in $CDCl_3$ at 298 K; 6.5 μL Thn^+ solution contain about 1 equivalent of oxidant. The relative abundance of each oxidation state was obtained as the intensity of the ^{19}F NMR signals assigned to the oxidation state divided by the maximum ^{19}F signal intensity for the oxidation state. The intensities of the ^{19}F NMR signals of the CF_3 groups of **T6$_C$** in the different oxidation states were obtained at the chemical shifts reported in Table 6.8.

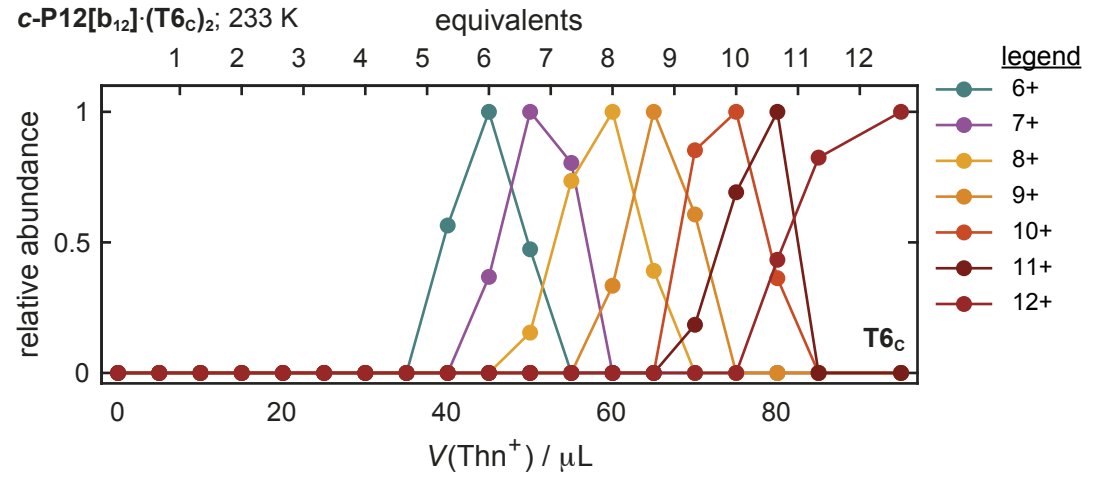


Figure 6.32: Speciation curve for the different oxidation states observed in the ^{19}F NMR titration of ***c*-P12[$\mathbf{b_{12}}$]·($\mathbf{T6_C}$)$_2$** with **ThnBArF$_{20}$** in $CDCl_3$ at 233 K; 7.5 μL Thn^+ solution contain about 1 equivalent of oxidant. The relative abundance of each oxidation state was obtained as the intensity of the ^{19}F NMR signals assigned to the oxidation state divided by the maximum ^{19}F signal intensity for the oxidation state. The intensities of the ^{19}F NMR signals of the CF_3 groups of **T6$_C$** in the different oxidation states were obtained at the chemical shifts reported in Table 6.9.

NMR Reduction Titrations and Speciation Curves

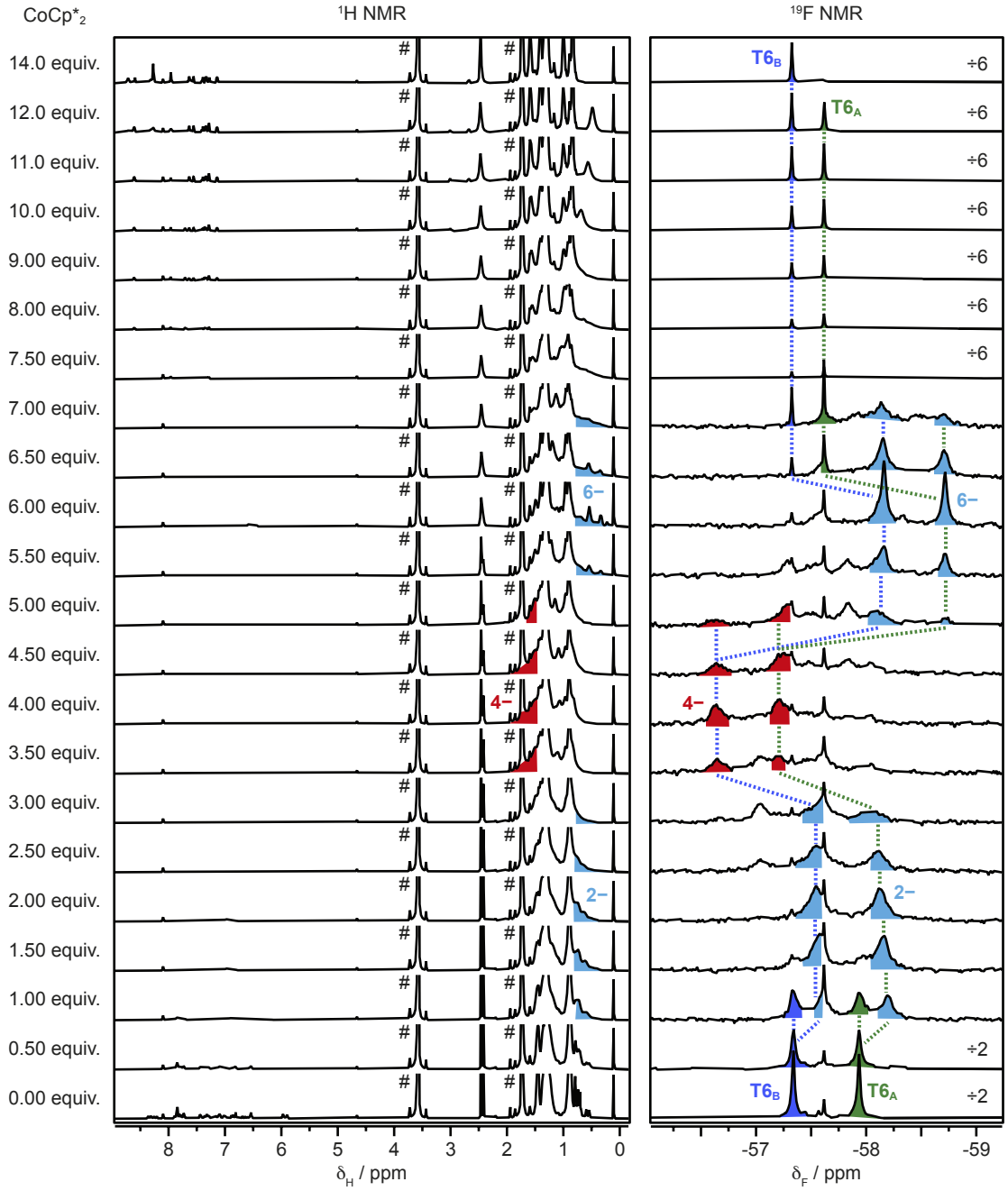


Figure 6.33: Summary of the ^{1}H and ^{19}F NMR titration of ***c*-P12[b_6f_6]·T6$_A$·T6$_B$** (500/471 MHz, 298 K) with **CoCp*$_2$** in THF-d_8; 2 μL **CoCp*$_2$** solution contain about 1 equivalent of reducing agent. Shifted THS and CF_3 resonances indicating global antiaromaticity are highlighted in red; those indicating global aromaticity are highlighted in blue. Peaks assigned with # arise from THF-d_8.

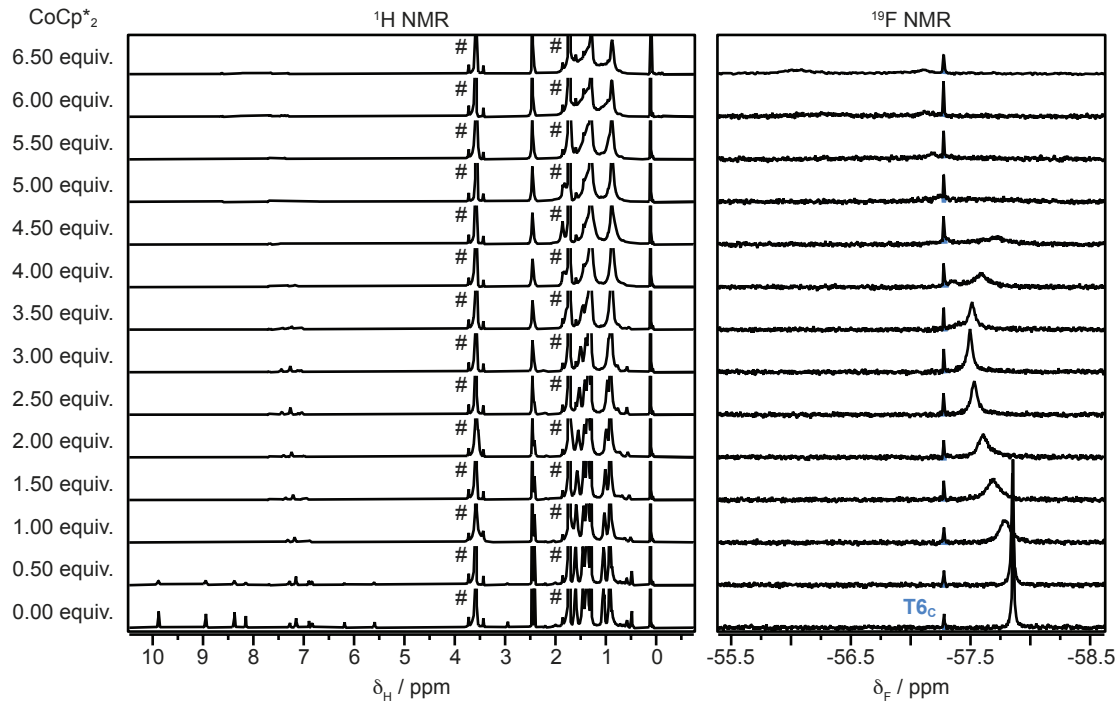


Figure 6.34: Summary of the ^{1}H and ^{19}F NMR titration of ***c*-P12[b$_{12}$]·(T6$_{C}$)$_2$** (500/471 MHz, 298 K) with **CoCp*$_2$** in THF-d_8 until the 6– state; 2 μL **CoCp*$_2$** solution contain about 1 equivalent of reducing agent. Peaks assigned with # arise from THF-d_8.

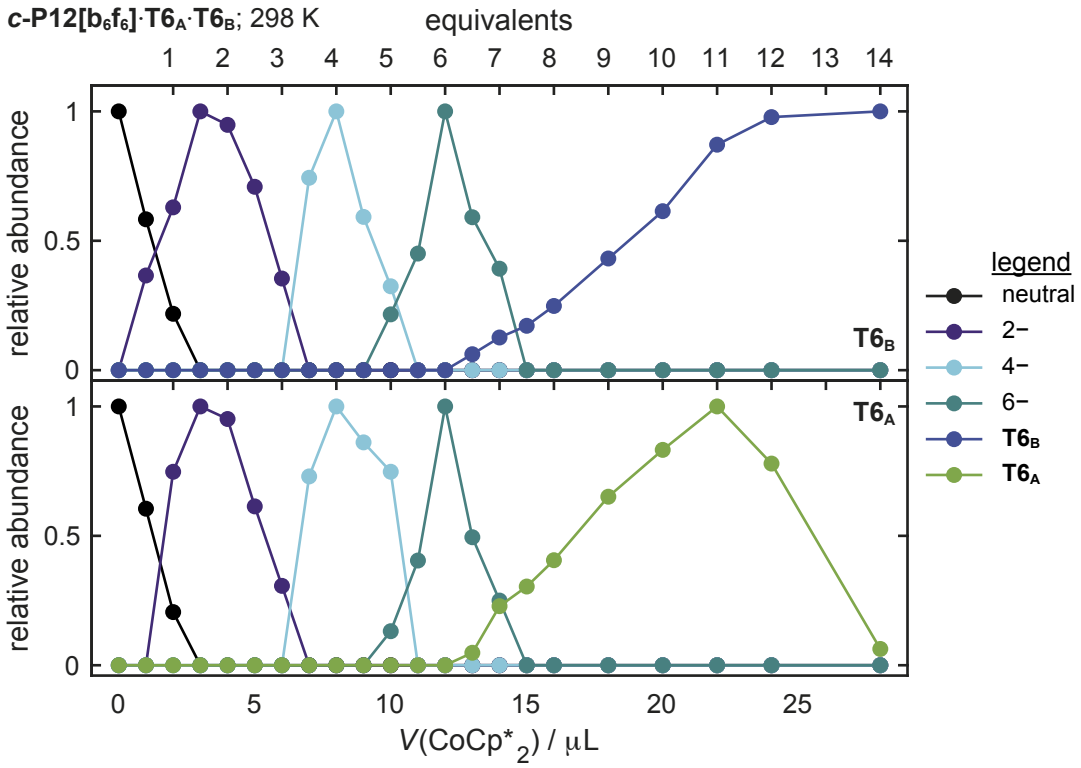


Figure 6.35: Speciation curve for the different oxidation states observed in the ^{19}F NMR titration of ***c*-P12[b_6f_6]·T6$_A$·T6$_B$** with **CoCp*$_2$** in THF-d_8 at 298 K; 2 μL **CoCp*$_2$** solution contain about 1 equivalent of reducing agent. Two independent speciation curves were calculated using the ^{19}F NMR resonances of the two templates **T6$_B$** and **T6$_A$** and are shown in the top and bottom panels, respectively. The relative abundance of each oxidation state was obtained as the intensity of the ^{19}F NMR signals assigned to the oxidation state divided by the maximum ^{19}F signal intensity for the oxidation state. The intensities of the ^{19}F NMR signals of the CF_3 groups of **T6$_A$** and **T6$_B$** in the different oxidation states were obtained at the chemical shifts reported in Table 6.11.

Summary of Experimental Results and NICS Calculations

Negative NICS/$\Delta\delta$ values and $4n$+2 Hückel classification correspond to aromaticity; positive NICS/$\Delta\delta$ values and $4n$ Hückel classification to antiaromaticity. NICS(0) values were calculated in the center of the nanoring complexes using DFT (BLYP35/6-31G*) without template. The chemical shift differences $\Delta\delta$ for different oxidation states Q of the nanoring complexes were calculated based on the change in chemical shift with respect to the free template ($\Delta\delta_{\mathrm{T6}} = \delta_{\mathrm{T6,bound}} - \delta_{\mathrm{T6,unbound}}$) and based on the chemical shift changes relative to the neutral nanoring complex ($\Delta\delta = \delta_Q - \delta_0$). The chemical shifts of ht unbound templates are as follows:

δ_{F}(**T6$_{\mathbf{A}}$**, $CDCl_3$, 298 K) = −59.77 ppm; δ_{F}(**T6$_{\mathbf{B}}$**, $CDCl_3$, 298 K) = −59.48 ppm; δ_{F}(**T6$_{\mathbf{B}}$**, $CDCl_3$, 233 K) = −59.95 ppm; δ_{F}(**T6$_{\mathbf{C}}$**, $CDCl_3$, 298 K) = −59.43 ppm; δ_{F}(**T6$_{\mathbf{C}}$**, $CDCl_3$, 233 K) = −59.87 ppm; δ_{F}(**T6$_{\mathbf{A}}$**, THF-d_8, 298 K) = −57.62 ppm; δ_{F}(**T6$_{\mathbf{B}}$**, THF-d_8, 298 K) = −57.35 ppm.

Table 6.3: Summary of the DFT (BLYP35/6-31G*) calculated NICS values for the study of global (anti)aromaticity in oxidized ***c*-P12[b$_6$f$_6$]**.

Q	NICS(0)$_{\mathrm{ZZ}}$	NICS(0)$_{\mathrm{iso}}$
0	0.4	−0.3
2+	5.0	1.3
4+	80.0	35.2
6+	−38.6	−13.0
8+	26.1	8.7

Table 6.4: Summary of the ^{19}F chemical shifts (δ_{CF_3}, ppm) and chemical shift differences $\Delta\delta_{T6}$ and $\Delta\delta$ in the NMR oxidation titration of ***c*-P12[b_6f_6]·T6$_A$·T6$_B$** in $CDCl_3$ at 298 K. [a]local aromatic currents observed; [b]triplet ground state results in Baird antiaromaticity.

Q	πe^-	Hückel classification	**T6$_B$**			**T6$_A$**		
			δ_{CF_3}	$\Delta\delta_{T6}$	$\Delta\delta$	δ_{CF_3}	$\Delta\delta_{T6}$	$\Delta\delta$
0	144/120	$4n\pi$[a]	−59.89	−0.41	0.00	−60.65	−0.88	0.00
1+	143/119	–	−60.57	−1.09	−0.68	−61.35	−1.58	−0.70
2+	142/118	$4n+2\pi$[b]	−59.30	0.18	0.59	−60.08	−0.31	0.57
3+	141/117	–	−57.47	2.01	2.42	−58.26	1.51	2.39
4+	140/116	$4n\pi$	−57.39	2.09	2.50	−58.18	1.59	2.47
5+	139/115	–	−59.01	0.47	0.88	−59.75	0.02	0.90
6+	138/114	$4n+2\pi$	−60.10	−0.62	−0.21	−60.80	−1.03	−0.15
7+	137/113	–	−59.24	0.24	0.65	−59.94	−0.17	0.71
8+	136/112	$4n\pi$	−58.41	1.07	1.48	−59.11	0.66	1.54
9+	135/111	–	−58.57	0.91	1.32	−59.23	0.54	1.42
10+	134/110	$4n+2\pi$	−59.00	0.48	0.89	−59.60	0.17	1.05
11+	133/109	–	−59.05	0.43	0.84	−59.61	0.16	1.04
12+	132/108	$4n\pi$	−59.03	0.45	0.86	−59.57	0.20	1.08

Table 6.5: Summary of the ^{19}F chemical shifts (δ_{CF_3}, ppm) and chemical shift differences $\Delta\delta_{T6}$ and $\Delta\delta$ in the NMR oxidation titration of ***c*-P12[b_6f_6]·(T6$_B$)$_2$** in $CDCl_3$ at 298 K. [a]local aromatic currents observed; [b]triplet ground state results in Baird antiaromaticity.

Q	πe^-	Hückel classification	**T6$_B$**		
			δ_{CF_3}	$\Delta\delta_{T6}$	$\Delta\delta$
0	144/120	$4n\pi$[a]	−60.24	−0.76	0.00
1+	143/119	–	−60.98	−1.50	−0.74
2+	142/118	$4n+2\pi$[b]	−59.66	−0.18	0.58
3+	141/117	–	−57.89	1.59	2.35
4+	140/116	$4n\pi$	−57.77	1.71	2.47
5+	139/115	–	−59.37	0.11	0.87
6+	138/114	$4n+2\pi$	−60.48	−1.00	−0.24
7+	137/113	–	−59.66	−0.18	0.58
8+	136/112	$4n\pi$	−58.95	0.53	1.29

Table 6.6: Summary of the ^{19}F chemical shifts (δ_{CF_3}, ppm) and chemical shift differences $\Delta\delta_{T6}$ and $\Delta\delta$ in the NMR oxidation titration of ***c*-P12[$\mathbf{b_6f_6}$]·($\mathbf{T6_B}$)$_2$** in $CDCl_3$ at 233 K. [a]local aromatic currents observed.

Q	πe^-	Hückel classification	**$\mathbf{T6_B}$** δ_{CF_3}	$\Delta\delta_{T6}$	$\Delta\delta$
0	144/120	$4n\pi$[a]	−61.44	−1.49	0.00
1+	143/119	–	−62.31	−2.36	−0.87
3+	141/117	–	−57.32	2.63	4.12
4+	140/116	$4n\pi$	−57.02	2.93	4.42
5+	139/115	–	−59.48	0.47	1.96
6+	138/114	$4n+2\pi$	−62.38	−2.43	−0.94

Table 6.7: Summary of the DFT (BLYP35/6-31G*) calculated NICS values for the study of global (anti)aromaticity in oxidized ***c*-P12[$\mathbf{b_{12}}$]**.

Q	NICS(0)$_{ZZ}$	NICS(0)$_{iso}$
0	0.2	−0.4
6+	−33.7	−11.6
8+	36.8	12.0
10+	−41.8	−14.0
12+	1.6	0.6

Table 6.8: Summary of the ^{19}F chemical shifts (δ_{CF_3}, ppm) and chemical shift differences $\Delta\delta_{T6}$ and $\Delta\delta$ in the NMR oxidation titration of ***c*-P12[$\mathbf{b_{12}}$]·($\mathbf{T6_C}$)$_2$** in $CDCl_3$ at 298 K. [a]local aromatic currents observed.

Q	πe^-	Hückel classification	**$\mathbf{T6_C}$** δ_{CF_3}	$\Delta\delta_{T6}$	$\Delta\delta$
0	168	$4n\pi$[a]	−60.20	−0.77	0.00
6+	162	$4n+2\pi$	−60.63	−1.20	−0.43
7+	161	–	−58.01	1.42	2.19
8+	160	$4n\pi$	−57.27	2.16	2.93
9+	159	–	−59.43	0.00	0.77
10+	158	$4n+2\pi$	−61.19	−1.76	−0.99
12+	156	$4n\pi$	−59.15	0.28	1.05

Table 6.9: Summary of the ^{19}F chemical shifts (δ_{CF_3}, ppm) and chemical shift differences $\Delta\delta_{T6}$ and $\Delta\delta$ in the NMR oxidation titration of ***c*-P12[b$_{12}$]·(T6$_C$)$_2$** in $CDCl_3$ at 233 K. [a]local aromatic currents observed.

Q	πe^-	Hückel classification	**T6$_C$** δ_{CF_3}	$\Delta\delta_{T6}$	$\Delta\delta$
0	168	$4n\pi$[a]	−60.74	−0.87	0.00
6+	162	$4n+2\pi$	−62.45	−2.58	−1.71
7+	161	–	−57.16	2.71	3.58
8+	160	$4n\pi$	−55.11	4.76	5.63
9+	159	–	−58.92	0.95	1.82
10+	158	$4n+2\pi$	−63.58	−3.71	−2.84
11+	157	–	−59.64	0.23	1.10
12+	156	$4n\pi$	−59.52	0.35	1.22

Table 6.10: Summary of the DFT (BLYP35/6-31G*) calculated NICS values for the study of global (anti)aromaticity in reduced ***c*-P12[b$_6$f$_6$]**.

Q	NICS(0)$_{ZZ}$	NICS(0)$_{iso}$
0	0.4	−0.3
2−	−21.2	−7.6
4−	205	67.7
6−	−34.9	−12.2

Table 6.11: Summary of the ^{19}F chemical shifts (δ_{CF_3}, ppm) and chemical shift differences $\Delta\delta_{T6}$ and $\Delta\delta$ in the NMR reduction titration of ***c*-P12[b$_6$f$_6$]·T6$_A$·T6$_B$** in THF-d_8 at 298 K. [a]local aromatic currents observed.

Q	πe^-	Hückel classification	**T6$_B$** δ_{CF_3}	$\Delta\delta_{T6}$	$\Delta\delta$	**T6$_A$** δ_{CF_3}	$\Delta\delta_{T6}$	$\Delta\delta$
0	144/120	$4n\pi$[a]	−57.34	0.01	0.00	−57.93	−0.31	0.00
2−	146/122	$4n+2\pi$	−57.55	−0.20	−0.21	−58.16	−0.54	−0.23
4−	148/124	$4n\pi$	−56.64	0.71	0.70	−57.22	0.40	0.71
6−	150/126	$4n+2\pi$	−58.16	−0.81	−0.82	−58.72	−1.10	−0.79

References

[1] R. Willstätter, "CHLOROPHYLL", *J. Am. Chem. Soc.* **1915**, *37*, 323–345.

[2] R. J. Cogdell, A. Gall, J. Köhler, "The architecture and function of the light-harvesting apparatus of purple bacteria: from single molecules to in vivo membranes", *Q. Rev. Biophys.* **2006**, *39*, 227–324.

[3] T. Mirkovic, E. E. Ostroumov, J. M. Anna, R. van Grondelle, Govindjee, G. D. Scholes, "Light Absorption and Energy Transfer in the Antenna Complexes of Photosynthetic Organisms", *Chem. Rev.* **2017**, *117*, 249–293.

[4] X. Huang, J. T. Groves, "Oxygen Activation and Radical Transformations in Heme Proteins and Metalloporphyrins", *Chem. Rev.* **2018**, *118*, 2491–2553.

[5] C. C. Hsia, "Respiratory function of hemoglobin", *N. Engl. J. Med.* **1998**, *338*, 239–247.

[6] I. Hanukoglu in *Advances in Molecular and Cell Biology*, *Vol. 14*, (Ed.: E. E. Bittar), Elsevier, **1996**, pp. 29–56.

[7] H. Michel, J. Behr, A. Harrenga, A. Kannt, "Cytochrome c oxidase: structure and spectroscopy", *Annu. Rev. Biophys. Biomol. Struct.* **1998**, *27*, 329–356.

[8] M. O. Senge, M. Davis, "Porphyrin (porphine) — A neglected parent compound with potential", *J. Porphyr. Phthalocyanines* **2010**, *14*, 557–567.

[9] E. D. Becker, R. B. Bradley, "Effects of "ring currents" on the NMR spectra of porphyrins", *J. Chem. Phys.* **1959**, *31*, 1413–1414.

[10] B. J. Littler, Y. Ciringh, J. S. Lindsey, "Investigation of Conditions Giving Minimal Scrambling in the Synthesis of trans-Porphyrins from Dipyrromethanes and Aldehydes", *J. Org. Chem.* **1999**, *64*, 2864–2872.

[11] B. J. Littler, M. A. Miller, C.-H. Hung, R. W. Wagner, D. F. O'Shea, P. D. Boyle, J. S. Lindsey, "Refined Synthesis of 5-Substituted Dipyrromethanes", *J. Org. Chem.* **1999**, *64*, 1391–1396.

[12] S. Hiroto, Y. Miyake, H. Shinokubo, "Synthesis and Functionalization of Porphyrins through Organometallic Methodologies", *Chem. Rev.* **2017**, *117*, 2910–3043.

[13] T. Tanaka, A. Osuka, "Chemistry of meso-Aryl-Substituted Expanded Porphyrins: Aromaticity and Molecular Twist", *Chem. Rev.* **2017**, *117*, 2584–2640.

[14] C. G. Claessens, D. González-Rodríguez, T. Torres, "Subphthalocyanines: singular nonplanar aromatic compounds-synthesis, reactivity, and physical properties", *Chem. Rev.* **2002**, *102*, 835–853.

[15] L. Cuesta, J. L. Sessler, "Pi-metal complexes of tetrapyrrolic systems. A novel coordination mode in "porphyrin-like" chemistry", *Chem. Soc. Rev.* **2009**, *38*, 2716–2729.

[16] P. J. Brothers, J. P. Collman, "The organometallic chemistry of transition-metal porphyrin complexes", *Acc. Chem. Res.* **1986**, *19*, 209–215.

[17] M.-S. Liao, S. Scheiner, "Electronic structure and bonding in metal porphyrins, metal=Fe, Co, Ni, Cu, Zn", *J. Chem. Phys.* **2002**, *117*, 205–219.

[18] L. Bogani, W. Wernsdorfer, "Molecular spintronics using single-molecule magnets", *Nat. Mater.* **2008**, *7*, 179–186.

[19] J. J. Le Roy, J. Cremers, I. A. Thomlinson, M. Slota, W. K. Myers, P. H. Horton, S. J. Coles, H. L. Anderson, L. Bogani, "Tailored homo- and hetero- lanthanide porphyrin dimers: a synthetic strategy for integrating multiple spintronic functionalities into a single molecule", *Chem. Sci.* **2018**, *9*, 8474–8481.

[20] T. Pei, J. O. Thomas, S. Sopp, M.-Y. Tsang, N. Dotti, J. Baugh, N. F. Chilton, S. Cardona-Serra, A. Gaita-Ariño, H. L. Anderson, L. Bogani, "Exchange-induced spin polarization in a single magnetic molecule junction", *Nat. Commun.* **2022**, *13*, 4506.

[21] B. E. Bode, J. Plackmeyer, T. F. Prisner, O. Schiemann, "PELDOR measurements on a nitroxide-labeled Cu(II) porphyrin: orientation selection, spin-density distribution, and conformational flexibility", *J. Phys. Chem. A* **2008**, *112*, 5064–5073.

[22] M. Di Valentin, M. Albertini, M. G. Dal Farra, E. Zurlo, L. Orian, A. Polimeno, M. Gobbo, D. Carbonera, "Light-Induced Porphyrin-Based Spectroscopic Ruler for Nanometer Distance Measurements", *Chem. Eur. J.* **2016**, *22*, 17204–17214.

[23] S. Richert, J. Cremers, H. L. Anderson, C. R. Timmel, "Exploring template-bound dinuclear copper porphyrin nanorings by EPR spectroscopy", *Chem. Sci.* **2016**, *7*, 6952–6960.

[24] C.-J. Yu, S. von Kugelgen, M. D. Krzyaniak, W. Ji, W. R. Dichtel, M. R. Wasielewski, D. E. Freedman, "Spin and Phonon Design in Modular Arrays of Molecular Qubits", *Chem. Mater.* **2020**, *32*, 10200–10206.

[25] D. Ranieri, A. Privitera, F. Santanni, K. Urbanska, G. J. Strachan, B. Twamley, E. Salvadori, Y.-K. Liao, M. Chiesa, M. O. Senge, F. Totti, L. Sorace, R. Sessoli, "A Heterometallic Porphyrin Dimer as a Potential Quantum Gate: Magneto-Structural Correlations and Spin Coherence Properties", *Angew. Chem. Int. Ed.* **2023**, *62*, e202312936.

[26] S. von Kugelgen, M. D. Krzyaniak, M. Gu, D. Puggioni, J. M. Rondinelli, M. R. Wasielewski, D. E. Freedman, "Spectral Addressability in a Modular Two Qubit System", *J. Am. Chem. Soc.* **2021**, *143*, 8069–8077.

[27] C. Costentin, S. Drouet, M. Robert, J.-M. Savéant, "A local proton source enhances CO2 electroreduction to CO by a molecular Fe catalyst", *Science* **2012**, *338*, 90–94.

[28] H. Rao, L. C. Schmidt, J. Bonin, M. Robert, "Visible-light-driven methane formation from CO2 with a molecular iron catalyst", *Nature* **2017**, *548*, 74–77.

[29] D. J. Martin, C. F. Wise, M. L. Pegis, J. M. Mayer, "Developing Scaling Relationships for Molecular Electrocatalysis through Studies of Fe-Porphyrin-Catalyzed O2 Reduction", *Acc. Chem. Res.* **2020**, *53*, 1056–1065.

[30] J. W. Buchler, C. Dreher, F. M. Künzel in *Metal Complexes with Tetrapyrrole Ligands III*, (Eds.: J. W. Buchler, C. Dreher, F. M. Künzel, S. Licoccia, R. Paolesse, J. Šima), Springer Berlin Heidelberg, Berlin, Heidelberg, **1995**, pp. 1–69.

[31] J. R. Miller, G. D. Dorough, "Pyridinate Complexes of Some Metallo-derivatives of Tetraphenylporphine and Tetraphenylchlorin1", *J. Am. Chem. Soc.* **1952**, *74*, 3977–3981.

[32] S. Venkataramani, U. Jana, M. Dommaschk, F. D. Sönnichsen, F. Tuczek, R. Herges, "Magnetic bistability of molecules in homogeneous solution at room temperature", *Science* **2011**, *331*, 445–448.

[33] M. Sakuragi, K. Ichimura, H. Sakuragi, "Photosensitized Oxygenation of Olefins with Zinc Tetraphenylporphine-1,4-Diazabicyclo[2.2.2]octane Complex", *Bull. Chem. Soc. Jpn.* **1992**, *65*, 1944–1949.

[34] H. Imai, S. Nakagawa, E. Kyuno, "Recognition of axial ligands by a zinc porphyrin host on the basis of nonpolar interligand interaction", *J. Am. Chem. Soc.* **1992**, *114*, 6719–6723.

[35] P. Bhyrappa, V. Krishnan, M. Nethaji, "Solvation and axial ligation properties of (2,3,7,8,12,13,17,18-octabromo-5,10,15,20-tetraphenylporphyrinato)zinc(II)", *J. Chem. Soc. Dalton Trans.* **1993**, 1901–1906.

[36] P. S. Bols, H. L. Anderson, "Template-Directed Synthesis of Molecular Nanorings and Cages", *Acc. Chem. Res.* **2018**, *51*, 2083–2092.

[37] S.-P. Wang, Y.-F. Shen, B.-Y. Zhu, J. Wu, S. Li, "Recent advances in the template-directed synthesis of porphyrin nanorings", *Chem. Commun.* **2016**, *52*, 10205–10216.

[38] C. O. Dietrich-Buchecker, J. P. Sauvage, J. P. Kintzinger, "Une nouvelle famille de molecules : les metallo-catenanes", *Tetrahedron Lett.* **1983**, *24*, 5095–5098.

[39] J. E. Beves, B. A. Blight, C. J. Campbell, D. A. Leigh, R. T. McBurney, "Strategies and tactics for the metal-directed synthesis of rotaxanes, knots, catenanes, and higher order links", *Angew. Chem. Int. Ed.* **2011**, *50*, 9260–9327.

[40] J.-F. Ayme, J. E. Beves, C. J. Campbell, D. A. Leigh, "Template synthesis of molecular knots", *Chem. Soc. Rev.* **2013**, *42*, 1700–1712.

[41] D. Zhang, T. K. Ronson, J. R. Nitschke, "Functional Capsules via Subcomponent Self-Assembly", *Acc. Chem. Res.* **2018**, *51*, 2423–2436.

[42] D. H. Busch in *The Pedersen Memorial Issue*, (Eds.: R. M. Izatt, J. S. Bradshaw), Springer Netherlands, Dordrecht, **1992**, pp. 389–395.

[43] S. Anderson, H. L. Anderson, J. K. M. Sanders, "Expanding roles for templates in synthesis", *Acc. Chem. Res.* **1993**, *26*, 469–475.

[44] H. J. Hogben, J. K. Sprafke, M. Hoffmann, M. Pawlicki, H. L. Anderson, "Stepwise effective molarities in porphyrin oligomer complexes: preorganization results in exceptionally strong chelate cooperativity", *J. Am. Chem. Soc.* **2011**, *133*, 20962–20969.

[45] M. Hoffmann, C. J. Wilson, B. Odell, H. L. Anderson, "Template-directed synthesis of a pi-conjugated porphyrin nanoring", *Angew. Chem. Int. Ed.* **2007**, *46*, 3122–3125.

[46] R. Haver, H. L. Anderson, "Synthesis and properties of porphyrin nanotubes", *Helv. Chim. Acta* **2019**, *102*, e1800211.

[47] J. Cremers, R. Haver, M. Rickhaus, J. Q. Gong, L. Favereau, M. D. Peeks, T. D. W. Claridge, L. M. Herz, H. L. Anderson, "Template-Directed Synthesis of a Conjugated Zinc Porphyrin Nanoball", *J. Am. Chem. Soc.* **2018**, *140*, 5352–5355.

[48] P. Neuhaus, A. Cnossen, J. Q. Gong, L. M. Herz, H. L. Anderson, "A Molecular Nanotube with Three-Dimensional π-Conjugation", *Angew. Chem. Int. Ed.* **2015**, *54*, 7344–7348.

[49] H. Gotfredsen, J.-R. Deng, J. M. Van Raden, M. Righetto, J. Hergenhahn, M. Clarke, A. Bellamy-Carter, J. Hart, J. O'Shea, T. D. W. Claridge, F. Duarte, A. Saywell, L. M. Herz, H. L. Anderson, "Bending a photonic wire into a ring", *Nat. Chem.* **2022**, *14*, 1436–1442.

[50] J. Pruchyathamkorn, W. J. Kendrick, A. T. Frawley, A. Mattioni, F. Caycedo-Soler, S. F. Huelga, M. B. Plenio, H. L. Anderson, "A Complex Comprising a Cyanine Dye Rotaxane and a Porphyrin Nanoring as a Model Light-Harvesting System", *Angew. Chem. Int. Ed.* **2020**, *59*, 16455–16458.

[51] M. D. Peeks, C. E. Tait, P. Neuhaus, G. M. Fischer, M. Hoffmann, R. Haver, A. Cnossen, J. R. Harmer, C. R. Timmel, H. L. Anderson, "Electronic delocalization in the radical cations of porphyrin oligomer molecular wires", *J. Am. Chem. Soc.* **2017**, *139*, 10461–10471.

[52] C. E. Tait, P. Neuhaus, M. D. Peeks, H. L. Anderson, C. R. Timmel, "Transient EPR Reveals Triplet State Delocalization in a Series of Cyclic and Linear π-Conjugated Porphyrin Oligomers", *J. Am. Chem. Soc.* **2015**, *137*, 8284–8293.

[53] M. Jirásek, M. Rickhaus, L. Tejerina, H. L. Anderson, "Experimental and Theoretical Evidence for Aromatic Stabilization Energy in Large Macrocycles", *J. Am. Chem. Soc.* **2021**, *143*, 2403–2412.

[54] M. Jirásek, H. L. Anderson, M. D. Peeks, "From Macrocycles to Quantum Rings: Does Aromaticity Have a Size Limit?", *Acc. Chem. Res.* **2021**.

[55] M. Rickhaus, M. Jirasek, L. Tejerina, H. Gotfredsen, M. D. Peeks, R. Haver, H.-W. Jiang, T. D. W. Claridge, H. L. Anderson, "Global aromaticity at the nanoscale", *Nat. Chem.* **2020**, *12*, 236–241.

[56] M. D. Peeks, T. D. W. Claridge, H. L. Anderson, "Aromatic and antiaromatic ring currents in a molecular nanoring", *Nature* **2017**, *541*, 200–203.

[57] S. Richert, J. Cremers, I. Kuprov, M. D. Peeks, H. L. Anderson, C. R. Timmel, "Constructive quantum interference in a bis-copper six-porphyrin nanoring", *Nat. Commun.* **2017**, *8*, 14842.

[58] H. L. Anderson, "Building molecular wires from the colours of life: conjugated porphyrin oligomers", *Chem. Commun.* **1999**, 2323–2330.

[59] M. Gouterman, "Spectra of porphyrins", *J. Mol. Spectrosc.* **1961**, *6*, 138–163.

[60] M. Gouterman, G. H. Wagnière, L. C. Snyder, "Spectra of porphyrins", *J. Mol. Spectrosc.* **1963**, *11*, 108–127.

[61] D. Beljonne, G. E. O'Keefe, P. J. Hamer, R. H. Friend, H. L. Anderson, J. L. Brédas, "Investigation of the linear and nonlinear optical response of edge-linked conjugated zinc porphyrin oligomers by optical spectroscopy and configuration interaction techniques", *J. Chem. Phys.* **1997**, *106*, 9439–9460.

[62] V. N. Nemykin, R. G. Hadt, "Interpretation of the UV-vis spectra of the meso(ferrocenyl)-containing porphyrins using a TDDFT approach: is Gouterman's classic four-orbital model still in play?", *J. Phys. Chem. A* **2010**, *114*, 12062–12066.

[63] T. Hashimoto, Y.-K. Choe, H. Nakano, K. Hirao, "Theoretical Study of the Q and B Bands of Free-Base, Magnesium, and Zinc Porphyrins, and Their Derivatives", *J. Phys. Chem. A* **1999**, *103*, 1894–1904.

[64] P. N. Taylor, J. Huuskonen, R. T. Aplin, H. L. Anderson, G. Rumbles, E. Williams, "Conjugated porphyrin oligomers from monomer to hexamer", *Chem. Commun.* **1998**, 909–910.

[65] M. Drobizhev, Y. Stepanenko, Y. Dzenis, A. Karotki, A. Rebane, P. N. Taylor, H. L. Anderson, "Extremely strong near-IR two-photon absorption in conjugated porphyrin dimers: quantitative description with three-essential-states model", *J. Phys. Chem. B* **2005**, *109*, 7223–7236.

[66] H. L. Anderson, "Conjugated Porphyrin Ladders", *Inorg. Chem.* **1994**, *33*, 972–981.

[67] M. Hoffmann, J. Kärnbratt, M.-H. Chang, L. M. Herz, B. Albinsson, H. L. Anderson, "Enhanced pi conjugation around a porphyrin[6] nanoring", *Angew. Chem. Int. Ed.* **2008**, *47*, 4993–4996.

[68] J. K. Sprafke, D. V. Kondratuk, M. Wykes, A. L. Thompson, M. Hoffmann, R. Drevinskas, W.-H. Chen, C. K. Yong, J. Kärnbratt, J. E. Bullock, M. Malfois, M. R. Wasielewski, B. Albinsson, L. M. Herz, D. Zigmantas, D. Beljonne, H. L. Anderson, "Belt-shaped π-systems: relating geometry to electronic structure in a six-porphyrin nanoring", *J. Am. Chem. Soc.* **2011**, *133*, 17262–17273.

[69] P. Parkinson, D. V. Kondratuk, C. Menelaou, J. Q. Gong, H. L. Anderson, L. M. Herz, "Chromophores in Molecular Nanorings: When Is a Ring a Ring?", *J. Phys. Chem. Lett.* **2014**, *5*, 4356–4361.

[70] A. Schweiger, G. Jeschke, *Principles of Pulse Electron Paramagnetic Resonance*, Oxford University Press, **2001**.

[71] D. Goldfarb, S. Stoll, *EPR Spectroscopy: Fundamentals and Methods*, John Wiley & Sons, **2018**.

[72] J. A. Weil, J. R. Bolton, *Electron paramagnetic resonance: Elementary theory and practical applications*, 2nd ed., Wiley-Interscience, Newy York, **2007**.

[73] N. M. Atherton, *Principles of electron spin resonance*, Ellis Horwood Ltd, Publisher, Harlow, England, **1993**.

[74] V. Chechik, E. Carter, D. Murphy, *Electron Paramagnetic Resonance*, Oxford University Press, **2016**.

[75] D. H. McIntyre, *Quantum Mechanics: A Paradigms Approach*, Cambridge University Press, **2022**.

[76] W. Gerlach, O. Stern, "Der experimentelle Nachweis der Richtungsquantelung im Magnetfeld", *Z. Phys.* **1922**, *9*, 349–352.

[77] H. M. McConnell, "Indirect Hyperfine Interactions in the Paramagnetic Resonance Spectra of Aromatic Free Radicals", *J. Chem. Phys.* **1956**, *24*, 764–766.

[78] H. M. McConnell, D. B. Chesnut, "Theory of isotropic hyperfine interactions in π-electron radicals", *J. Chem. Phys.* **1958**, *28*, 107–117.

[79] A. Meyer, S. Dechert, S. Dey, C. Höbartner, M. Bennati, "Measurement of Angstrom to Nanometer Molecular Distances with 19 F Nuclear Spins by EPR/ENDOR Spectroscopy", *Angew. Chem. Int. Ed.* **2020**, *59*, 373–379.

[80] N. M. Atherton, J. F. Shackleton, "Proton hyperfine couplings in VO(H2O)2+5: The validity of the point-dipole approximation", *Chem. Phys. Lett.* **1984**, *103*, 302–304.

[81] D. Goldfarb, "High field ENDOR as a characterization tool for functional sites in microporous materials", *Phys. Chem. Chem. Phys.* **2006**, *8*, 2325–2343.

[82] J. R. Norris, R. A. Uphaus, H. L. Crespi, J. J. Katz, "Electron spin resonance of chlorophyll and the origin of signal I in photosynthesis", *Proc. Natl. Acad. Sci. U. S. A.* **1971**, *68*, 625–628.

[83] G. Moise, L. Tejerina, M. Rickhaus, H. L. Anderson, C. R. Timmel, "Spin delocalization in the radical cations of porphyrin molecular wires: A new perspective on EPR approaches", *J. Phys. Chem. Lett.* **2019**, *10*, 5708–5712.

[84] T. M. Wilson, T. Hori, M.-C. Yoon, N. Aratani, A. Osuka, D. Kim, M. R. Wasielewski, "Rapid intramolecular hole hopping in meso-meso and meta-phenylene linked linear and cyclic multiporphyrin arrays", *J. Am. Chem. Soc.* **2010**, *132*, 1383–1388.

[85] J. Rawson, P. J. Angiolillo, M. J. Therien, "Extreme electron polaron spatial delocalization in π-conjugated materials", *Proc. Natl. Acad. Sci. U. S. A.* **2015**, *112*, 13779–13783.

[86] K. Susumu, P. R. Frail, P. J. Angiolillo, M. J. Therien, "Conjugated chromophore arrays with unusually large hole polaron delocalization lengths", *J. Am. Chem. Soc.* **2006**, *128*, 8380–8381.

[87] S. Richert, C. E. Tait, C. R. Timmel, "Delocalisation of photoexcited triplet states probed by transient EPR and hyperfine spectroscopy", *J. Magn. Reson.* **2017**, *280*, 103–116.

[88] G. Moise, A. J. Redman, S. Richert, W. K. Myers, I. Bulut, P. S. Bolls, M. Rickhaus, J. Sun, H. L. Anderson, C. R. Timmel, "The impact of spin-orbit coupling on fine-structure and spin polarisation in photoexcited porphyrin triplet states", *J. Magn. Reson.* **2023**, *355*, 107546.

[89] A. W. Hornig, J. S. Hyde, "Paramagnetic resonance in triplet naphthalene at liquid helium temperatures", *Mol. Phys.* **1963**, *6*, 33–41.

[90] J. H. van der Waals, M. S. de Groot, "Paramagnetic resonance in phosphorescent aromatic hydrocarbons. I: Naphthalene", *Mol. Phys.* **1959**, *2*, 333–340.

[91] S. Weber in *eMagRes*, John Wiley & Sons, Ltd, Chichester, UK, **2017**, pp. 255–270.

[92] C. E. Tait, M. D. Krzyaniak, S. Stoll, "Computational tools for the simulation and analysis of spin-polarized EPR spectra", *J. Magn. Reson.* **2023**, *349*, 107410.

[93] M. D. E. Forbes, L. E. Jarocha, S. Sim, V. F. Tarasov in *Advances in Physical Organic Chemistry*, *Vol. 47*, (Eds.: I. H. Williams, N. H. Williams), Academic Press, **2013**, pp. 1–83.

[94] W. B. Mims, "Pulsed endor experiments", *Proc. R. Soc. Lond. A Math. Phys. Sci.* **1997**, *283*, 452–457.

[95] E. R. Davies, "A new pulse endor technique", *Phys. Lett. A* **1974**, *47*, 1–2.

[96] A. Aviram, M. A. Ratner, "Molecular rectifiers", *Chem. Phys. Lett.* **1974**, *29*, 277–283.

[97] T. Li, V. K. Bandari, O. G. Schmidt, "Molecular Electronics: Creating and Bridging Molecular Junctions and Promoting Its Commercialization", *Adv. Mater.* **2023**, *35*, e2209088.

[98] T. A. Su, M. Neupane, M. L. Steigerwald, L. Venkataraman, C. Nuckolls, "Chemical principles of single-molecule electronics", *Nat. Rev. Mat.* **2016**, *1*, 1–15.

[99] N. Xin, J. Guan, C. Zhou, X. Chen, C. Gu, Y. Li, M. A. Ratner, A. Nitzan, J. F. Stoddart, X. Guo, "Concepts in the design and engineering of single-molecule electronic devices", *Nat. Rev. Phys.* **2019**, *1*, 211–230.

[100] C. J. Lambert, "Basic concepts of quantum interference and electron transport in single-molecule electronics", *Chem. Soc. Rev.* **2015**, *44*, 875–888.

[101] C. M. Guédon, H. Valkenier, T. Markussen, K. S. Thygesen, J. C. Hummelen, S. J. van der Molen, "Observation of quantum interference in molecular charge transport", *Nat. Nanotechnol.* **2012**, *7*, 305–309.

[102] J. Park, A. N. Pasupathy, J. I. Goldsmith, C. Chang, Y. Yaish, J. R. Petta, M. Rinkoski, J. P. Sethna, H. D. Abruña, P. L. McEuen, D. C. Ralph, "Coulomb blockade and the Kondo effect in single-atom transistors", *Nature* **2002**, *417*, 722–725.

[103] W. Liang, M. P. Shores, M. Bockrath, J. R. Long, H. Park, "Kondo resonance in a single-molecule transistor", *Nature* **2002**, *417*, 725–729.

[104] P. Zwick, D. Dulić, H. S. J. van der Zant, M. Mayor, "Porphyrins as building blocks for single-molecule devices", *Nanoscale* **2021**, *13*, 15500–15525.

[105] M. Jurow, A. E. Schuckman, J. D. Batteas, C. M. Drain, "Porphyrins as Molecular Electronic Components of Functional Devices", *Coord. Chem. Rev.* **2010**, *254*, 2297–2310.

[106] A. K. Burrell, M. R. Wasielewski, "Porphyrin-based nanostructures: routes to molecular electronics", *J. Porphyr. Phthalocyanines* **2000**, *04*, 401–406.

[107] W. M. Campbell, A. K. Burrell, D. L. Officer, K. W. Jolley, "Porphyrins as light harvesters in the dye-sensitised TiO2 solar cell", *Coord. Chem. Rev.* **2004**, *248*, 1363–1379.

[108] T. Tanaka, A. Osuka, "Conjugated porphyrin arrays: synthesis, properties and applications for functional materials", *Chem. Soc. Rev.* **2015**, *44*, 943–969.

[109] A. K. Burrell, D. L. Officer, P. G. Plieger, D. C. Reid, "Synthetic routes to multiporphyrin arrays", *Chem. Rev.* **2001**, *101*, 2751–2796.

[110] D. Holten, D. F. Bocian, J. S. Lindsey, "Probing electronic communication in covalently linked multiporphyrin arrays. A guide to the rational design of molecular photonic devices", *Acc. Chem. Res.* **2002**, *35*, 57–69.

[111] Y. Nakamura, N. Aratani, A. Osuka, "Cyclic porphyrin arrays as artificial photosynthetic antenna: synthesis and excitation energy transfer", *Chem. Soc. Rev.* **2007**, *36*, 831–845.

[112] V. Posligua, A. Aziz, R. Haver, M. D. Peeks, H. L. Anderson, R. Grau-Crespo, "Band Structures of Periodic Porphyrin Nanostructures", *J. Phys. Chem. C* **2018**, *122*, 23790–23798.

[113] A. Tsuda, A. Osuka, "Fully conjugated porphyrin tapes with electronic absorption bands that reach into infrared", *Science* **2001**, *293*, 79–82.

[114] Z. Chen, J.-R. Deng, S. Hou, X. Bian, J. L. Swett, Q. Wu, J. Baugh, L. Bogani, G. A. D. Briggs, J. A. Mol, C. J. Lambert, H. L. Anderson, J. O. Thomas, "Phase-Coherent Charge Transport through a Porphyrin Nanoribbon", *J. Am. Chem. Soc.* **2023**, *145*, 15265–15274.

[115] E. Leary, B. Limburg, A. Alanazy, S. Sangtarash, I. Grace, K. Swada, L. J. Esdaile, M. Noori, M. T. González, G. Rubio-Bollinger, H. Sadeghi, A. Hodgson, N. Agraı T, S. J. Higgins, C. J. Lambert, H. L. Anderson, R. J. Nichols, "Bias-driven conductance increase with length in porphyrin tapes", *J. Am. Chem. Soc.* **2018**, *140*, 12877–12883.

[116] J. Rawson, P. J. Angiolillo, P. R. Frail, I. Goodenough, M. J. Therien, "Electron Spin Relaxation of Hole and Electron Polarons in π-Conjugated Porphyrin Arrays: Spintronic Implications", *J. Phys. Chem. B* **2015**, *119*, 7681–7689.

[117] R. H. Clarke, D. R. Hobart, W. R. Leenstra, "The triplet state of the chlorophyll dimer", *J. Am. Chem. Soc.* **1979**, *101*, 2416–2423.

[118] A. J. Hoff, I. I. Proskuryakov, "Triplet EPR spectra of the primary electron donor in bacterial photosynthesis at temperatures between 15 and 296 K", *Chem. Phys. Lett.* **1985**, *115*, 303–310.

[119] F. Lendzian, H. van Willigen, S. Sastry, K. Möbius, H. Scheer, R. Feick, "Proton endor study of the photoexcited triplet state PT in Rps. sphaeroides R-26 photosynthetic reaction centres", *Chem. Phys. Lett.* **1985**, *118*, 145–150.

[120] F. Lendzian, R. Bittl, A. Telfer, W. Lubitz, "Hyperfine structure of the photoexcited triplet state 3P680 in plant PS II reaction centres as determined by pulse ENDOR spectroscopy", *Biochim. Biophys. Acta* **2003**, *1605*, 35–46.

[121] J. Andréasson, J. Kajanus, J. Mårtensson, B. Albinsson, "Triplet Energy Transfer in Porphyrin Dimers: Comparison between π- and σ-Chromophore Bridged Systems", *J. Am. Chem. Soc.* **2000**, *122*, 9844–9845.

[122] P. J. Angiolillo, V. S.-Y. Lin, J. M. Vanderkooi, M. J. Therien, "EPR spectroscopy and photophysics of the lowest photoactivated triplet state of a series of highly conjugated (porphinato)Zn arrays", *J. Am. Chem. Soc.* **1995**, *117*, 12514–12527.

[123] R. Shediac, M. H. B. Gray, H. T. Uyeda, R. C. Johnson, J. T. Hupp, P. J. Angiolillo, M. J. Therien, "Singlet and Triplet Excited States of Emissive, Conjugated Bis(porphyrin) Compounds Probed by Optical and EPR Spectroscopic Methods", *J. Am. Chem. Soc.* **2000**, *122*, 7017–7033.

[124] M. Bennati, A. Grupp, M. Mehring, P. Bäuerle, "Pulsed EPR Spectroscopy of the Photoexcited Triplet States of Thiophene Oligomers in Frozen Solution", *J. Phys. Chem.* **1996**, *100*, 2849–2853.

[125] P. J. Angiolillo, J. Rawson, P. R. Frail, M. J. Therien, "The evolution of spin distribution in the photoexcited triplet state of ethyne-elaborated porphyrins", *Chem. Commun.* **2013**, *49*, 9722–9724.

[126] S. Richert, B. Limburg, H. L. Anderson, C. R. Timmel, "On the Influence of the Bridge on Triplet State Delocalization in Linear Porphyrin Oligomers", *J. Am. Chem. Soc.* **2017**, *139*, 12003–12008.

[127] A. Köhler, J. S. Wilson, R. H. Friend, M. K. Al-Suti, M. S. Khan, A. Gerhard, H. Bässler, "The singlet–triplet energy gap in organic and Pt-containing phenylene ethynylene polymers and monomers", *J. Chem. Phys.* **2002**, *116*, 9457–9463.

[128] M. Ball, B. Zhang, Y. Zhong, B. Fowler, S. Xiao, F. Ng, M. Steigerwald, C. Nuckolls, "Conjugated Macrocycles in Organic Electronics", *Acc. Chem. Res.* **2019**, *52*, 1068–1078.

[129] C. Zhong, Y. Yan, Q. Peng, Z. Zhang, T. Wang, X. Chen, J. Wang, Y. Wei, T. Yang, L. Xie, "Structure-Property Relationship of Macrocycles in Organic Photoelectric Devices: A Comprehensive Review", *Nanomaterials (Basel)* **2023**, *13*.

[130] M. Ball, Y. Zhong, B. Fowler, B. Zhang, P. Li, G. Etkin, D. W. Paley, J. Decatur, A. K. Dalsania, H. Li, S. Xiao, F. Ng, M. L. Steigerwald, C. Nuckolls, "Macrocyclization in the Design of Organic n-Type Electronic Materials", *J. Am. Chem. Soc.* **2016**, *138*, 12861–12867.

[131] W. Liu, H. Zhang, S. Liang, T. Wang, S. He, Y. Hu, R. Zhang, H. Ning, J. Ren, A. Bakulin, F. Gao, J. Yuan, Y. Zou, "The Synthesis of a Multiple D-A Conjugated Macrocycle and Its Application in Organic Photovoltaic", *Angew. Chem. Int. Ed.* **2023**, *62*, e202311645.

[132] S. Izumi, H. F. Higginbotham, A. Nyga, P. Stachelek, N. Tohnai, P. d. Silva, P. Data, Y. Takeda, S. Minakata, "Thermally Activated Delayed Fluorescent Donor-Acceptor-Donor-Acceptor π-Conjugated Macrocycle for Organic Light-Emitting Diodes", *J. Am. Chem. Soc.* **2020**, *142*, 1482–1491.

[133] F. Zhao, J. Zhao, H. Liu, Y. Wang, J. Duan, C. Li, J. Di, N. Zhang, X. Zheng, P. Chen, "Synthesis of π-Conjugated Chiral Organoborane Macrocycles with Blue to Near-Infrared Emissions and the Diradical Character of Cations", *J. Am. Chem. Soc.* **2023**, *145*, 10092–10103.

[134] I. Roy, A. H. G. David, P. J. Das, D. J. Pe, J. F. Stoddart, "Fluorescent cyclophanes and their applications", *Chem. Soc. Rev.* **2022**, *51*, 5557–5605.

[135] O. Fenwick, J. K. Sprafke, J. Binas, D. V. Kondratuk, F. Di Stasio, H. L. Anderson, F. Cacialli, "Linear and cyclic porphyrin hexamers as near-infrared emitters in organic light-emitting diodes", *Nano Lett.* **2011**, *11*, 2451–2456.

[136] B. Zhang, M. T. Trinh, B. Fowler, M. Ball, Q. Xu, F. Ng, M. L. Steigerwald, X.-Y. Zhu, C. Nuckolls, Y. Zhong, "Rigid, Conjugated Macrocycles for High Performance Organic Photodetectors", *J. Am. Chem. Soc.* **2016**, *138*, 16426–16431.

[137] Q. Huang, G. Zhuang, H. Jia, M. Qian, S. Cui, S. Yang, P. Du, "Photoconductive Curved-Nanographene/Fullerene Supramolecular Heterojunctions", *Angew. Chem. Int. Ed.* **2019**, *58*, 6244–6249.

[138] B. Zhang, R. Hernández Sánchez, Y. Zhong, M. Ball, M. W. Terban, D. Paley, S. J. L. Billinge, F. Ng, M. L. Steigerwald, C. Nuckolls, "Hollow organic capsules assemble into cellular semiconductors", *Nat. Commun.* **2018**, *9*, 1957.

[139] R. Frydrych, T. Lis, W. Bury, J. Cybińska, M. Stępień, "Feeding a Molecular Squid: A Pliable Nanocarbon Receptor for Electron-Poor Aromatics", *J. Am. Chem. Soc.* **2020**, *142*, 15604–15613.

[140] L. You, D. Zha, E. V. Anslyn, "Recent Advances in Supramolecular Analytical Chemistry Using Optical Sensing", *Chem. Rev.* **2015**, *115*, 7840–7892.

[141] A. Heckmann, C. Lambert, "Organic mixed-valence compounds: a playground for electrons and holes", *Angew. Chem. Int. Ed.* **2012**, *51*, 326–392.

[142] C. Y. Liu, M. Meng, Introduction and fundamentals of mixed-valence chemistry, **2023**.

[143] R. A. Marcus, "On the theory of oxidation-reduction reactions involving electron transfer. I", *J. Chem. Phys.* **1956**, *24*, 966–978.

[144] R. A. Marcus, "Electron transfer reactions in chemistry. Theory and experiment", *Rev. Mod. Phys.* **1993**, *65*, 599–610.

[145] N. S. Hush, "Distance Dependence of Electron Transfer Rates", *Coord. Chem. Rev.* **1985**, *64*, 135–157.

[146] N. S. Hush, "Homogeneous and heterogeneous optical and thermal electron transfer", *Electrochim. Acta* **1968**, *13*, 1005–1023.

[147] M. R. Talipov, A. Boddeda, Q. K. Timerghazin, R. Rathore, "Key Role of End-Capping Groups in Optoelectronic Properties of Poly-p-phenylene Cation Radicals", *J. Phys. Chem. C Nanomater. Interfaces* **2014**, *118*, 21400–21408.

[148] M. B. Robin, P. Day in *Advances in Inorganic Chemistry and Radiochemistry*, Advances in inorganic chemistry and radiochemistry, Elsevier, **1968**, pp. 247–422.

[149] B. S. Brunschwig, S. Ehrenson, N. Sutin, "Solvent reorganization in optical and thermal electron-transfer processes", *J. Phys. Chem.* **1986**, *90*, 3657–3668.

[150] G. Heimel, "The Optical Signature of Charges in Conjugated Polymers", *ACS Cent Sci* **2016**, *2*, 309–315.

[151] P. A. Lane, X. Wei, Z. V. Vardeny, "Studies of charged excitations in pi -conjugated oligomers and polymers by optical modulation", *Phys. Rev. Lett.* **1996**, *77*, 1544–1547.

[152] M. Wohlgenannt, "Polarons in π-conjugated semiconductors: absorption spectroscopy and spin-dependent recombination", *Physica Status Solidi A Appl. Res.* **2004**, *201*, 1188–1204.

[153] P. R. Schleyer, "Introduction: aromaticity", *Chem. Rev.* **2001**, *101*, 1115–1118.

[154] G. Merino, M. Solà, I. Fernández, C. Foroutan-Nejad, P. Lazzeretti, G. Frenking, H. L. Anderson, D. Sundholm, F. P. Cossío, M. A. Petrukhina, J. Wu, J. I. Wu, A. Restrepo, "Aromaticity: Quo Vadis", *Chem. Sci.* **2023**, *14*, 5569–5576.

[155] E. Hückel, "Quantentheoretische Beiträge zum Benzolproblem", *Z. Phys.* **1931**, *70*, 204–286.

[156] E. Hückel, "Quanstentheoretische Beiträge zum Benzolproblem", *Z. Phys.* **1931**, *72*, 310–337.

[157] E. Hückel, "Quantentheoretische Beiträge zum Problem der aromatischen und ungesättigten Verbindungen. III", *Z. Phys.* **1932**, *76*, 628–648.

[158] K. Yates, *Hückel Molecular Orbital Theory*, Elsevier, **2012**.

[159] P. W. Atkins, J. De Paula, J. Keeler, *Atkins' Physical Chemistry*, Oxford University Press, **2018**.

[160] J. E. Lennard-Jones, "The electronic structure of some diatomic molecules", *Trans. Faraday Soc.* **1929**, *25*, 668–686.

[161] A. A. Frost, B. Musulin, "A mnemonic device for molecular orbital energies", *J. Chem. Phys.* **1953**, *21*, 572–573.

[162] M. Kertesz, C. H. Choi, S. Yang, "Conjugated polymers and aromaticity", *Chem. Rev.* **2005**, *105*, 3448–3481.

[163] M. K. Cyrański, T. M. Krygowski, "Two sources of the decrease of aromaticity: Bond length alternation and bond elongation. Part I. An analysis based on benzene ring deformations", *Tetrahedron* **1999**, *55*, 6205–6210.

[164] T. M. Krygowski, M. Cyrański, "Separation of the energetic and geometric contributions to the aromaticity of π-electron carbocyclics", *Tetrahedron* **1996**, *52*, 1713–1722.

[165] J. D. Roberts, M. C. Caserio, *Basic Principles of Organic Chemistry*, W. A. Benjamin, **1977**.

[166] P. R. von Schleyer, H. Jiao, "What is aromaticity?", *J. Macromol. Sci. Part A Pure Appl. Chem.* **1996**, *68*, 209–218.

[167] T. M. Krygowski, M. K. Cyrański, "Structural aspects of aromaticity", *Chem. Rev.* **2001**, *101*, 1385–1419.

[168] J. A. Gomes, R. B. Mallion, "Aromaticity and ring currents", *Chem. Rev.* **2001**, *101*, 1349–1383.

[169] H. C. Longuet-Higgins, L. Salem, "The alternation of bond lengths in long conjugated chain molecules", *Proc. R. Soc. Lond. A Math. Phys. Sci.* **1997**, *251*, 172–185.

[170] M. J. S. Dewar, G. J. Gleicher, "Ground States of Conjugated Molecules. II. Allowance for Molecular Geometry1a,b", *J. Am. Chem. Soc.* **1965**, *87*, 685–692.

[171] I. Casademont-Reig, E. Ramos-Cordoba, M. Torrent-Sucarrat, E. Matito, "How do the Hückel and Baird Rules Fade away in Annulenes?", *Molecules* **2020**, *25*.

[172] C. S. Wannere, P. von Ragué Schleyer, "How aromatic are large (4n + 2)pi annulenes?", *Org. Lett.* **2003**, *5*, 865–868.

[173] T. Soya, W. Kim, D. Kim, A. Osuka, "Stable [48]-, [50]-, and [52]dodecaphyrins(1.1.0.1.1.0.1.1.0.1.1.0): the largest Hückel aromatic molecules", *Chem. Eur. J.* **2015**, *21*, 8341–8346.

[174] T. Yoneda, T. Soya, S. Neya, A. Osuka, "[62]Tetradecaphyrin and Its Mono- and Bis-Zn(II) Complexes", *Chem. Eur. J.* **2016**, *22*, 14518–14522.

[175] T. Soya, H. Mori, A. Osuka, "Quadruply Twisted Hückel-Aromatic Dodecaphyrin", *Angew. Chem. Int. Ed.* **2018**, *57*, 15882–15886.

[176] M. D. Peeks, M. Jirasek, T. D. W. Claridge, H. L. Anderson, "Global Aromaticity and Antiaromaticity in Porphyrin Nanoring Anions", *Angew. Chem. Int. Ed.* **2019**, *58*, 15717–15720.

[177] M. D. Peeks, J. Q. Gong, K. McLoughlin, T. Kobatake, R. Haver, L. M. Herz, H. L. Anderson, "Aromaticity and Antiaromaticity in the Excited States of Porphyrin Nanorings", *J. Phys. Chem. Lett.* **2019**, *10*, 2017–2022.

[178] I. S. Grant, W. R. Phillips, *Electromagnetism*, Wiley, **1990**.

[179] P. v. R. Schleyer, C. Maerker, A. Dransfeld, H. Jiao, N. J. R. van Eikema Hommes, "Nucleus-Independent Chemical Shifts: A Simple and Efficient Aromaticity Probe", *J. Am. Chem. Soc.* **1996**, *118*, 6317–6318.

[180] J.-R. Deng, D. Bradley, M. Jirásek, H. L. Anderson, M. D. Peeks, "Correspondence on "How Aromatic Are Molecular Nanorings? The Case of a Six-Porphyrin Nanoring"", *Angew. Chem. Int. Ed.* **2022**, *61*, e202201231.

[181] J. L. Bredas, G. B. Street, "Polarons, bipolarons, and solitons in conducting polymers", *Acc. Chem. Res.* **1985**, *18*, 309–315.

[182] V. Coropceanu, J. Cornil, D. A. da Silva Filho, Y. Olivier, R. Silbey, J.-L. Brédas, "Charge transport in organic semiconductors", *Chem. Rev.* **2007**, *107*, 926–952.

[183] D. K. Campbell, A. R. Bishop, K. Fesser, "Polarons in quasi-one-dimensional systems", *Phys. Rev. B Condens. Matter* **1982**, *26*, 6862–6874.

[184] T. Sakanoue, H. Sirringhaus, "Band-like temperature dependence of mobility in a solution-processed organic semiconductor", *Nat. Mater.* **2010**, *9*, 736–740.

[185] H. Bässler, A. Köhler in *Unimolecular and Supramolecular Electronics I: Chemistry and Physics Meet at Metal-Molecule Interfaces*, (Ed.: R. M. Metzger), Springer Berlin Heidelberg, Berlin, Heidelberg, **2012**, pp. 1–65.

[186] A. A. Bakulin, A. Rao, V. G. Pavelyev, P. H. M. van Loosdrecht, M. S. Pshenichnikov, D. Niedzialek, J. Cornil, D. Beljonne, R. H. Friend, "The role of driving energy and delocalized States for charge separation in organic semiconductors", *Science* **2012**, *335*, 1340–1344.

[187] H. Tamura, I. Burghardt, "Ultrafast charge separation in organic photovoltaics enhanced by charge delocalization and vibronically hot exciton dissociation", *J. Am. Chem. Soc.* **2013**, *135*, 16364–16367.

[188] R. Ghosh, F. C. Spano, "Excitons and polarons in organic materials", *Acc. Chem. Res.* **2020**, *53*, 2201–2211.

[189] M. Moser, A. Savva, K. Thorley, B. D. Paulsen, T. C. Hidalgo, D. Ohayon, H. Chen, A. Giovannitti, A. Marks, N. Gasparini, A. Wadsworth, J. Rivnay, S. Inal, I. McCulloch, "Polaron Delocalization in Donor-Acceptor Polymers and its Impact on Organic Electrochemical Transistor Performance", *Angew. Chem. Int. Ed.* **2021**, *60*, 7777–7785.

[190] A. B. Matheson, A. Ruseckas, S. J. Pearson, I. D. W. Samuel, "Hole delocalization as a driving force for charge pair dissociation in organic photovoltaics", *Mater. Horiz.* **2019**, *6*, 1050–1056.

[191] J. Niklas, T. Zheng, A. Neshchadin, K. L. Mardis, L. Yu, O. G. Poluektov, "Polaron and Exciton Delocalization in Oligomers of High-Performance Polymer PTB7", *J. Am. Chem. Soc.* **2020**, *142*, 1359–1366.

[192] S. Schott, U. Chopra, V. Lemaur, A. Melnyk, Y. Olivier, R. Di Pietro, I. Romanov, R. L. Carey, X. Jiao, C. Jellett, M. Little, A. Marks, C. R. McNeill, I. McCulloch, E. R. McNellis, D. Andrienko, D. Beljonne, J. Sinova, H. Sirringhaus, "Polaron spin dynamics in high-mobility polymeric semiconductors", *Nat. Phys.* **2019**, *15*, 814–822.

[193] S. Watanabe, K. Ando, K. Kang, S. Mooser, Y. Vaynzof, H. Kurebayashi, E. Saitoh, H. Sirringhaus, "Polaron spin current transport in organic semiconductors", *Nat. Phys.* **2014**, *10*, 308–313.

[194] J. Tsurumi, H. Matsui, T. Kubo, R. Häusermann, C. Mitsui, T. Okamoto, S. Watanabe, J. Takeya, "Coexistence of ultra-long spin relaxation time and coherent charge transport in organic single-crystal semiconductors", *Nat. Phys.* **2017**, *13*, 994–998.

[195] G. Bullard, F. Tassinari, C.-H. Ko, A. K. Mondal, R. Wang, S. Mishra, R. Naaman, M. J. Therien, "Low-Resistance Molecular Wires Propagate Spin-Polarized Currents", *J. Am. Chem. Soc.* **2019**, *141*, 14707–14711.

[196] T. Hines, I. Diez-Perez, J. Hihath, H. Liu, Z.-S. Wang, J. Zhao, G. Zhou, K. Müllen, N. Tao, "Transition from tunneling to hopping in single molecular junctions by measuring length and temperature dependence", *J. Am. Chem. Soc.* **2010**, *132*, 11658–11664.

[197] Q. Lu, K. Liu, H. Zhang, Z. Du, X. Wang, F. Wang, "From tunneling to hopping: a comprehensive investigation of charge transport mechanism in molecular junctions based on oligo(p-phenylene ethynylene)s", *ACS Nano* **2009**, *3*, 3861–3868.

[198] R. C. Bruce, R. Wang, J. Rawson, M. J. Therien, W. You, "Valence Band Dependent Charge Transport in Bulk Molecular Electronic Devices Incorporating Highly Conjugated Multi-[(Porphinato)Metal] Oligomers", *J. Am. Chem. Soc.* **2016**, *138*, 2078–2081.

[199] Z. Li, T.-H. Park, J. Rawson, M. J. Therien, E. Borguet, "Quasi-ohmic single molecule charge transport through highly conjugated meso-to-meso ethyne-bridged porphyrin wires", *Nano Lett.* **2012**, *12*, 2722–2727.

[200] H. S. Cho, D. H. Jeong, S. Cho, D. Kim, Y. Matsuzaki, K. Tanaka, A. Tsuda, A. Osuka, "Photophysical properties of porphyrin tapes", *J. Am. Chem. Soc.* **2002**, *124*, 14642–14654.

[201] G. Sedghi, L. J. Esdaile, H. L. Anderson, S. Martin, D. Bethell, S. J. Higgins, R. J. Nichols, "Comparison of the conductance of three types of porphyrin-based molecular wires: β,meso,β-fused tapes, meso-Butadiyne-linked and twisted meso-meso linked oligomers", *Adv. Mater.* **2012**, *24*, 653–657.

[202] N. Algethami, H. Sadeghi, S. Sangtarash, C. J. Lambert, "The Conductance of Porphyrin-Based Molecular Nanowires Increases with Length", *Nano Lett.* **2018**, *18*, 4482–4486.

[203] J. O. Thomas, J. K. Sowa, B. Limburg, X. Bian, C. Evangeli, J. L. Swett, S. Tewari, J. Baugh, G. C. Schatz, G. A. D. Briggs, H. L. Anderson, J. A. Mol, "Charge transport through extended molecular wires with strongly correlated electrons", *Chem. Sci.* **2021**, *12*, 11121–11129.

[204] F. C. Grozema, C. Houarner-Rassin, P. Prins, L. D. A. Siebbeles, H. L. Anderson, "Supramolecular control of charge transport in molecular wires", *J. Am. Chem. Soc.* **2007**, *129*, 13370–13371.

[205] A. J. Cohen, P. Mori-Sánchez, W. Yang, "Insights into current limitations of density functional theory", *Science* **2008**, *321*, 792–794.

[206] M. Kaupp, M. Renz, M. Parthey, M. Stolte, F. Würthner, C. Lambert, "Computational and spectroscopic studies of organic mixed-valence compounds: where is the charge?", *Phys. Chem. Chem. Phys.* **2011**, *13*, 16973–16986.

[207] M. Renz, K. Theilacker, C. Lambert, M. Kaupp, "A reliable quantum-chemical protocol for the characterization of organic mixed-valence compounds", *J. Am. Chem. Soc.* **2009**, *131*, 16292–16302.

[208] J. C. Walton in *Encyclopedia of Radicals in Chemistry, Biology and Materials*, John Wiley & Sons, Ltd, Chichester, UK, **2012**.

[209] M. Rohrer, P. Gast, K. Möbius, T. F. Prisner, "Anisotropic motion of semiquinones in photosynthetic reaction centers of Rhodobacter sphaeroides R26 and in frozen isopropanol solution as measured by pulsed high-field EPR at 95 GHz", *Chem. Phys. Lett.* **1996**, *259*, 523–530.

[210] E. G. Bagryanskaya, D. N. Polovyanenko, M. V. Fedin, L. Kulik, A. Schnegg, A. Savitsky, K. Möbius, A. W. Coleman, G. S. Ananchenko, J. A. Ripmeester, "Multifrequency EPR study of the mobility of nitroxides in solid-state calixarene nanocapsules", *Phys. Chem. Chem. Phys.* **2009**, *11*, 6700–6707.

[211] C. E. Jackson, C.-Y. Lin, J. van Tol, J. M. Zadrozny, "Orientation dependence of phase memory relaxation in the V(IV) ion at high frequencies", *Chem. Phys. Lett.* **2020**, *739*, 137034.

[212] T. Ikeda, N. Aratani, A. Osuka, "Synthesis of extremely pi-extended porphyrin tapes from hybrid meso-meso linked porphyrin arrays: an approach towards the conjugation length", *Chem. Asian J.* **2009**, *4*, 1248–1256.

[213] B. S. Brunschwig, C. Creutz, N. Sutin, "Optical transitions of symmetrical mixed-valence systems in the Class II-III transition regime", *Chem. Soc. Rev.* **2002**, *31*, 168–184.

[214] M. R. Talipov, M. V. Ivanov, R. Rathore, "Inclusion of Asymptotic Dependence of Reorganization Energy in the Modified Marcus-Based Multistate Model Accurately Predicts Hole Distribution in Poly-p-phenylene Wires", *J. Phys. Chem. C* **2016**, *120*, 6402–6408.

[215] K. J. Thorley, "Estimation of Polaron Delocalization Lengths in Conjugated Organic Polymers", *J. Phys. Chem. B* **2023**, *127*, 5102–5114.

[216] D. A. Stanfield, Z. Mehmedović, B. J. Schwartz, "Vibrational Stark Effect Mapping of Polaron Delocalization in Chemically Doped Conjugated Polymers", *Chem. Mater.* **2021**, *33*, 8489–8500.

[217] R. Ghosh, A. R. Chew, J. Onorato, V. Pakhnyuk, C. K. Luscombe, A. Salleo, F. C. Spano, "Spectral Signatures and Spatial Coherence of Bound and Unbound Polarons in P3HT Films: Theory Versus Experiment", *J. Phys. Chem. C* **2018**, *122*, 18048–18060.

[218] M. Krejčik, M. Daněk, F. Hartl, "Simple construction of an infrared optically transparent thin-layer electrochemical cell: Applications to the redox reactions of ferrocene, Mn2(CO)10 and Mn(CO)3(3,5-di-t-butyl-catecholate)", *J. Electroanal. Chem. Interfacial Electrochem.* **1991**, *317*, 179–187.

[219] J. Jaumot, R. Gargallo, A. de Juan, R. Tauler, "A graphical user-friendly interface for MCR-ALS: a new tool for multivariate curve resolution in MATLAB", *Chemometrics Intellig. Lab. Syst.* **2005**, *76*, 101–110.

[220] J. Jaumot, A. de Juan, R. Tauler, "MCR-ALS GUI 2.0: New features and applications", *Chemometrics Intellig. Lab. Syst.* **2015**, *140*, 1–12.

[221] The MathWorks, Inc., Natick, Massachusetts, United States, MATLAB.

[222] M. J. Frisch, G. W. Trucks, H. B. Schlegel, G. E. Scuseria, M. A. Robb, J. R. Cheeseman, G. Scalmani, V. Barone, G. A. Petersson, H. Nakatsuji, X. Li, M. Caricato, A. V. Marenich, J. Bloino, B. G. Janesko, R. Gomperts, B. Mennucci, H. P. Hratchian, J. V. Ortiz, A. F. Izmaylov, J. L. Sonnenberg, Williams, F. Ding, F. Lipparini, F. Egidi, J. Goings, B. Peng, A. Petrone, T. Henderson, D. Ranasinghe, V. G. Zakrzewski, J. Gao, N. Rega, G. Zheng, W. Liang, M. Hada, M. Ehara, K. Toyota, R. Fukuda, J. Hasegawa, M. Ishida, T. Nakajima, Y. Honda, O. Kitao, H. Nakai, T. Vreven, K. Throssell, J. A. Montgomery, Jr, J. E. Peralta, F. Ogliaro, M. J. Bearpark, J. J. Heyd, E. N. Brothers, K. N. Kudin, V. N. Staroverov, T. A. Keith, R. Kobayashi, J. Normand, K. Raghavachari, A. P. Rendell, J. C. Burant, S. S. Iyengar, J. Tomasi, M. Cossi, J. M. Millam, M. Klene, C. Adamo, R. Cammi, J. W. Ochterski, R. L. Martin, K. Morokuma, O. Farkas, J. B. Foresman, D. J. Fox, Gaussian 16 Rev. C.01, Wallingford, CT, **2016**.

[223] R. Ditchfield, W. J. Hehre, J. A. Pople, "Self-Consistent Molecular-Orbital Methods. IX. An Extended Gaussian-Type Basis for Molecular-Orbital Studies of Organic Molecules", *J. Chem. Phys.* **1971**, *54*, 724–728.

[224] W. J. Hehre, R. Ditchfield, J. A. Pople, "Self—Consistent Molecular Orbital Methods. XII. Further Extensions of Gaussian—Type Basis Sets for Use in Molecular Orbital Studies of Organic Molecules", *J. Chem. Phys.* **1972**, *56*, 2257–2261.

[225] P. C. Hariharan, J. A. Pople, "The influence of polarization functions on molecular orbital hydrogenation energies", *Theor. Chim. Acta* **1973**, *28*, 213–222.

[226] V. A. Rassolov, J. A. Pople, M. A. Ratner, T. L. Windus, "6-31G* basis set for atoms K through Zn", *J. Chem. Phys.* **1998**, *109*, 1223–1229.

[227] H. Iikura, T. Tsuneda, T. Yanai, K. Hirao, "A long-range correction scheme for generalized-gradient-approximation exchange functionals", *J. Chem. Phys.* **2001**, *115*, 3540–3544.

[228] A. Najibi, M. Casanova-Páez, L. Goerigk, "Analysis of Recent BLYP- and PBE-Based Range-Separated Double-Hybrid Density Functional Approximations for Main-Group Thermochemistry, Kinetics, and Noncovalent Interactions", *J. Phys. Chem. A* **2021**, *125*, 4026–4035.

[229] A. Najibi, L. Goerigk, "The Nonlocal Kernel in van der Waals Density Functionals as an Additive Correction: An Extensive Analysis with Special Emphasis on the B97M-V and ωB97M-V Approaches", *J. Chem. Theory Comput.* **2018**, *14*, 5725–5738.

[230] F. Neese, "The ORCA program system", *Wiley Interdiscip. Rev. Comput. Mol. Sci.* **2012**, *2*, 73–78.

[231] F. Neese, "Software update: The ORCA program system—Version 5.0", *Wiley Interdiscip. Rev. Comput. Mol. Sci.* **2022**, *12*.

[232] F. Furche, R. Ahlrichs, "Adiabatic time-dependent density functional methods for excited state properties", *J. Chem. Phys.* **2002**, *117*, 7433–7447.

[233] T. M. Henderson, A. F. Izmaylov, G. Scalmani, G. E. Scuseria, "Can short-range hybrids describe long-range-dependent properties?", *J. Chem. Phys.* **2009**, *131*, 044108.

[234] B. Mennucci, J. Tomasi, R. Cammi, J. R. Cheeseman, M. J. Frisch, F. J. Devlin, S. Gabriel, P. J. Stephens, "Polarizable Continuum Model (PCM) Calculations of Solvent Effects on Optical Rotations of Chiral Molecules", *J. Phys. Chem. A* **2002**, *106*, 6102–6113.

[235] V. Barone in *Recent Advances in Density Functional Methods*, Recent Advances in Computational Chemistry, WORLD SCIENTIFIC, **1995**, pp. 287–334.

[236] V. Barone, "Inclusion of Hartree–Fock exchange in density functional methods. Hyperfine structure of second row atoms and hydrides", *J. Chem. Phys.* **1994**, *101*, 6834–6838.

[237] V. Barone, "Characterization of the potential energy surface of the HO2 molecular system by a density functional approach", *J. Chem. Phys.* **1994**, *101*, 10666–10676.

[238] S. Stoll, A. Schweiger, "EasySpin, a comprehensive software package for spectral simulation and analysis in EPR", *J. Magn. Reson.* **2006**, *178*, 42–55.

[239] W. Kaim, A. Klein, M. Glöckle, "Exploration of mixed-valence chemistry: inventing new analogues of the Creutz-Taube ion", *Acc. Chem. Res.* **2000**, *33*, 755–763.

[240] J. Schäfer, M. Holzapfel, B. Mladenova, D. Kattnig, I. Krummenacher, H. Braunschweig, G. Grampp, C. Lambert, "Hole transfer processes in meta- and para-conjugated mixed valence compounds: Unforeseen effects of bridge substituents and solvent dynamics", *J. Am. Chem. Soc.* **2017**, *139*, 6200–6209.

[241] C. Hua, P. W. Doheny, B. Ding, B. Chan, M. Yu, C. J. Kepert, D. M. D'Alessandro, "Through-space intervalence charge transfer as a mechanism for charge delocalization in metal–organic frameworks", *J. Am. Chem. Soc.* **2018**, *140*, 6622–6630.

[242] S. Barlow, C. Risko, S. A. Odom, S. Zheng, V. Coropceanu, L. Beverina, J.-L. Brédas, S. R. Marder, "Tuning delocalization in the radical cations of 1,4-bis[4-(diarylamino)styryl]benzenes, 2,5-bis[4-(diarylamino)styryl]thiophenes, and 2,5-bis[4-(diarylamino)styryl]pyrroles through substituent effects", *J. Am. Chem. Soc.* **2012**, *134*, 10146–10155.

[243] J. Hankache, O. S. Wenger, "Organic mixed valence", *Chem. Rev.* **2011**, *111*, 5138–5178.

[244] C. Joachim, J. K. Gimzewski, A. Aviram, "Electronics using hybrid-molecular and mono-molecular devices", *Nature* **2000**, *408*, 541–548.

[245] J.-P. Launay, "Electron transfer in molecular binuclear complexes and relation with electron transport through nanojunctions", *Coord. Chem. Rev.* **2013**, *257*, 1544–1554.

[246] W. B. Davis, W. A. Svec, M. A. Ratner, M. R. Wasielewski, "Molecular-wire behaviour in p -phenylenevinylene oligomers", *Nature* **1998**, *396*, 60–63.

[247] U. Scherf, E. J. W. List, "Semiconducting polyfluorenes—towards reliable structure–property relationships", *Adv. Mater.* **2002**, *14*, 477.

[248] J. H. Burroughes, D. D. C. Bradley, A. R. Brown, R. N. Marks, K. Mackay, R. H. Friend, P. L. Burns, A. B. Holmes, "Light-emitting diodes based on conjugated polymers", *Nature* **1990**, *347*, 539–541.

[249] L. Li, X. Dong, J. Li, J. Wei, "A short review on NIR-II organic small molecule dyes", *Dyes Pigm.* **2020**, *183*, 108756.

[250] V. Launay, A. Caron, G. Noirbent, D. Gigmes, F. Dumur, J. Lalevée, "NIR organic dyes as innovative tools for reprocessing/recycling of plastics: Benefits of the photothermal activation in the near-infrared range", *Adv. Funct. Mater.* **2021**, *31*, 2006324.

[251] B. Li, M. Zhao, F. Zhang, "Rational Design of Near-Infrared-II Organic Molecular Dyes for Bioimaging and Biosensing", *ACS Materials Lett.* **2020**, *2*, 905–917.

[252] P. Day, *Molecules Into Materials: Case Studies in Materials Chemistry – Mixed Valency, Magnetism and Superconductivity*, World Scientific, **2007**.

[253] G. Saito, Y. Yoshida, "Organic superconductors", *Chem. Rec.* **2011**, *11*, 124–145.

[254] H. Bronstein, C. B. Nielsen, B. C. Schroeder, I. McCulloch, "The role of chemical design in the performance of organic semiconductors", *Nat Rev Chem* **2020**, *4*, 66–77.

[255] B. Lüssem, M. Riede, K. Leo, "Doping of organic semiconductors", *Phys. Status Solidi* **2013**, *210*, 9–43.

[256] J. Cremer, P. Bäuerle, M. M. Wienk, R. A. J. Janssen, "High open-circuit voltage poly(ethynylene bithienylene):Fullerene solar cells", *Chem. Mater.* **2006**, *18*, 5832–5834.

[257] S. Hu, W. Liu, L. Guo, R. Zhang, X. Gu, K. Meng, Y. Qin, A. Guo, T. Yang, C. Zhang, X. Yang, S. Lu, M. Wu, K. Lu, T. Tan, E. Zhou, Z. Wei, X. Sun, "Continuous room-temperature spin-injection modulation achieved by spin-filtering competition in molecular spin valves", *Adv. Mater.* **2023**, *35*, e2300055.

[258] Y. Adhikari, T. Liu, H. Wang, Z. Hua, H. Liu, E. Lochner, P. Schlottmann, B. Yan, J. Zhao, P. Xiong, "Interplay of structural chirality, electron spin and topological orbital in chiral molecular spin valves", *Nat. Commun.* **2023**, *14*, 5163.

[259] S. Ding, Y. Tian, W. Hu, "Cornerstone of molecular spintronics: Strategies for reliable organic spin valves", *Nano Res.* **2021**, *14*, 3653–3668.

[260] M. Urdampilleta, S. Klyatskaya, J.-P. Cleuziou, M. Ruben, W. Wernsdorfer, "Supramolecular spin valves", *Nat. Mater.* **2011**, *10*, 502–506.

[261] G. Binasch, P. Grünberg, F. Saurenbach, W. Zinn, "Enhanced magnetoresistance in layered magnetic structures with antiferromagnetic interlayer exchange", *Phys. Rev. B Condens. Matter* **1989**, *39*, 4828–4830.

[262] M. N. Baibich, J. M. Broto, A. Fert, Nguyen Van Dau F, F. Petroff, P. Etienne, G. Creuzet, A. Friederich, J. Chazelas, "Giant magnetoresistance of (001)Fe/(001)Cr magnetic superlattices", *Phys. Rev. Lett.* **1988**, *61*, 2472–2475.

[263] N. S. Lai, W. H. Lim, C. H. Yang, F. A. Zwanenburg, W. A. Coish, F. Qassemi, A. Morello, A. S. Dzurak, "Pauli spin blockade in a highly tunable silicon double quantum dot", *Sci. Rep.* **2011**, *1*, 110.

[264] R. Li, F. E. Hudson, A. S. Dzurak, A. R. Hamilton, "Pauli Spin Blockade of Heavy Holes in a Silicon Double Quantum Dot", *Nano Lett.* **2015**, *15*, 7314–7318.

[265] S. Amaha, W. Izumida, T. Hatano, S. Teraoka, S. Tarucha, J. A. Gupta, D. G. Austing, "Two- and three-electron Pauli spin blockade in series-coupled triple quantum dots", *Phys. Rev. Lett.* **2013**, *110*, 016803.

[266] P. M. Burrezo, X. Zhu, S.-F. Zhu, Q. Yan, J. T. López Navarrete, H. Tsuji, E. Nakamura, J. Casado, "Planarization, fusion, and strain of carbon-bridged phenylenevinylene oligomers enhance π-electron and charge conjugation: a dissectional vibrational Raman study", *J. Am. Chem. Soc.* **2015**, *137*, 3834–3843.

[267] E. Leary, B. Limburg, A. Alanazy, S. Sangtarash, I. Grace, K. Swada, L. J. Esdaile, M. Noori, M. T. González, G. Rubio-Bollinger, H. Sadeghi, A. Hodgson, N. Agraı T, S. J. Higgins, C. J. Lambert, H. L. Anderson, R. J. Nichols, "Bias-Driven Conductance Increase with Length in Porphyrin Tapes", *J. Am. Chem. Soc.* **2018**, *140*, 12877–12883.

[268] J.-R. Deng, M. T. González, H. Zhu, H. L. Anderson, E. Leary, "Ballistic Conductance through Porphyrin Nanoribbons", *J. Am. Chem. Soc.* **2024**.

[269] F. Montaigne, M. Hehn, A. Schuhl, "Tunnel barrier parameters and magnetoresistance in the parabolic band model", *Phys. Rev. B Condens. Matter* **2001**, *64*, 144402.

[270] R. C. Sousa, J. J. Sun, V. Soares, P. P. Freitas, A. Kling, M. F. da Silva, J. C. Soares, "Temperature dependence and annealing effects on spin dependent tunnel junctions", *J. Appl. Phys.* **1999**, *85*, 5258–5260.

[271] P. Rottländer, M. Hehn, O. Lenoble, A. Schuhl, "Tantalum oxide as an alternative low height tunnel barrier in magnetic junctions", *Appl. Phys. Lett.* **2001**, *78*, 3274–3276.

[272] C. J. Hondros, K. Aravindu, J. R. Diers, D. Holten, J. S. Lindsey, D. F. Bocian, "Effects of linker torsional constraints on the rate of ground-state hole transfer in porphyrin dyads", *Inorg. Chem.* **2012**, *51*, 11076–11086.

[273] J. R. Diers, M. Taniguchi, D. Holten, J. S. Lindsey, D. F. Bocian, "Probing the rate of hole transfer in oxidized porphyrin dyads using thallium hyperfine clocks", *J. Am. Chem. Soc.* **2010**, *132*, 12121–12132.

[274] E. J. Nieves-Bernier, J. R. Diers, M. Taniguchi, D. Holten, D. F. Bocian, J. S. Lindsey, "Probing the rate of hole transfer in oxidized synthetic chlorin dyads via site-specific (13)C-labeling", *J. Org. Chem.* **2010**, *75*, 3193–3202.

[275] T. Quintes, M. Mayländer, S. Richert, "Properties and applications of photoexcited chromophore-radical systems", *Nat. Rev. Chem.* **2023**, *7*, 75–90.

[276] M. Mayländer, S. Chen, E. R. Lorenzo, M. R. Wasielewski, S. Richert, "Exploring photogenerated molecular quartet states as spin qubits and qudits", *J. Am. Chem. Soc.* **2021**, *143*, 7050–7058.

[277] Y. Qiu, H. J. Eckvahl, A. Equbal, M. D. Krzyaniak, M. R. Wasielewski, "Enhancing coherence times of chromophore-radical molecular qubits and qudits by rational design", *J. Am. Chem. Soc.* **2023**.

[278] M. Mayländer, P. Thielert, T. Quintes, A. Vargas Jentzsch, S. Richert, "Room temperature electron spin coherence in photogenerated molecular spin qubit candidates", *J. Am. Chem. Soc.* **2023**, *145*, 14064–14069.

[279] V. S. Iyudin, Y. E. Kandrashkin, V. K. Voronkova, V. S. Tyurin, E. N. Kirichenko, "Time-resolved EPR spectra of photoexcited copper porphyrin", *Appl. Magn. Reson.* **2011**, *40*, 75–89.

[280] M. Gouterman, R. A. Mathies, B. E. Smith, W. S. Caughey, "Porphyrins. XIX. Tripdoublet and quartet luminescence in Cu and VO complexes", *J. Chem. Phys.* **1970**, *52*, 3795–3802.

[281] V. Rozenshtein, A. Berg, H. Levanon, U. Krueger, D. Stehlik, Y. Kandrashkin, A. Van Der Est, "Light-induced electron spin polarization in the ground state of water-soluble copper porphyrins", *Isr. J. Chem.* **2003**, *43*, 373–381.

[282] A. J.-T. Lou, T. J. Marks, "A Twist on Nonlinear Optics: Understanding the Unique Response of π-Twisted Chromophores", *Acc. Chem. Res.* **2019**, *52*, 1428–1438.

[283] Y. Shi, D. Frattarelli, N. Watanabe, A. Facchetti, E. Cariati, S. Righetto, E. Tordin, C. Zuccaccia, A. Macchioni, S. L. Wegener, C. L. Stern, M. A. Ratner, T. J. Marks, "Ultra-High-Response, Multiply Twisted Electro-optic Chromophores: Influence of π-System Elongation and Interplanar Torsion on Hyperpolarizability", *J. Am. Chem. Soc.* **2015**, *137*, 12521–12538.

[284] I. D. L. Albert, T. J. Marks, M. A. Ratner, "Conformationally-Induced Geometric Electron Localization. Interrupted Conjugation, Very Large Hyperpolarizabilities, and Sizable Infrared Absorption in Simple Twisted Molecular Chromophores", *J. Am. Chem. Soc.* **1997**, *119*, 3155–3156.

[285] P. Parkinson, C. E. I. Knappke, N. Kamonsutthipaijit, K. Sirithip, J. D. Matichak, H. L. Anderson, L. M. Herz, "Ultrafast energy transfer in biomimetic multistrand nanorings", *J. Am. Chem. Soc.* **2014**, *136*, 8217–8220.

[286] S. Paul, C. Govind, V. Karunakaran, "Planarity and length of the bridge control rate and efficiency of intramolecular singlet fission in pentacene dimers", *J. Phys. Chem. B* **2021**, *125*, 231–239.

[287] J. Heinzer, "Fast computation of exchange-broadened isotropic E.S.R. spectra", *Mol. Phys.* **1971**, *22*, 167–177.

[288] G. K. Fraenkel, "Line widths and frequency shifts in electron spin resonance spectra", *J. Phys. Chem.* **1967**, *71*, 139–171.

[289] K. M. Salikhov, "New Paradigm of Spin Exchange and its Manifestations in EPR Spectroscopy", *Appl. Magn. Reson.* **2020**, *51*, 297–325.

[290] A. Hudson, G. R. Luckhurst, "Electron resonance line shapes of radicals in solution", *Chem. Rev.* **1969**, *69*, 191–225.

[291] B. P. Engler, L. A. Harrah, Viscosity and density of 2-methyltetrahydrofuran as a function of temperature, tech. rep., **1979**.

[292] J. H. Freed, G. K. Fraenkel, "Theory of linewidths in electron spin resonance spectra", *J. Chem. Phys.* **1963**, *39*, 326–348.

[293] F. Bloch, "Nuclear Induction", *Phys. Rev.* **1946**, *70*, 460–474.

[294] H. S. Gutowsky, D. W. McCall, C. P. Slichter, "Nuclear magnetic resonance multiplets in liquids", *J. Chem. Phys.* **1953**, *21*, 279–292.

[295] H. M. McConnell, "Reaction rates by nuclear magnetic resonance", *J. Chem. Phys.* **1958**, *28*, 430–431.

[296] M. Zalibera, A. S. Jalilov, S. Stoll, I. A. Guzei, G. Gescheidt, S. F. Nelsen, "Monotrimethylene-bridged bis-p-phenylenediamine radical cations and dications: spin states, conformations, and dynamics", *J. Phys. Chem. A* **2013**, *117*, 1439–1448.

[297] K. A. Kozhanov, M. P. Bubnov, I. A. Teplova, G. A. Abakumov, V. K. Cherkasov, "Carbonyl o-semiqunonato rhodium complexes with diphosphine ligands. Effect of diphosphine bite angle on reactivity and dynamic processes in their coordination sphere. EPR study", *J. Mol. Struct.* **2017**, *1147*, 541–548.

[298] H. Eyring, "The Activated Complex in Chemical Reactions", *J. Chem. Phys.* **1935**, *3*, 107–115.

[299] M. G. Evans, M. Polanyi, "Some applications of the transition state method to the calculation of reaction velocities, especially in solution", *Trans. Faraday Soc.* **1935**, *31*, 875–894.

[300] M. D. Newton, N. Sutin, "Electron Transfer Reactions in Condensed Phases", *Annu. Rev. Phys. Chem.* **1984**, *35*, 437–480.

[301] G. Y. Zhu, Y. Qin, M. Meng, S. Mallick, H. Gao, X. Chen, T. Cheng, Y. N. Tan, X. Xiao, M. J. Han, M. F. Sun, C. Y. Liu, "Crossover between the adiabatic and nonadiabatic electron transfer limits in the Landau-Zener model", *Nat. Commun.* **2021**, *12*, 456.

[302] D. R. Kattnig, B. Mladenova, G. Grampp, C. Kaiser, A. Heckmann, C. Lambert, "Electron Paramagnetic Resonance Spectroscopy of Bis(triarylamine) Paracyclophanes as Model Compounds for the Intermolecular Charge-Transfer in Solid State Materials for Optoelectronic Applications", *J. Phys. Chem. C* **2009**, *113*, 2983–2995.

[303] M. Gilbert, B. Albinsson, "Photoinduced charge and energy transfer in molecular wires", *Chem. Soc. Rev.* **2015**, *44*, 845–862.

[304] M. P. Eng, T. Ljungdahl, J. Mårtensson, B. Albinsson, "Triplet excitation energy transfer in porphyrin-based donor–bridge–acceptor systems with conjugated bridges of varying length: an experimental and DFT study", *J. Phys. Chem. B* **2006**, *110*, 6483–6491.

[305] J. Andréasson, A. Kyrychenko, J. Mårtensson, B. Albinsson, "Temperature and viscosity dependence of the triplet energy transfer process in porphyrin dimers", *Photochem. Photobiol. Sci.* **2002**, *1*, 111–119.

[306] H. Levanon, J. R. Norris, "The photoexcited triplet state and photosynthesis", *Chem. Rev.* **1978**, *78*, 185–198.

[307] C. E. Tait, P. Neuhaus, H. L. Anderson, C. R. Timmel, "Triplet state delocalization in a conjugated porphyrin dimer probed by transient electron paramagnetic resonance techniques", *J. Am. Chem. Soc.* **2015**, *137*, 6670–6679.

[308] W. G. van Dorp, W. H. Schoemaker, M. Soma, J. H. van der Waals, "The lowest triplet state of free base porphin", *Mol. Phys.* **1975**, *30*, 1701–1721.

[309] A. J. Redman, G. Moise, S. Richert, E. J. Viere, W. K. Myers, M. J. Therien, C. R. Timmel, "EPR of Photoexcited Triplet-State Acceptor Porphyrins", *J. Phys. Chem. C Nanomater. Interfaces* **2021**, *125*, 11782–11790.

[310] S. Sinnecker, F. Neese, "Spin-spin contributions to the zero-field splitting tensor in organic triplets, carbenes and biradicals-a density functional and ab initio study", *J. Phys. Chem. A* **2006**, *110*, 12267–12275.

[311] C. E. Tait, P. Neuhaus, M. D. Peeks, H. L. Anderson, C. R. Timmel, "Excitation wavelength-dependent EPR study on the influence of the conformation of multiporphyrin arrays on triplet state delocalization", *Phys. Chem. Chem. Phys.* **2016**, *18*, 5275–5280.

[312] V. Barone, M. Cossi, "Quantum Calculation of Molecular Energies and Energy Gradients in Solution by a Conductor Solvent Model", *J. Phys. Chem. A* **1998**, *102*, 1995–2001.

[313] M. Cossi, N. Rega, G. Scalmani, V. Barone, "Energies, structures, and electronic properties of molecules in solution with the C-PCM solvation model", *J. Comput. Chem.* **2003**, *24*, 669–681.

[314] A. Klamt, G. Schüürmann, "COSMO: a new approach to dielectric screening in solvents with explicit expressions for the screening energy and its gradient", *J. Chem. Soc. Perkin Trans. 2* **1993**, 799–805.

[315] J. Andzelm, C. Kölmel, A. Klamt, "Incorporation of solvent effects into density functional calculations of molecular energies and geometries", *J. Chem. Phys.* **1995**, *103*, 9312–9320.

[316] W. Lu, C. M. Lieber, "Nanoelectronics from the bottom up", *Nat. Mater.* **2007**, *6*, 841–850.

[317] K.-S. Lee, *Polymers for Photonics Applications I*, Springer Science & Business Media, **2002**.

[318] Y. Sun, N. C. Giebink, H. Kanno, B. Ma, M. E. Thompson, S. R. Forrest, "Management of singlet and triplet excitons for efficient white organic light-emitting devices", *Nature* **2006**, *440*, 908–912.

[319] B. T. Luppi, D. Majak, M. Gupta, E. Rivard, K. Shankar, "Triplet excitons: improving exciton diffusion length for enhanced organic photovoltaics", *J. Mater. Chem. A Mater. Energy Sustain.* **2019**, *7*, 2445–2463.

[320] D. Stich, F. Späth, H. Kraus, A. Sperlich, V. Dyakonov, T. Hertel, "Triplet–triplet exciton dynamics in single-walled carbon nanotubes", *Nat. Photonics* **2013**, *8*, 139–144.

[321] N. V. Korovina, C. H. Chang, J. C. Johnson, "Spatial separation of triplet excitons drives endothermic singlet fission", *Nat. Chem.* **2020**, *12*, 391–398.

[322] C. Hetzer, B. S. Basel, S. M. Kopp, F. Hampel, F. J. White, T. Clark, D. M. Guldi, R. R. Tykwinski, "Chromophore Multiplication To Enable Exciton Delocalization and Triplet Diffusion Following Singlet Fission in Tetrameric Pentacene", *Angew. Chem. Int. Ed.* **2019**, *58*, 15263–15267.

[323] M. R. Wasielewski, M. D. E. Forbes, N. L. Frank, K. Kowalski, G. D. Scholes, J. Yuen-Zhou, M. A. Baldo, D. E. Freedman, R. H. Goldsmith, T. Goodson, 3rd, M. L. Kirk, J. K. McCusker, J. P. Ogilvie, D. A. Shultz, S. Stoll, K. B. Whaley, "Exploiting chemistry and molecular systems for quantum information science", *Nat Rev Chem* **2020**, *4*, 490–504.

[324] T. Mani, "Molecular qubits based on photogenerated spin-correlated radical pairs for quantum sensing", *Chem. Phys. Rev.* **2022**, *3*.

[325] D. P. DiVincenzo, "The physical implementation of quantum computation", *Fortschr. Phys.* **2000**, *48*, 771–783.

[326] J. R. Palmer, M. L. Williams, R. M. Young, K. R. Peinkofer, B. T. Phelan, M. D. Krzyaniak, M. R. Wasielewski, "Oriented Triplet Excitons as Long-Lived Electron Spin Qutrits in a Molecular Donor-Acceptor Single Cocrystal", *J. Am. Chem. Soc.* **2024**, *146*, 1089–1099.

[327] Y.-X. Wang, Z. Liu, Y.-H. Fang, S. Zhou, S.-D. Jiang, S. Gao, "Coherent manipulation and quantum phase interference in a fullerene-based electron triplet molecular qutrit", *npj Quantum Information* **2021**, *7*, 1–8.

[328] A. P. Monkman, H. D. Burrows, I. Hamblett, S. Navarathnam, M. Svensson, M. R. Andersson, "The effect of conjugation length on triplet energies, electron delocalization and electron–electron correlation in soluble polythiophenes", *J. Chem. Phys.* **2001**, *115*, 9046–9049.

[329] S. Richert, G. Bullard, J. Rawson, P. J. Angiolillo, M. J. Therien, C. R. Timmel, "On the Importance of Electronic Symmetry for Triplet State Delocalization", *J. Am. Chem. Soc.* **2017**, *139*, 5301–5304.

[330] G. J. Wilson, D. P. Arnold, "Time-dependent density functional molecular orbital and excited state calculations on bis(porphyrinyl)butadiynes in the monocationic, neutral, monoanionic, and dianionic oxidation states", *J. Phys. Chem. A* **2005**, *109*, 6104–6113.

[331] M. D. Peeks, P. Neuhaus, H. L. Anderson, "Experimental and computational evaluation of the barrier to torsional rotation in a butadiyne-linked porphyrin dimer", *Phys. Chem. Chem. Phys.* **2016**, *18*, 5264–5274.

[332] C.-G. Zhan, J. A. Nichols, D. A. Dixon, "Ionization Potential, Electron Affinity, Electronegativity, Hardness, and Electron Excitation Energy: Molecular Properties from Density Functional Theory Orbital Energies", *J. Phys. Chem. A* **2003**, *107*, 4184–4195.

[333] R. F. Kelley, S. J. Lee, T. M. Wilson, Y. Nakamura, D. M. Tiede, A. Osuka, J. T. Hupp, M. R. Wasielewski, "Intramolecular energy transfer within butadiyne-linked chlorophyll and porphyrin dimer-faced, self-assembled prisms", *J. Am. Chem. Soc.* **2008**, *130*, 4277–4284.

[334] F. V. A. Camargo, C. R. Hall, H. L. Anderson, S. R. Meech, I. A. Heisler, "Time resolved structural dynamics of butadiyne-linked porphyrin dimers", *Struct Dyn* **2016**, *3*, 023608.

[335] I. V. Rubtsov, K. Susumu, G. I. Rubtsov, M. J. Therien, "Ultrafast singlet excited-state polarization in electronically asymmetric ethyne-bridged bis[(porphinato)zinc(II)] complexes", *J. Am. Chem. Soc.* **2003**, *125*, 2687–2696.

[336] M. K. Kuimova, M. Hoffmann, M. U. Winters, M. Eng, M. Balaz, I. P. Clark, H. A. Collins, S. M. Tavender, C. J. Wilson, B. Albinsson, H. L. Anderson, A. W. Parker, D. Phillips, "Determination of the triplet state energies of a series of conjugated porphyrin oligomers", *Photochem. Photobiol. Sci.* **2007**, *6*, 675–682.

[337] S. D. Dimitrov, B. C. Schroeder, C. B. Nielsen, H. Bronstein, Z. Fei, I. McCulloch, M. Heeney, J. R. Durrant, "Singlet Exciton Lifetimes in Conjugated Polymer Films for Organic Solar Cells", *Polymers* **2016**, *8*.

[338] R. Englman, J. Jortner, "The energy gap law for radiationless transitions in large molecules", *Mol. Phys.* **1970**, *18*, 145–164.

[339] C. Erker, T. Basché, "The Energy Gap Law at Work: Emission Yield and Rate Fluctuations of Single NIR Emitters", *J. Am. Chem. Soc.* **2022**, *144*, 14053–14056.

[340] P. O. Andersson, S. M. Bachilo, R.-L. Chen, T. Gillbro, "Solvent and Temperature Effects on Dual Fluorescence in a Series of Carotenes. Energy Gap Dependence of the Internal Conversion Rate", *J. Phys. Chem.* **1995**, *99*, 16199–16209.

[341] N. Notsuka, H. Nakanotani, H. Noda, K. Goushi, C. Adachi, "Observation of Nonradiative Deactivation Behavior from Singlet and Triplet States of Thermally Activated Delayed Fluorescence Emitters in Solution", *J. Phys. Chem. Lett.* **2020**, *11*, 562–566.

[342] T. J. Penfold, E. Gindensperger, C. Daniel, C. M. Marian, "Spin-Vibronic Mechanism for Intersystem Crossing", *Chem. Rev.* **2018**, *118*, 6975–7025.

[343] M. Kasha, "Characterization of electronic transitions in complex molecules", *Discuss. Faraday Soc.* **1950**, *9*, 14–19.

[344] R. Mansour, J. M. Toldo, S. Mukherjee, M. Pinheiro, Jr, M. Barbatti, "Temperature effects on the internal conversion of excited adenine and adenosine", *Phys. Chem. Chem. Phys.* **2023**, *25*, 27083–27093.

[345] Z. Yang, Z. Mao, Z. Xie, Y. Zhang, S. Liu, J. Zhao, J. Xu, Z. Chi, M. P. Aldred, "Recent advances in organic thermally activated delayed fluorescence materials", *Chem. Soc. Rev.* **2017**, *46*, 915–1016.

[346] F. B. Dias, T. J. Penfold, A. P. Monkman, "Photophysics of thermally activated delayed fluorescence molecules", *Methods Appl Fluoresc* **2017**, *5*, 012001.

[347] F. Metz, S. Friedrich, G. Hohlneicher, "What is the leading mechanism for the nonradiative decay of the lowest triplet state of aromatic hydrocarbons?", *Chem. Phys. Lett.* **1972**, *16*, 353–358.

[348] D. A. Antheunis, J. Schmidt, J. H. van der Waals, "Spin-forbidden radiationless processes in isoelectronic molecules: Anthracene, acridine and phenazine", *Mol. Phys.* **1974**, *27*, 1521–1541.

[349] S. Siegel, H. S. Judeikis, "A Magnetophotoselection Study of the Polarizations of the Absorption Bands of Some Structurally Related Hydrocarbons and Heterocyclic Molecules1", *J. Phys. Chem.* **1966**, *70*, 2205–2211.

[350] M. C. Thurnauer, J. R. Norris, "The ordering of the zero field triplet spin sublevels in the chlorophylls. A magnetophotoselection study", *Chem. Phys. Lett.* **1977**, *47*, 100–105.

[351] M. C. Thurnauer, J. R. Norris, "Magnetophotoselection applied to the triplet state observed by EPR in photosynthetic bacteria", *Biochem. Biophys. Res. Commun.* **1976**, *73*, 501–506.

[352] A. Toffoletti, Z. Wang, J. Zhao, M. Tommasini, A. Barbon, "Precise determination of the orientation of the transition dipole moment in a Bodipy derivative by analysis of the magnetophotoselection effect", *Phys. Chem. Chem. Phys.* **2018**, *20*, 20497–20503.

[353] S. G. Balasubramani, G. P. Chen, S. Coriani, M. Diedenhofen, M. S. Frank, Y. J. Franzke, F. Furche, R. Grotjahn, M. E. Harding, C. Hättig, A. Hellweg, B. Helmich-Paris, C. Holzer, U. Huniar, M. Kaupp, A. Marefat Khah, S. Karbalaei Khani, T. Müller, F. Mack, B. D. Nguyen, S. M. Parker, E. Perlt, D. Rappoport, K. Reiter, S. Roy, M. Rückert, G. Schmitz, M. Sierka, E. Tapavicza, D. P. Tew, C. van Wüllen, V. K. Voora, F. Weigend, A. Wodyński, J. M. Yu, "TURBOMOLE: Modular program suite for ab initio quantum-chemical and condensed-matter simulations", *J. Chem. Phys.* **2020**, *152*, 184107.

[354] V. N. Staroverov, G. E. Scuseria, J. Tao, J. P. Perdew, "Comparative assessment of a new nonempirical density functional: Molecules and hydrogen-bonded complexes", *J. Chem. Phys.* **2003**, *119*, 12129–12137.

[355] J. Tao, J. P. Perdew, V. N. Staroverov, G. E. Scuseria, "Climbing the density functional ladder: nonempirical meta-generalized gradient approximation designed for molecules and solids", *Phys. Rev. Lett.* **2003**, *91*, 146401.

[356] A. Tsuda, H. Furuta, A. Osuka, "Completely Fused Diporphyrins and Triporphyrin", *Angew. Chem. Int. Ed.* **2000**, *39*, 2549–2552.

[357] A. Tsuda, H. Furuta, A. Osuka, "Syntheses, structural characterizations, and optical and electrochemical properties of directly fused diporphyrins", *J. Am. Chem. Soc.* **2001**, *123*, 10304–10321.

[358] Y. Yamaguchi, "Time-dependent density functional calculations of fully π-conjugated zinc oligoporphyrins", *J. Chem. Phys.* **2002**, *117*, 9688–9694.

[359] T. G. Pedersen, T. B. Lynge, P. K. Kristensen, P. M. Johansen, "Theoretical study of conjugated porphyrin polymers", *Thin Solid Films* **2005**, *477*, 182–186.

[360] S. Ohmori, H. Kawabata, K. Tokunaga, H. Tachikawa, "Molecular design of high performance fused porphyrin one-dimensional wire: A DFT study", *Thin Solid Films* **2009**, *518*, 901–905.

[361] R. M. Metzger, "Unimolecular electronics", *Chem. Rev.* **2015**, *115*, 5056–5115.

[362] L. Dou, Y. Liu, Z. Hong, G. Li, Y. Yang, "Low-Bandgap Near-IR Conjugated Polymers/Molecules for Organic Electronics", *Chem. Rev.* **2015**, *115*, 12633–12665.

[363] L. Ren, T. Y. Gopalakrishna, I.-H. Park, Y. Han, J. Wu, "Porphyrin/Quinoidal-Bithiophene-Based Macrocycles and Their Dications: Template-Free Synthesis and Global Aromaticity", *Angew. Chem. Int. Ed.* **2020**, *59*, 2230–2234.

[364] M.-C. Yoon, Z. S. Yoon, S. Cho, D. Kim, A. Takagi, T. Matsumoto, T. Kawai, T. Hori, X. Peng, N. Aratani, A. Osuka, "A hexagonal prismatic porphyrin array: synthesis, STM detection, and efficient energy hopping in near-infrared region", *J. Phys. Chem. A* **2007**, *111*, 9233–9239.

[365] H. Sato, K. Tashiro, H. Shinmori, A. Osuka, Y. Murata, K. Komatsu, T. Aida, "Positive heterotropic cooperativity for selective guest binding via electronic communications through a fused zinc porphyrin array", *J. Am. Chem. Soc.* **2005**, *127*, 13086–13087.

[366] Y. Nakamura, N. Aratani, H. Shinokubo, A. Takagi, T. Kawai, T. Matsumoto, Z. S. Yoon, D. Y. Kim, T. K. Ahn, D. Kim, A. Muranaka, N. Kobayashi, A. Osuka, "A directly fused tetrameric porphyrin sheet and its anomalous electronic properties that arise from the planar cyclooctatetraene core", *J. Am. Chem. Soc.* **2006**, *128*, 4119–4127.

[367] Y. Nakamura, N. Aratani, A. Osuka, "Experimental and theoretical investigations into the paratropic ring current of a porphyrin sheet", *Chem. Asian J.* **2007**, *2*, 860–866.

[368] Y. Nakamura, N. Aratani, K. Furukawa, A. Osuka, "Synthesis and characterizations of free base and Cu(II) complex of a porphyrin sheet", *Tetrahedron* **2008**, *64*, 11433–11439.

[369] L.-A. Fendt, H. Fang, M. E. Plonska-Brzezinska, S. Zhang, F. Cheng, C. Braun, L. Echegoyen, F. Diederich, "*meso,meso*-linked and triply fused diporphyrins with mixed-metal ions: Synthesis and electrochemical investigations", *European J. Org. Chem.* **2007**, *2007*, 4659–4673.

[370] T. Tanaka, B. S. Lee, N. Aratani, M.-C. Yoon, D. Kim, A. Osuka, "Synthesis and properties of hybrid porphyrin tapes", *Chem. Eur. J.* **2011**, *17*, 14400–14412.

[371] S. Cho, M.-C. Yoon, K. S. Kim, P. Kim, D. Kim, "Electron delocalization in various triply linked zinc(II) porphyrin arrays: role of antiaromatic junctions between aromatic porphyrins", *Phys. Chem. Chem. Phys.* **2011**, *13*, 16175–16181.

[372] M. Makino, J.-I. Aihara, "Macrocyclic aromaticity of porphyrin units in fully conjugated oligoporphyrins", *J. Phys. Chem. A* **2012**, *116*, 8074–8084.

[373] R. R. Valiev, G. V. Baryshnikov, R. T. Nasibullin, D. Sundholm, H. Ågren, "When are Antiaromatic Molecules Paramagnetic?", *J. Phys. Chem. C* **2020**, *124*, 21027–21035.

[374] G. Povie, Y. Segawa, T. Nishihara, Y. Miyauchi, K. Itami, "Synthesis of a carbon nanobelt", *Science* **2017**, *356*, 172–175.

[375] Q. Zhang, Y.-E. Zhang, S. Tong, M.-X. Wang, "Hydrocarbon Belts with Truncated Cone Structures", *J. Am. Chem. Soc.* **2020**, *142*, 1196–1199.

[376] Y. Li, Y. Segawa, A. Yagi, K. Itami, "A Nonalternant Aromatic Belt: Methylene-Bridged [6]Cycloparaphenylene Synthesized from Pillar[6]arene", *J. Am. Chem. Soc.* **2020**, *142*, 12850–12856.

[377] Y. Yamaguchi, "Theoretical prediction of electronic structures of fully pi-conjugated zinc oligoporphyrins with curved surface structures", *J. Chem. Phys.* **2004**, *120*, 7963–7970.

[378] N. Fukui, T. Kim, D. Kim, A. Osuka, "Porphyrin Arch-Tapes: Synthesis, Contorted Structures, and Full Conjugation", *J. Am. Chem. Soc.* **2017**, *139*, 9075–9088.

[379] N. Fukui, A. Osuka, "Singly and Doubly 1,2-Phenylene-Inserted Porphyrin Arch-Tape Dimers: Synthesis and Highly Contorted Structures", *Angew. Chem. Int. Ed.* **2018**, *57*, 6304–6308.

[380] J. Song, N. Aratani, H. Shinokubo, A. Osuka, "A porphyrin nanobarrel that encapsulates C(60)", *J. Am. Chem. Soc.* **2010**, *132*, 16356–16357.

[381] S. Xue, D. Kuzuhara, N. Aratani, H. Yamada, "Synthesis of a Porphyrin(2.1.2.1) Nanobelt and Its Ability To Bind Fullerene", *Org. Lett.* **2019**, *21*, 2069–2072.

[382] S. Liu, D. V. Kondratuk, S. A. L. Rousseaux, G. Gil-Ramírez, M. C. O'Sullivan, J. Cremers, T. D. W. Claridge, H. L. Anderson, "Caterpillar track complexes in template-directed synthesis and correlated molecular motion", *Angew. Chem. Int. Ed.* **2015**, *54*, 5355–5359.

[383] M. C. O'Sullivan, J. K. Sprafke, D. V. Kondratuk, C. Rinfray, T. D. W. Claridge, A. Saywell, M. O. Blunt, J. N. O'Shea, P. H. Beton, M. Malfois, H. L. Anderson, "Vernier templating and synthesis of a 12-porphyrin nano-ring", *Nature* **2011**, *469*, 72–75.

[384] R. Haver, L. Tejerina, H.-W. Jiang, M. Rickhaus, M. Jirasek, I. Grübner, H. J. Eggimann, L. M. Herz, H. L. Anderson, "Tuning the Circumference of Six-Porphyrin Nanorings", *J. Am. Chem. Soc.* **2019**, *141*, 7965–7971.

[385] S. M. Kopp, H. Gotfredsen, J.-R. Deng, T. D. W. Claridge, H. L. Anderson, "Global Aromaticity in a Partially Fused 8-Porphyrin Nanoring", *J. Am. Chem. Soc.* **2020**, *142*, 19393–19401.

[386] M. Bednarz, P. Reineker, E. Mena-Osteritz, P. Bäuerle, "Optical absorption spectra of linear and cyclic thiophenes—selection rules manifestation", *J. Lumin.* **2004**, *110*, 225–231.

[387] B. M. Wong, "Optoelectronic Properties of Carbon Nanorings: Excitonic Effects from Time-Dependent Density Functional Theory", *J. Phys. Chem. C Nanomater. Interfaces* **2009**, *113*, 21921–21927.

[388] D. Sundholm, S. Taubert, F. Pichierri, "Calculation of absorption and emission spectra of [n]cycloparaphenylenes: the reason for the large Stokes shift", *Phys. Chem. Chem. Phys.* **2010**, *12*, 2751–2757.

[389] J. M. D. Coey, *Magnetism and Magnetic Materials*, Cambridge University Press, **2019**.

[390] R. R. Valiev, H. Fliegl, D. Sundholm, "Closed-shell paramagnetic porphyrinoids", *Chem. Commun.* **2017**, *53*, 9866–9869.

[391] R. R. Valiev, H. Fliegl, D. Sundholm, "Optical and magnetic properties of antiaromatic porphyrinoids", *Phys. Chem. Chem. Phys.* **2017**, *19*, 25979–25988.

[392] D. Sundholm, H. Fliegl, R. J. F. Berger, "Calculations of magnetically induced current densities: theory and applications", *Wiley Interdiscip. Rev. Comput. Mol. Sci.* **2016**, *6*, 639–678.

[393] L. Banci, M. Piccioli, A. Scozzafava, "Advances in the NMR investigation of paramagnetic molecules in solution", *Coord. Chem. Rev.* **1992**, *120*, 1–28.

[394] A. J. Pell, G. Pintacuda, C. P. Grey, "Paramagnetic NMR in solution and the solid state", *Prog. Nucl. Magn. Reson. Spectrosc.* **2019**, *111*, 1–271.

[395] M. U. Winters, E. Dahlstedt, H. E. Blades, C. J. Wilson, M. J. Frampton, H. L. Anderson, B. Albinsson, "Probing the efficiency of electron transfer through porphyrin-based molecular wires", *J. Am. Chem. Soc.* **2007**, *129*, 4291–4297.

[396] H. M. Marques, I. Cukrowski, "Molecular mechanics modelling of porphyrins. Using artificial neural networks to develop metal parameters for four-coordinate metalloporphyrins", *Phys. Chem. Chem. Phys.* **2002**, *4*, 5878–5887.

[397] H. M. Marques, I. Cukrowski, "Molecular mechanics parameters for the modelling of four-coordinate Zn(II) porphyrins", *Phys. Chem. Chem. Phys.* **2003**, *5*, 5499–5506.

[398] E. Goldstein, B. Ma, J.-H. Lii, N. L. Allinger, "Molecular mechanics calculations (MM3) on nitriles and alkynes", *J. Phys. Org. Chem.* **1996**, *9*, 191–202.

[399] P. D. Jarowski, F. Diederich, K. N. Houk, "Structures and stabilities of diacetylene-expanded polyhedranes by quantum mechanics and molecular mechanics", *J. Org. Chem.* **2005**, *70*, 1671–1678.

[400] J. J. P. Stewart, "Optimization of parameters for semiempirical methods VI: more modifications to the NDDO approximations and re-optimization of parameters", *J. Mol. Model.* **2013**, *19*, 1–32.

[401] O. A. Vydrov, G. E. Scuseria, "Assessment of a long-range corrected hybrid functional", *J. Chem. Phys.* **2006**, *125*, 234109.

[402] O. A. Vydrov, J. Heyd, A. V. Krukau, G. E. Scuseria, "Importance of short-range versus long-range Hartree-Fock exchange for the performance of hybrid density functionals", *J. Chem. Phys.* **2006**, *125*, 074106.

[403] O. A. Vydrov, G. E. Scuseria, J. P. Perdew, "Tests of functionals for systems with fractional electron number", *J. Chem. Phys.* **2007**, *126*, 154109.

[404] Z. Chen, C. S. Wannere, C. Corminboeuf, R. Puchta, P. v. R. Schleyer, "Nucleus-independent chemical shifts (NICS) as an aromaticity criterion", *Chem. Rev.* **2005**, *105*, 3842–3888.

[405] R. Herges, D. Geuenich, "Delocalization of Electrons in Molecules", *J. Phys. Chem. A* **2001**, *105*, 3214–3220.

[406] R. L. Martin, "Natural transition orbitals", *J. Chem. Phys.* **2003**, *118*, 4775–4777.

[407] A. Li, X. Zhang, S. Wang, K. Wei, P. Du, "Synthesis and Physical Properties of a Perylene Diimide-Embedded Chiral Conjugated Macrocycle", *Org. Lett.* **2023**, *25*, 1183–1187.

[408] H. M. Bergman, G. R. Kiel, R. J. Witzke, D. P. Nenon, A. M. Schwartzberg, Y. Liu, T. D. Tilley, "Shape-Selective Synthesis of Pentacene Macrocycles and the Effect of Geometry on Singlet Fission", *J. Am. Chem. Soc.* **2020**, *142*, 19850–19855.

[409] A. H. G. David, A. Garci, S. Abid, X. Li, R. M. Young, J. S. W. Seale, J. E. Hornick, C. S. Azad, Y. Jiao, I. Roy, I. Akpinar, T. Kesharwani, C. L. Stern, M. R. Wasielewski, J. F. Stoddart, "Divinylanthracene-Containing Tetracationic Organic Cyclophane with Near-Infrared Photoluminescence", *J. Am. Chem. Soc.* **2023**, *145*, 9182–9190.

[410] Á. Vidal-Vidal, E. M. Cabaleiro-Lago, C. Silva López, O. N. Faza, "Rational Design of Efficient Environmental Sensors: Ring-Shaped Nanostructures Can Capture Quat Herbicides", *ACS Omega* **2018**, *3*, 16976–16988.

[411] M. L. Ball, B. Zhang, Q. Xu, D. W. Paley, V. C. Ritter, F. Ng, M. L. Steigerwald, C. Nuckolls, "Influence of Molecular Conformation on Electron Transport in Giant, Conjugated Macrocycles", *J. Am. Chem. Soc.* **2018**, *140*, 10135–10139.

[412] Y. Li, H. Kono, T. Maekawa, Y. Segawa, A. Yagi, K. Itami, "Chemical Synthesis of Carbon Nanorings and Nanobelts", *Acc. Mater. Res.* **2021**, *2*, 681–691.

[413] Y. Wang, X.-S. Ke, S. Lee, S. Kang, V. M. Lynch, D. Kim, J. L. Sessler, "Pyrene-Bridged Expanded Carbaporphyrin Nanobelts", *J. Am. Chem. Soc.* **2022**, *144*, 9212–9216.

[414] D. Imoto, A. Yagi, K. Itami, "Carbon Nanobelts: Brief History and Perspective", *Precision Chemistry* **2023**, *1*, 516–523.

[415] A. Borissov, Y. K. Maurya, L. Moshniaha, W.-S. Wong, M. Żyła-Karwowska, M. Stępień, "Recent Advances in Heterocyclic Nanographenes and Other Polycyclic Heteroaromatic Compounds", *Chem. Rev.* **2022**, *122*, 565–788.

[416] H. Kono, Y. Li, R. Zanasi, G. Monaco, F. F. Summa, L. T. Scott, A. Yagi, K. Itami, "Methylene-Bridged [6]-, [8]-, and [10]Cycloparaphenylenes: Size-Dependent Properties and Paratropic Belt Currents", *J. Am. Chem. Soc.* **2023**, *145*, 8939–8946.

[417] F. F. Summa, G. Monaco, L. T. Scott, R. Zanasi, "Disentangling the Contributions to the Proton Magnetic Shielding in Carbon Nanohoops and Nanobelts: Evidence for a Paratropic Belt-Current", *J. Phys. Chem. Lett.* **2020**, *11*, 7489–7494.

[418] M. A. Majewski, W. Stawski, J. M. Van Raden, M. Clarke, J. Hart, J. N. O'Shea, A. Saywell, H. L. Anderson, "Covalent Template-Directed Synthesis of a Spoked 18-Porphyrin Nanoring", *Angew. Chem. Int. Ed.* **2023**, *62*, e202302114.

[419] C. E. Colwell, T. W. Price, T. Stauch, R. Jasti, "Strain visualization for strained macrocycles", *Chem. Sci.* **2020**, *11*, 3923–3930.

[420] P. S. Bols, M. Rickhaus, L. Tejerina, H. Gotfredsen, K. Eriksen, M. Jirasek, H. L. Anderson, "Allosteric Cooperativity and Template-Directed Synthesis with Stacked Ligands in Porphyrin Nanorings", *J. Am. Chem. Soc.* **2020**, *142*, 13219–13226.

[421] A. Hocquet, M. Langgård, "An Evaluation of the MM+ Force Field", *Molecular modeling annual* **1998**, *4*, 94–112.

[422] C. Janiak, "A critical account on π–π stacking in metal complexes with aromatic nitrogen-containing ligands", *J. Chem. Soc. Dalton Trans.* **2000**, 3885–3896.

[423] I. Dance, "Distance criteria for crystal packing analysis of supramolecular motifs", *New J. Chem.* **2003**, *27*, 22–27.

[424] S. Pronk, S. Páll, R. Schulz, P. Larsson, P. Bjelkmar, R. Apostolov, M. R. Shirts, J. C. Smith, P. M. Kasson, D. van der Spoel, B. Hess, E. Lindahl, "GROMACS 4.5: a high-throughput and highly parallel open source molecular simulation toolkit", *Bioinformatics* **2013**, *29*, 845–854.

[425] L. Fomina, B. Vazquez, E. Tkatchouk, S. Fomine, "The Glaser reaction mechanism. A DFT study", *Tetrahedron* **2002**, *58*, 6741–6747.

[426] R. C. Haddon, "The application of the Biot-Savart law to the ring current analysis of proton chemical shifts—I", *Tetrahedron* **1972**, *28*, 3613–3633.

[427] N. C. Baird, "Quantum organic photochemistry. II. Resonance and aromaticity in the lowest 3.pi..pi.* state of cyclic hydrocarbons", *J. Am. Chem. Soc.* **1972**, *94*, 4941–4948.

[428] K. C. Sahoo, M. S. Kumaraswami, D. Usharani, H. Rath, "Conformationally Rigid Ethynylene-Cumulene Conjugated Aromatic [30] Heteroannulenes with NIR Absorption: Synthesis, Spectroscopic and Theoretical Characterization", *J. Org. Chem.* **2019**, *84*, 5203–5212.